Ideal GLM-MHD

a new mathematical model for simulating astrophysical plasmas

Inaugural–Dissertation

zur

Erlangung des Doktorgrades

der Mathematisch-Naturwissenschaftlichen Fakultät

der

Universität zu Köln

vorgelegt von

Dominik Derigs
aus Frechen

Köln
2018

Berichterstatter

Prof. Dr. Stefanie Walch-Gassner
Prof. Dr. Simon Trebst

Tag der mündlichen Prüfung: 14.09.2018

Zusammenfassung

Magnetfelder sind in der Astrophysik allgegenwärtig. Aufgrund vielfältiger Hinweise, dass sie in einer großen Zahl von astrophysikalischen Prozessen eine dominante Rolle einnehmen können, sollten ihre Auswirkungen nicht leichtfertig vernachlässigt werden. Analytische Modelle berücksichtigen hingegen oftmals keine Magnetfelder oder nur unter starker Modellvereinfachung, die dann jedoch ihre Aussagefähigkeit deutlich reduzieren kann. Aufgrund dessen hat sich die Computerphysik als modernes Forschungsgebiet entwickelt. Mithilfe hochentwickelter Simulationen komplexer numerischer Modelle gewinnt sie Einblicke in ansonsten nicht zugängliche physikalische Prozesse.

Das am häufigsten verwendete Modell zur Simulation von Plasma, die idealen MHD-Gleichungen, hat zwei entscheidende Nachteile: Es begrenzt weder das Wachstum von numerisch verursachten magnetischen Monopolen, noch sind die meisten auf ihr basierenden numerischen Schema konform mit den Gesetzen der Thermodynamik, speziell dem zweiten Hauptsatz.

In meiner Arbeit, die ich interdisziplinär zwischen Mathematik und theoretischer Physik durchgeführt habe, entwickelte ich das erste thermodynamisch konsistente Modell mit wirkungsvoller eingebauter Korrektur von Divergenzfehlern in magnetischen Feldern. Mein neues Galilei-invariante Modell eignet sich für die Simulation magnetisierter Plasmen unter extremen Bedingungen wie sie typischerweise in astrophysikalischen Szenarien auftreten. Es wird als die „idealen GLM-MHD Gleichungen“ bezeichnet und beschreibt neun charakteristische Plasmawellen.

Die Genauigkeit und Robustheit meines Verfahrens wird anhand einer Reihe von Tests mithilfe des adaptiven Multi-Physik Simulationscode `FLASH` demonstriert. Ein astrophysikalisches Anwendungsszenario wird ausführlich diskutiert.

Abstract

Magnetic fields are ubiquitous in space. As there is strong evidence that magnetic fields play an important role in a variety of astrophysical processes, they should not be neglected recklessly. However, analytic models in astrophysical either do often not take magnetic fields into account or can do this after limiting simplifications reducing their overall predictive power. Therefore, computational astrophysics has evolved as a modern field of research using sophisticated computer simulations to gain insight into physical processes.

The ideal MHD equations, which are the most often used basis for simulating magnetized plasmas, have two critical drawbacks: Firstly, they do not limit the growth of numerically caused magnetic monopoles, and, secondly, most numerical schemes built from the ideal MHD equations are not conformable with thermodynamics.

In my work, at the interplay of math and physics, I developed and presented the first thermodynamically consistent model with effective inbuilt divergence cleaning. My new Galilean-invariant model is suitable for simulating magnetized plasmas under extreme conditions as those typically encountered in astrophysical scenarios. The new model is called the “ideal GLM-MHD” equations and supports nine wave solutions.

The accuracy and robustness of my numerical implementation are demonstrated with a number of tests, including comparisons to other schemes available within in the multi-physics, multi-scale adaptive mesh refinement (AMR) simulation code `FLASH`. A possible astrophysical application scenario is discussed in detail.

Acknowledgment

[Acknowledgements have been removed in the online version]

Contents

Typesetting by the author using TEX Live 2018.
Printed in Germany on acid-free paper.

1 Introduction

The natural sciences use mathematical models to describe the world we observe. Such models are abstractions based on mathematical concepts and language. This enables scientists to predict the behavior of various complex systems.

Traditionally, the investigation of such systems has been conducted to find analytical solutions of more and more refined mathematical models. However, if the complexity of non-linear interactions makes a model or the given initial conditions too complicated, no analytic treatment is possible without oversimplifying the model to such a degree that interesting effects are no longer present. Hence, numerical simulations, which can treat non-linear systems without oversimplifying them, have become a useful tool to model arbitrary physical systems. Nowadays, numerical simulations can be found as an everyday tool in a wide range of applications.

A classic example where numerical simulations shine is the field of astrophysics. Most astrophysical processes, such as molecular cloud or star formation, span too many temporal and spatial scales to be suitable for laboratory experiments. Furthermore, as most astrophysical processes rely on complex interactions between various physical phenomena such as gravity, heating, cooling, and radiation, the development of analytical solutions is often impossible without applying limiting simplifications to the models. Although simple astrophysical models have undoubtedly provided us with valuable insights in the past, purely analytical models tend to suffer from rough approximations or a lack of completeness, limiting their overall predictive power.

To overcome these limitations, computational astrophysics has evolved as a modern field of research. Its core task is to deliver theoretical predictions where analytic models fail to explain interesting phenomena.

1.1 The omnipresence of magnetic fields

The existence of magnetic fields in the interstellar medium (ISM) was first shown more than half a century ago by Hiltner (1951) and Hall (1951). Today, magnetic fields are believed to play an important role in all kinds of astrophysical processes. They have been observed on almost every

scale from stars and planets to the interstellar medium (see, e.g., Beck, 2009; Crutcher, 2012; Li et al., 2014; Haverkorn, 2015) up to galaxies where they are suggested to play a vital role for the entire evolution and the efficiency of galaxy formation across cosmic times (see, e.g., the recent review by Naab & Ostriker, 2017). In particular, large-scale magnetic fields are nowadays observed in almost every galaxy with hints of their presence in high-redshift galaxies, suggesting an early origin for magnetic fields (Bernet et al., 2008; Wolfe et al., 2008). The source of these magnetic fields is still vigorously debated (Planck Collaboration et al., 2016b).

Over the last few decades, radio observations revealed that galaxies generally host magnetic fields and that the interstellar medium typically has magnetic fields on the order of a few μG (Beck & Hoernes, 1996; Beck, 2004; Sur et al., 2012). Magnetic fields can easily be a dominant contribution for the overall gas dynamics as their energies are often comparable with the kinetic energy of the flows themselves (Naab & Ostriker, 2017, Sec. 3.4). Moreover, it has been shown that the magnetic pressure can often be significantly higher than the thermal pressure (Boulares & Cox, 1990; Ferrière, 2001; Cox, 2005). Hence, astrophysical models should not neglect their possible effects recklessly.

This importance of magnetic effects on the dynamics of astrophysical flows has been confirmed on multiple scales:

- Entire galaxies (Beck, 2001; Beck, 2009; Hanasz et al., 2009; Kotarba et al., 2009; Pakmor & Springel, 2013; Beck, 2015; Rieder & Teyssier, 2017),
- The interstellar medium (Avillez & Breitschwerdt, 2005; Koyama & Ostriker, 2009a; Koyama & Ostriker, 2009b; Hill et al., 2012; Kim & Ostriker, 2015; Walch et al., 2015; Girichidis et al., 2016; Pardi et al., 2017),
- Molecular clouds (Shu et al., 1987; McKee, 1999; Padoan & Nordlund, 1999; Heitsch & Burkert, 2002; Banerjee et al., 2009; Vázquez-Semadeni et al., 2011; Hennebelle & Iffrig, 2014; Körtgen & Banerjee, 2015; Banerjee & Körtgen, 2015; Planck Collaboration et al., 2016a; Federrath, 2016; Lee et al., 2017; Seifried et al., 2018a; see also the review by Mac Low & Klessen, 2004, especially chapter IV.F),
- Star-formation regions (Hennebelle & Fromang, 2008; Hennebelle & Teyssier, 2008; Hennebelle & Ciardi, 2009; Peters et al., 2011; Seifried et al., 2011b; Seifried et al., 2011a; Körtgen & Banerjee, 2015; Klassen et al., 2017).

Understanding the role of magnetic fields in the formation and evolution of molecular clouds is also critical for understanding the process of star formation. An example is the observed inefficiency of star formation. Considering the low temperatures, molecular clouds should be highly gravitationally unstable and collapse on their global mean freefall timescale. However, they are observed to live about 10-100 times longer, i.e., the star formation rate (SFR) per freefall time is only a few percent (Federrath, 2015). Besides turbulence and stellar feedback, magnetic fields have been suggested being the primary regulator of SFR and an important supporter against gravitational collapse of unstable regions, either statically or dynamically through MHD waves (McKee, 1999; Mac Low & Klessen, 2004; Crutcher, 2012; Li et al., 2017). Using different observational techniques (polarized emission from aligned dust grains measured by Houde et al., 2004; Chandrasekhar-Fermi method

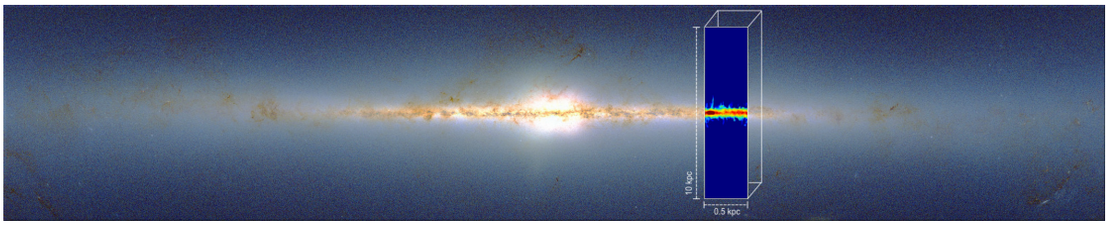

Fig. 1.1: The SILCC project: Simulated volume ($500 \times 500 \times 10\,000$ pc) by Walch et al. (2015) overlayed on the 2MASS survey's view of the entire Milky Way seen from Earth.

applied by Crutcher, 2004 and Novak et al., 2009; Zeeman effect measured by Crutcher et al., 2010), all evidence seems to point to the presence of dynamically important magnetic fields in molecular cloud clumps with hydrogen number densities of $n_{\rm H} \gtrapprox 3000\,{\rm cm}^{-3}$ (Draine, 2011, Sec. 32.10). However, the exact value for the transition from sub- to supercritical regions, needed for gravitational collapse to surpass the magnetic support is still unclear (see, e.g., Körtgen & Banerjee, 2015; Valdivia et al., 2016; Zamora-Avilés et al., 2018).

There are basically two approaches that can be taken to increase our understanding of the role of magnetic fields in astrophysical contexts. The first one is to simplify a problem down to a point where analytic solutions are possible. As mentioned before, such solutions only allow to focus on a few narrow aspects of the problem as the results may depend largely on the particular chosen simplifications themselves and are limited in their predictive power.

The second approach is to undertake detailed numerical simulations, which in general involves solving a complex multi-physics framework numerically. An example for such modern simulations are those carried out by the SILCC[1] collaboration, include magnetic fields in their endeavor of attaining a deeper understanding of the full life-cycle of molecular clouds (Walch et al., 2015; Girichidis et al., 2016; Gatto et al., 2016; Peters et al., 2017a; Peters et al., 2017b). The SILCC collaboration developed an encompassing multi-physics framework, including the effects of magnetic fields, self-gravity, heating and cooling at different gas metallicities, molecule formation and dissociation, and stellar feedback. They use a vertically stratified model of a disk galaxy with solar neighborhood conditions (see Fig. 1.1 for an illustration). To date, this is still not included by any other research group for this type of three-dimensional simulations. With this code at hand, the SILCC collaboration has recently demonstrated the feasibility of models that simulate the entire formation history of molecular clouds (MCs) forming out of the diffuse ISM down to resolutions of 0.06 pc (Seifried et al., 2017; Seifried et al., 2018a). These simulations have been found to accurately model the chemical evolution of MCs.

1.2 Magnetic fields in simulations

The diffuse interstellar medium (ISM) is generally highly conductive and largely ionized. Due to this, magnetic fields mostly follow the plasma and idealized assumptions (vanishing resistivity and

[1] SILCC = **SI**mulating the **L**ife-**C**ycle of molecular **C**louds

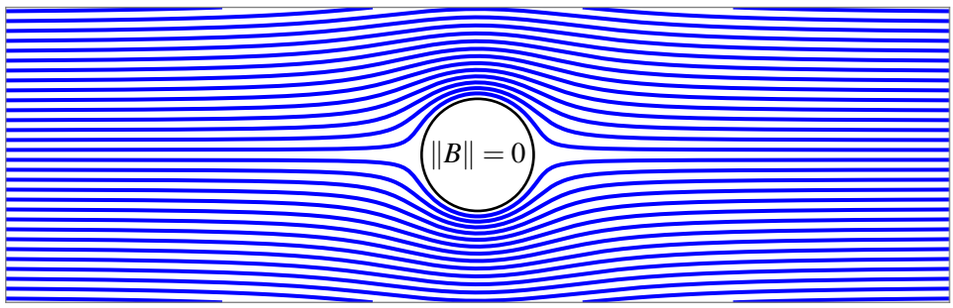

Fig. 1.2: Magnetic field lines (blue) close to a field-free region. Due to the divergence-free condition, field lines are conditioned globally to wrap around the region with zero magnetic field.

viscosity) are justified. Such systems can be described using the ideal magnetohydrodynamics (ideal MHD) equations. The ideal MHD equations are the most often used tool for modeling magnetized plasmas.

Unfortunately, the ideal MHD equations have two important drawbacks. Firstly, they do not control the growth of numerically caused magnetic field divergence errors. Secondly, an often overlooked complication is that, after having addressed the issue of magnetic field divergence control, the resulting schemes are most often no longer conformable with the second law of thermodynamics, also known as the *entropy inequality*. Numerical schemes that are guaranteed to conform with the second law of thermodynamics are called *entropy stable* schemes.

The major cause for magnetic field divergence in finite volume schemes is the inaccurate assumption of the locality of the problem. Whereas the hydrodynamic quantities of the fluid (density, momentum, pressure) are defined purely locally in a fluid, this is not the case for magnetic fields as the magnetic field divergence-free condition, which should be fulfilled at any point of the fluid at any time, globally constrains the magnetic field topology: Although one might only modify a small region in space, the magnetic field topology in the entire vicinity can be distorted (see Fig. 1.2). Numerical simulations are usually unable to handle this as they manipulate magnetic fields using purely local numerical fluxes. Hence, no magnetic field correction on larger scales is included although Gauß's law,

$$\nabla \cdot \boldsymbol{B} = 0, \tag{1.1}$$

clearly states that regions of reduced field strength *cannot* only be local.

Having this in mind, it is not surprising that numerical discretization errors can lead to an uncontrolled growth of magnetic field divergence,

$$\frac{\partial}{\partial t}(\nabla \cdot \boldsymbol{B}) = O\left(\Delta x^m, \Delta t^n\right) \tag{1.2}$$

(Brackbill & Barnes, 1980, eq. 2).

Inconsistent magnetic fields are not only unphysical, they also almost certainly cause numerical instabilities like negative internal energies inevitably leading to a break down of the simulation.

This underlines the need for so-called *divergence cleaning* techniques which are designed to limit the growth of the numerically caused magnetic field divergence.

1.3 Divergence cleaning techniques

Over the last decades, several methods for controlling the growth of magnetic divergence in numerical simulations emerged:

The eight-wave formulation

Powell et al. (1999) and others (see, e.g., Sjögreen et al., 2017, Sec. 6.1) observed a notable increase of numerical robustness when augmenting the ideal MHD equations with a specific non-conservative term first found by Godunov (1972). A careful analysis reveals a new MHD wave advecting the numerically caused divergence errors away from their origin. As this new wave manifests itself as a new eighth eigenvalue of the hyperbolic ideal MHD equation system, this modification is often called the "eight-wave" formulation. Taking the divergence of the induction equation of the ideal MHD equations, one obtains

$$\frac{\partial}{\partial t}(\nabla \cdot \boldsymbol{B}) + \nabla \cdot (\boldsymbol{u}(\nabla \cdot \boldsymbol{B})) = 0. \tag{1.3}$$

This equation describes the *conservation* and *advection* of the magnetic field divergence, $\nabla \cdot \boldsymbol{B}$, by the so-called *divergence-wave*.

As described in Derigs et al. (2016), relying on magnetic field divergence cleaning by the eight-wave scheme is typically insufficient to ensure a satisfactory divergence cleaning of the scheme. Although this method can be implemented in agreement with thermodynamics, it is especially problematic at stagnation points of flows as magnetic field divergence can build up due to the dependence of the divergence cleaning on the local fluid velocity (Derigs et al., 2018b, Sec. 3.1).

The projection method

The *projection method*, described by Brackbill & Barnes, 1980 and Marder, 1987, is implemented for divergence cleaning as a post-processing step performed after each MHD integration cycle. As such, it has the immediate benefit of being implementable without changing the underlying numerical scheme. It has successfully been applied by, e.g., Zachary et al. (1994) and Balsara (1998) and others. This method is called projection method as the magnetic field is projected into a space of divergence-free vector field solutions. This approach offers two variants, a scalar or vector divergence-cleaning, depending on the choice of real or Fourier spaces in which the divergence-cleaning is performed.

While having proven to be robust, its parabolic nature makes implementations computationally expensive on parallel systems. Furthermore, it is still unclear if entropy stable schemes can at all be constructed using the projection method.

Constrained transport

The *constrained transport* method developed by Evans & Hawley (1988) and Balsara & Spicer (1999) ensures a discretely vanishing magnetic field divergence by representing magnetic fields on staggered mesh cell faces (rather than cell centers). On such a grid, the MHD equations can be discretized such that they preserve the solenoidality of the magnetic field through Stokes' theorem. Also in the case of constrained transport, it is unclear if entropy stable schemes can be constructed. Researchers in astrophysics typically avoid staggered mesh based solvers as they are known for their additional memory requirements (see e.g. Derigs et al., 2016, Sec. 4.5) although recent developments have made this issue less severe.

Generalized Lagrangian multiplier

Munz et al. (2000, Sec. 3) investigated how one can incorporate the divergence-free condition into simulations computing the movement of charged particles in electromagnetic fields. They did so by introducing a new scalar field also known as *generalized Lagrangian multiplier* (*GLM*). Due to the additional degree of freedom that is added by this new field, it becomes possible to couple the divergence-free condition into the ideal MHD equations. This extension of the ideal MHD system is useful for schemes which are meant to be implemented for large-scale computations on parallel architectures as the model remains purely hyperbolic.

The GLM method has similarly been used by Dedner et al. (2002) who focused on ways of coupling the divergence-free constraint to the ideal MHD equations. Unfortunately, all three modifications of the ideal MHD equations Dedner et al. presented are unsuitable for constructing a thermodynamically consistent schemes as shown in Derigs et al. (2018b, Sec. 4.1).

In contrast to other divergence cleaning schemes, the GLM method has the great advantage to directly couple into the mathematical model. It does not require any multi-step or post-processing implementations, making it highly suitable for parallelized systems.

Goal of this thesis

As it is of great importance to handle the (numerically caused) magnetic field divergence correctly, I focused my recent research on reconciling entropy stability with effective divergence cleaning. It seems mandatory to be able to guarantee not only a thermodynamically consistent fluid behavior but to simultaneously ensure that the used magnetic field divergence treatment complies with the entropy inequality.

After trying to create provably entropy stable schemes for a variety of divergence cleaning methods, I found a way to formulate a new thermodynamically consistent model for ideal MHD where I utilize the GLM technique to couple Gauß's law to the ideal MHD equations in a novel entropy consistent way. I call this new mathematical model the *ideal GLM-MHD equations*.

As demonstrated in Derigs et al. (2018b), many numerical schemes are not constructed to comply with the universally valid laws of thermodynamics. Aim of my research was to derive a new mathematical model suitable for computing magnetized ideal plasmas under extreme conditions as those found in many astrophysical environments. I characterized and tested my new model for standard test problems commonly found in the literature as well as for real scientific scenarios. For this, I implemented my numerical scheme in the multi-physics simulation code `FLASH` (Fryxell et al., 2000).

While my primary research interest focus is on developing highly accurate, physically consistent schemes for astrophysical applications, it should be pointed out that my work is directly applicable to other applications dealing with plasmas under extreme conditions. Examples for such an applications are nuclear fusion power research and geophysics. I give more detail about the applicability of my scheme beyond astrophysics in the Outlook chapter.

Structure of this thesis

This thesis is organized as follows:

After this introductory part, I discuss the necessary theoretical foundations. I start with a short revision of the principles of fluid dynamics (Sec. 2.1) and the finite volume method (Sec. 2.2). Thereafter, I shortly describe the specialties of astrophysical plasmas (Sec. 2.3), and introduce the ideal MHD equations at the continuous level (Sec. 2.4).

These preparatory sections are followed by a synoptic introduction to the concept of entropy in Sec. 2.5 and Sec. 2.6. An interesting observation of these two sections is that entropy is not only an important measure to ensure thermodynamic consistency but turns out to be even inherently linked to the divergence-free constraint.

The shortcoming of the discrete ideal MHD model eventually led to the development of my new mathematical model described in Chapter 3.

In Chapter 4, I include a compilation of three published research articles I recently wrote. Each individual paper is prefaced by its full bibliographic record, a short summary placing them in context of this thesis, and an overview of the individual contributions of my co-authors.

Thereafter, in Chapter 5, I provide technical details about my implementation of the new scheme for the multi-physics code `FLASH`. Herein, I also describe fundamental limitations of the `FLASH` simulation code.

To demonstrate the utility of my new scheme in an astrophysical context, I apply my scheme to a state-of-the-art astrophysical simulation. The setup as well as the results, including a detailed comparison to the previously used numerical scheme are given in Chapter 6.

Finally, in Chapters 7 and 8, I give a summarizing conclusion of my work and carefully describe several possibilities for future work continuing the development of the new ideal GLM-MHD model.

In the Appendix, I include a comparison of colliding flow solutions obtained using a reference solver. I performed these comparisons to highlight possible discrepancies between different implementations of the non-conservative ideal MHD terms discussed in Derigs et al. (2018b, Sec. 3.8). This comparison is necessary as the reference solver that is used in several international research groups does not use the physically mandated term as described in Derigs et al. (2018b, Sec. 2).

On the last page of the appendix, I shortly comment on measurement endeavors and why we still cannot exclude the existence of magnetic monopoles.

2 | Theoretical background

This chapter serves to establish notation as well as to highlight a few points of interest. More specific introductions are also given in the individual publications included in this thesis.

2.1 Fluid dynamics

One might argue that most parts of the Universe are gaseous and should, therefore, be described by kinetic gas theory describing a gas as a large number of particles, all of which are in rapid motion. These particles are constantly colliding with each other giving rise to a certain amount of randomness. It is evident that a description of the cosmos based on all the atoms and molecules it is composed of is unsuitable, as simulating trillions of billions of particles is untractable based on the limited capabilities of humankind.

There is extensive literature available showing that we do not have to treat astrophysical systems using kinetic gas theory. Instead, we use the *fluid approximation*[2] when studying astrophysical problems. The fluid approximation (also known as the *fluid limit*) has the significant advantage of approximating the evolution of a given stochastic process to describe macroscopic properties such as density or pressure. Obviously, a sufficient number of gas particles must be available to make meaningful definitions of these macroscopic properties. Furthermore, the fluid approximation is only valid if variations in the macroscopic quantities we observe are slow compared to the time scale of microscopic processes in the fluid we want to model. Luckily, for astrophysical processes (on the scales we observe them) both requirements are always fulfilled.

[2] In common usage, *fluid* is often used as a synonym for *liquid*, however, in science, fluids are a subset of the phases of matter also including gases and plasmas.

Fluid approximation in a nutshell

We can always apply the fluid approximation to astrophysical problems when the mean free path of the fluid is much smaller than the scale of interest.

Interesting models in physics are formulated as systems of conservation laws,

$$\frac{\partial \boldsymbol{q}}{\partial t} + \nabla \cdot \boldsymbol{f} = 0, \tag{2.1}$$

where $\boldsymbol{q}$, and $\boldsymbol{f}(\boldsymbol{q}, \nabla \boldsymbol{q})$ are the set of conserved variables and the vector of (physical) fluxes depending on them and their gradients, respectively.

The behavior of fluids can be described by the Navier-Stokes equations, a set of partial differential equations which are conservation laws for mass, momentum, and energy. The study of fluids in motion is commonly called *fluid dynamics* or *hydrodynamics*.

2.2 The finite volume method

The finite volume (FV) approximation assumes that the quantities in question are constant within small volumes, the so-called *cells*.This subdivison of the continuous spatial domain into a finite number of cells, is known as *discretization* of the fluid. It inevitably implies a trade-off between a precise description of a physical system and the available computational resources.

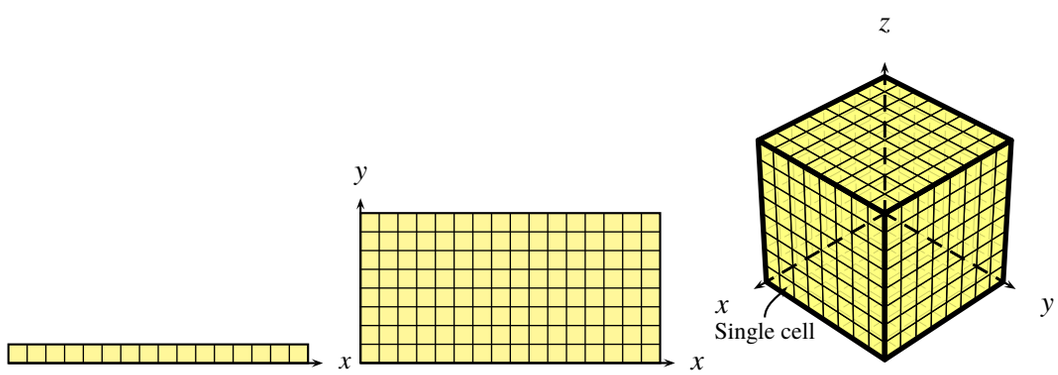

Fig. 2.1: Exemplary computational grids

Grid-based simulations deal with the evolution of fluids by solving the evolution equations of fluids for each cell on such a computational grid (see Fig. 2.1 for illustrations of simple one-, two- and three-dimensional grids). The cell quantities are affected by fluxes through their surfaces which couple the local cell with the rest of the fluid. In Fig. 2.2, I show an example for fluxes in a one-dimensional grid with three cells.

Assume we are looking at cell i, we need to determine the fluxes describing how much of a quantity is flowing *in* ($\boldsymbol{F}_{i-1/2}$, green arrow) and how much is flowing *out* ($\boldsymbol{F}_{i+1/2}$, red arrow) of cell i.

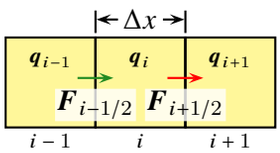

Fig. 2.2: Discretization in 1D showing interface fluxes associated with cell i.

Balancing these fluxes and assuming that the spatial dimension is discretized in uniform cells of size Δx, the temporal change of the conserved quantities $\boldsymbol{q}$ is

$$\frac{\mathrm{d}}{\mathrm{d}t}\,\boldsymbol{q}_i = \frac{\boldsymbol{F}_{i-1/2} - \boldsymbol{F}_{i+1/2}}{\Delta x}. \tag{2.2}$$

Numerical algorithms engineered to compute the interface fluxes $\boldsymbol{F}$ are often called *Riemann solvers*, as the interface fluxes can be computed by the solution of the so-called *Riemann problem*, that is a one-dimensional initial-value problem of two interacting, initially constant states separated by a single jump. Note that there is no exact-closed form solution of the Riemann problems found in fluid dynamics (Toro, 2009, p. 115). Commonly seen "exact" Riemann solvers iteratively compute the solution of the Riemann problem. Although they are typically very accurate, they have several drawbacks such as high computational costs. They are also not guaranteed to converge to a solution, resulting in a possible break-down of the scheme.

To overcome these problems, so-called "approximate" Riemann solvers have been developed. Due to their reduced costs, this kind of Riemann solvers is used in almost all modern implementations. Although they lack the ability to compute the interface fluxes *exactly*, various publications have found that they do not degrade the overall accuracy of numerical schemes as much detail of the solution to the Riemann problem is averaged over before the next time step. This is mostly caused by low-order time integration schemes and comparably low spatial resolutions in simulations.

In this thesis, I carefully describe how to derive approximate Riemann solvers for magnetized fluids that respect the fundamental laws of thermodynamics. I apply the technique to derive an approximate Riemann solver for my new ideal GLM-MHD model.

2.3 Astrophysical plasma

The continuing increase in the significance of simulations for various fields drives the development of numerical schemes. As both, the vast majority of the Universe, and, e.g., the interior of nuclear fusion reactors, are filled with fluid in the so-called *plasma* state, fluid dynamics simulations became a major instrument for such disciplines.

Plasmas are quasi-neutral, electrically conducting fluids. Examples for various kinds of plasma range from the heliosphere to the magnetospheres of planets, to the jets in active galactic nuclei (AGN), and to the gases of the interstellar and intergalactic media. The accepted view is that a vast

majority of the matter in the visible (baryonic) Universe is plasma (see, e.g., Chiuderi & Velli, 2015, Chap. 1).

The Navier-Stokes equations, named after Claude-Louis Navier and George Gabriel Stokes, describe the motion of viscous fluid substances. Unfortunately, the viscosity terms in the Navier-Stokes equations give an extreme complexity so one typically tries to assess the importance of these terms for the targeted application. The Reynolds number conveniently describes the ratio between the relative importance of inertial and viscous forces,

$$\mathcal{R}_e = \frac{\bar{u}L}{\nu}, \tag{2.3}$$

where $\bar{u}$ is the mean velocity, L the characteristic length scale and ν the kinematic viscosity of the fluid.

For $\mathcal{R}_e \gg 1$, inertial forces dominate the system. Fortunately, in the interstellar medium, one commonly finds $\mathcal{R}_e$ of up to 10^{10} such that viscous forces can safely be ignored (Burkhart, 2014, p. 3). The ability to neglect viscosity terms dramatically simplifies the Navier-Stokes equations (which involve higher-order spatial derivatives) to the Euler equations (involving only first order derivatives):

The Euler equations

$$\frac{\partial \rho}{\partial t} + \nabla \cdot (\rho \boldsymbol{u}) = 0, \tag{2.4a}$$

$$\frac{\partial \rho \boldsymbol{u}}{\partial t} + \nabla \cdot (\rho(\boldsymbol{u} \otimes \boldsymbol{u}) + p\mathbf{I}) = 0, \tag{2.4b}$$

$$\frac{\partial E}{\partial t} + \nabla \cdot \left(\boldsymbol{u} \left(\frac{1}{2}\rho \|\boldsymbol{u}\|^2 + \frac{\gamma p}{\gamma - 1} \right) \right) = 0. \tag{2.4c}$$

The three-dimensional Euler equations are given by eq. (2.4a-c). The conserved fluid quantities are density ρ, momentum $\rho\boldsymbol{u} = \{\rho u, \rho v, \rho w\}$, and total energy E. They are defined in the domain $\Omega \subset \mathbb{R}^3$.

Thermal pressure and energy are linked by the ideal gas law first introduced by Clapeyron (1834):

$$p = (\gamma - 1)E_{\text{int}}, \tag{2.5}$$

with the internal energy computed as the difference between the conserved total fluid energy and the kinetic energy of the gas,

$$E_{\text{int}} = E - \frac{1}{2}\rho \|\boldsymbol{u}\|^2, \tag{2.6}$$

and the ratio of specific heat capacities, $\gamma = \frac{c_p}{c_v}$.

2.4 Ideal MHD

As plasmas are electrically conducting, one must extend the hydrodynamic equations when magnetic fields are present. Incorporating the effects of magnetic fields, one arrives at the field of magnetohydrodynamics (*MHD*). As high electrical conductivity is ubiquitous in the ISM (resistivity is negligible), we can use *ideal* magnetohydrodynamics (*ideal MHD*). The ideal MHD equations are especially appealing as they allows one to capture as much physics as possible with a still fairly simple mathematical model.

It is straightforward to obtain the ideal MHD equations by coupling the compressible Euler equations through the Lorentz force,

$$\boldsymbol{F}_{\mathrm{L}} = q\,(\boldsymbol{E} + \boldsymbol{u} \times \boldsymbol{B}), \tag{2.7}$$

with Maxwell's equations for electromagnetism,

$$\nabla \cdot \boldsymbol{E} = \frac{\rho_e}{\varepsilon_0}, \tag{2.8a}$$

$$\nabla \cdot \boldsymbol{B} = \mu_0 \rho_m, \tag{2.8b}$$

$$\nabla \times \boldsymbol{B} = \frac{1}{c^2}\frac{\partial \boldsymbol{E}}{\partial t} + \mu_0 \boldsymbol{j}_e, \tag{2.8c}$$

$$-\nabla \times \boldsymbol{E} = \frac{\partial \boldsymbol{B}}{\partial t} + \mu_0 \boldsymbol{j}_m \tag{2.8d}$$

(Jackson et al., 2006, Sec. 6.11).

Here, $\boldsymbol{E}$ and $\boldsymbol{B}$ are the electric and magnetic field densities. The charge densities are $\rho_{e,m}$, where the subscript e refers to electric charges and m refers to magnetic charges. A similar distinction is made for the current densities, $\boldsymbol{j}_{e,m} := \rho_{e,m}\boldsymbol{u}$. The equations (2.8a-d) are invariant under a global duality transformation that mixes electric and magnetic fields (Jackson et al., 2006). It is important to note that I do not imply the non-existence of magnetic monopoles. By this, I keep the equations as general as possible. The importance of these derivations become particularly relevant when designing numerical methods for MHD as demonstrated in Derigs et al. (2018b, Sec. 2).

The ideal MHD equations, obtained from combining the general Maxwell equations (2.8a-d) through the Lorentz force to the Euler equations (2.4a-c), are given by eq. (2.9a-d). For the sake of clarity, I highlight the difference to the Euler equations in blue.

The ideal MHD equations

$$\frac{\partial}{\partial t}\begin{bmatrix}\rho\\ \rho\boldsymbol{u}\\ E\\ \boldsymbol{B}\end{bmatrix} + \nabla\cdot\begin{bmatrix}\rho\boldsymbol{u}\\ \rho(\boldsymbol{u}\otimes\boldsymbol{u}) + \left(p + \frac{1}{2}\|\boldsymbol{B}\|^2\right)\mathbf{I} - \boldsymbol{B}\otimes\boldsymbol{B}\\ \boldsymbol{u}\left(\frac{1}{2}\rho\|\boldsymbol{u}\|^2 + \frac{\gamma p}{\gamma-1} + \|\boldsymbol{B}\|^2\right) - \boldsymbol{B}(\boldsymbol{u}\cdot\boldsymbol{B})\\ \boldsymbol{u}\otimes\boldsymbol{B} - \boldsymbol{B}\otimes\boldsymbol{u}\end{bmatrix} = -(\nabla\cdot\boldsymbol{B})\begin{bmatrix}0\\ \boldsymbol{B}\\ \boldsymbol{u}\cdot\boldsymbol{B}\\ \boldsymbol{u}\end{bmatrix}. \tag{2.9a-d}$$

The system is closed by a new pressure equation now including magnetic energy,

$$p = (\gamma - 1)\left(E - \frac{1}{2}\rho\|\boldsymbol{u}\|^2 - \frac{1}{2}\|\boldsymbol{B}\|^2\right), \tag{2.10}$$

and Gauß's law for magnetism,

$$\nabla \cdot \boldsymbol{B} = 0, \tag{2.11}$$

which is nothing different than eq. (2.8b) with $\rho_m = 0$. It is essential to note that this condition is *not* inbuilt in the ideal MHD equations and is a constraint that is to be fulfilled separately. This independence is essential for being able to design entropy stable schemes as I did in the present work.

I carefully described the entire derivation of the ideal MHD equations in my third publication (pp. 84 - 88 in this thesis) where I put particular emphasis on the importance of not doing rash simplifications such as $\nabla \cdot \boldsymbol{B} \equiv 0$. Such assumptions restrict the applicability of the obtained equations to a narrower set of possible fluid configurations. I will herein only present the final result of the derivations to avoid unnecessary repetition as the derivations are mostly technical. I will, nevertheless, point out some of the essential findings here.

We see that the ideal MHD equations are in conservative form provided that $\nabla \cdot \boldsymbol{B} = 0$. However, for any small violation of (2.11), the ideal MHD equations loose their exact conservation property in all quantities except density. Many researchers see this as an unfavorable property and, in fact, due to this reason, many publications and implementations of the ideal MHD equations simply ignore the right-hand side of (2.9a-d). However, as I have shown in Derigs et al., 2018b (p. 87 in this thesis), neglecting these non-conservative terms may easily cause the modeled plasma to behave in a physically incorrect way. When we look at the projection of the Lorentz force onto the magnetic field,

$$\boldsymbol{F}_L \cdot \frac{\boldsymbol{B}}{\|\boldsymbol{B}\|} = -(\nabla \cdot \boldsymbol{B})\|\boldsymbol{B}\|, \tag{2.12}$$

it becomes clear that any non-negligible magnetic field divergence leads to an artificial force parallel to the magnetic field lines as eq. (2.12) $\neq 0$. When we, however, take the non-conservative terms on the right-hand side of (2.9a-d) into account, there are no artificial forces present regardless of the magnitude of the magnetic field divergence.

It is interesting to note that Godunov (1972) found the same non-conservative terms for symmetrizability of the partial differential equation (PDE) system using an altogether different approach for his derivations. The formulation of the ideal MHD system presented in (2.9a-d) supports eight traveling plane wave solutions and is hence often referred to as the *eight-wave formulation*. As the non-conservative term on the right-hand side is proportional to the divergence of the magnetic field, it is, on the continuous level, nothing but adding zero in a clever way.

A remarkable outcome is that the obtained set of equations is known to have a number of desirable properties lacking in the classical ideal MHD equations: The system (2.9a-d) is not only symmetrizable (Godunov, 1972; Barth, 1999), but it is also invariant under a Galilean transformation (translation with a constant velocity). Galilean invariance is considered necessary property of any well-posed theory in non-relativistic physics.

2.5 Entropy

Thermodynamics plays a vital role in describing and predicting the behavior of systems we observe in our everyday life. The fundamentals are described in three laws. They are solely based on empirical observations but have not been disproved to date.

There is yet another important property of the thermodynamical laws: they describe how a system can *not* behave. Hence, they can decide which fluid behavior is physically meaningful and which is not.

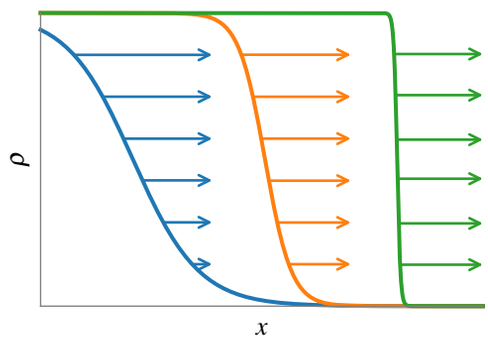

Fig. 2.3: Due to steepening, an initially smooth profile can evolve into a discontinuity that can no longer be resolved on a finite grid. The arrows indicate the velocity of the right-going shock front at three different times.

It is well known that for the Euler and ideal MHD equations, discontinuities in all physical quantities may develop even from smooth initial data (see also Fig. 2.3). It turns out that solutions for discontinuous data are not unique and, although all of the solutions of the Riemann problem are mathematically valid, some of them might represent physically impossible fluid configurations. To rule those out, one needs to supplement the PDE system by an additional admissibility criterion.

Fortunately, entropy can be used as such a criterion for the physical relevance of a given solution. Investigations of hyperbolic PDEs, modeling entropy consistent fluid dynamics, have been the subject of research for over fifty years (Godunov, 1961; Lax, 1967; Kružkov, 1970; Godunov, 1972; Kuznetsov, 1976; Mock, 1980; Harten, 1983; Tadmor, 1984; Tadmor, 1987; Merriam, 1989; Tadmor, 2003; Roe, 2006; Ismail & Roe, 2009; Fjordholm et al., 2012; Tadmor, 2016; Winters & Gassner, 2016; Derigs et al., 2016; Derigs et al., 2017; Winters et al., 2017; Derigs et al., 2018a; Derigs et al., 2018b).

In the case of the Euler equations (and also ideal MHD), entropy is defined as the *physical entropy density*,

$$S(\boldsymbol{q}) = -\frac{\rho s}{\gamma - 1} \quad \text{with} \quad s = \ln \frac{p}{\rho^\gamma} \tag{2.13}$$

(Landau, 1959, p. 315).

Entropy, is conserved in smooth (continuous) flows,

$$\frac{\partial}{\partial t} S + \nabla \cdot (\boldsymbol{u} S) = 0, \tag{2.14a}$$

and decreasing in shock waves (discontinuous flows),

$$\frac{\partial}{\partial t} S + \nabla \cdot (\boldsymbol{u} S) \leq 0, \tag{2.14b}$$

turning the balance law eq. (2.14a) into an inequality. Note that the sign is a matter of convention: Whereas, in thermodynamics, entropy is described to only grow, mathematics and computational physics define entropy to be only decreasing.

In the present work, I chose the mathematical sign convention as it is the commonly used convention in the Journal of Computational Physics (JCP) in which I published my articles.

Entropy sign convention

If I would define the entropy in the thermodynamical sense (as an only *increasing* quantity),

$$S(\boldsymbol{q}) = \frac{\rho s}{\gamma - 1}, \tag{2.15}$$

then eq. (2.14b) would become

$$\frac{\partial}{\partial t} S + \nabla \cdot (\boldsymbol{u} S) \geq 0. \tag{2.16}$$

A prime example of the usefulness of entropy stability as a physically motivated admissibility criterion is that certain numerical schemes tend to "square" an initially smooth pulse (Merriam, 1989, Sec. 5.6). As such solutions have unphysical entropy production rates, entropy-aware schemes avoid them by construction as they are designed to discard unphysical flow configurations (see also Derigs et al., 2018b, Sec.5.7, p. 116 in this thesis).

2.6 Entropy aware schemes

A method is said to be *entropy conservative* if the local changes of entropy are the same as described by the entropy equality (2.14a). It is said to be *entropy stable* if entropy is not only always conserved but can also be "generated"[3]. This process is described by the entropy *in*equality (2.14b).

From the second law of thermodynamics, kinetic and magnetic energy can be transformed irreversibly into internal energy (heat). If additional dissipation is not included in an entropy conservative method, spurious oscillations will develop near discontinuities as energy is re-distributed among its available forms at the smallest resolvable scale (Mishra, 2011).

[3] If entropy generation means reduction or increase in entropy depends on the sign convention.

We know that entropy is only conserved in purely smooth solutions. However, solutions to the Euler and ideal MHD equations may develop discontinuities of significant strength even from smooth initial conditions. Hence, entropy *conserving* schemes are only a first step into the direction of entropy *stable* methods. Only these methods can be applied to arbitrary fluid configurations.

To obtain an entropy stable scheme, one contracts the ideal MHD equations into entropy space. For this, Mock (1980) suggested defining *entropy variables*, which, in the case of the ideal MHD equations are given by

$$\boldsymbol{v} = \frac{\partial S(\boldsymbol{q})}{\partial \boldsymbol{q}} = \begin{bmatrix} \frac{\gamma - s}{\gamma - 1} - \beta \|\boldsymbol{u}\|^2 \\ 2\beta u \\ 2\beta v \\ 2\beta w \\ -2\beta \\ 2\beta B_1 \\ 2\beta B_2 \\ 2\beta B_3 \end{bmatrix}, \tag{2.17}$$

where $S(\boldsymbol{q})$ and $\boldsymbol{q}$ are the physical entropy density (2.13), and the vector of conserved variables,

$$\boldsymbol{q} = \begin{bmatrix} \rho \\ \rho u \\ \rho v \\ \rho w \\ E \\ B_1 \\ B_2 \\ B_3 \end{bmatrix}, \tag{2.18}$$

respectively. The commonly used notation for the vector field components is $\boldsymbol{B} = [B_1, B_2, B_3]^\intercal$ and $\boldsymbol{u} = [u, v, w]^\intercal$.

For convenience, I introduce a new quantity proportional to the inverse temperature,

$$\beta = \frac{\rho}{2p} \propto T^{-1}, \tag{2.19}$$

as suggested by Chandrashekar (2013).

Thanks to the strongly convex mathematical entropy function $S(\boldsymbol{q})$, the mapping $\boldsymbol{q} \rightarrow \boldsymbol{v}$ is one-to-one and one can use the entropy variables to contract the hyperbolic conservation law (2.1) into entropy space,

$$\boldsymbol{v}^\intercal \cdot \left(\frac{\partial \boldsymbol{q}}{\partial t} + \nabla \cdot \boldsymbol{f} \right) = 0 \tag{2.20}$$

(Mock, 1980; Harten, 1983).

After many manipulations, one sees that the ideal MHD equations in form (2.9a-d) are entropy consistent as the obtained entropy law,

$$\frac{\partial}{\partial t} S + \nabla \cdot (\boldsymbol{u} S) = 0, \tag{2.21}$$

is identical to the entropy equality (2.14a). Thus, the system (2.9a-d) is suitable for construction entropy conservative schemes. Although not immediately apparent, this result is significant. I will come back to this when describing the new mathematical model I derived for this work.

The full derivation of entropy aware schemes is rather lengthy and technical. I carefully described the procedure in Derigs et al. (2018b, Sec. 3.1) which is part of this thesis. For the sake of brevity, I present here only the results of this derivation.

To simplify the discussion, but without lack of generality, I limit my analysis to the x-dimension. As all dimensions are decoupled from each other,

$$\nabla \cdot \boldsymbol{f} = \frac{\partial}{\partial x}\boldsymbol{f}_x + \frac{\partial}{\partial y}\boldsymbol{f}_y + \frac{\partial}{\partial z}\boldsymbol{f}_z, \tag{2.22}$$

the extension to two or three spatial dimensions is straightforward. I described the procedure of extending one-dimensional fluxes to multiple dimensions in Derigs et al. (2016, Sec. 3.1, p. 40 in this thesis) and more extensively in Derigs et al. (2018a, beginning of Sec. 4.2, not included in this thesis).

For the sake of convenience, I drop the x subscript from the flux vectors in the following.

2.6.1 Kinetic energy preservation

Correct simulation of the evolution of kinetic energy is a crucial requirement for accurate simulations. A prime example are simulations involving turbulence, where there is an energy cascade between the different eddy scales. Jameson (2008) detailed that the interface fluxes of a conservative scheme can be constructed such that spurious kinetic energy cannot be produced by the numerical fluxes. He denoted such schemes *kinetic energy preserving* (KEP) schemes. The construction of a KEP scheme requires the fluxes of the continuity and momentum equations to be constructed in a specific manner. The kinetic energy preserving property is desirable as traditional Riemann solvers ("Godunov schemes") are found to have wrong order of kinetic energy dissipation and entropy production which leads to excessive damping of flow structures (Thornber et al., 2008; Chandrashekar, 2013).

As I have shown in Derigs et al. (2017), the kinetic energy preserving property is favorable regarding robustness of the numerical scheme particularly at high Mach numbers.

2.6.2 Entropy conserving scheme

In a numerical finite volume code, the continuous fluxes given in (2.9a-d) are computed at discrete cell interfaces. The discrete *kinetic energy preserving entropy conserving* (KEPEC) numerical

flux at an interface described by the fluid configuration on its left (L) and right (R) side, reads

$$\boldsymbol{f}^{\text{KEPEC}} := \begin{bmatrix} \rho^{\ln} \{\!\{u\}\!\} \\ \rho^{\ln} \{\!\{u\}\!\}^2 + \overline{p}_{\text{tot}} - \{\!\{B_1\}\!\}^2 \\ \rho^{\ln} \{\!\{u\}\!\} \{\!\{v\}\!\} - \{\!\{B_1\}\!\} \{\!\{B_2\}\!\} \\ \rho^{\ln} \{\!\{u\}\!\} \{\!\{w\}\!\} - \{\!\{B_1\}\!\} \{\!\{B_3\}\!\} \\ f_E^* \\ 0 \\ \{\!\{u\}\!\} \{\!\{B_2\}\!\} - \{\!\{v\}\!\} \{\!\{B_1\}\!\} \\ \{\!\{u\}\!\} \{\!\{B_3\}\!\} - \{\!\{w\}\!\} \{\!\{B_1\}\!\} \end{bmatrix}, \tag{2.23a-h}$$

with the averaged total pressure

$$\overline{p}_{\text{tot}} = \tilde{p} + \frac{1}{2}\Big(\{\!\{B_1^2\}\!\} + \{\!\{B_2^2\}\!\} + \{\!\{B_3^2\}\!\} \Big), \tag{2.24}$$

and the discrete total energy flux

$$\begin{aligned} f_E^* = {} & \frac{f_a^*}{2(\gamma-1)\beta^{\ln}} - \frac{1}{2} f_a^* \Big(\{\!\{u^2\}\!\} + \{\!\{v^2\}\!\} + \{\!\{w^2\}\!\} \Big) + f_b^* \{\!\{u\}\!\} + f_c^* \{\!\{v\}\!\} + f_d^* \{\!\{w\}\!\} + f_f^* \{\!\{B_1\}\!\} \\ & + f_g^* \{\!\{B_2\}\!\} + f_h^* \{\!\{B_3\}\!\} - \frac{1}{2} \Big(\{\!\{uB_1^2\}\!\} + \{\!\{uB_2^2\}\!\} + \{\!\{uB_3^2\}\!\} \Big) + \{\!\{B_1\}\!\} \Big(\{\!\{uB_1\}\!\} + \{\!\{vB_2\}\!\} + \{\!\{wB_3\}\!\} \Big) \end{aligned} \tag{2.25}$$

(Derigs et al., 2018b, Sec. 4.2). The numerical flux indices $f_{(\cdot)}^*$ represent the individual flux components in (2.23).

The β averaged pressure is

$$\tilde{p} = \frac{\{\!\{\rho\}\!\}}{2\,\{\!\{\beta\}\!\}}. \tag{2.26}$$

The average of a quantity is defined as

$$\{\!\{\cdot\}\!\} := \frac{(\cdot)_{\text{L}} + (\cdot)_{\text{R}}}{2}. \tag{2.27}$$

When applied to vectors, the average operators are evaluated separately for each vector component.

The logarithmic mean is defined as

$$(\cdot)^{\ln} = \frac{[\![\cdot]\!]}{[\![\ln(\cdot)]\!]}, \tag{2.28}$$

where the jump in a quantity is defined as

$$[\![\cdot]\!] = (\cdot)_{\text{R}} - (\cdot)_{\text{L}}. \tag{2.29}$$

A numerically stable procedure to compute the logarithmic mean is described by Ismail & Roe (2009, App. B).

The discrete non-conservative term on the right-hand side of the ideal MHD equations is

$$\Upsilon_i^x := \frac{[\![B_1]\!]}{2\Delta x}\left(\begin{bmatrix} 0 \\ \boldsymbol{B}_\mathrm{L} \\ (\boldsymbol{u}\cdot\boldsymbol{B})_\mathrm{L} \\ \boldsymbol{u}_\mathrm{L} \end{bmatrix}\right)_{i-1/2} + \frac{[\![B_1]\!]}{2\Delta x}\left(\begin{bmatrix} 0 \\ \boldsymbol{B}_\mathrm{R} \\ (\boldsymbol{u}\cdot\boldsymbol{B})_\mathrm{R} \\ \boldsymbol{u}_\mathrm{R} \end{bmatrix}\right)_{i+1/2}. \tag{2.30}$$

A numerical scheme build upon (2.23) and (2.30) conserves the discrete entropy by construction.

2.6.3 Entropy stable scheme

From the second law of thermodynamics, we know that kinetic and magnetic energy can irreversibly be transformed into heat. This process is known as *dissipation* of energy. To respect this fundamental physical process, the numerical scheme has to ensure that enough entropy is added to the solution discretely satisfying the entropy inequality (2.14b).

The easiest and arguably most straightforward way of creating an entropy stable flux function is to augment an entropy conserving baseline flux (as described in the preceding subsection) by a suitable dissipation operator. The resulting *kinetic energy preserving and entropy **stable*** (*KEPE**S***) flux,

$$\boldsymbol{f}^{\mathrm{KEPE\mathbf{S}}} = \boldsymbol{f}^{\mathrm{KEPE\mathbf{C}}} - \frac{1}{2}\mathbf{D}\,[\![\boldsymbol{q}]\!], \tag{2.31}$$

is applicable to arbitrary flows. Finding suitable dissipation operators $\mathbf{D}$ such that the dissipation is guaranteed to fulfill the entropy inequality is a major difficulty.

Scalar dissipation operator

A particularly simple dissipation operator is

$$\mathbf{D}_\mathrm{scalar} = |\mathbf{\Lambda}_\mathrm{scalar}| \tag{2.32}$$

with the scalar diagonal matrix

$$\mathbf{\Lambda}_\mathrm{scalar} = \mathrm{diag}(\lambda_\mathrm{max}, \ldots, \lambda_\mathrm{max}), \tag{2.33}$$

where λ_max is the largest eigenvalue of the ideal MHD system. The matrix $\mathbf{\Lambda}_\mathrm{scalar}$ is a diagonal 8-by-8 matrix.

If λ_max is the largest *global* eigenvalue, eq. (2.32) describes a *Lax-Friedrichs like* dissipation scheme (Lax, 1954). Although being known for stability, such schemes are also known for their diffusivity, especially around shocks. The reason for this lies in the choice of the wave speed: Dissipating according to the maximum wave speed present in the solution does not take into account the local fluid properties.

Choosing $\lambda_{\max}$ as the *local* maximum eigenvalue in only the adjacent cells leads to a considerable improvement in sharpness of results. Such schemes are known as *local* Lax-Friedrichs like or also *Rusanov like* schemes (Rusanov, 1962).

As I have shown in Derigs et al. (2017, Sec. 4, pp. 74-76 in this thesis), the dissipation operator in form (2.32) is not provably entropy stable. For achieving provable entropy stability, we have to transform (2.31) from conservative into entropy space,

$$\frac{1}{2}\mathbf{D}\,[\![\boldsymbol{q}]\!] \;\rightarrow\; \frac{1}{2}\mathbf{D}\,\mathbf{H}\,[\![\boldsymbol{v}]\!], \tag{2.34}$$

with a matrix $\mathbf{H} := \frac{\partial \boldsymbol{v}}{\partial \boldsymbol{q}}$ relating the conservative and entropy spaces. This is in agreement with the observation of Barth (1999) who realized that entropy stable dissipation schemes should incorporate the jump in entropy variables rather than in conservative variables. However, it turns out that the matrix $\mathbf{H}$ is asymmetric and hence generally unsuitable for constructing entropy stable schemes.

Fortunately, I found that it is possible to derive a suitable matrix $\hat{\mathcal{H}}$ by relaxing the equality $[\![\boldsymbol{q}]\!] = \mathbf{H}\,[\![\boldsymbol{v}]\!]$ in the total energy jump so that the equality reduces to an asymptotic approximation,

$$([\![\boldsymbol{q}]\!])_i = (\hat{\mathcal{H}}\,[\![\boldsymbol{v}]\!])_i \tag{2.35}$$

for $i = \{1,2,3,4,6,7,8\}$ and

$$([\![\boldsymbol{q}]\!])_5 \simeq (\hat{\mathcal{H}}\,[\![\boldsymbol{v}]\!])_5. \tag{2.36}$$

The resulting matrix

$$\hat{\mathcal{H}} = \begin{bmatrix}
\rho^{\ln} & \rho^{\ln}\{\!\{u\}\!\} & \rho^{\ln}\{\!\{v\}\!\} & \rho^{\ln}\{\!\{w\}\!\} & \overline{E} & 0 & 0 & 0 \\
\rho^{\ln}\{\!\{u\}\!\} & \rho^{\ln}\{\!\{u\}\!\}^2 + \{\!\{p\}\!\} & \rho^{\ln}\{\!\{u\}\!\}\{\!\{v\}\!\} & \rho^{\ln}\{\!\{u\}\!\}\{\!\{w\}\!\} & (\overline{E} + \{\!\{p\}\!\})\{\!\{u\}\!\} & 0 & 0 & 0 \\
\rho^{\ln}\{\!\{v\}\!\} & \rho^{\ln}\{\!\{v\}\!\}\{\!\{u\}\!\} & \rho^{\ln}\{\!\{v\}\!\}^2 + \{\!\{p\}\!\} & \rho^{\ln}\{\!\{v\}\!\}\{\!\{w\}\!\} & (\overline{E} + \{\!\{p\}\!\})\{\!\{v\}\!\} & 0 & 0 & 0 \\
\rho^{\ln}\{\!\{w\}\!\} & \rho^{\ln}\{\!\{w\}\!\}\{\!\{u\}\!\} & \rho^{\ln}\{\!\{w\}\!\}\{\!\{v\}\!\} & \rho^{\ln}\{\!\{w\}\!\}^2 + \{\!\{p\}\!\} & (\overline{E} + \{\!\{p\}\!\})\{\!\{w\}\!\} & 0 & 0 & 0 \\
\overline{E} & (\overline{E} + \{\!\{p\}\!\})\{\!\{u\}\!\} & (\overline{E} + \{\!\{p\}\!\})\{\!\{v\}\!\} & (\overline{E} + \{\!\{p\}\!\})\{\!\{w\}\!\} & \hat{\mathcal{H}}_{5,5} & \tau\{\!\{B_1\}\!\} & \tau\{\!\{B_2\}\!\} & \tau\{\!\{B_3\}\!\} \\
0 & 0 & 0 & 0 & \tau\{\!\{B_1\}\!\} & \tau & 0 & 0 \\
0 & 0 & 0 & 0 & \tau\{\!\{B_2\}\!\} & 0 & \tau & 0 \\
0 & 0 & 0 & 0 & \tau\{\!\{B_3\}\!\} & 0 & 0 & \tau
\end{bmatrix}, \tag{2.37}$$

with

$$\hat{\mathcal{H}}_{5,5} = \frac{1}{\rho^{\ln}}\left(\frac{(p^{\ln})^2}{\gamma - 1} + \overline{E}^2\right) + \{\!\{p\}\!\}\left(\{\!\{u\}\!\}^2 + \{\!\{v\}\!\}^2 + \{\!\{w\}\!\}^2\right) + \tau\sum_{i=1}^{3}\left(\{\!\{B_i\}\!\}^2\right), \tag{2.38}$$

$$p^{\ln} = \frac{\rho^{\ln}}{2\beta^{\ln}}, \quad \{\!\{p\}\!\} = \frac{\{\!\{\rho\}\!\}}{2\,\{\!\{\beta\}\!\}}, \quad \overline{E} = \frac{p^{\ln}}{\gamma - 1} + \frac{1}{2}\rho^{\ln}\overline{\|\boldsymbol{u}\|^2}, \tag{2.39}$$

$$\overline{\|\boldsymbol{u}\|^2} = 2\left(\{\!\{u\}\!\}^2 + \{\!\{v\}\!\}^2 + \{\!\{w\}\!\}^2\right) - \left(\{\!\{u^2\}\!\} + \{\!\{v^2\}\!\} + \{\!\{w^2\}\!\}\right), \quad \text{and} \quad \tau = \frac{\{\!\{p\}\!\}}{\{\!\{\rho\}\!\}} \tag{2.40}$$

is symmetric positive definite (see Derigs et al., 2017, Appendix A, for the proof).

As the derivation of this matrix is very technical and adds little additional information to this introduction, I only note that it is extensively described in Derigs et al. (2017, Sec. 4, pp. 74ff in this thesis).

Using the said matrix, I derived a provably entropy stable scheme with scalar dissipation:

$$\boldsymbol{f}^{\mathrm{KEPES}} = \boldsymbol{f}^{\mathrm{KEPEC}} - \frac{1}{2}\mathbf{D}_{\mathrm{scalar}}\hat{\mathcal{H}}\,[\![\boldsymbol{v}]\!] \tag{2.41}$$

Being the most straightforward choice for a dissipation scheme, the scalar dissipation has some drawbacks. One of them is that a scalar dissipation term cannot resolve contact discontinuities exactly and will always add dissipation on interfaces separating zones of different densities. Furthermore, it cannot dissipate selectively based on the waves present in the solution but will always introduce much more dissipation than a selective dissipation scheme (Winters & Gassner, 2016, Sec. 6.4).

Selective dissipation scheme

A more complex dissipation operator is

$$\mathbf{D}_{\mathrm{matrix}} = \mathbf{R}|\mathbf{\Lambda}_{\mathrm{matrix}}|\mathbf{R}^{-1}, \tag{2.42}$$

where $\mathbf{R}$ is the matrix of right eigenvectors and $\mathbf{\Lambda}_{\mathrm{matrix}}$ is the diagonal matrix composed of the eigenvalues of the flux Jacobian for the eight-wave ideal MHD system,

$$\mathbf{\Lambda}_{\mathrm{matrix}} = \mathrm{diag}(\lambda_{+\mathrm{f}}, \lambda_{+\mathrm{s}}, \lambda_{+\mathrm{a}}, \lambda_{\mathrm{E}}, \lambda_{\mathrm{D}}, \lambda_{-\mathrm{s}}, \lambda_{-\mathrm{a}}, \lambda_{-\mathrm{f}}),$$

with the wave speeds of two fast and slow magnetoacoustic waves ($\pm$f, $\pm$s), two Alfvén waves ($\pm$a), an entropy wave (E), and a divergence wave (D). Using the eigenvector scaling theorem of Barth (1999), it is possible to relate the entropy Jacobian $\mathbf{H}$ and the right eigenvectors $\mathbf{R}$, to create a positive diagonal matrix such that

$$\mathbf{H} = \mathbf{R}\mathbf{T}\mathbf{R}^{\mathsf{T}}, \tag{2.43}$$

with a positive diagonal scaling matrix $\mathbf{T}$. To ensure that this entropy scaling exists, it must be possible to symmetrize the system of PDEs. Fortunately, the ideal MHD equations with non-conservative terms are symmetrizable as I pointed out in Sec. 2.4. Roe & Balsara (2006) showed that the right eigenvectors may exhibit several forms of degeneracy. We obtained discrete right eigenvectors and values free from these degeneracies in Winters et al. (2017).

The selective dissipation scheme is similar to Roe's scheme (Roe, 2006; Ismail & Roe, 2009), however, it gives greatly increased robustness, as we showed in Derigs et al. (2017) and Winters et al. (2017).

Hybrid dissipation scheme

In Derigs et al. (2016) and Derigs et al. (2018b) we found that using a *hybrid* dissipation scheme, continuously blending the scalar and the selective dissipation schemes, has additional benefits in the robustness of our entropy stable numerical scheme.

In the hybrid scheme, eq. (2.41) and eq. (2.42) are combined[4]. The diagonal matrix of eigenvalues is scaled to continuously blend the two schemes. The hybrid scheme has an identical form to (2.42),

$$\mathbf{D}_{\text{hybrid}} = \mathbf{R}|\mathbf{\Lambda}_{\text{hybrid}}|\mathbf{R}^{-1}, \tag{2.44}$$

where the hybrid matrix is given by

$$|\mathbf{\Lambda}_{\text{hybrid}}| = (1 - \Xi)\,|\mathbf{\Lambda}_{\text{matrix}}| + \Xi\,|\mathbf{\Lambda}_{\text{scalar}}|, \tag{2.45}$$

with the parameter-free pressure-based smoothness indicator

$$\Xi = \sqrt{\frac{|p_{\text{L}} - p_{\text{R}}|}{p_{\text{L}} + p_{\text{R}}}} \in [0, 1] \tag{2.46}$$

(Derigs et al., 2016, Sec. 3.5.2, p. 46 in this thesis). I depict the course of the smoothness indicator in dependence of the ration of pressures in Fig. 2.4.

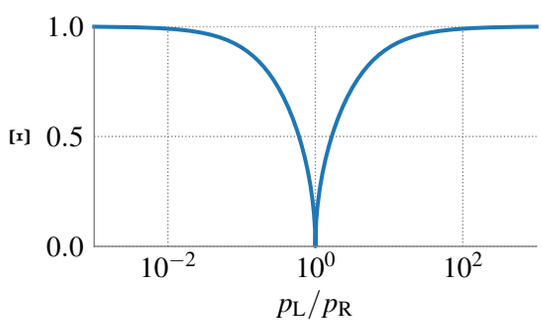

Fig. 2.4: Parameter-free pressure-based smoothness indicator Ξ. The case $\Xi \approx 0$ corresponds to a smooth solution whereas $\Xi \longrightarrow 1$ indicates a strong shock.

Combining eq. (2.31), and eq. (2.43) – (2.45), the hybrid entropy stable flux has the form

$$\boldsymbol{f}^{\text{KEPES}} = \boldsymbol{f}^{\text{KEPEC}} - \frac{1}{2}\mathbf{R}|\mathbf{\Lambda}_{\text{hybrid}}|\mathbf{R}^{-1}(\mathbf{R}\mathbf{T}\mathbf{R}^{\intercal})\,[\![\boldsymbol{v}]\!] = \boldsymbol{f}^{\text{KEPEC}} - \frac{1}{2}\mathbf{R}|\mathbf{\Lambda}_{\text{hybrid}}|\mathbf{T}\mathbf{R}^{\intercal}\,[\![\boldsymbol{v}]\!]\,. \tag{2.47}$$

The pressure-based smoothness indicator (2.46) applies the more dissipative scalar term near strong shocks and the less dissipative matrix term in smooth regions near rarefaction waves and at contact discontinuities to ensure more accurate resolution of these features. I describe a possible extension of this smoothness indicator to increase accuracy in the Outlook chapter (Sec. 8.2).

Using eq. (2.47), I can get the discrete form of the entropy inequality (see Derigs et al., 2018a, Sec. 4.3.2),

$$\frac{\partial}{\partial t}S + [\![uS]\!] \leq -\frac{1}{2}\,[\![\boldsymbol{v}]\!]^{-1}\,\mathbf{R}|\mathbf{\Lambda}_{\text{hybrid}}|\mathbf{T}\mathbf{R}^{\intercal}\,[\![\boldsymbol{v}]\!]\,, \tag{2.48}$$

[4] this is possible as $\mathbf{R}\mathbf{R}^{-1} = \mathbf{I}$

where $[\![uS]\!]$ is the discrete analog of $\frac{\partial}{\partial x}(uS)$. As the right-hand side,

$$\frac{1}{2}[\![\boldsymbol{v}]\!]^{-1}\,\mathbf{R}|\boldsymbol{\Lambda}_{\text{hybrid}}|\mathbf{T}\mathbf{R}^{\intercal}\,[\![\boldsymbol{v}]\!] \geq 0 \tag{2.49}$$

is a quadratic form (and is as such positive), we have

$$\frac{\partial}{\partial t}S + [\![uS]\!] \leq 0. \tag{2.50}$$

This proves that the numerical scheme (2.47) is entropy stable as it satisfies the entropy inequality in a discrete sense.

Entropy sign convention

If I define the entropy in the thermodynamical sense as described in eq. (2.15), this leads to an inversion of the sign on the entropy variables, $\boldsymbol{v}_{\text{pos}} = -\boldsymbol{v}$. The entropy inequality would then be described by eq. (2.52). The entropy stable flux (2.47) would be

$$\boldsymbol{f}^{\text{KEPES}} = \boldsymbol{f}^{\text{KEPEC}} + \frac{1}{2}\mathbf{R}|\boldsymbol{\Lambda}_{\text{hybrid}}|\mathbf{T}\mathbf{R}^{\intercal}\left[\!\left[\boldsymbol{v}_{\text{pos}}\right]\!\right]. \tag{2.51}$$

As eq. (2.49) still holds, we have see that eq. (2.51) similarly fulfills the entropy inequality (2.16):

$$\frac{\partial}{\partial t}S + [\![uS]\!] \geq 0. \tag{2.52}$$

3 | The ideal GLM-MHD equations

The ideal GLM-MHD equations are a new mathematical model ensuring entropy stability with effective inbuilt hyperbolic divergence cleaning. They couple Gauß's law to the ideal MHD equations in a novel entropy consistent way. Similar to Dedner et al. (2002), the idea is not to strictly enforce the divergence-free condition (2.11), but rather to construct a scheme that is designed to evolve towards a divergence-free state. For this, I investigated many options to couple the divergence of the magnetic field into Faraday's equation and found that a scheme with a Galilean-invariant hyperbolic ansatz has favorable properties (see Derigs et al., 2018b, Sec. 3.4, pp. 88-91 in this thesis, for the full derivation from first principles). The new mathematical model I derived for thermodynamically consistent ideal MHD simulations reads:

The ideal GLM-MHD equations

$$\frac{\partial}{\partial t}\begin{bmatrix}\rho\\ \rho\boldsymbol{u}\\ E\\ \boldsymbol{B}\\ \psi\end{bmatrix}+\nabla\cdot\begin{bmatrix}\rho\boldsymbol{u}\\ \rho(\boldsymbol{u}\otimes\boldsymbol{u})+\left(p+\frac{1}{2}\|\boldsymbol{B}\|^2\right)\mathbf{I}-\boldsymbol{B}\otimes\boldsymbol{B}\\ \boldsymbol{u}\left(\frac{1}{2}\rho\|\boldsymbol{u}\|^2+\frac{\gamma p}{\gamma-1}+\|\boldsymbol{B}\|^2\right)-\boldsymbol{B}(\boldsymbol{u}\cdot\boldsymbol{B})+c_h\psi\boldsymbol{B}\\ \boldsymbol{u}\otimes\boldsymbol{B}-\boldsymbol{B}\otimes\boldsymbol{u}+c_h\psi\mathbf{I}\\ c_h\boldsymbol{B}\end{bmatrix}=-\Upsilon_{\mathrm{GLM}}. \tag{3.1a-e}$$

For the sake of convenience, I highlight the difference of my new mathematical model to the eight-wave formulations of the ideal MHD equations (2.9a-d) in red.

The GLM-MHD equations feature a new non-conservative term

$$\Upsilon_{\mathrm{GLM}}:=(\nabla\cdot\boldsymbol{B})\begin{bmatrix}0\\ \boldsymbol{B}\\ \boldsymbol{u}\cdot\boldsymbol{B}\\ \boldsymbol{u}\\ 0\end{bmatrix}+(\nabla\psi)\cdot\begin{bmatrix}\mathbf{0}\\ 0\\ \boldsymbol{u}\psi\\ 0\\ \boldsymbol{u}\end{bmatrix}, \tag{3.2}$$

and an extended thermodynamic pressure equation,

$$p=(\gamma-1)\left(E-\frac{1}{2}\rho\|\boldsymbol{u}\|^2-\frac{1}{2}\|\boldsymbol{B}\|^2-\frac{1}{2}\psi^2\right). \tag{3.3}$$

The newly introduced divergence-correcting field is denoted by ψ, where c_h is the new hyperbolic divergence cleaning speed. My definition of the generalized Lagrangian multiplier ψ, compared to the definition of Dedner et al. (2002), results in a favorable set of entropy variables reducing the complexity of the thermodynamic analysis. It is easily seen that for zero magnetic field divergence, the correcting field is constant and the highlighted contributions in (3.1a-e) vanish, returning the model to the ideal MHD equations (2.9a-d). Thus, the GLM modifications are consistent to the ideal MHD model and correctly restore the continuous limit.

An important ingredient in my new model is that one needs to account for a form of magnetic field correction energy carried by the ψ field. This is because the ψ field couples into the induction equation,

$$\frac{\mathrm{d}}{\mathrm{d}t}\boldsymbol{B} = \nabla \times (\boldsymbol{u} \times \boldsymbol{B}) - c_h \nabla \psi, \tag{3.4}$$

and therefore alters the magnetic field and the energy stored therein. It stands to reason that the correcting field contains some form of energy for which should be accounted. As the thermal energy is computed by subtracting the kinetic and magnetic energies from the total energy, any information regarding loss/gain of magnetic energy would be falsely attributed to thermal energy. In Derigs et al. (2018b, eq. (3.12), p. 90 in this thesis), I found this additional ψ energy to be

$$E_\psi = \frac{1}{2}\psi^2. \tag{3.5}$$

The similarity of this new energy to the magnetic field energy, $E_{\mathrm{mag}} = \frac{1}{2}\|\boldsymbol{B}\|^2$ is undeniable. Including this term in the total energy directly leads to the modifications in the total energy equation (3.1c) and non-conservative term (3.2).

As the derived model is entirely new, I performed a full eigenstructure analysis in Derigs et al. (2018b, Sec. 3.6, p. 92f in this thesis). The fast and slow magnetoacoustic (f/s), the Alfvén (a) and the entropy (e) waves are identical to the ideal MHD case, whereas the divergence wave of the eight-wave formulation splits into new left and right-going GLM waves. The eigenvalues of the new ideal GLM-MHD system are

$$\lambda_{\pm\mathrm{f}} = u \pm c_f, \tag{3.6a}$$
$$\lambda_{\pm\mathrm{s}} = u \pm c_s, \tag{3.6b}$$
$$\lambda_{\pm\mathrm{a}} = u \pm c_a, \tag{3.6c}$$
$$\lambda_{\mathrm{e}} = u, \tag{3.6d}$$
$$\lambda_{\pm\psi} = u \pm c_h, \tag{3.6e}$$

with

$$a^2 = \gamma\,\frac{p}{\rho}, \quad \boldsymbol{b} = \frac{\boldsymbol{B}}{\sqrt{\rho}}, \quad c_{\mathrm{a}}^2 = b_1^2, \quad \text{and}$$
$$c_{\mathrm{f,s}}^2 = \frac{1}{2}\left(a^2 + \|\boldsymbol{b}\|^2 \pm \sqrt{(a^2 + \|\boldsymbol{b}\|^2)^2 - 4a^2 b_1^2}\right), \tag{3.7}$$

where c_{f} and c_{s} are the fast and slow magnetoacoustic wave speeds, respectively, and c_{a} is the Alfvén wave speed. In the equations for $c_{\mathrm{f,s}}^2$, the plus sign corresponds to the fast magnetoacoustic speed

c_f, whereas the minus sign corresponds to the slow magnetoacoustic speed c_s. All eigenvalues are real and simple (they have an algebraic multiplicity of one). Hence, the ideal GLM-MHD scheme is *strictly hyperbolic*. However, note that this is only true as long as magnetic fields are present. If there are zero magnetic fields (compressible Euler equations), some waves may coincide.

As my system supports nine traveling waves, I call it the *nine-wave scheme* in the style of denoting the ideal MHD system (supporting eight waves) as the eight-wave scheme.

Galilean invariance

The ideal GLM-MHD equation are invariant under a Galilean transformation, i.e., invariant to a transformation into a frame of reference moving with a constant relative velocity $\boldsymbol{u}_0$,

$$\boldsymbol{x}' = \boldsymbol{x} - \boldsymbol{u}_0 t, \quad \boldsymbol{u}' = \boldsymbol{u} - \boldsymbol{u}_0, \quad t' = t,$$

as they show the expected transformation behavior of:

$$\frac{\mathrm{d}}{\mathrm{d}t'} = \frac{\mathrm{d}}{\mathrm{d}t} \quad \text{and} \quad \frac{\partial}{\partial t'} = \frac{\partial}{\partial t} + \boldsymbol{u}_0 \cdot \nabla$$

When setting $\psi = c_h = 0$, one immediately gets the eight-wave formulation. Both GLM waves join to form the commonly known (single) divergence wave with eigenvalue $\lambda_\mathrm{D} = u$.

3.1 The cleaning speed c_h

The cleaning velocity, c_h, is the velocity with which the correction of the magnetic field is propagated into the surrounding medium. Hence, the hyperbolic cleaning is most effective when c_h is as high as possible. Unfortunately, we cannot increase the cleaning velocity to an arbitrarily high value as it is coupled into the CFL condition through the $\lambda_{\pm\psi}$ wave speed. Hence, beyond a certain maximum value, it will affect the time step of the simulation which is undesirable in most cases. In Derigs et al. (2018b, Sec. 3.7, p. 93 in this thesis), I carefully investigated the maximum possible cleaning speed under the condition

$$\lambda_{\pm\psi} \leq \max(\lambda_{\pm\mathrm{f}}, \lambda_{\pm\mathrm{a}}, \lambda_{\pm\mathrm{s}}, \lambda_\mathrm{E}) \tag{3.8}$$

resulting in a maximum CFL-compliant cleaning velocity

$$c_h \leq \max_\Omega(c_f), \tag{3.9}$$

where $\max_\Omega(c_f)$ is the maximum fast magnetoacoustic wave speed in the entire simulation. This result is favorable as it ensures that there will always be a non-vanishing cleaning speed.

A local, instead of a global, definition of c_h can be advantageous regarding a locally higher cleaning efficiency. Unfortunately, spatially varying cleaning speeds cannot be implemented in an entropy-consistent way. In comparison to the discrete scheme I derived one would have to include

c_h in the jumps of the total entropy update (Derigs et al., 2018b, eq. (4.41), p. 100 in this thesis) as highlighted in red:

$$[\![\boldsymbol{v}]\!] \cdot \boldsymbol{f}^* = [\![\rho u]\!] + \left[\!\!\left[\beta u \|\boldsymbol{B}^2\|\right]\!\!\right] + 2\,[\![\beta B_1 c_h \psi]\!] - 2\,\{\!\{B_1\}\!\}\,[\![\beta(\boldsymbol{u}\cdot\boldsymbol{B})]\!] \tag{3.10}$$

This leads to slightly increased complexity as $[\![\beta B_1 c_h \psi]\!]$ will contain more mixed terms than what I showed in Derigs et al. (2018b, eq. (A.6)):

$$\begin{aligned}
[\![\beta B_1 c_h \psi]\!] &= \{\!\{\beta\}\!\}\,[\![B_1 c_h \psi]\!] + \{\!\{B_1 c_h \psi\}\!\}\,[\![\beta]\!] \\
&= \{\!\{\beta\}\!\}\left(\{\!\{B_1\}\!\}\,[\![c_h]\!]\,\psi + \{\!\{\psi\}\!\}\,[\![c_h B_1]\!]\right) + \{\!\{B_1 c_h \psi\}\!\}\,[\![\beta]\!] \\
&= \{\!\{\beta\}\!\}\left(\{\!\{B_1\}\!\}\left(\{\!\{c_h\}\!\}\,[\![\psi]\!] + \{\!\{\psi\}\!\}\,[\![c_h]\!]\right) + \{\!\{\psi\}\!\}\left(\{\!\{c_h\}\!\}\,[\![B_1]\!] + \{\!\{B_1\}\!\}\,[\![c_h]\!]\right)\right) + \{\!\{B_1 c_h \psi\}\!\}\,[\![\beta]\!] \\
&= [\![\psi]\!]\,\{\!\{\beta\}\!\}\,\{\!\{B_1\}\!\}\,\{\!\{c_h\}\!\} + [\![B_1]\!]\,\{\!\{\beta\}\!\}\,\{\!\{\psi\}\!\}\,\{\!\{c_h\}\!\} + [\![c_h]\!]\,2\,\{\!\{\beta\}\!\}\,\{\!\{\psi\}\!\}\,\{\!\{B_1\}\!\} + [\![\beta]\!]\,\{\!\{B_1 c_h \psi\}\!\}
\end{aligned} \tag{3.11}$$

Unfortunately, due to the absence of c_h in the entropy variables, this results in an additional equation when comparing to (A.7a) - (A.7i) in my paper. This equation,

$$[\![c_h]\!]\,(\{\!\{\beta\}\!\}\,\{\!\{\psi\}\!\}\,\{\!\{B_1\}\!\}) = 0, \tag{3.12}$$

turns out to be problematic. As $\{\!\{\beta\}\!\} > 0$ and $\{\!\{\psi\}\!\}\,\{\!\{B_1\}\!\} \not\equiv 0$, eq. (3.12) inevitably requires $[\![c_h]\!] = 0$. Hence, it seems not possible to construct an entropy aware discrete GLM-MHD scheme with spatially varying cleaning speeds.

3.2 Physical interpretation of the GLM correction

As described before, magnetic fields affect the surrounding fluid *only locally* through the Lorentz force. Changes in the magnetic field topology are, however, *non-local* as the magnetic field is globally constrained by the divergence-free condition (2.11). As the ideal MHD system does not include this fundamental constraint, the global field topology stays unconstrained and magnetic field divergence emerges. Although the ideal MHD equations in form (2.9a-d) correctly treat non-zero magnetic field divergence, numerical instabilities can still occur due to energy piling up in the magnetic field at stagnation points.

The ideal GLM-MHD equations are a substantial improvement over the ideal MHD equations concerning magnetic field divergence treatment. Through the new scalar field ψ, I couple the divergence-free constraint into the system. It takes care of propagating the corrections, which are necessary to maintain the physical correctness of the solution, outwards into the ambient medium with the "cleaning" speed c_h.

The ultimate effect of the GLM correction can best be made clear with a simple example. In Figs. 3.1 to 3.4, I show the temporal evolution of a simulation starting from purposely defined non-divergence-free initial conditions. The initial conditions in many variables are constant

(uniform density, pressure, zero velocity). I add a homogeneous magnetic field in x-direction, where I cut out a cylindrical region in the center of the computational domain. An equivalent physical experiment would be a region with a homogeneous magnetic field having a superconducting wire at its center. The truncated magnetic field leads to a significant initial magnetic field divergence,

$$\nabla \boldsymbol{B} = \frac{\partial}{\partial x} B_x \neq 0. \tag{3.13}$$

In this section, I use $B_{\{x,y,z\}}$ instead of $B_{\{1,2,3\}}$ for the sake of readability.

Fig. 3.1 illustrates the initial conditions which feature a significant initial magnetic field divergence. On the top panel, I show a slice of the magnetic field (left: x-component, right: y-component). On the bottom left, I plot the scalar field ψ for visualization purpose and the magnetic field divergence on the bottom right. I overplot magnetic field lines (in red) in the top left panel. In Fig. 3.2, I plot the same quantities only a few time steps after the initial conditions. The magnetic field lines become bend around the region with zero magnetic fields as the scheme corrects the magnetic field topology. One can nicely see the generated correction field in the ψ plot (bottom left).

Fig. 3.3 shows the evolution of the simulation after a few more timesteps. The ψ wave is isotropically expanding from the initial magnetic field discontinues around the cylindrical region. As it propagates outward, it is correcting the magnetic field topology in the area through which it travels. Accordingly, the $\nabla \cdot \boldsymbol{B}$ plot shows that the strong initial magnetic field divergence at the center of the computations domain has decreased notably (bottom right panel). As expected, there is some "new" magnetic field divergence at the front of the GLM wave as the magnetic field is just being corrected here and, in front of the ψ wave, the magnetic field is still uncorrected, creating a kink in the magnetic field lines. As can be seen in the top right panel, magnetic energy is redistributed from B_x into the B_y component to correct the magnetic field topology. The magnetic field lines start to bend around the region of zero magnetic fields as expected and depicted in the introduction (Fig. 1.2) so that the magnetic field outside of the radius of influence of the ψ wave is still identical to the initial state.

In Fig. 3.4, I plot the magnetic field after one Alfvén wave crossing time. The initial magnetic field divergence is removed, and the system is brought into a configuration in agreement with Gauß's law (2.11). The numerical solution obeys the second law of thermodynamics and is in this sense physically meaningful. It reached an almost stationary state already at $t \approx 80\,\%$ of the Alfvén crossing time. This is not surprising as the correction speed, c_h, is given by the fast magnetoacoustic wave and we have $c_\mathrm{f} \geq c_\mathrm{a}$.

Of course, this example is rather academic but it nevertheless provides valuable information to support the physical interpretation of the entropy-consistent GLM correction. More realistic tests involve simulations where errors in the divergence-free constraint are (continuously) generated by the numerical scheme over time. Such tests, as the MHD rotor or the Orszag-Tang MHD vortex, start from purely smooth initial data and generate non-trivial magnetic field configurations involving fast shocks.

I carefully tested my scheme using these and other tests in Derigs et al. (2018b, Sec. 5, pp. 107-117 in this thesis). Comparisons to reference solutions computed with a constraint transport scheme prove the applicability of my new scheme for such benchmark tests.

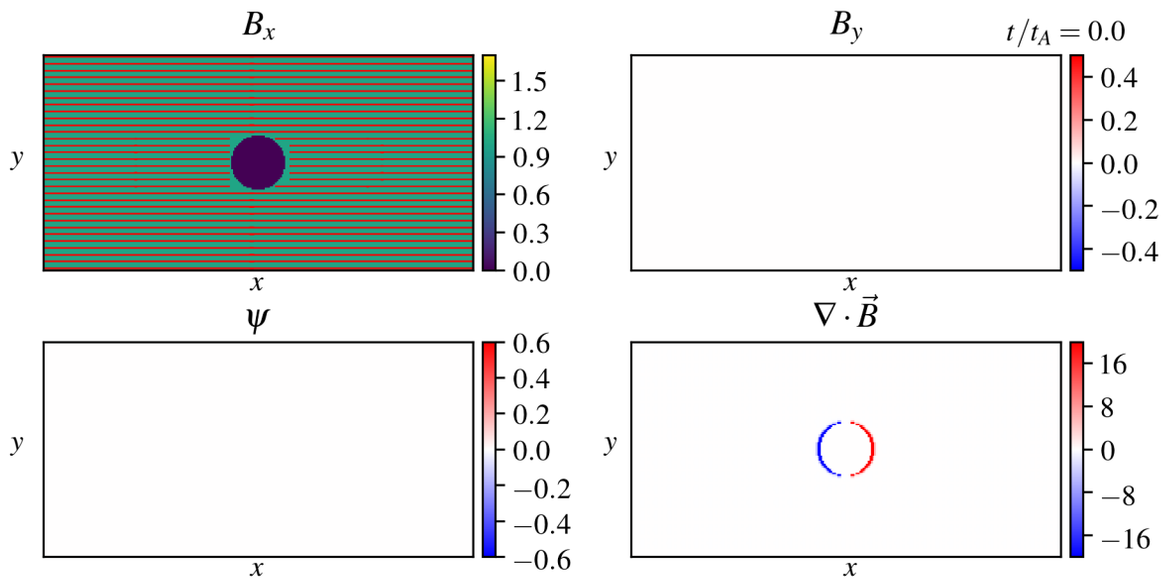

Fig. 3.1: GLM divergence correction test: Initial conditions set. The magnetic field is set up in x-direction where I exclude a cylindric region, causing a notable initial violation of the divergence-free constraint as can be seen on the bottom right plot. I overplot magnetic field lines (in red) in the top left panel.

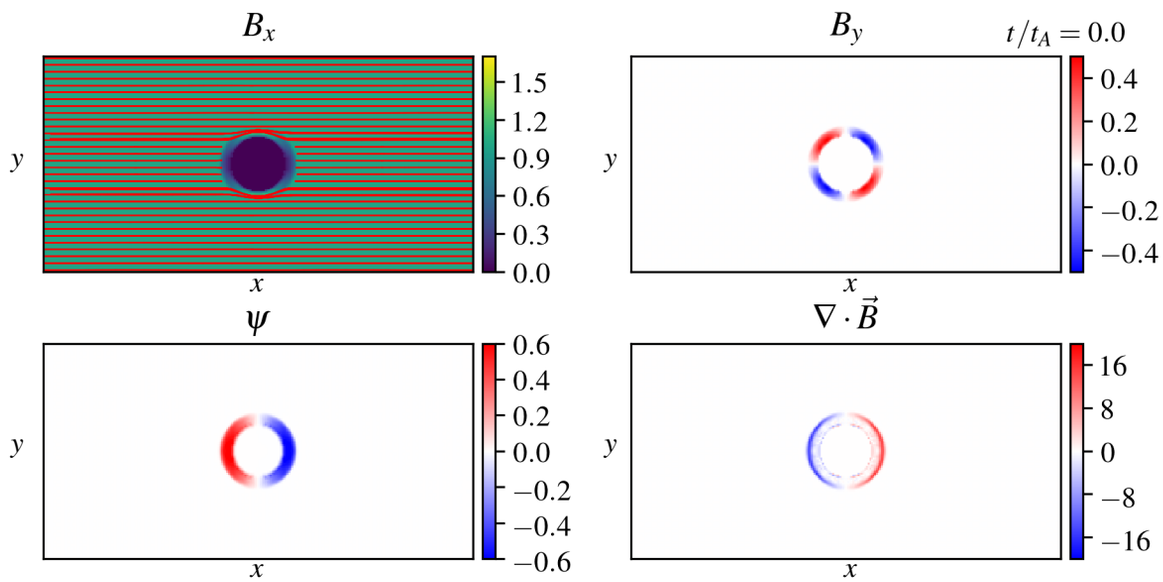

Fig. 3.2: GLM divergence correction test: Snapshot only shortly after the initial conditions. The correction is constantly propagating the necessary magnetic field corrections outwards, reducing the strength of the local magnetic field divergence at the origin.

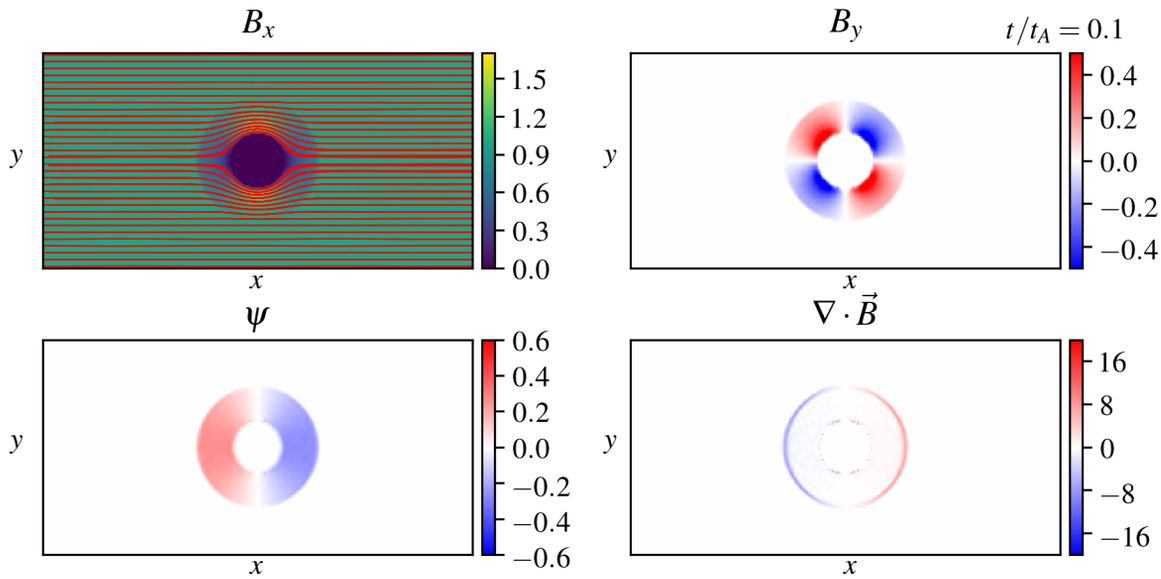

Fig. 3.3: GLM divergence correction test: Snapshot after 10 % of the Alfvén crossing time. As the ψ wave is propagating outwards, the magnetic field topology is corrected.

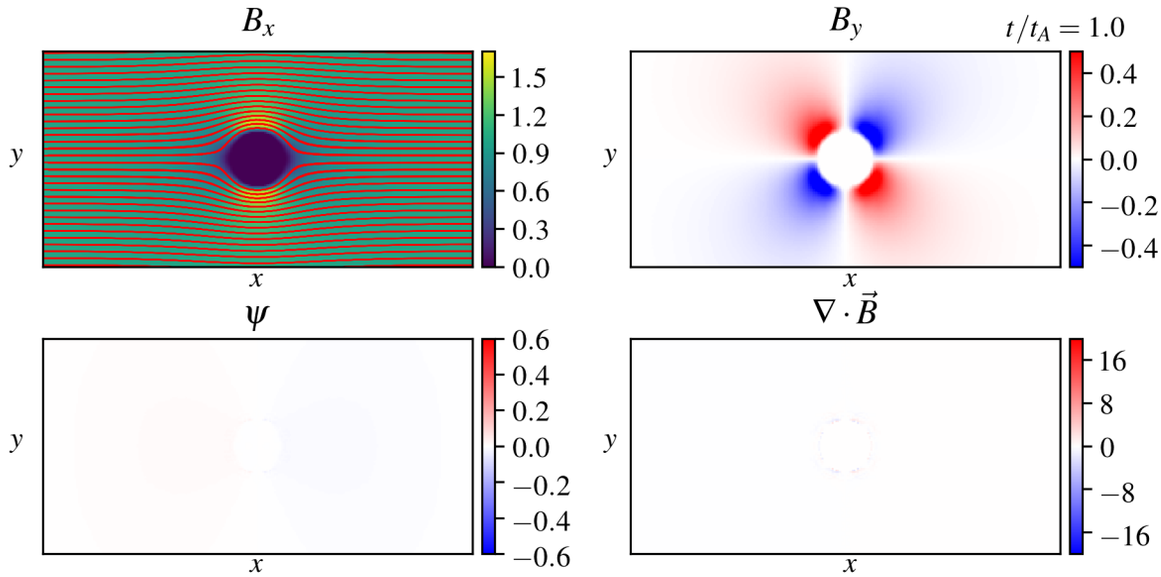

Fig. 3.4: GLM divergence correction test: Snapshot after one Alfvén wave crossing time. The magnetic field has been brought into a physically consistent configuration. The simulation reached an almost stationary configuration at this point. The scanable hyperlink to the right links to a movie showing the temporal evolution of the GLM divergence correction test.

4 | Publications

This cumulative dissertation is based on work that has been presented in the internationally respected *Journal of Computational Physics* (JCP) that focuses on computational aspects and algorithmic development to numerically model physical problems. This journal was established in 1966 and generally seeks to emphasize numerical methods that cross disciplinary boundaries. **All articles included in this thesis are accepted and have been published.**

4.1 Contribution overview

This section contrasts my own contributions to the paper with the contributions of my collaborators and co-authors. I am the main contributor in all included articles. Dr. Andrew Winters, Prof. Dr. Stefanie Walch, and Prof. Dr.-Ing. Gregor Gassner assisted significantly in my research.

Prof. Dr. Stefanie Walch primarily supervised my work and helped me in finding the correct physics interpretations for observed phenomena and continuously supported my endeavor of developing a new numerical scheme for the simulation of astrophysical phenomena. She was my first point of call whenever I had questions.

Prof. Dr.-Ing. Gregor Gassner showed me the way into mathematical modeling and the underlying mathematical concepts of entropy stability. His support, especially for the numerical aspects of this work, was essential for all, and especially my third article in which I derived the new mathematical model, the ideal GLM-MHD equations.

Dr. Andrew Winters is an expert in the field of entropy stable methods. He helped me understand the various derivation techniques I used throughout my research and continuously assisted me with complex derivations (see individual contributions mentioned before each included article).

The new ideas we generated in our regular interdisciplinary meetings eventually lead to all three works. Hence, they are included as authors on all publications as they contributed to all aspects of my research. Without their help, none of the included works would have been possible.

4.2 Publication I

Derigs, D., Winters, A. R., Gassner, G. J., Walch, S., (Apr. 2016). "A novel high-order, entropy stable, 3D AMR MHD solver with guaranteed positive pressure." In: *Journal of Computational Physics* 317, pp. 223–256. ISSN: 0021-9991.
DOI: 10.1016/j.jcp.2016.04.048. arXiv: 1605.03572.

The first paper presented in this cumulative thesis describes the technical details of an implementation of a significantly extended variant of the entropy-stable solver described in Winters & Gassner (2016). I implemented the scheme into the multi-physics, multi-scale adaptive mesh refinement (AMR) simulation code FLASH (Fryxell et al., 2000). The accuracy, robustness and computational efficiency is demonstrated with a number of tests, including comparisons to available MHD implementations in FLASH.

Contribution overview

I developed and implemented the numerical scheme, performed all simulations, and analyzed them. Andrew Winters and Gregor Gassner gave advise while I developed a new high-order adaptive mesh refinement (AMR) scheme based on the first-order scheme they presented in Winters & Gassner (2016). Stefanie Walch gave advise and helped me clarifying the needs for astrophysical applications.

Stefanie Walch, Gregor Gassner and Andrew Winters edited the paper.

Journal of Computational Physics 317 (2016) 223–256

Contents lists available at ScienceDirect

Journal of Computational Physics

www.elsevier.com/locate/jcp

A novel high-order, entropy stable, 3D AMR MHD solver with guaranteed positive pressure

Dominik Derigs [a,*], Andrew R. Winters [b], Gregor J. Gassner [b], Stefanie Walch [a]

[a] *I. Physikalisches Institut, Universität zu Köln, Zülpicher Straße 77, 50937 Köln, Germany*
[b] *Mathematisches Institut, Universität zu Köln, Weyertal 86-90, 50931 Köln, Germany*

ARTICLE INFO

Article history:
Received 21 January 2016
Received in revised form 11 April 2016
Accepted 24 April 2016
Available online 28 April 2016

Keywords:
Magnetohydrodynamics
FLASH
Entropy stable
Finite volume schemes
Pressure positivity

ABSTRACT

We describe a high-order numerical magnetohydrodynamics (MHD) solver built upon a novel non-linear entropy stable numerical flux function that supports eight travelling wave solutions. By construction the solver conserves mass, momentum, and energy and is entropy stable. The method is designed to treat the divergence-free constraint on the magnetic field in a similar fashion to a hyperbolic divergence cleaning technique. The solver described herein is especially well-suited for flows involving strong discontinuities. Furthermore, we present a new formulation to guarantee positivity of the pressure. We present the underlying theory and implementation of the new solver into the multi-physics, multi-scale adaptive mesh refinement (AMR) simulation code FLASH (http://flash.uchicago.edu). The accuracy, robustness and computational efficiency is demonstrated with a number of tests, including comparisons to available MHD implementations in FLASH.

1. Introduction

Modelling complex non-linear astrophysical phenomena is a central task in the field of astrophysics where laboratory experiments are very difficult if not entirely impossible. Examples of interesting phenomena include the study of stellar evolution, like the star formation process and supernovae explosions, pre-stellar accretion discs and many more. Using simulations allows us to study the internals of complex systems that cannot been seen in experiments and observations.

In astrophysics, a flow involving magnetized gas is typically ionized, compressible, and often supersonic. Since the interstellar gas has essentially infinite conductivity [1], we treat the flow by solving the ideal magnetohydrodynamics (MHD) equations. From the hyperbolic nature of the ideal MHD equations, it is known that discontinuous solutions may develop even from smooth initial data. Obtaining stable numerical results for the variety of physical flow regimes is extremely challenging, particularly for the natural requirement that the numerical scheme must be both accurate and robust. In this paper, we present a novel three-dimensional high-order, conservative, quasi-multifluid, entropy stable, eight wave MHD solver developed for the numerical modelling of MHD flows. It is equally well suited for one, two, or three-dimensional hydrodynamics (HD) and MHD simulations.

The core of the novel MHD solver is the use of entropy stable flux functions developed in [2]. Entropy stable algorithms have the benefit that, by construction, the numerical method is nearly isentropic in smooth regions and entropy is guaranteed to be increasing near discontinuities. Thus, the numerics precisely follow the physics of the second law of ther-

* Corresponding author.
E-mail address: derigs@ph1.uni-koeln.de (D. Derigs).

http://dx.doi.org/10.1016/j.jcp.2016.04.048
0021-9991/

modynamics. Another advantage of entropy stable approximations is that one can limit the amount of dissipation added to the numerical approximation to guarantee entropy stability. The development and investigation of entropy stable algorithms for the ideal MHD equations has been considered by several authors [3–5,2].

The entropy stable formulation also addresses the issue of divergence cleaning for approximate solutions of the ideal MHD equations. The proof of entropy stability in [2] required an additional source term that acts analogously to a hyperbolic divergence cleaning technique [6]. That is, errors introduced into the divergence-free condition are advected away with the fluid velocity.

The scheme handles another major robustness issue in numerical approximations of state-of-the-art high-order MHD solvers – the possible appearance of negative pressures. Negative pressures are a numerical artifact arising due to the problem of finite numerical precision. This phenomenon has been reported frequently in the literature [7–23]. In current codes, negative pressures are avoided by adding artificially high amounts of dissipation or by introducing non-conservative low pressure limits. Negative pressures can arise due the fact that the internal energy is obtained by subtracting the kinetic and magnetic energies from the conserved total energy. In many situations, such as high Mach number or low plasma β flows ($\beta \propto p/\|\boldsymbol{B}\|^2$), the internal energy can be several orders of magnitude smaller then either the kinetic or magnetic energies. Thus, discretisation errors in the total energy could be significant enough to result in negative pressures. The inevitable consequence is the failure of the numerical scheme.

We describe how the novel solver uses the entropy as an auxiliary equation to eliminate this issue and derive a novel expression for the pressure which completely avoids the subtraction problem. The new pressure positivity guaranteeing formulation is not tied to any specific numerical flux function. It remains general and it is straightforward to retrofit into any existing HD/MHD schemes if the underlying numerical approximation is constructed in a way that satisfies certain criteria on the entropy (see Sec. 3.6).

The new solver achieves high-order accuracy in space and time while remaining attractive from a computational point of view. The numerical scheme is extended to high-order in space with spatial reconstruction techniques. In particular, we use a third order spatial approximation with the newly developed reconstruction technique of Schmidtmann et al. [24]. High-order accuracy in time is obtained using the family of strong stability preserving (SSP) Runge–Kutta methods developed by Gottlieb et al. [25].

We provide here details of the novel solver as well as its implementation into the multi-scale multi-physics simulation code `FLASH` [26,27]. `FLASH` is publicly available and has a wide international user base. The remainder of this paper is organized as follows: Sec. 2 provides the necessary background information to discuss the novel numerical solver. In Sec. 3 we describe, in detail, the new solver. The most important aspects of which are the entropy stable numerical fluxes and the new pressure positivity guaranteeing formulation. Sec. 4 presents a variety of numerical results that demonstrate the utility of the new solver. We compare our results to already available MHD implementations in `FLASH` where applicable. Sec. 5, presents our concluding remarks.

2. Governing equations and discretisation

We first provide the necessary background to discuss the novel MHD solver. This includes a brief description of the ideal MHD equations, the concept of entropy conservation and stability, and an outline of the finite volume scheme used for the spatial discretisation.

2.1. Ideal MHD equations

The ideal MHD model assumes that a fluid is a good electric conductor and neglects non-ideal effects, e.g. viscosity or resistivity. It is governed by a system of conservation laws

$$\frac{\partial}{\partial t}\begin{bmatrix}\rho\\ \rho\boldsymbol{u}\\ E\\ \boldsymbol{B}\end{bmatrix} + \nabla\cdot\begin{bmatrix}\rho\boldsymbol{u}\\ \rho(\boldsymbol{u}\otimes\boldsymbol{u}) + \left(p+\frac{1}{2}\|\boldsymbol{B}\|^2\right)\mathbf{I} - \boldsymbol{B}\otimes\boldsymbol{B}\\ \boldsymbol{u}\left(E+p+\frac{1}{2}\|\boldsymbol{B}\|^2\right) - \boldsymbol{B}(\boldsymbol{u}\cdot\boldsymbol{B})\\ \boldsymbol{B}\otimes\boldsymbol{u} - \boldsymbol{u}\otimes\boldsymbol{B}\end{bmatrix} = 0, \tag{2.1}$$

$$\nabla\cdot\boldsymbol{B} = 0, \tag{2.2}$$

where ρ, $\rho\boldsymbol{u}$, and E are the mass, momenta, and total specific energy of the plasma system, p is the thermal pressure, $\mathbf{I}$ is the identity matrix, and $\boldsymbol{B}$ is the magnetic field, also referred to as magnetic flux density. Since our velocities are non-relativistic, Maxwell's displacement current may be ignored in the Lorentz force term. We consider the non-dimensional form of the ideal MHD equations. Details concerning physical units can be found in Appendix D.

Numerical methods for multidimensional ideal MHD must satisfy some discrete version of the divergence-free condition (2.2). There are several approaches to control the error in $\nabla\cdot\boldsymbol{B}$ and in depth review of many methods can be found in Tóth [17]. The thermal pressure is related to the conserved quantities through the ideal gas law for problems in which relativistic, viscous, and resistive effects can be neglected:

$$p = (\gamma - 1)\left(E - \frac{\rho}{2}\|\boldsymbol{u}\|^2 - \frac{1}{2}\|\boldsymbol{B}\|^2\right) \tag{2.3}$$

with the ratio of specific heats $\gamma > 1$.

Note that if we take the divergence of Faraday's equation the magnetic continuity equation

$$\frac{\partial}{\partial t}(\nabla \cdot \boldsymbol{B}) + \nabla \cdot \big(\boldsymbol{u}(\nabla \cdot \boldsymbol{B})\big) = 0, \tag{2.4}$$

is obtained. From (2.4) we see that the divergence of the magnetic field may be treated as an advected scalar. Thereby, the robustness and accuracy of a numerical scheme can be significantly improved [28]. This improvement is primarily because the advection of the generated errors prevents the accumulation at fixed locations. The eigenmode which is advected with the flow in (2.4) is referred to as the *divergence wave*.

We include the Janhunen source term [18] in the ideal MHD equations (2.1) which is proportional to $\nabla \cdot \boldsymbol{B}$. The use of a source term to control the error in the divergence free condition has known issues, such as errors can build up at stagnation points as well as in periodic or closed domains. The only mechanism present to remove these divergence errors is the numerical dissipation of a scheme, but true hyperbolic divergence cleaning methods can remove such limitations [6]. However, the Janhunen source term preserves the conservation of mass, momentum, total energy and allows for the construction of an entropy stable approximation [2]. We explicitly "clean" magnetic field divergence errors in a post-processing step, as will be described later. The governing equations in conjunction with the Janhunen source term are now a system of balance laws

$$\frac{\partial}{\partial t}\begin{bmatrix}\rho\\ \rho\boldsymbol{u}\\ E\\ \boldsymbol{B}\end{bmatrix} + \nabla\cdot\begin{bmatrix}\rho\boldsymbol{u}\\ \rho(\boldsymbol{u}\otimes\boldsymbol{u}) + \left(p + \frac{1}{2}\|\boldsymbol{B}\|^2\right)\mathbf{I} - \boldsymbol{B}\otimes\boldsymbol{B}\\ \boldsymbol{u}\left(E + p + \frac{1}{2}\|\boldsymbol{B}\|^2\right) - \boldsymbol{B}(\boldsymbol{u}\cdot\boldsymbol{B})\\ \boldsymbol{B}\otimes\boldsymbol{u} - \boldsymbol{u}\otimes\boldsymbol{B}\end{bmatrix} = -(\nabla\cdot\boldsymbol{B})\begin{bmatrix}0\\ \boldsymbol{0}\\ 0\\ \boldsymbol{u}\end{bmatrix}. \tag{2.5}$$

Note that the expression "source term" is common in this context, even though the term actually involves spatial derivatives.

To simplify the discussion of the new solver we first consider the modified ideal MHD system (2.5) in one spatial dimension

$$\frac{\partial}{\partial t}\boldsymbol{Q} + \frac{\partial}{\partial x}\boldsymbol{F} = \boldsymbol{\Upsilon}, \tag{2.6}$$

where $\boldsymbol{Q} = \boldsymbol{Q}(x,t)$ is the vector of conservative variables, $\boldsymbol{F}(\boldsymbol{Q})$ the flux vector, and $\boldsymbol{\Upsilon}(\boldsymbol{Q})$ is the vector source term

$$\boldsymbol{Q} = \begin{bmatrix}\rho\\ \rho u\\ \rho v\\ \rho w\\ E\\ B_1\\ B_2\\ B_3\end{bmatrix}, \qquad \boldsymbol{F} = \begin{bmatrix}\rho u\\ \rho u^2 + p + \frac{1}{2}\|\boldsymbol{B}\|^2 - B_1^2\\ \rho u v - B_1 B_2\\ \rho u w - B_1 B_3\\ u\left(E + p + \frac{1}{2}\|\boldsymbol{B}\|^2\right) - B_1(\boldsymbol{u}\cdot\boldsymbol{B})\\ 0\\ u B_2 - v B_1\\ u B_3 - w B_1\end{bmatrix}, \qquad \boldsymbol{\Upsilon} = -\frac{\partial B_1}{\partial x}\begin{bmatrix}0\\ 0\\ 0\\ 0\\ 0\\ u\\ v\\ w\end{bmatrix}. \tag{2.7}$$

In Sec. 3.1 we provide a detailed discussion of the multi-dimensional extension of the solver.

2.2. Entropy conservation and stability

This section serves as a brief introduction to entropy and numerical partial differential equations. A thorough review of this topic has been presented by Tadmor [29]. Work specifically related to entropy and the ideal MHD equations can be found in [4,2].

It is well-known that solutions of balance laws like (2.6) may develop discontinuities in finite time, so we consider solutions of the balance laws (2.6) in the weak sense. Unfortunately, the weak solution is not unique. Thus, we require an additional admissibility condition on the solution to guarantee that the numerical approximation will converge to a weak solution that is consistent with the second law of thermodynamics. In the case of ideal MHD a suitable condition can be defined in terms of the physical entropy density, as defined by Landau [30, p. 315], divided by the constant $(\gamma - 1)$ for convenience, i.e.

$$S(\boldsymbol{Q}) = \frac{\rho s}{\gamma - 1} \quad \text{with} \quad s = \ln\left(p\rho^{-\gamma}\right), \tag{2.8}$$

where γ is the adiabatic index and s is the entropy per particle. The approximation obeys the second law of thermodynamics and is based on an entropy condition for two regimes:

1. For smooth solutions, one can design numerical methods to be ***entropy conservative*** if, discretely, the local changes of entropy are the same as predicted by the continuous entropy conservation law

$$\frac{\partial}{\partial t}S + \frac{\partial}{\partial x}\mathscr{F} = 0, \tag{2.9}$$

where we define the corresponding entropy flux

$$\mathscr{F}(\mathbf{Q}) = uS = \frac{\rho u s}{\gamma - 1}\,. \tag{2.10}$$

2. For discontinuous solutions, the approximation is said to be ***entropy stable*** if the entropy always possesses the correct sign and the numerical scheme produces more entropy than an entropy conservative scheme and satisfies the entropy inequality

$$\frac{\partial}{\partial t}S + \frac{\partial}{\partial x}\mathscr{F} \geq 0. \tag{2.11}$$

From the second law of thermodynamics, kinetic as well as magnetic energy can be transformed irreversibly into heat (internal energy). If additional dissipation is not included in an entropy conservative method, spurious oscillations will develop near discontinuities as energy is re-distributed at the smallest resolvable scale [31]. A numerical scheme requires a diffusion operator to match such a physical process.

For the entropy stable solver discussed in this paper we use the provably entropy stable approximate Riemann solver derived in [2].

2.3. Finite volume scheme

The finite volume method is a discretisation technique for partial differential equations especially useful for the approximation of systems of hyperbolic conservations laws. The finite volume method is designed to approximate conservation laws in their integral form, e.g.,

$$\int_V \mathbf{Q}_t \,\mathrm{d}x + \int_{\partial V} \boldsymbol{F}\cdot\hat{\boldsymbol{n}}\,\mathrm{d}S = 0. \tag{2.12}$$

In one spatial dimension we divide the interval, V, into cells

$$V_i = \left[x_{i-1/2}, x_{i+1/2}\right], \tag{2.13}$$

and the integral equation of a balance law with a source term becomes

$$\frac{\mathrm{d}}{\mathrm{d}t}\int_{x_{i-1/2}}^{x_{i+1/2}} \mathbf{Q}\,\mathrm{d}x + \left[\boldsymbol{F}^*\left(x_{i+1/2}\right) - \boldsymbol{F}^*\left(x_{i-1/2}\right)\right] = \int_{x_{i-1/2}}^{x_{i+1/2}} \boldsymbol{\Upsilon}\,\mathrm{d}x. \tag{2.14}$$

A common approximation is to assume a constant solution within the cell [32, p. 436]:

$$\int_{x_{i-1/2}}^{x_{i+1/2}} \mathbf{Q}\,\mathrm{d}x \approx \int_{x_{i-1/2}}^{x_{i+1/2}} \mathbf{Q}_i\,\mathrm{d}x = \mathbf{Q}_i\Delta x_i. \tag{2.15}$$

Note that the finite volume solution is typically discontinuous at the boundaries of the cells. To resolve this, we introduce the idea of a "numerical flux", $\boldsymbol{F}^*(\mathbf{Q}_R, \mathbf{Q}_L)$, often derived from the (approximate) solution of a Riemann problem. The function $\boldsymbol{F}^*$ takes the two states of the solution at an element interface and returns a single flux value. For consistency, we require that

$$\boldsymbol{F}^*(\mathbf{Q}, \mathbf{Q}) = \boldsymbol{F}, \tag{2.16}$$

that is, the numerical flux is equivalent to the physical flux if the states on each side of the interface are identical.

Next, we address the discretisation of the source term $\boldsymbol{\Upsilon}$ in (2.14). There is a significant amount of freedom in the source term discretisation. The explicit discretisation of the source term is given in Sec. 3.4. We note that the discrete source term at each left $(i-1/2)$ and right $(i+1/2)$ interface will contribute in cell i. So, the semi-discrete finite volume method is

$$\left(\mathbf{Q}_t\right)_i + \frac{1}{\Delta x_i}\left[\boldsymbol{F}^*_{i+1/2} - \boldsymbol{F}^*_{i-1/2}\right] = \frac{1}{2}\left(\boldsymbol{\Upsilon}_{i-1/2} + \boldsymbol{\Upsilon}_{i+1/2}\right). \tag{2.17}$$

3. Description of the novel entropy stable MHD solver

Here we describe the FLASH implementation of the entropy stable ES solver in three spatial dimensions. In Sec. 3.1 we discuss the extension of the solver to three dimensions using dimensional splitting. Sec. 3.2 presents a spatial reconstruction scheme used to achieve a high-order approximation. We describe the explicit time integration technique in Sec. 3.3. The entropy conservative and entropy stable numerical flux functions are described in Sec. 3.4 and Sec. 3.5, respectively. The new strategy to numerically guarantee the positivity of the pressure is described in Sec. 3.6. The adaptive mesh refinement (AMR) functionality of FLASH and the new implementation is found in Sec. 3.7. Next, in Sec. 3.8, a brief summary of a quasi-multifluid implementation is provided. Sec. 3.9 describes how to couple gravity into the entropy stable solver. The treatment of the divergence-free condition in higher spatial dimensions is described in Sec. 3.10. Finally, Sec. 3.11 summarizes the MHD update procedure in FLASH.

3.1. Multi-dimensionality

We extend the one-dimensional set of MHD equations (2.6) to two or three spatial dimensions. In the case of an underlying grid structure that is logically rectangular[1] (like Cartesian grid geometries) a simple and efficient way of extending the one-dimensional Riemann solver to higher spatial dimensions is to use *dimensional splitting*. The method of dimensional splitting has become popular in fluid dynamics as it allows us to apply our knowledge about one-dimensional systems directly to multi-dimensional systems. Using the dimensional splitting method, one-dimensional problems along each coordinate direction are solved in turn to determine the fluxes across the faces of a finite volume cell. It has proven to be an inexpensive way of extending one-dimensional high-resolution methods to higher dimensions [32, p. 103].

We experience that in multi-physics simulations, commonly performed using FLASH, the MHD solver accounts for less than 10% of the overall CPU time (e.g. [33]). Thus, an MHD discretisation which allows large time steps is beneficial for the overall computational efficiency of the multi-physics framework. It is well-known that dimensionally split schemes give larger time steps than comparable unsplit schemes where the dimensionality directly enters the CFL condition. Although the technique of dimensional splitting reduces the accuracy of the solver to formally second-order, the overall increase in efficiency is often favourable for practical applications.

If the three-dimensional semi-discrete problem can be written in the form of

$$\left(\mathbf{Q}_t\right)_i + \mathbf{A}(\mathbf{Q}) + \mathbf{B}(\mathbf{Q}) + \mathbf{C}(\mathbf{Q}) = 0, \tag{3.1}$$

then the total update (3.1) can be split up into an *x-sweep*

$$\left(\mathbf{Q}_t\right)_i + \mathbf{A}(\mathbf{Q}) = 0, \tag{3.2}$$

a *y-sweep*

$$\left(\mathbf{Q}_t\right)_i + \mathbf{B}(\mathbf{Q}) = 0, \tag{3.3}$$

and a *z-sweep*

$$\left(\mathbf{Q}_t\right)_i + \mathbf{C}(\mathbf{Q}) = 0, \tag{3.4}$$

where $\mathbf{A}(\mathbf{Q})$, $\mathbf{B}(\mathbf{Q})$, and $\mathbf{C}(\mathbf{Q})$ are operators for the vector of quantities $\mathbf{Q}$ in x, y, and z-directions, respectively. Each of the sweep operators is a compact notation to write the numerical flux and source term contributions for a given spatial direction. For example, the operator $\mathbf{A}(\mathbf{Q})$ in three dimensions has the form

$$\mathbf{A}(\mathbf{Q}) = \frac{1}{\Delta x_i}\left(\boldsymbol{F}^*_{i+1/2,j,k} - \boldsymbol{F}^*_{i-1/2,j,k}\right) - \frac{1}{2}\left(\boldsymbol{\Upsilon}_{i-1/2,j,k} + \boldsymbol{\Upsilon}_{i+1/2,j,k}\right). \tag{3.5}$$

Therefore, in each sweep direction, separate solutions of the Riemann problem and source term values are computed to update the quantities stored in $\mathbf{Q}^n$ according to (2.17).

To compute the sweeps in y- and z-directions, any direction dependent quantities, i.e. velocity and magnetic field components, are rotated in order to solve them with the same algorithm that is used for the x-sweep.

3.2. Spatial reconstruction

The finite volume method used by the FLASH framework approximates the solution with quantities which are constant within each cell. If one considers these values as point-wise approximations of the solution located at each cell centre, this method computes the numerical interface fluxes at a distance of $\Delta x/2$ from an interface. Rather than using piecewise constant data, we use *reconstructed* quantities within each cell, $(\tilde{\mathbf{Q}}_i)_{\mathrm{L,R}}$. Reconstruction functions, $(\boldsymbol{p}_i)_{\mathrm{L,R}}$, allow the computation of the approximated interface quantities

[1] Not strictly rectangular since cells of different spatial sizes are allowed to coexist on the same grid.

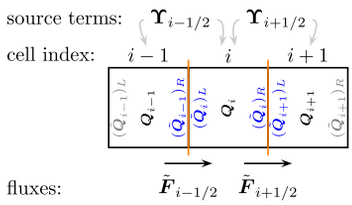

Fig. 1. Graphical representation of the quantities used in (3.7) and (3.8). Reconstructed quantities used for the computation of the numerical fluxes are highlighted in blue. The cell-centred quantities are printed in black. (For interpretation of the references to colour in this figure legend, the reader is referred to the web version of this article.)

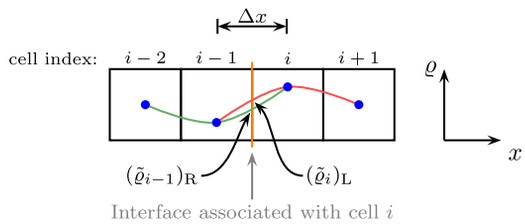

Fig. 2. Principle of our spatial reconstruction. This example shows the parabolic reconstruction of a specific density pattern. The cell-centred quantities, ρ_{i-2}, ρ_{i-1}, ρ_i, and ρ_{i+1}, are represented by dots. Our scheme uses a local three-point stencil and is thereby computationally very efficient.

$$(\tilde{\boldsymbol{Q}}_i)_L = \boldsymbol{Q}_i - \frac{1}{2}(\boldsymbol{p}_i)_L, \quad \text{and} \quad (\tilde{\boldsymbol{Q}}_i)_R = \boldsymbol{Q}_i + \frac{1}{2}(\boldsymbol{p}_i)_R. \tag{3.6}$$

The reconstructed quantities (3.6) are then used to compute high-order accurate numerical fluxes in the finite volume scheme (2.17), i.e.

$$\tilde{\boldsymbol{F}}_{i-1/2} = \boldsymbol{F}^*\Big((\tilde{\boldsymbol{Q}}_{i-1})_R, (\tilde{\boldsymbol{Q}}_i)_L\Big) \quad \text{and} \quad \tilde{\boldsymbol{F}}_{i+1/2} = \boldsymbol{F}^*\Big((\tilde{\boldsymbol{Q}}_i)_R, (\tilde{\boldsymbol{Q}}_{i+1})_L\Big). \tag{3.7}$$

The resulting high-order accurate semi-discrete approximation, reorganizing (2.17), is of the form

$$(\boldsymbol{Q}_t)_i = \frac{1}{\Delta x_i}\left(\tilde{\boldsymbol{F}}_{i-1/2} - \tilde{\boldsymbol{F}}_{i+1/2}\right) + \frac{1}{2}\left(\boldsymbol{\Upsilon}_{i-1/2} + \boldsymbol{\Upsilon}_{i+1/2}\right), \tag{3.8}$$

as illustrated in Fig. 1.

For our reconstruction we use the third order accurate shock capturing limiting procedure for numerical solutions of hyperbolic conservation laws recently described by Schmidtmann et al. [24]. Their scheme utilizes a local piecewise-parabolic reconstruction away from discontinuities (see Fig. 2) and reads

$$(\boldsymbol{p}_i)_L = \boldsymbol{p}(\boldsymbol{Q}_{i-1}, \boldsymbol{Q}_i, \boldsymbol{Q}_{i+1}) = +\frac{2}{3}\boldsymbol{Q}_{i-1} - \frac{1}{3}\boldsymbol{Q}_i - \frac{1}{6}\boldsymbol{Q}_{i+1} = \frac{2\boldsymbol{\delta}_{\boldsymbol{i-\frac{1}{2}}} - \boldsymbol{\delta}_{i+\frac{1}{2}}}{3}, \tag{3.9}$$

$$(\boldsymbol{p}_i)_R = \boldsymbol{p}(\boldsymbol{Q}_{i+1}, \boldsymbol{Q}_i, \boldsymbol{Q}_{i-1}) = -\frac{1}{6}\boldsymbol{Q}_{i-1} - \frac{1}{3}\boldsymbol{Q}_i + \frac{2}{3}\boldsymbol{Q}_{i+1} = \frac{2\boldsymbol{\delta}_{\boldsymbol{i+\frac{1}{2}}} - \boldsymbol{\delta}_{i-\frac{1}{2}}}{3}, \tag{3.10}$$

with

$$\boldsymbol{\delta}_{i-\frac{1}{2}} = \boldsymbol{Q}_i - \boldsymbol{Q}_{i-1} \quad \text{and} \quad \boldsymbol{\delta}_{i+\frac{1}{2}} = \boldsymbol{Q}_{i+1} - \boldsymbol{Q}_i. \tag{3.11}$$

However, such a reconstruction is known to cause oscillations in non-smooth solutions. This can be seen as a direct consequence of Godunov's Theorem [34]. To avoid oscillations, we use the limiting procedure of Schmidtmann et al. [24] to switch to a lower-order accurate reconstruction near large gradients, shocks and discontinuities.

3.3. Strong stability preserving time integration

The solution of a system of hyperbolic conservation laws may not be smooth. In such cases inaccurate time-integration schemes can suffer from poor performance such as an excessively small time step size due to the presence of spurious oscillations as well as the progressive smearing, clipping or squaring of the numerical approximation. To alleviate such performance issues, we consider a third order accurate explicit high-order *strong-stability-preserving* (SSP) low-storage Runge–Kutta time-integration scheme [25]. Such schemes are also referred to in the literature as *total variation diminishing* (TVD) [35]. However, Gottlieb et al. [36] showed this moniker is misleading as their strong stability property holds in any

norm and not only the TVD norm. We complete the discretisation of the reconstructed method (3.8) with the third order SSP Runge–Kutta scheme:

$$\mathbf{Q}' = \mathbf{Q}^n + \Delta t \cdot \mathbf{Q}_t(\mathbf{Q}^n), \tag{3.12}$$

$$\mathbf{Q}'' = \frac{3}{4}\mathbf{Q}^n + \frac{1}{4}\Big(\mathbf{Q}' + \Delta t \cdot \mathbf{Q}_t(\mathbf{Q}')\Big), \tag{3.13}$$

$$\mathbf{Q}^{n+1} = \frac{1}{3}\mathbf{Q}^n + \frac{2}{3}\Big(\mathbf{Q}'' + \Delta t \cdot \mathbf{Q}_t(\mathbf{Q}'')\Big). \tag{3.14}$$

SSP Runge–Kutta schemes consist of convex combinations of explicit forward Euler integration. Thus, the family of methods are guaranteed to be stable under the same time step restriction [25]. We find that the third order SSP Runge–Kutta time integration enables us to use larger time steps, which is favourable in our multi-physics framework.

To select a stable time step for a computational run we use the CFL condition

$$\Delta t \leq \texttt{CFL} \cdot \min\left[\frac{\Delta x}{\lambda^x_{\max}}, \frac{\Delta y}{\lambda^y_{\max}}, \frac{\Delta z}{\lambda^z_{\max}}\right], \tag{3.15}$$

where $\lambda^d_{\max}$ is the speed of the largest wave at time step n travelling in $d = \{x, y, z\}$ direction, $\texttt{CFL}$ is the user-definable CFL coefficient, $\texttt{CFL} \in (0, 1]$. If $\lambda_{\max}$ is known exactly, then the choice $\texttt{CFL} = 1.0$ may be adequate [37, p. 222]. However, $\lambda_{\max}$ is usually computed in some approximate way. Thus, a more conservative choice for the CFL coefficient is typically used in practice (e.g. $\texttt{CFL} = 0.8$).

3.4. Entropy conserving numerical flux

For the entropy analysis of the ideal MHD equations the divergence-free condition is incorporated into the system of conservation laws as a source term [38,18]. Both the Powell [28] and Janhunen [18] source terms treats the magnetic field as an advected scalar. However, the Janhunen source term remains conservative in the momentum and total energy equations and restores the positivity of the Riemann problem as well as Lorentz invariance [39].

The discussion of the entropy conserving numerical flux function of [2] requires the introduction of some notation. We introduce the jump $[\![\cdot]\!]$, the arithmetic mean $(\cdot)^{\mathrm{A}}$ as well as the logarithmic mean $(\cdot)^{\ln}$ of the left/right states, denoted by $(\cdot)_{\mathrm{L}}$ and $(\cdot)_{\mathrm{R}}$, respectively. These operators are defined as

$$[\![\cdot]\!] = (\cdot)_{\mathrm{R}} - (\cdot)_{\mathrm{L}}, \qquad (\cdot)^{\mathrm{A}} = \frac{(\cdot)_{\mathrm{L}} + (\cdot)_{\mathrm{R}}}{2}, \qquad \text{and} \qquad (\cdot)^{\ln} = \frac{[\![\cdot]\!]}{[\![\ln(\cdot)]\!]}. \tag{3.16}$$

A numerically stable procedure to compute the logarithmic mean is described by Ismail and Roe [40, Appendix B]. For convenience we also introduce

$$z_1 = \sqrt{\frac{\rho}{p}}, \qquad \text{and} \qquad z_5 = \sqrt{\rho p}. \tag{3.17}$$

3.4.1. Source term discretisation

It was shown in [2] that the Janhunen source term can be used to design numerical schemes that guarantee the discrete conservation of the entropy density for the ideal MHD equations. Guaranteeing this discrete conservation of the entropy density requires a particular discretisation of the Janhunen source term:

$$\frac{1}{2}\left(\boldsymbol{\Upsilon}_{i-1/2} + \boldsymbol{\Upsilon}_{i+1/2}\right), \tag{3.18}$$

with

$$\boldsymbol{\Upsilon}_{i-1/2} = -[\![B_1]\!]_{i-1/2} \begin{bmatrix} 0 \\ 0 \\ 0 \\ 0 \\ 0 \\ \frac{(uz_1^2)^{\mathrm{A}}(B_1)^{\mathrm{A}}}{(\Delta x z_1^2 B_1)^{\mathrm{A}}} \\ \frac{(vz_1^2)^{\mathrm{A}}(B_2)^{\mathrm{A}}}{(\Delta x z_1^2 B_2)^{\mathrm{A}}} \\ \frac{(wz_1^2)^{\mathrm{A}}(B_3)^{\mathrm{A}}}{(\Delta x z_1^2 B_3)^{\mathrm{A}}} \end{bmatrix}_{i-1/2}, \quad \text{and} \quad \boldsymbol{\Upsilon}_{i+1/2} = -[\![B_1]\!]_{i+1/2} \begin{bmatrix} 0 \\ 0 \\ 0 \\ 0 \\ 0 \\ \frac{(uz_1^2)^{\mathrm{A}}(B_1)^{\mathrm{A}}}{(\Delta x z_1^2 B_1)^{\mathrm{A}}} \\ \frac{(vz_1^2)^{\mathrm{A}}(B_2)^{\mathrm{A}}}{(\Delta x z_1^2 B_2)^{\mathrm{A}}} \\ \frac{(wz_1^2)^{\mathrm{A}}(B_3)^{\mathrm{A}}}{(\Delta x z_1^2 B_3)^{\mathrm{A}}} \end{bmatrix}_{i+1/2}. \tag{3.19}$$

3.4.2. Entropy conserving flux function

The recently developed provably entropy conserving flux of Winters and Gassner [2] reads:

$$\boldsymbol{F}^{*,\mathrm{ec}} = \begin{bmatrix} \hat{\rho}\hat{u}_1 \\ \hat{p}_1 + \hat{\rho}\hat{u}_1^2 + \frac{1}{2}\left(\mathring{B}_1 + \mathring{B}_2 + \mathring{B}_3\right) - \mathring{B}_1 \\ \hat{\rho}\hat{u}_1\hat{v}_1 - \widehat{B_1 B_2} \\ \hat{\rho}\hat{u}_1\hat{w}_1 - \widehat{B_1 B_3} \\ \frac{\gamma}{\gamma-1}\hat{u}_1\hat{p}_2 + \frac{1}{2}\hat{\rho}\hat{u}_1\left(\hat{u}_1^2 + \hat{v}_1^2 + \hat{w}_1^2\right) + \hat{u}_2\left(\hat{B}_2^2 + \hat{B}_3^2\right) - \hat{B}_1\left(\hat{v}_2\hat{B}_2 + \hat{w}_2\hat{B}_3\right) \\ 0 \\ \hat{u}_2\hat{B}_2 - \hat{v}_2\hat{B}_1 \\ \hat{u}_2\hat{B}_3 - \hat{w}_2\hat{B}_1 \end{bmatrix}, \tag{3.20}$$

with the averaged quantities and products

$$\begin{aligned}
&\hat{\rho} = (z_1)^{\mathsf{A}}\,(z_5)^{\ln}, && \hat{p}_1 = \frac{(z_5)^{\mathsf{A}}}{(z_1)^{\mathsf{A}}}, && \hat{p}_2 = \frac{\gamma+1}{2\gamma}\frac{(z_5)^{\ln}}{(z_1)^{\ln}} + \frac{\gamma-1}{2\gamma}\frac{(z_5)^{\mathsf{A}}}{(z_1)^{\mathsf{A}}}, \\
&\hat{u}_1 = \frac{(z_1 u)^{\mathsf{A}}}{(z_1)^{\mathsf{A}}}, && \hat{v}_1 = \frac{(z_1 v)^{\mathsf{A}}}{(z_1)^{\mathsf{A}}}, && \hat{w}_1 = \frac{(z_1 w)^{\mathsf{A}}}{(z_1)^{\mathsf{A}}}, \\
&\hat{u}_2 = \frac{\left(z_1^2 u\right)^{\mathsf{A}}}{\left(z_1^2\right)^{\mathsf{A}}}, && \hat{v}_2 = \frac{\left(z_1^2 v\right)^{\mathsf{A}}}{\left(z_1^2\right)^{\mathsf{A}}}, && \hat{w}_2 = \frac{\left(z_1^2 w\right)^{\mathsf{A}}}{\left(z_1^2\right)^{\mathsf{A}}}, \\
&\hat{B}_1 = (B_1)^{\mathsf{A}}, && \hat{B}_2 = (B_2)^{\mathsf{A}}, && \hat{B}_3 = (B_3)^{\mathsf{A}}, \quad \widehat{B_1 B_2} = (B_1 B_2)^{\mathsf{A}}, \\
&\mathring{B}_1 = \left(B_1^2\right)^{\mathsf{A}}, && \mathring{B}_2 = \left(B_2^2\right)^{\mathsf{A}}, && \mathring{B}_3 = \left(B_3^2\right)^{\mathsf{A}}, \quad \widehat{B_1 B_3} = (B_1 B_3)^{\mathsf{A}}.
\end{aligned} \tag{3.21}$$

In the case of smooth solutions, the entropy conserving flux (3.20) conserves the entropy density of the system up to the precision of the scheme. In order for the numerical scheme to be applicable for possibly non-smooth solutions we must extend the purely entropy *conserving* flux to become an entropy *stable* flux.

3.5. Entropy stabilization

Entropy conserving approximations suffer breakdown in the presence of discontinuities, which results in large oscillations in post-shock regions. Therefore, we require dissipation to be added to the approximation in an entropy consistent manner to guarantee discrete satisfaction of the entropy inequality (2.11). The work [2] derived two provably entropy stable approximate Riemann solvers for the ideal MHD equations. In this work we present a new hybrid entropy stable approximation that continuously combines these two entropy stable fluxes. This introduces explicit non-linearity to permit the calculation of sharp shock fronts and contact discontinuities.

3.5.1. Entropy stable flux functions

To build an entropy stable approximation we use the entropy conservative approximation (3.20) as a baseline. In particular the work [2] presented two possible dissipation terms that can be added to the entropy conserving scheme:

`ES-Roe`: a *matrix dissipation* entropy stabilization. Similar to a Roe type method it selectively applies dissipation to each of the travelling wave solutions, particularly close to shocks.

`ES-LLF`: a *scalar dissipation* entropy stabilization. A simple, local Lax–Friedrichs type dissipation mechanism. Due to the simplicity of `ES-LLF` it cannot distinguish between the various waves present in the MHD flow and can, therefore, lead to a severe smearing of the approximation near discontinuities.

Here we outline the construction of the `ES-Roe` stabilization. The `ES-LLF` stabilization follows almost immediately. To build the matrix dissipation term we first select the dissipation matrix to be $|\widehat{\mathbf{A}}|$. That is the absolute value of the flux Jacobian for the ideal MHD 8-wave formulation:

$$\widehat{\mathbf{A}} = \boldsymbol{F}_{\boldsymbol{Q}} + \mathbf{P} = \mathbf{A} + \mathbf{P}, \tag{3.22}$$

where $\mathbf{A}$ is the flux Jacobian for the homogeneous ideal MHD equations and $\mathbf{P}$ is the Powell source term [28] written in matrix form, i.e.

$$\mathbf{P}\frac{\partial \mathbf{Q}}{\partial x} = \begin{bmatrix} 0 & 0 & 0 & 0 & 0 & 0 & 0 & 0 \\ 0 & 0 & 0 & 0 & 0 & B_1 & 0 & 0 \\ 0 & 0 & 0 & 0 & 0 & B_2 & 0 & 0 \\ 0 & 0 & 0 & 0 & 0 & B_3 & 0 & 0 \\ 0 & 0 & 0 & 0 & 0 & \boldsymbol{u}\cdot\boldsymbol{B} & 0 & 0 \\ 0 & 0 & 0 & 0 & 0 & u & 0 & 0 \\ 0 & 0 & 0 & 0 & 0 & v & 0 & 0 \\ 0 & 0 & 0 & 0 & 0 & w & 0 & 0 \end{bmatrix} \frac{\partial}{\partial x} \begin{bmatrix} \rho \\ \rho u \\ \rho v \\ \rho w \\ \rho e \\ B_1 \\ B_2 \\ B_3 \end{bmatrix} = \frac{\partial B_1}{\partial x} \begin{bmatrix} 0 \\ B_1 \\ B_2 \\ B_3 \\ \boldsymbol{u}\cdot\boldsymbol{B} \\ u \\ v \\ w \end{bmatrix}. \tag{3.23}$$

The design of the entropy stable matrix dissipation term requires the specific form of the flux Jacobian (3.22) because it must be possible to relate the eigenvectors of (3.22) to the entropy Jacobian matrix [41]. This relationship is referred to as creating entropy scaled eigenvectors, e.g. [41,42]. To ensure that this entropy scaling exists, the system of PDEs must be symmetrizable. It is known that the Powell source term restores the symmetric property to the ideal MHD system [42,38], whereas the Janhunen source term does not restore symmetry. However, both source terms allow to contract the MHD equation to the entropy evolution equation and hence both source terms can be used to construct entropy conserving (or stable) discretisations. We choose the Janhunen source term to construct the entropy conservative discretisation, as this gives us conservation of mass, momentum and energy unlike a method based on the Powell source term. Thus, the consistent symmetric part of the flux is based on the Janhunen source term. As long as the additional stabilization term is guaranteed to dissipate entropy, the scheme is entropy stable. Hence, for the design of the stabilization term only, we are considering the flux Jacobian that incorporates the Powell source term, as this guarantees that the entropy scaled eigenvectors exist for the ideal MHD system, which is necessary in order to get the Roe type dissipation term.

The matrix type stabilization term requires the eigenstructure of the dissipation matrix (3.22)

$$\widehat{\mathbf{A}} = \widehat{\mathbf{R}}\mathbf{D}\widehat{\mathbf{R}}^{-1}. \tag{3.24}$$

The matrix $\widehat{\mathbf{A}}$ supports eight propagating plane-wave solutions:

- two fast magnetoacoustic waves ($\pm f$),
- two slow magnetoacoustic waves ($\pm s$),
- two Alfvén waves ($\pm a$),
- an entropy wave (E),
- a divergence wave (D).

It is known that a naively scaled set of right eigenvectors will exhibit several forms of degeneracy that are carefully described by Roe and Balsara [43]. We follow the same rescaling procedure of Roe and Balsara to improve the numerical behaviour of the fast/slow magnetoacoustic eigenvectors. The matrix of right eigenvectors is

$$\widehat{\mathbf{R}} = [\,\widehat{\boldsymbol{r}}_{+\mathrm{f}}\,|\,\widehat{\boldsymbol{r}}_{+\mathrm{a}}\,|\,\widehat{\boldsymbol{r}}_{+\mathrm{s}}\,|\,\widehat{\boldsymbol{r}}_{\mathrm{E}}\,|\,\widehat{\boldsymbol{r}}_{\mathrm{D}}\,|\,\widehat{\boldsymbol{r}}_{-\mathrm{s}}\,|\,\widehat{\boldsymbol{r}}_{-\mathrm{a}}\,|\,\widehat{\boldsymbol{r}}_{-\mathrm{f}}\,], \tag{3.25}$$

with the eigenvectors $\widehat{\boldsymbol{r}}$, and corresponding eigenvalues λ [42,43,2]

Entropy and Divergence Waves: $\lambda_{E,D} = u$

$$\widehat{\boldsymbol{r}}_E = \begin{bmatrix} 1 \\ u \\ v \\ w \\ \frac{\|\boldsymbol{u}\|^2}{2} \\ 0 \\ 0 \\ 0 \end{bmatrix}, \quad \widehat{\boldsymbol{r}}_D = \begin{bmatrix} 0 \\ 0 \\ 0 \\ 0 \\ B_1 \\ 1 \\ 0 \\ 0 \end{bmatrix}, \tag{3.26}$$

Alfvén Waves: $\lambda_{\pm a} = u \pm b_1$

$$\widehat{\boldsymbol{r}}_{\pm a} = \begin{bmatrix} 0 \\ 0 \\ \pm\rho^{\frac{3}{2}}\beta_3 \\ \mp\rho^{\frac{3}{2}}\beta_2 \\ \mp\rho^{\frac{3}{2}}(\beta_2 w - \beta_3 v) \\ 0 \\ -\rho\beta_3 \\ \rho\beta_2 \end{bmatrix}, \tag{3.27}$$

Magnetoacoustic Waves: $\lambda_{\pm f,\pm s} = u \pm c_{f,s}$

$$\widehat{\boldsymbol{r}}_{\pm f} = \begin{bmatrix} \alpha_f \rho \\ \alpha_f \rho (u \pm c_f) \\ \rho \left(\alpha_f v \mp \alpha_s c_s \beta_2 \sigma(b_1)\right) \\ \rho \left(\alpha_f w \mp \alpha_s c_s \beta_3 \sigma(b_1)\right) \\ \Psi_{\pm f} \\ 0 \\ \alpha_s a \beta_2 \sqrt{\rho} \\ \alpha_s a \beta_3 \sqrt{\rho} \end{bmatrix}, \qquad \widehat{\boldsymbol{r}}_{\pm s} = \begin{bmatrix} \alpha_s \rho \\ \alpha_s \rho (u \pm c_s) \\ \rho \left(\alpha_s v \pm \alpha_f c_f \beta_2 \sigma(b_1)\right) \\ \rho \left(\alpha_s w \pm \alpha_f c_f \beta_3 \sigma(b_1)\right) \\ \Psi_{\pm s} \\ 0 \\ -\alpha_f a \beta_2 \sqrt{\rho} \\ -\alpha_f a \beta_3 \sqrt{\rho} \end{bmatrix}, \tag{3.28}$$

where we introduced several convenience variables

$$\begin{aligned}
\Psi_{\pm s} &= \frac{\alpha_s \rho \|\boldsymbol{u}\|^2}{2} - a \alpha_f \rho b_\perp + \frac{\alpha_s \rho a^2}{\gamma - 1} \pm \alpha_s c_s \rho u \pm \alpha_f c_f \rho \sigma(b_1)(v\beta_2 + w\beta_3), \\
\Psi_{\pm f} &= \frac{\alpha_f \rho \|\boldsymbol{u}\|^2}{2} + a \alpha_s \rho b_\perp + \frac{\alpha_f \rho a^2}{\gamma - 1} \pm \alpha_f c_f \rho u \mp \alpha_s c_s \rho \sigma(b_1)(v\beta_2 + w\beta_3), \\
c_a^2 &= b_1^2, \quad c_{f,s}^2 = \frac{1}{2}\left((a^2 + b^2) \pm \sqrt{(a^2 + b^2)^2 - 4a^2 b_1^2}\right), \quad a^2 = \gamma \frac{p}{\rho}, \\
b^2 &= b_1^2 + b_2^2 + b_3^2, \quad b_\perp^2 = b_2^2 + b_3^2, \quad \boldsymbol{b} = \frac{\boldsymbol{B}}{\sqrt{\rho}}, \quad \beta_{1,2,3} = \frac{b_{1,2,3}}{b_\perp}, \\
\alpha_f^2 &= \frac{a^2 - c_s^2}{c_f^2 - c_s^2}, \quad \alpha_s^2 = \frac{c_f^2 - a^2}{c_f^2 - c_s^2}, \quad \sigma(\omega) = \begin{cases} +1 & \text{if } \omega \geq 0, \\ -1 & \text{otherwise} \end{cases}.
\end{aligned} \tag{3.29}$$

In (3.29), for the wave speed computation $c_{f,s}^2$, the plus sign corresponds to the fast magnetoacoustic speed, c_f^2, and the minus sign corresponds to the slow magnetoacoustic speed, c_s^2.

The entropy stable dissipation term is built from three components:

- Entropy scaled matrix of right eigenvectors: $\mathring{\mathbf{R}} = \widehat{\mathbf{R}}\sqrt{\mathbf{T}}$, where $\mathbf{T}$ is the diagonal scaling matrix

$$\mathbf{T} = \operatorname{diag}\left(\frac{1}{2\rho\gamma}, \frac{p}{2\rho^3}, \frac{1}{2\rho\gamma}, \frac{\rho(\gamma-1)}{\gamma}, \frac{p}{\rho}, \frac{1}{2\rho\gamma}, \frac{p}{2\rho^3}, \frac{1}{2\rho\gamma}\right). \tag{3.30}$$

  For the complete motivation and details on the entropy scaling of eigenvectors see Barth [42].
- Diagonal matrix of eigenvalues: For `ES-Roe` each wave component is weighted with a different eigenvalue, whereas `ES-LLF` weights all wave components identically

$$|\mathbf{D}_{\mathtt{ES-Roe}}| = \operatorname{diag}\big(|\lambda_{+f}|, |\lambda_{+a}|, |\lambda_{+s}|, |\lambda_E|, |\lambda_D|, |\lambda_{-s}|, |\lambda_{-a}|, |\lambda_{-f}|\big), \tag{3.31a}$$

$$|\mathbf{D}_{\mathtt{ES-LLF}}| = \operatorname{diag}\big(\lambda_{\max}, \lambda_{\max}, \lambda_{\max}, \lambda_{\max}, \lambda_{\max}, \lambda_{\max}, \lambda_{\max}, \lambda_{\max}\big). \tag{3.31b}$$

  The maximum eigenvalue $\lambda_{\max}$ is given by

$$\lambda_{\max} = \max\left(|\lambda_{+f}|, |\lambda_{+a}|, |\lambda_{+s}|, |\lambda_E|, |\lambda_D|, |\lambda_{-s}|, |\lambda_{-a}|, |\lambda_{-f}|\right). \tag{3.32}$$

- Jump in the entropy vector: $[\![\boldsymbol{v}]\!]$
  The term $[\![\boldsymbol{v}]\!]$ is the jump between left and right states of the entropy vector, which is defined as a vector field whose components are partial derivatives of the entropy density (2.8) with respect to the fluid quantities $\mathbf{Q}$,

$$\boldsymbol{v} = \frac{\mathrm{d}S}{\mathrm{d}\mathbf{Q}} = -\left[\frac{\gamma - s}{\gamma - 1} - \frac{\rho\|\boldsymbol{u}\|^2}{2p}, \frac{\rho u}{p}, \frac{\rho v}{p}, \frac{\rho w}{p}, -\frac{\rho}{p}, \frac{\rho B_1}{p}, \frac{\rho B_2}{p}, \frac{\rho B_3}{p}\right]^\mathsf{T}, \tag{3.33}$$

  with the physical entropy, s, defined in (2.8).

The general form of the `ES-Roe`, and `ES-LLF` numerical flux functions is

$$\boldsymbol{F}_{\mathtt{ES}} = \boldsymbol{F}^{*,\mathrm{ec}} + \frac{1}{2}\mathring{\mathbf{R}}|\mathbf{D}|\mathring{\mathbf{R}}^T[\![\boldsymbol{v}]\!], \tag{3.34}$$

where $\boldsymbol{F}^{*,\mathrm{ec}}$ is the entropy conserving numerical flux (3.20). Note that the only difference between the `ES-Roe` and `ES-LLF` stabilizations is in the selection of the diagonal matrix of eigenvalues $\mathbf{D}$. The matrix of right eigenvectors and the

eigenvalues are discretely computed from the previously defined average quantities (3.21) to ensure consistency, in the presence of vanishing magnetic fields, with the entropy stable Euler solver of Ismail and Roe [40].

3.5.2. Hybrid entropy stabilization

Chandrashekar [44] points out that most, if not all, schemes which resolve grid aligned stationary contact discontinuities exactly suffer from the carbuncle effect as the profiles around shocks can exhibit spurious oscillations. This can also be true in our case as our flux function guarantees only the correct sign of the entropy but not necessarily the correct amount of entropy production. However, a flux function must generate *enough* entropy across a shock to guarantee monotonicity [45]. The usual fix for this problem, i.e. increasing the amount of induced dissipation, causes poor resolution of features of boundary layers or near shocks. Another possibility is to switch the numerical scheme to a more dissipative one only near shocks and use a high resolution Riemann solver in smooth parts of the flow [46]. It is straightforward to implement such an idea in the current context because entropy stable schemes have the freedom to select the eigenvalues that essentially control the amount of dissipation.

The local Lax–Friedrichs type scalar dissipation, `ES-LLF`, effectively suppresses the carbuncle phenomenon. However, we want to use the more accurate Roe type matrix dissipation, `ES-Roe`, in regions without large pressure jumps to be able to track smooth parts of the solutions with more accuracy. To achieve this goal we construct a *hybrid entropy stabilization* scheme, called `ES-Hybrid`, that blends the `ES-Roe` and the `ES-LLF` scheme continuously. In the hybrid scheme, a new diagonal matrix of eigenvalues is defined as

$$|\mathbf{D}_{\texttt{ES-Hybrid}}(\Xi)| = (1-\Xi)|\mathbf{D}_{\texttt{ES-Roe}}| + \Xi|\mathbf{D}_{\texttt{ES-LLF}}|, \tag{3.35}$$

with the limits

$$\begin{aligned} \lim_{\Xi\to 0} |\mathbf{D}_{\texttt{ES-Hybrid}}(\Xi)| &= |\mathbf{D}_{\texttt{ES-Roe}}|, \\ \lim_{\Xi\to 1} |\mathbf{D}_{\texttt{ES-Hybrid}}(\Xi)| &= |\mathbf{D}_{\texttt{ES-LLF}}|. \end{aligned} \tag{3.36}$$

As was done in [44], we define the parameter $\Xi \in [0,1]$ using a simple local pressure jump indicator

$$\Xi = \left| \frac{p_L - p_R}{p_L + p_R} \right|^{1/2}. \tag{3.37}$$

From the design of the pressure indicator (3.37), the scheme uses mainly the less dissipative `ES-Roe` scheme for smooth parts of the flow (but also near e.g. contact discontinuities), while the more dissipative `ES-LLF` entropy-stabilization is used near strong shocks.

3.6. Pressure positivity guaranteeing formulation

We next address the issue that negative pressures may be introduced by a numerical scheme. This has been described in previous publications, e.g. [22,19,20]. We present here a general and physically motivated solution to the specific numerical issue of negative pressures.

In a classical higher order Godunov method, the internal energy and thereby the thermal pressure, p_{th}, is obtained by subtracting the kinetic and magnetic energies from the conserved total energy (2.3). In many situations, as in high-Mach number or low plasma-beta flows ($\beta \propto p/\|\boldsymbol{B}\|^2$), the internal energy can be several orders of magnitude smaller then the kinetic or magnetic energies. Thus, discretisation errors in the total energy might be significant enough to result in negative pressures leading to a failure of the numerical scheme. This problem is often addressed by enforcing low pressure limits. However, it is questionable if the simulation can then still give a physically meaningful solution. Therefore, it is important to design a conservative pressure positivity *guaranteeing* scheme that is physically convincing.

3.6.1. Previous investigations

Ryu et al. [22] state that in regions where the gas is very cold compared to the bulk kinetic energy, the flow cannot be treated using the total energy approach as the errors in calculating the total energy can be larger than the internal energy itself. In order to overcome this difficulty, they solve an entropy conservation equation and extract the pressure directly wherever the internal energy is much less than the kinetic energy, i.e. $E_{\text{th}}/E_{\text{kin}} \ll 1$. They present several different criteria used to select whether to compute the pressure from the total energy or from their entropy formulation.

Balsara and Spicer [19] extend the idea of Ryu et al. to MHD flows and present two strategies to prevent negative pressures. Their “strategy 1” is to use the pressure computed from the entropy density only in those cells where the thermal pressure could potentially become negative. In all other cells, they use the thermal pressure given by (2.3). Their “strategy 2” uses the pressure computed from the entropy everywhere except in regions near strong magnetosonic shocks or a flow configuration that may develop such shocks. They justify the validity of their approach by noting that their work deals with magnetospheric problems. There are no shocks present in a magnetosphere, but there still remains a positivity problem.

Li [15] extends the ideas of Balsara and Spicer to an implementation of two new equations: The entropy equation used in [19] and an internal energy equation. Similar to the previously mentioned works, he points out that these equations should not be used close to or within regions that contain shocks. His shock detection scheme sets a floor value for the internal energy in cells near a shock.

Balsara [20] presents a general strategy to address problems where the positivity of density and pressure is uncertain. His work addresses the problem that positivity can be lost when using reconstruction schemes. He presents a self-adjusting strategy for enforcing the positivity of the pressure. However, we realize that the positivity problem of pressure can also be encountered with schemes that are first-order accurate in space and as such do not utilize a reconstruction scheme. This is due to the problem of subtracting large numbers with accordingly large discretisation errors as stated above.

The work of Ersoy et al. [10] relies on improving the resolution in problematic regions. They utilize a discrete measure of the entropy in order to stabilize their computation. They use the local *entropy production* as a mesh refinement criterion on their computational grid.

3.6.2. Derivation of a new pressure formulation

The current solver is built from an entropic perspective. Thus, at any time in the computation, we can compute the entropy density as well as the discrete entropy flux. With these tools we determine a value for the pressure that is guaranteed to be positive. From the computed entropy density for each cell within the computational domain, we use (2.8) to derive a new expression for the pressure in the cells:

$$p_s = \exp\left[\frac{\gamma-1}{\rho}S + \gamma\ln(\rho)\right]. \tag{3.38}$$

From (3.38), it is immediately clear that this "entropy pressure" will always be positive as $\exp(x) > 0, \;\; x \in \mathbb{R}$. Hence, our solver fulfils the desired property of being pressure positivity guaranteeing under all circumstances.

We note that our scheme can be used in a similar way as described by Balsara and Spicer [19]. However, our scheme includes a proper treatment of the entropy at shocks. It is applicable in all regions of the flow and not only in sufficiently smooth regions.

The current scheme is: Use the "normal" scheme as long as the internal energy is large enough after the update with the criterion $E_{\text{int}}/E_{\text{tot}} >$ `smalleint` with the user-definable parameter `smalleint` that defaults to 0.01. If the internal energy is smaller than the criterion, we switch to the entropy pressure formulation without violating the conservation of total energy.

3.6.3. Implementation of the entropy pressure formulation

It is straightforward for a given semi-discrete finite volume method to compute the entropy update of the method. This is because we know how to convert the equations into entropy space. We contract the semi-discrete equations (possibly including some reconstruction technique) (3.8) with the entropy vector (3.33) to obtain

$$\boldsymbol{v}^T\left(\boldsymbol{Q}_t\right)_i = \boldsymbol{v}^T\left(\frac{1}{\Delta x_i}\left(\tilde{\boldsymbol{F}}_{i-1/2} - \tilde{\boldsymbol{F}}_{i+1/2}\right) + \frac{1}{2}\left(\boldsymbol{\Upsilon}_{i-1/2} + \boldsymbol{\Upsilon}_{i+1/2}\right)\right). \tag{3.39}$$

From the chain rule and definition of the entropy vector (3.33) we know that

$$\boldsymbol{v}^T\left(\boldsymbol{Q}_t\right)_i = (S_t)_i\,. \tag{3.40}$$

So, we have an expression for the time evolution of the entropy density

$$(S_t)_i = \boldsymbol{v}^T\left(\frac{1}{\Delta x_i}\left(\tilde{\boldsymbol{F}}_{i-1/2} - \tilde{\boldsymbol{F}}_{i+1/2}\right) + \frac{1}{2}\left(\boldsymbol{\Upsilon}_{i-1/2} + \boldsymbol{\Upsilon}_{i+1/2}\right)\right), \tag{3.41}$$

where, as was shown in [2], the entropy stable fluxes provide a discrete approximation to the spatial derivative of the entropy flux, i.e.

$$\frac{\partial}{\partial x}(uS) \approx \boldsymbol{v}^T\left(\frac{1}{\Delta x_i}\left(\tilde{\boldsymbol{F}}_{i-1/2} - \tilde{\boldsymbol{F}}_{i+1/2}\right) + \frac{1}{2}\left(\boldsymbol{\Upsilon}_{i-1/2} + \boldsymbol{\Upsilon}_{i+1/2}\right)\right). \tag{3.42}$$

Thus, we see that (3.41) is a consistent, discrete update for the entropy. This new discrete equation for the entropy density can be added to the MHD system (2.5) and evolved in time with the other fluid quantities. We reiterate that, by construction, the entropy stable approximation will guarantee that entropy is consistent with the second law of thermodynamics everywhere. Thus, the proposed positive pressure guaranteeing method is valid in any region of the flow. The implemented procedure is:

1. We update the entropy density S^{n+1} with the same time integration scheme used to obtain $\boldsymbol{Q}^{n+1}$.
2. If the updated energies violate the criterion $E_{\text{int}}^{n+1}/E_{\text{tot}}^{n+1} >$ `smalleint`, we use (3.38) to get p_s^{n+1}.
3. Finally, we recompute the updated internal energy from p_s^{n+1} to make the scheme consistent.

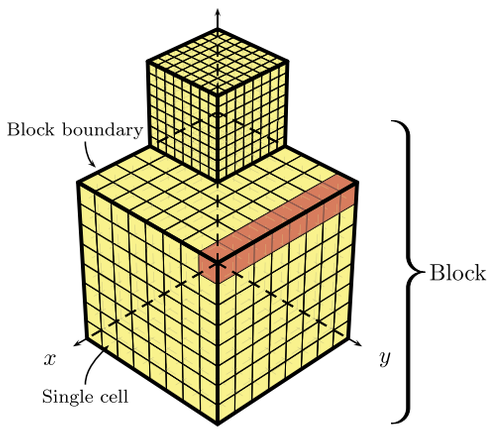

Fig. 3. Two blocks with different levels of refinement (i.e. mesh resolution). A single x sweep is highlighted in red. The guard cells are not shown in this figure.

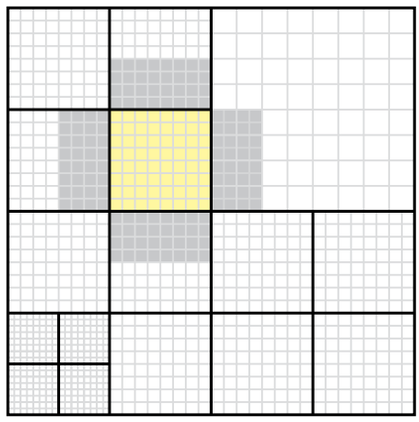

Fig. 4. An adaptive grid 2D simulation with different levels of refinement. The interior cells of one of the blocks are highlighted in yellow. The according guard cells are shown in grey. Guard cells that extend into blocks having a different grid size are interpolated. (For interpretation of the references to colour in this figure legend, the reader is referred to the web version of this article.)

3.7. AMR functionality

FLASH incorporates an adaptive mesh refinement (AMR) strategy using the PARAMESH library [47], through which the grid is organized in a block structured, oct-tree adaptive grid. The presented entropy stable solver is fully incorporated into FLASH's AMR functionality to optimize computational costs. For completeness we briefly discuss the underlying AMR structure, and parallelization in FLASH. With AMR, the local spatial resolution can be dynamically controlled. This allows the maximization of the computational efficiency of the overall simulation as higher resolution is placed only where it is needed.

Parallelization is achieved by dividing the computational domain into several *blocks* (sub-domains). A block contains a number of computational cells (NXB, NYB, and NZB in the x, y, and z-direction, respectively). The default block contains NX | Y | ZB = 8. Each block is surrounded by a fixed number of *guard cells* in each spatial direction, providing the block with information from its neighbouring blocks. The complete computational domain consists of a number of blocks (most likely with different physical sizes). The three-dimensional structure of the blocks is sketched in Fig. 3, while a simple two-dimensional slice through an adaptive grid is shown in Fig. 4. Three rules apply in the creation of refined blocks:

1. A refined block must be one-half of the size of the parent block in each spatial dimension (e.g. each refinement of a block gives 8 additional blocks in three-dimensional computations).
2. Refined blocks must fit within the parent block and are not allowed to overlap into other blocks (they have to be aligned).
3. Blocks sharing a common border are not allowed to differ in more than one level of refinement.

Each block contains all information about local and neighbouring cells, making the blocks with the surrounding guard cells self-contained computational domains which allows efficient parallel computation using the Message Passing Interface (MPI) framework. We configure AMR in such a way that adaptive refinement is allowed after each two consecutive time steps (nrefs = 2).

3.8. Quasi-multifluid implementation

The ability to track the exact composition of a gas is of central importance in astrophysical simulations as they include detailed chemical networks to treat heating, cooling, as well as molecule formation and destruction to mimic the behaviour of the interstellar medium (ISM) [48,33,49].

In order to track the different chemical species in the gas, advection equations of the form

$$\frac{\partial X_\ell \rho}{\partial t} + \nabla \cdot (X_\ell \rho \boldsymbol{u}) = 0, \tag{3.43}$$

are solved, where X_ℓ is the fractional abundance of the ℓth species (H, H^+, H^2, He, etc.) with the unity constraint $\sum_\ell X_\ell = 1$. For each species the flow of the quantity is calculated by multiplying the fractional abundances of the species in the cells with the total density fluxes. Our scheme was originally devised for a perfect gas with a constant ratio of specific heats, γ.

We generalize our scheme for a multi-species fluid with variable γ by adopting a mean value of γ at the cell interfaces as suggested by Murawski [50].

We implement the multi-species advection in a similar way as recommended by Plewa & Müller [51] (known as Consistent Multi-fluid Advection (CMA) method). That is, we ensure that the species fluxes are consistent during the advection. Note that many existing schemes instead normalize the abundances after the advection step. However, as Glover et al. [52] pointed out, this procedure lacks any formal justification and can lead to large systematic errors in the abundance of the least abundant chemical species.

In addition to the multifluid approach using different chemical species, we implement mass tracer fields (also called mass scalars or tracerfields). These are field variables which are advected similar to species mass fractions by an equation of the form

$$\frac{\partial \psi \rho}{\partial t} + \nabla \cdot (\psi \rho \boldsymbol{u}) = 0\,, \tag{3.44}$$

where ψ is the mass fraction, and $\psi\rho$ is the partial density of the traced mass.

Our implementation of the mass tracer fields into the MHD solver allows the use of any number of such fields. Thus, the mass tracer fields are a flexible tool for tracing different mass quantities according to individual requirements. For example, a mass tracer field could be used to follow the distribution of metals in the interstellar gas with virtually no additional computational costs.

3.9. Coupling to gravity

The inclusion of gravity in the ideal MHD equations (2.1) introduces a force into the right-hand side of the momentum equations

$$\frac{\partial}{\partial t}\rho\boldsymbol{u} + \nabla \cdot \left[\rho(\boldsymbol{u}\otimes\boldsymbol{u}) + \left(p + \frac{1}{2}\|\boldsymbol{B}\|^2\right)\mathbf{I} - \boldsymbol{B}\otimes\boldsymbol{B}\right] = -\rho\nabla\phi\,, \tag{3.45}$$

where the gravitational potential ϕ satisfies Poisson's equation

$$\nabla^2\phi = 2\pi G\rho\,, \tag{3.46}$$

with the universal gravitational constant G that is an empirical physical constant involved in the calculations of gravitational forces between two bodies.

`FLASH` provides several algorithms for solving the Poisson equation (3.46). We tested our implementation with a Barns & Hut tree-based algorithm implemented by R. Wünsch (`Poisson/BHTree`) [53] and the Fourier transform-based multigrid algorithm Poisson solver (`Poisson/Multigrid`) [54].

3.10. Magnetic field divergence treatment

Within the MHD equations (2.1), the divergence free condition of the magnetic field (2.2) is not modelled directly. While this constraint is physically fulfilled at any time, we will see that care must be taken to fulfil this constraint numerically.

The extension to higher spatial dimensions, as described in Sec. 3.1, has been performed in a straightforward manner by relying on the Cartesian grid structure. In one dimension the divergence-free condition implies that the longitudinal component of the magnetic field is constant over time. However, this conclusion does not generalize to two and three spatial dimensions.

Instead, due to discretisation errors, a non-zero divergence of the magnetic field occurs over time which inevitably leads to the issue that the conservation of the magnetic flux cannot be maintained. These discretisation errors effectively generate numerical *magnetic monopoles* that grow exponentially during the computation and cause the magnetic field to no longer be solenoidal. From the equations of ideal MHD (2.1) it is clear that these monopoles cause an artificial force parallel to $\boldsymbol{B}$.

In Sec. 2.1, we noted that errors in the divergence-free condition are dealt with by treating the divergence of the magnetic field as an additional fluid quantity to prevent accumulation of errors when the divergence is non-zero in the computational domain. The eigenmode which is advected with the flow in (2.4) is referred to as the *divergence wave*. This procedure might be understood as a form of *divergence cleaning* for the magnetic field. However, numerical experiments show that this approach might not be sufficient to maintain adequate divergence-free magnetic fields throughout simulations.

Concerning divergence cleaning, there are different techniques available (see e.g. [55]). One particular example is the elliptic projection, based on the Helmholtz decomposition, originally developed by Chorin [56]. Brackbill and Barnes [57] and Marder [58] developed a *projection method* in the context of the MHD equations. This method effectively suppresses the growth of unphysical magnetic monopoles locally as shown by Murawski [50] and Tóth [17]. The projection method has successfully been applied by e.g. Zachary et al. [21], Balsara [59], and more recently by Crockett et al. [60]. We implement the projection method for divergence cleaning as a separate post-processing step and note that our original scheme remains unchanged.

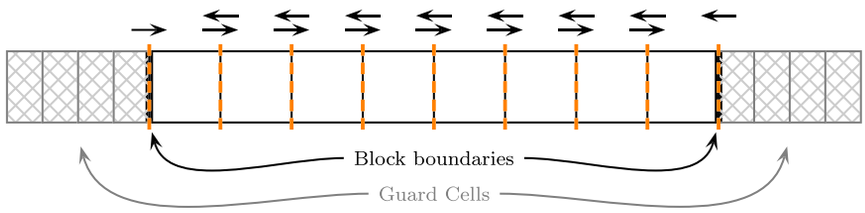

Fig. 5. Principle of the one-dimensional solution update with four guard cells.

The general downside of this scheme may be the high computational costs caused by the projection approach. Our implementation is based of the realization that although the divergence problem is of elliptical character, its influence is only local. Accordingly, we design our implementation of the projection method in a way that is purely local and thereby computationally favourable.

To enforce the divergence-free constraint we subtract the portion of the magnetic field that violates $\nabla \cdot \boldsymbol{B} = 0$. Suppose that the divergence of the magnetic field in the computation is non-zero. An easy fix to this problem is the addition of a correction field $\tilde{\boldsymbol{B}}$ such that

$$\nabla \cdot \left(\boldsymbol{B} + \tilde{\boldsymbol{B}}\right) = 0. \tag{3.47}$$

To guarantee physical consistency of the magnetic field correction, it is clear that $\tilde{\boldsymbol{B}}$ must not cause any additional current

$$\boldsymbol{j} \propto \nabla \times \tilde{\boldsymbol{B}} = 0. \tag{3.48}$$

Hence, we conclude that $\tilde{\boldsymbol{B}}$ must have the form

$$\tilde{\boldsymbol{B}} = \nabla \phi, \tag{3.49}$$

where ϕ is a scalar potential. Combining (3.47) and (3.49) we obtain

$$\Delta \phi = \nabla^2 \phi = -\nabla \cdot \boldsymbol{B}. \tag{3.50}$$

Note that the Laplace operator, Δ, has the physical interpretation for non-equilibrium diffusion as the extent to which a point represents a source or sink of some concentration. The resulting scalar potential can then be used to evaluate $\tilde{\boldsymbol{B}}$ according to (3.49) and, thus, clean the magnetic field $\boldsymbol{B}$:

$$\boldsymbol{B}\Big|_{\nabla \cdot \boldsymbol{B}=0} = \boldsymbol{B} + \tilde{\boldsymbol{B}}. \tag{3.51}$$

By the projection of the cell-centred magnetic fields onto the space of divergence-free magnetic fields, one is left with fields at the next time step which are divergence-free to very good approximation. We note that projecting the magnetic field in the way described is consistent with the underlying cell-centred scheme.

An alternative approach to divergence cleaning that should be mentioned is the constraint transport method developed by Evans and Hawley [61] or Balsara and Spicer [62] (reviewed in [17]). In this approach, the divergence-free constraint is satisfied by placing the staggered magnetic field at cell faces instead of cell centres. On such a grid, the MHD equations can be approximated such that they preserve numerical solenoidality of the magnetic field by construction. Note that Balsara and Kim [63] found advantages for the staggered-mesh in their comparison between divergence-*cleaning* and divergence-*free* methods for stringent test cases. However, the staggered grid approach has the downside of being much more expensive in terms of storage. In addition, it is not clear if provably stable schemes can be constructed for staggered-meshes [64].

The precise implementation of our divergence cleaning approach is described in further detail in Appendix B.

3.11. MHD update procedure

On logically Cartesian grid geometries, it is straightforward to solve multi-dimensional problems as sets of one-dimensional problems by using the *dimensional split* approach. This approach is the principle of the new `ES` solver. The MHD equations are solved as one-dimensional problems along each coordinate direction in turn (x, y, and z-sweeps) in order to determine the fluxes through the finite volume cell surfaces.

Each one-dimensional *sweep* (like the one highlighted in Fig. 5) works as follows:

1. First, the quantities are converted from primitive to conservative form (e.g. velocity to momentum).
2. For y and z-sweeps the solution array is rotated such that we solve this sweep as if it would be an x-sweep. This allow us to use our one-dimensional algorithms without modification.
3. For each cell within the array, the reconstructed quantities $(\tilde{\boldsymbol{Q}}_{i-1})_{\mathrm{R}}$ and $(\tilde{\boldsymbol{Q}}_{i})_{\mathrm{L}}$ are computed using the spatial reconstruction scheme (see Sec. 3.2) at the current time.

4. Then, the entropy stable numerical fluxes as well as the source terms are computed using the algorithms described in Secs. 3.4 and 3.5.

The default behaviour is to use the `ES-Hybrid` flux due to its flexibility. However, the user can easily change which flux function the computation uses with a single switch. Depending on the settings, either the entropy conserving fluxes, $\boldsymbol{F}^{*,\mathtt{ec}}$, the matrix dissipation entropy stable fluxes, $\boldsymbol{F}_{\mathtt{ES-Roe}}$, the scalar dissipation entropy stable fluxes, $\boldsymbol{F}_{\mathtt{ES-LLF}}$, or the hybrid entropy stable fluxes, $\boldsymbol{F}_{\mathtt{ES-Hybrid}}$ are used.

5. After this preparation, the solution array is updated using the time integration scheme described above.
6. The updated internal energies are then derived from the updated total energy.

We update the total energy as it is a conserved quantity. From the updated total energy, we derive the internal energy by subtracting the magnetic and kinetic energies as suggested in [65]:

$$E_{\text{int}}^{n+1} = E_{\text{tot}}^{n+1} - \left(E_{\text{mag}}^{n+1} + E_{\text{kin}}^{n+1}\right) \quad \text{with} \quad E_{\text{mag}}^{n} = \frac{1}{2}\left\|\boldsymbol{B}^{n}\right\|^2, \quad \text{and} \quad E_{\text{kin}}^{n} = \frac{1}{2}\rho^{n}\left\|\boldsymbol{u}^{n}\right\|^2 \tag{3.52}$$

If the computed internal energy fails the criterion $E_{\text{int}}/E_{\text{tot}} > \mathtt{smalleint}$, then the total energy update is done with the pressure computed from the entropy density described in Sec. 3.6.

7. Finally, the variables are converted to primitive form as other `FLASH` modules expect primitive variables.
8. In higher dimensions, the divergence cleaning procedure, described in Sec. 3.10, is used to diffuse away errors in the divergence-free condition as a post-processing step.

4. Numerical results

We demonstrate the utility, robustness, and accuracy of the new solver by computing the solution to several well-known HD and MHD test problems. The version of `FLASH` on hand is 4.3 as of 18th July, 2015. We consider six numerical test cases to test the performance of our new solver and compare to results obtained using already available MHD solver implementations for `FLASH`. A test that extends the well-known Shu–Osher test to MHD is presented in Sec. 4.1 which is used to test the `ES` scheme's artificial dissipation in 1D. The propagation of smooth Alfvén waves is studied in Sec. 4.2. We forgo the presentation of further one-dimensional results as we felt multi-dimensional results were more valuable to the present discussion. The application of the entropy stable MHD solver to the shock tube problems of Brio and Wu [66], Ryu and Jones [67], and Torrilhon [68] can be found in Winters and Gassner [2]. In Sec. 4.3 we further explore the accuracy of the method in multiple spatial dimensions by considering the Orszag–Tang vortex problem. The MHD rotor problem originally proposed by Balsara [62] is investigated in Sec. 4.4. The MHD Rotor is also used in Sec. 4.5 to compare CPU timing and memory consumption of the new `ES` solver and the other schemes. Sec. 4.6 provides an example of using gravity with the new solver by considering the Jeans instability. We note that the Jeans instability is a pure HD configuration and demonstrates that the new MHD solver remains applicable to flows with vanishing magnetic fields. Finally, we test the conservation of the available MHD schemes using the involving MHD blast wave test discussed in Sec. 4.7. All tests, except the Jeans instability test, are performed using dimensionless units. Each test is run with $\mathtt{CFL} = 0.8$ unless specified otherwise.

4.1. MHD version of Shu–Osher test (1D)

The test proposed by Shu and Osher [69] is commonly used to test a scheme's ability to resolve small-scale fluid features in the presence of a supersonic shock. A sinusoidal density/entropy perturbation is added downstream of a Mach 3 shock wave. The interaction of the shock wave with the perturbations gives rise to complex fluid features as the shock amplifies the initial oscillations. This test is an excellent testbed to measure the numerical (artificial) viscosity of a scheme. Additionally, the presence of a supersonic shock is used to demonstrate the robustness and stability of a scheme [70]. We consider a complex MHD version of the Shu–Osher problem recently developed by Susanto [71]. We present the initial conditions for this test in Table 1. The left and right boundaries are taken sufficiently far from the initial discontinuity such that they do not influence the solution. This test has no analytic solution, so we compute a reference solution on a highly refined grid using the `MHD_8Wave` solver for comparison.

Fig. 6 shows the density at $t = 0.7$ for all solvers. Using the same number of cells, we see that the `ES-Hybrid` solver captures the small-scale flow features much better than the other schemes available in `FLASH`. Also, no stability or overshoot problems are visible in the solutions.

According to previous investigations, e.g. [73], a scheme is considered "acceptable" for capturing supersonic turbulence if the dynamics can be captured well with 400 cells. However, the entropy stable scheme is also able to resolve the dynamics of the flow with a much lower spatial resolution (the result used in Fig. 6 is 208 cells in total).

Table 1
Initial conditions and runtime parameters: MHD Shu–Osher test (1D).

	$x \leq x_0$	$x > x_0$
ρ	3.5	$1 + 0.2\sin(5x)$
u	5.8846	0
v	1.1198	0
w	0	0
p	42.0267	1
B_1	1	1
B_2	3.6359	1
B_3	0	0

Domain size	$\{x_{\min}, x_{\max}\} = \{-5, 5\}$
Initial shock location	$x_0 = -4$
Boundary conditions	Zero-gradient ("outflow")
Simulation end time	$t_{\max} = 0.7$
Adiabatic index	$\gamma = 5/3$

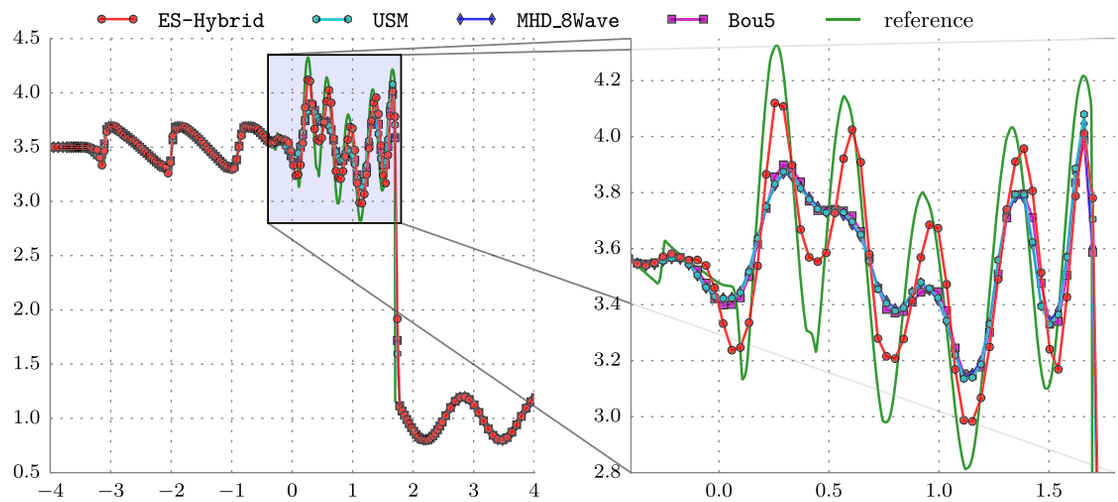

Fig. 6. Density of the MHD Shu–Osher problem at $t = 0.7$. These plots be compared to Fig. 1 of [72] or Fig. 3.9 of [71]. We used an adaptive grid resolution of up to 256 cells. The reference solution is computed on a uniform grid of 4096 cells.

Table 2
Initial conditions and runtime parameters: Smooth Alfvén wave test (1D, 2D).

Density ρ	1.0
Pressure p	0.1
Velocity $\boldsymbol{u}$	$B_\perp \cdot (-\sin(\alpha), \cos(\alpha), 0)^\intercal + B_z \cdot (0, 0, 1)^\intercal$
Mag. field $\boldsymbol{B}$	$B_\parallel \cdot (\cos(\alpha), \sin(\alpha), 0)^\intercal + \boldsymbol{u}$

Domain size	$\{x, y\}_{\min} = \{0.0, 0.0\}$ $\{x, y\}_{\max} = \{1/\cos(\alpha), 1/\sin(\alpha)\}$
Boundary conditions	Periodic
Simulation end time	$t_{\max} = 5.0$
Adiabatic index	$\gamma = 5/3$

4.2. Smooth Alfvén wave (1D, 2D)

The smooth Alfvén wave test [17] is used to compare the accuracy of MHD schemes for smooth flows. The initial circularly polarized Alfvén wave propagates across a periodic domain. For the 2D test, we incline the smooth Alfvén wave by an angle of $\alpha = 45°$ relative to the x-axis. The Alfvén wave speed is $|v_A| = B_\parallel/\sqrt{\rho} = 1$ and thus, the wave is expected to return to its initial state at each time $t \in \mathbb{N}$. This test is run to a final time $t_{\max} = 5.0$ with a CFL number of 0.6. We introduce additional notation for a perpendicular coordinate $x_\parallel = x \cdot \cos(\alpha) + y \cdot \sin(\alpha)$ as well as the parallel, $B_\parallel = 1.0$, and perpendicular, $B_\perp = 0.1\sin(2\pi x_\parallel)$, magnetic fields. The field in z-direction is given by $B_z = 0.1\cos(2\pi x_\parallel)$. The initial conditions listed in Table 2 ensure that the magnetic pressure is constant.

The ability to propagate Alfvén waves over long times and distances is crucial for e.g. MHD turbulence simulations. If the Alfvén waves are damped strongly because of inherent numerical dissipation in a scheme, the code will fail to capture the resulting turbulence behaviour correctly as MHD turbulence is mainly sustained by Alfvén waves [74].

4.2.1. One dimensional test

In the one dimensional smooth Alfvén wave test we check the spatial high resolution properties of our scheme. For sufficiently smooth fields, i.e. in cases where discontinuous features are absent, the used reconstruction technique is designed to achieve third order accuracy (see Sec. 3.2).

To test the accuracy of our scheme, we run several simulations with varying resolutions and compute the L_1 and L_2 errors for the quantity $B_\perp = B_y\cos(\alpha) - B_x\sin(\alpha)$ as described in Appendix E. The obtained errors are plotted as a function

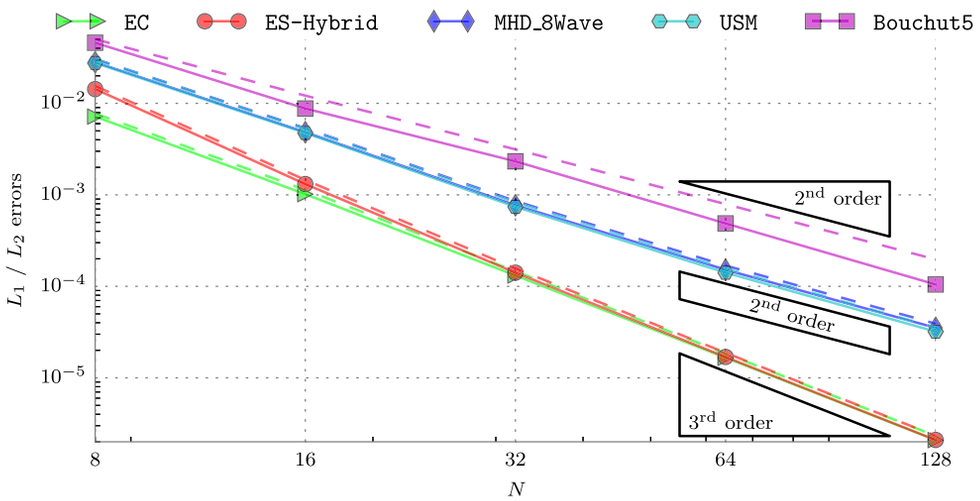

Fig. 7. L_1 (solid lines) and L_2 (dashed lines) errors measured with the smooth Alfvén wave test in 1D. We omit the lines for the `ES-Roe` and `ES-LLF` schemes as they are visually indistinguishable from `ES-Hybrid` (cf. Table 3).

Table 3
Computed errors and experimental order of convergence (EOC) for B_2 after five oscillation of the Alfvén wave in one dimension ($t = 5.0$). Sorted by increasing errors from left to right.

		EC	ES-Roe	ES-Hybrid	ES-LLF	USM	MHD_8Wave	Bouchut5
$N = 8$	L_1 error	$7.17 \cdot 10^{-3}$	$< 1.43 \cdot 10^{-2}$	$= 1.43 \cdot 10^{-2}$	$= 1.43 \cdot 10^{-2}$	$< 2.76 \cdot 10^{-2}$	$\approx 2.81 \cdot 10^{-2}$	$< 4.60 \cdot 10^{-2}$
	L_2 error	$7.76 \cdot 10^{-3}$	$< 1.55 \cdot 10^{-2}$	$= 1.55 \cdot 10^{-2}$	$= 1.55 \cdot 10^{-2}$	$< 3.00 \cdot 10^{-2}$	$\approx 3.06 \cdot 10^{-2}$	$< 5.03 \cdot 10^{-2}$
$N = 16$	L_1 error	$1.02 \cdot 10^{-3}$	$< 1.31 \cdot 10^{-3}$	$= 1.31 \cdot 10^{-3}$	$= 1.31 \cdot 10^{-3}$	$< 4.74 \cdot 10^{-3}$	$< 4.84 \cdot 10^{-3}$	$< 8.78 \cdot 10^{-3}$
	L_2 error	$1.13 \cdot 10^{-3}$	$< 1.46 \cdot 10^{-3}$	$= 1.46 \cdot 10^{-3}$	$= 1.46 \cdot 10^{-3}$	$< 5.24 \cdot 10^{-3}$	$< 5.35 \cdot 10^{-3}$	$< 1.21 \cdot 10^{-2}$
	EOC (L_1)	2.82	3.45	3.45	3.45	2.54	2.54	2.39
	EOC (L_2)	2.78	3.41	3.41	3.41	2.52	2.52	2.05
$N = 32$	L_1 error	$1.31 \cdot 10^{-4}$	$< 1.41 \cdot 10^{-4}$	$= 1.41 \cdot 10^{-4}$	$= 1.41 \cdot 10^{-4}$	$< 7.41 \cdot 10^{-4}$	$< 7.69 \cdot 10^{-4}$	$< 2.33 \cdot 10^{-3}$
	L_2 error	$1.46 \cdot 10^{-4}$	$< 1.57 \cdot 10^{-4}$	$= 1.57 \cdot 10^{-4}$	$= 1.57 \cdot 10^{-4}$	$< 8.24 \cdot 10^{-4}$	$< 8.56 \cdot 10^{-4}$	$< 3.14 \cdot 10^{-3}$
	EOC (L_1)	2.95	3.22	3.22	3.22	2.68	2.65	1.92
	EOC (L_2)	2.95	3.21	3.21	3.21	2.67	2.64	1.95
$N = 64$	L_1 error	$1.66 \cdot 10^{-5}$	$\approx 1.69 \cdot 10^{-5}$	$= 1.69 \cdot 10^{-5}$	$= 1.69 \cdot 10^{-5}$	$\ll 1.41 \cdot 10^{-4}$	$< 1.52 \cdot 10^{-4}$	$< 4.87 \cdot 10^{-4}$
	L_2 error	$1.85 \cdot 10^{-5}$	$\approx 1.88 \cdot 10^{-5}$	$= 1.88 \cdot 10^{-5}$	$= 1.88 \cdot 10^{-5}$	$\ll 1.57 \cdot 10^{-4}$	$< 1.69 \cdot 10^{-4}$	$< 7.92 \cdot 10^{-4}$
	EOC (L_1)	2.98	3.06	3.06	3.06	2.39	2.34	2.25
	EOC (L_2)	2.99	3.06	3.06	3.06	2.39	2.34	1.99
$N = 128$	L_1 error	$2.09 \cdot 10^{-6}$	$\approx 2.10 \cdot 10^{-6}$	$= 2.10 \cdot 10^{-6}$	$= 2.10 \cdot 10^{-6}$	$\ll 3.20 \cdot 10^{-5}$	$< 3.52 \cdot 10^{-5}$	$< 1.05 \cdot 10^{-4}$
	L_2 error	$2.32 \cdot 10^{-6}$	$\approx 2.33 \cdot 10^{-6}$	$= 2.33 \cdot 10^{-6}$	$= 2.33 \cdot 10^{-6}$	$\ll 3.55 \cdot 10^{-5}$	$< 3.91 \cdot 10^{-5}$	$< 1.97 \cdot 10^{-4}$
	EOC (L_1)	2.99	3.01	3.01	3.01	2.14	2.11	2.22
	EOC (L_2)	2.99	3.01	3.01	3.01	2.14	2.11	2.01

of the number of grid points in logarithmic scale in Fig. 7 and are listed in Table 3. As can be seen, third order accuracy is achieved, already at very low resolutions.

Fig. 8 shows $B_\perp$ vs. $x_\perp$ at time $t = 5$ for the one dimensional Alfvén wave test. As we know that the solution is smooth, we disable the entropy stabilization term described in Sec. 2.2 and obtain an entropy conserving `EC` scheme (▶—▶). The `EC` solution shows very little dissipation. Note that the `EC` scheme is only applicable to smooth solutions and should not be used for arbitrary flows. We observe that the different `ES` schemes (▼—▼, △—△, and ●—●) resolve the Alfvén wave with the least dissipation of all tested MHD solvers (except the entropy conserving scheme) while their results are virtually identical. The `MHD_8Wave` implementation (◆—◆) [28,70] as well as the unsplit `USM` implementation (⬢—⬢) [75,76,70] are considerably more diffusive. They show second order convergence. Finally, we note that the `Bouchut5` implementation (■—■) [12] has the highest measured amount of dissipation for this one dimensional test case.

4.2.2. Two dimensional test

Fig. 9 shows $B_\perp$ vs. $x_\perp$ at time $t = 5$ for the two dimensional Alfvén wave test. The `EC` solution (▶—▶) shows again very little dissipation. As before, the `ES` schemes resolve the Alfvén wave with the least dissipation of all tested MHD solvers while the `ES-Roe` scheme (▼—▼) is least dissipative and the `ES-LLF` scheme (△—△) is slightly more diffusive. As expected for smooth problems, the `ES-Hybrid` scheme (●—●) gives results that are identical to those computed using the

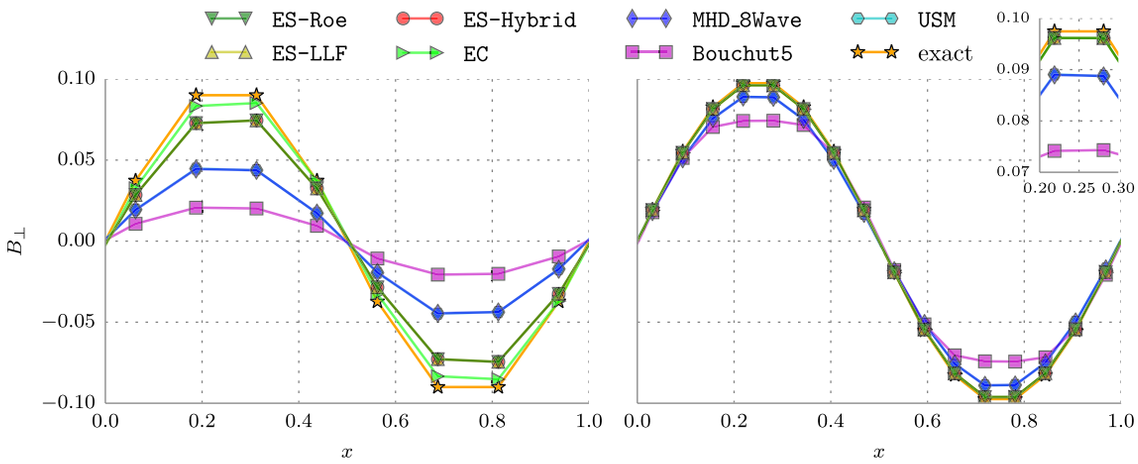

Fig. 8. Smooth Alfvén wave test after five crossing times. For the left plot, we used a fixed grid of 8 cells. For the right plot we use a grid of 16 cells. The *exact* solution shows the initial configuration at the given resolution.

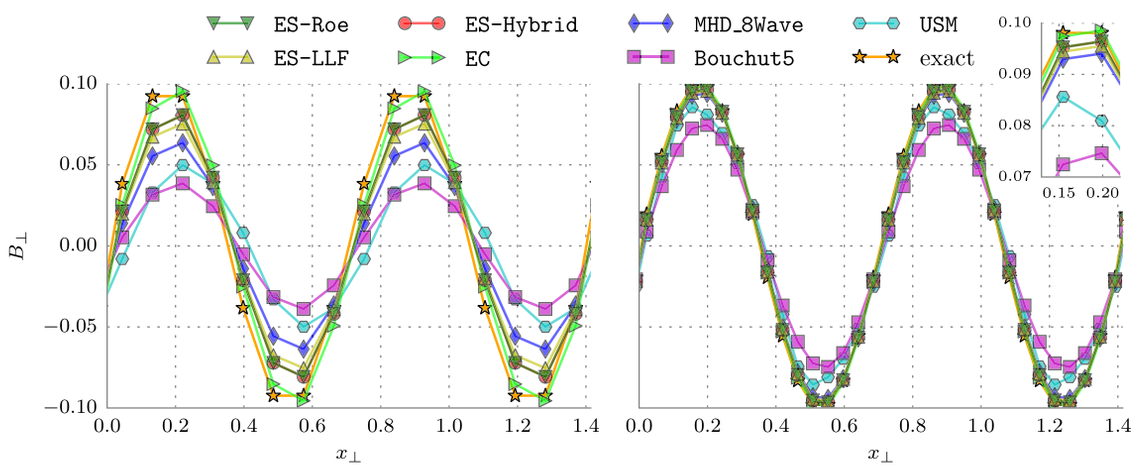

Fig. 9. Smooth Alfvén wave test after five crossing times. These plots be compared to Fig. 8 of [17] or Fig. 4 of [4]. For the left plot, we used a fixed grid of 16×16 cells. For the right plot we use a grid of 32×32 cells. The *exact* solution shows the initial configuration at the given resolution. We use `CFL` $= 0.6$ to remove artificial wave steeping effects in the `USM` solver solution.

`ES-Roe` scheme. The `MHD_8Wave` implementation (◆) gives similar results compared to the `ES` solver but is slightly more diffusive. The unsplit `USM` implementation (⬢) shows a higher dissipation compared to the `ES` or `MHD_8Wave` implementations and its zero-crossing points are clearly shifted at the lower resolution run. We find that the `Bouchut5` implementation (■) has the highest amount of dissipation for this smooth test case. Note that the dissipation of the Alfvén waves is significantly reduced in higher dimensions if multidimensional Riemann solvers with sub-structure are used, as was shown by Balsara [74].

In Fig. 10 we plot the evolution of the conserved quantities as well as the individual energies. Looking, for example, at the magnetic energy, E_{mag}, it can be seen that the `EC` scheme introduces the least amount of dissipation. It is followed by our entropy stable schemes `ES-Roe`/`ES-Hybrid` and `ES-LLF`. The `MHD_8Wave` and the `USM` implementations show higher dissipation while the `Bouchut5` implementation shows the highest amount of dissipation. If one would only look at the internal energy, one might conclude that the `MHD_8Wave` solver introduces even less dissipation that the `ES` schemes. However, one has to be cautious with such a conclusion because both `MHD_8Wave` as well as `Bouchut5` fail to preserve total energy conservation.

We list the computed L_1 and L_2 errors for the quantity $B_\perp$ in Table 4. They support our conclusions given above, e.g. `ES-Roe` and `ES-Hybrid` give identical solutions for smooth problems. Due to dimensional splitting, the obtained results are only second-order accurate in space.

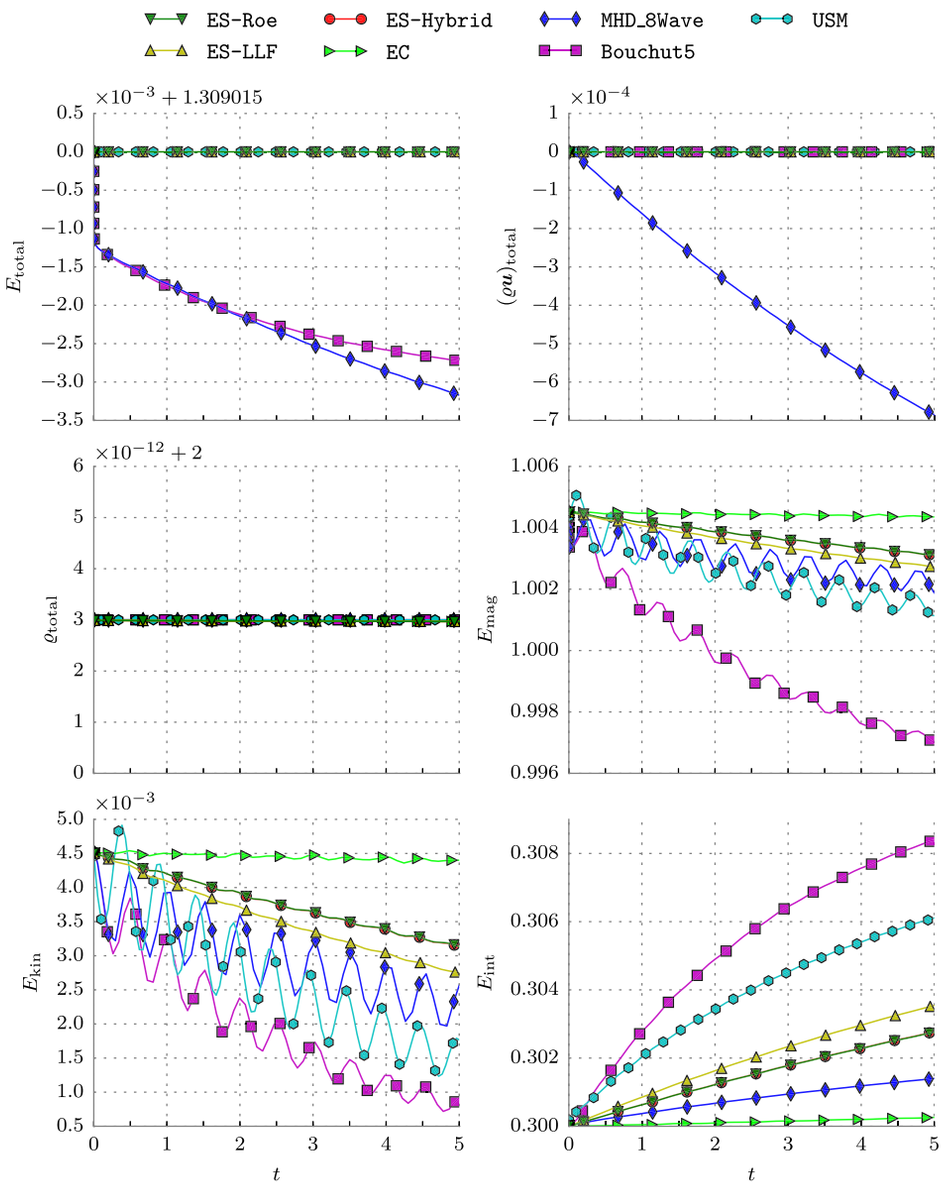

Fig. 10. Evolution of the conserved quantities as well as the individual energies in the smooth Alfvén wave test over five crossing times (16×16 cells).

4.3. Orszag–Tang MHD vortex (2D)

The Orszag–Tang vortex problem [77] is a two-dimensional, spatially periodic problem well suited for studies of MHD turbulence. Thus, it has become a classical test for numerical MHD schemes. It includes dissipation of kinetic and magnetic energy, magnetic reconnection, formation of high-density jets, dynamic alignment and the emergence and manifestation of small-scale structures. The Orszag–Tang MHD vortex problem starts from non-random, smooth initial data. As the flow evolves it gradually becomes increasingly complex, forming intermediate shocks. Thus, this problem demonstrates the transition from initially smooth data to compressible, supersonic MHD turbulence. The initial data is chosen such that the root mean square values of the velocity and the magnetic fields as well as the initial Mach number are all one. The average plasma beta is $\beta = \frac{10}{3}$.

Additionally, we compute the experimental convergence order for the available MHD schemes after 10% of the total runtime. At this time, the solution is already very complex but still smooth. As there is no analytic solution available, we compare to a high resolution simulation obtained using our entropy-conserving (`EC`) scheme on an uniform grid of

Table 4
Computed errors and experimental order of convergence (EOC) for $B_\perp$ after five oscillation of the Alfvén wave in two dimensions ($t = 5.0$). Sorted by increasing errors from left to right.

		EC	ES-Roe	ES-Hybrid	ES-LLF	MHD_8Wave	USM	Bouchut5
$N = 16$	L_1 error	$8.34 \cdot 10^{-3}$	$< 1.34 \cdot 10^{-2}$	$= 1.34 \cdot 10^{-2}$	$< 1.62 \cdot 10^{-2}$	$< 2.43 \cdot 10^{-2}$	$< 3.96 \cdot 10^{-2}$	$< 4.15 \cdot 10^{-2}$
	L_2 error	$9.26 \cdot 10^{-3}$	$< 1.47 \cdot 10^{-2}$	$= 1.48 \cdot 10^{-2}$	$< 1.80 \cdot 10^{-2}$	$< 2.69 \cdot 10^{-2}$	$< 4.39 \cdot 10^{-2}$	$< 4.54 \cdot 10^{-2}$
$N = 32$	L_1 error	$1.83 \cdot 10^{-3}$	$< 2.36 \cdot 10^{-3}$	$= 2.36 \cdot 10^{-3}$	$< 2.76 \cdot 10^{-3}$	$< 3.61 \cdot 10^{-3}$	$< 1.11 \cdot 10^{-2}$	$< 1.67 \cdot 10^{-2}$
	L_2 error	$2.05 \cdot 10^{-3}$	$< 2.64 \cdot 10^{-3}$	$= 2.64 \cdot 10^{-3}$	$< 3.06 \cdot 10^{-3}$	$< 3.94 \cdot 10^{-3}$	$< 1.19 \cdot 10^{-2}$	$< 1.84 \cdot 10^{-2}$
	EOC (L_1)	2.19	2.50	2.51	2.55	2.75	1.83	1.31
	EOC (L_2)	2.17	2.48	2.49	2.56	2.77	1.88	1.30
$N = 64$	L_1 error	$4.36 \cdot 10^{-4}$	$< 4.73 \cdot 10^{-4}$	$= 4.73 \cdot 10^{-4}$	$< 5.10 \cdot 10^{-4}$	$< 6.78 \cdot 10^{-4}$	$< 4.03 \cdot 10^{-3}$	$< 7.79 \cdot 10^{-3}$
	L_2 error	$4.93 \cdot 10^{-4}$	$< 5.37 \cdot 10^{-4}$	$= 5.37 \cdot 10^{-4}$	$< 5.73 \cdot 10^{-4}$	$< 7.38 \cdot 10^{-4}$	$< 4.85 \cdot 10^{-3}$	$< 8.65 \cdot 10^{-3}$
	EOC (L_1)	2.06	2.32	2.32	2.44	2.41	1.46	1.10
	EOC (L_2)	2.06	2.30	2.30	2.41	2.42	1.30	1.09
$N = 128$	L_1 error	$1.08 \cdot 10^{-4}$	$\approx 1.10 \cdot 10^{-4}$	$= 1.10 \cdot 10^{-4}$	$\approx 1.12 \cdot 10^{-4}$	$< 1.56 \cdot 10^{-4}$	$< 1.57 \cdot 10^{-3}$	$< 3.87 \cdot 10^{-3}$
	L_2 error	$1.22 \cdot 10^{-4}$	$\approx 1.25 \cdot 10^{-4}$	$= 1.25 \cdot 10^{-4}$	$\approx 1.28 \cdot 10^{-4}$	$< 1.73 \cdot 10^{-4}$	$< 1.89 \cdot 10^{-3}$	$< 4.30 \cdot 10^{-3}$
	EOC (L_1)	2.01	2.10	2.10	2.18	2.12	1.36	1.01
	EOC (L_2)	2.01	2.10	2.10	2.16	2.09	1.36	1.01

Table 5
Initial conditions and runtime parameters: Orszag–Tang MHD vortex test.

Density ρ	1.0
Pressure p	$1.0/\gamma$
Velocity $\boldsymbol{u}$	$(-\sin(2\pi y), \sin(2\pi x), 0.0)^\intercal$
Mag. field $\boldsymbol{B}$	$\frac{1}{\gamma}(-\sin(2\pi y), \sin(4\pi x), 0.0)^\intercal$

Domain size	$\{x, y\}_{\min} = \{0.0, 0.0\}$ $\{x, y\}_{\max} = \{1.0, 1.0\}$
Boundary conditions	All: periodic
Adaptive refinement on	Density, magnetic field
Simulation end time	$t_{\max} = 0.5$
Adiabatic index	$\gamma = 5/3$

Table 6
Computed errors and experimental order of convergence (EOC) for $p_{\text{mag}} = \frac{1}{2}\|\boldsymbol{B}\|^2$ before the onset of discontinuities in the Orszag–Tang MHD vortex test ($t = 0.05$).

		EC	ES-Hybrid	Bouchut5	USM	MHD_8Wave
$N = 16$	L_1 error	$6.59 \cdot 10^{-3}$	$< 7.00 \cdot 10^{-3}$	$< 7.25 \cdot 10^{-3}$	$< 8.08 \cdot 10^{-3}$	$< 8.18 \cdot 10^{-3}$
	L_2 error	$8.51 \cdot 10^{-3}$	$< 8.71 \cdot 10^{-3}$	$< 9.32 \cdot 10^{-3}$	$< 1.02 \cdot 10^{-2}$	$\approx 1.03 \cdot 10^{-2}$
$N = 32$	L_1 error	$1.60 \cdot 10^{-3}$	$\approx 1.63 \cdot 10^{-3}$	$< 2.08 \cdot 10^{-3}$	$\approx 2.09 \cdot 10^{-3}$	$\approx 2.12 \cdot 10^{-3}$
	L_2 error	$2.02 \cdot 10^{-3}$	$\approx 2.06 \cdot 10^{-3}$	$< 2.65 \cdot 10^{-3}$	$\approx 2.69 \cdot 10^{-3}$	$\approx 2.63 \cdot 10^{-3}$
	EOC (L_1)	2.04	2.10	1.80	1.95	1.95
	EOC (L_2)	2.07	2.08	1.81	1.93	1.96
$N = 64$	L_1 error	$4.01 \cdot 10^{-4}$	$\approx 3.99 \cdot 10^{-4}$	$< 5.13 \cdot 10^{-4}$	$< 5.55 \cdot 10^{-4}$	$\approx 5.55 \cdot 10^{-4}$
	L_2 error	$5.17 \cdot 10^{-4}$	$\approx 5.14 \cdot 10^{-4}$	$< 6.60 \cdot 10^{-4}$	$< 7.25 \cdot 10^{-4}$	$> 7.06 \cdot 10^{-4}$
	EOC (L_1)	2.00	2.03	2.02	1.91	1.93
	EOC (L_2)	1.97	2.00	2.01	1.81	1.90

1024×1024 cells. We compute the L_1 and L_2 errors as well as the experimental order of convergence and list them in Table 6. They coincide with our results presented in the preceding section. As in Sec. 4.2, we find the results to be at most second-order accurate in space due to dimensional splitting.

Fig. 11 displays the evolution of the density of a plasma given the initial conditions listed in Table 5. As the solution evolves in time, the initial vortex splits into two vortices. Sharp gradients accumulate and the vortex pattern becomes increasingly complex due to highly non-linear interactions between multiple intermediate shock waves travelling at different speeds. The result compares very well with results given in the literature, e.g. [78–80], as well as with the solution of the Orszag–Tang MHD vortex obtained using the `MHD_8Wave`, the `Bouchut5`, and the unsplit `USM` implementations (shown in Fig. 12).

4.4. MHD rotor (2D)

The MHD rotor problem [62] describes a rapidly spinning dense cylinder embedded in a magnetized, homogeneous medium at rest. Due to centrifugal forces, the dense cylinder is in non-equilibrium. As the rotor spins with the given initial rotating velocity, the initially uniform magnetic field will wind up the rotor. The wrapping of the rotor by the magnetic field leads to strong torsional Alfvén waves launched into the ambient fluid. Due to the onset and propagation of strong Alfvén waves, this test is relevant for the understanding of star formation. The initial conditions are listed in Table 7.

This test demonstrates that our solver is able to resolve torsional Alfvén waves, which is particularly visible in the plot of the magnetic pressure (right plot in Fig. 13). The Mach number M (see Fig. 13) shows that the rotor is, up to a certain

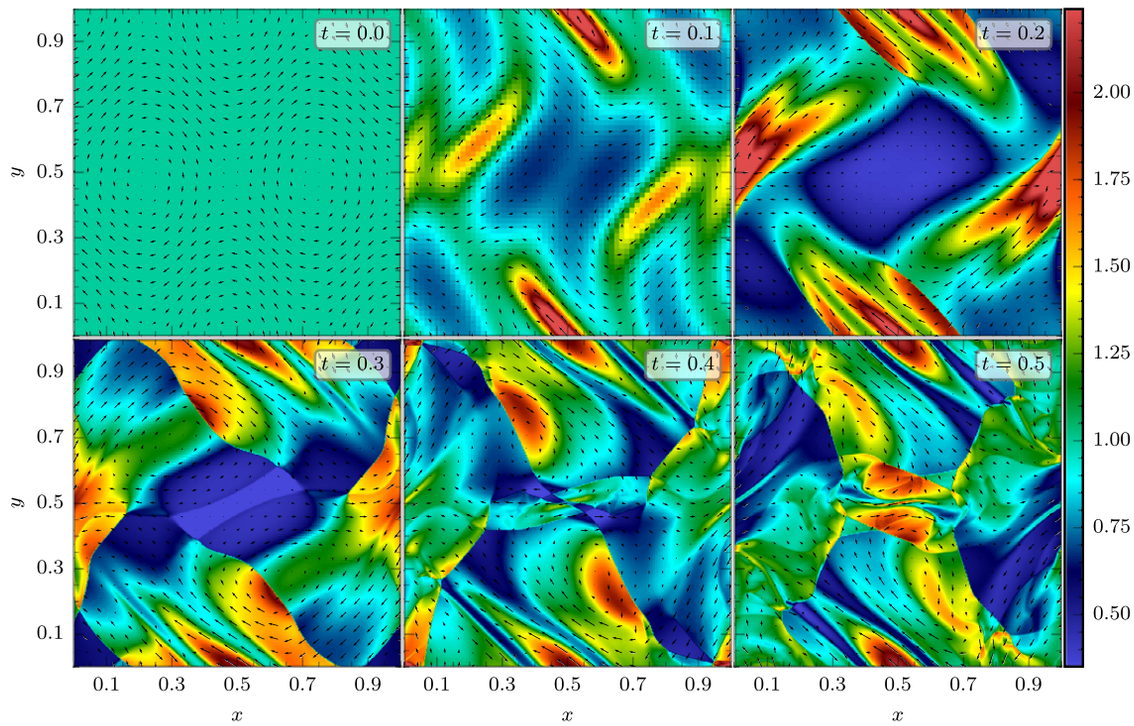

Fig. 11. Orszag–Tang MHD vortex test: Density plots with superimposed magnetic field directions. `ES-Hybrid` scheme with an adaptive grid resolution up to 512×512. The time step is shown in the upper right corner of each plot. These plots can be compared to e.g. Fig. 1 of [78]. The lower right plot ($t = 0.5$) can be compared to e.g. Fig. 10 of [79] and Fig. 14 of [80].

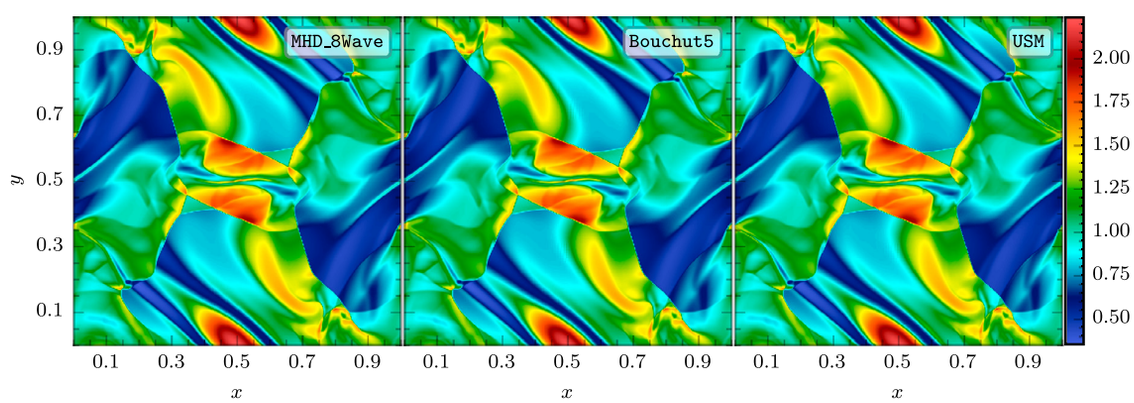

Fig. 12. Orszag–Tang MHD vortex test: Density plots with an adaptive grid resolution up to 512×512 at $t = 0.5$. The MHD solver used is given in the upper right corner of each plot.

radial distance, still in uniform rotation. Beyond this radius, the rotor has exchanged momentum with its environment and decelerated. In the left plot of Fig. 13 we present the magnetic field superimposed on the fluid density, ρ. It is clearly seen that the magnetic field basically maintains its initial shape outside of the region of influence of the Alfvén waves. Inside, the magnetic field is refracted by the MHD discontinuities. In Fig. 14 we present six snapshots of the evolution of the fluid density (as well as the AMR grid) up to the final time $t = t_{\text{max}}$. This is shortly before the torsional Alfvén waves leave the computational domain and after the cylinder has rotated almost 180°.

4.5. Comparison of computational efficiency (2D)

We perform a memory and CPU time comparison on a uniform grid. We compare the new `ES` solver implementation against the Bouchut 5 wave (`Bouchut5`) [12], Powell's 8 wave (`MHD_8Wave`) [28], and the unsplit staggered mesh (`USM`)

Table 7
Initial conditions and runtime parameters: MHD rotor test.

	$r \le r_0$	$r \in (r_0, r_1)$	$r \ge r_1$
ρ	10.0	$1.0 + 9.0 f(r)$	1.0
p	1.0	1.0	1.0
B_1	$5/\sqrt{4\pi}$	$5/\sqrt{4\pi}$	$5/\sqrt{4\pi}$
B_2	0.0	0.0	0.0
B_3	0.0	0.0	0.0
u	$-20.0\Delta y$	$-20.0 f(r)\Delta y$	0.0
v	$20.0\Delta x$	$20.0 f(r)\Delta x$	0.0
w	0.0	0.0	0.0

With $r = \sqrt{(x - x_{\text{centre}})^2 + (y - y_{\text{centre}})^2}$, $\Delta x = (x - x_{\text{centre}})$, $\Delta y = (y - y_{\text{centre}})$, and $f(r) = \frac{r_1 - r}{r_1 - r_0}$

Domain size	$\{x, y\}_{\text{min}} = \{0.0, 0.0\}$ $\{x, y\}_{\text{max}} = \{1.0, 1.0\}$
Inner radius	$r_0 = 0.1$
Outer radius	$r_1 = 0.115$
x-Centre	$x_{\text{centre}} = 0.5$
y-Centre	$y_{\text{centre}} = 0.5$
Boundary conditions	All: zero-gradient ("outflow")
Adaptive refinement on	Density, magnetic field
Simulation end time	$t_{\text{max}} = 0.15$
Adiabatic index	$\gamma = 1.4$

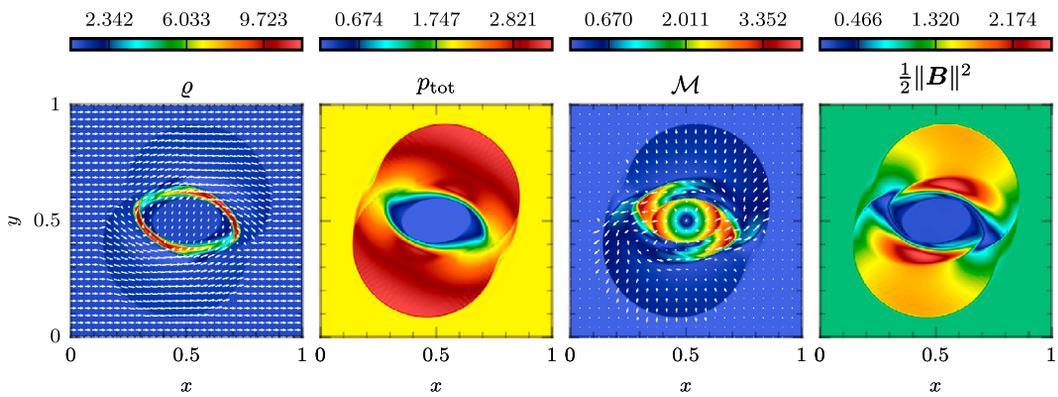

Fig. 13. MHD rotor test: Adaptive grid resolution up to 512×512. From left to right: density ρ with overlayed magnetic field, total pressure $p_{\text{tot}} = p + p_{\text{mag}}$, Mach number $\mathcal{M}$ with overlayed velocity vectors, and magnetic pressure $p_{\text{mag}} = \frac{1}{2}\|\boldsymbol{B}\|^2$. This plot can directly be compared to Fig. 7 of [2], Fig. 14 of [79], and Fig. 2 of [62].

[75,76] solver implementations applied to the MHD Rotor problem, described in the preceding section. For this test we use identical runtime parameters. The AMR grid is fixed to level 5.

We present the results of the study in Table 8. Note that the effective computational costs are very implementation specific. We see that the `ES` solver uses slightly less memory than the other schemes. The `ES` solver needs more computational time per time step since the Runge–Kutta time integration scheme involves the full flux computation and spatial reconstruction procedure in each of the intermediate stages. The higher computational costs per time step can be – at least partially – compensated by choosing a larger `CFL` coefficient. We neglect this benefit here and run all simulations with a fixed `CFL` number to give a fair comparison. For `USM` we use a second order accurate Roe-type Riemann solver, previously used for the numerical tests in [76].

4.6. Gravitational instability

A particularly simple example of gravitational instability was discovered by Jeans [81]. This phenomenon is of great astrophysical interest in the context of star formation and cosmic structure growth. The configuration is a useful test for the coupling of multi-dimensional gravity to hydrodynamics in a computational code. The Jeans instability allows one to study the pressure dominated and gravity dominated limits as well as the numerical method's behaviour between the two limits. We start from an infinite homogeneous medium at rest and consider a small perturbation in density. We shall suppose that the initial fluctuations in density and pressure take place adiabatically, so that $p_0 = \gamma \rho_0$. The initial conditions for this test are summarized in Table 9. We use the direct multigrid fast Fourier transform Poisson solver (`Grid/GridSolvers/Multigrid/fft`) for the computation of the gravitational source term.

We obtain the dispersion relation of a self-gravitating fluid by solving the perturbed wave equations by planar wave solutions in Fourier space. From the relation,

$$\omega^2 = a_0^2 k^2 - 4\pi G \rho_0, \tag{4.1}$$

we define the *Jeans wavenumber*

$$k_J = \frac{\sqrt{4\pi G \rho_0}}{a_0} \approx 2.75 \tag{4.2}$$

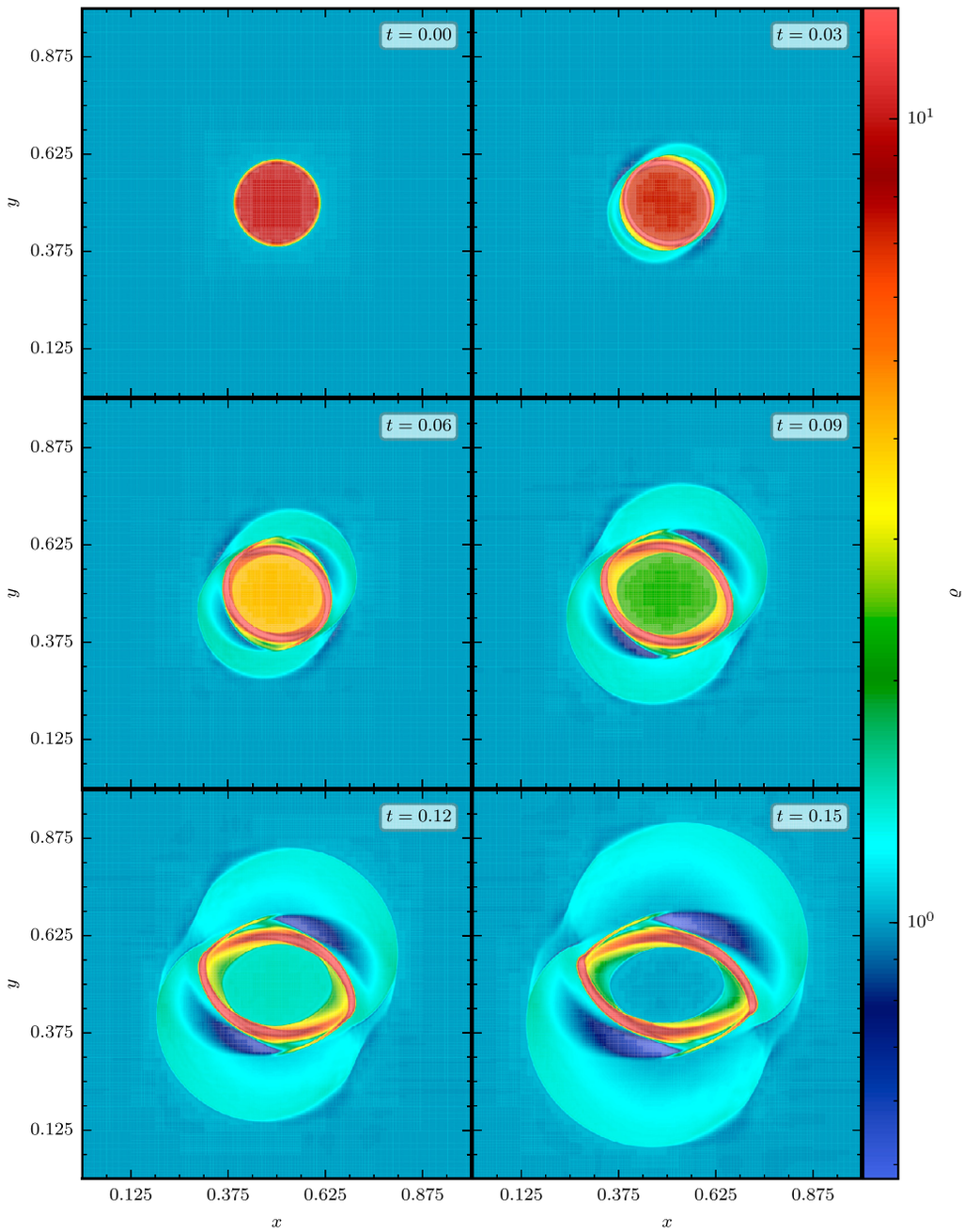

Fig. 14. MHD rotor test: Density evolution on a logarithmic scale with superimposed AMR grid. Adaptive grid resolution up to level 8 (up to 1024×1024 cells).

with the gravitational constant, $G = 6.674 \cdot 10^{-8}\ \mathrm{cm^3\,g^{-1}\,s^{-2}}$, and the adiabatic sound speed $a_0 = \sqrt{\gamma\, p_0/\rho_0} \approx 1.29\ \mathrm{cm\,s^{-1}}$ where the given numbers correspond to the initial conditions used. The Jeans wavenumber number is very important as it defines a scale on which gravitational effect become dominant in astrophysical systems. As long as $k > k_J$, the perturbation is stable and oscillates with a real frequency of ω. This is the case with our chosen initial conditions, as $k \approx 11 > 2.75 \approx k_J$. However, if $k < k_J$, the perturbation grows exponentially in time as ω is purely imaginary. An overdense region would become denser and denser, leading to gravitational collapse [82]. We compute the oscillation frequency, ω, by measuring the time interval required for the energy to undergo exactly ten oscillations. The analytical expression for the kinetic, internal, and potential energies are provided in Appendix A.

Table 8
Comparison of computational efficiency. The memory consumption is measured for the whole `flash4` process, while the computational time corresponds only to the time used by the MHD solver as given by `FLASH`'s code performance summary.

Scheme	Memory consumption (MB)	CPU time (s)
`ES`	**88.5**	**11.18**
`Bouchut5`	90.7	7.43
`MHD_8Wave`	95.4	7.80
`USM`	143.5	12.16

Table 9
Runtime parameters and initial conditions: Jeans Instability test (2D).

Density ρ [g cm^{-3}]	$\rho_0 \cdot [1 + \delta(\boldsymbol{x})]$
Pressure p [dyn cm^{-2}]	$p_0 \cdot [1 + \gamma\delta(\boldsymbol{x})]$
Perturbation $\delta(\boldsymbol{x})$	$\delta_0 \cdot \cos(\boldsymbol{k} \cdot \boldsymbol{x})$
Velocity $\boldsymbol{u}$ [cm s^{-1}]	$\mathbf{0}$
Magnetic field $\boldsymbol{B}$ [G]	$\mathbf{0}$

With $\rho_0 = 1.5 \cdot 10^7$ g cm^{-3}, $\delta_0 = 1 \cdot 10^{-3}$, and $p_0 = 1.5 \cdot 10^7$ dyn cm^{-2}

Domain size [cm]	$\{x, y\}_{\min} = \{0.0, 0.0\}$ $\{x, y\}_{\max} = \{1.0, 1.0\}$
Boundary conditions	All: periodic
Simulation end time [s]	$t_{\max} = 5.0$
Adiabatic index	$\gamma = 5/3$
Wave vector $\boldsymbol{k}$ [cm^{-1}]	$2\pi/\lambda$ with $\boldsymbol{\lambda} = (0.5, 0, 0)^\intercal$

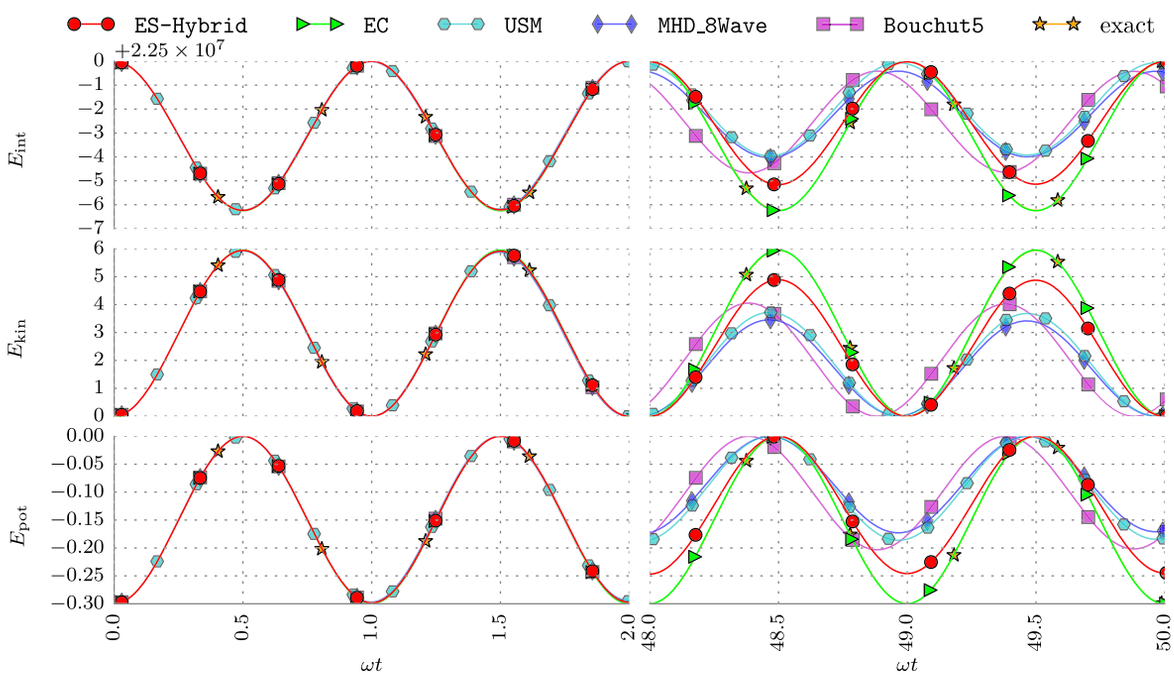

Fig. 15. Jeans Gravitational Instability test: Plot of internal, kinetic, and gravitational energies. (Left) The energy changes for all solvers agree well early in the computation. (Right) As time progresses we see the dissipation of energy by each solver differs. The `ES` solver exhibits the least dissipation of the solvers tested and shows the best agreement with the analytic solution. We use a fixed resolution of 64×64 cells. We give the *exact* solution in Appendix A.

The resulting kinetic and internal (thermal) energies as functions of ωt are shown in Fig. 15. We performed the simulations using a uniform resolution of 64×64 grid cells and chose a small CFL coefficient of $\texttt{CFL} = 0.1$ to limit the maximum time step for all solvers. The small CFL coefficient is not chosen for stability reasons, but to ensure enough data is generated to create smooth plots. As can be seen in Fig. 15, all solvers agree well in the beginning. Again, the `EC` scheme can be used as the solution is smooth. We note that the `EC` scheme shows essentially no dissipation even at the final time $t = 5.0$. All remaining solvers dissipate energy in some capacity. We see from Fig. 15 that the `ES` solver is considerably less dissipative than the other tested solvers. Furthermore, the `ES` scheme agrees well with the analytic solution, while the other schemes fail to maintain the exact oscillation period at later times and dissipate much of the energy of the dynamics.

Table 10
Initial conditions and runtime parameters: MHD blast wave test.

	$r \le r_0$	$r \in (r_0, r_1)$	$r \ge r_1$
ρ	1.0	1.0	1.0
p	1000.0	$0.1 + 999.9\, f(r)$	0.1
B_1	$\frac{100}{\sqrt{4\pi}}$	$\frac{100}{\sqrt{4\pi}}$	$\frac{100}{\sqrt{4\pi}}$
B_2	0.0	0.0	0.0
B_3	0.0	0.0	0.0
u	0.0	0.0	0.0
v	0.0	0.0	0.0
w	0.0	0.0	0.0

With $r = \sqrt{(x - x_{\text{centre}})^2 + (y - y_{\text{centre}})^2}$,
and $f(r) = \frac{r_1 - r}{r_1 - r_0}$

Domain size	$\{x, y, z\}_{\min} = \{-0.5, -0.5, -0.5\}$ $\{x, y, z\}_{\max} = \{0.5, 0.5, 0.5\}$
Inner radius	$r_0 = 0.09$
Outer radius	$r_1 = 0.1$
Explosion centre	$\boldsymbol{x}_{\text{centre}} = (0.0, 0.0, 0.0)$
Boundary conditions	All: periodic
Adaptive refinement on	Density, pressure
Simulation end time	$t_{\max} = 0.01$
Adiabatic index	$\gamma = 1.4$

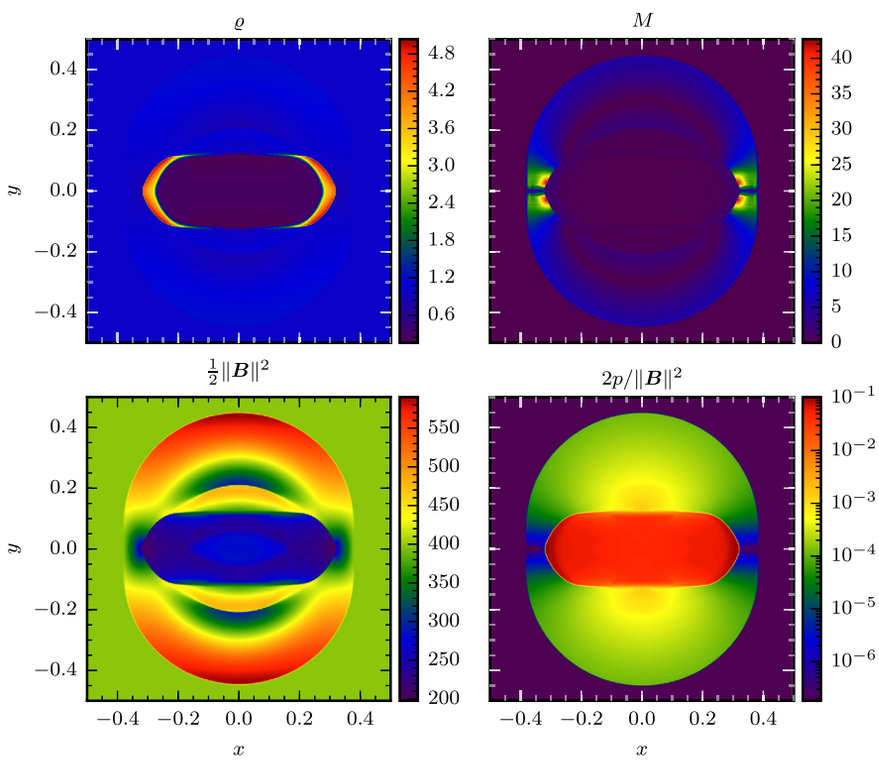

Fig. 16. MHD blast wave test: Adaptive grid resolution up to 512×512. Top left: density ρ. Top right: Mach number M. Lower left: magnetic pressure $p_{\text{mag}} = \frac{1}{2}\|\boldsymbol{B}\|^2$. Lower right: Plasma-$\beta = p/p_{\text{mag}}$. The density and magnetic pressure plots can be compared to Fig. 13 of [79]. The plots of density and magnetic pressure can directly be compared to Fig. 4 of [62].

4.7. MHD blast wave (2D, 3D)

The two-dimensional version of the MHD blast wave problem was studied by [62]. We use an extended three-dimensional version to demonstrate the robustness of our scheme in simulations involving regimes with low thermal pressures and high kinetic as well as magnetic energies in three dimensions. This test problem leads to the onset of strong MHD discontinuities, relevant to astrophysical phenomena where magnetic fields can have strong dynamical effects. It describes an initially circular pressure pulse. We choose here a relative magnitude of 10^4 for comparison with [62]. The initial conditions used are listed in Table 10.

The chosen initial conditions result in a very low plasma-β parameter, $\beta = 2p/\boldsymbol{B}^2 \approx 2.5 \cdot 10^{-4}$. The MHD explosion emits fast magnetosonic shock waves propagating with high velocities. The explosion is highly anisotropic and the displacement of the gas in the transverse y and z-direction is inhibited. This leads to the phenomenon that the explosion bubble is strongly distorted according to the initial magnetic field (in the x-direction). Furthermore, we see that the Mach number spans a broad range from 0 up to 42. As can be seen from the results in Fig. 16 showing the density, Mach number, magnetic

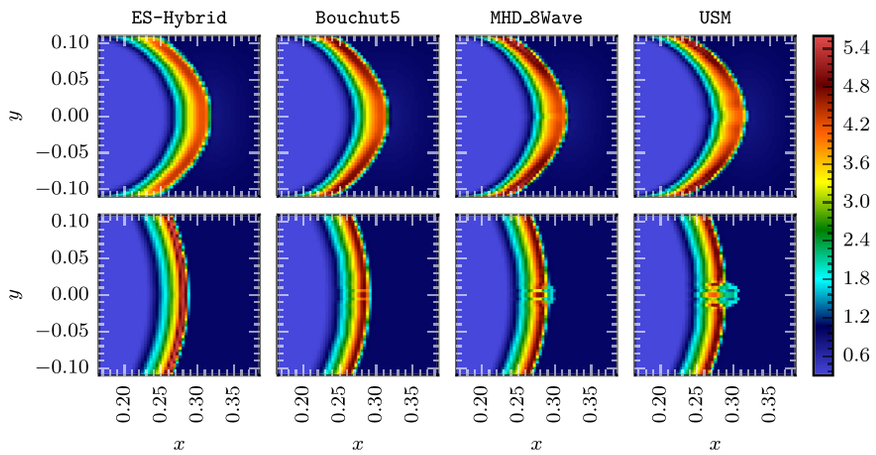

Fig. 17. MHD blast wave test: Linear density plots. Top: $B_1 = 100/\sqrt{4\pi}$. Bottom: $B_1 = 0$.

pressure and the plasma-β at $t = 0.01$, the out-going blast wave shows no grid alignment effect. We also tested the new `ES` solver with relative pressure magnitudes of 10^5 and 10^6 without finding any numerical defects.

In Fig. 17, we show zoomed linear density plots of the fast expanding shock front computed with our `ES-Hybrid`, the `Bouchut5` [12], the unsplit `USM` [76,75], and the `MHD_8Wave` [28] solvers. As can be seen, the blast wave front has a elliptical shape as is expected due to the strong influence of the magnetic field. If we run the same simulation without magnetic fields, i.e. the hydrodynamic limit $\boldsymbol{B} = \mathbf{0}$, we observe numerical defects close to the Cartesian grid axes in all simulation runs except the one using the `ES` solver. Ismail et al. [45] showed that even schemes which have increased dissipation and do not show 1D shock instabilities can still suffer from the carbuncle phenomenon in multiple dimensions. We emphasize that there are no numerical artifacts in the hydrodynamic limit when using the `ES-Hybrid` solver.

Fig. 18 shows the evolution of the conserved quantities as well as the individual energies. We observe that the `ES` scheme is mass, momentum, and total energy conservative also in this extreme test. The other MHD solvers fail to maintain the conservation of total energy by a small amount. Also, the `MHD_8Wave` solver fails to preserve the conservation of momentum as expected with the addition of the Powell source term. All solvers conserve mass up to machine precision. Fig. 19 shows a 3D variant of this test [70].

5. Conclusion

In this work we describe and test an implementation of a high-order, entropy stable numerical method for MHD problems. Entropy stable numerical fluxes serve as the core of the new entropy stable MHD solver. The implementation is implemented as a new module for the multi-physics `FLASH` framework [26] offering adaptive mesh refinement and large-scale, multi-processor simulations.

The new scheme is implemented with three entropy stable variants: Roe type dissipation (`ES-Roe`), local Lax–Friedrichs type dissipation (`ES-LLF`), and a hybrid dissipation term that uses a pressure switch to use `ES-Roe` in smooth regions and the more dissipative `ES-LLF` near pressure discontinuities (`ES-Hybrid`). The integration in time uses a strong stability preserving (SSP) Runge–Kutta method.

The numerical approximation is built from an entropic point of view. Thus, at a given time, it is possible to compute the current entropy density for all cells in the computational domain. We exploit this additional knowledge of the entropy and reformulate the computation to guarantee positivity of the pressure while maintaining the conservation of the total energy of the system. This reformulation prevents non-physical negative pressures which can occur numerically if the internal energy is a small fraction of the total energy.

We presented a variety of numerical results for the new entropy stable solver implementation for HD and MHD flows in multiple spatial dimensions. These numerical tests served to demonstrate the flexibility and robustness of the new solver. The testing included a recently developed shock-tube experiment, smooth Alfvén wave propagation, the Orszag–Tang MHD vortex, the MHD Rotor, and the strong MHD explosion test. The coupling of gravity to our new solver has been tested using the Jeans instability test. We compared the physical aspects of the numerical results, CPU timing and memory consumption of the new entropy stable scheme against the 8-wave, Bouchut 5-wave and unsplit MHD solver implementations already available for `FLASH`.

We found in these comparisons that the newly implemented entropy stable approximation was the most accurate in smooth regions of a flow. Also, it was shown that the entropy stable scheme was the only one that maintains the conservation of total energy during the computation.

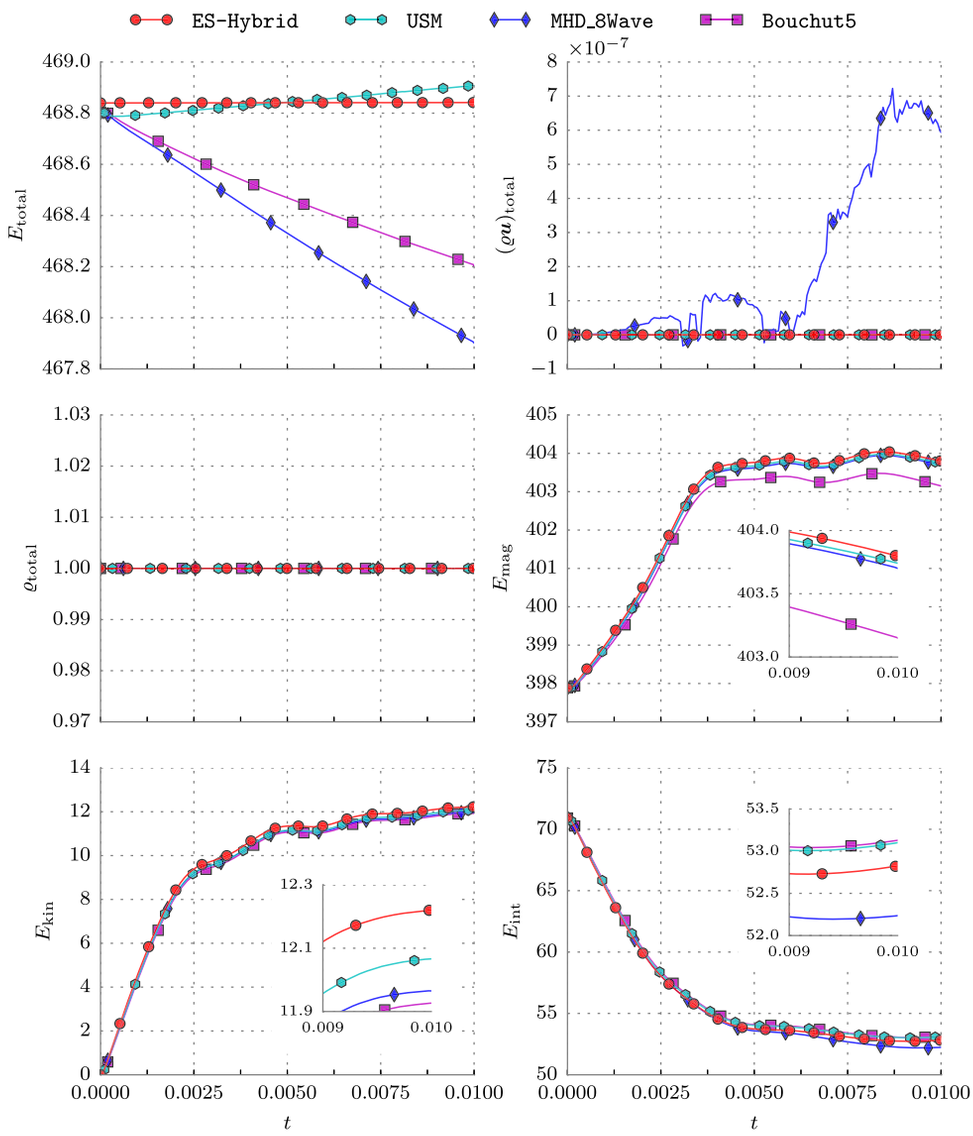

Fig. 18. MHD blast wave test: Evolution of the total conserved quantities as well as the individual energies in the $B_x = 100/\sqrt{4\pi}$ simulation run. It can easily be seen that the ES solver preserves the total energy well while the other schemes fail to preserve the total energy.

The new FLASH MHD module is freely available upon contact with the corresponding author.

Acknowledgements

We thank the anonymous referee for their useful comments, which helped to improve this article. Dominik Derigs and Stefanie Walch acknowledge the support of the Bonn–Cologne Graduate School for Physics and Astronomy (BCGS), which is funded through the Excellence Initiative, as well as the Sonderforschungsbereich (SFB) 956 on the “Conditions and impact of star formation”. Stefanie Walch thanks the Deutsche Forschungsgemeinschaft (DFG) for funding through the SPP 1573 “The physics of the interstellar medium” and SFB 956. This work has been partially performed using the Cologne High Efficiency Operating Platform for Sciences (CHEOPS) HPC cluster at the Regionales Rechenzentrum Köln (RRZK), University of Cologne, Germany. The software used in this work was developed in part by the DOE NNSA ASC- and DOE Office of Science ASCR-supported FLASH Center for Computational Science at the University of Chicago. To create some of the figures, we have used the free visualization software YT [83].

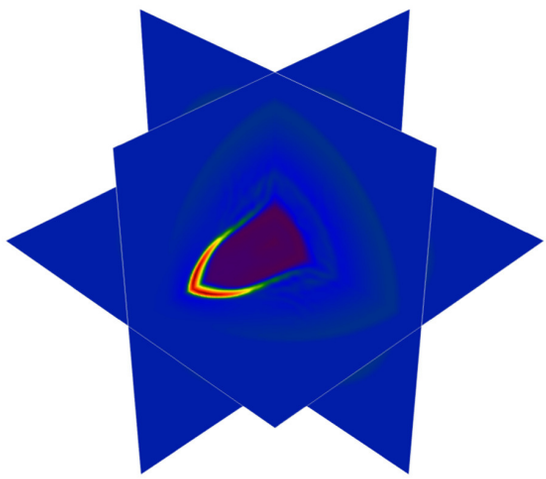

Fig. 19. MHD blast wave test: Adaptive grid resolution up to $128 \times 128 \times 128$ cells. Three-slice plot. Linear plot of density, ρ, using the same colour range as used in Fig. 16.

Appendix A. Analytic solution of the gravitational instability test

We list here the analytic solution for the gravitational instability test as given in [82,70].
Kinetic energy:

$$E_{\text{kin}}(t) = \frac{1}{8}\frac{\rho_0 \delta_0^2 |\omega|^2 L^2}{k^2}\Big(1 - \cos(2\omega t)\Big) \tag{A.1}$$

Internal energy:

$$E_{\text{int}}(t) - E_{\text{int}}(0) = -\frac{1}{8}\rho_0 a_0^2 \delta^2 L^2 \Big(1 - \cos(2\omega t)\Big) \tag{A.2}$$

Potential energy:

$$E_{\text{pot}}(t) = -\frac{1}{2}\frac{\pi G \rho_0^2 \delta_0^2 L^2}{k^2}\Big(1 + \cos(2\omega t)\Big) \tag{A.3}$$

where L is the length of the computational domain, and k is the magnitude of the wave vector $\boldsymbol{k}$.

Appendix B. Diffusive magnetic field correction

We present here the equations used for the implementation of the diffusive divergence error method described in Sec. 3.10. First and second derivatives are approximated by central second-order finite differences. Fig. B.1 illustrates the location of the different indices in the two dimensional case.

$$\begin{aligned}\tilde{B_1'} = \partial_x^2 B_1 + \partial_x(\partial_y B_2) + \partial_x(\partial_z B_3) = {} & \frac{B_{1,i+1,j,k} - 2B_{1,i,j,k} + B_{1,i-1,j,k}}{\Delta x^2} \\ & + \frac{\frac{B_{2,i+1,j+1,k} - B_{2,i+1,j-1,k}}{2\Delta y} - \frac{B_{2,i-1,j+1,k} - B_{2,i-1,j-1,k}}{2\Delta y}}{2\Delta x} \\ & + \frac{\frac{B_{3,i+1,j,k+1} - B_{3,i+1,j,k-1}}{2\Delta z} - \frac{B_{3,i-1,j,k+1} - B_{3,i-1,j,k-1}}{2\Delta z}}{2\Delta x}\end{aligned} \tag{B.1}$$

$$\begin{aligned}\tilde{B_2'} = \partial_y^2 B_2 + \partial_y(\partial_x B_1) + \partial_y(\partial_z B_3) = {} & \frac{B_{2,i,j+1,k} - 2B_{2,i,j,k} + B_{2,i,j-1,k}}{\Delta y^2} \\ & + \frac{\frac{B_{1,i+1,j+1,k} - B_{1,i-1,j+1,k}}{2\Delta x} - \frac{B_{1,i+1,j-1,k} - B_{1,i-1,j-1,k}}{2\Delta x}}{2\Delta y} \\ & + \frac{\frac{B_{3,i,j+1,k+1} - B_{3,i,j+1,k-1}}{2\Delta z} - \frac{B_{3,i,j-1,k+1} - B_{3,i,j-1,k-1}}{2\Delta z}}{2\Delta y}\end{aligned} \tag{B.2}$$

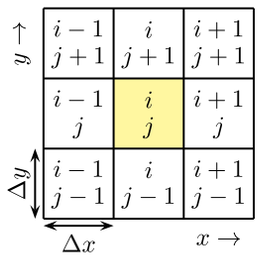

Fig. B.1. Illustration of index locations in 2D.

$$\tilde{B_3'} = \partial_z^2 B_3 + \partial_z(\partial_x B_1) + \partial_z(\partial_y B_2) = \frac{B_{3,i,j,k+1} - 2B_{3,i,j,k} + B_{3,i,j,k-1}}{\Delta z^2} + \frac{\frac{B_{1,i+1,j,k+1} - B_{1,i-1,j,k+1}}{2\Delta x} - \frac{B_{1,i+1,j,k-1} - B_{1,i-1,j,k-1}}{2\Delta x}}{2\Delta z} + \frac{\frac{B_{2,i,j+1,k+1} - B_{2,i,j-1,k+1}}{2\Delta y} - \frac{B_{2,i,j+1,k-1} - B_{2,i,j-1,k-1}}{2\Delta y}}{2\Delta z} \tag{B.3}$$

$$\tilde{\boldsymbol{B}} = \frac{\Delta x^2 \Delta y^2 \Delta z^2}{\Delta x^2 \Delta y^2 + \Delta x^2 \Delta z^2 + \Delta y^2 \Delta z^2} \left(\tilde{B_1'}, \tilde{B_2'}, \tilde{B_3'} \right)^\mathsf{T} \tag{B.4}$$

In 2D, we instead have:

$$\tilde{\boldsymbol{B}} = \frac{\Delta x^2 \Delta y^2}{\Delta x^2 + \Delta y^2} \left(\tilde{B_1'}, \tilde{B_2'}, 0 \right)^\mathsf{T} \tag{B.5}$$

Note that in 2D computations the dark red highlighted parts are zero and can be neglected.

Appendix C. Flowchart

In this section we provide flowcharts to detail and outline the workflow of the new ES MHD solver. We divide the flowchart description of the algorithm into three parts. The first, shown in Fig. C.4, depicts the global solver procedure for a single stage (of the possibly multi-stage) Runge–Kutta method. The second flowchart in Fig. C.2 displays the workflow for the computation of the numerical fluxes. The third flowchart in Fig. C.3 displays the workflow for the update of the solution array.

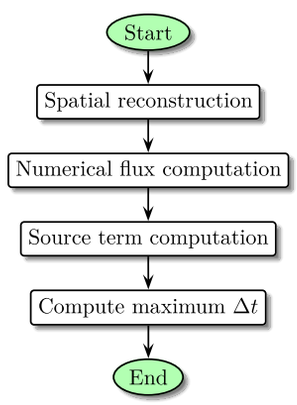

Fig. C.2. Flowchart showing the flux computation procedure of the ES solver. For a full description see Fig. C.4.

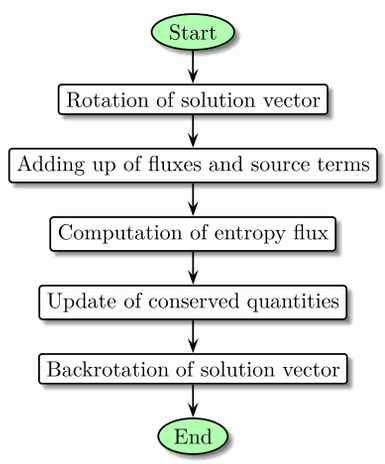

Fig. C.3. Flowchart showing the solution update procedure of the ES solver. For a full description see Fig. C.4.

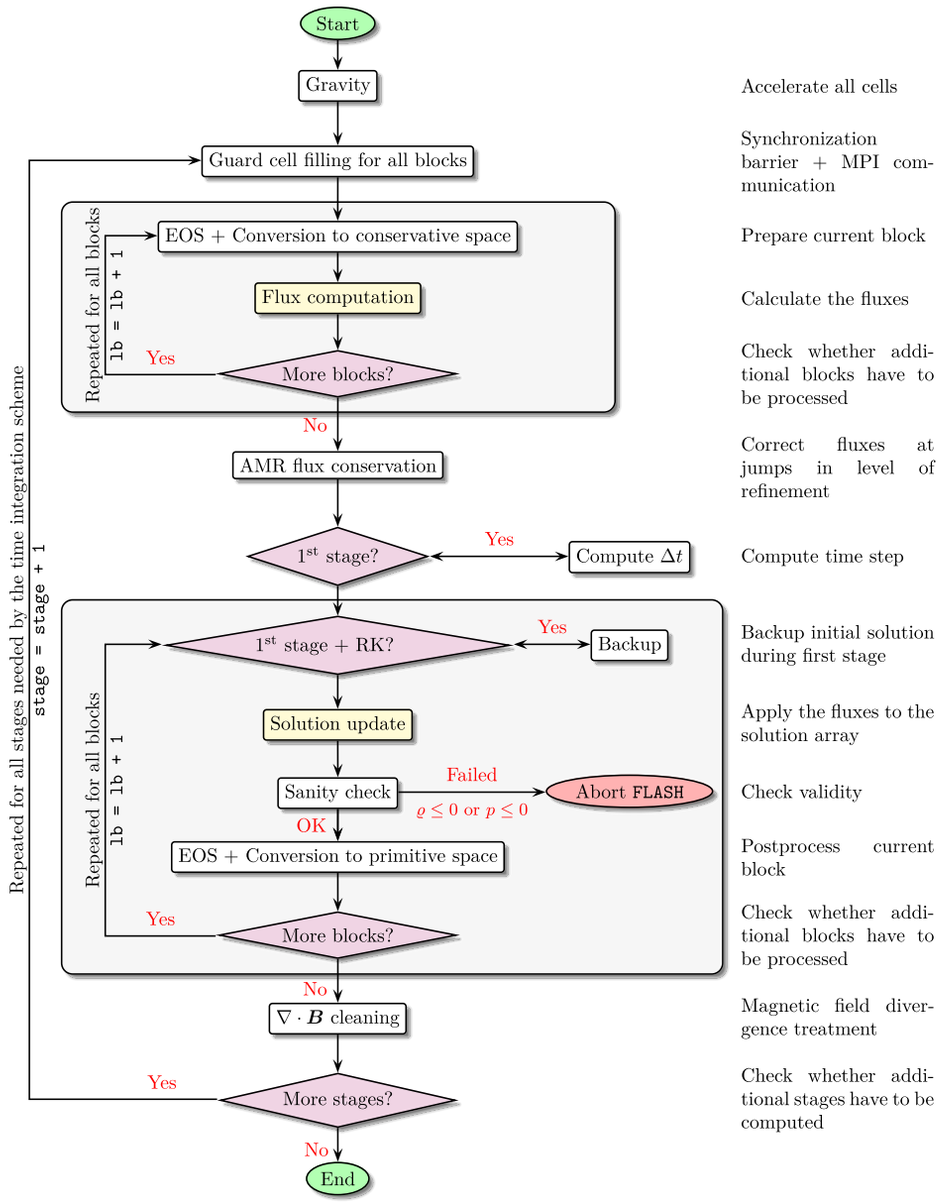

Fig. C.4. Flowchart showing the principle of operation of the ES solver. The steps "Flux computation" and "Solution update" is depicted in separate flowcharts, shown in Fig. C.2 and C.3, respectively.

Appendix D. Dimensional MHD equations

The dimensional MHD equations are given by

$$\frac{\partial}{\partial t}\begin{bmatrix}\rho\\ \rho\boldsymbol{u}\\ E\\ \boldsymbol{B}\end{bmatrix}+\nabla\cdot\begin{bmatrix}\rho\boldsymbol{u}\\ \rho(\boldsymbol{u}\otimes\boldsymbol{u})+\left(p+\frac{\|\boldsymbol{B}\|^2}{2\mu_0}\right)\mathbf{I}-\frac{\boldsymbol{B}\otimes\boldsymbol{B}}{\mu_0}\\ \boldsymbol{u}\left(E+p+\frac{\|\boldsymbol{B}\|^2}{2\mu_0}\right)-\frac{\boldsymbol{B}(\boldsymbol{u}\cdot\boldsymbol{B})}{\mu_0}\\ \boldsymbol{B}\otimes\boldsymbol{u}-\boldsymbol{u}\otimes\boldsymbol{B}\end{bmatrix}=0, \tag{D.1}$$

where the thermal pressure is related to the conserved quantities through the ideal gas law:

Table D.1
Simulation units with different settings of the compilation-time parameter `HY_UNIT`.

Unit system		Non-dimensional	SI	CGS
`#define HY_UNIT`		0	1	2
Length	ℓ	1	m	cm
Time	t	1	s	s
Density	ϱ	1	$\mathrm{kg\,m^{-3}}$	$\mathrm{g\,cm^{-3}}$
Velocities	$\boldsymbol{u}$	1	$\mathrm{m\,s^{-1}}$	$\mathrm{cm\,s^{-1}}$
Specific energy	E	1	$\mathrm{J\,m^{-3}}$	$\mathrm{erg\,cm^{-3}}$
Pressure	p	1	$\mathrm{N\,m^{-2}}$	$\mathrm{dyn\,cm^{-2}}$
Magnetic field	B	1	T	G
with $\mu_0 =$		1	$4\pi \cdot 10^{-7}\ \mathrm{T^2\,m^3\,J^{-1}}$	$4\pi\ \mathrm{G^2\,cm^3\,erg^{-1}}$

$$p = (\gamma - 1)\left(E - \frac{\rho}{2}\|\boldsymbol{u}\|^2 - \frac{\|\boldsymbol{B}\|^2}{2\mu_0}\right). \tag{D.2}$$

The unit system is determined at compilation time through the user-definable parameter `HY_UNIT` in the `ES.h` parameter file. In non-dimensional units, (D.1) and (D.2) are identical to (2.1) and (2.3).

The chosen unit system leads to different internal conversion factors within our implementation. The resulting units of the simulation quantities are listed in Table D.1. Depending on the setting, the according vacuum permeability constant, μ_0, is chosen. Note that both the specific energy, E, and the pressure, p, are of the same units.

Appendix E. Error norms and the experimental order of convergence

The discrete L_1- and L_2-errors are defined by

$$\|\Delta u(t)\|_{L_1} = \frac{1}{N^d}\sum_{i,j=1}^{N}\left|u_{i,j}^{\text{exact}} - u_{i,j}^{\text{solution}}\right|, \quad \text{and} \quad \|\Delta u(t)\|_{L_2} = \sqrt{\frac{1}{N^d}\sum_{i,j=1}^{N}\left(u_{i,j}^{\text{exact}} - u_{i,j}^{\text{solution}}\right)^2},$$

where N is the number or grid points in each direction, and d is the number of spatial dimensions. After computing the norms of the errors, we obtain the experimental order of convergence (EOC) using

$$\text{EOC}(i \to j) = \frac{\log\left(\|\Delta u_i(t)\|\right) - \log\left(\|\Delta u_j(t)\|\right)}{\log\left(N_i/N_j\right)}. \tag{E.1}$$

Appendix F. Supplementary material

Supplementary material related to this article can be found online at http://dx.doi.org/10.1016/j.jcp.2016.04.048.

References

[1] D.W. Goldsmith, Thermal instabilities in interstellar gas heated by cosmic rays, Astrophys. J. 161 (1970) 41–54, http://dx.doi.org/10.1086/150511.
[2] A.R. Winters, G.J. Gassner, Affordable, entropy conserving and entropy stable flux functions for the ideal MHD equations, J. Comput. Phys. 304 (2016) 72–108, http://dx.doi.org/10.1016/j.jcp.2015.09.055.
[3] F. Bouchut, C. Klingenberg, K. Waagan, A multiwave approximate Riemann solver for ideal MHD based on relaxation, I: theoretical framework, Numer. Math. 108 (1) (2007) 7–42, http://dx.doi.org/10.1007/s00211-007-0108-8.
[4] P. Chandrashekar, C. Klingenberg, Entropy stable finite volume scheme for ideal compressible MHD on 2-D Cartesian meshes, SIAM J. Numer. Anal. 54 (2) (2016) 1313–1340, http://dx.doi.org/10.1137/15M1013626.
[5] J.A. Rossmanith, High-order discontinuous Galerkin finite element methods with globally divergence-free constrained transport for ideal MHD, ArXiv e-prints, arXiv:1310.4251.
[6] A. Dedner, F. Kemm, D. Kröner, C.-D. Munz, T. Schnitzer, M. Wesenberg, Hyperbolic divergence cleaning for the MHD equations, J. Comput. Phys. 175 (2) (2002) 645–673, http://dx.doi.org/10.1006/jcph.2001.6961.
[7] A.J. Christlieb, Y. Liu, Q. Tang, Z. Xu, Positivity-preserving finite difference weighted ENO schemes with constrained transport for ideal magnetohydrodynamic equations, SIAM J. Sci. Comput. 37 (4) (2015) A1825–A1845, http://dx.doi.org/10.1137/140971208.
[8] F. Huazheng, F. Xueshang, Splitting based scheme for three-dimensional MHD with dual time stepping, Chin. J. Space Sci. 35 (1) (2015) 9, http://dx.doi.org/10.11728/cjss2015.01.009.
[9] C.M. Xisto, J.C. Páscoa, P.J. Oliveira, A pressure-based high resolution numerical method for resistive MHD, J. Comput. Phys. 275 (2014) 323–345, http://dx.doi.org/10.1016/j.jcp.2014.07.009.
[10] M. Ersoy, F. Golay, L. Yushchenko, Adaptive multiscale scheme based on numerical density of entropy production for conservation laws, Cent. Eur. J. Math. 11 (8) (2013) 1392–1415, http://dx.doi.org/10.2478/s11533-013-0252-6.
[11] D.S. Spicer, H. Luo, J.E. Dorband, K.M. Olson, P.J. MacNeice, A new 3D, fully parallel, unstructured AMR MHD high order Godunov code for modeling Sun–Earth connection phenomena, J. Atmos. Sol.-Terr. Phys. 4 (2013), preprint, submitted for publication. The article can be found and downloaded from http://einstein.physics.drexel.edu/~solarweather/unstructuredcode.pdf.
[12] K. Waagan, C. Federrath, C. Klingenberg, A robust numerical scheme for highly compressible magnetohydrodynamics: nonlinear stability, implementation and tests, J. Comput. Phys. 230 (9) (2011) 3331–3351, http://dx.doi.org/10.1016/j.jcp.2011.01.026.

[13] X. Zhang, C.-W. Shu, On positivity-preserving high order discontinuous Galerkin schemes for compressible Euler equations on rectangular meshes, J. Comput. Phys. 229 (23) (2010) 8918–8934, http://dx.doi.org/10.1016/j.jcp.2010.08.016.
[14] V. Wheatley, H. Kumar, P. Huguenot, On the role of Riemann solvers in discontinuous Galerkin methods for magnetohydrodynamics, J. Comput. Phys. 229 (3) (2010) 660–680, http://dx.doi.org/10.1016/j.jcp.2009.10.003.
[15] S. Li, A simple dual implementation to track pressure accurately, in: N.V. Pogorelov, E. Audit, G.P. Zank (Eds.), Numerical Modeling of Space Plasma Flows, in: Astronomical Society of the Pacific Conference Series, vol. 385, 2008, pp. 273–278.
[16] S. Li, H. Li, R. Cen, CosmoMHD: a cosmological magnetohydrodynamics code, Astrophys. J. Suppl. Ser. 174 (2008) 1–12, http://dx.doi.org/10.1086/521302, arXiv:astro-ph/0611863.
[17] G. Tóth, The $\nabla \cdot B = 0$ constraint in shock-capturing magnetohydrodynamics codes, J. Comput. Phys. 161 (2) (2000) 605–652, http://dx.doi.org/10.1006/jcph.2000.6519.
[18] P. Janhunen, A positive conservative method for magnetohydrodynamics based on HLL and Roe methods, J. Comput. Phys. 160 (2) (2000) 649–661, http://dx.doi.org/10.1006/jcph.2000.6479.
[19] D.S. Balsara, D. Spicer, Maintaining pressure positivity in magnetohydrodynamic simulations, J. Comput. Phys. 148 (1) (1999) 133–148, http://dx.doi.org/10.1006/jcph.1998.6108.
[20] D.S. Balsara, Self-adjusting, positivity preserving high order schemes for hydrodynamics and magnetohydrodynamics, J. Comput. Phys. 231 (22) (2012) 7504–7517, http://dx.doi.org/10.1016/j.jcp.2012.01.032.
[21] A.L. Zachary, A. Malagoli, P. Colella, A higher-order Godunov method for multidimensional ideal magnetohydrodynamics, SIAM J. Sci. Comput. 15 (2) (1994) 263–284, http://dx.doi.org/10.1137/0915019.
[22] D. Ryu, J.P. Ostriker, H. Kang, R. Cen, A cosmological hydrodynamic code based on the total variation diminishing scheme, Astrophys. J. 414 (1993) 1–19, http://dx.doi.org/10.1086/173051.
[23] B. Einfeldt, C.-D. Munz, P.L. Roe, B. Sjögreen, On Godunov-type methods near low densities, J. Comput. Phys. 92 (2) (1991) 273–295, http://dx.doi.org/10.1016/0021-9991(91)90211-3.
[24] B. Schmidtmann, B. Seibold, M. Torrilhon, Relations between WENO3 and third-order limiting in finite volume methods, J. Sci. Comput., http://dx.doi.org/10.1007/s10915-015-0151-z.
[25] S. Gottlieb, On high order strong stability preserving Runge–Kutta and multi step time discretizations, J. Sci. Comput. 25 (1) (2005) 105–128, http://dx.doi.org/10.1007/s10915-004-4635-5.
[26] B. Fryxell, K. Olson, P. Ricker, F.X. Timmes, M. Zingale, D.Q. Lamb, P. MacNeice, R. Rosner, J.W. Truran, H. Tufo, FLASH: an adaptive mesh hydrodynamics code for modeling astrophysical thermonuclear flashes, Astrophys. J. Suppl. Ser. 131 (2000) 273–334, http://dx.doi.org/10.1086/317361.
[27] A. Dubey, L.B. Reid, K. Weide, K. Antypas, M.K. Ganapathy, K. Riley, D.J. Sheeler, A. Siegal, Extensible component-based architecture for FLASH, a massively parallel, multiphysics simulation code, Parallel Comput. 35 (10–11) (2009) 512–522, http://dx.doi.org/10.1016/j.parco.2009.08.001.
[28] K.G. Powell, P.L. Roe, T.J. Linde, T.I. Gombosi, D.L. De Zeeuw, A solution-adaptive upwind scheme for ideal magnetohydrodynamics, J. Comput. Phys. 154 (2) (1999) 284–309, http://dx.doi.org/10.1006/jcph.1999.6299.
[29] E. Tadmor, Entropy stability theory for difference approximations of nonlinear conservation laws and related time-dependent problems, Acta Numer. 12 (2003) 451–512, http://dx.doi.org/10.1017/s0962492902000156.
[30] L.D. Landau, Fluid Mechanics, vol. 6, Pergamon, 1959.
[31] S. Mishra, Entropy stable high-order schemes for systems of conservation laws, in: Modern Techniques in the Numerical Solution of Partial Differential Equations.
[32] R.J. LeVeque, D. Mihalas, E.A. Dorfi, E. Müller, Computational Methods for Astrophysical Fluid Flow, Saas-Fee Advanced Course, Lecture Notes 1997 Swiss Society for Astrophysics and Astronomy, vol. 27, Springer Science & Business, Media, 1998.
[33] S. Walch, P. Girichidis, T. Naab, A. Gatto, S.C.O. Glover, R. Wünsch, R.S. Klessen, P.C. Clark, T. Peters, D. Derigs, C. Baczynski, The SILCC (simulating the lifecycle of molecular clouds) project, I: chemical evolution of the supernova-driven ISM, Mon. Not. R. Astron. Soc. 454 (1) (2015) 238–268, http://dx.doi.org/10.1093/mnras/stv1975.
[34] S.K. Godunov, A difference method for numerical calculation of discontinuous solutions of the equations of hydrodynamics, Mat. Sb. 89 (3) (1959) 271–306.
[35] C.-W. Shu, Total-variation-diminishing time discretizations, SIAM J. Sci. Stat. Comput. 9 (6) (1988) 1073–1084, http://dx.doi.org/10.1137/0909073.
[36] S. Gottlieb, C.-W. Shu, E. Tadmor, Strong stability-preserving high-order time discretization methods, SIAM Rev. 43 (1) (2001) 89–112, http://dx.doi.org/10.1137/S003614450036757X.
[37] E.F. Toro, Riemann Solvers and Numerical Methods for Fluid Dynamics: A Practical Introduction, 3rd edition, Springer, 2009.
[38] S. Godunov, Symmetric form of the equations of magnetohydrodynamics, Numer. Methods Mech. Contin. Med. 1 (1972) 26–34.
[39] P.J. Dellar, A note on magnetic monopoles and the one-dimensional MHD Riemann problem, J. Comput. Phys. 172 (1) (2001) 392–398, http://dx.doi.org/10.1006/jcph.2001.6815.
[40] F. Ismail, P.L. Roe, Affordable, entropy-consistent Euler flux functions, II: entropy production at shocks, J. Comput. Phys. 228 (15) (2009) 5410–5436, http://dx.doi.org/10.1016/j.jcp.2009.04.021.
[41] M.L. Merriam, An entropy-based approach to nonlinear stability, NASA Tech. Memo. 101086 (64) (1989) 1–154.
[42] T.J. Barth, Numerical methods for gasdynamic systems on unstructured meshes, in: D. Kröner, M. Ohlberger, C. Rohde (Eds.), An Introduction to Recent Developments in Theory and Numerics for Conservation Laws, in: Lecture Notes in Computational Science and Engineering, vol. 5, Springer, Berlin, Heidelberg, 1999, pp. 195–285.
[43] P.L. Roe, D.S. Balsara, Notes on the eigensystem of magnetohydrodynamics, SIAM J. Appl. Math. 56 (1) (1996) 57–67, http://dx.doi.org/10.1137/S003613999427084X.
[44] P. Chandrashekar, Kinetic energy preserving and entropy stable finite volume schemes for compressible Euler and Navier–Stokes equations, arXiv:1209.4994.
[45] F. Ismail, P.L. Roe, H. Nishikawa, A proposed cure to the carbuncle phenomenon, in: H. Deconinck, E. Dick (Eds.), Computational Fluid Dynamics 2006, Springer, Berlin, Heidelberg, 2009, pp. 149–154.
[46] J.J. Quirk, A contribution to the great Riemann solver debate, Int. J. Numer. Methods Fluids 18 (6) (1994) 555–574, http://dx.doi.org/10.1002/fld.1650180603.
[47] K. Olson, PARAMESH: a parallel, adaptive grid tool, in: A. Deane, A. Ecer, G. Brenner, D. Emerson, J. McDonough, J. Periaux, N. Satofuka, D. Tromeur-Dervout (Eds.), Parallel Computational Fluid Dynamics 2005, Elsevier, Amsterdam, 2006, pp. 341–348.
[48] A. Gatto, S. Walch, M.-M.M. Low, T. Naab, P. Girichidis, S.C.O. Glover, R. Wünsch, R.S. Klessen, P.C. Clark, C. Baczynski, T. Peters, J.P. Ostriker, J.C. Ibáñez-Mejía, S. Haid, Modelling the supernova-driven ISM in different environments, Mon. Not. R. Astron. Soc. 449 (1) (2015) 1057–1075, http://dx.doi.org/10.1093/mnras/stv324.
[49] S.C.O. Glover, P.C. Clark, Molecular cooling in the diffuse interstellar medium, Mon. Not. R. Astron. Soc. 437 (2014) 9–20, http://dx.doi.org/10.1093/mnras/stt1809, arXiv:1305.7365.
[50] K. Murawski, Analytical and Numerical Methods for Wave Propagation in Fluid Media, Stability, Vibration and Control of Systems, Series A, World Scientific Pub. Co. Inc., 2003.

[51] T. Plewa, E. Müller, The consistent multi-fluid advection method, Astron. Astrophys. 342 (1999) 179–191, arXiv:astro-ph/9807241.
[52] S.C.O. Glover, C. Federrath, M.-M. Mac Low, R.S. Klessen, Modelling CO formation in the turbulent interstellar medium, Mon. Not. R. Astron. Soc. 404 (2010) 2–29, http://dx.doi.org/10.1111/j.1365-2966.2009.15718.x, arXiv:0907.4081.
[53] J. Barnes, P. Hut, A hierarchical O(N log N) force-calculation algorithm, Nature 324 (1986) 446–449, http://dx.doi.org/10.1038/324446a0.
[54] P.M. Ricker, A direct multigrid Poisson solver for oct-tree adaptive meshes, Astrophys. J. Suppl. Ser. 176 (2008) 293–300, http://dx.doi.org/10.1086/526425, arXiv:0710.4397.
[55] C. Altmann, Explicit discontinuous Galerkin methods for magnetohydrodynamics, Ph.D. thesis, Universität Stuttgart, Holzgartenstr. 16, 70174 Stuttgart, 2012, http://elib.uni-stuttgart.de/opus/volltexte/2013/7998.
[56] A.J. Chorin, The numerical solution of the Navier–Stokes equations for an incompressible fluid, Bull. Am. Math. Soc. 73 (6) (1967) 928–931.
[57] J.U. Brackbill, D.C. Barnes, The effect of nonzero $\nabla \cdot b$ on the numerical solution of the magnetohydrodynamic equations, J. Comput. Phys. 35 (3) (1980) 426–430, http://dx.doi.org/10.1016/0021-9991(80)90079-0.
[58] B. Marder, A method for incorporating Gauss' law into electromagnetic {PIC} codes, J. Comput. Phys. 68 (1) (1987) 48–55, http://dx.doi.org/10.1016/0021-9991(87)90043-X.
[59] D.S. Balsara, Total variation diminishing scheme for adiabatic and isothermal magnetohydrodynamics, Astrophys. J. Suppl. Ser. 116 (1) (1998) 133–153, http://dx.doi.org/10.1086/313093.
[60] R.K. Crockett, P. Colella, R.T. Fisher, R.I. Klein, C.F. McKee, An unsplit, cell-centered Godunov method for ideal MHD, J. Comput. Phys. 203 (2005) 422–448, http://dx.doi.org/10.1016/j.jcp.2004.08.021.
[61] C.R. Evans, J.F. Hawley, Simulation of magnetohydrodynamic flows – a constrained transport method, Astrophys. J. 332 (1988) 659–677, http://dx.doi.org/10.1086/166684.
[62] D.S. Balsara, D. Spicer, A staggered mesh algorithm using high order Godunov fluxes to ensure solenoidal magnetic fields in magnetohydrodynamic simulations, J. Comput. Phys. 149 (2) (1999) 270–292, http://dx.doi.org/10.1006/jcph.1998.6153.
[63] D.S. Balsara, J. Kim, A comparison between divergence-cleaning and staggered-mesh formulations for numerical magnetohydrodynamics, Astrophys. J. 602 (2004) 1079–1090, http://dx.doi.org/10.1086/381051.
[64] K. Waagan, A positive MUSCL-Hancock scheme for ideal magnetohydrodynamics, J. Comput. Phys. 228 (23) (2009) 8609–8626, http://dx.doi.org/10.1016/j.jcp.2009.08.020.
[65] P. Colella, P.R. Woodward, The piecewise parabolic method (PPM) for gas-dynamical simulations, J. Comput. Phys. 54 (1) (1984) 174–201, http://dx.doi.org/10.1016/0021-9991(84)90143-8.
[66] M. Brio, C.C. Wu, An upwind differencing scheme for the equations of ideal magnetohydrodynamics, J. Comput. Phys. 75 (2) (1988) 400–422, http://dx.doi.org/10.1016/0021-9991(88)90120-9.
[67] D. Ryu, T.W. Jones, Numerical magnetohydrodynamics in astrophysics: algorithm and tests for one-dimensional flow, Astrophys. J. 442 (1995) 228–258, http://dx.doi.org/10.1086/175437.
[68] M. Torrilhon, Uniqueness conditions for Riemann problems of ideal magnetohydrodynamics, J. Plasma Phys. 69 (3) (2003) 253–276, http://dx.doi.org/10.1017/s0022377803002186.
[69] C.-W. Shu, S. Osher, Efficient implementation of essentially non-oscillatory shock-capturing schemes, II, J. Comput. Phys. 83 (1) (1989) 32–78, http://dx.doi.org/10.1007/978-3-642-60543-7_14.
[70] Flash Center for Computational Science, University of Chicago, FLASH user's guide. http://flash.uchicago.edu/site/flashcode/user_support/flash4_ug_4p3.pdf.
[71] A. Susanto, High-order finite-volume schemes for magnetohydrodynamics, Ph.D. thesis, University of Waterloo, 2014, https://uwspace.uwaterloo.ca/handle/10012/8597.
[72] R. Balasubramanian, K. Anandhanarayanan, An ideal magnetohydrodynamics solver with artificial compressibility analogy divergence-cleaning, pp. 1–8, http://www.nal.res.in/CFDsympo16/FULL%20PAPERS-AeSICFD16/CP5.pdf, 2014.
[73] V.K. Chakravarthy, K. Arora, D. Chakraborty, A simple hybrid finite volume solver for compressible turbulence, Int. J. Numer. Methods Fluids 77 (2015) 707–731, http://dx.doi.org/10.1002/fld.4000.
[74] D.S. Balsara, Multidimensional Riemann problem with self-similar internal structure, part I: application to hyperbolic conservation laws on structured meshes, J. Comput. Phys. 277 (2014) 163–200, http://dx.doi.org/10.1016/j.jcp.2014.07.053.
[75] D. Lee, A solution accurate, efficient and stable unsplit staggered mesh scheme for three dimensional magnetohydrodynamics, J. Comput. Phys. 243 (2013) 269–292, http://dx.doi.org/10.1016/j.jcp.2013.02.049.
[76] D. Lee, A.E. Deane, An unsplit staggered mesh scheme for multidimensional magnetohydrodynamics, J. Comput. Phys. 228 (4) (2009) 952–975, http://dx.doi.org/10.1016/j.jcp.2008.08.026.
[77] S.A. Orszag, C.-M. Tang, Small-scale structure of two-dimensional magnetohydrodynamic turbulence, J. Fluid Mech. 90 (01) (1979) 129–143, http://dx.doi.org/10.1017/s002211207900210x.
[78] J. Balbás, E. Tadmor, A central differencing simulation of the Orszag Tang vortex system, IEEE Trans. Plasma Sci. 33 (2005) 470–471, http://dx.doi.org/10.1109/TPS.2005.845282.
[79] P. Londrillo, L. Del Zanna, High-order upwind schemes for multidimensional magnetohydrodynamics, Astrophys. J. 530 (2000) 508–524, http://dx.doi.org/10.1086/308344, arXiv:astro-ph/9910086.
[80] W. Dai, P.R. Woodward, A simple finite difference scheme for multidimensional magnetohydrodynamical equations, J. Comput. Phys. 142 (2) (1998) 331–369, http://dx.doi.org/10.1006/jcph.1998.5944.
[81] J.H. Jeans, The stability of a spherical nebula, Philos. Trans. R. Soc., Math. Phys. Eng. Sci. 199 (312–320) (1902) 1–53, http://dx.doi.org/10.1098/rsta.1902.0012.
[82] S. Chandrasekhar, Hydrodynamic and Hydromagnetic Stability, Dover Books on Physics Series, Dover Publications, 1961.
[83] M.J. Turk, B.D. Smith, J.S. Oishi, S. Skory, S.W. Skillman, T. Abel, M.L. Norman, yt: a multi-code analysis toolkit for astrophysical simulation data, Astrophys. J. Suppl. Ser. 192 (2011) 9+, http://dx.doi.org/10.1088/0067-0049/192/1/9, arXiv:1011.3514.

4.3 Publication II

Derigs, D., Winters, A. R., Gassner, G. J., Walch, S., (Feb. 2017). "A novel averaging technique for discrete entropy-stable dissipation operators for ideal MHD." In: *Journal of Computational Physics* 330, pp. 624–632. ISSN: 0021-9991.
DOI: 10.1016/j.jcp.2016.10.055. arXiv: 1610.06584.

The second paper presented in this cumulative thesis is a follow-up to the first paper. It is concerned with constructing robust fluxes and dissipation terms within the framework of entropy stable approximations. The core motivation of this work is that we discovered that the widely used formulation of Ismail & Roe (2009) can exhibit unphysical mass transfer and easily breaks down for initial conditions commonly found in astrophysical simulations.

In this paper, I present a derivation technique for uniquely defined discrete entropy stable schemes. It is the foundation stone for a few follow-up works that have already been published (see, e.g., Winters et al., 2017)

Contribution overview

The work presented in this publication has been entirely performed by me. The group discussions with Andrew Winters, Gregor Gassner, and Stefanie Walch allowed me to show the results in a context highlighting the importance for state-of-the-art schemes.

Stefanie Walch, Gregor Gassner and Andrew Winters edited the paper.

Journal of Computational Physics 330 (2017) 624–632

Contents lists available at ScienceDirect

Journal of Computational Physics

www.elsevier.com/locate/jcp

A novel averaging technique for discrete entropy-stable dissipation operators for ideal MHD

Dominik Derigs [a,*], Andrew R. Winters [b], Gregor J. Gassner [b], Stefanie Walch [a]

[a] *I. Physikalisches Institut, Universität zu Köln, Zülpicher Straße 77, 50937 Köln, Germany*
[b] *Mathematisches Institut, Universität zu Köln, Weyertal 86-90, 50931 Köln, Germany*

ARTICLE INFO

Article history:
Received 30 May 2016
Received in revised form 21 October 2016
Accepted 25 October 2016
Available online 31 October 2016

Keywords:
Magnetohydrodynamics
Entropy stable
Entropy Jacobian
Kinetic energy preserving

ABSTRACT

Entropy stable schemes can be constructed with a specific choice of the numerical flux function. First, an entropy conserving flux is constructed. Secondly, an entropy stable dissipation term is added to this flux to guarantee dissipation of the discrete entropy. Present works in the field of entropy stable numerical schemes are concerned with thorough derivations of entropy conservative fluxes for ideal MHD. However, as we show in this work, if the dissipation operator is not constructed in a very specific way, it cannot lead to a generally stable numerical scheme.

The two main findings presented in this paper are that the entropy conserving flux of Ismail & Roe can easily break down for certain initial conditions commonly found in astrophysical simulations, and that special care must be taken in the derivation of a discrete dissipation matrix for an entropy stable numerical scheme to be robust.

We present a convenient novel averaging procedure to evaluate the entropy Jacobians of the ideal MHD and the compressible Euler equations that yields a discretization with favorable robustness properties.

1. Introduction

The applications of ideal magnetohydrodynamics (MHD) are ubiquitous in science and engineering. Accordingly, the design of numerical schemes for the approximation of this particular set of hyperbolic conservation laws has undergone extensive development. The ideal MHD model assumes that a fluid is a good electric conductor and neglects non-ideal effects, *e.g.* viscosity or resistivity. It is governed by a system of conservation laws together with the divergence-free condition

$$\frac{\partial}{\partial t}\boldsymbol{q}+\nabla\cdot\boldsymbol{f}=\frac{\partial}{\partial t}\begin{bmatrix}\varrho\\ \varrho\boldsymbol{u}\\ E\\ \boldsymbol{B}\end{bmatrix}+\nabla\cdot\begin{bmatrix}\varrho\boldsymbol{u}\\ \varrho(\boldsymbol{u}\otimes\boldsymbol{u})+\left(p+\frac{1}{2}\|\boldsymbol{B}\|^2\right)\mathbf{I}-\boldsymbol{B}\otimes\boldsymbol{B}\\ \boldsymbol{u}\left(\frac{1}{2}\varrho\|\boldsymbol{u}\|^2+\frac{\gamma p}{\gamma-1}+\|\boldsymbol{B}\|^2\right)-\boldsymbol{B}(\boldsymbol{u}\cdot\boldsymbol{B})\\ \boldsymbol{u}\otimes\boldsymbol{B}-\boldsymbol{B}\otimes\boldsymbol{u}\end{bmatrix}=\mathbf{0}, \tag{1.1}$$

where ϱ, $\varrho\boldsymbol{u}$, and E are the mass, momenta, and total specific energy of the plasma system, p is the thermal pressure, $\mathbf{I}$ is the 3×3 identity matrix, and $\boldsymbol{B}$ is the magnetic field, also referred to as magnetic flux density. $\boldsymbol{f}$ is the multidimensional flux function.

* Corresponding author.
E-mail address: derigs@ph1.uni-koeln.de (D. Derigs).

http://dx.doi.org/10.1016/j.jcp.2016.10.055
0021-9991/

It is well-known that solutions to (1.1) may contain discontinuities in the form of shocks, even for smooth initial data. Hence, solutions are sought in the weak sense [1]. However, weak solutions are not unique and need to be supplemented with extra admissibility criteria. Following the work of *e.g.* [2–5], we use the concept of entropy stability to construct discretizations that agree with the second law of thermodynamics.

In this paper we describe a technique suitable for the derivation of a flux dissipation term that guarantees entropy stability. Sec. 2 provides the necessary background of entropy numerical fluxes. In Sec. 3 we motivate our choice for the baseline entropy conserving flux and apply our technique to derive a simple dissipation operator in Sec. 4. In Sec. 5 we investigate the computational costs of our modifications. Finally, in Sec. 6, we revisit the two main findings of this work using simple numerical tests from the field of astrophysics.

2. Entropy stable numerical flux functions

For smooth solutions, one can design numerical methods to be ***entropy conservative*** if, discretely, the local changes of entropy are the same as predicted by the continuous entropy conservation law. For discontinuous solutions, the approximation is said to be ***entropy stable*** if the entropy always possesses the correct sign and the numerical scheme produces more entropy than an entropy conservative scheme and satisfies the entropy inequality (where we use the mathematical notation that entropy is a decaying function)

$$\frac{\partial}{\partial t} S + \nabla \cdot (\boldsymbol{u} S) \leq 0, \tag{2.1}$$

with the entropy density $S = -\frac{\varrho s}{\gamma - 1}$, the corresponding entropy flux $\boldsymbol{u}S$, and the specific nondimensional thermodynamic entropy $s = \ln\left(p\varrho^{-\gamma}\right)$, where $\gamma = \frac{c_p}{c_v}$ is the ratio of specific heats [2]. Because entropy conservative schemes will produce high-frequency oscillations near shocks (see *e.g.* [3]), we need to add a carefully designed dissipation term to ensure that the entropy is guaranteed to dissipate.

Therefore, in order to create an entropy stable numerical approximation, we use a suitable entropy conserving flux as a base and add a numerical dissipation term. The resulting numerical flux is of the form

$$\boldsymbol{f}^* = \boldsymbol{f}^{*,ec} - \frac{1}{2}\mathbf{D}\left[\!\left[\boldsymbol{q}\right]\!\right], \tag{2.2}$$

where $\mathbf{D}$ is a suitable dissipation operator, and $\boldsymbol{q}$ is the vector of conserved quantities. We define the jump operator as $[\![\cdot]\!] = (\cdot)_\mathrm{R} - (\cdot)_\mathrm{L}$. Of utmost concern for entropy stability is to formulate the dissipation term in (2.2) such that the numerical flux fulfills the entropy inequality (2.1).

If we make the choice of $\mathbf{D}$ to be

$$\mathbf{D} = |\lambda_{\max}|\mathbf{I}, \tag{2.3}$$

where $\lambda_{\max}$ is the largest eigenvalue of the ideal MHD system, we can rewrite the dissipation term

$$\frac{1}{2}\mathbf{D}\left[\!\left[\boldsymbol{q}\right]\!\right] = \frac{1}{2}|\lambda_{\max}|\mathbf{I}\left[\!\left[\boldsymbol{q}\right]\!\right], \tag{2.4a}$$

$$= \frac{1}{2}|\lambda_{\max}|\boldsymbol{\mathcal{H}}\left[\!\left[\boldsymbol{v}\right]\!\right], \tag{2.4b}$$

where $\boldsymbol{v}$ is the vector of entropy variables and $\boldsymbol{\mathcal{H}} = \frac{\partial \boldsymbol{v}}{\partial \boldsymbol{q}}$ is a matrix that relates the variables in conserved and entropy space. This particularly simple choice for the dissipation term leads to a *scalar dissipation term*. Note that a scalar dissipation term cannot resolve contact discontinuities exactly, as it will always add dissipation on surfaces that separate zones of different densities. The reformulation of the dissipation term to incorporate the jump in entropy variables (rather than the jump in conservative variables) is done to be able to guarantee entropy stability [6]. The question is how should the entropy Jacobian be evaluated at the interface, where values from left and right are available.

3. Break down of Ismail and Roe's entropy conservative scheme and the KEPEC flux

First, we consider the widely used Ismail and Roe (IR) entropy conservative flux for Euler flows (see *e.g.* [7,8]). Define the arithmetic mean and the logarithmic mean of any strictly positive quantity as

$$\{\{\cdot\}\} = \frac{(\cdot)_\mathrm{L} + (\cdot)_\mathrm{R}}{2}, \quad (\cdot)^{\ln} = \frac{[\![\cdot]\!]}{[\![\ln(\cdot)]\!]},$$

where a stable numerical algorithm to compute the logarithmic mean when $(\cdot)_\mathrm{R} \approx (\cdot)_\mathrm{L}$ is given in [8, App. B].

Using the parameter vector $\boldsymbol{z}$, the mass flux at an interface is given by

$$f_\varrho^{\mathrm{IR}} = \tilde{\varrho}\tilde{u}, \quad \text{where} \quad \tilde{\varrho} = \{\{z_1\}\}z_3^{\ln}, \quad \text{and} \quad \tilde{u} = \frac{\{\{z_2\}\}}{\{\{z_1\}\}} \quad \text{with} \quad \boldsymbol{z} = \left[\sqrt{\frac{\varrho}{p}}, \sqrt{\frac{\varrho}{p}}u, \sqrt{\varrho p}\right]^\mathsf{T}. \tag{3.1}$$

Consider the following initial conditions representing a very simplified form of a strong shock in a uniform moving medium,

$$\gamma = 1.4, \quad \boldsymbol{p}_{\mathrm{L}} = [1, 10, 1], \quad \text{and} \quad \boldsymbol{p}_{\mathrm{R}} = \left[1, 10, 10^{-6}\right] \quad \text{with} \quad \boldsymbol{p} = [\varrho, u, p]. \tag{3.2}$$

Using a Finite Volume (FV) update (see *e.g.* [2]) with a CFL coefficient of $c = 0.6$ we find

$$\varrho'_{\mathrm{L}} \approx -37.5 \quad \text{and} \quad \varrho'_{\mathrm{R}} \approx 37.5$$

after the first time step (see also section 6). Clearly, the greatly overestimated mass flux is unphysical and the scheme breaks down. Note that the wrong mass flux cannot be compensated by the stabilization term, since any stabilization in the mass flux is proportional to the jump in density, which is zero according to (3.2).

If we, however, use the kinetic energy preserving entropy-conservative (KEPEC) flux presented by Chandrashekar [9] and recently extended to ideal MHD by Winters & Gassner [3], the mass flux is

$$f_{\varrho}^{\mathrm{KEPEC}} = \varrho^{\ln}\{\{u\}\}. \tag{3.3}$$

We obtain the updated densities

$$\varrho'_{\mathrm{L}} \approx 1.0 - 9 \times 10^{-10} \quad \text{and} \quad \varrho'_{\mathrm{R}} \approx 1.0 + 9 \times 10^{-10}.$$

Note that even for much higher pressure jumps, there is no pathological behavior as seen in the mass flux with the $\boldsymbol{z}$ parametrization (3.1). Since example conditions given in (3.2) are typical in astrophysical simulations, we conclude that the IR scheme is not suitable as an underlying entropy conservative scheme when constructing entropy stable schemes in a general way. Therefore, we use the KEPEC flux as the baseline entropy conserving flux in (2.2).

We further note that this example will equally fail in the case of ideal MHD.

4. Derivation technique for the discrete entropy Jacobian

The entropy variables for an ideal gas with entropy $s = -(\gamma - 1)\ln(\varrho) - \ln(\beta) - \ln(2)$ are

$$\boldsymbol{v} = \frac{\partial S}{\partial \boldsymbol{q}} = \left[\frac{\gamma - s}{\gamma - 1} - \beta\|\boldsymbol{u}\|^2,\ 2\beta u, 2\beta v, 2\beta w, -2\beta, 2\beta B_1, 2\beta B_2, 2\beta B_3\right]^{\mathsf{T}}, \quad \beta = \frac{\varrho}{2p} \propto \frac{1}{T}. \tag{4.1}$$

The goal is to derive the averages in such a way that the relation $[\![\boldsymbol{q}]\!] = \mathcal{H}[\![\boldsymbol{v}]\!]$ holds. The entries of the matrix $\mathcal{H}$ are derived step-by-step through the solution of 64 linear equations:

$$[\![\boldsymbol{q}]\!] = \left[\!\!\left[\begin{bmatrix} \varrho \\ \varrho u \\ \varrho v \\ \varrho w \\ E \\ B_1 \\ B_2 \\ B_3 \end{bmatrix}\right]\!\!\right] \overset{!}{=} \begin{bmatrix} \mathcal{H}_{1,1} & \mathcal{H}_{1,2} & \dots & \dots & \mathcal{H}_{1,7} & \mathcal{H}_{1,8} \\ \mathcal{H}_{2,1} & \mathcal{H}_{2,2} & \dots & \dots & \mathcal{H}_{2,7} & \mathcal{H}_{2,8} \\ \vdots & \vdots & \ddots & \ddots & \vdots & \vdots \\ \vdots & \vdots & \ddots & \ddots & \vdots & \vdots \\ \mathcal{H}_{7,1} & \mathcal{H}_{7,2} & \dots & \dots & \mathcal{H}_{7,7} & \mathcal{H}_{7,8} \\ \mathcal{H}_{8,1} & \mathcal{H}_{8,2} & \dots & \dots & \mathcal{H}_{8,7} & \mathcal{H}_{8,8} \end{bmatrix} \left[\!\!\left[\begin{bmatrix} \frac{\gamma - s}{\gamma - 1} - \beta\|\boldsymbol{u}\|^2 \\ 2\beta u \\ 2\beta v \\ 2\beta w \\ -2\beta \\ 2\beta B_1 \\ 2\beta B_2 \\ 2\beta B_3 \end{bmatrix}\right]\!\!\right] = \mathcal{H}[\![\boldsymbol{v}]\!]. \tag{4.2}$$

The procedure is to multiply each row of $\mathcal{H}$ with the expanded jump in the entropy variables. By examining each equation individually, all unknown entries of the discrete matrix are found.

The derivation of the first row of $\mathcal{H}$ is straightforward and therefore serves as an excellent example for the derivation technique. First, we use properties of the linear jump operator [3] to expand the jump in both the conservative and the entropy variables

$$[\![\boldsymbol{q}]\!] = \left[\!\!\left[\begin{bmatrix} \varrho \\ \varrho u \\ \varrho v \\ \varrho w \\ E \\ B_1 \\ B_2 \\ B_3 \end{bmatrix}\right]\!\!\right] = \begin{bmatrix} [\![\varrho]\!] \\ \{\{\varrho\}\}[\![u]\!] + \{\{u\}\}[\![\varrho]\!] \\ \{\{\varrho\}\}[\![v]\!] + \{\{v\}\}[\![\varrho]\!] \\ \{\{\varrho\}\}[\![w]\!] + \{\{w\}\}[\![\varrho]\!] \\ \left(\frac{\{\{\beta^{-1}\}\}}{2(\gamma-1)} + \frac{1}{2}\overline{\{\{\boldsymbol{u}^2\}\}}\right)[\![\varrho]\!] + \{\{\varrho\}\}\left(\{\{u\}\}[\![u]\!] + \{\{v\}\}[\![v]\!] + \{\{w\}\}[\![w]\!]\right) - \frac{\{\{\varrho\}\}}{2\overline{\beta^2}(\gamma-1)}[\![\beta]\!] + \sum_{i=1}^{3}\{\{B_i\}\}[\![B_i]\!] \\ [\![B_1]\!] \\ [\![B_2]\!] \\ [\![B_3]\!] \end{bmatrix},$$

$$[\![\boldsymbol{v}]\!] = \left[\!\!\left[\begin{bmatrix} \frac{\gamma-s}{\gamma-1} - \beta\|\boldsymbol{u}\|^2 \\ 2\beta u \\ 2\beta v \\ 2\beta w \\ -2\beta \\ 2\beta B_1 \\ 2\beta B_2 \\ 2\beta B_3 \end{bmatrix}\right]\!\!\right] = \begin{bmatrix} \frac{[\![\varrho]\!]}{\varrho^{\ln}} + \frac{[\![\beta]\!]}{\beta^{\ln}(\gamma-1)} - \Big(\{\{u^2\}\} + \{\{v^2\}\} + \{\{w^2\}\}\Big)[\![\beta]\!] - 2\{\{\beta\}\}\Big(\{\{u\}\}[\![u]\!] + \{\{v\}\}[\![v]\!] + \{\{w\}\}[\![w]\!]\Big) \\ 2\{\{\beta\}\}[\![u]\!] + 2\{\{u\}\}[\![\beta]\!] \\ 2\{\{\beta\}\}[\![v]\!] + 2\{\{v\}\}[\![\beta]\!] \\ 2\{\{\beta\}\}[\![w]\!] + 2\{\{w\}\}[\![\beta]\!] \\ -2[\![\beta]\!] \\ 2\{\{\beta\}\}[\![B_1]\!] + 2\{\{B_1\}\}[\![\beta]\!] \\ 2\{\{\beta\}\}[\![B_2]\!] + 2\{\{B_2\}\}[\![\beta]\!] \\ 2\{\{\beta\}\}[\![B_3]\!] + 2\{\{B_3\}\}[\![\beta]\!] \end{bmatrix},$$

with

$$\overline{\beta^2} = 2\{\{\beta\}\}^2 - \{\{\beta^2\}\}, \text{ and } \overline{\{\{\boldsymbol{u}^2\}\}} = \{\{u^2\}\} + \{\{v^2\}\} + \{\{w^2\}\}.$$

According to (4.2), the entries of the first row of $\boldsymbol{\mathcal{H}}$ can be obtained by solving

$$\begin{aligned}[\![\varrho]\!] = {} & \boldsymbol{\mathcal{H}}_{1,1}\left(\frac{[\![\varrho]\!]}{\varrho^{\ln}} + \frac{[\![\beta]\!]}{\beta^{\ln}(\gamma-1)} - \Big(\{\{u^2\}\} + \{\{v^2\}\} + \{\{w^2\}\}\Big)[\![\beta]\!] - 2\{\{\beta\}\}\Big(\{\{u\}\}[\![u]\!] + \{\{v\}\}[\![v]\!] + \{\{w\}\}[\![w]\!]\Big)\right) \\ & + \boldsymbol{\mathcal{H}}_{1,2}\left(2\{\{\beta\}\}[\![u]\!] + 2\{\{u\}\}[\![\beta]\!]\right) + \boldsymbol{\mathcal{H}}_{1,3}\left(2\{\{\beta\}\}[\![v]\!] + 2\{\{v\}\}[\![\beta]\!]\right) + \boldsymbol{\mathcal{H}}_{1,4}\left(2\{\{\beta\}\}[\![w]\!] + 2\{\{w\}\}[\![\beta]\!]\right) \\ & + \boldsymbol{\mathcal{H}}_{1,5}\left(-2[\![\beta]\!]\right) + \boldsymbol{\mathcal{H}}_{1,6}\left(2\{\{\beta\}\}[\![B_1]\!] + 2\{\{B_1\}\}[\![\beta]\!]\right) + \boldsymbol{\mathcal{H}}_{1,7}\left(2\{\{\beta\}\}[\![B_2]\!] + 2\{\{B_2\}\}[\![\beta]\!]\right) \\ & + \boldsymbol{\mathcal{H}}_{1,8}\left(2\{\{\beta\}\}[\![B_3]\!] + 2\{\{B_3\}\}[\![\beta]\!]\right). \end{aligned}$$

From this equation, we directly obtain the entries of the first row of the discretized entropy Jacobian,

$$\boldsymbol{\mathcal{H}}_1 = \begin{bmatrix} \varrho^{\ln} & \varrho^{\ln}\{\{u\}\} & \varrho^{\ln}\{\{v\}\} & \varrho^{\ln}\{\{w\}\} & \overline{E} & 0 & 0 & 0 \end{bmatrix}, \tag{4.3}$$

where we introduced additional notation for compactness

$$p^{\ln} = \frac{\varrho^{\ln}}{2\beta^{\ln}}, \quad \overline{E} = \frac{p^{\ln}}{\gamma-1} + \frac{1}{2}\varrho^{\ln}\overline{\|\boldsymbol{u}\|^2}, \quad \text{and} \quad \overline{\|\boldsymbol{u}\|^2} = 2\left(\{\{u\}\}^2 + \{\{v\}\}^2 + \{\{w\}\}^2\right) - \left(\{\{u^2\}\} + \{\{v^2\}\} + \{\{w^2\}\}\right).$$

One finds that the forthright solution of (4.2) leads to an asymmetric, *i.e.* not provably entropy stable, matrix $\boldsymbol{\mathcal{H}}$. Hence, it is not possible to derive a symmetric matrix such that the equality $[\![\boldsymbol{q}]\!] = \boldsymbol{\mathcal{H}}[\![\boldsymbol{v}]\!]$ holds exactly for all components of $\boldsymbol{q}$. However, if special care is taken during the expansion of the total energy term, a matrix $\hat{\boldsymbol{\mathcal{H}}}$ that obeys the required property can be found. It guarantees equality in all but the jump in energy term where the equality reduces to an asymptotic one. The modified jump in total energy reads

$$\begin{aligned}\overline{[\![E]\!]} = {} & \left(\frac{1}{2(\gamma-1)\beta^{\ln}} + \frac{1}{2}\overline{\|\boldsymbol{u}\|^2}\right)[\![\varrho]\!] - \frac{\varrho^{\ln}}{2(\gamma-1)}\frac{[\![\beta]\!]}{(\beta^{\ln})^2} + \{\{\varrho\}\}\left(\{\{u\}\}[\![u]\!] + \{\{v\}\}[\![v]\!] + \{\{w\}\}[\![w]\!]\right) \\ & + \sum_{i=1}^{3}\left(\{\{B_i\}\}[\![B_i]\!]\right) \simeq [\![E]\!]. \end{aligned} \tag{4.4}$$

Using $\overline{[\![E]\!]}$ in place of $[\![E]\!]$, we can solve (4.2) using the previously described technique where we have $([\![\boldsymbol{q}]\!])_i = (\hat{\boldsymbol{\mathcal{H}}}[\![\boldsymbol{v}]\!])_i$ for $i = \{1,2,3,4,6,7,8\}$ and $([\![\boldsymbol{q}]\!])_5 \simeq (\hat{\boldsymbol{\mathcal{H}}}[\![\vec{v}]\!])_5$. We get the complete dissipation matrix

$$\hat{\boldsymbol{\mathcal{H}}} = \begin{bmatrix} \varrho^{\ln} & \varrho^{\ln}\{\{u\}\} & \varrho^{\ln}\{\{v\}\} & \varrho^{\ln}\{\{w\}\} & \overline{E} & 0 & 0 & 0 \\ \varrho^{\ln}\{\{u\}\} & \varrho^{\ln}\{\{u\}\}^2 + \{\{p\}\} & \varrho^{\ln}\{\{u\}\}\{\{v\}\} & \varrho^{\ln}\{\{u\}\}\{\{w\}\} & \left(\overline{E} + \{\{p\}\}\right)\{\{u\}\} & 0 & 0 & 0 \\ \varrho^{\ln}\{\{v\}\} & \varrho^{\ln}\{\{v\}\}\{\{u\}\} & \varrho^{\ln}\{\{v\}\}^2 + \{\{p\}\} & \varrho^{\ln}\{\{v\}\}\{\{w\}\} & \left(\overline{E} + \{\{p\}\}\right)\{\{v\}\} & 0 & 0 & 0 \\ \varrho^{\ln}\{\{w\}\} & \varrho^{\ln}\{\{w\}\}\{\{u\}\} & \varrho^{\ln}\{\{w\}\}\{\{v\}\} & \varrho^{\ln}\{\{w\}\}^2 + \{\{p\}\} & \left(\overline{E} + \{\{p\}\}\right)\{\{w\}\} & 0 & 0 & 0 \\ \overline{E} & \left(\overline{E} + \{\{p\}\}\right)\{\{u\}\} & \left(\overline{E} + \{\{p\}\}\right)\{\{v\}\} & \left(\overline{E} + \{\{p\}\}\right)\{\{w\}\} & \hat{\boldsymbol{\mathcal{H}}}_{5,5} & \tau\{\{B_1\}\} & \tau\{\{B_2\}\} & \tau\{\{B_3\}\} \\ 0 & 0 & 0 & 0 & \tau\{\{B_1\}\} & \tau & 0 & 0 \\ 0 & 0 & 0 & 0 & \tau\{\{B_2\}\} & 0 & \tau & 0 \\ 0 & 0 & 0 & 0 & \tau\{\{B_3\}\} & 0 & 0 & \tau \end{bmatrix}, \tag{4.5}$$

with

$$\hat{\boldsymbol{\mathcal{H}}}_{5,5} = \frac{1}{\varrho^{\ln}}\left(\frac{(p^{\ln})^2}{\gamma-1} + \overline{E}^2\right) + \{\{p\}\}\left(\{\{u\}\}^2 + \{\{v\}\}^2 + \{\{w\}\}^2\right) + \tau\sum_{i=1}^{3}\left(\{\{B_i\}\}^2\right), \quad \{\{p\}\} = \frac{\{\{\varrho\}\}}{2\{\{\beta\}\}}, \quad \text{and} \quad \tau = \frac{\{\{p\}\}}{\{\{\varrho\}\}}.$$

The discrete entropy Jacobian for the compressible Euler equations is

$$\hat{\boldsymbol{\mathcal{H}}}_{\text{Euler}} = \begin{bmatrix} \varrho^{\ln} & \varrho^{\ln}\{\{u\}\} & \varrho^{\ln}\{\{v\}\} & \varrho^{\ln}\{\{w\}\} & \overline{E} \\ \varrho^{\ln}\{\{u\}\} & \varrho^{\ln}\{\{u\}\}^2 + \{\{p\}\} & \varrho^{\ln}\{\{u\}\}\{\{v\}\} & \varrho^{\ln}\{\{u\}\}\{\{w\}\} & \left(\overline{E} + \{\{p\}\}\right)\{\{u\}\} \\ \varrho^{\ln}\{\{v\}\} & \varrho^{\ln}\{\{v\}\}\{\{u\}\} & \varrho^{\ln}\{\{v\}\}^2 + \{\{p\}\} & \varrho^{\ln}\{\{v\}\}\{\{w\}\} & \left(\overline{E} + \{\{p\}\}\right)\{\{v\}\} \\ \varrho^{\ln}\{\{w\}\} & \varrho^{\ln}\{\{w\}\}\{\{u\}\} & \varrho^{\ln}\{\{w\}\}\{\{v\}\} & \varrho^{\ln}\{\{w\}\}^2 + \{\{p\}\} & \left(\overline{E} + \{\{p\}\}\right)\{\{w\}\} \\ \overline{E} & \left(\overline{E} + \{\{p\}\}\right)\{\{u\}\} & \left(\overline{E} + \{\{p\}\}\right)\{\{v\}\} & \left(\overline{E} + \{\{p\}\}\right)\{\{w\}\} & \frac{1}{\varrho^{\ln}}\left(\frac{(p^{\ln})^2}{\gamma-1} + \overline{E}^2\right) + \{\{p\}\}\left(\{\{u\}\}^2 + \{\{v\}\}^2 + \{\{w\}\}^2\right) \end{bmatrix}. \tag{4.6}$$

Clearly, the discrete entropy Jacobian matrices (4.5) and (4.6) are symmetric. It is straightforward, albeit laborious, to verify using Sylvester's criterion that the discrete matrices are symmetric positive definite (SPD). Due to the structure of the dissipation term (2.4b), the SPD property of the new matrices guarantees that the numerical flux (2.2) complies with the entropy inequality (2.1) discretely.

Next, we exemplarily test the equality (2.4a) = (2.4b) for a single entry of the obtained matrix for ideal MHD (4.5), namely the mass flux using the initial conditions (3.2). If we use the discrete entropy Jacobian derived in this work, we find

$$\hat{\boldsymbol{\mathcal{H}}}_1 = \left[\varrho^{\ln} \quad \varrho^{\ln}\{\{u\}\} \quad \varrho^{\ln}\{\{v\}\} \quad \varrho^{\ln}\{\{w\}\} \quad \frac{p^{\ln}}{\gamma-1} + \frac{1}{2}\varrho^{\ln}\overline{\|\boldsymbol{u}\|^2} \quad 0 \quad 0 \quad 0 \right]$$
$$\Rightarrow \hat{\boldsymbol{\mathcal{H}}}_1 \cdot [\![\boldsymbol{v}]\!] = 0 = [\![\varrho]\!]$$

as expected.

If we, however, chose a naive averaging, this equality does not hold any longer. Assume that all entries of the entropy Jacobian are given by arithmetic means of the primitive variables, *e.g.*

$$\boldsymbol{H}_1 = \left[\{\{\varrho\}\} \quad \{\{\varrho\}\}\{\{u\}\} \quad \{\{\varrho\}\}\{\{v\}\} \quad \{\{\varrho\}\}\{\{w\}\} \quad \frac{\{\{p\}\}}{\gamma-1} + \frac{1}{2}\{\{\varrho\}\}\{\{\boldsymbol{u}^2\}\} \right] \quad \text{we find}$$
$$\Rightarrow \boldsymbol{H}_1 \cdot [\![\boldsymbol{v}]\!] \approx 1.25 \times 10^6 \neq [\![\varrho]\!],$$

which will inevitably lead to negative densities for any practical CFL coefficient.

This short numerical experiment highlights the main massage of this work that even if one uses a suitable baseline entropy conserving flux, the stabilization term still has to be constructed carefully in order to obtain a stable numerical scheme.

We can use this to create a local Lax–Friedrichs (LLF) like numerical scheme

$$\boldsymbol{f}^{\text{KEPES,LLF}} = \boldsymbol{f}^{\text{KEPEC}} - \frac{1}{2}|\lambda_{\max}^{\text{local}}|\hat{\boldsymbol{\mathcal{H}}}\,[\![\boldsymbol{v}]\!] \tag{4.7}$$

where

$$\lambda_{\max}^{\text{local}} = \max(\lambda_{\max,\text{R}}, \lambda_{\max,\text{L}}) \tag{4.8}$$

is the largest of the local ideal MHD wave speeds (*i.e.* eigenvectors of the ideal MHD system)

$$\lambda_{\pm\text{f}} = u \pm c_\text{f}, \qquad \lambda_{\pm\text{s}} = u \pm c_\text{s}, \qquad \lambda_{\pm\text{a}} = u \pm c_\text{a}, \qquad \lambda_{\text{D,E}} = u \tag{4.9}$$

with

$$c_\text{a}^2 = b_1^2, \quad c_{\text{f,s}}^2 = \frac{1}{2}\left(a^2 + \|\boldsymbol{b}\|^2 \pm \sqrt{(a^2+\|\boldsymbol{b}\|^2)^2 - 4a^2b_1^2}\right), \tag{4.10}$$
$$a^2 = \gamma\,\frac{p}{\varrho}, \quad \boldsymbol{b} = \frac{\boldsymbol{B}}{\sqrt{\varrho}}, \quad b_\perp^2 = b_2^2 + b_3^2, \quad \text{and} \quad \beta_{1,2,3} = \frac{b_{1,2,3}}{b_\perp},$$

where c_f and c_s are the fast and slow magnetoacoustic wave speeds, respectively. c_a is the Alfvén wave speed. In (4.10), the plus sign corresponds to the fast magnetoacoustic speed, c_f, and the minus sign corresponds to the slow magnetoacoustic speed, c_s. Some eigenvalues may coincide depending on the magnetic field strength and direction. Hence, the complete set of eigenvectors is not obtained in a straightforward way [10,11].

5. A note on computational complexity

We are interested in the computational complexity of our proposed scheme in comparison to the IR scheme and less complicated dissipation operators. In order to quantitatively investigate the numerical complexity we prepared a benchmark program written in `FORTRAN`. We take the full numerical flux functions from [2, (3.20)] (IR flux) and [3, (B.3)] (KEPEC flux) and compute the fluxes from random initial conditions.

In Table 1, we list the computational time in CPUs needed for ten million iterations on a single core. We disable the automatic code optimization of the compiler (*i.e.* `ifort -O0 test.F90`) for a fair comparison of the numerical complexity of the algorithms. As can be seen, the entropy conserving flux of Ismail and Roe (IR) is about 60% more costly than the kinetic energy preserving entropy conserving flux (KEPEC). This might be surprising on the first hand, but one has to keep in mind that the IR flux makes use of the complex $\boldsymbol{z}$ vector parametrization, introducing a considerable amount of hidden additional complexity.

A second question goes towards the computational costs of the entropy stable fluxes where the new matrix dissipation operator we found requires very specific averages. Therefore, we want to compare the computational time needed to compute the scheme given by (4.7) to three numerical schemes:

Table 1
Computing the entropy conserving flux.

IR EC flux	KEPEC flux
1.553 ± 0.007	0.975 ± 0.002

Table 2
Computing the stabilization terms.

non-ES scheme	naive $\mathbf{H}$ matrix	new $\hat{\mathcal{H}}$ matrix
0.227 ± 0.002	5.467 ± 0.007	6.063 ± 0.010

Non-ES scheme This scheme is given by a simple LLF stabilization:

$$\boldsymbol{f}^{\text{non-ES,LLF}} = \boldsymbol{f}^{\text{KEPEC}} - \frac{1}{2}|\lambda_{\max}^{\text{local}}|\,[\![\boldsymbol{q}]\!]\,. \tag{5.1}$$

Ad hoc dissipation operator We arbitrarily choose arithmetic means in the entropy Jacobian:

$$\boldsymbol{f}^{\text{KEPES,naive}} = \boldsymbol{f}^{\text{KEPEC}} - \frac{1}{2}|\lambda_{\max}^{\text{local}}|\mathbf{H}\,[\![\boldsymbol{v}]\!]\,. \tag{5.2}$$

This procedure is consistent with present literature since it has not been mentioned before that special care has to be taken when selecting the dissipation operator.

New dissipation operator For this scheme, we use the entropy Jacobian derived in this work:

$$\boldsymbol{f}^{\text{KEPES}} = \boldsymbol{f}^{\text{KEPEC}} - \frac{1}{2}|\lambda_{\max}^{\text{local}}|\hat{\mathcal{H}}\,[\![\boldsymbol{v}]\!]\,. \tag{5.3}$$

Note that the scheme given by (5.3) is identical to (4.7).

The three schemes given by (5.1)–(5.3) rely on the same baseline flux, the kinetic energy preserving entropy conservative (KEPEC) ideal MHD flux. The only difference is in the selection of the stabilization term.

As can be seen in Table 2, the non-entropy stable, very simple dissipation term is much faster than the computation involving the entropy Jacobian matrix. However, as shown in the numerical results section, both (5.1) and (5.2) lead to a breakdown of the scheme in the first timestep. Although (5.3) is the most expensive stabilization in this comparison, it is the only stable scheme that does not suffer from a breakdown. We find that the computation of the new $\hat{\mathcal{H}}$ matrix involves about 27% higher computational costs compared to the H matrix with ad hoc averages. This only minor increase in computational costs can be attributed to the fact that, although we have to compute more complicated averages, we precalculate them once and use the stored result when filling the matrix.

Note that a significant portion of the execution time ($\approx 40\%$) is spend in the `FORTRAN` function `MATMUL` used to multiply the entropy Jacobian with the jump of the entropy vector. Hence, an optimized version may increase the computational efficiency considerably.

6. Numerical tests

We illustrate the increased robustness of the scheme derived in this work by considering two simple one dimensional test problems.

6.1. Shock in fast moving magnetized background medium – breakdown of the IR scheme

As a first robustness test, we consider a demanding problem involving a shock traveling though a fast moving and magnetized medium. This test represents typical situations in large-scale astrophysical simulations namely supernova explosions in various environments, *e.g.* [12]. We take the first numerical experiment given in this paper (3.2) and create a full numerical test. The test is computed on a uniform grid of 256 cells with a CFL coefficient of 0.8 and a domain size of $x \in [-1, 1]$. We select uniform density, $\varrho = 1$, uniform velocity of the background $\boldsymbol{u} = [10, 0, 0]^\intercal$ as well as a uniform background magnetic field $\boldsymbol{B} = [1 \times 10^{-2}, 0, 0]$. To simulate the strong explosion, we inject a pressure discontinuity with $p_{\text{in}} = 1.0$ at $|x_{\text{in}}| \leq 0.1$. Outside of this injection region, we set $p_{\text{out}} = 1 \times 10^{-6}$. We use periodic boundary conditions and compute the solution at $t_{\text{end}} = 5 \times 10^{-2}$ using an ideal gas equation of state with an adiabatic index of $\gamma = 5/3$.

The result of this test is shown in Fig. 1. We observe that the IR scheme fails during the first time step even for greatly lowered CFL coefficients. However, this test can easily be computed using the KEPEC + the new scalar dissipation flux derived in this work (4.7). As expected, two shock fronts develop, propagating outwards. The "explosion" is moving to the right with the initial background velocity, leading to a final displacement of $u \cdot t_{\text{end}} = 0.5$ at $t_{\text{end}} = 5 \times 10^{-2}$.

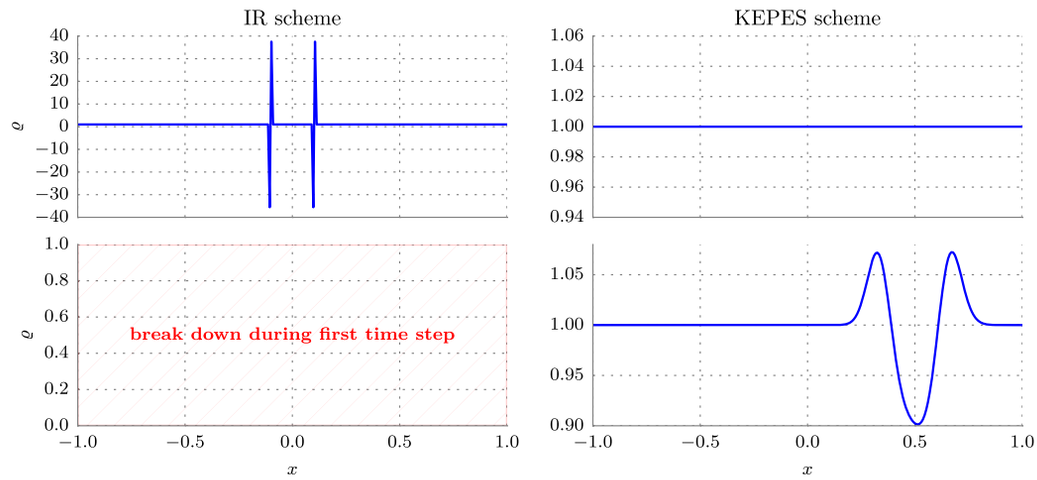

Fig. 1. Result of the fast shock propagating through a magnetized medium which is moving in x-direction with a constant speed. We show the result of the first time step ($t \approx 4 \times 10^{-4}$, top) and the set simulation end time ($t_{\text{end}} = 5 \times 10^{-2}$, bottom). The IR scheme (left) fails in the first time step, while the new scheme derived in this work (right) is stable.

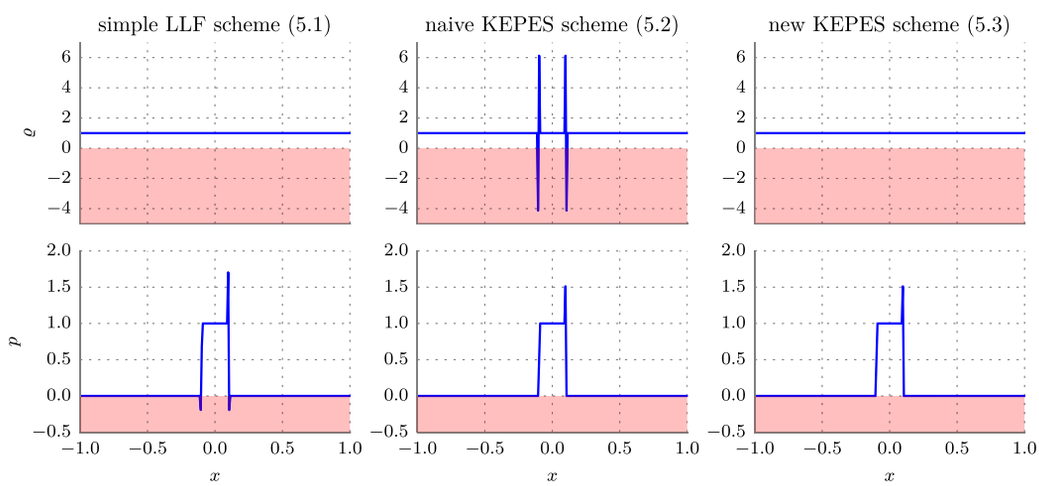

Fig. 2. Density (top) and thermal pressure (bottom) plots of the shock propagating through a fast magnetized medium test at $t \approx 4 \times 10^{-4}$. The simple LLF scheme (left) over-stabilizes the total energy update, leading to a break down because of negative pressures. The KEPES scheme with the naively averaged dissipation operator (center) produces both negative densities and pressures. The scheme involving the correctly averaged dissipation operator (right) is stable.

6.2. Importance of the averaging in the dissipation operator

As a second robustness test, we use the previously described test case and use the three different stabilizations terms described in section 5. We find that the two stabilizations which are not carefully constructed for entropy stability fail for the demanding test case described above.

In Fig. 2 we see a failure of the simple non-entropy stable LLF scheme (left) as well as of the scheme involving the naively averaged entropy Jacobian $\mathbf{H}$ (middle). The LLF scheme overestimates the stabilization of the total energy and hence leads to negative thermal pressures in two cells. The naive KEPES scheme breaks down because the required equalities $[\![\boldsymbol{q}]\!] \simeq \mathbf{H} \cdot [\![\boldsymbol{v}]\!]$ are not approximated well for very large jumps in neither the conservative nor the entropy variables. Therefore, this demanding test triggers a breakdown of the scheme, leading to large negative densities ($\min(\varrho) \approx -4$) as well as small negative pressures ($\min(p) \approx -1.4 \times 10^{-5}$). In direct comparison, we see that interchanging the discrete entropy Jacobian matrix[1] is sufficient to make the scheme robust.

[1] Which is the only difference between (5.2) and (5.3).

7. Conclusion

In this work we present a technique that is convenient for the derivation of discrete entropy Jacobian operators. We exemplarily apply the technique to a very simple choice of a Rusanov-like mean value entropy Jacobian that guarantees fulfillment of the entropy inequality for ideal MHD and the compressible Euler equations. It emerges that a unique averaging technique is required and it is shown that a discrete SPD entropy Jacobian matrix can be obtained choosing specific averages during the expansion of the jump in total energy.

As a baseline flux, we choose the kinetic energy preserving entropy conservative flux recently presented in [3,9] since we experience unphysical results with the entropy conserving flux of Ismail and Roe for shocks in moving media as we show using a simple test problem in the numerical results section. Future work on the field of entropy-stable approximations can benefit from the knowledge of the required averaging technique presented in this paper. Follow up work will describe more complex matrix dissipation terms.

Acknowledgements

DD and SW acknowledge the support of the Bonn–Cologne Graduate School for Physics and Astronomy (BCGS), which is funded through the Excellence Initiative (GSC 260), as well as the Sonderforschungsbereich (SFB) 956 on the "Conditions and impact of star formation". SW thanks the Deutsche Forschungsgemeinschaft (DFG) for funding through the SPP 1573 "The physics of the interstellar medium".

Appendix A. Application of Sylvester's criterion

We give here the eight determinants of the leading principal minors (M_{1-8}) of the obtained matrix for ideal MHD $\hat{\mathcal{H}}$ (4.5). Since $\varrho, p, \tau > 0, \gamma > 1$, the SPD property is immediately clear.

$$
\begin{aligned}
|M_1| &= \left|\left[\varrho^{\ln}\right]\right| = \varrho^{\ln},\\
|M_2| &= \left|\begin{bmatrix} \varrho^{\ln} & \varrho^{\ln}\{\{u\}\} \\ \varrho^{\ln}\{\{u\}\} & \varrho^{\ln}\{\{u\}\}^2 + \{\{p\}\} \end{bmatrix}\right| = \varrho^{\ln}\{\{p\}\},\\
|M_3| &= \left|\begin{bmatrix} \varrho^{\ln} & \varrho^{\ln}\{\{u\}\} & \varrho^{\ln}\{\{v\}\} \\ \varrho^{\ln}\{\{u\}\} & \varrho^{\ln}\{\{u\}\}^2 + \{\{p\}\} & \varrho^{\ln}\{\{u\}\}\{\{v\}\} \\ \varrho^{\ln}\{\{v\}\} & \varrho^{\ln}\{\{v\}\}\{\{u\}\} & \varrho^{\ln}\{\{v\}\}^2 + \{\{p\}\} \end{bmatrix}\right| = \varrho^{\ln}(\{\{p\}\})^2,\\
|M_4| &= \cdots = \varrho^{\ln}(\{\{p\}\})^3,\\
|M_5| &= \cdots = \varrho^{\ln}(\{\{p\}\})^3 \left(\tau\left(\{\{B_1\}\}^2 + \{\{B_2\}\}^2 + \{\{B_3\}\}^2\right) + 2\frac{p^{\ln}}{\gamma-1}\frac{p^{\ln}}{\varrho^{\ln}}\right),\\
|M_6| &= \cdots = \varrho^{\ln}(\{\{p\}\})^3\tau \left(\tau\left(\{\{B_2\}\}^2 + \{\{B_3\}\}^2\right) + 2\frac{p^{\ln}}{\gamma-1}\frac{p^{\ln}}{\varrho^{\ln}}\right),\\
|M_7| &= \cdots = \varrho^{\ln}(\{\{p\}\})^3\tau^2 \left(\tau\{\{B_3\}\}^2 + 2\frac{p^{\ln}}{\gamma-1}\frac{p^{\ln}}{\varrho^{\ln}}\right),\\
|M_8| &= |\hat{\mathcal{H}}| = \cdots = 2\frac{(\{\{p\}\})^3 (p^{\ln})^2 \tau^3}{(\gamma-1)}.
\end{aligned}
$$

References

[1] U.S. Fjordholm, S. Mishra, E. Tadmor, Arbitrarily high-order accurate entropy stable essentially nonoscillatory schemes for systems of conservation laws, SIAM J. Numer. Anal. 50 (2) (2012) 544–573, http://dx.doi.org/10.1137/110836961.

[2] D. Derigs, A.R. Winters, G.J. Gassner, S. Walch, A novel high-order, entropy stable, 3D AMR MHD solver with guaranteed positive pressure, J. Comput. Phys. 317 (2016) 223–256, http://dx.doi.org/10.1016/j.jcp.2016.04.048.

[3] A.R. Winters, G.J. Gassner, Affordable, entropy conserving and entropy stable flux functions for the ideal MHD equations, J. Comput. Phys. 304 (2016) 72–108, http://dx.doi.org/10.1016/j.jcp.2015.09.055.

[4] U.S. Fjordholm, S. Mishra, E. Tadmor, Well-balanced and energy stable schemes for the shallow water equations with discontinuous topography, J. Comput. Phys. 230 (14) (2011) 5587–5609, http://dx.doi.org/10.1016/j.jcp.2011.03.042.

[5] E. Tadmor, The numerical viscosity of entropy stable schemes for systems of conservation laws, Math. Comput. 49 (179) (1987) 91–103, http://dx.doi.org/10.2307/2008251.

[6] T.J. Barth, Numerical methods for gasdynamic systems on unstructured meshes, in: D. Kröner, M. Ohlberger, C. Rohde (Eds.), An Introduction to Recent Developments in Theory and Numerics for Conservation Laws, in: Lecture Notes in Computational Science and Engineering, vol. 5, Springer, Berlin, Heidelberg, 1999, pp. 195–285.

[7] P.L. Roe, Affordable, entropy consistent flux functions, in: Eleventh International Conference on Hyperbolic Problems: Theory, Numerics and Applications, Lyon, 2006.
[8] F. Ismail, P.L. Roe, Affordable, entropy-consistent Euler flux functions, II: entropy production at shocks, J. Comput. Phys. 228 (15) (2009) 5410–5436, http://dx.doi.org/10.1016/j.jcp.2009.04.021.
[9] P. Chandrashekar, Kinetic energy preserving and entropy stable finite volume schemes for compressible Euler and Navier–Stokes equations, Commun. Comput. Phys. 14 (2013) 1252–1286, http://dx.doi.org/10.4208/cicp.170712.010313a.
[10] M. Brio, C.C. Wu, An upwind differencing scheme for the equations of ideal magnetohydrodynamics, J. Comput. Phys. 75 (2) (1988) 400–422, http://dx.doi.org/10.1016/0021-9991(88)90120-9.
[11] P. Cargo, G. Gallice, Roe matrices for ideal MHD and systematic construction of Roe matrices for systems of conservation laws, J. Comput. Phys. 136 (2) (1997) 446–466, http://dx.doi.org/10.1006/jcph.1997.5773.
[12] A. Gatto, S. Walch, M.-M.M. Low, T. Naab, P. Girichidis, S.C.O. Glover, R. Wünsch, R.S. Klessen, P.C. Clark, C. Baczynski, T. Peters, J.P. Ostriker, J.C. Ibáñez Mejía, S. Haid, Modelling the supernova-driven ISM in different environments, Mon. Not. R. Astron. Soc. 449 (1) (2015) 1057–1075, http://dx.doi.org/10.1093/mnras/stv324.

4.4 Publication III

Derigs, D., Winters, A. R., Gassner, G. J., Walch, S., Bohm, M., (July 2018b). "Ideal GLM-MHD: About the entropy consistent nine-wave magnetic field divergence diminishing ideal magnetohydrodynamics equations." In: *Journal of Computational Physics* 364, pp. 420–467. ISSN: 0021-9991.
DOI: 10.1016/j.jcp.2018.03.002. arXiv: 1711.06269.

The third paper presented in this cumulative thesis presents a modified form of the ideal magneto-hydrodynamic (MHD) equations with the aid of generalized Lagrangian multiplier (GLM) to incorporate the divergence-free condition. Moreover, we consider non-zero magnetic field divergence and develop the ideal MHD equations from compressible Euler equations to include a non-conservative term that is proportional to the divergence-free condition. Importantly, this non-conservative term guarantees that the Lorentz force is correctly captured when $\nabla \cdot \boldsymbol{B} \neq 0$. Finally, an entropy-stable numerical flux function is derived and employed on the AMR code `FLASH` for a representative number of numerical test cases.

One of the prominent novelties in this research is the idea of evolving towards a divergence-free state instead of strictly enforcing the divergence-free condition from the outset. Proper consideration is given to the effect of the non-conservative terms (magnetic field divergence) in general. To underline the importance of our work in a more general physics framework, a continuous entropy analysis of several well-known MHD formulations with the GLM ansatz is performed to demonstrate that they fail to follow the second law of thermodynamics discretely.

Contribution overview

The topic of this extensive work is the development of a new mathematical model we propose as a replacement for the long used ideal MHD model. This work would not been possible without the continued support from my collaborators. I did all derivations in this work (except section 4.3.2) myself. I furthermore did all simulations, analyzed and interpreted them.

Stefanie Walch helped me with the correct physical interpretation of the consequences of my findings especially in the second chapter. Furthermore, she provided general advise throughout my entire research and raised questions that where interesting to address.

Gregor Gassner assisted me in finding, e.g., a technique to extend the scheme to arbitrary high spatial order retaining the entropy stability property. Moreover, he suggested numerical tests and gave invaluable advise that helped strengthen the entire article.

Andrew Winters derived the GLM-based changes for the matrix dissipation terms (section 4.3.2) for my new model based on the techniques we developed in Winters et al. (2017).

Marvin Bohm contributed the idea of assuming a specific form of the ideal MHD non-conservative term from the outset of the derivations. This enabled me to greatly simplify the derivation of

the discrete entropy stable schemes and slightly reduce the overall arithmetic complexity of the scheme. I extended and applied his suggestion to my new ideal GLM-MHD system.

Stefanie Walch, Gregor Gassner and Andrew Winters edited the paper.

Journal of Computational Physics 364 (2018) 420–467

Contents lists available at ScienceDirect

Journal of Computational Physics

www.elsevier.com/locate/jcp

Ideal GLM-MHD: About the entropy consistent nine-wave magnetic field divergence diminishing ideal magnetohydrodynamics equations

Dominik Derigs [a,*], Andrew R. Winters [b], Gregor J. Gassner [b], Stefanie Walch [a], Marvin Bohm [b]

[a] *I. Physikalisches Institut, Universität zu Köln, Zülpicher Straße 77, 50937 Köln, Germany*
[b] *Mathematisches Institut, Universität zu Köln, Weyertal 86-90, 50931 Köln, Germany*

ARTICLE INFO

Article history:
Received 16 November 2017
Received in revised form 28 February 2018
Accepted 1 March 2018
Available online 8 March 2018

Keywords:
Magnetohydrodynamics
Entropy stability
Divergence-free magnetic field
Divergence cleaning

ABSTRACT

The paper presents two contributions in the context of the numerical simulation of magnetized fluid dynamics. First, we show how to extend the ideal magnetohydrodynamics (MHD) equations with an inbuilt magnetic field divergence cleaning mechanism in such a way that the resulting model is consistent with the second law of thermodynamics. As a byproduct of these derivations, we show that not all of the commonly used divergence cleaning extensions of the ideal MHD equations are thermodynamically consistent. Secondly, we present a numerical scheme obtained by constructing a specific finite volume discretization that is consistent with the discrete thermodynamic entropy. It includes a mechanism to control the discrete divergence error of the magnetic field by construction and is Galilean invariant. We implement the new high-order MHD solver in the adaptive mesh refinement code `FLASH` where we compare the divergence cleaning efficiency to the constrained transport solver available in `FLASH` (unsplit staggered mesh scheme).

1. Introduction

Widespread applications of the ideal magnetohydrodynamic (MHD) equations emerged in many disciplines, including, but not limited to, astrophysical and magnetically confined fusion plasma applications. The mentioned applications, usually deal with extreme conditions like near vacuum up to ultra-high density environments where shocks of varying type and strength are the rule rather than the exception. Hence, the accuracy and robustness of numerical simulation codes are very important.

Yet, the mathematical model of ideal MHD has some shortcomings that can cause the results to become unphysical. As neither the full set of universally valid thermodynamics laws nor the divergence-free condition of the magnetic field is directly coupled into the classic mathematical model of ideal MHD, it is possible to obtain physically invalid solutions.

In order to single out physically relevant solutions, we have to augment the system with additional admissibility criteria. One admissibility criterion in the case of ideal MHD is the divergence-free condition of the magnetic field that is expressed by Gauß's law for magnetism

* Corresponding author.
E-mail address: derigs@ph1.uni-koeln.de (D. Derigs).

https://doi.org/10.1016/j.jcp.2018.03.002
0021-9991/

$$\nabla \cdot \boldsymbol{B} = 0. \tag{1.1}$$

The implementation of (1.1) into a numerical approximation is a major difficulty. As detailed in the early 1980s by Brackbill and Barnes [1, eq. (2)], numerical discretization errors always have a noticeable impact on the temporal evolution of the magnetic field divergence:

$$\frac{\partial}{\partial t}(\nabla \cdot \boldsymbol{B}) = 0 + \mathcal{O}\big(\Delta x^m,\ \Delta t^n\big), \tag{1.2}$$

where Δx and Δt are the space and time discretization steps, and $m, n \geq 0$ are scheme dependent constants that also depend on the smoothness of the problem. Since the advent of sufficiently powerful computers, many approaches have been proposed to address this issue and "clean" such errors, including projection methods, constrained transport, and hyperbolic divergence cleaning. We give a brief overview over these methods with special focus on the hyperbolic divergence cleaning as we find it particularly useful in the context of highly efficient, highly parallelizable numerical schemes for large-scale applications.

Another natural admissibility criterion is given by the universally valid laws of thermodynamics. Most numerical schemes do not take the second law of thermodynamics directly into account but rather equip the system with a minute amount of diffusion. We seek to derive a numerical scheme that complies with the laws of thermodynamics and especially the second law, *i.e.* the entropy inequality. Following the work of *e.g.* [2–5], we use this law as an additional admissibility criterion to construct discretizations that agree with the laws of thermodynamics. In this way, we enforce that the solution does not converge towards physically irrelevant solutions which increases their numerical robustness, as thermodynamically impossible physical processes that could *e.g.* lead to negative thermal pressures are forbidden.

In this work, we derive a new mathematical model that is built to explicitly take into account all the mentioned relevant physics in order to impede unphysical results of numerical simulations. We start from first principles to avoid commonly done simplifications that, as we explain herein, make the typically used classic mathematical model of ideal MHD unsuitable in describing the behavior of physical flows in certain regimes of numerically computed, discrete solutions.

For this, we derive a new system of equations, which we deem the ideal GLM-MHD equations, that allows the construction of a novel magnetic field divergence diminishing scheme that naturally complies with thermodynamics. Furthermore, we investigate our new model in great detail and present both the methods we use as well as the details to allow a straightforward implementation of our scheme into the reader's own simulation code.

We shortly summarize the new contributions presented in this work:

- We derive the ideal MHD equations from the compressible Euler equations where we explicitly allow non-zero magnetic field divergence in Maxwell's equations. We physically motivate and highlight important findings (Sec. 2)
- We derive a new physically motivated mathematical model, the *ideal GLM-MHD equations* which we thoroughly investigate from both mathematical and physical perspectives (Sec. 3.4)
- We derive entropy stable numerical flux functions. We give all necessary details to code the high-order scheme we are describing in a straightforward manner (Secs. 4.2 and 4.3)

2. The ideal MHD equations in the case of $\nabla \cdot \boldsymbol{B} \neq 0$

We begin with the three-dimensional compressible Euler equations describing non-magnetized single-fluid flows. We then couple the effect of magnetic fields to the model. We find that the classic model of ideal MHD in the form of conservation laws is not valid for arbitrary flows, but only for fluids where (1.1) holds *exactly*. Interestingly, our derivations reveal results that are known from previous publications [6,7] while our independent and fundamentally different approach motivates these findings with a solely physically motivated mindset which eases the interpretation.

An important first step is, due to the findings of Brackbill and Barnes [1, eq. (2)], see also (1.2), that we shouldn't assume the divergence-free condition of the magnetic field (1.1) is fulfilled *exactly* at *all* times in numerical simulations. In fact, Dirac [8] showed that quantum mechanics does not preclude the existence of isolated magnetic monopoles although physicists often reason that magnetic monopoles are unlikely to exist. Their reasoning mainly comes from the fact that quantum mechanics, as it is usually established, seems possible only when there are no isolated magnetic monopoles. Dirac, however, disproved this view. One of the most important theoretical motivations of introducing magnetic monopoles is to obtain Maxwell's equations in symmetric form with regard to charges. Note that the Maxwell equations retain all their properties, such as invariance under a global duality transformation that mixes electric and magnetic fields [9], when magnetic monopoles are included, whether or not they exist.

During the derivation of the classic ideal MHD equations in conservative form, (1.1) is used to simplify the computations. However, this ultimately destroys the validity of the system of ideal MHD equations for flows where the divergence-free condition is not fulfilled to a certain extent, which is generally the case in discrete approximations. This is commonly found in simulations due to errors caused by any given numerical approximation. Note that this more general form of the ideal MHD equations is, of course, perfectly valid in the case of $\nabla \cdot \boldsymbol{B} = 0$, as the only difference is that certain terms aren't neglected early on in the derivation.

We start from the three-dimensional compressible Euler equations written compactly as a system of conservation laws,

$$\frac{\partial}{\partial t}\boldsymbol{q} + \nabla\cdot\boldsymbol{f} = \frac{\partial}{\partial t}\begin{bmatrix}\varrho\\ \varrho\boldsymbol{u}\\ E\end{bmatrix} + \nabla\cdot\begin{bmatrix}\varrho\boldsymbol{u}\\ \varrho(\boldsymbol{u}\otimes\boldsymbol{u}) + p\mathbf{I}\\ \boldsymbol{u}\left(\frac{1}{2}\varrho\|\boldsymbol{u}\|^2 + \frac{\gamma p}{\gamma-1}\right)\end{bmatrix} = \begin{bmatrix}0\\ \boldsymbol{F}\\ E_\mathrm{a}\end{bmatrix}, \quad \begin{matrix}\text{(a)}\\ \text{(b)}\\ \text{(c)}\end{matrix} \tag{2.1}$$

where ϱ, $\varrho\boldsymbol{u}$, and E are the density, volume specific momenta, and total energy density of the plasma system, p is the thermal pressure, $\mathbf{I}$ is the 3×3 identity matrix. $\boldsymbol{F}$ and E_a denote the sum of all (external) forces and energy source terms which are important for the fluid. The multidimensional flux function is denoted by $\boldsymbol{f}$. The flux Jacobian has only real eigenvalues and the right eigenvectors are linearly independent, *i.e.* the compressible Euler equations are hyperbolic. We assume that the total energy and the thermal pressure are related through the ideal gas law

$$p = \varrho RT = (\gamma-1)\left(E - \frac{1}{2}\varrho\|\boldsymbol{u}\|^2\right), \tag{2.2}$$

with the ratio of specific heats, $\gamma = \frac{c_p}{c_v}$.

For coupling electromagnetic fields to the fluid, we must examine the equations which describe their behavior. The generalized Maxwell's equations for non-vanishing magnetic charge densities are

$$\nabla\cdot\boldsymbol{E} = \frac{\rho_e}{\varepsilon_0}, \quad \text{(a)} \qquad \nabla\cdot\boldsymbol{B} = \mu_0\rho_m, \quad \text{(b)} \qquad \nabla\times\boldsymbol{B} = \frac{1}{c^2}\frac{\partial\boldsymbol{E}}{\partial t} + \mu_0\boldsymbol{j}_e, \quad \text{(c)} \qquad -\nabla\times\boldsymbol{E} = \frac{\partial\boldsymbol{B}}{\partial t} + \mu_0\boldsymbol{j}_m, \quad \text{(d)} \tag{2.3}$$

where $\boldsymbol{E}$ and $\boldsymbol{B}$ are the electric and magnetic fields [9, Sec. 6.11]. The charge densities are $\rho_{e,m}$, where the subscript e refers to electric charges and m refers to magnetic charges. A similar distinction is made for the current densities, $\boldsymbol{j}_{e,m} := \rho_{e,m}\boldsymbol{u}$. The equations (2.3) are invariant under a global duality transformation that mixes electric and magnetic fields [9]. This underlines that the limitation $\rho_m = 0$ is only a convention.

By investigating how the magnetic field influences the fluid we can integrate the effects of magnetic fields into the compressible Euler equations. For this, we consider the Lorentz force caused by the electric and magnetic fields, denoted by $\boldsymbol{F}_L$. In our derivations, we assume that the magnetic field in the only cause of external forces, *i.e.* $\boldsymbol{F}\equiv\boldsymbol{F}_L$ and use it on the right-hand side momentum equation (2.1b). If the system contains additional forces, *e.g.* gravitational acceleration or radiation, these forces need to be added to the momentum equation as well. The most general form of the Lorentz force is

$$\boldsymbol{F}_L = q_e\left(\boldsymbol{E} + \boldsymbol{u}\times\boldsymbol{B}\right) + q_m\left(\boldsymbol{B} - \frac{\boldsymbol{u}\times\boldsymbol{E}}{c^2}\right), \tag{2.4}$$

where $q_{e,m}$ are the electric and magnetic charges. Note that the second term on the right-hand side vanishes for $q_m \propto \nabla\cdot\boldsymbol{B} = 0$, see [10]. The total Lorentz force per unit volume is then

$$\boldsymbol{F}_L = e_e(n_i - n_e)\boldsymbol{E} + e_e(n_i\boldsymbol{u}_i - n_e\boldsymbol{u}_e)\times\boldsymbol{B} + e_m(n_i - n_e)\boldsymbol{B} - e_m\frac{n_i\boldsymbol{u}_i - n_e\boldsymbol{u}_e}{c^2}\times\boldsymbol{E} \tag{2.5}$$

where the ions and electrons are denoted by subscripts i, and e, respectively. Their number densities are $n_{i,e}$. The unit charges of electric and magnetic monopoles are denoted by e_e and e_m, respectively. The quasi-neutrality assumption, $n := n_i = n_e$, that is due to the single-fluid model leads to

$$\begin{aligned}\boldsymbol{F}_L &= ne_e(\boldsymbol{u}_I - \boldsymbol{u}_E)\times\boldsymbol{B} - \frac{ne_m}{c^2}(\boldsymbol{u}_I - \boldsymbol{u}_E)\boldsymbol{E}\\ &= \boldsymbol{j}_e\times\boldsymbol{B} - \frac{1}{c^2}\boldsymbol{j}_m\times\boldsymbol{E},\end{aligned} \tag{2.6}$$

where we can use the magnetic current density given by (2.3b)

$$\boldsymbol{j}_m = \rho_m\boldsymbol{u} = \mu_0^{-1}(\nabla\cdot\boldsymbol{B})\boldsymbol{u}. \tag{2.7}$$

We use the ideal Ohm's law for ionized fluids in motion,

$$\boldsymbol{E} + \boldsymbol{u}\times\boldsymbol{B} = \eta\boldsymbol{j}_e = 0, \tag{2.8}$$

with the assumption of vanishing resistivity, $\eta = 0$, *i.e.* infinite conductivity of the plasma which is an essential assumption of ideal MHD, to obtain

$$\begin{aligned}\boldsymbol{F}_L &= \boldsymbol{j}_e\times\boldsymbol{B} + \frac{1}{c^2}\boldsymbol{j}_m\times(\boldsymbol{u}\times\boldsymbol{B})\\ &= \frac{1}{\mu_0}\left(\nabla\times\boldsymbol{B} - \frac{1}{c^2}\frac{\partial\boldsymbol{E}}{\partial t}\right)\times\boldsymbol{B} + \frac{1}{c^2}(\nabla\cdot\boldsymbol{B})\boldsymbol{u}\times(\boldsymbol{u}\times\boldsymbol{B}).\end{aligned} \tag{2.9}$$

With this result, we add the magnetic forces into the momentum equation to obtain the non-divergence-free form of the ideal MHD momentum equation

$$\frac{\partial}{\partial t}(\varrho \boldsymbol{u}) + \nabla \cdot \left(\varrho(\boldsymbol{u} \otimes \boldsymbol{u}) + \left(p + \frac{1}{2\mu_0}\|\boldsymbol{B}\|^2\right)\mathbf{I} - \frac{\boldsymbol{B} \otimes \boldsymbol{B}}{\mu_0} \right) = \frac{\nabla \cdot \boldsymbol{B}}{\mu_0} \left(\frac{1}{c^2}\boldsymbol{u} \times (\boldsymbol{u} \times \boldsymbol{B}) - \boldsymbol{B} \right) - \frac{1}{\mu_0 c^2} \frac{\partial \boldsymbol{E}}{\partial t} \times \boldsymbol{B}. \tag{2.10}$$

In the non-relativistic limit, $\|\boldsymbol{u}\| \ll c$, (2.10) simplifies to become

$$\frac{\partial}{\partial t}(\varrho \boldsymbol{u}) + \nabla \cdot \left(\varrho(\boldsymbol{u} \otimes \boldsymbol{u}) + \left(p + \frac{1}{2\mu_0}\|\boldsymbol{B}\|^2\right)\mathbf{I} - \frac{\boldsymbol{B} \otimes \boldsymbol{B}}{\mu_0} \right) = -\frac{\nabla \cdot \boldsymbol{B}}{\mu_0}\boldsymbol{B} \tag{2.11}$$

as the displacement current, where the rightmost term in (2.10) can be neglected for a Newtonian theory of MHD [11, Sec. 3.1.4]. We observe that (2.11) reduces to the standard form of the momentum equation in the ideal MHD equation system for $\nabla \cdot \boldsymbol{B} \to 0$. Note that the non-relativistic limit is not a restriction in our derivations, but a natural assumption as we chose to start from the compressible Euler equations (2.1) which are themselves derived for the non-relativistic case.

Now that we accounted for the influence of the magnetic field on the fluid in the momentum equation, we must add a new evolution equation for the magnetic field components to the system of equations. From (2.3), we obtain the generalized induction equation

$$\frac{\partial \boldsymbol{B}}{\partial t} = -\nabla \times \boldsymbol{E} - \mu_0 \boldsymbol{j}_m. \tag{2.12}$$

Using (2.8) we get

$$\frac{\partial \boldsymbol{B}}{\partial t} - \nabla \times (\boldsymbol{u} \times \boldsymbol{B}) = -\mu_0 \boldsymbol{j}_m = -(\nabla \cdot \boldsymbol{B})\boldsymbol{u}. \tag{2.13}$$

The obtained induction equation (2.13) is added in the system of compressible Euler equations to model the evolution of the magnetic field.

To close the system of the generalized ideal MHD equations, we need to compute the total energy equation including the effects of the aforementioned modifications. The total energy update equations is

$$\frac{\partial E}{\partial t} = \frac{\partial}{\partial t}\left(\frac{1}{2}\varrho\|\boldsymbol{u}\|^2 + \epsilon + \frac{1}{2}\|\boldsymbol{B}\|^2 \right). \tag{2.14}$$

After many manipulations, that can be found in Appendix E, we find

$$\frac{\partial E}{\partial t} + \nabla \cdot \left(\boldsymbol{u}\left(\frac{1}{2}\varrho\|\boldsymbol{u}\|^2 + \frac{\gamma p}{\gamma - 1} + \frac{\|\boldsymbol{B}\|^2}{2\mu_0} \right) - \frac{\boldsymbol{B}(\boldsymbol{u} \cdot \boldsymbol{B})}{\mu_0} \right) = -\mu_0^{-1}(\nabla \cdot \boldsymbol{B})(\boldsymbol{u} \cdot \boldsymbol{B}), \tag{2.15}$$

which is the commonly known form of the ideal MHD total energy conservation law equipped with a non-conservative part on the right hand side. Note that, for the sake of convenience, we set $\mu_0 = 1$ hereafter to express the ideal MHD equations in dimensionless units. See Appendix G for a full presentation of the ideal MHD equations in physical units.

We summarize the ideal MHD equations in their general form to be

$$\frac{\partial}{\partial t}\boldsymbol{q} + \nabla \cdot \boldsymbol{f} = \frac{\partial}{\partial t}\begin{bmatrix} \varrho \\ \varrho\boldsymbol{u} \\ E \\ \boldsymbol{B} \end{bmatrix} + \nabla \cdot \begin{bmatrix} \varrho\boldsymbol{u} \\ \varrho(\boldsymbol{u} \otimes \boldsymbol{u}) + \left(p + \frac{1}{2}\|\boldsymbol{B}\|^2\right)\mathbf{I} - \boldsymbol{B} \otimes \boldsymbol{B} \\ \boldsymbol{u}\left(\frac{1}{2}\varrho\|\boldsymbol{u}\|^2 + \frac{\gamma p}{\gamma - 1} + \|\boldsymbol{B}\|^2\right) - \boldsymbol{B}(\boldsymbol{u} \cdot \boldsymbol{B}) \\ \boldsymbol{u} \otimes \boldsymbol{B} - \boldsymbol{B} \otimes \boldsymbol{u} \end{bmatrix} = -(\nabla \cdot \boldsymbol{B}) \begin{bmatrix} 0 \\ \boldsymbol{B} \\ \boldsymbol{u} \cdot \boldsymbol{B} \\ \boldsymbol{u} \end{bmatrix} \begin{matrix} \text{(a)} \\ \text{(b)} \\ \text{(c)} \\ \text{(d)} \end{matrix} \tag{2.16}$$

with the new pressure equation that includes the magnetic energy

$$p = (\gamma - 1)\left(E - \frac{1}{2}\varrho\|\boldsymbol{u}\|^2 - \frac{1}{2}\|\boldsymbol{B}\|^2 \right) \tag{2.17}$$

defined in the domain $\Omega \subset \mathbb{R}^3$.

A remarkable outcome of the physically motivated derivation is that we obtain a set of equations which is known to have a number of desirable properties lacking in the classical ideal MHD equations. The system (2.16a–d) is not only symmetrizable [12] but also Galilean invariant [3,7,13]. The non-conservative terms found on the right hand side were first mentioned by Godunov [6] who investigated whether the equations of ideal MHD can be put into symmetric hyperbolic form. Interestingly, he found the same additional non-conservative terms were required to obtain a PDE system that is symmetrizable, he took an altogether different approach. The formulation of ideal MHD system considered here is often referred to as the *eight-wave* formulation, because it supports eight traveling plane wave solutions. As the non-conservative term on the right hand side is proportional to the divergence of the magnetic field, it is, on the continuous level, nothing but adding zero in a clever way. Further advantages are that the flux Jacobian has only real eigenvalues and the right eigenvectors are linearly

independent, *i.e.* the ideal MHD equations in form (2.16a–d) are hyperbolic. We will further investigate on the importance of these consequences later in this work.

Numerical simulations of this system are known to be more stable than the same numerical methods applied to the original ideal MHD equations. This has been demonstrated by Powell [7] and numerically confirmed by others (see *e.g.* [14, Sec. 6.1]). From the derivations allowing for $\nabla \cdot \boldsymbol{B} \neq 0$ a new physical understanding for the addition of the non-conservative terms emerge and it is clear that their appearance are essential parts of the system. We conclude that the classical ideal MHD equations are invalid for regions where $\nabla \cdot \boldsymbol{B} \neq 0$ even if this deviation is only minor when the divergence of the magnetic field is controlled to a sufficient degree. This is due to the fact that classical ideal MHD models contain the divergence-free condition as a decoupled partial differential equation and hence assume that $\nabla \cdot \boldsymbol{B} \neq 0$ can never happen. However, our fundamentally physically motivated derivation reveals that classical numerical schemes which neglect the magnetic field divergence terms on the right hand side of (2.16a–d) may discretely describe the wrong physics if they cannot assure (1.1) pointwise.

Without the non-conservative terms, a modeled magnetized fluid may not behave in a physically correct way if the magnetic field divergence is not negligible. To highlight this, we investigate what effect the Lorentz force has on the fluid with and without the derived non-conservative terms:

1. Lorentz force **with** non-conservative terms

$$\begin{aligned}\boldsymbol{F}_L &= \boldsymbol{j}_e \times \boldsymbol{B} = (\nabla \times \boldsymbol{B}) \times \boldsymbol{B} \\ &= -\nabla \cdot \left(\frac{1}{2} \|\boldsymbol{B}\|^2 - \boldsymbol{B} \otimes \boldsymbol{B} \right) - (\nabla \cdot \boldsymbol{B}) \boldsymbol{B}\end{aligned} \tag{2.18}$$

   The projection of the Lorentz force onto the magnetic field is

$$\boldsymbol{F}_L \cdot \frac{\boldsymbol{B}}{\|\boldsymbol{B}\|} = 0, \tag{2.19}$$

   so $\boldsymbol{F}_L \perp \boldsymbol{B}$ as expected and the fluid does not feel a force parallel to the magnetic field lines even in the presence of non-vanishing magnetic field divergence.
2. Lorentz force **without** non-conservative terms

$$\hat{\boldsymbol{F}}_L = -\nabla \cdot \left(\frac{1}{2} \|\boldsymbol{B}\|^2 - \boldsymbol{B} \otimes \boldsymbol{B} \right) \tag{2.20}$$

   The projection of this form of the Lorentz force onto the magnetic field is

$$\hat{\boldsymbol{F}}_L \cdot \frac{\boldsymbol{B}}{\|\boldsymbol{B}\|} = -(\nabla \cdot \boldsymbol{B}) \|\boldsymbol{B}\|. \tag{2.21}$$

   We see that a modeled magnetized fluid only behaves correctly if the magnetic field divergence is zero or at least negligible. In case of any notable non-zero magnetic field divergence, the fluid feels an artificial force parallel to the magnetic field lines. This leads to physically wrong behavior and makes it clear that the ideal MHD system without the correct choice of non-conservative terms is invalid in the case of $\nabla \cdot \boldsymbol{B} \neq 0$. Note that $\hat{\boldsymbol{F}}_L$ is identical to the divergence of the Maxwell stress tensor for vanishing electric fields.

In the eight-wave formulation of ideal MHD, the magnetic field divergence is an advected quantity with the fluid. This can easily be seen by taking the divergence of the induction equation (2.16d),

$$\begin{aligned}&\frac{\partial}{\partial t}(\nabla \cdot \boldsymbol{B}) = -\nabla \cdot \big(\nabla \times (\boldsymbol{u} \times \boldsymbol{B})\big) - \mu_0 \nabla \cdot \boldsymbol{j}_m) = -\nabla \cdot (\mu_0 \boldsymbol{j}_m) = -\nabla \cdot \big(\boldsymbol{u}(\nabla \cdot \boldsymbol{B})\big), \\ \Rightarrow \quad &\frac{\partial}{\partial t}(\nabla \cdot \boldsymbol{B}) + \nabla \cdot (\boldsymbol{u}(\nabla \cdot \boldsymbol{B})) = 0.\end{aligned} \tag{2.22}$$

The appearance of the non-conservative term in the total energy equations can be understood using similar reasoning. Assume a positive magnetic field divergence which may also be expressed as a *source* of magnetic field. Such a source may generate additional magnetic and/or kinetic energy when moving through the fluid. If, however, we artificially enforce total energy conservation by neglecting the non-conservative term on the total energy, this *increase* in energy can inevitably lead to a *loss* of internal energy. This is due to the fact that internal energy is the reminder of the subtraction of the other energies from the total energy (2.17). Hence, errors in the computation of the energies will always be shifted into the computed internal energy. It is clear that in a region with sufficiently strong magnetic sources, the pressure could easily become negative if the total energy is not corrected accordingly from the magnetic fields. If, however, the non-conservative term is included, then the gain in total energy is accounted by the non-conservative term in the total energy evolution equation. In other words, as we do not strictly enforce total energy conservation. Thus, the thermal energy is not artificially modified and the positivity of a numerical scheme is improved.

Furthermore, the non-conservative terms are necessary to ensure Galilean invariance of the system for any $\nabla \cdot \boldsymbol{B} \neq 0$. Note that Galilean invariance is a necessary property of any well-posed theory in non-relativistic physics.

Although we derive the ideal MHD equations for the general case of arbitrary $\nabla \cdot \boldsymbol{B}$, we want to minimize the magnetic field divergence everywhere in numerical simulations to match the evolution simulation results to the observational constraint (1.1). Hence, the remainder of this paper is concerned with the derivation of an entropy stable scheme that starts from the equations derived in this section. The scheme we build will discretely satisfy the second law of thermodynamics as well as minimize the divergence of the magnetic field by construction.

3. Incorporating the divergence-free constraint into the model

In this section, we investigate the coupling of the magnetic field divergence into the ideal MHD equations. The investigations in this section are, in principle, self-sufficient and independent from any non-conservative parts being present in the system of equations. However, we will merge new findings with our results from Sec. 2 wherever appropriate to construct a mathematical model that is valid in regions of non-vanishing magnetic field divergence.

There exist different ways of enforcing (1.1) discretely, commonly called *divergence cleaning* techniques as they are designed to "clean up" divergence errors made by the numerical algorithms. Many schemes are designed to "treat" the divergence errors in the magnetic field, but never get rid of them entirely. The conventional divergence cleaning methods are shortly described in the following.

3.1. Non-conservative term approach

With the non-conservative term approach (also known as source term approach, *e.g.* [7]), a *non-conservative term* is added to the system of conservation laws that acts to minimize magnetic field divergence. Source terms generally lead to a loss of conservation in the quantities they affect which may be undesirable. The non-conservative term we use in this work can be understood as advecting non-zero magnetic field divergence with the fluid speed (2.22). As the authors found in previous work (*e.g.* [2]) such a divergence advection is especially problematic at stagnation points of the flow where magnetic field divergence can build up due to the dependence of the divergence cleaning on the local fluid velocity. Hence, the non-conservative term approach is typically insufficient to ensure the numerical fulfillment of (1.1) on its own.

3.2. Projection method

An alternative approach is the *projection method* described by Brackbill and Barnes [1] and Marder [15]. The projection method has successfully been applied by, *e.g.* Zachary et al. [16], Balsara [17], and more recently by Crockett et al. [18] as well as the authors [2]. The projection method is implemented for divergence cleaning as a completely separate post-processing step, *i.e.* the original scheme remains unchanged. It has been extensively described by the authors in [2, Sec. 3.10]. In essence, the projection method acts as a source term and affects the conservation of the magnetic field, but it changes the magnetic field components in an unpredictable way. Therefore, it is unclear if cleaning the divergence errors with a projection method can build a numerical scheme that is thermodynamically consistent.

3.3. Constrained transport

Another approach is the *constrained transport method* developed by Evans and Hawley [19] or Balsara and Spicer [20] (reviewed in [21]). This method originally comes from the staggered-mesh scheme of Yee [22] for electromagnetism in a vacuum. Technically, the divergence-free constraint is satisfied by representing the magnetic field as cell face averaged quantities (as opposed to the usual choice of cell center volume averages). On such a grid, the MHD equations can be approximated such that they preserve numerical solenoidality of the magnetic field by construction through Stokes' theorem. Note that Balsara and Kim [23] found advantages for the staggered-mesh in their comparison between divergence-*cleaning* and divergence-*free* methods for stringent test cases. However, it is not clear if provably entropy stable schemes can be constructed for staggered-meshes [24].

3.4. Generalized Lagrangian multipliers

As detailed by Munz et al. [25], the divergence constraint for the electric field can be coupled with the induction equation by introducing a new real scalar field ψ also known as *generalized Lagrangian multiplier* (GLM). Dedner et al. [26] applied this technique to ideal MHD in order to incorporate the divergence-free condition (1.1) into the ideal MHD equations. However, as we will show later, the GLM modification of the ideal MHD equations as presented by Dedner et al. is inconsistent with the second law of thermodynamics as we show in Sec. 4.1.1.

In this work, we describe a novel entropy consistent formulation involving generalized Lagrangian multipliers. We call the resulting scheme the ideal GLM-MHD system. Similar to Dedner et al., the idea is not to enforce the divergence-free condition (1.1) exactly, but rather to construct a scheme that is designed to evolve towards a divergence-free state.

We couple the divergence of the magnetic field to Faraday's equation and add a new evolution equation for ψ using a hyperbolic ansatz. The new equations read:

$$\frac{\mathrm{d}}{\mathrm{d}t}\boldsymbol{B} = \nabla\times(\boldsymbol{u}\times\boldsymbol{B}) \quad\Longrightarrow\quad \frac{\mathrm{d}}{\mathrm{d}t}\boldsymbol{B} = \nabla\times(\boldsymbol{u}\times\boldsymbol{B}) - c_h\nabla\psi\,, \quad \frac{\mathrm{d}}{\mathrm{d}t}\psi := -c_h(\nabla\cdot\boldsymbol{B}) \tag{3.1}$$

where we highlight the modifications in red. Note that we specified (3.1) using Lagrangian derivatives, also known as convective derivatives. The advantage is that this directly leads to a Galilean invariant formulation.

The newly introduced *divergence-correcting field* is denoted by ψ, where c_h is the *hyperbolic divergence cleaning speed*. Our definition of the generalized Lagrangian multiplier ψ, compared to the definition of Dedner et al. results in a nicer set of entropy variables reducing the complexity of the forthcoming thermodynamic analysis. It is easily seen that for vanishing magnetic field divergence the correcting field $\psi\to 0$ and the highlighted contributions in (3.1) vanish, returning the model to the ideal MHD equations as derived in Sec. 2. Thus, the GLM modifications to the ideal MHD model are consistent and correctly restore the continuous limit.

Before we continue, we re-write (3.1) into a form similar to (2.16) for the sake of convenience:

$$\frac{\partial}{\partial t}\boldsymbol{B} + \nabla\cdot(\boldsymbol{u}\otimes\boldsymbol{B} - \boldsymbol{B}\otimes\boldsymbol{u} + c_h\psi\mathbf{I}) + \boldsymbol{u}(\nabla\cdot\boldsymbol{B}) = 0, \tag{3.2a}$$

$$\frac{\partial}{\partial t}\psi + c_h(\nabla\cdot\boldsymbol{B}) + \boldsymbol{u}\cdot\nabla\psi = 0, \tag{3.2b}$$

where we again highlight the modification with respect to (2.16d) in red.

If we assume that the solution is sufficiently smooth, such that all derivatives are well defined, we differentiate with respect to time and space to obtain the following relations from (3.2):

$$\frac{\partial}{\partial t}(\nabla\cdot\boldsymbol{B}) = -\nabla\cdot\big(\boldsymbol{u}(\nabla\cdot\boldsymbol{B})\big) - c_h\nabla^2\psi = -\frac{1}{c_h}\frac{\partial^2}{\partial t^2}\psi - \frac{1}{c_h}\frac{\partial}{\partial t}(\boldsymbol{u}\cdot\nabla\psi), \text{ and} \tag{3.3}$$

$$\frac{\partial}{\partial t}(\nabla^2\psi) = -c_h\nabla^2(\nabla\cdot\boldsymbol{B}) - \nabla^2(\boldsymbol{u}\cdot\nabla\psi) = -c_h^{-1}\frac{\partial}{\partial t}\nabla\cdot\big(\boldsymbol{u}(\nabla\cdot\boldsymbol{B})\big) - c_h^{-1}\frac{\partial^2}{\partial t^2}(\nabla\cdot\boldsymbol{B}). \tag{3.4}$$

From these relations, it is straightforward to derive wave equations for both the magnetic field divergence as well as the correcting field ψ

$$\frac{\partial^2}{\partial t^2}(\nabla\cdot\boldsymbol{B}) - c_h^2\nabla^2(\nabla\cdot\boldsymbol{B}) - c_h\nabla^2(\boldsymbol{u}\cdot\nabla\psi) + \frac{\partial}{\partial t}\nabla\cdot(\boldsymbol{u}(\nabla\cdot\boldsymbol{B})) = 0, \tag{3.5}$$

and

$$\frac{\partial^2}{\partial t^2}\psi \qquad - c_h^2\nabla^2\psi \qquad - c_h\nabla\cdot(\boldsymbol{u}\cdot\nabla\psi) + \frac{\partial}{\partial t}\big(\boldsymbol{u}\cdot\nabla\psi\big) = 0. \tag{3.6}$$

We see that the two wave equations (3.5) and (3.6) are coupled through the term $c_h\nabla\cdot(\boldsymbol{u}\cdot\nabla\psi)$ and we look at a combined wave equation,

$$\frac{\partial^2}{\partial t^2}(\nabla\cdot\boldsymbol{B}) - c_h^2\nabla^2(\nabla\cdot\boldsymbol{B}) + \frac{\partial}{\partial t}\nabla\big(\boldsymbol{u}(\nabla\cdot\boldsymbol{B})\big) = \frac{\partial^2}{\partial t^2}(\hat{\nabla}\psi) - c_h^2\nabla^2(\hat{\nabla}\psi) + \frac{\partial}{\partial t}\nabla(\boldsymbol{u}\cdot(\hat{\nabla}\psi)), \tag{3.7}$$

where we used the notation $\hat{\nabla}\psi := \sum_{i=x,y,z}\frac{\partial\psi}{\partial i}$.

Here, we see a complex interaction between the divergence treatment due to the advection of the magnetic monopoles with the fluid velocity, $\boldsymbol{u}$, and the newly introduced GLM correction field, ψ, as well as the hyperbolic cleaning speed, c_h. This complex interaction is expected as ψ and $\boldsymbol{B}$ are not independent quantities, but a gradient in ψ is created by a non-zero divergence in the magnetic field. As such, we investigate the behavior of the magnetic field divergence based on (3.7). It is important to note that the effects described in the following take place simultaneously. However, for the sake of simplicity, we split the analysis into separate parts and discuss the effect as if they are independent.

Wave components in (3.7):

$$\frac{\partial^2}{\partial t^2}(\nabla\cdot\boldsymbol{B}) - c_h^2\nabla^2(\nabla\cdot\boldsymbol{B}) = 0 \tag{3.8}$$

This part is a wave equation describes the isotropic propagation of $\nabla\cdot\boldsymbol{B}$ with constant speed c_h. So, local divergence errors by this part of (3.7) are isotropically propagated away from where they have been created with finite speed c_h. Looking back at the initially discussed source term approach, it becomes clear that the GLM approach does not suffer from the problem of accumulating magnetic field divergence at stagnation points of the fluid as this term is independent of the fluid velocity, $\boldsymbol{u}$, and we always have $c_h > 0$.

$$\frac{\partial^2}{\partial t^2}(\hat{\nabla}\psi) - c_h^2\nabla^2(\hat{\nabla}\psi) = 0 \tag{3.9}$$

We see that $\hat{\nabla}\psi$ propagates isotropically with constant speed c_h, just as the magnetic field divergence.

Advective components in (3.7):

$$\frac{\partial}{\partial t}(\nabla\cdot\boldsymbol{B}) + \nabla\cdot(\boldsymbol{u}(\nabla\cdot\boldsymbol{B})) = 0 \tag{3.10}$$

This equation is a standard advection equation describing the transport of $\nabla\cdot\boldsymbol{B}$ by bulk motion. It is clear that (3.10), as a continuity equation, conserves $\nabla\cdot\boldsymbol{B}$ by construction. This part is a direct consequence of the non-conservative terms we derived in Section 2 and corresponds to the "divergence wave" of the well-known eight-wave formulation.

$$\frac{\partial}{\partial t}(\hat{\nabla}\psi) + \nabla\cdot(\boldsymbol{u}(\hat{\nabla}\psi)) = 0 \tag{3.11}$$

As before, we see that $\hat{\nabla}\psi$ behaves identically to the magnetic field divergence in that it is advected with the flow. Just like (3.10), this passive advection equation is an expected result for a Galilean invariant formulation.

In (3.1) we introduce the possibility to advect the divergence error with the correcting field ψ. Also, the correcting field couples into the induction and therefore can alter the magnetic field. This transfer of information between the magnetic field components and the correcting field is important for divergence cleaning, but raises the question of how can ψ affect the magnetic energy $E_{\text{mag}} = \frac{1}{2}\|\boldsymbol{B}\|^2$. It stands to reason that the correcting field contains some form of "energy" for which we should account. As the thermal energy is computed by subtracting the kinetic and magnetic energies from the total energy, any information regarding loss/gain of magnetic energy would be falsely attributed into thermal energy.

Tricco and Price [27] investigated the effect of Dedner et al.'s GLM modification of the ideal MHD equations in the framework of smoothed particles hydrodynamics (SPH). They pointed out that the energy contained within the ψ field should be defined such that, in the absence of damping terms, any change in magnetic energy should be balanced by a corresponding change in the energy stored in the correcting field. Hence, we introduce a new kind of energy stored in the ψ field, E_ψ, which becomes a new component of the total fluid energy, E, for ensuring total energy conservation. As $\boldsymbol{B}$ and ψ both have units of magnetic fields, and because we observe a surprising symmetry between B_1 and ψ in the one-dimensional form of (3.1) for vanishing fluid velocities,

$$(B_1)_t + c_h(\psi)_x + u(B_1)_x = 0, \quad \text{and} \quad (\psi)_t + c_h(B_1)_x + u(\psi)_x = 0,$$

we make the ansatz

$$E_\psi := \frac{1}{2}\psi^2. \tag{3.12}$$

Since we introduce a new form of energy into the system, we must account for its temporal evolution. Therefore, we investigate the effect which the modifications (3.2a) and (3.2b) have on the conservation law for the total energy, $E = \frac{p}{\gamma-1} + \frac{\varrho}{2}\|\boldsymbol{u}\|^2 + \frac{1}{2}\|\boldsymbol{B}\|^2 + \frac{1}{2}\psi^2$. To do so we examine the evolution of the magnetic energy

$$\frac{\partial}{\partial t}\left(\frac{1}{2}\|\boldsymbol{B}\|^2\right) = \boldsymbol{B}\cdot\underbrace{\frac{\partial\boldsymbol{B}}{\partial t}}_{(3.2a)} = -\boldsymbol{B}\cdot\nabla(\boldsymbol{u}\otimes\boldsymbol{B} - \boldsymbol{B}\otimes\boldsymbol{u}) - c_h\boldsymbol{B}\cdot\nabla\psi + (\boldsymbol{B}\cdot\boldsymbol{u})(\nabla\cdot\boldsymbol{B}), \tag{3.13}$$

as well as a contribution from the new ψ field energy (3.12)

$$\frac{\partial}{\partial t}\left(\frac{1}{2}\psi^2\right) = \psi\cdot\underbrace{\frac{\partial\psi}{\partial t}}_{(3.2b)} = -c_h\psi(\nabla\cdot\boldsymbol{B}) + \boldsymbol{u}\psi(\nabla\psi). \tag{3.14}$$

Since

$$c_h\boldsymbol{B}\cdot\nabla\psi + c_h\psi(\nabla\cdot\boldsymbol{B}) = c_h\nabla\cdot(\psi\boldsymbol{B}),$$

we find that the correct form of the total energy conservation equation for ideal GLM-MHD is given by

$$\frac{\partial}{\partial t}\left(\frac{1}{2}\varrho\|\boldsymbol{u}\|^2 + \frac{p}{\gamma-1} + \frac{1}{2}\|\boldsymbol{B}\|^2 + \frac{1}{2}\psi^2\right) = -\nabla\cdot\left(\boldsymbol{u}\left(\frac{1}{2}\varrho\|\boldsymbol{u}\|^2 + \frac{p}{\gamma-1} + p + \|\boldsymbol{B}\|^2\right) - \boldsymbol{B}(\boldsymbol{u}\cdot\boldsymbol{B}) + c_h\psi\boldsymbol{B}\right)$$
$$- (\boldsymbol{B}\cdot\boldsymbol{u})(\nabla\cdot\boldsymbol{B}) + \boldsymbol{u}\psi(\nabla\psi). \tag{3.15}$$

Hence, the new **ideal GLM-MHD system** reads

$$\boxed{\frac{\partial}{\partial t}\boldsymbol{q}+\nabla\cdot\boldsymbol{f}=\frac{\partial}{\partial t}\begin{bmatrix}\varrho\\ \varrho\boldsymbol{u}\\ E\\ \boldsymbol{B}\\ \psi\end{bmatrix}+\nabla\cdot\begin{bmatrix}\varrho\boldsymbol{u}\\ \varrho(\boldsymbol{u}\otimes\boldsymbol{u})+\left(p+\frac{1}{2}\|\boldsymbol{B}\|^2\right)\mathbf{I}-\boldsymbol{B}\otimes\boldsymbol{B}\\ \boldsymbol{u}\left(\frac{1}{2}\varrho\|\boldsymbol{u}\|^2+\frac{\gamma p}{\gamma-1}+\|\boldsymbol{B}\|^2\right)-\boldsymbol{B}(\boldsymbol{u}\cdot\boldsymbol{B})+c_h\psi\boldsymbol{B}\\ \boldsymbol{u}\otimes\boldsymbol{B}-\boldsymbol{B}\otimes\boldsymbol{u}+c_h\psi\mathbf{I}\\ c_h\boldsymbol{B}\end{bmatrix}=-\boldsymbol{\Upsilon}_{\mathrm{GLM}},}\quad\begin{matrix}\text{(a)}\\ \text{(b)}\\ \text{(c)}\\ \text{(d)}\\ \text{(e)}\end{matrix}\tag{3.16}$$

with

$$\boldsymbol{\Upsilon}_{\mathrm{GLM}}:=(\nabla\cdot\boldsymbol{B})\begin{bmatrix}0\\ \boldsymbol{B}\\ \boldsymbol{u}\cdot\boldsymbol{B}\\ \boldsymbol{u}\\ 0\end{bmatrix}+(\nabla\psi)\cdot\begin{bmatrix}\mathbf{0}\\ 0\\ \boldsymbol{u}\psi\\ 0\\ \boldsymbol{u}\end{bmatrix}\tag{3.17}$$

and the new thermodynamic pressure

$$p=(\gamma-1)\,\epsilon\qquad\text{and}\qquad\epsilon=E-\frac{1}{2}\varrho\|\boldsymbol{u}\|^2-\frac{1}{2}\|\boldsymbol{B}\|^2-\frac{1}{2}\psi^2.\tag{3.18}$$

If the divergence of the magnetic field is zero, the new system is identical to the original ideal MHD system (2.16). If, however, the initial solution does not satisfy the divergence-free constraint then the deviations will decay. This new set of equations ensures that any magnetic divergence caused by inaccuracies of a numerical method for the ideal GLM-MHD system remains small.

The ideal GLM-MHD system is invariant under a Galilean transformation, *i.e.* invariant to a transformation into a frame of reference moving with a constant relative velocity $\boldsymbol{u}_0$ ($\boldsymbol{x}'=\boldsymbol{x}-\boldsymbol{u}_0t$, $\boldsymbol{u}'=\boldsymbol{u}-\boldsymbol{u}_0$, $t'=t$). It shows the correct transformation behavior of $\frac{\mathrm{d}}{\mathrm{d}t'}=\frac{\mathrm{d}}{\mathrm{d}t}$ and $\frac{\partial}{\partial t'}=\frac{\partial}{\partial t}+\boldsymbol{u}_0\cdot\nabla$.

Next, we investigate the structure of the obtained ideal GLM-MHD system and discuss crucial properties such as the hyperbolicity as well as the partially altered eigenstructure of the new system. We then compare the new set of equations to existing formulations in the beginning of the next section.

3.5. Multi-dimensional structure of the ideal GLM-MHD equations

To simplify the discussion of the new system we write (3.16) in one-dimensional form,

$$\frac{\partial}{\partial t}\boldsymbol{q}+\frac{\partial}{\partial x}\boldsymbol{f}^x+\boldsymbol{\Upsilon}^x=\mathbf{0},\tag{3.19}$$

where $\boldsymbol{q}=\boldsymbol{q}(\boldsymbol{x},t)$ is the vector of conservative variables, $\boldsymbol{f}^x(\boldsymbol{q})$ is the flux vector in x-direction, and $\boldsymbol{\Upsilon}$ is the non-conservative term.

$$\boldsymbol{q}=\begin{bmatrix}\varrho & \varrho u & \varrho v & \varrho w & E & B_1 & B_2 & B_3 & \psi\end{bmatrix}^{\mathsf{T}},\tag{3.20}$$

$$\boldsymbol{f}^x=\begin{bmatrix}\varrho\,u\\ \varrho u^2+p+\frac{1}{2}\|\boldsymbol{B}\|^2-B_1B_1\\ \varrho\,u\,v-B_1B_2\\ \varrho\,u\,w-B_1B_3\\ u\hat{E}-B_1(\boldsymbol{u}\cdot\boldsymbol{B})+c_h\psi B_1\\ c_h\psi\\ u\,B_2-v\,B_1\\ u\,B_3-w\,B_1\\ c_hB_1\end{bmatrix},\qquad\boldsymbol{\Upsilon}^x=\frac{\partial B_1}{\partial x}\begin{bmatrix}0\\ B_1\\ B_2\\ B_3\\ \boldsymbol{u}\cdot\boldsymbol{B}\\ u\\ v\\ w\\ 0\end{bmatrix}+\frac{\partial\psi}{\partial x}\begin{bmatrix}0\\ 0\\ 0\\ 0\\ u\psi\\ 0\\ 0\\ 0\\ u\end{bmatrix},\tag{3.21}$$

with

$$\hat{E}:=\frac{1}{2}\varrho\|\boldsymbol{u}\|^2+\frac{\gamma p}{\gamma-1}+\|\boldsymbol{B}\|^2.\tag{3.22}$$

We limit the analysis of the ideal GLM-MHD system (3.16) to one spatial dimension in the following. The main motivation for this restriction is because the analysis of the eigenstructure as well as the derivation of the numerical fluxes described

later in this work proved to be quite intense. However, this restriction is done without loss of generality because the spatial dimensions are decoupled. Thus, for completeness, we summarize the results of the derivations in the y and z-direction in Appendix F.

3.6. Eigenvalues of the ideal GLM-MHD system

An important step in the investigation of the properties of the system is to compute the eigenvalues of the ideal GLM-MHD system, which are the speeds of the different waves involved in the solution. In doing so we find that the new ideal GLM-MHD system does not show a degeneracy of the eigenvalues like in the eight-wave formulation of ideal MHD where the entropy and divergence waves travel with the same speed, and hence have the same eigenvalue [7, Sec. 3.5.1].

First, we compute the flux Jacobian of the ideal GLM-MHD system

$$\mathbf{A}^x := \frac{\partial \boldsymbol{f}^x}{\partial \boldsymbol{q}} =$$

$$\begin{bmatrix}
0 & 1 & 0 & 0 & 0 & 0 & 0 & 0 & 0 \\
\frac{1}{2}(\gamma-1)\|\boldsymbol{u}\|^2 - u^2 & u(3-\gamma) & v(1-\gamma) & w(1-\gamma) & \gamma-1 & -B_1\gamma & B_2(2-\gamma) & B_3(2-\gamma) & \psi(1-\gamma) \\
-uv & v & u & 0 & 0 & -B_2 & -B_1 & 0 & 0 \\
-uw & w & 0 & u & 0 & -B_3 & 0 & -B_1 & 0 \\
A_{5,1} & A_{5,2} & uv(1-\gamma) - \frac{B_1 B_2}{\varrho} & uw(1-\gamma) - \frac{B_1 B_3}{\varrho} & u\gamma & c_h\psi - u\gamma B_1 - vB_2 - wB_3 & B_2 u(2-\gamma) - B_1 v & B_3 u(2-\gamma) - B_1 w & B_1 c_h - \psi u\gamma \\
0 & 0 & 0 & 0 & 0 & 0 & 0 & 0 & c_h \\
\frac{B_1 v - B_2 u}{\varrho} & \frac{B_2}{\varrho} & -\frac{B_1}{\varrho} & 0 & 0 & -v & u & 0 & 0 \\
\frac{B_1 w - B_3 u}{\varrho} & \frac{B_3}{\varrho} & 0 & -\frac{B_1}{\varrho} & 0 & -w & 0 & u & 0 \\
0 & 0 & 0 & 0 & 0 & c_h & 0 & 0 & 0
\end{bmatrix}, \tag{3.23}$$

with

$$A^x_{5,1} = -2\gamma u\left(E - \frac{1}{2}\psi^2\right) + 2B_1(\boldsymbol{u}\cdot\boldsymbol{B} + uB_1) + 2u(\gamma-1)\left(\varrho\|\boldsymbol{u}\|^2\right) + u(\gamma-2)\left(\frac{1}{2}\|\boldsymbol{B}\|^2\right), \tag{3.24}$$

$$A^x_{5,2} = -\frac{1}{2}(\gamma-1)\left(\|\boldsymbol{u}\|^2 + 2u^2\right) + \frac{\gamma}{\varrho}\left(E - \frac{1}{2}\|\boldsymbol{B}\|^2 - \frac{1}{2}\psi^2\right) + \frac{B_2^2 + B_3^2}{\varrho}. \tag{3.25}$$

We then add the non-conservative term written in matrix form

$$\boldsymbol{\Upsilon}^x = \frac{\partial B_1}{\partial x}\begin{bmatrix} 0 \\ B_1 \\ B_2 \\ B_3 \\ \boldsymbol{u}\cdot\boldsymbol{B} \\ u \\ v \\ w \\ 0 \end{bmatrix} + \frac{\partial \psi}{\partial x}\begin{bmatrix} 0 \\ 0 \\ 0 \\ 0 \\ u\psi \\ 0 \\ 0 \\ 0 \\ u \end{bmatrix} = \begin{bmatrix}
0&0&0&0&0&0&0&0&0 \\
0&0&0&0&0&B_1&0&0&0 \\
0&0&0&0&0&B_2&0&0&0 \\
0&0&0&0&0&B_3&0&0&0 \\
0&0&0&0&0&\boldsymbol{u}\cdot\boldsymbol{B}&0&0&u\psi \\
0&0&0&0&0&u&0&0&0 \\
0&0&0&0&0&v&0&0&0 \\
0&0&0&0&0&w&0&0&0 \\
0&0&0&0&0&0&0&0&u
\end{bmatrix} \frac{\partial}{\partial x}\begin{bmatrix} \varrho \\ \varrho u \\ \varrho v \\ \varrho w \\ E \\ B_1 \\ B_2 \\ B_3 \\ \psi \end{bmatrix} := \hat{\boldsymbol{\Upsilon}}^x \frac{\partial \boldsymbol{q}}{\partial x}, \tag{3.26}$$

to (3.23) and obtain

$$\mathbf{A}^x_{\boldsymbol{\Upsilon}} := \mathbf{A}^x + \hat{\boldsymbol{\Upsilon}}^x =$$

$$\begin{bmatrix}
0 & 1 & 0 & 0 & 0 & 0 & 0 & 0 & 0 \\
\frac{1}{2}(\gamma-1)\|\boldsymbol{u}\|^2 - u^2 & u(3-\gamma) & v(1-\gamma) & w(1-\gamma) & \gamma-1 & B_1(1-\gamma) & B_2(2-\gamma) & B_3(2-\gamma) & \psi(1-\gamma) \\
-uv & v & u & 0 & 0 & 0 & -B_1 & 0 & 0 \\
-uw & w & 0 & u & 0 & 0 & 0 & -B_1 & 0 \\
A_{5,1} & A_{5,2} & uv(1-\gamma) - \frac{B_1 B_2}{\varrho} & uw(1-\gamma) - \frac{B_1 B_3}{\varrho} & u\gamma & c_h\psi - uB_1(1-\gamma) & B_2 u(2-\gamma) - B_1 v & B_3 u(2-\gamma) - B_1 w & c_h B_1 + u\psi(1-\gamma) \\
0 & 0 & 0 & 0 & 0 & u & 0 & 0 & c_h \\
\frac{B_1 v - B_2 u}{\varrho} & \frac{B_2}{\varrho} & -\frac{B_1}{\varrho} & 0 & 0 & 0 & u & 0 & 0 \\
\frac{B_1 w - B_3 u}{\varrho} & \frac{B_3}{\varrho} & 0 & -\frac{B_1}{\varrho} & 0 & 0 & 0 & u & 0 \\
0 & 0 & 0 & 0 & 0 & c_h & 0 & 0 & u
\end{bmatrix}. \tag{3.27}$$

From (3.27) we compute the eigenvalues of the ideal GLM-MHD system in x-direction:

$$\lambda^x_{\pm \mathrm{f}} = u \pm c_{\mathrm{f}}, \qquad \lambda^x_{\pm \mathrm{s}} = u \pm c_{\mathrm{s}}, \qquad \lambda^x_{\pm \mathrm{a}} = u \pm c_{\mathrm{a}}, \qquad \lambda^x_{\mathrm{E}} = u, \qquad \lambda^x_{\pm\psi} = u \pm c_h, \tag{3.28}$$

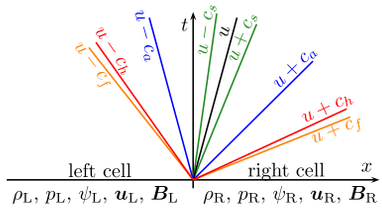

Fig. 1. Spacetime sketch of a typical Riemann fan spanned by the eigenvalues (3.28) with some global c_h that equals the fastest magnetoacoustic speed present in the entire numerical simulation. We do this to not affect the global time step size, see Section 3.7.

with

$$c_a^2 = b_1^2, \quad c_{f,s}^2 = \frac{1}{2}\left(a^2 + \|\boldsymbol{b}\|^2 \pm \sqrt{(a^2 + \|\boldsymbol{b}\|^2)^2 - 4a^2 b_1^2}\right), \; a^2 = \gamma\,\frac{p}{\varrho}, \quad \boldsymbol{b} = \frac{\boldsymbol{B}}{\sqrt{\varrho}}, \tag{3.29}$$

where c_f and c_s are the fast and slow magnetoacoustic wave speeds, respectively, and c_a is the Alfvén wave speed. In (3.29), the plus sign corresponds to the fast magnetoacoustic speed, c_f, and the minus sign corresponds to the slow magnetoacoustic speed, c_s. We find that all eigenvalues have multiplicity one. They are depicted in Fig. 1 Note that, however, some eigenvalues may coincide depending on the magnetic field strength and direction. Hence, it is not straightforward to compute the complete set of eigenvectors [28,29].

We see that the divergence wave, commonly found when analyzing the original ideal MHD system in conjunction with the source term, splits into a left and a right going ψ-wave. If we set $\psi = c_h = 0$, $\mathbf{A}^x_{\boldsymbol{\Upsilon}}$ becomes identical to the flux Jacobian matrix of the eight-wave formulation of the ideal MHD equations and we recover a single divergence wave with eigenvalue $\lambda^x_D = u$.

We note that due to $\lambda^x_{\pm\psi} \neq c_h$, we find that the commonly chosen approximation to set $c_h = \max(\lambda)$ (see *e.g.* [30, Section 3.4]) may lead to a violation of the CFL criterion, which may cause robustness issues when the CFL number is not adapted accordingly.

3.7. The hyperbolic propagation speed c_h

An important issue is how to select the cleaning wave speed c_h. We implement the new numerical scheme for the ideal GLM-MHD system in the multi-physics code FLASH (see [2]) where we often experience that the MHD solver accounts for 10% of the overall CPU time in real applications (see *e.g.* [31]). As such, it is important to determine a cleaning speed c_h such that the propagation of the ψ field is most effective, but does not influence the size of the time step compared to standard ideal MHD implementations. We immediately see that this requirement is fulfilled by choosing c_h to be the difference between the maximum eigenvalue, $\lambda_{\max}$, and the maximum fluid speed,

$$c_h = \lambda_{\max} - u_{\max,\Omega}, \tag{3.30}$$

where $u_{\max,\Omega} = \max_{\Omega}(|u|, |v|, |w|)$ is the largest (physical) speed found in the entire simulation domain.

If the fluid speed is zero (*i.e.* at stagnation points) the divergence correction is most effective with $c_h = \lambda_{\max}$. If $u_{\max,\Omega} \neq 0$, then c_h is reduced such that neither of the ψ eigenvalues exceed the maximum of the remaining wave speeds to guarantee that the GLM modification does not negatively affect the time step of the simulation. Note that (3.30) also suggests that the simple and commonly used choice $c_h = a \cdot \lambda_{\max}$ may be inappropriate for *any* value of $a \in (0, 1]$.

Note that it is possible to select values for c_h that exceed (3.30). However, this would lead to the approximation being dominated by the ψ-wave and, hence, will shrink the time step size. Nevertheless, this will result in (even) faster correction of the magnetic field divergence, although the authors have not felt this necessary in the numerical results obtained for this work. Another possibility, although rarely seen in the literature, could be a local, instead of a global value for the hyperbolic cleaning speed, c_h. However, this would add c_h as yet another field variable which we want to avoid in the highly parallelized targeted framework. Nonetheless, we mention this as a feasible part of future works.

3.8. Alternative non-conservative terms

From the derivations of the generalized ideal MHD equations for non-vanishing magnetic field divergence, we found that particular non-conservative terms are necessary to ensure the validity of the numerical scheme in situations in which (1.1) is not fulfilled exactly. However, it is known that schemes which do not preserve exact conservation of the physical quantities can produce erroneous shock speeds, *e.g.* [13]. In cases where $\nabla \cdot \boldsymbol{B} = 0$, there is no non-conservative contribution to any of the physical quantities. Note that this is not only the case for vanishing magnetic fields, but for arbitrary configurations, given that a numerical approximation is properly initialized. Even in the presence of $\nabla \cdot \boldsymbol{B} \neq 0$, the non-conservative part in *e.g.* the total energy equation could be attributed to excess energy in the magnetic field caused by sources/sinks present

in the solution. The importance of the non-conservative term in the momentum equations has already been discussed in Sec. 2 and is important to ensure $\boldsymbol{F}_L \perp \boldsymbol{B}$ wherever $\nabla \cdot \boldsymbol{B} \neq 0$.

Nevertheless, there are at least three possibilities to construct an entropy stable scheme for ideal MHD:

1. The full non-conservative terms as derived in Sec. 2:
$$\boldsymbol{\Upsilon}^{\text{magnetic}} = \underbrace{\left(\frac{\partial B_1}{\partial x} + \frac{\partial B_2}{\partial y} + \frac{\partial B_3}{\partial z}\right)}_{\nabla\cdot\boldsymbol{B}} \begin{bmatrix} 0 & B_1 & B_2 & B_3 & \boldsymbol{u}\cdot\boldsymbol{B} & u & v & w & 0 \end{bmatrix}^\intercal . \tag{3.31}$$
2. Only the non-conservative terms needed to ensure $\boldsymbol{F}_L \perp \boldsymbol{B}$:
$$\boldsymbol{\Upsilon}^{\text{magnetic}}_{\text{BB}} := \underbrace{\left(\frac{\partial B_1}{\partial x} + \frac{\partial B_2}{\partial y} + \frac{\partial B_3}{\partial z}\right)}_{\nabla\cdot\boldsymbol{B}} \begin{bmatrix} 0 & B_1 & B_2 & B_3 & 0 & 0 & 0 & 0 & 0 \end{bmatrix}^\intercal . \tag{3.32}$$
This non-conservative terms have first been suggested by Brackbill and Barnes [1].
3. Furthermore, Janhunen [13] presented non-conservative terms that add the advection of the magnetic field, see (2.22), but preserve the conservation in all thermodynamics quantities:
$$\boldsymbol{\Upsilon}^{\text{magnetic}}_{\text{J}} := \underbrace{\left(\frac{\partial B_1}{\partial x} + \frac{\partial B_2}{\partial y} + \frac{\partial B_3}{\partial z}\right)}_{\nabla\cdot\boldsymbol{B}} \begin{bmatrix} 0 & 0 & 0 & 0 & 0 & u & v & w & 0 \end{bmatrix}^\intercal . \tag{3.33}$$

The conservative formulation, *i.e.* $\boldsymbol{\Upsilon}_0 := \boldsymbol{0}$, of the ideal MHD equations is *not* entropy consistent as demonstrated by Godunov in the 1970s [6]. Because $\boldsymbol{v}\cdot\boldsymbol{\Upsilon}^{\text{magnetic}} = \boldsymbol{v}\cdot\boldsymbol{\Upsilon}^{\text{magnetic}}_{\text{BB}} = \boldsymbol{v}\cdot\boldsymbol{\Upsilon}^{\text{magnetic}}_{\text{J}} = 2\beta(\boldsymbol{u}\cdot\boldsymbol{B})$, all of the non-conservative terms mentioned are interchangeable in an entropic sense. That is, they all ensure entropy consistency of the scheme. We note that only the first one, $\boldsymbol{\Upsilon}^{\text{magnetic}}$, symmetrizes the PDE system [6] and complies with our derivation of the ideal MHD equations in the general case where $\nabla \cdot \boldsymbol{B} \neq 0$.

Earlier publications, *e.g.* [14, Sec. 6.1], investigated all four non-conservative terms choices, including the non-entropy consistent fully conservative formulation, and found that the full non-conservative terms, $\boldsymbol{\Upsilon}^{\text{magnetic}}$, has the best properties with respect to numerical stability and accuracy in the sense of convergence to analytic solutions. We found little difference between the full and the Janhunen non-conservative terms in all of our numerical tests, however, due to the reasoning given in Sec. 2, we perform all numerical tests in the following section using the full non-conservative terms (3.31). An exception to this is a two-dimensional shock tube test described in Sec. 5.5, as this test is specifically designed to show a breakdown of the eight-wave formulation. Here, we explicitly test the scheme also against the non-conservative terms that was suggested by Janhunen, $\boldsymbol{\Upsilon}^{\text{magnetic}}_{\text{J}}$, but find no notable difference to using the full non-conservative terms.

3.9. Alternative GLM ansatz

We also considered alternative entropy-consistent GLM-modifications. If one uses an Eulerian instead of a Lagrangian ansatz for the ψ evolution equation (compare to (3.1)),
$$\frac{\mathrm{d}}{\mathrm{d}t}\boldsymbol{B} = \nabla \times (\boldsymbol{u} \times \boldsymbol{B}) \quad \Longrightarrow \quad \frac{\mathrm{d}}{\mathrm{d}t}\boldsymbol{B} = \nabla \times (\boldsymbol{u} \times \boldsymbol{B}) - c_h \nabla \psi \,, \quad \frac{\partial}{\partial t}\psi := -c_h(\nabla \cdot \boldsymbol{B}), \tag{3.34}$$
we obtain the same fluxes as before (3.16), however with a slightly simpler source term:
$$\boldsymbol{\Upsilon}_{\text{GLM,alt}} := (\nabla \cdot \boldsymbol{B}) \begin{bmatrix} 0 & \boldsymbol{B} & \boldsymbol{u}\cdot\boldsymbol{B} & \boldsymbol{u} & 0 \end{bmatrix}^\intercal \tag{3.35}$$
Although one can see the absence of the non-conservative $\psi\boldsymbol{u}\cdot\nabla\psi$ term on the right hand side of the total energy equation as an advantage, the resulting scheme is not Galilean invariant. This is immediately seen by computing the eigenstructure of this alternative system. While all other wave speeds stay the same, the GLM wave speeds takes the form
$$\lambda_{\pm\psi,\text{alt}} = \frac{1}{2}\left(u \pm \sqrt{u^2 + 4c_h^2}\right). \tag{3.36}$$
They are clearly not Galilean invariant. However, Galilean invariance is an important physical property for our new scheme and therefore we do not pursue this alternative ansatz any further in this work. Nevertheless, it should be noted that using (3.34), one can build an entropy stable scheme, *e.g.* [32]. We derived and implemented a numerical scheme for this alternative ansatz and find similar results without Galilean invariance. However, we observe slightly reduced robustness.

4. Deriving an entropy stable numerical scheme

In this section, we briefly introduce the concept of entropy conservation and stability on the continuous level for the ideal GLM-MHD equations and derive numerical flux functions that can be used to implement an entropy stable numerical scheme for ideal MHD simulations. Furthermore, we perform an entropy analysis for several known GLM formulations. A broader introduction to the concept of entropy has been given by the authors in [2,3] as well as in the pioneering works of Tadmor [5,33] and Barth [34].

We want to construct a numerical scheme that not only complies with a subset of the thermodynamical laws, but that is in agreement with *all* universally valid laws of thermodynamics – including the second law of thermodynamics, *i.e.* the entropy inequality.

We define the physical entropy density, divided by the constant $(\gamma - 1)$ for convenience to be

$$S(\boldsymbol{q}) = -\frac{\varrho s}{\gamma - 1} \qquad \text{with} \qquad s = \ln \frac{p}{\varrho^\gamma} = -(\gamma - 1)\ln(\varrho) - \ln(\beta) - \ln(2) \qquad \text{and} \qquad \beta = \frac{\varrho}{2p} \propto \frac{1}{T}, \tag{4.1}$$

where s is the entropy per particle, and β is the inverse temperature. An approximation obeys the second law of thermodynamics in two regimes:

1. For smooth solutions, we can design numerical methods to be ***entropy conservative*** if, discretely, the local changes of entropy are the same as predicted by the continuous entropy conservation law

$$\frac{\partial}{\partial t} S + \nabla \cdot (\boldsymbol{u} S) = 0. \tag{4.2a}$$

2. For discontinuous solutions, the approximation is said to be ***entropy stable*** if the entropy always possesses the correct sign (where we use the mathematical notation that entropy is a decaying function) and the numerical scheme produces more entropy than an entropy conservative scheme and satisfies the entropy inequality

$$\frac{\partial}{\partial t} S + \nabla \cdot (\boldsymbol{u} S) \leq 0, \tag{4.2b}$$

that can be interpreted as the entropy conservation law (4.2a) augmented with a non-positive entropy source term.

For switching from conserved to entropy space, we introduce the entropy variables

$$\boldsymbol{v} = \frac{\partial S}{\partial \boldsymbol{q}} = \left[\frac{\gamma - s}{\gamma - 1} - \beta \|\boldsymbol{u}\|^2,\ 2\beta u,\ 2\beta v,\ 2\beta w,\ -2\beta,\ 2\beta B_1,\ 2\beta B_2,\ 2\beta B_3,\ 2\beta \psi \right]^\mathsf{T}. \tag{4.3}$$

4.1. Continuous entropy analysis

Now that we prepared the necessary framework for an entropy analysis, we are interested in the agreement of the proposed new ideal GLM-MHD system (3.16) with (4.2a). We examine how the individual components of the ideal GLM-MHD flux contract into entropy space to see if it is possible to construct schemes from (3.16) which comply with the continuous entropy conservation law. In addition, we analyze the applicability of entropy analysis to different ideal MHD + GLM systems already available in the literature.

To increase the clarity of the following derivations, we split the new flux into three pieces:

$$\boldsymbol{f}^x = \boldsymbol{f}^{x,\text{hydro}} + \boldsymbol{f}^{x,\text{magnetic}} + \boldsymbol{f}^{x,\psi} = \begin{bmatrix} \varrho u \\ \varrho u^2 + p \\ \varrho u v \\ \varrho u w \\ u\left(\frac{1}{2}\varrho \|\boldsymbol{u}\|^2 + \frac{\gamma p}{\gamma - 1}\right) \\ 0 \\ 0 \\ 0 \\ 0 \end{bmatrix} + \begin{bmatrix} 0 \\ \frac{1}{2}\|\boldsymbol{B}\|^2 - B_1 B_1 \\ -B_1 B_2 \\ -B_1 B_3 \\ u\|\boldsymbol{B}\|^2 - B_1(\boldsymbol{u} \cdot \boldsymbol{B}) \\ 0 \\ u B_2 - v B_1 \\ u B_3 - w B_1 \\ 0 \end{bmatrix} + c_h \begin{bmatrix} 0 \\ 0 \\ 0 \\ 0 \\ \psi B_1 \\ \psi \\ 0 \\ 0 \\ B_1 \end{bmatrix}. \tag{4.4}$$

We contract the ideal GLM-MHD system (3.16) into entropy space using the entropy variables (4.3) and, for convenience, multiply by $\frac{1}{2\beta}$. The non-conservative term, $\boldsymbol{\Upsilon}$, is defined in (3.21). Looking at the individual components of the flux one after another we obtain

$$\frac{1}{2\beta}\boldsymbol{v}\cdot\frac{\partial}{\partial x}\boldsymbol{f}^{x,\text{hydro}} = \left(\frac{1}{2\beta}\frac{\gamma-s}{\gamma-1}-\frac{1}{2}\|\boldsymbol{u}\|^2\right)(\varrho u)_x + u(\varrho u^2+p) + v(\varrho uv)_x + w(\varrho uw)_x - \left(u\left(\frac{\gamma p}{\gamma-1}+\frac{1}{2}\varrho\|\boldsymbol{u}\|^2\right)\right)_x = \cdots = -\frac{1}{2\beta}\left(\frac{\varrho us}{\gamma-1}\right)_x = \frac{1}{2\beta}(uS)_x, \tag{4.5}$$

$$\begin{aligned}\frac{1}{2\beta}\boldsymbol{v}\cdot\left(\frac{\partial}{\partial x}\boldsymbol{f}^{x,\text{magnetic}}+\boldsymbol{\Upsilon}^{x,\text{magnetic}}\right) &= u\left(\frac{1}{2}\|\boldsymbol{B}\|^2-B_1B_1\right)_x - v\big(B_1B_2\big)_x - w\big(B_1B_3\big)_x - \\ &\quad \Big(u\|\boldsymbol{B}^2\| - B_1(\boldsymbol{u}\cdot\boldsymbol{B})\Big)_x + B_2(uB_2-vB_1)_x + B_3(uB_3-wB_1)_x - \\ &\quad u(B_1)_xB_1 + v(B_1)_xB_2 + w(B_1)_xB_3 - \\ &\quad ((B_1)_xuB_1 + (B_1)_xvB_2 + (B_1)_xwB_3) + \\ &\quad B_1(B_1)_xu + B_2(B_1)_xv + B_3(B_1)_xw = \cdots = 0,\end{aligned} \tag{4.6}$$

$$\begin{aligned}\frac{1}{2\beta}\boldsymbol{v}\cdot\left(\frac{\partial}{\partial x}\boldsymbol{f}^{x,\psi}+\boldsymbol{\Upsilon}^{x,\psi}\right) &= -c_h(\psi B_1)_x - u\psi(\psi)_x + c_hB_1(\psi)_x + c_h\psi(B_1)_x + \psi u(\psi)_x \\ &= c_h\left[-(B_1\psi)_x + B_1(\psi)_x + \psi(B_1)_x\right] + u\psi(\psi)_x - u\psi(\psi)_x = 0\end{aligned} \tag{4.7}$$

where we introduce the abbreviated notation $(\cdot)_x = \frac{\partial(\cdot)}{\partial x}$. This gives an overall contribution of

$$\boldsymbol{v}\cdot\left(\frac{\partial}{\partial x}\boldsymbol{f}^{x}+\boldsymbol{\Upsilon}^{x}\right) = \boldsymbol{v}\cdot\left(\frac{\partial}{\partial x}\boldsymbol{f}^{x,\text{hydro}}+\frac{\partial}{\partial x}\boldsymbol{f}^{x,\text{magnetic}}+\frac{\partial}{\partial x}\boldsymbol{f}^{x,\psi}+\boldsymbol{\Upsilon}^{x,\text{magnetic}}+\boldsymbol{\Upsilon}^{x,\psi}\right) = (uS)_x. \tag{4.8}$$

From the definition of the entropy variables, $\boldsymbol{v}\cdot\boldsymbol{q}_t = S_t$, we immediately obtain the entropy conservation law in one spatial dimension,

$$\boldsymbol{v}\cdot\left(\boldsymbol{q}_t+\frac{\partial}{\partial x}\boldsymbol{f}^{x}+\boldsymbol{\Upsilon}^{x}\right) = S_t + (uS)_x = 0. \tag{4.9}$$

We perform the same computations for the remaining two spatial dimensions

$$\boldsymbol{v}\cdot\left(\frac{\partial}{\partial y}\boldsymbol{f}^{y}+\boldsymbol{\Upsilon}^{y}\right) = (uS)_y = 0, \tag{4.10}$$

$$\boldsymbol{v}\cdot\left(\frac{\partial}{\partial z}\boldsymbol{f}^{z}+\boldsymbol{\Upsilon}^{z}\right) = (uS)_z = 0, \tag{4.11}$$

and find the entropy balance law in three dimensions

$$\boldsymbol{v}\cdot(\nabla\cdot\boldsymbol{f}+\boldsymbol{\Upsilon}) = \nabla\cdot(\boldsymbol{u}S) \quad\Longrightarrow\quad \boldsymbol{v}\cdot(\boldsymbol{q}_t+\nabla\cdot\boldsymbol{f}+\boldsymbol{\Upsilon}) = S_t+\nabla\cdot(\boldsymbol{u}S) = 0. \tag{4.12}$$

This equation is identical to the continuous entropy conservation law (4.2a). Therefore, the new ideal GLM-MHD system is suitable for building an entropy conserving numerical scheme. Note that when omitting the non-conservative terms, entropy consistency is lost for the ideal MHD equations [3,12].

In the remainder of this section, we compute the entropy balance equation for GLM-modified ideal MHD systems which have been presented in the literature to highlight that our system is the first presented consistent ideal MHD system with GLM divergence treatment that is fully compatible with thermodynamics.

4.1.1. Continuous entropy analysis of Dedner et al.'s ansatz

Dedner et al. [26] presented the first GLM modified ideal MHD system. Their hyperbolic and conservative modification of the ideal MHD equations (their eq. (25)) reads

$$\frac{\partial}{\partial t}\boldsymbol{q}+\nabla\cdot\boldsymbol{f}_{\text{D}} = \frac{\partial}{\partial t}\begin{bmatrix}\varrho\\ \varrho\boldsymbol{u}\\ E\\ \boldsymbol{B}\\ \psi\end{bmatrix} + \nabla\cdot\begin{bmatrix}\varrho\boldsymbol{u}\\ \varrho(\boldsymbol{u}\otimes\boldsymbol{u})+\left(p+\frac{1}{2}\|\boldsymbol{B}\|^2\right)\mathbf{I}-\boldsymbol{B}\otimes\boldsymbol{B}\\ \boldsymbol{u}\left(E+p+\frac{1}{2}\|\boldsymbol{B}\|^2\right)-\boldsymbol{B}(\boldsymbol{u}\cdot\boldsymbol{B})\\ \boldsymbol{u}\otimes\boldsymbol{B}-\boldsymbol{B}\otimes\boldsymbol{u}+\psi\mathbf{I}\\ c_h^2\boldsymbol{B}\end{bmatrix} = -\frac{c_h^2}{c_p^2}\begin{bmatrix}0\\ \boldsymbol{0}\\ 0\\ \boldsymbol{0}\\ \psi\end{bmatrix} = -\boldsymbol{\Upsilon}_{\text{D}}, \tag{4.13}$$

with

$$p = (\gamma-1)\left(E-\frac{1}{2}\varrho\|\boldsymbol{u}\|^2-\frac{1}{2}\|\boldsymbol{B}\|^2\right). \tag{4.14}$$

The entropy variables for this system are

$$\boldsymbol{v}_{\mathrm{D}} = \frac{\partial S}{\partial \boldsymbol{q}} = \left[\frac{\gamma - s}{\gamma - 1} - \beta\|\boldsymbol{u}\|^2,\ 2\beta u,\ 2\beta v,\ 2\beta w,\ -2\beta,\ 2\beta B_1,\ 2\beta B_2,\ 2\beta B_3,\ 0\right]^{\mathsf{T}}. \tag{4.15}$$

Repeating the computations presented above for Dedner et al.'s equations, we obtain

$$\boldsymbol{v}_{\mathrm{D}} \cdot (\nabla \cdot \boldsymbol{f}_{\mathrm{D}} + \boldsymbol{\Upsilon}_{\mathrm{D}}) = \nabla \cdot (\boldsymbol{u} S) + 2\beta\big[-(\boldsymbol{u} \cdot \boldsymbol{B}) \cdot (\nabla \cdot \boldsymbol{B}) + \boldsymbol{B} \cdot \nabla\psi\big] \neq \nabla \cdot (\boldsymbol{u} S), \tag{4.16}$$

which is not conformable with the continuous entropy conservation law (4.2a) and, as such, it cannot be used to construct an entropy conserving scheme. At first glance it seems like we could still fulfill (4.2b) to construct an entropy stable scheme. However, this is not possible either, because we cannot guarantee the correct sign of the term $(\boldsymbol{u} \cdot \boldsymbol{B}) \cdot (\nabla \cdot \boldsymbol{B}) - \boldsymbol{B} \cdot \nabla\psi$.

It is well known that a non-conservative term that is proportional to the magnetic field divergence is necessary for entropy consistency, *e.g.* [3,12]. However, when we repeat the computation including the non-conservative terms we found in this work, we cancel only one of the extraneous terms from (4.16). Even when assuming $c_p \to \infty$, one further term remains

$$\boldsymbol{v}_{\mathrm{D}} \cdot (\nabla \cdot \boldsymbol{f}_{\mathrm{D}} + \boldsymbol{\Upsilon}_{\mathrm{D}} + \boldsymbol{\Upsilon}) = \nabla \cdot (\boldsymbol{u} S) + 2\beta \boldsymbol{B} \cdot \nabla\psi \neq \nabla \cdot (\boldsymbol{u} S), \tag{4.17}$$

which is still not conformable with the continuous entropy conservation law or stability as we cannot predict the sign of the product $\boldsymbol{B} \cdot \nabla\psi$.

Note that due to the zero value in the ninth component of the entropy variables in the scheme of Dedner et al., (4.16), the mapping between physical and entropy space is not bijective. As such, a one-to-one correspondence between conservative and entropy space does not exist. Hence, the equations (4.13) are not suitable for constructing an entropy stable scheme [33, Section 2].

4.1.2. Continuous entropy analysis of Dedner et al.'s ansatz (extended version)

In the same work, Dedner et al. also presented an *extended* GLM system, which involves additional non-conservative terms. They call this system (their eq. (24)) the *extended* GLM (EGLM) formulation of the MHD equations which has been adapted in many other works, *e.g.* [35–37]. This extended system is given by

$$\frac{\partial}{\partial t}\boldsymbol{q} + \nabla \cdot \boldsymbol{f}_{\mathrm{D}} = \frac{\partial}{\partial t}\begin{bmatrix} \varrho \\ \varrho\boldsymbol{u} \\ E \\ \boldsymbol{B} \\ \psi \end{bmatrix} + \nabla \cdot \begin{bmatrix} \varrho\boldsymbol{u} \\ \varrho(\boldsymbol{u} \otimes \boldsymbol{u}) + \left(p + \frac{1}{2}\|\boldsymbol{B}\|^2\right)\mathbf{I} - \boldsymbol{B} \otimes \boldsymbol{B} \\ \boldsymbol{u}\left(E + p + \frac{1}{2}\|\boldsymbol{B}\|^2\right) - \boldsymbol{B}(\boldsymbol{u} \cdot \boldsymbol{B}) \\ \boldsymbol{u} \otimes \boldsymbol{B} - \boldsymbol{B} \otimes \boldsymbol{u} + \psi\mathbf{I} \\ c_h^2 \boldsymbol{B} \end{bmatrix} = \begin{bmatrix} 0 \\ -(\nabla \cdot \boldsymbol{B})\boldsymbol{B} \\ -\boldsymbol{B} \cdot \nabla\psi \\ \mathbf{0} \\ -\frac{c_h^2}{c_p^2}\psi \end{bmatrix} = -\boldsymbol{\Upsilon}_{\mathrm{EGLM}}. \tag{4.18}$$

Doing the entropy contraction for Dedner et al.'s EGLM equations, we find

$$\boldsymbol{v}_{\mathrm{D}} \cdot (\nabla \cdot \boldsymbol{f}_{\mathrm{D}} + \boldsymbol{\Upsilon}_{\mathrm{EGLM}}) = \nabla \cdot (\boldsymbol{u} S), \tag{4.19}$$

which is in agreement with the continuous entropy conservation law (4.2a). However, the zero in the ninth entropy variable makes the construction of an entropy conservative scheme impossible. Furthermore, it is in conflict with the general term we found when deriving the ideal MHD equations in Sec. 2. The non-conservative terms in the total energy contribution is not proportional to the magnetic field divergence and hence may be of significant magnitude. Nevertheless, our finding underlines Dedner et al.'s observation that their EGLM scheme has superior robustness properties, since it is in agreement with thermodynamics.

4.1.3. Continuous entropy analysis of Dedner et al.'s ansatz (extended version, Galilean invariant)

In the same work, Dedner et al. presented a third scheme which is a variant of his *extended* GLM system (their eq. (38)) that includes the eight-wave formulation to achieve Galilean invariance. We will call this system Galilean invariant extended GLM (GI-EGLM) for convenience. It is given by

$$\frac{\partial}{\partial t}\boldsymbol{q} + \nabla \cdot \boldsymbol{f}_{\mathrm{D}} = \frac{\partial}{\partial t}\begin{bmatrix} \varrho \\ \varrho\boldsymbol{u} \\ E \\ \boldsymbol{B} \\ \psi \end{bmatrix} + \nabla \cdot \begin{bmatrix} \varrho\boldsymbol{u} \\ \varrho(\boldsymbol{u} \otimes \boldsymbol{u}) + \left(p + \frac{1}{2}\|\boldsymbol{B}\|^2\right)\mathbf{I} - \boldsymbol{B} \otimes \boldsymbol{B} \\ \boldsymbol{u}\left(E + p + \frac{1}{2}\|\boldsymbol{B}\|^2\right) - \boldsymbol{B}(\boldsymbol{u} \cdot \boldsymbol{B}) \\ \boldsymbol{u} \otimes \boldsymbol{B} - \boldsymbol{B} \otimes \boldsymbol{u} + \psi\mathbf{I} \\ c_h^2 \boldsymbol{B} \end{bmatrix} = -\boldsymbol{\Upsilon}_{\text{GI-EGLM}}, \tag{4.20}$$

with

$$\boldsymbol{\Upsilon}_{\text{GI-EGLM}} := \begin{bmatrix} 0 \\ (\nabla\cdot\boldsymbol{B})\boldsymbol{B} \\ (\boldsymbol{u}\cdot\boldsymbol{B})(\nabla\cdot\boldsymbol{B}) + \boldsymbol{B}\cdot\nabla\psi \\ \boldsymbol{u}(\nabla\cdot\boldsymbol{B}) \\ \boldsymbol{u}\cdot\nabla\psi + \frac{c_h^2}{c_p^2}\psi \end{bmatrix}. \tag{4.21}$$

Doing the entropy contraction for Dedner et al.'s GI-EGLM equations, we find

$$\boldsymbol{v}_{\text{D}}\cdot(\nabla\cdot\boldsymbol{f}_{\text{D}} + \boldsymbol{\Upsilon}_{\text{GI-EGLM}}) = \nabla\cdot(\boldsymbol{u}S). \tag{4.22}$$

We have again obtained the continuous entropy conservation law (4.2a), however, the same limitations as with the EGLM terms (preceding section) apply. These equations seem to be the most preferable of the equations Dedner et al. presented as they are both in agreement with the continuous entropy conservation law as also contain the non-conservative we found to be necessary in Section 2 for $\nabla\cdot\boldsymbol{B}\neq 0$. Nevertheless, they are not suitable for constructing entropy stable numerical schemes as the mapping between physical and entropy space, given by (4.16), is not bijective.

4.1.4. Continuous entropy analysis of Mackey and Lim's ansatz

Mackey and Lim [38] presented a version of Dedner et al.'s ansatz with improved performance. They modified the total energy flux to be

$$\boldsymbol{f}_{\text{ML}} = \boldsymbol{f}_{\text{D}} + \begin{bmatrix} 0 \\ \boldsymbol{0} \\ \begin{bmatrix} B_1 f_{\text{D}}^{B_1} \\ B_2 f_{\text{D}}^{B_2} \\ B_3 f_{\text{D}}^{B_3} \end{bmatrix} \\ \boldsymbol{0} \\ 0 \end{bmatrix}, \tag{4.23}$$

to address gas pressure dips which appear ahead of oblique shocks in axisymmetric models of magnetized jets. The entropy variables remain unchanged, $\boldsymbol{v}_{\text{ML}} = \boldsymbol{v}_{\text{D}}$, and we obtain

$$\boldsymbol{v}_{\text{ML}}\cdot(\nabla\cdot\boldsymbol{f}_{\text{ML}}) = \nabla\cdot(\boldsymbol{u}S) - 2\beta\big[(\boldsymbol{u}\cdot\boldsymbol{B})\cdot(\nabla\cdot\boldsymbol{B}) + \boldsymbol{B}\cdot(\nabla\psi) + \nabla\cdot(\psi\boldsymbol{B})\big] \neq \nabla\cdot(\boldsymbol{u}S), \tag{4.24}$$

which is not conformable with the continuous entropy inequality (4.2a,b) either.

We repeat the computation including the non-conservative terms we found and obtain

$$\boldsymbol{v}_{\text{ML}}\cdot(\nabla\cdot\boldsymbol{f}_{\text{ML}} + \boldsymbol{\Upsilon}) = \nabla\cdot(\boldsymbol{u}S) - 2\beta\big[\boldsymbol{B}\cdot(\nabla\psi) + \nabla\cdot(\psi\boldsymbol{B})\big] \neq \nabla\cdot(\boldsymbol{u}S), \tag{4.25}$$

which is still not conformable with the continuous entropy conservation law as we cannot predict the sign of neither $\boldsymbol{B}\cdot(\nabla\psi)$ nor $\nabla\cdot(\psi\boldsymbol{B})$.

4.1.5. Continuous entropy analysis of Tricco and Price's ansatz

Tricco and Price [27,39] presented a constrained formulation of Dedner et al.'s hyperbolic divergence cleaning for SPH. The constraint they impose is that magnetic energy modified due to the cleaning process must be balanced by a new kind of correction energy which is correlated to ψ. We repeat their derivations with our definition of (3.12) and verified the same behavior for our scheme. Their modified form of the ideal MHD equations for SPH reads (their eqs. (5) and (6) in [39])

$$\frac{\partial}{\partial t}\boldsymbol{q} + \nabla\cdot\boldsymbol{f}_{\text{TP}} = \frac{\partial}{\partial t}\begin{bmatrix} \varrho \\ \varrho\boldsymbol{u} \\ E \\ \boldsymbol{B} \\ \psi \end{bmatrix} + \nabla\cdot\begin{bmatrix} \varrho\boldsymbol{u} \\ \varrho(\boldsymbol{u}\otimes\boldsymbol{u}) + \big(p + \frac{1}{2}\|\boldsymbol{B}\|^2\big)\mathbf{I} - \boldsymbol{B}\otimes\boldsymbol{B} \\ \boldsymbol{u}\big(\frac{1}{2}\varrho\|\boldsymbol{u}\|^2 + \frac{\gamma p}{\gamma-1} + \|\boldsymbol{B}\|^2\big) - \boldsymbol{B}(\boldsymbol{u}\cdot\boldsymbol{B}) \\ \boldsymbol{u}\otimes\boldsymbol{B} - \boldsymbol{B}\otimes\boldsymbol{u} + \psi\mathbf{I} \\ c_h^2\boldsymbol{B} \end{bmatrix} = -\boldsymbol{\Upsilon}_{\text{TP}}, \tag{4.26}$$

with

$$\boldsymbol{\Upsilon}_{\text{TP}} := \begin{bmatrix} 0 \\ \boldsymbol{0} \\ 0 \\ \boldsymbol{u}(\nabla\cdot\boldsymbol{B}) \\ \frac{1}{2}\psi(\nabla\cdot\boldsymbol{u}) + \boldsymbol{u}\cdot\nabla\psi \end{bmatrix}, \tag{4.27}$$

and

$$p = (\gamma - 1)\left(E - \frac{1}{2}\varrho\|\boldsymbol{u}\|^2 - \frac{1}{2}\|\boldsymbol{B}\|^2 - \frac{1}{2}\frac{\psi^2}{c_h^2}\right). \tag{4.28}$$

The entropy variables for this system are

$$\boldsymbol{v}_{\mathrm{TP}} = \frac{\partial S}{\partial \boldsymbol{q}} = \left[\frac{\gamma - s}{\gamma - 1} - \beta\|\boldsymbol{u}\|^2,\ 2\beta u,\ 2\beta v,\ 2\beta w,\ -2\beta,\ 2\beta B_1,\ 2\beta B_2,\ 2\beta B_3,\ 2\beta c_h^{-2}\psi\right]^{\mathsf{T}}. \tag{4.29}$$

We find

$$\boldsymbol{v}_{\mathrm{TP}} \cdot \left(\nabla \cdot \boldsymbol{f}_{\mathrm{TP}} + \boldsymbol{\Upsilon}_{\mathrm{TP}}\right) = \nabla \cdot (\boldsymbol{u}S) + \frac{\beta}{c_h^2}\nabla \cdot (\psi^2 \boldsymbol{u}) \neq \nabla \cdot (\boldsymbol{u}S), \tag{4.30}$$

which is inconsistent with the entropy conservation law such that – although the modified ideal MHD system of Tricco and Price are valid in the framework of SPH – it can neither be used to construct an entropy conserving nor an entropy stable scheme for a FV scheme as we can not predict the sign of the term $\nabla \cdot (\psi^2 \boldsymbol{u})$. Repeating the computation including the non-conservative terms we found earlier also in the momentum and total energy equations does not change the result (4.30) as the two additional terms cancel in entropy space.

To summarize, we demonstrated that it is important to account for energy transfers between the magnetic field and a correcting field used to control numerical errors in the divergence-free constraint. This lead to a modification of the total energy equation (as well as the induction equations) that ensures the model remains in agreement with the second law of thermodynamics. Additionally, we showed that the entropy analysis of other proposed GLM-type hyperbolic divergence methods from the literature are incompatible to build numerical approximations that discretely satisfy entropy conservation.

For implementing our new mathematical model as an algorithm usable for computer simulations, it has to be *discretized*. We will see that although the divergence diminishing property of the ideal GLM-MHD system rather trivially extends from continuous into discrete space, we have to pay special attention to the transfer of the entropy consistency property into a discrete numerical algorithm.

4.2. Derivation of an entropy conserving numerical scheme

In this section we describe the derivation of an entropy conserving approximation for the ideal GLM-MHD equations (3.16). We drop the superscripts $(\cdot)^x$ for convenience as the following derivation is concerned with the derivation of the numerical scheme in x-direction only. Note that we do this without loss of generality. As shown in [2, Sec. 3.1] and [3, Appendix A], the flux derivations easily extend to higher spatial dimensions. The derivations shown herein are closely related to the derivations done by Winters and Gassner [3] and Chandrashekar and Klingenberg [40] for entropy stable fluxes.

4.2.1. Discrete entropy conservation

When we contract the ideal GLM-MHD equations with the entropy variables, we obtain the entropy conservation law with additional terms proportional to the magnetic field divergence,

$$\frac{\partial}{\partial t}S + \nabla \cdot \boldsymbol{F} + 2\beta(\boldsymbol{u} \cdot \boldsymbol{B})(\nabla \cdot \boldsymbol{B}) = 0. \tag{4.31}$$

Hence, to ease the following derivations, we assume that we can rewrite the non-conservative terms using a homogeneous function of degree one, with respect to the entropy variables, in the form [12,40]

$$\phi(\boldsymbol{v}) := \boldsymbol{v} \cdot \frac{\partial \phi}{\partial \boldsymbol{v}} = 2\beta(\boldsymbol{u} \cdot \boldsymbol{B}). \tag{4.32}$$

A suitable candidate function is

$$\phi(\boldsymbol{v}) = \frac{v_2 v_6 + v_3 v_7 + v_4 v_8}{v_5}, \tag{4.33}$$

where differentiating with respect to the entropy variables,

$$\frac{\partial \phi}{\partial \boldsymbol{v}} = \begin{bmatrix} 0 & \boldsymbol{B} & \boldsymbol{u} \cdot \boldsymbol{B} & \boldsymbol{u} & 0 \end{bmatrix}^{\mathsf{T}} =: \boldsymbol{\Phi} \tag{4.34}$$

reveals the vector components of the non-conservative term (3.21), which is now connected through

$$\boldsymbol{\Upsilon} = (\nabla \cdot \boldsymbol{B})\boldsymbol{\Phi} = (\nabla \cdot \boldsymbol{B})\frac{\partial \phi}{\partial \boldsymbol{v}}. \tag{4.35}$$

Hence, in the following, we consider the one dimensional PDE system in the form

$$\frac{\partial}{\partial t}\boldsymbol{q} + \frac{\partial}{\partial x}\boldsymbol{f} + \boldsymbol{\Phi}(\boldsymbol{v})(\nabla \cdot \boldsymbol{B}) = \boldsymbol{0}, \tag{4.36}$$

that is identical to (3.19) but contains the order one homogeneity condition (4.32).

We assume left and right cell-averages, denoted by L and R, with cell sizes Δx_L and Δx_R separated by a common interface. We discretize the one-dimensional ideal GLM-MHD equations (3.19) semi-discretely and derive an approximation for the fluxes at the interface in between the two adjacent cells (the $i+1/2$ interface):

$$\Delta x_\mathrm{L}\frac{\partial}{\partial t}\boldsymbol{q}_\mathrm{L} = \boldsymbol{f}_\mathrm{L} - \boldsymbol{f}^* - \frac{\Delta x_\mathrm{L}}{2}\frac{[\![B_1]\!]}{\Delta x_\mathrm{L}}\boldsymbol{\Phi}_\mathrm{L}, \qquad \text{and} \qquad \Delta x_\mathrm{R}\frac{\partial}{\partial t}\boldsymbol{q}_\mathrm{R} = \boldsymbol{f}^* - \boldsymbol{f}_\mathrm{R} - \frac{\Delta x_\mathrm{R}}{2}\frac{[\![B_1]\!]}{\Delta x_\mathrm{R}}\boldsymbol{\Phi}_\mathrm{R}, \tag{4.37}$$

where the adjacent states L and R are separated by a numerical interface flux $\boldsymbol{f}^*$. We define the jump in a quantity as $[\![\cdot]\!] := (\cdot)_\mathrm{R} - (\cdot)_\mathrm{L}$. Note that both cells are also affected by the physical fluxes $\boldsymbol{f}_{\mathrm{L,R}}$.

Next, we convert (4.37) from physical to entropy space to get the semi-discrete entropy update in each cell

$$\Delta x_\mathrm{L}\frac{\partial}{\partial t}S_\mathrm{L} = \boldsymbol{v}_\mathrm{L}\cdot\left(\boldsymbol{f}_\mathrm{L} - \boldsymbol{f}^* - \frac{[\![B_1]\!]}{2}\boldsymbol{\Phi}_\mathrm{L}\right) \quad \text{(a)} \qquad \text{and} \qquad \Delta x_\mathrm{R}\frac{\partial}{\partial t}S_\mathrm{R} = \boldsymbol{v}_\mathrm{R}\cdot\left(\boldsymbol{f}^* - \boldsymbol{f}_\mathrm{R} - \frac{[\![B_1]\!]}{2}\boldsymbol{\Phi}_\mathrm{R}\right), \quad \text{(b)} \tag{4.38}$$

where we again use that $S_t = \boldsymbol{v}\cdot\boldsymbol{q}_t$.

By combining (4.38a,b), setting $\Delta x_\mathrm{L} = \Delta x_\mathrm{R} =: \Delta x$ and using the homogeneity condition $\boldsymbol{v}\cdot\boldsymbol{\Phi} = \phi$ (see (4.32)), we obtain the total entropy update

$$\Delta x\frac{\partial}{\partial t}(S_\mathrm{L} + S_\mathrm{R}) = [\![\boldsymbol{v}]\!]\cdot\boldsymbol{f}^* - [\![\boldsymbol{v}\cdot\boldsymbol{f}]\!] - \{\!\{\phi\}\!\}\,[\![B_1]\!]\,, \tag{4.39}$$

where the average of a state is defined as $\{\!\{\cdot\}\!\} := ((\cdot)_\mathrm{L} + (\cdot)_\mathrm{R})/2$. When applied to vectors, the average and jump operators are evaluated separately for each vector component.

To have the finite volume update satisfy the discrete entropy conservation law, the entropy flux due to the finite volume flux must coincide with the discrete entropy flux $\boldsymbol{u}S$ from (4.2a). We define the entropy flux potential as [40]

$$\Psi = \boldsymbol{v}\cdot\boldsymbol{f} - uS + \phi B_1 = \varrho u + \beta u\|\boldsymbol{B}^2\| + 2\beta c_h B_1\psi \tag{4.40}$$

and rewrite (4.39) using the linearity of the jump operator to obtain

$$[\![\boldsymbol{v}]\!]\cdot\boldsymbol{f}^* = [\![\Psi]\!] - \{\!\{B_1\}\!\}\,[\![\phi]\!] = [\![\varrho u]\!] + \left[\!\!\left[\beta u\|\boldsymbol{B}^2\|\right]\!\!\right] + 2c_h\,[\![\beta\psi B_1]\!] - 2\,\{\!\{B_1\}\!\}\,[\![\beta(\boldsymbol{u}\cdot\boldsymbol{B})]\!]\,, \tag{4.41}$$

where we used that

$$\{\!\{\phi\}\!\}\,[\![B_1]\!] = [\![\phi B_1]\!] - \{\!\{B_1\}\!\}\,[\![\phi]\!]\,. \tag{4.42}$$

We denote (4.41) as the *discrete entropy conservation condition* for the ideal GLM-MHD equations. Since this is a scalar equation, there are several possible solutions for the numerical flux vector $\boldsymbol{f}^*$. However, there is the additional requirement that the numerical flux must be consistent, *i.e.* $\boldsymbol{f}^*(\boldsymbol{q},\boldsymbol{q}) = \boldsymbol{f}$ severely limiting the number of possible solutions.

With all necessary components collected, we solve (4.41) to obtain the new entropy conserving numerical flux. The full derivation is shown in Appendix A. The numerical flux function reads

$$\boldsymbol{f}^{\mathrm{KEPEC,GLM}} = \begin{bmatrix} \varrho^{\ln}\{\!\{u\}\!\} \\ \varrho^{\ln}\{\!\{u\}\!\}^2 + \overline{p}_\mathrm{tot} - \{\!\{B_1\}\!\}^2 \\ \varrho^{\ln}\{\!\{u\}\!\}\{\!\{v\}\!\} - \{\!\{B_1\}\!\}\{\!\{B_2\}\!\} \\ \varrho^{\ln}\{\!\{u\}\!\}\{\!\{w\}\!\} - \{\!\{B_1\}\!\}\{\!\{B_3\}\!\} \\ f_5^* \\ c_h\{\!\{\psi\}\!\} \\ \{\!\{u\}\!\}\{\!\{B_2\}\!\} - \{\!\{v\}\!\}\{\!\{B_1\}\!\} \\ \{\!\{u\}\!\}\{\!\{B_3\}\!\} - \{\!\{w\}\!\}\{\!\{B_1\}\!\} \\ c_h\{\!\{B_1\}\!\} \end{bmatrix}, \tag{4.43}$$

with

$$\overline{p}_\mathrm{tot} = \tilde{p} + \frac{1}{2}\left(\left\{\!\!\left\{B_1^2\right\}\!\!\right\} + \left\{\!\!\left\{B_2^2\right\}\!\!\right\} + \left\{\!\!\left\{B_3^2\right\}\!\!\right\}\right), \text{ and} \tag{4.44}$$

$$f_5^* = f_1^*\left[\frac{1}{2(\gamma-1)\beta^{\ln}} - \frac{1}{2}\left(\left\{\!\!\left\{u^2\right\}\!\!\right\} + \left\{\!\!\left\{v^2\right\}\!\!\right\} + \left\{\!\!\left\{w^2\right\}\!\!\right\}\right)\right] + f_2^*\{\!\{u\}\!\} + f_3^*\{\!\{v\}\!\} + f_4^*\{\!\{w\}\!\} +$$

$$+ f_6^* \{\!\{B_1\}\!\} + f_7^* \{\!\{B_2\}\!\} + f_8^* \{\!\{B_3\}\!\} + f_9^* \{\!\{\psi\}\!\} - \frac{1}{2}\Big(\Big\{\!\Big\{ u B_1^2 \Big\}\!\Big\} + \Big\{\!\Big\{ u B_2^2 \Big\}\!\Big\} + \Big\{\!\Big\{ u B_3^2 \Big\}\!\Big\} \Big) +$$
$$+ \{\!\{B_1\}\!\} \Big(\{\!\{u B_1\}\!\} + \{\!\{v B_2\}\!\} + \{\!\{w B_3\}\!\} \Big) - c_h \{\!\{B_1 \psi\}\!\}, \tag{4.45}$$

the logarithmic mean $(\cdot)^{\ln} = \frac{[\![\cdot]\!]}{[\![\ln(\cdot)]\!]}$, and the specifically averaged pressure, $\tilde{p} = \frac{\{\!\{\varrho\}\!\}}{2\{\!\{\beta\}\!\}}$. A numerically stable procedure to compute the logarithmic mean is described by Ismail and Roe [41, App. B].

We compute the magnetic field divergence in the discretized non-conservative term using central differencing:

$$\boldsymbol{\Upsilon}_i^{x,\text{magnetic}} := \underbrace{\left(\frac{(B_1)_{i+1} - (B_1)_{i-1}}{2\Delta x} \right)}_{\text{central derivative}} \begin{bmatrix} 0 \\ \boldsymbol{B}_i \\ (\boldsymbol{u}\cdot\boldsymbol{B})_i \\ \boldsymbol{u}_i \\ 0 \end{bmatrix}$$
$$= \frac{1}{2\Delta x} \left\{ \left([\![B_1]\!] \begin{bmatrix} 0 \\ \boldsymbol{B}_{\mathrm{L}} \\ (\boldsymbol{u}\cdot\boldsymbol{B})_{\mathrm{L}} \\ \boldsymbol{u}_{\mathrm{L}} \\ 0 \end{bmatrix} \right)_{i-1/2} + \left([\![B_1]\!] \begin{bmatrix} 0 \\ \boldsymbol{B}_{\mathrm{R}} \\ (\boldsymbol{u}\cdot\boldsymbol{B})_{\mathrm{R}} \\ \boldsymbol{u}_{\mathrm{R}} \\ 0 \end{bmatrix} \right)_{i+1/2} \right\} \tag{4.46}$$

Similarly, we also find the ψ correlated non-conservative term

$$\boldsymbol{\Upsilon}_i^{x,\psi} := \left(\frac{(\psi)_{i+1} - (\psi)_{i-1}}{2\Delta x} \right) \begin{bmatrix} 0 \\ \boldsymbol{0} \\ (u\psi)_i \\ \boldsymbol{0} \\ u_i \end{bmatrix} = \frac{1}{2\Delta x} \left\{ \left([\![\psi]\!] \begin{bmatrix} 0 \\ 0 \\ (u\psi)_{\mathrm{L}} \\ 0 \\ u_{\mathrm{L}} \end{bmatrix} \right)_{i-1/2} + \left([\![\psi]\!] \begin{bmatrix} 0 \\ 0 \\ (u\psi)_{\mathrm{R}} \\ 0 \\ u_{\mathrm{R}} \end{bmatrix} \right)_{i+1/2} \right\} \tag{4.47}$$

The full discrete non-conservative term is simply given by the sum of the two terms presented above:

$$\boldsymbol{\Upsilon}_i^{x} = \boldsymbol{\Upsilon}_i^{x,\text{magnetic}} + \boldsymbol{\Upsilon}_i^{x,\psi} \tag{4.48}$$

We highlight that the newly derived numerical flux function (4.43) conserves the discrete entropy by construction. Furthermore, in the case of vanishing magnetic fields, the scheme is not only *entropy conserving* (EC), but also *kinetic energy preserving* (KEP) [42]. As has been shown by the authors, the kinetic energy preserving property is favorable in terms of robustness of the scheme particularly at high Mach numbers [43].

When investigating the consistency of the obtained numerical flux function (4.43) we assume that the left/right states are identical and find

$$\boldsymbol{f}^{\text{KEPEC,GLM}} = \begin{bmatrix} \varrho u \\ \varrho u^2 + p + \frac{1}{2}\|\boldsymbol{B}\|^2 - B_1^2 \\ \varrho u v - B_1 B_2 \\ \varrho u w - B_1 B_3 \\ u\big(\frac{1}{2}\varrho\|\boldsymbol{u}\|^2 + \frac{\gamma p}{\gamma-1} + \|\boldsymbol{B}\|^2\big) - B_1\big(\boldsymbol{u}\cdot\boldsymbol{B}\big) + c_h \psi B_1 \\ c_h \psi \\ u B_2 - v B_1 \\ u B_3 - w B_1 \\ c_h B_1 \end{bmatrix} = \boldsymbol{f}^x, \tag{4.49}$$

where we used that

$$u(B_2^2 + B_3^2) - B_1(v B_2 + w B_3) = u\|\boldsymbol{B}^2\| - B_1(\boldsymbol{u}\cdot\boldsymbol{B}). \tag{4.50}$$

Thus, we have shown that the newly derived entropy conservative numerical flux for the ideal GLM-MHD equations given by (4.43) is consistent with the physical flux, and, together with the discretization of the non-conservative terms (4.48), conserves the discrete entropy by construction. We note that the non-conservative terms (4.48) vanish when the left/right states are identical, reflecting convergence to the continuous case where the divergence of the magnetic field should vanish.

We stress that the presented way of deriving the entropy conservative scheme is not unique. We prefer the numerical flux presented herein as it avoids problematic non-conservative term discretizations which is what we found in previous works [44].

4.3. Derivation of an entropy stable numerical scheme

The entropy of a closed system is only conserved if the solution remains smooth. If additional dissipation is not included in an entropy conservative method, spurious oscillations will develop near discontinuities as energy is re-distributed at the smallest resolvable scale [45]. Hence, entropy conserving schemes may suffer breakdown in the presence of discontinuities. From the second law of thermodynamics we know that kinetic and/or magnetic energy can be transformed irreversibly into heat, which we denote as *dissipation* (also known as "thermalization"). Accordingly, we require dissipation is added to the approximation such that discrete satisfaction of the entropy inequality (4.2b) is guaranteed. A numerical scheme requires a diffusion operator to match such a physical process.

In order to create an entropy stable numerical flux function, we use the KEPEC flux (4.43) as a baseline flux and add a general form of numerical dissipation to compute a *kinetic energy preserving* and *entropy stable* (KEPES) numerical flux that is applicable to arbitrary flows

$$\boldsymbol{f}^{\text{KEPES}} = \boldsymbol{f}^{\text{KEPEC}} - \frac{1}{2}\mathbf{D}\,[\![\boldsymbol{q}]\!]\,, \tag{4.51}$$

where $\mathbf{D}$ is a suitable dissipation matrix that is guaranteed to cause a negative contribution in (4.2b).

4.3.1. Scalar dissipation term (Lax–Friedrichs and Rusanov schemes)

If we make the simple choice of $\mathbf{D}$ to be

$$\mathbf{D}_{\text{LF}} = |\lambda_{\max}^{\text{global}}|\mathbf{I}, \tag{4.52}$$

where $\lambda_{\max}^{\text{global}} = \max(\lambda_{\max,i=1,\dots,N})$ is the largest eigenvalue of the ideal GLM-MHD system in the whole computational domain, we can rewrite the dissipation term

$$\frac{1}{2}\mathbf{D}_{\text{LF}}\,[\![\boldsymbol{q}]\!] = \frac{1}{2}|\lambda_{\max}^{\text{global}}|\mathbf{I}\,[\![\boldsymbol{q}]\!] = \frac{1}{2}|\lambda_{\max}^{\text{global}}|\hat{\boldsymbol{\mathcal{H}}}\,[\![\boldsymbol{v}]\!] \simeq \frac{1}{2}|\lambda_{\max}^{\text{global}}|\boldsymbol{\mathcal{H}}\,[\![\boldsymbol{v}]\!]\,, \tag{4.53}$$

where $\hat{\boldsymbol{\mathcal{H}}} = \frac{\partial \boldsymbol{q}}{\partial \boldsymbol{v}}$ is a matrix that relates the variables in conserved and entropy space. This choice for the dissipation term leads to a *scalar dissipation term*, also called *Lax–Friedrichs* (LF) type dissipation. While the entropy Jacobian, $\hat{\boldsymbol{\mathcal{H}}}$, is easily found in continuous space, it was shown in [43] that it is highly non-trivial to discretize this matrix for use in a numerical scheme. The requirement is to average the quantities in such a way that the relation $[\![\boldsymbol{q}]\!] = \boldsymbol{\mathcal{H}}\,[\![\boldsymbol{v}]\!]$ holds whenever possible. The reformulation of the dissipation term to incorporate the jump in entropy variables (rather than the jump in conservative variables) is done to ensure entropy stability by guaranteeing a negative contribution in the entropy inequality [3].

The entries of the matrix $\boldsymbol{\mathcal{H}}$ are derived step-by-step through the solution of 81 equations similar to what was done in [43, Section 4] for the unmodified ideal MHD equations. Details are given in Appendix B. We summarize the symmetric $\boldsymbol{\mathcal{H}}$ matrix:

$$\boldsymbol{\mathcal{H}} = \begin{bmatrix}
\varrho^{\ln} & \varrho^{\ln}\{\!\{u\}\!\} & \varrho^{\ln}\{\!\{v\}\!\} & \varrho^{\ln}\{\!\{w\}\!\} & \overline{E} & 0 & 0 & 0 & 0 \\
\varrho^{\ln}\{\!\{u\}\!\} & \varrho^{\ln}\{\!\{u\}\!\}^2 + \tilde{p} & \varrho^{\ln}\{\!\{u\}\!\}\{\!\{v\}\!\} & \varrho^{\ln}\{\!\{u\}\!\}\{\!\{w\}\!\} & \left(\overline{E}+\tilde{p}\right)\{\!\{u\}\!\} & 0 & 0 & 0 & 0 \\
\varrho^{\ln}\{\!\{v\}\!\} & \varrho^{\ln}\{\!\{v\}\!\}\{\!\{u\}\!\} & \varrho^{\ln}\{\!\{v\}\!\}^2 + \tilde{p} & \varrho^{\ln}\{\!\{v\}\!\}\{\!\{w\}\!\} & \left(\overline{E}+\tilde{p}\right)\{\!\{v\}\!\} & 0 & 0 & 0 & 0 \\
\varrho^{\ln}\{\!\{w\}\!\} & \varrho^{\ln}\{\!\{w\}\!\}\{\!\{u\}\!\} & \varrho^{\ln}\{\!\{w\}\!\}\{\!\{v\}\!\} & \varrho^{\ln}\{\!\{w\}\!\}^2 + \tilde{p} & \left(\overline{E}+\tilde{p}\right)\{\!\{w\}\!\} & 0 & 0 & 0 & 0 \\
\overline{E} & \left(\overline{E}+\tilde{p}\right)\{\!\{u\}\!\} & \left(\overline{E}+\tilde{p}\right)\{\!\{v\}\!\} & \left(\overline{E}+\tilde{p}\right)\{\!\{w\}\!\} & \boldsymbol{\mathcal{H}}_{5,5} & \tau\{\!\{B_1\}\!\} & \tau\{\!\{B_2\}\!\} & \tau\{\!\{B_3\}\!\} & \tau\{\!\{\psi\}\!\} \\
0 & 0 & 0 & 0 & \tau\{\!\{B_1\}\!\} & \tau & 0 & 0 & 0 \\
0 & 0 & 0 & 0 & \tau\{\!\{B_2\}\!\} & 0 & \tau & 0 & 0 \\
0 & 0 & 0 & 0 & \tau\{\!\{B_3\}\!\} & 0 & 0 & \tau & 0 \\
0 & 0 & 0 & 0 & \tau\{\!\{\psi\}\!\} & 0 & 0 & 0 & \tau
\end{bmatrix}, \tag{4.54}$$

$$\overline{E} = \frac{1}{2}\varrho^{\ln}\overline{\|\boldsymbol{u}\|^2} + \frac{p^{\ln}}{\gamma-1}, \quad \tau = \frac{\{\!\{p\}\!\}}{\{\!\{\varrho\}\!\}} = \frac{1}{2\{\!\{\beta\}\!\}}, \quad \text{and} \tag{4.55}$$

$$\boldsymbol{\mathcal{H}}_{5,5} = \frac{1}{\varrho^{\ln}}\left(\frac{(p^{\ln})^2}{\gamma-1} + \overline{E}^2\right) + \tilde{p}\left(\{\!\{u\}\!\}^2 + \{\!\{v\}\!\}^2 + \{\!\{w\}\!\}^2\right) + \tau\sum_{i=1}^{3}\{\!\{B_i\}\!\}^2 + \tau\,\{\!\{\psi\}\!\}^2\,. \tag{4.56}$$

With the particular averaging of the matrix $\boldsymbol{\mathcal{H}}$ it can be shown that

$$([\![\boldsymbol{q}]\!])_i = (\boldsymbol{\mathcal{H}}\,[\![\boldsymbol{v}]\!])_i, \quad i = 1,2,3,4,6,7,8,9 \quad \text{and} \quad ([\![\boldsymbol{q}]\!])_5 \simeq (\boldsymbol{\mathcal{H}}\,[\![\boldsymbol{v}]\!])_5. \tag{4.57}$$

So, the equality holds for each term except for the jump in total energy. The relation that the jump in total energy only holds asymptotically was necessary to create a discrete dissipation operator that is still symmetric [43, Sec. 4]. It is straightforward, using Sylvester's criterion, to verify that the discrete matrix (4.54) is symmetric positive definite (SPD) [43, Appendix A].

Due to the structure of the dissipation term (4.53), the SPD property of the discrete matrix guarantees that the numerical flux

$$\boldsymbol{f}^{\mathrm{KEPES,LF}} = \boldsymbol{f}^{\mathrm{KEPEC}} - \frac{1}{2}|\lambda_{\max}^{\mathrm{global}}|\boldsymbol{\mathcal{H}}\,[\![\boldsymbol{v}]\!]\,, \tag{4.58}$$

complies with the entropy inequality (4.2b) on the discrete level. Although the LF flux is quite dissipative (especially for slow waves), it has the advantage that it very numerically stable, non-oscillatory [3], and easy to implement.

A natural reason for the diffusivity of LF lies in its global nature. The wave speeds involved are the maximum allowed speeds in the computational domain and do not take into account the local wave speeds of the solution. Indeed, Rusanov [46] showed that a less diffusive, yet stable scheme can be built using a local, instead of a global, wave speed measure. The resulting dissipation term is the *Rusanov* or *local Lax–Friedrichs* (LLF) stabilization term:

$$\boldsymbol{f}^{\mathrm{KEPES,LLF}} = \boldsymbol{f}^{\mathrm{KEPEC}} - \frac{1}{2}|\lambda_{\max}^{\mathrm{local}}|\boldsymbol{\mathcal{H}}\,[\![\boldsymbol{v}]\!] \qquad \text{with} \qquad \lambda_{\max}^{\mathrm{local}} = \max(\lambda_{\max,\mathrm{R}}, \lambda_{\max,\mathrm{L}}). \tag{4.59}$$

4.3.2. Matrix dissipation term

We create a less diffusive operator than LF or LLF if we select the dissipation matrix in (4.51) to be

$$\mathbf{D}_{\mathrm{MD}} = \boldsymbol{\mathcal{R}}|\boldsymbol{\Lambda}|\boldsymbol{\mathcal{R}}^{-1}, \tag{4.60}$$

where $\boldsymbol{\mathcal{R}}$ is the matrix of right eigenvectors and $\boldsymbol{\Lambda}$ is the diagonal matrix of the eigenvalues of the flux Jacobian for the ideal MHD system. Here we focus on the particular mean states at which the matrix $\boldsymbol{\mathcal{R}}$ is evaluated. For entropy stable schemes there exists a particular scaling of the eigenvectors that relates the matrix $\boldsymbol{\mathcal{R}}$ to the entropy Jacobian $\boldsymbol{\mathcal{H}}$ [12] such that

$$\boldsymbol{\mathcal{H}} = \boldsymbol{\mathcal{R}}\boldsymbol{\mathcal{Z}}\boldsymbol{\mathcal{R}}^{\mathsf{T}}. \tag{4.61}$$

The derivation and entropy scaling of the eigenvectors is provided in Appendix D. From this scaling we rewrite the dissipation term

$$\begin{aligned}\frac{1}{2}\mathbf{D}_{\mathrm{MD}}\,[\![\boldsymbol{q}]\!] &= \frac{1}{2}\boldsymbol{\mathcal{R}}|\boldsymbol{\Lambda}|\boldsymbol{\mathcal{R}}^{-1}\,[\![\boldsymbol{q}]\!] \simeq \frac{1}{2}\boldsymbol{\mathcal{R}}|\boldsymbol{\Lambda}|\boldsymbol{\mathcal{R}}^{-1}\boldsymbol{\mathcal{H}}\,[\![\boldsymbol{v}]\!] \quad \text{(in the sense of (4.57))} \\ &= \frac{1}{2}\boldsymbol{\mathcal{R}}|\boldsymbol{\Lambda}|\boldsymbol{\mathcal{R}}^{-1}\boldsymbol{\mathcal{R}}\boldsymbol{\mathcal{Z}}\boldsymbol{\mathcal{R}}^{\mathsf{T}}\,[\![\boldsymbol{v}]\!] = \frac{1}{2}\boldsymbol{\mathcal{R}}|\boldsymbol{\Lambda}|\boldsymbol{\mathcal{Z}}\boldsymbol{\mathcal{R}}^{\mathsf{T}}\,[\![\boldsymbol{v}]\!]\,.\end{aligned} \tag{4.62}$$

We already know the particular averaging needed for the matrix $\boldsymbol{\mathcal{H}}$ from (4.54). Next, we use these known averages and the condition (4.61) to determine the mean state evaluations for $\boldsymbol{\mathcal{R}}$ and $\boldsymbol{\mathcal{Z}}$. This creates a unique averaging procedure for the matrix dissipation term (4.62) while retaining the almost equal property (4.57).

It is straightforward, albeit laborious, to relate the entries of the matrix $\boldsymbol{\mathcal{H}}$ and determine the 81 individual components of the matrices $\boldsymbol{\mathcal{R}}$ and $\boldsymbol{\mathcal{Z}}$. An outline of the general technique and justification of the somewhat unconventional averaging strategies that result in the final form is provided in [44]. We forgo the algebraic details and after many manipulations, present the unique averaging procedure for the discrete eigenvector and scaling matrices.

Due to the complicated structure of the eigenvectors the presentation of the final form is divided into three parts. First, we give the specific averages for several convenience variables

$$\begin{aligned}
\hat{\Psi}_{\pm\mathrm{s}} &= \frac{\hat{\alpha}_{\mathrm{s}}\varrho^{\ln}\overline{\|\boldsymbol{u}\|^2}}{2} - a^{\beta}\hat{\alpha}_{\mathrm{f}}\varrho^{\ln}\bar{b}_{\perp} + \frac{\hat{\alpha}_{\mathrm{s}}\varrho^{\ln}(a^{\ln})^2}{\gamma-1} \pm \hat{\alpha}_{\mathrm{s}}\hat{c}_{\mathrm{s}}\varrho^{\ln}\{\!\{u\}\!\} \pm \hat{\alpha}_{\mathrm{f}}\hat{c}_{\mathrm{f}}\varrho^{\ln}\sigma(\bar{b}_1)(\{\!\{v\}\!\}\,\bar{\chi}_2 + \{\!\{w\}\!\}\,\bar{\chi}_3),\\
\hat{\Psi}_{\pm\mathrm{f}} &= \frac{\hat{\alpha}_{\mathrm{f}}\varrho^{\ln}\overline{\|\boldsymbol{u}\|^2}}{2} + a^{\beta}\hat{\alpha}_{\mathrm{s}}\varrho^{\ln}\bar{b}_{\perp} + \frac{\hat{\alpha}_{\mathrm{f}}\varrho^{\ln}(a^{\ln})^2}{\gamma-1} \pm \hat{\alpha}_{\mathrm{f}}\hat{c}_{\mathrm{f}}\varrho^{\ln}\{\!\{u\}\!\} \mp \hat{\alpha}_{\mathrm{s}}\hat{c}_{\mathrm{s}}\varrho^{\ln}\sigma(\bar{b}_1)(\{\!\{v\}\!\}\,\bar{\chi}_2 + \{\!\{w\}\!\}\,\bar{\chi}_3),\\
\hat{c}_{\mathrm{a}}^2 &= \bar{b}_1^2, \quad \hat{c}_{\mathrm{f,s}}^2 = \frac{1}{2}\left((\bar{a}^2+\bar{b}^2) \pm \sqrt{(\bar{a}^2+\bar{b}^2)^2 - 4\bar{a}^2\bar{b}_1^2}\right), \quad \tilde{p} = \frac{\{\!\{\varrho\}\!\}}{2\,\{\!\{\beta\}\!\}}, \quad \bar{a}^2 = \gamma\frac{\tilde{p}}{\varrho^{\ln}},\\
(a^{\ln})^2 &= \gamma\frac{p^{\ln}}{\varrho^{\ln}}, \quad (a^{\beta})^2 = \gamma\frac{1}{2\,\{\!\{\beta\}\!\}}, \quad \bar{b}^2 = \bar{b}_1^2+\bar{b}_2^2+\bar{b}_3^2, \quad \bar{b}_{\perp}^2 = \bar{b}_2^2+\bar{b}_3^2, \quad \bar{\chi}_{2,3} = \frac{\bar{b}_{2,3}}{\bar{b}_{\perp}},\\
\bar{b}_{1,2,3}^2 &= \frac{\{\!\{B_{1,2,3}\}\!\}^2}{\varrho^{\ln}}, \quad \hat{\alpha}_{\mathrm{f}}^2 = \frac{\bar{a}^2-\hat{c}_{\mathrm{s}}^2}{\hat{c}_{\mathrm{f}}^2-\hat{c}_{\mathrm{s}}^2}, \quad \hat{\alpha}_{\mathrm{s}}^2 = \frac{\hat{c}_{\mathrm{f}}^2-\bar{a}^2}{\hat{c}_{\mathrm{f}}^2-\hat{c}_{\mathrm{s}}^2}, \quad \sigma(\omega) = \begin{cases}+1 & \text{if } \omega \geq 0,\\ -1 & \text{otherwise}\end{cases}.
\end{aligned} \tag{4.63}$$

Next, we give the average of the right eigenvector matrix

$$\mathcal{R} = \left[\boldsymbol{r}_{+\mathrm{f}} \,|\, \boldsymbol{r}_{+\mathrm{a}} \,|\, \boldsymbol{r}_{+\mathrm{s}} \,|\, \boldsymbol{r}_{+\psi} \,|\, \boldsymbol{r}_{\mathrm{E}} \,|\, \boldsymbol{r}_{-\psi} \,|\, \boldsymbol{r}_{-\mathrm{s}} \,|\, \boldsymbol{r}_{-\mathrm{a}} \,|\, \boldsymbol{r}_{-\mathrm{f}} \right]. \tag{4.64}$$

Here each of the discrete eigenvectors are

GLM Waves: $\lambda_{\pm\psi}$

$$\boldsymbol{r}_{\pm\psi} = \begin{bmatrix} 0 \\ 0 \\ 0 \\ 0 \\ \{\!\{B_1\}\!\} \pm \{\!\{\psi\}\!\} \\ 1 \\ 0 \\ 0 \\ \pm 1 \end{bmatrix}, \tag{4.65}$$

Entropy Wave : λ_{E}

$$\boldsymbol{r}_{\mathrm{E}} = \begin{bmatrix} 1 \\ \{\!\{u\}\!\} \\ \{\!\{v\}\!\} \\ \{\!\{w\}\!\} \\ \frac{1}{2}\overline{\|\boldsymbol{u}\|^2} \\ 0 \\ 0 \\ 0 \\ 0 \end{bmatrix}, \tag{4.66}$$

Alfvén Waves: $\lambda_{\pm\mathrm{a}}$

$$\boldsymbol{r}_{\pm\mathrm{a}} = \begin{bmatrix} 0 \\ 0 \\ \pm \varrho^{\ln} \sqrt{\{\!\{\varrho\}\!\}}\, \bar{\chi}_3 \\ \mp \varrho^{\ln} \sqrt{\{\!\{\varrho\}\!\}}\, \bar{\chi}_2 \\ \mp \varrho^{\ln} \sqrt{\{\!\{\varrho\}\!\}} (\bar{\chi}_2 \{\!\{w\}\!\} - \bar{\chi}_3 \{\!\{v\}\!\}) \\ 0 \\ -\varrho^{\ln} \bar{\chi}_3 \\ \varrho^{\ln} \bar{\chi}_2 \\ 0 \end{bmatrix}, \tag{4.67}$$

Fast and Slow Magnetoacoustic Waves: $\lambda_{\pm\mathrm{f},\pm\mathrm{s}}$

$$\boldsymbol{r}_{\pm\mathrm{f}} = \begin{bmatrix} \hat{\alpha}_{\mathrm{f}} \varrho^{\ln} \\ \hat{\alpha}_{\mathrm{f}} \varrho^{\ln} (\{\!\{u\}\!\} \pm \hat{c}_f) \\ \varrho^{\ln} \left(\hat{\alpha}_{\mathrm{f}} \{\!\{v\}\!\} \mp \hat{\alpha}_{\mathrm{s}} \hat{c}_{\mathrm{s}} \bar{\chi}_2 \sigma(\bar{b}_1) \right) \\ \varrho^{\ln} \left(\hat{\alpha}_{\mathrm{f}} \{\!\{w\}\!\} \mp \hat{\alpha}_{\mathrm{s}} \hat{c}_{\mathrm{s}} \bar{\chi}_3 \sigma(\bar{b}_1) \right) \\ \hat{\Psi}_{\pm\mathrm{f}} \\ 0 \\ \hat{\alpha}_{\mathrm{s}} a^{\beta} \bar{\chi}_2 \sqrt{\varrho^{\ln}} \\ \hat{\alpha}_{\mathrm{s}} a^{\beta} \bar{\chi}_3 \sqrt{\varrho^{\ln}} \\ 0 \end{bmatrix}, \tag{4.68}$$

$$\boldsymbol{r}_{\pm\mathrm{s}} = \begin{bmatrix} \hat{\alpha}_{\mathrm{s}} \varrho^{\ln} \\ \hat{\alpha}_{\mathrm{s}} \varrho^{\ln} \left(\{\!\{u\}\!\} \pm \hat{c}_{\mathrm{s}} \right) \\ \varrho^{\ln} \left(\hat{\alpha}_{\mathrm{s}} \{\!\{v\}\!\} \pm \hat{\alpha}_{\mathrm{f}} \hat{c}_{\mathrm{f}} \bar{\chi}_2 \sigma(\bar{b}_1) \right) \\ \varrho^{\ln} \left(\hat{\alpha}_{\mathrm{s}} \{\!\{w\}\!\} \pm \hat{\alpha}_{\mathrm{f}} \hat{c}_{\mathrm{f}} \bar{\chi}_3 \sigma(\bar{b}_1) \right) \\ \hat{\Psi}_{\pm\mathrm{s}} \\ 0 \\ -\hat{\alpha}_{\mathrm{f}} a^{\beta} \bar{\chi}_2 \sqrt{\varrho^{\ln}} \\ -\hat{\alpha}_{\mathrm{f}} a^{\beta} \bar{\chi}_3 \sqrt{\varrho^{\ln}} \\ 0 \end{bmatrix}. \tag{4.69}$$

The mean state for the diagonal scaling matrix is

$$\mathcal{Z} = \mathrm{diag}\left(\frac{1}{2\gamma \varrho^{\ln}}, \frac{1}{4\{\!\{\beta\}\!\} (\varrho^{\ln})^2}, \frac{1}{2\gamma \varrho^{\ln}}, \frac{1}{4\{\!\{\beta\}\!\}}, \frac{\varrho^{\ln}(\gamma - 1)}{\gamma}, \frac{1}{4\{\!\{\beta\}\!\}}, \frac{1}{2\gamma \varrho^{\ln}}, \frac{1}{4\{\!\{\beta\}\!\} (\varrho^{\ln})^2}, \frac{1}{2\gamma \varrho^{\ln}} \right), \tag{4.70}$$

and the diagonal matrix of eigenvalues for the ideal GLM-MHD system is

$$\Lambda = \mathrm{diag}\left(\hat{\lambda}_{+\mathrm{f}} \,|\, \hat{\lambda}_{+\mathrm{a}} \,|\, \hat{\lambda}_{+\mathrm{s}} \,|\, \hat{\lambda}_{+\psi} \,|\, \hat{\lambda}_{\mathrm{E}} \,|\, \hat{\lambda}_{-\psi} \,|\, \hat{\lambda}_{-\mathrm{s}} \,|\, \hat{\lambda}_{-\mathrm{a}} \,|\, \hat{\lambda}_{-\mathrm{f}} \right), \tag{4.71}$$

where we describe the discrete evaluation of the wave speeds in the following subsection.

The final form of the entropy stable numerical flux with the matrix dissipation term takes the form [3,12]

$$\boldsymbol{f}^{*,\mathrm{KEPES,MD}} = \boldsymbol{f}^{*,\mathrm{KEPEC}} - \tfrac{1}{2} \mathcal{R} |\Lambda| \mathcal{Z} \mathcal{R}^{\mathsf{T}} [\![\boldsymbol{v}]\!]. \tag{4.72}$$

4.4. Discrete eigenvalues of the ideal GLM-MHD system

An important aspect of utmost concern for robustness and stability of the numerical scheme we construct is how to define the discrete wave speeds, λ, at the interfaces. From (3.28) we know that the wave speeds in continuous space are given by

$$\lambda_{\pm\mathrm{f}} = u \pm c_{\mathrm{f}}, \qquad \lambda_{\pm\mathrm{s}} = u \pm c_{\mathrm{s}}, \qquad \lambda_{\pm\mathrm{a}} = u \pm c_{\mathrm{a}}, \qquad \lambda_{\mathrm{E}} = u, \quad \text{and} \quad \lambda_{\pm\psi} = u \pm c_h. \tag{4.73}$$

However, in discretized space, we have to compute the eigenvalues at each interface from the discrete left and right states, $\boldsymbol{q}_{\mathrm{L,R}}$. First, we compute a discrete flux Jacobian as was described, in a different context, in [43]. From this matrix we compute the eigenvalues of the discrete ideal GLM-MHD system at the interface between the left and right cells and obtain:

$$\hat{\boldsymbol{\lambda}} = \begin{bmatrix} \hat{\lambda}_{+\mathrm{f}} \\ \hat{\lambda}_{+\mathrm{a}} \\ \hat{\lambda}_{+\mathrm{s}} \\ \hat{\lambda}_{+\psi} \\ \hat{\lambda}_{\mathrm{E}} \\ \hat{\lambda}_{-\psi} \\ \hat{\lambda}_{-\mathrm{s}} \\ \hat{\lambda}_{-\mathrm{a}} \\ \hat{\lambda}_{-\mathrm{f}} \end{bmatrix} = \begin{bmatrix} \{\!\{u\}\!\} + \hat{c}_{\mathrm{f}} \\ \{\!\{u\}\!\} + \hat{c}_{\mathrm{a}} \\ \{\!\{u\}\!\} + \hat{c}_{\mathrm{s}} \\ \{\!\{u\}\!\} + \{\!\{c_h\}\!\} \\ \{\!\{u\}\!\} \\ \{\!\{u\}\!\} - \{\!\{c_h\}\!\} \\ \{\!\{u\}\!\} - \hat{c}_{\mathrm{s}} \\ \{\!\{u\}\!\} - \hat{c}_{\mathrm{a}} \\ \{\!\{u\}\!\} - \hat{c}_{\mathrm{f}} \end{bmatrix} \begin{array}{l} \text{right going fast magnetoacoustic wave} \\ \text{right going Alfvén wave} \\ \text{right going slow magnetoacoustic wave} \\ \text{right going GLM wave} \\ \text{entropy wave} \\ \text{left going GLM wave} \\ \text{left going slow magnetoacoustic wave} \\ \text{left going Alfvén wave} \\ \text{left going fast magnetoacoustic wave} \end{array} \tag{4.74}$$

The precise form of the discrete speeds ($\hat{c}_{\mathrm{f,s,a}}$) as well as technical details are summarized in Appendix C.

4.5. Mixed hyperbolic/parabolic GLM ansatz

Dedner et al. [26], Wesenberg [47] and Tricco and Price [39] found that the best approximation of ψ may be obtained by a mixed hyperbolic/parabolic ansatz. Hence, we supplement (3.16e) with an additional source term

$$\boldsymbol{\Upsilon}^{\alpha} = \begin{bmatrix} 0 & \mathbf{0} & 0 & \mathbf{0} & \alpha\psi \end{bmatrix}^{\mathsf{T}}, \tag{4.75}$$

with the parabolic diffusion rate $\alpha \in [0, \infty)$ that controls the damping of the ψ field. Through the addition of this source term, the ψ field is no longer a conserved quantity, but is actively dissipated. Clearly, including such a dissipative term makes the derivation of an entropy *conserving* scheme impossible. However, if we carefully compute the entropy budget of the source term (4.75), we find that the contribution to the entropy is guaranteed to have the correct sign, *i.e.* it fulfills the entropy inequality and is still suitable for creating an entropy *stable* scheme,

$$\boldsymbol{v} \cdot (\boldsymbol{q}_t + \frac{\partial}{\partial x}\boldsymbol{f}^x + \boldsymbol{\Upsilon}^x + \boldsymbol{\Upsilon}^{\alpha}) \quad \Rightarrow \quad \frac{\partial}{\partial t} S + \nabla \cdot (\boldsymbol{u} S) = -2\beta\alpha\psi^2 \leq 0 \quad \text{with} \quad \alpha, \beta \geq 0. \tag{4.76}$$

The effect of this additional source term on the evolution of the total energy is found by looking at the temporal evolution of the ψ field,

$$\frac{\partial}{\partial t}\left(\frac{1}{2}\psi^2\right) = \psi \cdot \frac{\partial \psi}{\partial t} = -c_h \psi (\nabla \cdot \boldsymbol{B}) + \boldsymbol{u}\psi(\nabla\psi) + \alpha\psi^2. \tag{4.77}$$

The resulting system is given by (3.16) with an additional source term $\alpha\psi^2$ on the right hand side of the total energy. We chose to ignore this additional source term on the total energy equation, thus any energy dissipated from the ψ field directly enters the thermal pressure.

The source term (4.75) introduces a new free parameter α which requires further analysis. We see that for the purely hyperbolic case, *i.e.* $\alpha = 0$, we can derive an entropy conserving scheme. Furthermore, for any $\alpha > 0$, entropy is guaranteed to be dissipated but never destroyed. There are several choices one can make in selecting the damping parameter α. As discussed by Dedner et al. [26, Section 4], a favorable choice for the damping parameter is a fixed proportion of decay (parabolic) to transport (hyperbolic) with a ratio $c_r := c_p^2/c_h$ at all times. In their observation this choice of α resulted in satisfactory numerical results that are independent of the grid resolution or the scheme used. Dedner et al. [26, p. 661] define the optimal ratio as $c_r = 0.18$,

$$\alpha = \frac{c_h^2}{c_p^2} = \frac{c_h}{c_r} = \frac{c_h}{0.18}. \tag{4.78}$$

As we show in the numerical results section, the mixed GLM ansatz gives very good results and is in fact even necessary for periodic boundary conditions.

4.6. High-order accurate entropy stable scheme

The scheme we discussed so far is first order in space and still continuous in time. In the following subsections, we discuss its extension to the fully discrete case with high-order accuracy.

4.6.1. Temporal accuracy

A very simple time integrator is the Euler scheme, where the solution is advanced in small time steps in which the flux is assumed to be constant. The Euler scheme is only first-order accurate in *time*, *i.e.* the solution is accurate to $\mathcal{O}(\Delta t)$. Fortunately, the temporal order can be increased by replacing the time integrator by a suitable higher-order scheme, *e.g.* strong stability preserving (SSP) Runge–Kutta (RK) schemes [48]. However, high-order accurate time integrators come at significant additional computational costs so one has to always find a compromise between (temporal) accuracy and computational resources. For the numerical tests we present in this work, we use a third order SSPRK time integrator.

Table 1
High-order coefficients $\{\xi_{p,r}\}_{r=1}^{p}$ for up to 16th order accuracy. Coefficients for even higher order can be computed from (4.81).

Accuracy $2p$	$\xi_{p,1}$	$\xi_{p,2}$	$\xi_{p,3}$	$\xi_{p,4}$	$\xi_{p,5}$	$\xi_{p,6}$	$\xi_{p,7}$	$\xi_{p,8}$
2	1							
4	$\frac{4}{3}$	$-\frac{1}{6}$						
6	$\frac{3}{2}$	$-\frac{3}{10}$	$\frac{1}{30}$					
8	$\frac{8}{5}$	$-\frac{2}{5}$	$\frac{8}{105}$	$-\frac{1}{140}$				
10	$\frac{5}{3}$	$-\frac{10}{21}$	$\frac{5}{42}$	$-\frac{5}{252}$	$\frac{1}{630}$			
12	$\frac{12}{7}$	$-\frac{15}{28}$	$\frac{10}{63}$	$-\frac{1}{28}$	$\frac{2}{385}$	$-\frac{1}{2772}$		
14	$\frac{7}{4}$	$-\frac{7}{12}$	$\frac{7}{36}$	$-\frac{7}{132}$	$\frac{7}{660}$	$-\frac{7}{5148}$	$\frac{1}{12012}$	
16	$\frac{16}{9}$	$-\frac{28}{45}$	$\frac{112}{495}$	$-\frac{7}{99}$	$\frac{112}{6435}$	$-\frac{4}{1287}$	$\frac{16}{45045}$	$-\frac{1}{51480}$

4.6.2. Spatial accuracy

Unfortunately, higher spatial accuracy is harder to obtain for finite volume schemes because we only have cell-averaged quantities available, although we need interface values for computing the numerical fluxes. There are, essentially, two ways to achieve high-order accuracy in space: The first, and most often used one, is the technique of "spatial reconstruction" where an algorithm is used to deduce an interface value based on a certain stencil on the cell-averaged quantities. The simplest approximation is to assume that the values at the interfaces are identical to the cell-averages. Unsurprisingly, the solution obtained using such an approximation is only first-order accurate in *space*, *i.e.* the solution is accurate to $\mathcal{O}(\Delta x)$. There exists a vast amount of literature on the technique of spatial reconstruction. The authors give an extensive introduction in [49, Section 4.1].

The second approach, uses the fact that the entropy conserving flux describes the rate of change for the quantities over an interface and, as such, is a first order derivative with respect to time over a fixed volume. Using a suitable extrapolation, we can construct arbitrarily accurate entropy conservative interface fluxes through linear combinations of our computationally inexpensive entropy conservative flux derived in Section 4.2 as shown below.

Given suitable coefficients $\{\xi_{p,r}\}_{r=1}^{p}$ (see Table 1), the entropy conserving flux

$$ {}^{2p}\boldsymbol{f}^{\mathrm{EC}}_{i-1/2} := \sum_{r=1}^{p} \xi_{p,r} \sum_{s=1}^{r} \boldsymbol{f}^{\mathrm{EC}}(\boldsymbol{u}_{i-s}, \boldsymbol{u}_{i-s+r}) \tag{4.79} $$

is $2p$th-order accurate in space, *i.e.*

$$ \frac{1}{\Delta x}\left({}^{2p}\boldsymbol{f}^{\mathrm{EC}}_{i+1/2} - {}^{2p}\boldsymbol{f}^{\mathrm{EC}}_{i-1/2}\right) = \frac{\partial}{\partial x}\boldsymbol{f}(\boldsymbol{u})\Big|_{x=x_i} + \mathcal{O}(\Delta x^{2p}) \tag{4.80} $$

[50, Theorem 4.4]. The coefficients $\{\xi_{p,r}\}_{r=1}^{p}$ are obtained by solving the p linear equations given by

$$ \sum_{r=1}^{p} i\xi_{p,r} = 1, \quad \sum_{r=1}^{p} r^{2s-1}\xi_{p,r} = 0 \qquad (s = 2, \dots, p). \tag{4.81} $$

As an example, we summarize the second- to sixth-order accurate entropy conserving fluxes below:

- Second-order accurate EC interface flux ($p = 1$)

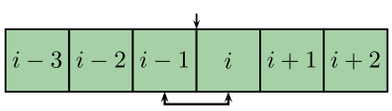

$$ {}^{2}\boldsymbol{f}^{\mathrm{EC}}_{i-1/2} = \boldsymbol{f}^{\mathrm{EC}}(\boldsymbol{u}_{i-1}, \boldsymbol{u}_i) \tag{4.82} $$

- Fourth-order accurate EC interface flux ($p = 2$)

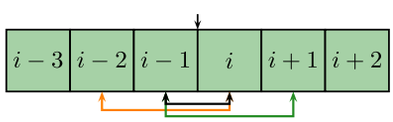

$$ \begin{aligned} {}^{4}\boldsymbol{f}^{\mathrm{EC}}_{i-1/2} = {} & \tfrac{4}{3}\boldsymbol{f}^{\mathrm{EC}}(\boldsymbol{u}_{i-1}, \boldsymbol{u}_i) \\ & -\tfrac{1}{6}\big(\boldsymbol{f}^{\mathrm{EC}}(\boldsymbol{u}_{i-2}, \boldsymbol{u}_i) \\ & \quad +\boldsymbol{f}^{\mathrm{EC}}(\boldsymbol{u}_{i-1}, \boldsymbol{u}_{i+1})\big) \end{aligned} \tag{4.83} $$

- Sixth-order accurate EC interface flux ($p = 3$)

$$ \begin{aligned} {}^{6}\boldsymbol{f}^{\mathrm{EC}}_{i-1/2} = {} & \frac{3}{2}\boldsymbol{f}(\boldsymbol{u}_{i-1}, \boldsymbol{u}_i) - \frac{3}{10}\big(\boldsymbol{f}(\boldsymbol{u}_{i-2}, \boldsymbol{u}_i) + \boldsymbol{f}(\boldsymbol{u}_{i-1}, \boldsymbol{u}_{i+1})\big) \\ & + \frac{1}{30}\big(\boldsymbol{f}(\boldsymbol{u}_{i-3}, \boldsymbol{u}_i) + \boldsymbol{f}(\boldsymbol{u}_{i-2}, \boldsymbol{u}_{i+1}) + \boldsymbol{f}(\boldsymbol{u}_{i-1}, \boldsymbol{u}_{i+2})\big) \end{aligned} \tag{4.84} $$

Up to now it is unknown how to discretize the non-conservative terms to obtain a high-order accurate approximation. The source term added to the numerical fluxes is given by

$$\boldsymbol{\Upsilon}^x = (\nabla\cdot\boldsymbol{B})^x \begin{bmatrix} 0 & \boldsymbol{B} & \boldsymbol{u}\cdot\boldsymbol{B} & \boldsymbol{u} & 0 \end{bmatrix}^\mathsf{T} + (\boldsymbol{u}\cdot(\nabla\psi))^x \begin{bmatrix} 0 & \boldsymbol{0} & \psi & \boldsymbol{0} & 1 \end{bmatrix}^\mathsf{T}, \tag{4.85}$$

where, in its discretized version, it is a high-order representation of the divergence and gradient operators in combination with the cell-centered quantities in cell i,

$${}^{2p}\boldsymbol{\Upsilon}_i^x = {}^{2p}(\nabla\cdot\boldsymbol{B})_i^x \begin{bmatrix} 0 & \boldsymbol{B} & \boldsymbol{u}\cdot\boldsymbol{B} & \boldsymbol{u} & 0 \end{bmatrix}_i^\mathsf{T} + {}^{2p}(\boldsymbol{u}\cdot(\nabla\psi))_i^x \begin{bmatrix} \boldsymbol{0} & 0 & \psi & 0 & 1 \end{bmatrix}_i^\mathsf{T} \tag{4.86}$$

with

$${}^{2p}(\nabla\cdot\boldsymbol{B})_i^x := \frac{1}{2\Delta x}\sum_{r=1}^{p}\xi_{p,r}(B_{1,i+r}-B_{1,i-r}) \qquad \text{and} \qquad {}^{2p}(\boldsymbol{u}\cdot(\nabla\psi))_i^x := \frac{u_i}{2\Delta x}\sum_{r=1}^{p}\xi_{p,r}(\psi_{i+r}-\psi_{i-r}) \tag{4.87}$$

Again, we summarize the resulting non-conservative terms for second- to sixth-order accuracy below:

- Second-order accurate magnetic field divergence ($p=1$)

$${}^{2}(\nabla\cdot\boldsymbol{B})_i^x = \frac{B_{1,i+1}-B_{1,i-1}}{2\Delta x} \tag{4.88}$$

$${}^{2}(\boldsymbol{u}\cdot\nabla\psi)_i = u_i\frac{\psi_{i+1}-\psi_{i-1}}{2\Delta x} \tag{4.89}$$

$${}^{2}\boldsymbol{\Upsilon}_i = {}^{2}(\nabla\cdot\boldsymbol{B})_i^x \begin{bmatrix} 0 & \boldsymbol{B} & \boldsymbol{u}\cdot\boldsymbol{B} & \boldsymbol{u} & 0 \end{bmatrix}_i^\mathsf{T} + {}^{2}(\boldsymbol{u}\cdot(\nabla\psi))_i^x \begin{bmatrix} 0 & \boldsymbol{0} & \psi & \boldsymbol{0} & 1 \end{bmatrix}_i^\mathsf{T} \tag{4.90}$$

- Fourth-order accurate magnetic field divergence ($p=2$)

$${}^{4}(\nabla\cdot\boldsymbol{B})_i^x = \frac{\frac{4}{3}(B_{1,i+1}-B_{1,i-1})-\frac{1}{6}(B_{i,i+2}-B_{i,i-2})}{2\Delta x} \tag{4.91}$$

$${}^{4}(\boldsymbol{u}\cdot\nabla\psi)_i = u_i\frac{\frac{4}{3}(\psi_{i+1}-\psi_{i-1})-\frac{1}{6}(\psi_{i+2}-\psi_{i-2})}{2\Delta x} \tag{4.92}$$

$${}^{4}\boldsymbol{\Upsilon}_i = {}^{4}(\nabla\cdot\boldsymbol{B})_i^x \begin{bmatrix} 0 & \boldsymbol{B} & \boldsymbol{u}\cdot\boldsymbol{B} & \boldsymbol{u} & 0 \end{bmatrix}_i^\mathsf{T} + {}^{4}(\boldsymbol{u}\cdot(\nabla\psi))_i^x \begin{bmatrix} 0 & \boldsymbol{0} & \psi & \boldsymbol{0} & 1 \end{bmatrix}_i^\mathsf{T} \tag{4.93}$$

- Sixth-order accurate magnetic field divergence ($p=3$)

$${}^{6}(\nabla\cdot\boldsymbol{B})_i^x = \frac{\frac{3}{2}(B_{1,i+1}-B_{1,i-1})-\frac{3}{10}(B_{1,i+2}-B_{1,i-2})+\frac{1}{60}(B_{1,i+3}-B_{1,i-3})}{2\Delta x} \tag{4.94}$$

$${}^{6}(\boldsymbol{u}\cdot\nabla\psi)_i^x = u_i\frac{\frac{3}{2}(\psi_{i+1}-\psi_{i-1})-\frac{3}{10}(\psi_{i+2}-\psi_{i-2})+\frac{1}{60}(\psi_{i+3}-\psi_{i-3})}{2\Delta x} \tag{4.95}$$

$${}^{6}\boldsymbol{\Upsilon}_i = {}^{6}(\nabla\cdot\boldsymbol{B})_i^x \begin{bmatrix} 0 & \boldsymbol{B} & \boldsymbol{u}\cdot\boldsymbol{B} & \boldsymbol{u} & 0 \end{bmatrix}_i^\mathsf{T} + {}^{6}(\boldsymbol{u}\cdot(\nabla\psi))_i^x \begin{bmatrix} 0 & \boldsymbol{0} & \psi & \boldsymbol{0} & 1 \end{bmatrix}_i^\mathsf{T} \tag{4.96}$$

Unfortunately, one cannot apply the same technique for the entropy stable part of the numerical fluxes. As detailed by Fjordholm [51, Sec. 3.2], a specific reconstruction procedure (preferably done in entropy rather than in conservative variables) can be used to ensure high-order entropy stability. To do so, we ensure that the sign of the reconstructed jump, ${}^{k}[\![\boldsymbol{v}]\!]_{i-1/2}$, is the same sign as the naive jump, $[\![\boldsymbol{v}]\!]_{i-1/2}$.

5. Numerical tests

We demonstrate the numerical magnetic divergence evolution of the new entropy stable numerical scheme for ideal GLM-MHD derived in this work by computing several ideal MHD test problems. We use the finite volume code `FLASH` in version 4.5. The technical aspects of our testbed are described in great detail in [2]. We use fourth-order accurate entropy-conservative as well as third-order accurate entropy-stable fluxes (limited reconstruction [52]) in space as well as a third-order accurate SSP RK time integration scheme [48] and a CFL coefficient of 0.8 for all tests. With our numerical tests we focus on the magnetic field divergence cleaning effectiveness of the new entropy stable ideal GLM-MHD system. A numerical validation of the entropy conservation properties of the new numerical flux is given as a supplementary test case.

Note that, given its nature, a suitable choice for the initial value for ψ is $\psi_0 = \psi(t=0) = 0$. This has two reasons:

1. Only gradients of ψ appear in the numerical fluxes. Hence, given divergence-free initial conditions, we should initialize the ψ field with a constant value everywhere such that $\nabla\psi_0 = \boldsymbol{0}$, initially.
2. We define the energy in the ψ field as $E_\psi = \frac{1}{2}\psi^2$. In a divergence-free state, it makes sense to have this "correction field energy" equal to zero, suggesting $\psi_0 = 0$ everywhere.

Table 2
Initial conditions and runtime parameters: artificial non-zero magnetic field divergence test (1D).

Density ϱ	1.0	Domain size	$\{x_{\min}, x_{\max}\} = \{-1, 1\}$
Pressure p	1.0	Boundary conditions	outflow or periodic
Velocity $\boldsymbol{u}$	$\mathbf{0}$	Simulation end time	$t_{\max} = 5.0$
Mag. field $\boldsymbol{B}$	$[B_1(x) \quad 0 \quad 0]^\intercal$	Adiabatic index	$\gamma = 1.4$

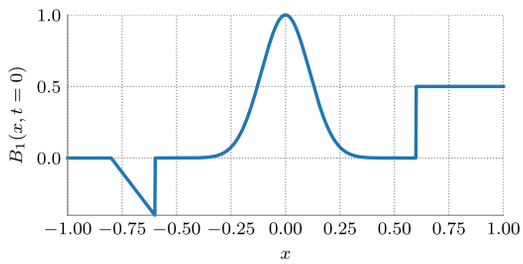

$$B_1(x) = \begin{cases} 0.0 & x \leq -0.8 \\ -2(x + 0.8) & -0.8 < x \leq -0.6 \\ \exp\left(-\frac{(x/0.11)^2}{2}\right) & -0.6 < x \leq 0.6 \\ 0.5 & x > 0.6 \end{cases} \tag{5.1}$$

Fig. 2. Initial x component of the magnetic field of the artificial non-zero magnetic field divergence test (1D).

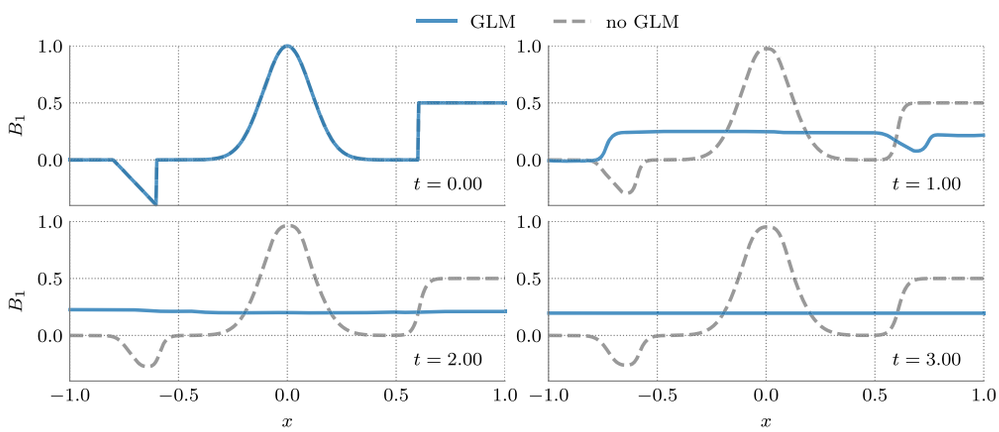

Fig. 3. Magnetic field B_1 of the artificial non-zero magnetic field divergence test at four different times. We show the magnetic field evolution computed using the new GLM-KEPES flux (blue lines), together with the solution obtained using the KEPES flux that is not using the GLM technique for divergence cleaning (dashed, gray lines). Note that $t = 1, 2, 3$ corresponds to one, two, and three Alfvén crossing times. (For interpretation of the colors in the figure(s), the reader is referred to the web version of this article.)

5.1. Artificial non-zero magnetic field divergence test (1D)

The behavior of any numerical scheme, given non-zero initial divergence is of high interest as non-zero divergence may also be caused by poorly chosen initial conditions. The scheme must deal with the divergence errors properly in order to produce a credible solution. This artificial numerical test starts from a magnetic field with non-zero divergence involving not only smooth gradients but also steps making it a more challenging test for the divergence cleaning method. The remaining quantities are flat. We select a fixed resolution of 256 uniformly distributed cells. We present the initial conditions for this test in Table 2. The magnetic field in the x-direction is given by (5.1) in Fig. 2. Note that these initial conditions intentionally violate the constraint $\nabla \cdot \boldsymbol{B} = 0$ by a significant amount.

In Fig. 3, we compare the result of this test against the one obtained using the kinetic energy preserving entropy stable (KEPES) solver for ideal MHD [43] at different times. The new GLM-KEPES solver treats the substantial initial divergence error correctly and removes any divergence in the magnetic field quickly. The KEPES solver is, however, only capable of dissipating the magnetic field slightly due to numerical dissipation caused by the spatial and temporal discretizations. Note that we can obtain similar results with our scheme if we enforce $c_h = 0$ throughout the simulation. It is obvious that a scheme that is not capable of removing significant divergence errors in the solution generates unsatisfactory numerical results. We set $\alpha = 0$ in this test case (hyperbolic cleaning only) and use outflow boundaries. In the following, we use periodic boundary conditions. Note that for outflow boundary conditions, the errors can quickly leave the computational domain. However, as can be seen in Fig. 4, a solely hyperbolic cleaning ($\alpha = 0$) is not sufficient to reduce the divergence for periodic boundary conditions. This is easily understood as the divergence error cannot be advected "out" of the com-

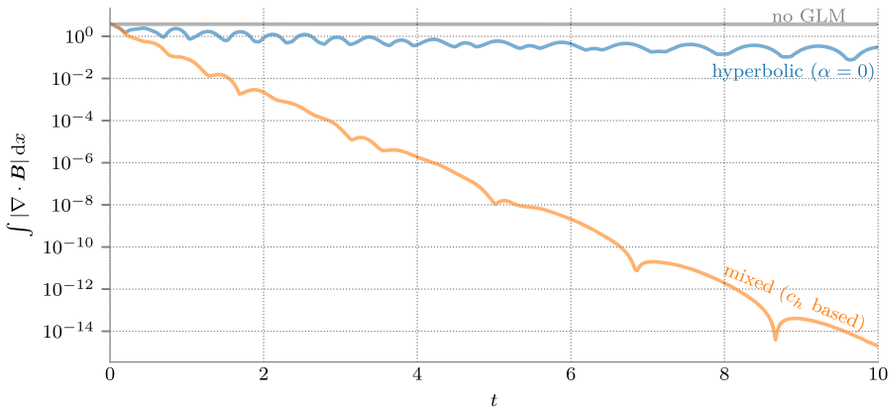

Fig. 4. Artificial non-zero magnetic field divergence test: Evolution of the integrated absolute magnetic field divergence in the artificial non-zero magnetic field divergence test in one dimension using periodic boundary conditions. It is clear the magnetic field divergence evolution with mixed cleaning is favorable.

Table 3
Initial conditions and runtime parameters: Divergence advection test (2D) [27].

$$\varrho = \begin{cases} 1.0 & \text{if } x \leq 0.5 \\ 2.0 & \text{else} \end{cases}$$

$$\boldsymbol{B} = \left[B_x \quad 0 \quad \tfrac{1}{\sqrt{4\pi}} \right]^{\mathsf{T}}, \quad \boldsymbol{u} = \boldsymbol{0}, \quad p = 6.0$$

$$B_x = \begin{cases} \frac{1}{\sqrt{4\pi}} \left(\left(\frac{r}{r_0} \right)^8 - 2 \left(\frac{r}{r_0} \right)^4 + 1 \right) & \text{if } r \leq r_0, \\ 0 & \text{else.} \end{cases}$$

Domain size	$x, y \in [-0.5, 1.5]$
Radial extent	$r_0 = 1/\sqrt{8}$
Boundary conditions	all: periodic
Simulation end time	$t_{\max} = 1.0$
Adiabatic index	$\gamma = 5/3$

with $r = \sqrt{x^2 + y^2}$

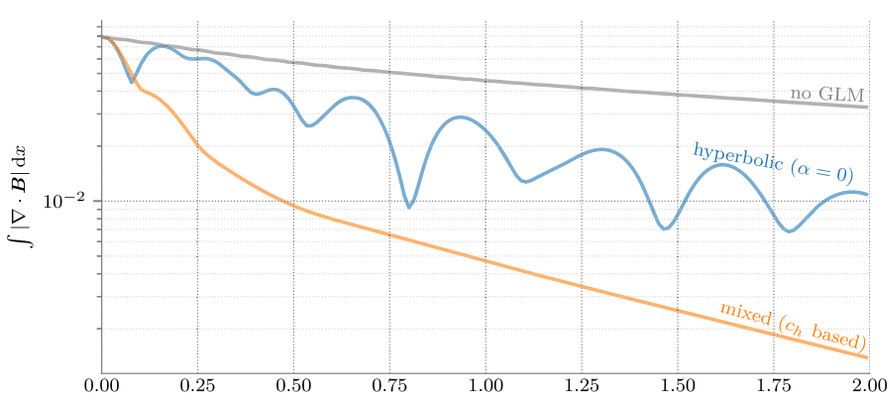

Fig. 5. Divergence advection test: Evolution of the integrated absolute magnetic field divergence in the advection test in two dimensions. We test various choices of the damping parameter.

putational domain anymore. Hence, additional damping is essential in order to reduce the divergence error over time, as suggested by Dedner et al. [26, Section 4], denoted by "mixed (c_h based)" in the figure.

5.2. Divergence advection test (2D)

Another simple test case for the cleaning efficiency is the two-dimensional divergence advection test presented by Tricco and Price [27, Sec. 5.2]. It consists of divergence in the magnetic field artificially induced in the initial conditions that is advected by a uniform flow and is a variant of the "peak in B_1" test presented by Dedner et al. [26, Sec. 5]. This test includes a density step that is used to examine the reflection and refraction of the divergence waves as they transit between media of different densities. The initial conditions are listed in Table 3.

Table 4
Initial conditions and runtime parameters: 2D MHD rotor test [2].

	$r \le r_0$	$r \in (r_0, r_1)$	$r \ge r_1$
ϱ	10.0	$1.0 + 9.0 f(r)$	1.0
p	1.0	1.0	1.0
B_1	$5/\sqrt{4\pi}$	$5/\sqrt{4\pi}$	$5/\sqrt{4\pi}$
B_2	0.0	0.0	0.0
B_3	0.0	0.0	0.0
u	$-20.0\Delta y$	$-20.0 f(r)\Delta y$	0.0
v	$20.0\Delta x$	$20.0 f(r)\Delta x$	0.0
w	0.0	0.0	0.0

with $f(r) = \frac{r_1 - r}{r_1 - r_0}$,
$r = \sqrt{(x - x_{\text{center}})^2 + (y - y_{\text{center}})^2}$,
$\Delta x = (x - x_{\text{center}})$, $\Delta y = (y - y_{\text{center}})$

Domain size	$x, y \in [0, 1]$
Inner radius	$r_0 = 0.1$
Outer radius	$r_1 = 0.115$
x-center	$x_{\text{center}} = 0.5$
y-center	$y_{\text{center}} = 0.5$
Boundary conditions	all: outflow
Adaptive refinement on	density, magnetic field
Simulation end time	$t_{\max} = 0.15$
Adiabatic index	$\gamma = 1.4$

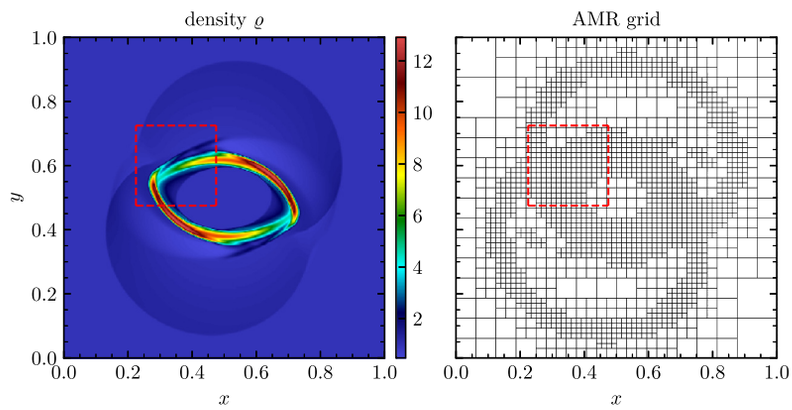

Fig. 6. MHD rotor test ($t = 0.15$): Adaptive grid resolution up to 512×512 (each shown rectangle encloses 8×8 cells). The marked area is shown in Fig. 7.

Our findings are plotted in Fig. 5. We find similar results compared to the one-dimensional test with periodic boundary conditions as the semi-adaptive choice suggested by Dedner et al. gives the best cleaning behavior.

5.3. MHD Rotor test

The MHD rotor problem [20] describes a rapidly spinning dense cylinder embedded in a magnetized, homogeneous medium at rest. Due to centrifugal forces, the dense cylinder is not in equilibrium. As the rotor spins with the given initial rotating velocity, the initially uniform magnetic field will wind up. The wrapping of the rotor by the magnetic field leads to strong toroidal Alfvén waves launched into the ambient fluid. The initial conditions are listed in Table 4.

The reference solution has been obtained using the unsplit staggered mesh (USM) solver implemented in `FLASH` [53]. The USM solver uses constrained transport to ensure the solenoidal constraint of the magnetic field on a staggered mesh geometry. An advantage of our numerical scheme, compared to the staggered mesh USM solver, is that it requires appreciably less memory (see *e.g.* [2, Sec. 4.5]). This makes our scheme computationally attractive on many modern supercomputing systems where simulations are commonly memory-limited, *e.g.* [31]. As can be seen in Figs. 6 and 7, the results obtained using the KEPES-GLM scheme show much smaller divergence artifacts and hence are much closer to the reference solution than the solution computed with the same numerical solver but without GLM correction (where we artificially set $c_h = 0$).

In the zoom-in figure (Fig. 7) we see density (top row) and pressure (2nd row) minima visible in the GLM solution at $(x, y) \approx (0.4, 0.64)$ which are absent in the reference solution. To check for a possible wrong behavior of our scheme we re-ran the reference solution, obtained with the unsplit staggered mesh solver of `FLASH`, with an adaptive resolution of up to 2048×2048 (four-fold). With the higher resolution run we confirm the extrema seen with our scheme and conclude that, in this test case, our scheme is able to capture finer details than the reference simulation on the same resolution.

The USM solver uses a formulation that ensures that the numerical divergence is zero at the cell face-centered magnetic fields,

$$(\nabla \cdot \boldsymbol{B})^{\text{face}}_{i,j} = \frac{b_{x,i+1/2,j} - b_{x,i-1/2,j}}{\Delta x} + \frac{b_{y,i,j+1/2} - b_{y,i,j-1/2}}{\Delta y}, \tag{5.2}$$

where $b_{x,y,z}$ describes the face-centered magnetic field components [53, eq. (20)]. Note that this way of computing the magnetic field divergence is different from our treatment of the magnetic fields at the cell-centers as defined in (4.48):

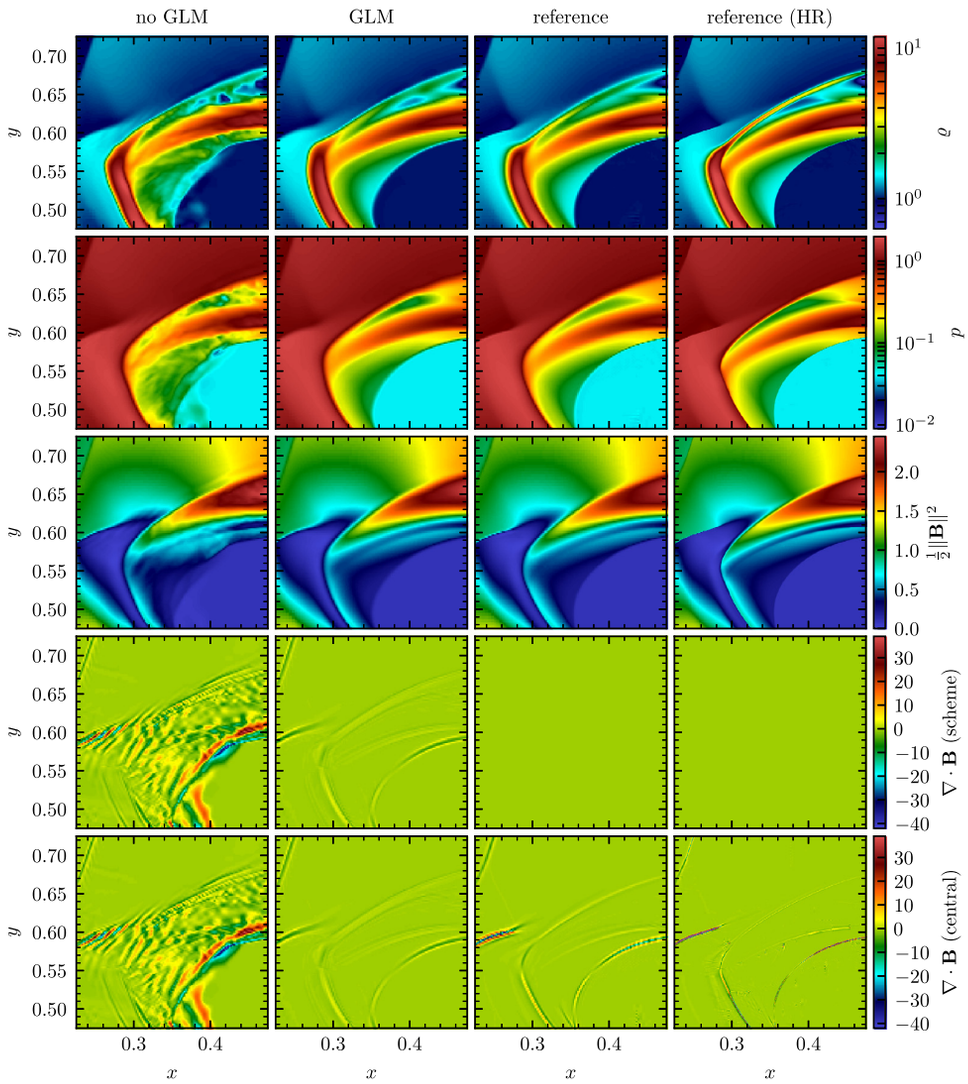

Fig. 7. MHD rotor test: Zoom-in plot of Fig. 6. Left to right: Disabled GLM, enabled GLM, and two reference solution obtained using the unsplit staggered mesh solver implemented in FLASH. The left reference solution is obtained on a similar (adaptive) grid, while the right reference solution (labeled "HR") is obtained on a grid that was 4× finer resolution in each spatial direction. Top to bottom: Gas density ϱ, gas pressure p, magnetic pressure, $\frac{1}{2}\|\boldsymbol{B}\|^2$, and magnetic field divergence (two plots). The upper magnetic field divergence plot shows the magnetic field divergence computed using the method that is used in the corresponding numerical scheme. The lower plot shows the magnetic field divergence computes using central-differencing over the cell-center variables (5.3). We see that in this context our GLM scheme shows a comparable result to the constrained transport scheme.

$$(\nabla \cdot \boldsymbol{B})^{\text{cell}}_{i,j} = \frac{B_{x,i+1,j} - B_{x,i-1,j}}{2\Delta x} + \frac{B_{y,i,j+1} - B_{y,i,j-1}}{2\Delta y} \tag{5.3}$$

We see that for the USM solver, the face-centered magnetic field divergence (5.2) is indeed on the order of machine precision at any time. Hence, the USM solver itself solves the ideal MHD equations always in regions with vanishing magnetic field divergence. However, the cell-centered magnetic field divergence (5.3) is not guaranteed to vanish. While this is not an issue for the scheme itself, it may be relevant for schemes that use the cell-centered values for post-processing the numerical results. In fact, we find that the cell-centered magnetic field divergence is comparable between our scheme with GLM correction and the USM result which highlights the effectiveness of our scheme, cf. the bottom panels in Fig. 7.

5.4. Orszag–Tang MHD vortex

The Orszag–Tang vortex problem [2,54] is a two-dimensional, spatially periodic problem well suited for studies of MHD turbulence. Thus, it has become a classical test for numerical MHD schemes. It includes dissipation of kinetic and magnetic

Table 5
Initial conditions and runtime parameters: Orszag–Tang MHD vortex [2].

Density ϱ	1.0
Pressure p	$1.0/\gamma$
Velocity $\boldsymbol{u}$	$\begin{bmatrix} -\sin(2\pi y) & \sin(2\pi x) & 0 \end{bmatrix}^\intercal$
Mag. field $\boldsymbol{B}$	$\gamma^{-1}\begin{bmatrix} -\sin(2\pi y) & \sin(4\pi x) & 0 \end{bmatrix}^\intercal$

Domain size	$x, y \in [0, 1]$
Boundary conditions	all: periodic
Adaptive refinement on	density, magnetic field
Simulation end time	$t_{\max} = 0.5$
Adiabatic index	$\gamma = 5/3$

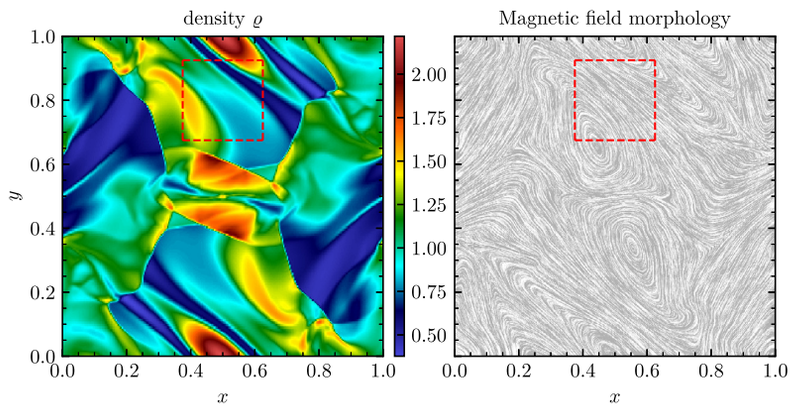

Fig. 8. Orszag–Tang MHD vortex: Adaptive grid resolution up to 256×256. The simulation domain is fully refined at the shown time, $t = 0.5$, for the given refinement criteria. The marked area is shown in Fig. 10.

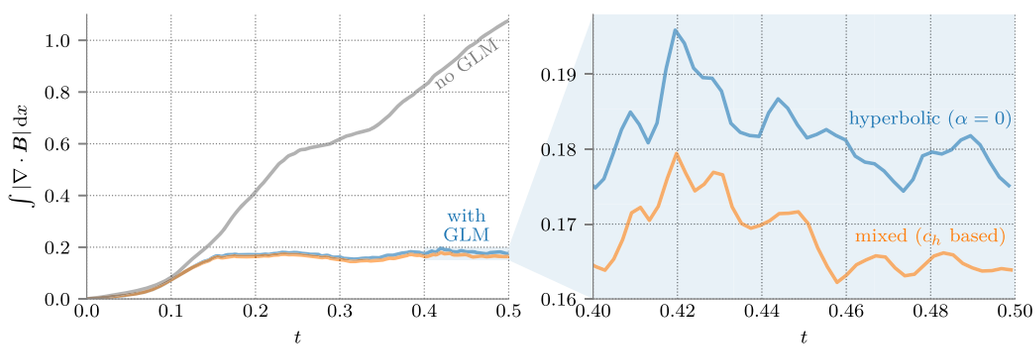

Fig. 9. Orszag–Tang MHD vortex: Evolution of the integrated absolute magnetic field divergence. We test various choices of the damping parameter. The numerical results shown in this section use the c_h based damping.

energy, magnetic reconnection, the formation of high-density jets, dynamic alignment and the emergence and manifestation of small-scale structures. The Orszag–Tang MHD vortex problem starts from non-random, smooth initial data. As the flow evolves it gradually becomes increasingly complex, forming intermediate shocks. Thus, this problem demonstrates the transition from initially smooth data to compressible, supersonic MHD turbulence.

Fig. 8 shows the density of the plasma at $t = 0.5$ given the initial conditions listed in Table 5. As the solution evolves in time, the initial vortex splits into two vortices. Sharp gradients accumulate and the vortex pattern becomes increasingly complex due to highly non-linear interactions between multiple intermediate shock waves traveling at different speeds. We compute the solution using a comparably low resolution of up to 256×256 in order to demonstrate that our numerical scheme is able to resolve sharp features on low to intermediate resolutions. The result compares very well with results given in the literature, *e.g.* [55–57].

In Fig. 9, we plot the temporal evolution of the integrated absolute magnetic field divergence in this test. In contrast to the first two test cases presented in this work, this test is different in that there is no initial magnetic field divergence but the magnetic field divergence is naturally generated by the numerical scheme as the simulation evolves. It is not surprising that the eight-wave ("no GLM") solution shows the largest divergence error. Again, the c_h based damping leads to an efficient divergence treatment.

As before, we see very good agreement between the GLM-KEPES and the USM reference solution (cf. Fig. 10). Again, the divergence errors contaminate the solution notably in the uncorrected case ("no GLM"), leading to unphysical oscillations in both, density and pressure.

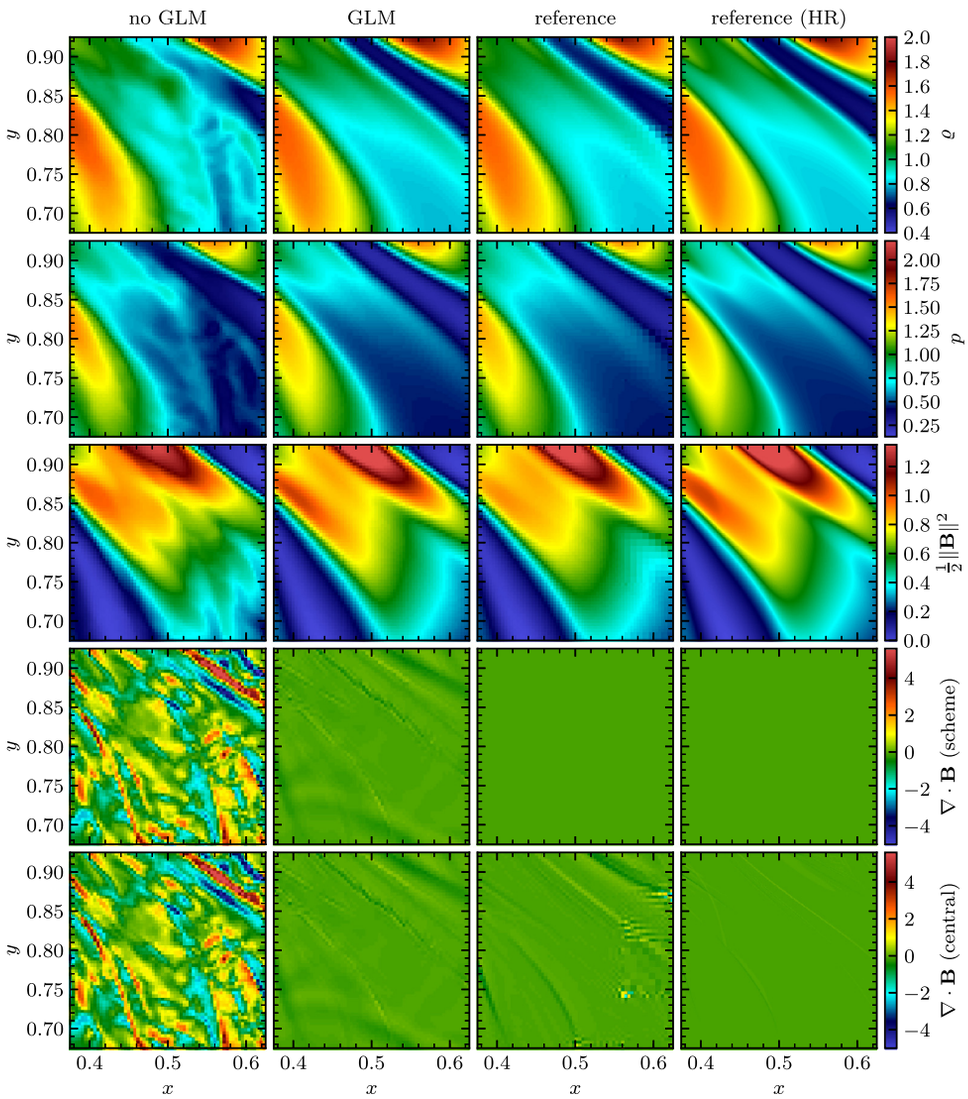

Fig. 10. Orszag–Tang MHD vortex: Zoom-in plot of Fig. 8. Left to right: Disabled GLM, enabled GLM, and two reference solutions obtained using the unsplit staggered mesh solver implemented in FLASH. The left reference solution is obtained on a similar (adaptive) grid, while the right reference solution (labeled "HR") is obtained on a uniform grid that was 4× finer in each spatial direction. Top to bottom: Gas density ϱ, gas pressure p, magnetic pressure, $\frac{1}{2}\|\boldsymbol{B}\|^2$, and magnetic field divergence (two plots). The upper magnetic field divergence plot shows the magnetic field divergence computed using the method that is used in the corresponding numerical scheme. The lower plot shows the magnetic field divergence computes using central-differencing over the cell-center variables (5.3). We see that our GLM scheme, again, shows a similar result to the constrained transport scheme (on the same grid) when looking at the cell-centered magnetic field divergence. Visible artifacts are caused by recent adaptive mesh refinements.

5.5. 2D shock tube test for the effect of the non-conservative terms

This oblique magnetized shock tube was first proposed by Ryu et al. [58]. Tóth used it later to show the failure of the conventional eight-wave scheme to obtain the correct values of the magnetic fields. The formulation he tested used the same non-conservative source term (2.16) in the evolution of the ideal MHD equations [21]. This shock tube is bounded by a left- and a right-going fast shock wave as well as a left- and right-facing slow rarefaction, a right-going slow shock wave, and a contact discontinuity. Thus, it is suitable for testing the correct behavior of a numerical code that is facing a variety of different MHD waves within the same solution. The initial conditions are described in Table 6.

The shock tube is rotated by an angle of $\theta = \tan^{-1}(2) \approx 63°$. Since the magnetic field is initially uniform, the initial conditions trivially fulfill (1.1) for any discretization of the divergence-free condition at any rotation angle. The computational domain is a narrow strip where the top and bottom boundaries are given by "shifted" periodic boundary conditions. We depict our realization of these boundary conditions in Fig. 11. Note that the realization of the shifted boundary conditions

Table 6
Initial conditions and runtime parameters.

	$x < x_{\text{shock}}$	$x > x_{\text{shock}}$
Density ϱ	1.0	
Pressure p	20.0	1.0
Velocity $u_\parallel$	10	-10
$u_\perp, w$	0	
Mag. field $[B_\parallel, B_\perp, B_z]$	$(4\pi)^{-0.5}\,[5 \quad 5 \quad 0]^\intercal$	

Domain size	$x \in [0, 1]\ \ y \in [0, 8/N]$
Boundary conditions	see text
Shock position	$x_{\text{shock}} = 0.5$
Simulation end time	$t_{\text{max}} = 0.08/\sqrt{5}$
Adiabatic index	$\gamma = 5/3$

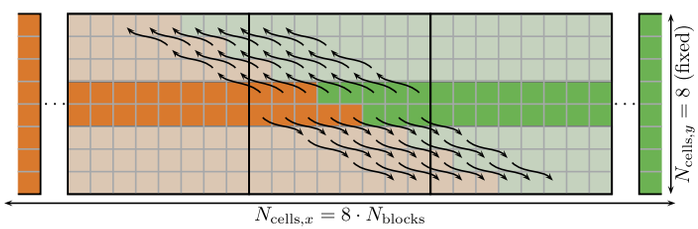

Fig. 11. Special boundary conditions for the 2D shock tube test. The outermost blocks are fixed to the initial conditions indicated by orange (left) and green (right) (color online). The inner blocks use special shifted periodic boundary conditions where the values of the inner computation domain (center unshaded cells) are copied to the surrounding cells (shaded cells) as indicated by the arrows. This can be done without changing the results of the computation due to $(-2, 1)$ translational symmetry [21, Sec. 6.3.2.].

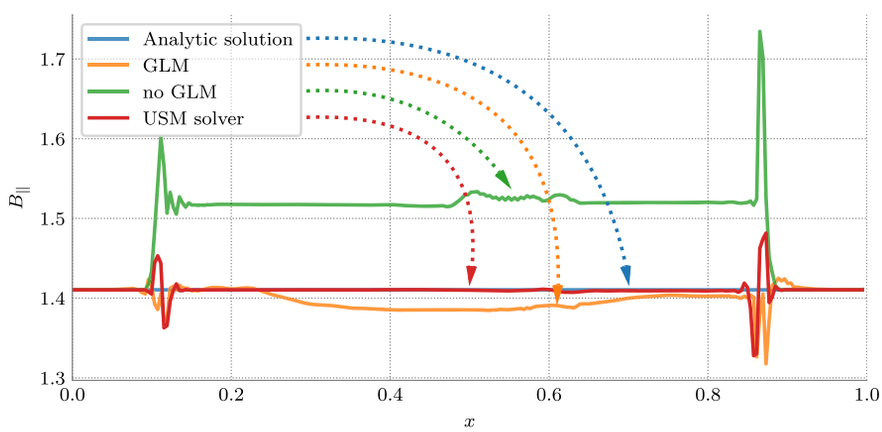

Fig. 12. 2D shock tube test: Plot of the parallel component of the magnetic field at $t = t_{\text{max}}$. As can be seen, the non-conservative terms have a notable influence on the perpendicular magnetic field, $B_\perp$. We see that the GLM correction improves the accuracy of the solution significantly. Furthermore, we note that the reduced form of the non-conservative terms (the "Janhunen" non-conservative terms) gives similar results as the results obtained using the full non-conservative terms as derived in Sec. 2.

is done by copying the cell values after each solver step according to the specific $(-2, 1)$ translational symmetry resulting from the chosen rotation angle. We ensure that the outermost cells still contain the initial conditions by ensuring that the simulation is ended before the shock reaches the boundaries of the computational domain. These specific boundary conditions ensure that effects coming from the boundaries of the computational domains do not influence the flow in our region of interest. Similar to Tóth, we use a uniform grid with $N_{\text{cells},x} = 256$, which translates into 32 blocks in x and 1 block in y direction in `FLASH`'s grid configuration. We compare our numerical results to the analytic solution of this test.

The parallel component of the magnetic field, $B_\parallel = B_1 \cos\theta + B_2 \sin\theta$ should be a constant for all time. Note that, we obtain similar errors to those found by Tóth for an entropy stable eight-wave scheme without GLM correction [21, Fig. 12]. Also, our baseline scheme yields similar results to what he found earlier for his scheme [21, Fig. 11]. If we, however, use our entropy stable GLM treatment at the same time, we see that the errors introduced by the non-conservative terms are reduced significantly (cfm. Fig. 12). Note that the solutions obtained when using the full vs. the reduced non-conservative terms are basically indistinguishable.

We chose this test as Tóth used it specifically to point to a potential weakness of the non-conservative formulation. However, he also points out that this scheme performs well in many other test cases. We see that our entropy-stable scheme which contains both, the eight-wave as well as GLM methods, greatly enhances the solution quality of this specific test case, making the scheme preferable in comparison to a standard eight-wave formulation.

Table 7
Initial conditions: Brio and Wu MHD shock tube [28].

	$x < x_{\text{shock}}$	$x \geq x_{\text{shock}}$
ϱ	1	0.125
p	1	0.1
$\boldsymbol{u}$	**0**	**0**
B_1	0.75	0.75
B_2	1	-1
B_3	0	0

Domain size	$x_{\text{min}} = 0, x_{\text{max}} = 1$
Initial shock position	$x_{\text{shock}} = 0.5$
Boundary conditions	all: periodic
Simulation end time	$t_{\text{max}} = 0.1$
Adiabatic index	$\gamma = 2.0$

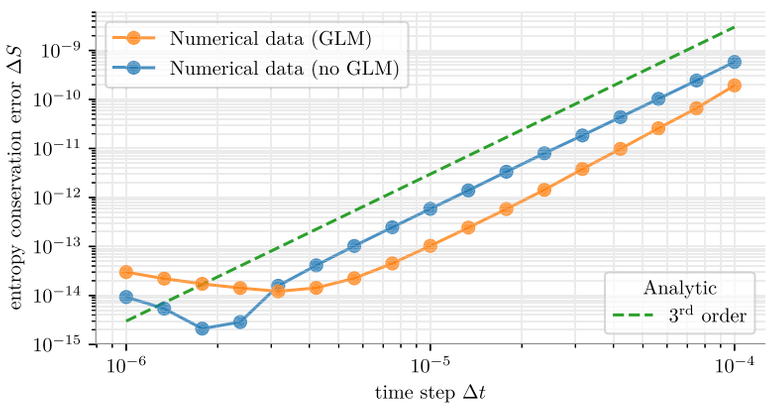

Fig. 13. Entropy conservation test, SSP RK3 time integration.

5.6. Entropy conservation test for the new ideal GLM-MHD system

The mathematical entropy conservation obtained in Sec. 4.2 is in the semi-discrete sense. That is, the discrete entropy is conserved up to the errors introduced by the temporal approximation. Hence, we can use the error in the conservation of the total entropy with respect to the chosen time step size as a measurement for the temporal discretization error. We use a 3rd order accurate SSP RK time integration scheme as mentioned in Sec. 4.6. Hence, we expect the entropy conservation error,

$$\Delta S := |S(t = 0) - S(t = t_{\text{end}})| \,,$$

to behave like

$$\Delta S \propto (\Delta t)^3. \tag{5.4}$$

As our test of choice, we run the two-dimensional version of the Brio and Wu magnetohydrodynamical shock tube problem [28] with a number of different fixed time step lengths Δt. This test includes discontinuities, a magnetic field and is performed in multiple dimensions and starts from discontinuous initial conditions. Hence, it utilizes the full set of features of the entropy aware scheme we derived in this work. We keep the previously used periodic boundary conditions to eliminate any possible influence from the boundaries of the domain and to ensure that we observe a closed system. We construct the two-dimensional initial conditions by rotating the one-dimensional conditions (see Table 7) at a 45° angle. The fluid is initially at rest on either side of the interface.

Note that the entropy conserving scheme cannot describe systems with discontinuities as it cannot add the physically needed dissipation. We limit the end time step to $t_{\text{end}} = 10^{-3}$ when the oscillations have not grown too large as to cause numerical instabilities. Our sole intention is to show that even under high stresses and with active divergence cleaning our scheme is still capable of conserving the thermodynamic entropy correctly.

We ran a number of simulations using logarithmically equally spaced time steps and plot the measured entropy conservation error. In Fig. 13, we see that for very fine temporal resolution (*i.e.* very small time steps) the approximation tapers around 10^{-14}. This is caused by the finite precision of the numerical approximation and expected due to floating point arithmetic issues [59]. We conclude there exists a natural limit for the accuracy of the entropy conservation in our scheme. This test demonstrates that we are able to successfully construct a numerical scheme that is capable of cleaning the divergence in agreement with the second law of thermodynamics.

Table 8
Initial conditions: Modified Sod shock tube test [60, Section 11.5.1].

	$x < x_{\text{shock}}$	$x \geq x_{\text{shock}}$
ϱ	1	0.125
p	1	0.1
u	0.75	0
v	0	0
w	0	0
$\boldsymbol{B}$	**0**	**0**

Domain size	$x_{\text{min}} = 0, x_{\text{max}} = 1$
Initial shock position	$x_{\text{shock}} = 0.5$
Boundary conditions	all: zero-gradient
Simulation end time	$t_{\text{max}} = 0.2$
Adiabatic index	$\gamma = 1.4$

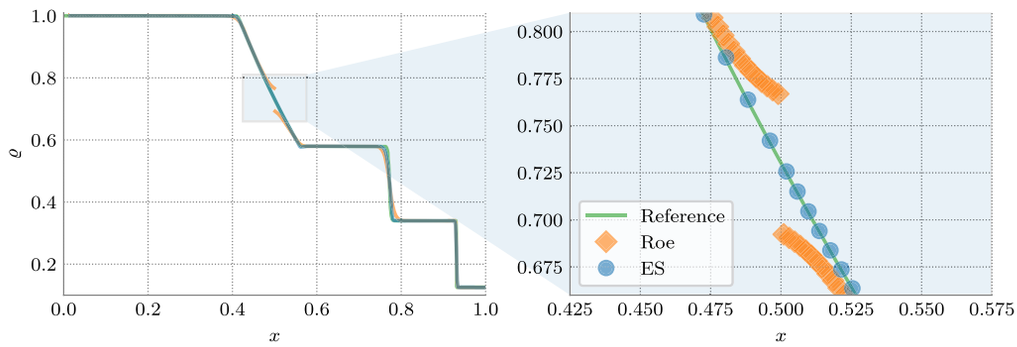

Fig. 14. Entropy consistency test (HD variant): Plot of the fluid density, ϱ, at $t = t_{\text{max}}$. On the right panel we show a zoom-in of the plot on the left. The entropy glitch of the original Roe scheme is apparent whereas there is no inconsistency visible in our numerical scheme.

5.7. Entropy consistency test

In this section, we elaborate on the importance of entropy consistency for the proposed ideal GLM-MHD scheme. Numerical tests suitable for assessing the entropic properties of numerical models have been summarized *e.g.* by Toro [60, Section 11.5]. We first look at the "entropy glitch" test and later amend this test with magnetic fields.

Toro describes a modified variant of Sod's well-known shock tube test [61, Section 3], where he added a constant velocity on the left side of the initial shock. We summarize the initial conditions in Table 8. The given initial conditions result in a solution that consists of a left sonic rarefaction wave, a contact discontinuity, and a right shock wave. This test nicely shows the necessity of entropy consistency, as some widely used schemes – such as the original Roe scheme – fail to numerically solve this test correctly when compared to the exact solution. The numerics can produce an unphysical jump feature in the rarefaction wave, also known as "entropy glitch". It arises in the presence of sonic rarefaction waves if schemes are not constructed with entropy consistency in mind [62]. In Fig. 14, we plot the numerical solution obtained on an adaptive grid of up to 512 cells using an implementation of the original Roe scheme in `FLASH`'s `USM` solver (parameter `RiemannSolver = "Roe"`), our numerical entropy stable scheme (denoted by "ES") and a highly-resolved (2048 cells, uniform grid) reference solution obtained using an LLF scheme. We immediately see that the numerical solution of the original Roe scheme exhibits a discontinuity within the wave. This discontinuity is not only unphysical, it also violates the entropy condition [60, Section 11.4.1]. Our numerical scheme is not affected by this issue and behaves just as expected. Note that we verified the absence of any unphysical discontinuity also for higher and lower resolution. The size of the jump of the entropy glitch reduces for increased resolution but never disappears completely. It is apparent that, using our numerical scheme, the reference solution is matched with a comparably lower adaptive resolution as in Fig. 14. Although the solution obtained using the Roe scheme fully resolves the region around the "entropy glitch", it still fails to obtain the correct physical result.

For assessing entropy consistency in the presence of magnetic fields, we design a new test. It seems an obvious choice to start the design of such a test from a well known MHD shock tube just as the one described by Brio and Wu [28]. We similarly add a constant velocity on the left-hand side where we precompute the velocity of the rarefaction wave in the solution to create a rarefaction wave with a sonic point in this new test case. We summarize the initial conditions proposed for this test in Table 9.

In Fig. 15, we plot the numerical solution. We see that, due to the compound wave in this MHD test, the left rarefaction wave is much smaller in the MHD case. Although clearly present, the entropy glitch could be overlooked with too low resolution and misinterpreted as a dissipative/dispersive effect. As before, we see an unphysical discontinuity in the left rarefaction wave that violates the entropy condition. In contrast, the result obtained using our numerical scheme is free of any entropy violating parts in the solution.

Table 9
Initial conditions: Modified Brio and Wu shock tube test.

	$x < x_{\text{shock}}$	$x \geq x_{\text{shock}}$
ϱ	1	0.125
p	1	0.1
u	1.75	0
v,w	0	0
B_1	0.75	0.75
B_2	1	−1
B_3	0	0

Domain size	$x_{\text{min}} = 0, x_{\text{max}} = 1$
Initial shock position	$x_{\text{shock}} = 0.5$
Boundary conditions	all: zero-gradient
Simulation end time	$t_{\text{max}} = 0.1$
Adiabatic index	$\gamma = 2.0$

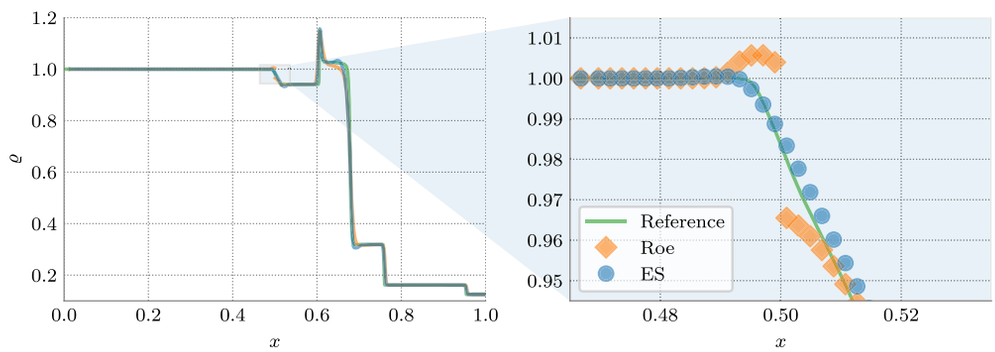

Fig. 15. Entropy consistency test (MHD variant): Plot of the fluid density, ϱ, at $t = t_{\text{max}}$. On the right panel we show a zoom-in of the plot on the left. The entropy glitch of the original Roe scheme is apparent whereas there is no inconsistency visible in our numerical scheme.

6. Conclusion

In this work, we describe a physically motivated mathematical model that is suitable for building numerical schemes for ideal MHD flows. We call our system the "ideal GLM-MHD equations" in agreement with earlier publications. The significance of our modifications is, as shown in this work, that they lead to the first entropy consistent hyperbolic formulation of the ideal MHD equations with effective inbuilt divergence cleaning. One major benefit of this approach is that divergence cleaning is done alongside the hydrodynamical flux computations so no additional communication or globally coupled computations are introduced when implementing our scheme. This underlines its usability for highly-parallelized numerical simulation codes as it does not only ease the process of parallelization but also allows unaffected scaling of the scheme on over dozens of thousands of computing cores.

We carefully investigate the properties of the proposed mathematical model and discuss the implications of, e.g., the new eigenvalues that come from the GLM waves while we explain how our new model converges to already known models in various limits such as vanishing cleaning speed, vanishing magnetic field divergence and altogether vanishing magnetic fields.

For demonstrating the numerical feasibility of our model, we derive a set of magnetic field divergence diminishing entropy conservative and entropy stable fluxes. Note that these can be used to build entropy stable numerical approximations that respect the fundamental laws of thermodynamics by construction. Our decision to build entropy stable numerical fluxes – in contrast to, *e.g.* HLL fluxes, was due to the fact that entropy stability plays a crucial dual role in ensuring both the physical relevance of the simulation results as well as the numerical robustness of the scheme.

We conclude our analysis and derivations with a section presenting numerical results obtained using the new entropy stable solver implementation for MHD flows in multiple spatial dimensions with adaptive mesh refinement. These numerical tests serve to demonstrate the flexibility of the new solver, the utility as well as the rigor of the implemented divergence diminishing formulation. We found that additional damping is not strictly needed when dealing with boundary conditions that allow the divergence errors to be advected out of the computational domain, but found the additionally possible ψ wave damping useful when this is not possible, e.g., due to periodic boundary conditions that do not allow the divergence errors to leave the simulation domain.

Acknowledgements

We thank the anonymous reviewers for their thorough review, insightful comments and suggestions on this work. In particular we appreciate the detailed comments and discussion about Galilean invariance.

Dominik Derigs and Stefanie Walch acknowledge the support of the Bonn-Cologne Graduate School for Physics and Astronomy (BCGS), which is funded through the Excellence Initiative (GSC 260), as well as the Sonderforschungsbereich (SFB) 956 on the "Conditions and impact of star formation". Stefanie Walch thanks the Deutsche Forschungsgemeinschaft (DFG) for funding through the SPP 1573 "The physics of the interstellar medium" and the funding from the European Research Council

via the ERC Starting Grant "The radiative interstellar medium" (RADFEEDBACK, project no. 679852). Gregor Gassner thanks the European Research Council for funding through the ERC Starting Grant "An Exascale aware and Un-crashable Space-Time-Adaptive Discontinuous Spectral Element Solver for Non-Linear Conservation Laws" (Extreme, project no. 71448). The software used in this work was in part developed by the DOE NNSA-ASC OASCR Flash Center at the University of Chicago. This work was partially performed on the Cologne High Efficiency Operating Platform for Sciences (CHEOPS) at the Regionales Rechenzentrum Köln (RRZK). The authors gratefully acknowledge the Gauss Centre for Supercomputing e.V. (www.gauss-centre.eu) for funding this project by providing computing time on the GCS supercomputer SuperMUC at Leibniz Supercomputing Centre (www.lrz.de).

Appendix A. Derivation of the entropy conserving numerical ideal GLM-MHD flux

First, we use the properties of the linear jump operator

$$\llbracket ab \rrbracket = \{\!\{b\}\!\} \llbracket a \rrbracket + \{\!\{a\}\!\} \llbracket b \rrbracket, \qquad \left\llbracket a^2 \right\rrbracket = 2 \{\!\{a\}\!\} \llbracket a \rrbracket,$$

to expand the jump in entropy variables

$$\begin{aligned}
\llbracket \boldsymbol{v} \rrbracket &= \left\llbracket \begin{bmatrix} \frac{\gamma - s}{\gamma - 1} - \beta \|\boldsymbol{u}\|^2 \\ 2\beta u \\ 2\beta v \\ 2\beta w \\ -2\beta \\ 2\beta B_1 \\ 2\beta B_2 \\ 2\beta B_3 \\ 2\beta \psi \end{bmatrix} \right\rrbracket \\
&= \begin{bmatrix} \frac{\llbracket \varrho \rrbracket}{\varrho^{\ln}} + \frac{\llbracket \beta \rrbracket}{\beta^{\ln}(\gamma-1)} - \left(\{\!\{u^2\}\!\} + \{\!\{v^2\}\!\} + \{\!\{w^2\}\!\} \right) \llbracket \beta \rrbracket - 2 \{\!\{\beta\}\!\} \left(\{\!\{u\}\!\} \llbracket u \rrbracket + \{\!\{v\}\!\} \llbracket v \rrbracket + \{\!\{w\}\!\} \llbracket w \rrbracket \right) \\ 2 \{\!\{\beta\}\!\} \llbracket u \rrbracket + 2 \{\!\{u\}\!\} \llbracket \beta \rrbracket \\ 2 \{\!\{\beta\}\!\} \llbracket v \rrbracket + 2 \{\!\{v\}\!\} \llbracket \beta \rrbracket \\ 2 \{\!\{\beta\}\!\} \llbracket w \rrbracket + 2 \{\!\{w\}\!\} \llbracket \beta \rrbracket \\ -2 \llbracket \beta \rrbracket \\ 2 \{\!\{\beta\}\!\} \llbracket B_1 \rrbracket + 2 \{\!\{B_1\}\!\} \llbracket \beta \rrbracket \\ 2 \{\!\{\beta\}\!\} \llbracket B_2 \rrbracket + 2 \{\!\{B_2\}\!\} \llbracket \beta \rrbracket \\ 2 \{\!\{\beta\}\!\} \llbracket B_3 \rrbracket + 2 \{\!\{B_3\}\!\} \llbracket \beta \rrbracket \\ 2 \{\!\{\beta\}\!\} \llbracket \psi \rrbracket + 2 \{\!\{\psi\}\!\} \llbracket \beta \rrbracket \end{bmatrix}. \qquad \text{(A.1)}
\end{aligned}$$

With the known jump in entropy variables, we expand the LHS of (4.41) componentwise to find

$$\begin{aligned}
\llbracket \boldsymbol{v} \rrbracket \cdot \boldsymbol{f}^* = f_1^* \Bigg(& \frac{\llbracket \varrho \rrbracket}{\varrho^{\ln}} + \frac{\llbracket \beta \rrbracket}{\beta^{\ln}(\gamma - 1)} - \left(\left\{\!\!\left\{ u^2 \right\}\!\!\right\} + \left\{\!\!\left\{ v^2 \right\}\!\!\right\} + \left\{\!\!\left\{ w^2 \right\}\!\!\right\} \right) \llbracket \beta \rrbracket \\
& - 2 \{\!\{\beta\}\!\} \left(\{\!\{u\}\!\} \llbracket u \rrbracket + \{\!\{v\}\!\} \llbracket v \rrbracket + \{\!\{w\}\!\} \llbracket w \rrbracket \right) \Bigg) \\
& + f_2^* \left(2 \{\!\{\beta\}\!\} \llbracket u \rrbracket + 2 \{\!\{u\}\!\} \llbracket \beta \rrbracket \right) + f_3^* \left(2 \{\!\{\beta\}\!\} \llbracket v \rrbracket + 2 \{\!\{v\}\!\} \llbracket \beta \rrbracket \right) + f_4^* \left(2 \{\!\{\beta\}\!\} \llbracket w \rrbracket + 2 \{\!\{w\}\!\} \llbracket \beta \rrbracket \right) \\
& + f_5^* \left(-2 \llbracket \beta \rrbracket \right) + f_6^* \left(2 \{\!\{\beta\}\!\} \llbracket B_1 \rrbracket + 2 \{\!\{B_1\}\!\} \llbracket \beta \rrbracket \right) + f_7^* \left(2 \{\!\{\beta\}\!\} \llbracket B_2 \rrbracket + 2 \{\!\{B_2\}\!\} \llbracket \beta \rrbracket \right) + f_8^* \left(2 \{\!\{\beta\}\!\} \llbracket B_3 \rrbracket \right. \\
& \left. + 2 \{\!\{B_3\}\!\} \llbracket \beta \rrbracket \right) + f_9^* \left(2 \{\!\{\beta\}\!\} \llbracket \psi \rrbracket + 2 \{\!\{\psi\}\!\} \llbracket \beta \rrbracket \right), \qquad \text{(A.2)}
\end{aligned}$$

where we introduce the logarithmic mean $(\cdot)^{\ln} = \frac{\llbracket \cdot \rrbracket}{\llbracket \ln(\cdot) \rrbracket}$. A numerically stable procedure to compute the logarithmic mean is described by Ismail and Roe [41, Appendix B]. In the algorithm to compute $(\cdot)^{\ln}$ we chose $\epsilon = 1 \times 10^{-3}$ to increase the accuracy of the entropy conservative approximation to close to machine precision.

Next, we expand the individual components on the RHS of (4.41) into combinations of linear jumps

$$\begin{aligned}
\llbracket \varrho u \rrbracket &= \{\!\{u\}\!\} \llbracket \varrho \rrbracket + \left\{\!\!\left\{ \varrho \right\}\!\!\right\} \llbracket u \rrbracket, \qquad \text{(A.3)} \\
\left\llbracket \beta u \| \boldsymbol{B}^2 \| \right\rrbracket &= \left\llbracket \beta u B_1^2 \right\rrbracket + \left\llbracket \beta u B_2^2 \right\rrbracket + \left\llbracket \beta u B_3^2 \right\rrbracket \\
&= \left\{\!\!\left\{ u B_1^2 \right\}\!\!\right\} \llbracket \beta \rrbracket + \{\!\{\beta\}\!\} \left(\left\{\!\!\left\{ B_1^2 \right\}\!\!\right\} \llbracket u \rrbracket + 2 \{\!\{u\}\!\} \{\!\{B_1\}\!\} \llbracket B_1 \rrbracket \right) \\
&\quad + \left\{\!\!\left\{ u B_2^2 \right\}\!\!\right\} \llbracket \beta \rrbracket + \{\!\{\beta\}\!\} \left(\left\{\!\!\left\{ B_2^2 \right\}\!\!\right\} \llbracket u \rrbracket + 2 \{\!\{u\}\!\} \{\!\{B_2\}\!\} \llbracket B_2 \rrbracket \right)
\end{aligned}$$

$$
\begin{aligned}
&+ \left\{\!\left\{ uB_3^2 \right\}\!\right\} [\![\beta]\!] + \{\!\{\beta\}\!\} \left(\left\{\!\left\{ B_3^2 \right\}\!\right\} [\![u]\!] + 2\,\{\!\{u\}\!\}\,\{\!\{B_3\}\!\}\,[\![B_3]\!] \right) \\
&= [\![\beta]\!] \left(\left\{\!\left\{ uB_1^2 \right\}\!\right\} + \left\{\!\left\{ uB_2^2 \right\}\!\right\} + \left\{\!\left\{ uB_3^2 \right\}\!\right\} \right) \\
&\quad + [\![u]\!] \left(\{\!\{\beta\}\!\} \left\{\!\left\{ B_1^2 \right\}\!\right\} + \{\!\{\beta\}\!\} \left\{\!\left\{ B_2^2 \right\}\!\right\} + \{\!\{\beta\}\!\} \left\{\!\left\{ B_3^2 \right\}\!\right\} \right) \\
&\quad + [\![B_1]\!] \left(2\,\{\!\{\beta\}\!\}\,\{\!\{u\}\!\}\,\{\!\{B_1\}\!\} \right) + [\![B_2]\!] \left(2\,\{\!\{\beta\}\!\}\,\{\!\{u\}\!\}\,\{\!\{B_2\}\!\} \right) + [\![B_3]\!] \left(2\,\{\!\{\beta\}\!\}\,\{\!\{u\}\!\}\,\{\!\{B_3\}\!\} \right), \qquad \text{(A.4)}
\end{aligned}
$$

$$
\begin{aligned}
[\![\beta(\boldsymbol{u}\cdot\boldsymbol{B})]\!] &= [\![\beta u B_1]\!] + [\![\beta v B_2]\!] + [\![\beta w B_3]\!] \\
&= [\![\beta]\!] \left(\{\!\{u B_1\}\!\} + \{\!\{v B_2\}\!\} + \{\!\{w B_3\}\!\} \right) + [\![u]\!]\,\{\!\{\beta\}\!\}\,\{\!\{B_1\}\!\} + [\![v]\!]\,\{\!\{\beta\}\!\}\,\{\!\{B_2\}\!\} + [\![w]\!]\,\{\!\{\beta\}\!\}\,\{\!\{B_3\}\!\} \\
&\quad + [\![B_1]\!]\,\{\!\{\beta\}\!\}\,\{\!\{u\}\!\} + [\![B_2]\!]\,\{\!\{\beta\}\!\}\,\{\!\{v\}\!\} + [\![B_3]\!]\,\{\!\{\beta\}\!\}\,\{\!\{w\}\!\}, \qquad \text{(A.5)}
\end{aligned}
$$

and

$$
\begin{aligned}
[\![\beta B_1 \psi]\!] &= \{\!\{\beta\}\!\}\,[\![B_1\psi]\!] + \{\!\{B_1\psi\}\!\}\,[\![\beta]\!] = \{\!\{\beta\}\!\} \left(\{\!\{B_1\}\!\}\,[\![\psi]\!] + \{\!\{\psi\}\!\}\,[\![B_1]\!] \right) + \{\!\{B_1\psi\}\!\}\,[\![\beta]\!] \\
&= [\![\psi]\!]\,\{\!\{\beta\}\!\}\,\{\!\{B_1\}\!\} + [\![B_1]\!]\,\{\!\{\beta\}\!\}\,\{\!\{\psi\}\!\} + [\![\beta]\!]\,\{\!\{B_1\psi\}\!\}. \qquad \text{(A.6)}
\end{aligned}
$$

After rewriting every term in the discrete entropy conservation equation (4.41) into linear jumps, we obtain the yet unknown components of the entropy conserving ideal GLM-MHD flux function:

$$
\begin{aligned}
&[\![\varrho]\!] : f_1^* \frac{[\![\varrho]\!]}{\varrho^{\ln}} = \{\!\{u\}\!\}\,[\![\varrho]\!] && \text{(A.7a)} \\
&[\![u]\!] : -2f_1^*\,\{\!\{\beta\}\!\}\,\{\!\{u\}\!\}\,[\![u]\!] + 2f_2^*\,\{\!\{\beta\}\!\}\,[\![u]\!] = \left\{\!\left\{ \varrho \right\}\!\right\} [\![u]\!] + \{\!\{\beta\}\!\} \left(\left\{\!\left\{ B_1^2 \right\}\!\right\} + \left\{\!\left\{ B_2^2 \right\}\!\right\} + \left\{\!\left\{ B_3^2 \right\}\!\right\} \right) [\![u]\!] - \\
&\qquad - 2\,\{\!\{\beta\}\!\}\,\{\!\{B_1\}\!\}^2\,[\![u]\!] && \text{(A.7b)} \\
&[\![v]\!] : -2f_1^*\,\{\!\{\beta\}\!\}\,\{\!\{v\}\!\}\,[\![v]\!] + 2f_3^*\,\{\!\{\beta\}\!\}\,[\![v]\!] = -2\,\{\!\{\beta\}\!\}\,\{\!\{B_1\}\!\}\,\{\!\{B_2\}\!\}\,[\![v]\!] && \text{(A.7c)} \\
&[\![w]\!] : -2f_1^*\,\{\!\{\beta\}\!\}\,\{\!\{w\}\!\}\,[\![w]\!] + 2f_4^*\,\{\!\{\beta\}\!\}\,[\![w]\!] = -2\,\{\!\{\beta\}\!\}\,\{\!\{B_1\}\!\}\,\{\!\{B_3\}\!\}\,[\![w]\!] && \text{(A.7d)} \\
&[\![B_1]\!] : 2f_6^*\,\{\!\{\beta\}\!\}\,[\![B_1]\!] = 2\,\{\!\{\beta\}\!\}\,\{\!\{B_1\}\!\}\,\{\!\{u\}\!\}\,[\![B_1]\!] - 2\,\{\!\{\beta\}\!\}\,\{\!\{B_1\}\!\}\,\{\!\{u\}\!\}\,[\![B_1]\!] + 2c_h\,\{\!\{\beta\}\!\}\,\{\!\{\psi\}\!\}\,[\![B_1]\!] \\
&\qquad = 2\,\{\!\{\beta\}\!\}\,c_h\,\{\!\{\psi\}\!\}\,[\![B_1]\!] && \text{(A.7e)} \\
&[\![B_2]\!] : 2f_7^*\,\{\!\{\beta\}\!\}\,[\![B_2]\!] = 2\,\{\!\{\beta\}\!\}\,\{\!\{B_2\}\!\}\,\{\!\{u\}\!\}\,[\![B_2]\!] - 2\,\{\!\{\beta\}\!\}\,\{\!\{B_1\}\!\}\,\{\!\{v\}\!\}\,[\![B_2]\!] && \text{(A.7f)} \\
&[\![B_3]\!] : 2f_8^*\,\{\!\{\beta\}\!\}\,[\![B_3]\!] = 2\,\{\!\{\beta\}\!\}\,\{\!\{B_3\}\!\}\,\{\!\{u\}\!\}\,[\![B_3]\!] - 2\,\{\!\{\beta\}\!\}\,\{\!\{B_1\}\!\}\,\{\!\{w\}\!\}\,[\![B_2]\!] && \text{(A.7g)} \\
&[\![\psi]\!] : 2f_9^*\,\{\!\{\beta\}\!\} = 2c_h\,\{\!\{\beta\}\!\}\,\{\!\{B_1\}\!\} && \text{(A.7h)} \\
&[\![\beta]\!] : \frac{f_1^*}{\beta^{\ln}(\gamma-1)}\,[\![\beta]\!] - f_1^* \left(\left\{\!\left\{ u^2 \right\}\!\right\} + \left\{\!\left\{ v^2 \right\}\!\right\} + \left\{\!\left\{ w^2 \right\}\!\right\} \right) [\![\beta]\!] + 2f_2^*\,\{\!\{u\}\!\}\,[\![\beta]\!] + 2f_3^*\,\{\!\{v\}\!\}\,[\![\beta]\!] \\
&\qquad + 2f_4^*\,\{\!\{w\}\!\}\,[\![\beta]\!] - 2f_5^*\,[\![\beta]\!] + 2f_6^*\,\{\!\{B_1\}\!\}\,[\![\beta]\!] + 2f_7^*\,\{\!\{B_2\}\!\}\,[\![\beta]\!] + 2f_8^*\,\{\!\{B_3\}\!\}\,[\![\beta]\!] + 2f_9^*\,\{\!\{\psi\}\!\}\,[\![\beta]\!] \\
&\qquad = \left(\left\{\!\left\{ uB_1^2 \right\}\!\right\} + \left\{\!\left\{ uB_2^2 \right\}\!\right\} + \left\{\!\left\{ uB_3^2 \right\}\!\right\} \right) [\![\beta]\!] - 2\,\{\!\{B_1\}\!\} \left(\{\!\{uB_1\}\!\} + \{\!\{vB_2\}\!\} + \{\!\{wB_3\}\!\} \right) [\![\beta]\!] \\
&\qquad + 2c_h\,\{\!\{B_1\psi\}\!\}\,[\![\beta]\!] && \text{(A.7i)}
\end{aligned}
$$

Solving (A.7a)–(A.7i) gives the numerical entropy conserving flux function $\boldsymbol{f}^*$:

$$
\begin{aligned}
&f_1^* = \varrho^{\ln}\,\{\!\{u\}\!\} && \text{(A.8a)} \\
&f_2^* = f_1^*\,\{\!\{u\}\!\} - \{\!\{B_1\}\!\}^2 + \frac{\left\{\!\left\{ \varrho \right\}\!\right\}}{2\,\{\!\{\beta\}\!\}} + \frac{1}{2} \left(\left\{\!\left\{ B_1^2 \right\}\!\right\} + \left\{\!\left\{ B_2^2 \right\}\!\right\} + \left\{\!\left\{ B_3^2 \right\}\!\right\} \right) && \text{(A.8b)} \\
&f_3^* = f_1^*\,\{\!\{v\}\!\} - \{\!\{B_1\}\!\}\,\{\!\{B_2\}\!\} && \text{(A.8c)} \\
&f_4^* = f_1^*\,\{\!\{w\}\!\} - \{\!\{B_1\}\!\}\,\{\!\{B_3\}\!\} && \text{(A.8d)} \\
&f_5^* = f_1^* \left[\frac{1}{2(\gamma-1)\beta^{\ln}} - \frac{1}{2} \left(\left\{\!\left\{ u^2 \right\}\!\right\} + \left\{\!\left\{ v^2 \right\}\!\right\} + \left\{\!\left\{ w^2 \right\}\!\right\} \right) \right] + f_2^*\,\{\!\{u\}\!\} + f_3^*\,\{\!\{v\}\!\} + f_4^*\,\{\!\{w\}\!\} \\
&\qquad + f_6^*\,\{\!\{B_1\}\!\} + f_7^*\,\{\!\{B_2\}\!\} + f_8^*\,\{\!\{B_3\}\!\} + f_9^*\,\{\!\{\psi\}\!\} - \frac{1}{2} \left(\left\{\!\left\{ uB_1^2 \right\}\!\right\} + \left\{\!\left\{ uB_2^2 \right\}\!\right\} + \left\{\!\left\{ uB_3^2 \right\}\!\right\} \right) \\
&\qquad + \{\!\{B_1\}\!\} \left(\{\!\{uB_1\}\!\} + \{\!\{vB_2\}\!\} + \{\!\{wB_3\}\!\} \right) - c_h\,\{\!\{B_1\psi\}\!\}. && \text{(A.8e)} \\
&f_6^* = c_h\,\{\!\{\psi\}\!\} && \text{(A.8f)} \\
&f_7^* = \{\!\{u\}\!\}\,\{\!\{B_2\}\!\} - \{\!\{v\}\!\}\,\{\!\{B_1\}\!\} && \text{(A.8g)}
\end{aligned}
$$

$$f_8^* = \{\!\{u\}\!\}\,\{\!\{B_3\}\!\} - \{\!\{w\}\!\}\,\{\!\{B_1\}\!\} \tag{A.8h}$$

$$f_9^* = c_h\,\{\!\{B_1\}\!\} \tag{A.8i}$$

Appendix B. Discrete version of the entropy Jacobian

The entries of the matrix $\boldsymbol{\mathcal{H}}$ are derived step-by-step through the solution of 81 equations in a similar fashion as done in [43] for the unmodified ideal MHD equations (64 equations):

$$[\![\boldsymbol{q}]\!] = \begin{bmatrix}[\![\varrho]\!]\\ [\![\varrho u]\!]\\ [\![\varrho v]\!]\\ [\![\varrho w]\!]\\ [\![E]\!]\\ [\![B_1]\!]\\ [\![B_2]\!]\\ [\![B_3]\!]\\ [\![\psi]\!]\end{bmatrix} \overset{!}{=} \begin{bmatrix} \boldsymbol{\mathcal{H}}_{1,1} & \boldsymbol{\mathcal{H}}_{1,2} & \cdots & \cdots & \cdots & \boldsymbol{\mathcal{H}}_{1,8} & \boldsymbol{\mathcal{H}}_{1,9}\\ \boldsymbol{\mathcal{H}}_{2,1} & \boldsymbol{\mathcal{H}}_{2,2} & \cdots & \cdots & \cdots & \boldsymbol{\mathcal{H}}_{2,8} & \boldsymbol{\mathcal{H}}_{2,9}\\ \vdots & \vdots & \ddots & \ddots & \ddots & \vdots & \vdots\\ \vdots & \vdots & \ddots & \ddots & \ddots & \vdots & \vdots\\ \vdots & \vdots & \ddots & \ddots & \ddots & \vdots & \vdots\\ \boldsymbol{\mathcal{H}}_{8,1} & \boldsymbol{\mathcal{H}}_{8,2} & \cdots & \cdots & \cdots & \boldsymbol{\mathcal{H}}_{8,8} & \boldsymbol{\mathcal{H}}_{9,9}\\ \boldsymbol{\mathcal{H}}_{9,1} & \boldsymbol{\mathcal{H}}_{9,2} & \cdots & \cdots & \cdots & \boldsymbol{\mathcal{H}}_{9,8} & \boldsymbol{\mathcal{H}}_{9,9} \end{bmatrix} \begin{bmatrix}[\![\frac{\gamma-s}{\gamma-1} - \beta\|\boldsymbol{u}\|^2]\!]\\ [\![2\beta u]\!]\\ [\![2\beta v]\!]\\ [\![2\beta w]\!]\\ [\![-2\beta]\!]\\ [\![2\beta B_1]\!]\\ [\![2\beta B_2]\!]\\ [\![2\beta B_3]\!]\\ [\![2\beta\psi]\!]\end{bmatrix} = \boldsymbol{\mathcal{H}}\,[\![\boldsymbol{v}]\!]\,. \tag{B.1}$$

First, we expand the jump in both the conservative and the entropy variables

$$[\![\boldsymbol{q}]\!] = \begin{bmatrix}[\![\varrho]\!]\\ [\![\varrho u]\!]\\ [\![\varrho v]\!]\\ [\![\varrho w]\!]\\ [\![E]\!]\\ [\![B_1]\!]\\ [\![B_2]\!]\\ [\![B_3]\!]\\ [\![\psi]\!]\end{bmatrix} = \begin{bmatrix} [\![\varrho]\!]\\ \{\!\{\varrho\}\!\}\,[\![u]\!] + \{\!\{u\}\!\}\,[\![\varrho]\!]\\ \{\!\{\varrho\}\!\}\,[\![v]\!] + \{\!\{v\}\!\}\,[\![\varrho]\!]\\ \{\!\{\varrho\}\!\}\,[\![w]\!] + \{\!\{w\}\!\}\,[\![\varrho]\!]\\ \left(\frac{1}{2(\gamma-1)\beta^{\ln}} + \frac{1}{2}\overline{\|\boldsymbol{u}\|^2}\right)[\![\varrho]\!] + \{\!\{\varrho\}\!\}\left(\{\!\{u\}\!\}\,[\![u]\!] + \{\!\{v\}\!\}\,[\![v]\!] + \{\!\{w\}\!\}\,[\![w]\!]\right) - \frac{\overline{\{\!\{\varrho\}\!\}}}{2(\gamma-1)\overline{\beta^2}}\,[\![\beta]\!] + \{\!\{B_1\}\!\}\,[\![B_1]\!] + \{\!\{B_2\}\!\}\,[\![B_2]\!] + \{\!\{B_3\}\!\}\,[\![B_3]\!] + \{\!\{\psi\}\!\}\,[\![\psi]\!]\\ [\![B_1]\!]\\ [\![B_2]\!]\\ [\![B_3]\!]\\ [\![\psi]\!] \end{bmatrix}, \tag{B.2}$$

$$[\![\boldsymbol{v}]\!] = \begin{bmatrix}[\![\frac{\gamma-s}{\gamma-1} - \beta\|\boldsymbol{u}\|^2]\!]\\ [\![2\beta u]\!]\\ [\![2\beta v]\!]\\ [\![2\beta w]\!]\\ [\![-2\beta]\!]\\ [\![2\beta B_1]\!]\\ [\![2\beta B_2]\!]\\ [\![2\beta B_3]\!]\\ [\![2\beta\psi]\!]\end{bmatrix} = \begin{bmatrix} \frac{[\![\varrho]\!]}{\varrho^{\ln}} + \frac{[\![\beta]\!]}{\beta^{\ln}(\gamma-1)} - \left(\{\!\{u^2\}\!\} + \{\!\{v^2\}\!\} + \{\!\{w^2\}\!\}\right)[\![\beta]\!] - 2\,\{\!\{\beta\}\!\}\left(\{\!\{u\}\!\}\,[\![u]\!] + \{\!\{v\}\!\}\,[\![v]\!] + \{\!\{w\}\!\}\,[\![w]\!]\right)\\ 2\,\{\!\{\beta\}\!\}\,[\![u]\!] + 2\,\{\!\{u\}\!\}\,[\![\beta]\!]\\ 2\,\{\!\{\beta\}\!\}\,[\![v]\!] + 2\,\{\!\{v\}\!\}\,[\![\beta]\!]\\ 2\,\{\!\{\beta\}\!\}\,[\![w]\!] + 2\,\{\!\{w\}\!\}\,[\![\beta]\!]\\ -2\,[\![\beta]\!]\\ 2\,\{\!\{\beta\}\!\}\,[\![B_1]\!] + 2\,\{\!\{B_1\}\!\}\,[\![\beta]\!]\\ 2\,\{\!\{\beta\}\!\}\,[\![B_2]\!] + 2\,\{\!\{B_2\}\!\}\,[\![\beta]\!]\\ 2\,\{\!\{\beta\}\!\}\,[\![B_3]\!] + 2\,\{\!\{B_3\}\!\}\,[\![\beta]\!]\\ 2\,\{\!\{\beta\}\!\}\,[\![\psi]\!] + 2\,\{\!\{\psi\}\!\}\,[\![\beta]\!] \end{bmatrix}, \tag{B.3}$$

with

$$\overline{\beta^2} = 2\,\{\!\{\beta\}\!\}^2 - \left\{\!\left\{\beta^2\right\}\!\right\}, \quad p^{\ln} = \frac{\varrho^{\ln}}{2\beta^{\ln}}, \quad \text{and} \quad \overline{\|\boldsymbol{u}\|^2} = 2\left(\{\!\{u\}\!\}^2 + \{\!\{v\}\!\}^2 + \{\!\{w\}\!\}^2\right) - \left(\left\{\!\left\{u^2\right\}\!\right\} + \left\{\!\left\{v^2\right\}\!\right\} + \left\{\!\left\{w^2\right\}\!\right\}\right). \tag{B.4}$$

Note that the jump in E contains the specific modifications found in [43] to allow the derivation of a symmetric dissipation matrix.

Appendix C. Discrete eigenvalues of the ideal GLM-MHD system

First, we transform the system into primitive variables as the analysis in conservative variables proved to be highly complicated. This is straightforward because we can swap between variable spaces with the matrix

$$\mathbf{M} = \frac{\partial \boldsymbol{q}}{\partial \boldsymbol{\omega}} = \begin{bmatrix} 1 & 0 & 0 & 0 & 0 & 0 & 0 & 0 & 0 \\ u & \varrho & 0 & 0 & 0 & 0 & 0 & 0 & 0 \\ v & 0 & \varrho & 0 & 0 & 0 & 0 & 0 & 0 \\ w & 0 & 0 & \varrho & 0 & 0 & 0 & 0 & 0 \\ \frac{1}{2}\|\boldsymbol{u}\|^2 & \varrho\, u & \varrho\, v & \varrho\, w & \frac{1}{\gamma-1} & B_1 & B_2 & B_3 & \psi \\ 0 & 0 & 0 & 0 & 0 & 1 & 0 & 0 & 0 \\ 0 & 0 & 0 & 0 & 0 & 0 & 1 & 0 & 0 \\ 0 & 0 & 0 & 0 & 0 & 0 & 0 & 1 & 0 \\ 0 & 0 & 0 & 0 & 0 & 0 & 0 & 0 & 1 \end{bmatrix}, \tag{C.1}$$

and its inverse which can be used to go back to conservative variables

$$\begin{aligned} \mathbf{M}^{-1} &= \frac{\partial \boldsymbol{\omega}}{\partial \boldsymbol{q}} \\ &= \begin{bmatrix} 1 & 0 & 0 & 0 & 0 & 0 & 0 & 0 & 0 \\ -\frac{u}{\varrho} & \frac{1}{\varrho} & 0 & 0 & 0 & 0 & 0 & 0 & 0 \\ -\frac{v}{\varrho} & 0 & \frac{1}{\varrho} & 0 & 0 & 0 & 0 & 0 & 0 \\ -\frac{w}{\varrho} & 0 & 0 & \frac{1}{\varrho} & 0 & 0 & 0 & 0 & 0 \\ \frac{\gamma-1}{2}\|\boldsymbol{u}\|^2 & u\,(1-\gamma) & v\,(1-\gamma) & w\,(1-\gamma) & \gamma-1 & B_1\,(1-\gamma) & B_2\,(1-\gamma) & B_3\,(1-\gamma) & \psi\,(1-\gamma) \\ 0 & 0 & 0 & 0 & 0 & 1 & 0 & 0 & 0 \\ 0 & 0 & 0 & 0 & 0 & 0 & 1 & 0 & 0 \\ 0 & 0 & 0 & 0 & 0 & 0 & 0 & 1 & 0 \\ 0 & 0 & 0 & 0 & 0 & 0 & 0 & 0 & 1 \end{bmatrix}, \end{aligned} \tag{C.2}$$

where $\boldsymbol{\xi}$ is the vector of primitive variables, $\boldsymbol{\xi} := \begin{bmatrix} \varrho & u & v & w & p & B_1 & B_2 & B_3 & \psi \end{bmatrix}^{\mathsf{T}}$.

The equation system

$$\frac{\partial}{\partial t}\boldsymbol{q} + \mathbf{A}_{\boldsymbol{\Upsilon}}\frac{\partial}{\partial x}\boldsymbol{q} = \mathbf{0} \tag{C.3}$$

can now be rewritten as

$$\begin{aligned} \mathbf{M}\frac{\partial}{\partial t}\boldsymbol{\xi} + \mathbf{A}_{\boldsymbol{\Upsilon}}\mathbf{M}\frac{\partial}{\partial x}\boldsymbol{\xi} &= 0, \\ \frac{\partial}{\partial t}\boldsymbol{\xi} + \mathbf{M}^{-1}\mathbf{A}_{\boldsymbol{\Upsilon}}\mathbf{M}\frac{\partial}{\partial x}\boldsymbol{\xi} &= 0, \\ \frac{\partial}{\partial t}\boldsymbol{\xi} + \mathbf{C}\frac{\partial}{\partial x}\boldsymbol{\xi} &= 0. \end{aligned} \tag{C.4}$$

Comparing (C.3) and (C.4) we find that the matrix $\mathbf{A}_{\boldsymbol{\Upsilon}}$ can be transformed to primitive space to obtain the primitive matrix $\mathbf{C} := \mathbf{M}^{-1}\mathbf{A}_{\boldsymbol{\Upsilon}}\mathbf{M}$

$$\mathbf{C} = \begin{bmatrix} u & \varrho & 0 & 0 & 0 & 0 & 0 & 0 & 0 \\ 0 & u & 0 & 0 & \frac{1}{\varrho} & 0 & \frac{B_2}{\varrho} & \frac{B_3}{\varrho} & 0 \\ 0 & 0 & u & 0 & 0 & 0 & -\frac{B_1}{\varrho} & 0 & 0 \\ 0 & 0 & 0 & u & 0 & 0 & 0 & -\frac{B_1}{\varrho} & 0 \\ 0 & \gamma\, p & 0 & 0 & u & 0 & 0 & 0 & 0 \\ 0 & 0 & 0 & 0 & 0 & u & 0 & 0 & c_h \\ 0 & B_2 & -B_1 & 0 & 0 & 0 & u & 0 & 0 \\ 0 & B_3 & 0 & -B_1 & 0 & 0 & 0 & u & 0 \\ 0 & 0 & 0 & 0 & 0 & c_h & 0 & 0 & u \end{bmatrix}. \tag{C.5}$$

The matrices $\mathbf{A}_{\boldsymbol{\Upsilon}}$ and $\mathbf{C}$ are *similar*, *i.e.* they have the same eigenvalues but not necessarily the same eigenvectors.[1]

From

$$\frac{\partial}{\partial t}\boldsymbol{\xi} + \mathbf{C}\frac{\partial}{\partial x}\boldsymbol{\xi} = \frac{\partial}{\partial t}\boldsymbol{\xi} + \begin{bmatrix} u & \varrho & 0 & 0 & 0 & 0 & 0 & 0 & 0 \\ 0 & u & 0 & 0 & \frac{1}{\varrho} & 0 & \frac{B_2}{\varrho} & \frac{B_3}{\varrho} & 0 \\ 0 & 0 & u & 0 & 0 & 0 & -\frac{B_1}{\varrho} & 0 & 0 \\ 0 & 0 & 0 & u & 0 & 0 & 0 & -\frac{B_1}{\varrho} & 0 \\ 0 & \gamma\, p & 0 & 0 & u & 0 & 0 & 0 & 0 \\ 0 & 0 & 0 & 0 & 0 & u & 0 & 0 & c_h \\ 0 & B_2 & -B_1 & 0 & 0 & 0 & u & 0 & 0 \\ 0 & B_3 & 0 & -B_1 & 0 & 0 & 0 & u & 0 \\ 0 & 0 & 0 & 0 & 0 & c_h & 0 & 0 & u \end{bmatrix} \begin{bmatrix} \varrho \\ u \\ v \\ w \\ p \\ B_1 \\ B_2 \\ B_3 \\ \psi \end{bmatrix}_x \tag{C.6}$$

$$= \frac{\partial}{\partial t}\boldsymbol{\xi} + \begin{bmatrix} u(\varrho)_x + \varrho(u)_x \\ u(u)_x + \frac{1}{\varrho}(p)_x + \frac{B_2}{\varrho}(B_2)_x + \frac{B_3}{\varrho}(B_3)_x \\ uv_x - \frac{B_1}{\varrho}(B_2)_x \\ uw_x - \frac{B_1}{\varrho}(B_3)_x \\ \gamma\, p(u)_x + u(p)_x \\ u(B_1)_x + c_h(\psi)_x \\ B_2(u)_x - B_1(v)_x + u(B_2)_x \\ B_3(u)_x - B_1(w)_x + u(B_3)_x \\ c_h(B_1)_x + u(\psi)_x \end{bmatrix} = \mathbf{0}, \tag{C.7}$$

we see that we cannot bring the system into flux form for primitive variables. Hence, we refrain from calling $\mathbf{C}$ the primitive flux Jacobian, since it is not possible to bring the system described by

$$\frac{\partial}{\partial t}\boldsymbol{\xi} + \mathbf{C}\frac{\partial}{\partial x}\boldsymbol{\xi} = \mathbf{0}, \tag{C.8}$$

into flux form for primitive variables. Therefore, unlike the matrix $\mathbf{A}$ in flux form, the coefficient matrix $\mathbf{C}$ in primitive variable form is not the flux Jacobian of *any* flux function $\boldsymbol{f}(\boldsymbol{\xi})$. We can easily see that, as the entries on the diagonal of $\mathbf{C}$ are all equal to u, and they are the only ones depending on u, the matrix $\mathbf{C}$ describes a Galilean invariant scheme [26, Section 3], as expected.

In the next step, we make the discrete ansatz, where we discretize the update of the primitive variables in the spatial dimension like

$$-\frac{\partial}{\partial t}\boldsymbol{\xi} = \mathbf{C}\frac{\partial}{\partial x}\boldsymbol{\xi} \tag{C.9}$$

$$= \int_L^R \left(\mathbf{C}\frac{\partial}{\partial x}\boldsymbol{\xi}\right) \mathrm{d}x \tag{C.10}$$

$$\approx \frac{\Delta x}{2} \sum_{k=\{\mathrm{L},\mathrm{R}\}} \left(\mathbf{C}\frac{\partial}{\partial x}\boldsymbol{\xi}\right)_k \tag{C.11}$$

[1] The eigenvectors are transformed according to the base changing matrix $\mathbf{M}$.

$$= \frac{\Delta x}{2}\left(\mathbf{C}_{\mathrm{L}}\frac{\boldsymbol{\xi}_{\mathrm{R}}-\boldsymbol{\xi}_{\mathrm{L}}}{\Delta x}+\mathbf{C}_{\mathrm{R}}\frac{\boldsymbol{\xi}_{\mathrm{R}}-\boldsymbol{\xi}_{\mathrm{L}}}{\Delta x}\right) \tag{C.12}$$

$$= \frac{1}{2}(\mathbf{C}_{\mathrm{L}}+\mathbf{C}_{\mathrm{R}})(\boldsymbol{\xi}_{\mathrm{R}}-\boldsymbol{\omega}_{\mathrm{L}}) \tag{C.13}$$

$$= \{\!\{\mathbf{C}\}\!\}\,[\![\boldsymbol{\omega}]\!]\,, \tag{C.14}$$

where we used the trapezoidal rule for approximating the integral on the RHS of (C.10) using the left and right states. We immediately see that the discretized version of the coefficient matrix, $\mathbf{C}$, is the continuous coefficient matrix, $\mathbf{C}$, arithmetically averaged in each entry, $\hat{\mathbf{C}} := \{\!\{\mathbf{C}\}\!\} = \frac{1}{2}(\mathbf{C}_{\mathrm{L}}+\mathbf{C}_{\mathrm{R}})$:

$$\hat{\mathbf{C}} = \begin{bmatrix}
\{\!\{u\}\!\} & \left\{\!\left\{\varrho\right\}\!\right\} & 0 & 0 & 0 & 0 & 0 & 0 & 0 \\
0 & \{\!\{u\}\!\} & 0 & 0 & \left\{\!\left\{\varrho^{-1}\right\}\!\right\} & 0 & \left\{\!\left\{\frac{B_2}{\varrho}\right\}\!\right\} & \left\{\!\left\{\frac{B_3}{\varrho}\right\}\!\right\} & 0 \\
0 & 0 & \{\!\{u\}\!\} & 0 & 0 & 0 & -\left\{\!\left\{\frac{B_1}{\varrho}\right\}\!\right\} & 0 & 0 \\
0 & 0 & 0 & \{\!\{u\}\!\} & 0 & 0 & 0 & -\left\{\!\left\{\frac{B_1}{\varrho}\right\}\!\right\} & 0 \\
0 & \gamma\,\{\!\{p\}\!\} & 0 & 0 & \{\!\{u\}\!\} & 0 & 0 & 0 & 0 \\
0 & 0 & 0 & 0 & 0 & \{\!\{u\}\!\} & 0 & 0 & \{\!\{c_h\}\!\} \\
0 & \{\!\{B_2\}\!\} & -\{\!\{B_1\}\!\} & 0 & 0 & 0 & \{\!\{u\}\!\} & 0 & 0 \\
0 & \{\!\{B_3\}\!\} & 0 & -\{\!\{B_1\}\!\} & 0 & 0 & 0 & \{\!\{u\}\!\} & 0 \\
0 & 0 & 0 & 0 & 0 & \{\!\{c_h\}\!\} & 0 & 0 & \{\!\{u\}\!\}
\end{bmatrix}. \tag{C.15}$$

The eigenvalues of $\hat{\mathbf{C}}$ are:

$$\hat{\boldsymbol{\lambda}} = \begin{bmatrix}
\{\!\{u\}\!\} - \frac{\sqrt{2\sqrt{\{\!\{B_1\}\!\}\left\{\!\left\{\frac{B_1}{\varrho}\right\}\!\right\}\{\!\{p\}\!\}\{\!\{\varrho^{-1}\}\!\}\gamma+\{\!\{p\}\!\}\{\!\{\varrho^{-1}\}\!\}\gamma+\{\!\{B_3\}\!\}\left\{\!\left\{\frac{B_3}{\varrho}\right\}\!\right\}+\{\!\{B_2\}\!\}\left\{\!\left\{\frac{B_2}{\varrho}\right\}\!\right\}+\{\!\{B_1\}\!\}\left\{\!\left\{\frac{B_1}{\varrho}\right\}\!\right\}}+\sqrt{-2\sqrt{\{\!\{B_1\}\!\}\left\{\!\left\{\frac{B_1}{\varrho}\right\}\!\right\}\{\!\{p\}\!\}\{\!\{\varrho^{-1}\}\!\}\gamma+\{\!\{p\}\!\}\{\!\{\varrho^{-1}\}\!\}\gamma+\{\!\{B_3\}\!\}\left\{\!\left\{\frac{B_3}{\varrho}\right\}\!\right\}+\{\!\{B_2\}\!\}\left\{\!\left\{\frac{B_2}{\varrho}\right\}\!\right\}+\{\!\{B_1\}\!\}\left\{\!\left\{\frac{B_1}{\varrho}\right\}\!\right\}}}{2} \\
\{\!\{u\}\!\} - \frac{\sqrt{2\sqrt{\{\!\{B_1\}\!\}\left\{\!\left\{\frac{B_1}{\varrho}\right\}\!\right\}\{\!\{p\}\!\}\{\!\{\varrho^{-1}\}\!\}\gamma+\{\!\{p\}\!\}\{\!\{\varrho^{-1}\}\!\}\gamma+\{\!\{B_3\}\!\}\left\{\!\left\{\frac{B_3}{\varrho}\right\}\!\right\}+\{\!\{B_2\}\!\}\left\{\!\left\{\frac{B_2}{\varrho}\right\}\!\right\}+\{\!\{B_1\}\!\}\left\{\!\left\{\frac{B_1}{\varrho}\right\}\!\right\}}-\sqrt{-2\sqrt{\{\!\{B_1\}\!\}\left\{\!\left\{\frac{B_1}{\varrho}\right\}\!\right\}\{\!\{p\}\!\}\{\!\{\varrho^{-1}\}\!\}\gamma+\{\!\{p\}\!\}\{\!\{\varrho^{-1}\}\!\}\gamma+\{\!\{B_3\}\!\}\left\{\!\left\{\frac{B_3}{\varrho}\right\}\!\right\}+\{\!\{B_2\}\!\}\left\{\!\left\{\frac{B_2}{\varrho}\right\}\!\right\}+\{\!\{B_1\}\!\}\left\{\!\left\{\frac{B_1}{\varrho}\right\}\!\right\}}}{2} \\
\{\!\{u\}\!\} + \frac{\sqrt{2\sqrt{\{\!\{B_1\}\!\}\left\{\!\left\{\frac{B_1}{\varrho}\right\}\!\right\}\{\!\{p\}\!\}\{\!\{\varrho^{-1}\}\!\}\gamma+\{\!\{p\}\!\}\{\!\{\varrho^{-1}\}\!\}\gamma+\{\!\{B_3\}\!\}\left\{\!\left\{\frac{B_3}{\varrho}\right\}\!\right\}+\{\!\{B_2\}\!\}\left\{\!\left\{\frac{B_2}{\varrho}\right\}\!\right\}+\{\!\{B_1\}\!\}\left\{\!\left\{\frac{B_1}{\varrho}\right\}\!\right\}}-\sqrt{-2\sqrt{\{\!\{B_1\}\!\}\left\{\!\left\{\frac{B_1}{\varrho}\right\}\!\right\}\{\!\{p\}\!\}\{\!\{\varrho^{-1}\}\!\}\gamma+\{\!\{p\}\!\}\{\!\{\varrho^{-1}\}\!\}\gamma+\{\!\{B_3\}\!\}\left\{\!\left\{\frac{B_3}{\varrho}\right\}\!\right\}+\{\!\{B_2\}\!\}\left\{\!\left\{\frac{B_2}{\varrho}\right\}\!\right\}+\{\!\{B_1\}\!\}\left\{\!\left\{\frac{B_1}{\varrho}\right\}\!\right\}}}{2} \\
\{\!\{u\}\!\} + \frac{\sqrt{2\sqrt{\{\!\{B_1\}\!\}\left\{\!\left\{\frac{B_1}{\varrho}\right\}\!\right\}\{\!\{p\}\!\}\{\!\{\varrho^{-1}\}\!\}\gamma+\{\!\{p\}\!\}\{\!\{\varrho^{-1}\}\!\}\gamma+\{\!\{B_3\}\!\}\left\{\!\left\{\frac{B_3}{\varrho}\right\}\!\right\}+\{\!\{B_2\}\!\}\left\{\!\left\{\frac{B_2}{\varrho}\right\}\!\right\}+\{\!\{B_1\}\!\}\left\{\!\left\{\frac{B_1}{\varrho}\right\}\!\right\}}+\sqrt{-2\sqrt{\{\!\{B_1\}\!\}\left\{\!\left\{\frac{B_1}{\varrho}\right\}\!\right\}\{\!\{p\}\!\}\{\!\{\varrho^{-1}\}\!\}\gamma+\{\!\{p\}\!\}\{\!\{\varrho^{-1}\}\!\}\gamma+\{\!\{B_3\}\!\}\left\{\!\left\{\frac{B_3}{\varrho}\right\}\!\right\}+\{\!\{B_2\}\!\}\left\{\!\left\{\frac{B_2}{\varrho}\right\}\!\right\}+\{\!\{B_1\}\!\}\left\{\!\left\{\frac{B_1}{\varrho}\right\}\!\right\}}}{2} \\
\{\!\{u\}\!\} - \sqrt{\{\!\{B_1\}\!\}\left\{\!\left\{\frac{B_1}{\varrho}\right\}\!\right\}} \\
\{\!\{u\}\!\} + \sqrt{\{\!\{B_1\}\!\}\left\{\!\left\{\frac{B_1}{\varrho}\right\}\!\right\}} \\
\{\!\{u\}\!\} - \{\!\{c_h\}\!\} \\
\{\!\{u\}\!\} + \{\!\{c_h\}\!\} \\
\{\!\{u\}\!\}
\end{bmatrix} \tag{C.16}$$

After many manipulations, we find a greatly simplified form of the discrete eigenvalues using the discrete wave speeds

$$\hat{c}_{\mathrm{a}} = |\hat{b}_1|, \qquad \hat{c}_{\mathrm{f,s}} = \frac{1}{2}\left(\sqrt{\hat{a}^2+\hat{b}^2+2\sqrt{\hat{a}^2\hat{b}_1^2}} \pm \sqrt{\hat{a}^2+\hat{b}^2-2\sqrt{\hat{a}^2\hat{b}_1^2}}\right), \tag{C.17}$$

with the special discrete averages

$$\hat{\boldsymbol{b}}^2 = \{\!\{\boldsymbol{B}\}\!\}\cdot\left\{\!\left\{\frac{\boldsymbol{B}}{\varrho}\right\}\!\right\}, \quad \hat{a}^2 = \gamma\,\{\!\{p\}\!\}\left\{\!\left\{\varrho^{-1}\right\}\!\right\}, \quad \hat{b}^2 = \hat{b}_1^2+\hat{b}_2^2+\hat{b}_3^2. \tag{C.18}$$

In (C.17), the plus sign corresponds to the fast magnetoacoustic speed, c_{f}, and the minus sign corresponds to the slow magnetoacoustic speed, c_{s}.

The simplified eigenvalues of the ideal GLM-MHD system are:

$$\hat{\boldsymbol{\lambda}} = \begin{bmatrix} \hat{\lambda}_{+\mathrm{f}} \\ \hat{\lambda}_{+\mathrm{a}} \\ \hat{\lambda}_{+\mathrm{s}} \\ \hat{\lambda}_{+\psi} \\ \hat{\lambda}_{\mathrm{E}} \\ \hat{\lambda}_{-\psi} \\ \hat{\lambda}_{-\mathrm{s}} \\ \hat{\lambda}_{-\mathrm{a}} \\ \hat{\lambda}_{-\mathrm{f}} \end{bmatrix} = \begin{bmatrix} \{\!\{u\}\!\} + \hat{c}_{\mathrm{f}} \\ \{\!\{u\}\!\} + \hat{c}_{\mathrm{a}} \\ \{\!\{u\}\!\} + \hat{c}_{\mathrm{s}} \\ \{\!\{u\}\!\} + \{\!\{c_h\}\!\} \\ \{\!\{u\}\!\} \\ \{\!\{u\}\!\} - \{\!\{c_h\}\!\} \\ \{\!\{u\}\!\} - \hat{c}_{\mathrm{s}} \\ \{\!\{u\}\!\} - \hat{c}_{\mathrm{a}} \\ \{\!\{u\}\!\} - \hat{c}_{\mathrm{f}} \end{bmatrix} \begin{matrix} \text{right going fast magnetoacoustic wave} \\ \text{right going Alfvén wave} \\ \text{right going slow magnetoacoustic wave} \\ \text{right going GLM wave} \\ \text{entropy wave} \\ \text{left going GLM wave} \\ \text{left going slow magnetoacoustic wave} \\ \text{left going Alfvén wave} \\ \text{left going fast magnetoacoustic wave} \end{matrix} \tag{C.19}$$

Appendix D. Eigenstructure

We outline the steps to obtain the eigenstructure of the flux Jacobian for the new ideal GLM-MHD system. For this one-dimensional analysis we forgo the addition of the matrix superscript $(\cdot)^x$ for the sake of convenience. We have already computed the flux Jacobian, $\mathbf{A}^x_{\boldsymbol{\Upsilon}}$, (3.27) for the new system. For an entropy stable numerical flux with a matrix dissipation term we require a relationship between the entropy Jacobian, $\mathbf{H}$, and the right eigenvectors, $\mathbf{R}$.

The eigendecomposition of the matrix $\mathbf{A}_{\boldsymbol{\Upsilon}}$ supports nine propagating plane-wave solutions:

- two fast magnetoacoustic waves ($\pm$f),
- two slow magnetoacoustic waves ($\pm$s),
- two Alfvén waves ($\pm$a),
- an entropy wave (E),
- two GLM waves ($\pm\psi$).

It is known that the right eigenvectors may exhibit several forms of degeneracy that are carefully described by Roe and Balsara [63]. We follow the same rescaling procedure of Roe and Balsara to improve the numerical behavior of the fast/slow magnetoacoustic eigenvectors.

To compute the eigenvectors it is more convenient to work with primitive variables, $\boldsymbol{\omega}$, and then convert back to conservative space as noted in Appendix C. Once we know the eigenvectors in primitive space, $\mathbf{R}_{\mathbf{C}}$ we return to conservative space by

$$\mathbf{R}\Lambda\mathbf{R}^{-1} = \mathbf{A}_{\mathbf{P}} = \mathbf{M}\mathbf{C}\mathbf{M}^{-1} = (\mathbf{M}\mathbf{R}_{\mathbf{C}})\boldsymbol{\Lambda}(\mathbf{M}\mathbf{R}_{\mathbf{C}})^{-1}, \tag{D.1}$$

with the eigenvalue matrix Λ. The matrix of right eigenvectors is given by

$$\mathbf{R} := \mathbf{M}\mathbf{R}_{\mathbf{C}} = \left[\boldsymbol{r}_{+\mathrm{f}} \,|\, \boldsymbol{r}_{+\mathrm{a}} \,|\, \boldsymbol{r}_{+\mathrm{s}} \,|\, \boldsymbol{r}_{+\psi} \,|\, \boldsymbol{r}_{\mathrm{E}} \,|\, \boldsymbol{r}_{-\psi} \,|\, \boldsymbol{r}_{-\mathrm{s}} \,|\, \boldsymbol{r}_{-\mathrm{a}} \,|\, \boldsymbol{r}_{-\mathrm{f}}\right], \tag{D.2}$$

with the eigenvectors $\boldsymbol{r}$:

GLM Waves: $\lambda_{\pm\psi} = u \pm c_h$, Entropy Wave: $\lambda_{\mathrm{E}} = u$, and Alfvén Waves: $\lambda_{\pm\mathrm{a}} = u \pm c_{\mathrm{a}}$

$$\boldsymbol{r}_{\pm\psi} = \begin{bmatrix} 0 \\ 0 \\ 0 \\ 0 \\ B_1 \pm \psi \\ 1 \\ 0 \\ 0 \\ \pm 1 \end{bmatrix}, \quad \boldsymbol{r}_{\mathrm{E}} = \begin{bmatrix} 1 \\ u \\ v \\ w \\ \frac{\|\boldsymbol{u}\|^2}{2} \\ 0 \\ 0 \\ 0 \\ 0 \end{bmatrix}, \quad \boldsymbol{r}_{\pm\mathrm{a}} = \begin{bmatrix} 0 \\ 0 \\ \pm\varrho^{\frac{3}{2}}\chi_3 \\ \mp\varrho^{\frac{3}{2}}\chi_2 \\ \mp\varrho^{\frac{3}{2}}(\chi_2 w - \chi_3 v) \\ 0 \\ -\varrho\chi_3 \\ \varrho\chi_2 \\ 0 \end{bmatrix}, \tag{D.3}$$

Magnetoacoustic Waves: $\lambda_{\pm f,\pm s} = u \pm c_{f,s}$

$$\boldsymbol{r}_{\pm f} = \begin{bmatrix} \alpha_f \varrho \\ \alpha_f \varrho (u \pm c_f) \\ \varrho \left(\alpha_f v \mp \alpha_s c_s \chi_2 \sigma(b_1)\right) \\ \varrho \left(\alpha_f w \mp \alpha_s c_s \chi_3 \sigma(b_1)\right) \\ \Psi_{\pm f} \\ 0 \\ \alpha_s a \chi_2 \sqrt{\varrho} \\ \alpha_s a \chi_3 \sqrt{\varrho} \\ 0 \end{bmatrix}, \qquad \boldsymbol{r}_{\pm s} = \begin{bmatrix} \alpha_s \varrho \\ \alpha_s \varrho (u \pm c_s) \\ \varrho \left(\alpha_s v \pm \alpha_f c_f \chi_2 \sigma(b_1)\right) \\ \varrho \left(\alpha_s w \pm \alpha_f c_f \chi_3 \sigma(b_1)\right) \\ \Psi_{\pm s} \\ 0 \\ -\alpha_f a \chi_2 \sqrt{\varrho} \\ -\alpha_f a \chi_3 \sqrt{\varrho} \\ 0 \end{bmatrix}, \tag{D.4}$$

where we introduced several convenience variables

$$\Psi_{\pm s} = \frac{\alpha_s \varrho \|\boldsymbol{u}\|^2}{2} - a \alpha_f \varrho b_\perp + \frac{\alpha_s \varrho a^2}{\gamma - 1} \pm \alpha_s c_s \varrho u \pm \alpha_f c_f \varrho \sigma(b_1)(v \chi_2 + w \chi_3), \quad b^2 = b_1^2 + b_2^2 + b_3^2,$$

$$\Psi_{\pm f} = \frac{\alpha_f \varrho \|\boldsymbol{u}\|^2}{2} + a \alpha_s \varrho b_\perp + \frac{\alpha_f \varrho a^2}{\gamma - 1} \pm \alpha_f c_f \varrho u \mp \alpha_s c_s \varrho \sigma(b_1)(v \chi_2 + w \chi_3), \quad b_\perp^2 = b_2^2 + b_3^2,$$

$$c_a^2 = b_1^2, \quad c_{f,s}^2 = \frac{1}{2}\left((a^2 + b^2) \pm \sqrt{(a^2 + b^2)^2 - 4a^2 b_1^2}\right), \quad a^2 = \gamma \frac{1}{2\beta}, \quad \boldsymbol{b}^2 = \frac{\boldsymbol{B}^2}{\varrho},$$

$$\alpha_f^2 = \frac{a^2 - c_s^2}{c_f^2 - c_s^2}, \quad \alpha_s^2 = \frac{c_f^2 - a^2}{c_f^2 - c_s^2}, \quad \chi_{1,2,3} = \frac{b_{1,2,3}}{b_\perp}, \quad \sigma(\omega) = \begin{cases} +1 & \text{if } \omega \geq 0, \\ -1 & \text{otherwise} \end{cases}.$$

Appendix E. Derivation of the total energy equation

The total energy equation (2.15) is obtained as described by (2.14):

$$\frac{\partial E}{\partial t} = \frac{\partial}{\partial t}\left(\frac{1}{2}\varrho \|\boldsymbol{u}\|^2 + \epsilon + \frac{1}{2}\|\boldsymbol{B}\|^2\right). \tag{E.1}$$

For now, we compute the contributions of the momentum and induction equation intentionally without the non-conservative terms to avoid confusion:

1. Kinetic energy *without* non-conservative term on the momentum equation

$$\begin{aligned} \frac{\partial}{\partial t}\left(\frac{1}{2}\varrho \|\boldsymbol{u}\|^2\right) &= \frac{\partial}{\partial t}\left(\frac{1}{2}\frac{(\varrho u)^2}{\varrho} + \frac{1}{2}\frac{(\varrho v)^2}{\varrho} + \frac{1}{2}\frac{(\varrho w)^2}{\varrho}\right) \\ &= u(\varrho u)_t + v(\varrho v)_t + w(\varrho w)_t - \frac{1}{2}\|\boldsymbol{u}\|^2(\varrho)_t \\ &= \underbrace{-\frac{1}{2}u^2\left(3\varrho(u)_x + u(\varrho)_x\right)}_{-\frac{1}{2}(\varrho u^2)_x} - u(p)_x - \frac{1}{2}u\left(-(B_1)_x^2 + (B_2)_x^2 + (B_3)_x^2\right) \\ &\quad \underbrace{-\frac{1}{2}\left(2\varrho u v(v)_x + \varrho v^2(u)_x + (\varrho)_x u v^2\right)}_{-\frac{1}{2}(\varrho u v)_x} \underbrace{-\frac{1}{2}\left(2\varrho u w(w)_x + \varrho w^2(u)_x + (\varrho)_x u w^2\right)}_{-\frac{1}{2}(\varrho u w)_x} \\ &\quad + \underbrace{v B_1(B_2)_x + v(B_1)_x B_2}_{v(B_1 B_2)_x} + \underbrace{w B_1(B_2)_x + w(B_1)_x B_2}_{w(B_1 B_3)_x} \\ &= -\left\{u\left(\frac{1}{2}\varrho \|\boldsymbol{u}\|^2\right)\right\}_x - u(p)_x - \frac{1}{2}u\left(-(B_1)_x^2 + (B_2)_x^2 + (B_3)_x^2\right) \\ &\quad + v(B_1 B_2)_x + w(B_1 B_3)_x \end{aligned} \tag{E.2}$$

2. Internal energy

$$\frac{\partial}{\partial t}\epsilon = \frac{1}{\gamma-1}\frac{\partial p}{\partial t} = \frac{-1}{\gamma-1}\left(u(p)_x + \gamma p(u)_x\right) \tag{E.3}$$

3. Magnetic energy *without* non-conservative term on the induction equation

$$\begin{aligned}\frac{\partial}{\partial t}\left(\frac{1}{2}\|\boldsymbol{B}\|^2\right) &= \boldsymbol{B}\cdot\left(\frac{\partial \boldsymbol{B}}{\partial t}\right) = \begin{bmatrix}B_1\\B_2\\B_3\end{bmatrix}\cdot\left(-\frac{\partial}{\partial x}\begin{bmatrix}0\\uB_2 - vB_1\\uB_3 - wB_1\end{bmatrix}\right)\\ &= -B_2(uB_2)_x + B_2(vB_1)_x - B_3(uB_3)_x + B_3(wB_1)_x\end{aligned} \tag{E.4}$$

Summing them all up, we obtain (we color code the individual contributions for the sake of readability)

$$\frac{\partial}{\partial t}\left(\frac{1}{2}\varrho\|\boldsymbol{u}\|^2\right) + \frac{\partial \epsilon}{\partial t} + \frac{\partial}{\partial t}\left(\frac{1}{2}\|\boldsymbol{B}\|^2\right) \tag{E.5}$$

$$\begin{aligned}&= -\left\{u\left(\frac{1}{2}\varrho\|\boldsymbol{u}\|^2\right)\right\}_x - u(p)_x - \frac{1}{2}u\left(-(B_1)_x^2 + (B_2)_x^2 + (B_3)_x^2\right) + v(B_1B_2)_x + w(B_1B_3)_x\\ &\quad - \frac{1}{\gamma-1}\left(u(p)_x + \gamma p(u)_x\right) - B_2(uB_2)_x + B_2(vB_1)_x - B_3(uB_3)_x + B_3(wB_1)_x\end{aligned} \tag{E.6}$$

$$\begin{aligned}&= -\left\{u\left(\frac{1}{2}\varrho\|\boldsymbol{u}\|^2\right)\right\}_x \underbrace{-\frac{u(p)_x + \gamma p(u)_x + \gamma u(p)_x - u(p)_x}{\gamma-1}}_{-\frac{\gamma}{\gamma-1}(up)_x}\\ &\quad + uB_1(B_1)_x \underbrace{-B_2^2(u)_x - u(B_2^2)_x}_{-(uB_2^2)_x} \underbrace{-B_3^2(u)_x - u(B_3^2)_x}_{-(uB_3^2)_x}\\ &\quad + \underbrace{vB_1(B_2)_x + 2vB_2(B_1)_x + B_1B_2(v)_x}_{(vB_1B_2)_x + vB_2(B_1)_x} + \underbrace{wB_1(B_3)_x + 2wB_3(B_1)_x + B_1B_3(w)_x}_{(wB_1B_3)_x + wB_3(B_1)_x}\end{aligned} \tag{E.7}$$

This means the total energy conservation law (using the induction equation and the given momentum conservation law *without* the non-conservative terms) is

$$\frac{\partial E}{\partial t} + \frac{\partial}{\partial x}\left(u\left(\frac{1}{2}\varrho\|\boldsymbol{u}\|^2 + \frac{\gamma p}{\gamma-1} + \|\boldsymbol{B}\|^2\right) - \boldsymbol{B}(\boldsymbol{u}\cdot\boldsymbol{B})\right) = \overset{\downarrow}{+}(B_1)_x(\boldsymbol{u}\cdot\boldsymbol{B}). \tag{E.8}$$

As can be seen from these derivations, we obtained a non-conservative term contributing in the total energy equation *although we started off from equations that do not contain non-conservative term*. It is this very specific (positive) contribution that cancels with one of the two (negative) $(B_1)_x(\boldsymbol{u}\cdot\boldsymbol{B})$ terms coming from the momentum and induction equations with non-conservative term:

1. Kinetic energy *with* non-conservative term

$$\begin{aligned}\frac{\partial}{\partial t}\left(\frac{1}{2}\varrho\|\boldsymbol{u}\|^2\right) &= u(\varrho u)_t + v(\varrho v)_t + w(\varrho w)_t - \frac{1}{2}\|\boldsymbol{u}\|^2(\varrho)_t\\ &= -\left\{u\left(\frac{1}{2}\varrho\|\boldsymbol{u}\|^2\right)\right\}_x - u(p)_x - \frac{1}{2}u\left(-(B_1)_x^2 + (B_2)_x^2 + (B_3)_x^2\right)\\ &\quad + v(B_1B_2)_x + w(B_1B_3)_x - (B_1)_x(\boldsymbol{u}\cdot\boldsymbol{B})\end{aligned} \tag{E.9}$$

2. Magnetic energy *with* non-conservative term

$$\begin{aligned}\frac{\partial}{\partial t}\left(\frac{1}{2}\|\boldsymbol{B}\|^2\right) &= \boldsymbol{B}\cdot\left(\frac{\partial \boldsymbol{B}}{\partial t}\right) = \begin{bmatrix}B_1\\B_2\\B_3\end{bmatrix}\cdot\left(-\frac{\partial}{\partial x}\begin{bmatrix}0\\uB_2 - vB_1\\uB_3 - wB_1\end{bmatrix} - (B_1)_x\begin{bmatrix}u\\v\\w\end{bmatrix}\right)\\ &= -B_2(uB_2)_x + B_2(vB_1)_x - B_3(uB_3)_x + B_3(wB_1)_x - (B_1)_x(\boldsymbol{B}\cdot\boldsymbol{u})\end{aligned} \tag{E.10}$$

Using the kinetic and magnetic energy contributions with non-conservative term as derived in Section 2 results in the shown equation (2.15):

$$\frac{\partial E}{\partial t} + \frac{\partial}{\partial x}\left(u\left(\frac{1}{2}\varrho\|\boldsymbol{u}\|^2 + \frac{\gamma p}{\gamma-1} + \|\boldsymbol{B}\|^2\right) - \boldsymbol{B}(\boldsymbol{u}\cdot\boldsymbol{B})\right) \overset{\downarrow}{=} -(B_1)_x(\boldsymbol{u}\cdot\boldsymbol{B}). \tag{E.11}$$

Appendix F. Ideal GLM-MHD equations in *y* and *z*-direction

For completeness, we summarize the ideal GLM-MHD equations in the two and three-dimensional case below:

$$\frac{\partial}{\partial t}\boldsymbol{q} + \frac{\partial}{\partial x}\boldsymbol{f}^x + \boldsymbol{\Upsilon} = \boldsymbol{0}, \qquad \text{in 1D} \tag{F.1}$$

$$\frac{\partial}{\partial t}\boldsymbol{q} + \frac{\partial}{\partial x}\boldsymbol{f}^x + \frac{\partial}{\partial y}\boldsymbol{f}^y + \boldsymbol{\Upsilon} = \boldsymbol{0}, \qquad \text{in 2D} \tag{F.2}$$

$$\frac{\partial}{\partial t}\boldsymbol{q} + \frac{\partial}{\partial x}\boldsymbol{f}^x + \frac{\partial}{\partial y}\boldsymbol{f}^y + \frac{\partial}{\partial z}\boldsymbol{f}^z + \boldsymbol{\Upsilon} = \boldsymbol{0}, \qquad \text{in 3D} \tag{F.3}$$

where $\boldsymbol{f}^{x,y,z}(\boldsymbol{q})$ are the flux vectors in x, y, and z-direction, and $\boldsymbol{\Upsilon}$ is the non-conservative term.

$$\boldsymbol{f}^x = \begin{bmatrix} \varrho\, u \\ \varrho u^2 + p + \frac{1}{2}\|\boldsymbol{B}\|^2 - B_1 B_1 \\ \varrho\, u\, v - B_1 B_2 \\ \varrho\, u\, w - B_1 B_3 \\ u\hat{E} - B_1(\boldsymbol{u}\cdot\boldsymbol{B}) + c_h\psi B_1 \\ c_h\psi \\ u\, B_2 - v\, B_1 \\ u\, B_3 - w\, B_1 \\ c_h B_1 \end{bmatrix}, \qquad \boldsymbol{f}^y = \begin{bmatrix} \varrho\, v \\ \varrho\, v\, u - B_2 B_1 \\ \varrho v^2 + p + \frac{1}{2}\|\boldsymbol{B}\|^2 - B_2 B_2 \\ \varrho\, v\, w - B_2 B_3 \\ v\hat{E} - B_2(\boldsymbol{u}\cdot\boldsymbol{B}) + c_h\psi B_2 \\ v\, B_1 - u\, B_2 \\ c_h\psi \\ v\, B_3 - w\, B_2 \\ c_h B_2 \end{bmatrix},$$

$$\boldsymbol{f}^z = \begin{bmatrix} \varrho\, w \\ \varrho\, w\, u - B_3 B_1 \\ \varrho\, w\, v - B_3 B_2 \\ \varrho w^2 + p + \frac{1}{2}\|\boldsymbol{B}\|^2 - B_3 B_3 \\ w\hat{E} - B_3(\boldsymbol{u}\cdot\boldsymbol{B}) + c_h\psi B_3 \\ w\, B_1 - u\, B_3 \\ w\, B_2 - v\, B_3 \\ c_h\psi \\ c_h B_3 \end{bmatrix}. \tag{F.4}$$

Appendix G. Dimensional ideal GLM-MHD equations

We used dimensionless quantities in this work for the sake of convenience as it allows us to hide some physical constants as they are set to one. However, as the authors have also shown in [2, Appendix D], our EC/ES schemes trivially extend to dimensional units, where the magnetic permeability, μ_0, has to explicitly be taken into account:

$$E_{\text{mag}} = \frac{1}{2\mu_0}\|\boldsymbol{B}\|^2, \tag{G.1}$$

$$E_\psi = \frac{1}{2\mu_0}\psi^2. \tag{G.2}$$

The dimensional ideal GLM-MHD equations are given by

$$\frac{\partial}{\partial t}\boldsymbol{q} + \nabla\cdot\boldsymbol{f} = \frac{\partial}{\partial t}\begin{bmatrix} \varrho \\ \varrho\boldsymbol{u} \\ E \\ \boldsymbol{B} \\ \psi \end{bmatrix} + \nabla\cdot\begin{bmatrix} \varrho\boldsymbol{u} & \text{(a)} \\ \varrho(\boldsymbol{u}\otimes\boldsymbol{u}) + \left(p + \frac{\|\boldsymbol{B}\|^2}{2\mu_0}\right)\mathbf{I} - \frac{\boldsymbol{B}\otimes\boldsymbol{B}}{\mu_0} & \text{(b)} \\ \boldsymbol{u}\left(\frac{1}{2}\varrho\|\boldsymbol{u}\|^2 + \frac{\gamma p}{\gamma-1} + \frac{\|\boldsymbol{B}\|^2}{\mu_0}\right) - \frac{\boldsymbol{B}(\boldsymbol{u}\cdot\boldsymbol{B})}{\mu_0} + \frac{c_h}{\mu_0}\psi\boldsymbol{B} & \text{(c)} \\ \boldsymbol{u}\otimes\boldsymbol{B} - \boldsymbol{B}\otimes\boldsymbol{u} + c_h\psi\mathbf{I} & \text{(d)} \\ c_h\boldsymbol{B} & \text{(e)} \end{bmatrix} = -\boldsymbol{\Upsilon}_{\text{GLM}}, \tag{G.3}$$

with

Table G.1
Simulation units determined by different values for μ_0 [2].

Unit system:		SI	CGS
Length	ℓ	m	cm
Time	t	s	s
Density	ϱ	$\mathrm{kg\,m^{-3}}$	$\mathrm{g\,cm^{-3}}$
Velocities	$\boldsymbol{u}$	$\mathrm{m\,s^{-1}}$	$\mathrm{cm\,s^{-1}}$
Specific energy	E	$\mathrm{J\,m^{-3}}$	$\mathrm{erg\,cm^{-3}}$
Pressure	p	$\mathrm{N\,m^{-2}}$	$\mathrm{dyn\,cm^{-2}}$
Magnetic field	B	T	G
Damping coefficient	α	$\mathrm{s^{-1}}$	$\mathrm{s^{-1}}$
	with $\mu_0 :=$	$4\pi \times 10^{-7}\ \mathrm{T^2\,m^3\,J^{-1}}$	$4\pi\ \mathrm{G^2\,cm^3\,erg^{-1}}$

$$\boldsymbol{\Upsilon}_{\mathrm{GLM}} := (\nabla \cdot \boldsymbol{B}) \begin{bmatrix} 0 \\ \mu_0^{-1}\boldsymbol{B} \\ \mu_0^{-1}\boldsymbol{u}\cdot\boldsymbol{B} \\ \boldsymbol{u} \\ 0 \end{bmatrix} + (\nabla\psi)\cdot \begin{bmatrix} \boldsymbol{0} \\ 0 \\ \mu_0^{-1}\boldsymbol{u}\psi \\ 0 \\ \boldsymbol{u} \end{bmatrix} \tag{G.4}$$

where the thermal pressure is related to the conserved quantities through the dimensional ideal gas law:

$$p = (\gamma - 1)\left(E - \frac{\varrho}{2}\|\boldsymbol{u}\|^2 - \frac{1}{2\mu_0}\left(\|\boldsymbol{B}\|^2 + \psi^2\right)\right). \tag{G.5}$$

The resulting units of the simulation quantities are can be determined by the chosen value for μ_0. They are listed in Table G.1. In non-dimensional units, one typically uses $\mu_0 = 1$, where (G.3) and (G.5) are identical to (3.16) and (3.18).

References

[1] J.U. Brackbill, D.C. Barnes, The effect of nonzero $\nabla \cdot B$ on the numerical solution of the magnetohydrodynamic equations, J. Comput. Phys. 35 (3) (1980) 426–430, https://doi.org/10.1016/0021-9991(80)90079-0.
[2] D. Derigs, A.R. Winters, G.J. Gassner, S. Walch, A novel high-order, entropy stable, 3D AMR MHD solver with guaranteed positive pressure, J. Comput. Phys. 317 (2016) 223–256, https://doi.org/10.1016/j.jcp.2016.04.048.
[3] A.R. Winters, G.J. Gassner, Affordable, entropy conserving and entropy stable flux functions for the ideal MHD equations, J. Comput. Phys. 304 (2016) 72–108, https://doi.org/10.1016/j.jcp.2015.09.055.
[4] U.S. Fjordholm, S. Mishra, E. Tadmor, Well-balanced and energy stable schemes for the shallow water equations with discontinuous topography, J. Comput. Phys. 230 (14) (2011) 5587–5609, https://doi.org/10.1016/j.jcp.2011.03.042.
[5] E. Tadmor, The numerical viscosity of entropy stable schemes for systems of conservation laws, Math. Comput. 49 (179) (1987) 91–103, https://doi.org/10.2307/2008251.
[6] S. Godunov, Symmetric form of the equations of magnetohydrodynamics, Numer. Methods Mech. Contin. Medium 1 (1972) 26–34.
[7] K.G. Powell, P.L. Roe, T.J. Linde, T.I. Gombosi, D.L. De Zeeuw, A solution-adaptive upwind scheme for ideal magnetohydrodynamics, J. Comput. Phys. 154 (2) (1999) 284–309, https://doi.org/10.1006/jcph.1999.6299.
[8] P.A.M. Dirac, Quantised singularities in the electromagnetic field, Proc. R. Soc., Math. Phys. Eng. Sci. 133 (821) (1931) 60–72, https://doi.org/10.1098/rspa.1931.0130.
[9] J.D. Jackson, C. Witte, K. Muller, Klassische Elektrodynamik, (Überarbeitete Auflage) (German Edition), 4th edition, Walter de Gruyter, 2006.
[10] F. Moulin, Magnetic monopoles and Lorentz force, Nuovo Cimento B 116 (2001) 869, arXiv:math-ph/0203043.
[11] G.I. Ogilvie, Lecture notes: astrophysical fluid dynamics, ArXiv e-prints arXiv:1604.03835.
[12] T.J. Barth, Numerical methods for gasdynamic systems on unstructured meshes, in: D. Kröner, M. Ohlberger, C. Rohde (Eds.), An Introduction to Recent Developments in Theory and Numerics for Conservation Laws, in: Lect. Notes Comput. Sci. Eng., vol. 5, Springer Berlin Heidelberg, 1999, pp. 195–285.
[13] P. Janhunen, A positive conservative method for magnetohydrodynamics based on HLL and Roe methods, J. Comput. Phys. 160 (2) (2000) 649–661, https://doi.org/10.1006/jcph.2000.6479.
[14] B. Sjögreen, H.C. Yee, D. Kotov, Skew-symmetric splitting and stability of high order central schemes, J. Phys. Conf. Ser. 837 (2017) 012019, https://doi.org/10.1088/1742-6596/837/1/012019.
[15] B. Marder, A method for incorporating Gauss' law into electromagnetic PIC codes, J. Comput. Phys. 68 (1) (1987) 48–55, https://doi.org/10.1016/0021-9991(87)90043-X.
[16] A.L. Zachary, A. Malagoli, P. Colella, A higher-order Godunov method for multidimensional ideal magnetohydrodynamics, SIAM J. Sci. Comput. 15 (2) (1994) 263–284, https://doi.org/10.1137/0915019.
[17] D.S. Balsara, Total variation diminishing scheme for adiabatic and isothermal magnetohydrodynamics, Astrophys. J. Suppl. Ser. 116 (1) (1998) 133–153, https://doi.org/10.1086/313093.
[18] R.K. Crockett, P. Colella, R.T. Fisher, R.I. Klein, C.F. McKee, An unsplit, cell-centered Godunov method for ideal MHD, J. Comput. Phys. 203 (2005) 422–448, https://doi.org/10.1016/j.jcp.2004.08.021.
[19] C.R. Evans, J.F. Hawley, Simulation of magnetohydrodynamic flows – a constrained transport method, Astrophys. J. 332 (1988) 659–677, https://doi.org/10.1086/166684.
[20] D.S. Balsara, D. Spicer, A staggered mesh algorithm using high order Godunov fluxes to ensure solenoidal magnetic fields in magnetohydrodynamic simulations, J. Comput. Phys. 149 (2) (1999) 270–292, https://doi.org/10.1006/jcph.1998.6153.
[21] G. Tóth, The $\nabla \cdot B = 0$ constraint in shock-capturing magnetohydrodynamics codes, J. Comput. Phys. 161 (2) (2000) 605–652, https://doi.org/10.1006/jcph.2000.6519.
[22] K.S. Yee, Numerical solution of initial boundary value problems involving Maxwell's equations in isotropic media, IEEE Trans. Antennas Propag. 14 (3) (1966) 302–307, https://doi.org/10.1109/TAP.1966.1138693.

[23] D.S. Balsara, J. Kim, A comparison between divergence-cleaning and staggered-mesh formulations for numerical magnetohydrodynamics, Astrophys. J. 602 (2004) 1079–1090, https://doi.org/10.1086/381051.
[24] K. Waagan, A positive MUSCL-Hancock scheme for ideal magnetohydrodynamics, J. Comput. Phys. 228 (23) (2009) 8609–8626, https://doi.org/10.1016/j.jcp.2009.08.020.
[25] C.-D. Munz, P. Omnes, R. Schneider, E. Sonnendrücker, U. Voß, Divergence correction techniques for Maxwell solvers based on a hyperbolic model, J. Comput. Phys. 161 (2) (2000) 484–511, https://doi.org/10.1006/jcph.2000.6507.
[26] A. Dedner, F. Kemm, D. Kröner, C.-D. Munz, T. Schnitzer, M. Wesenberg, Hyperbolic divergence cleaning for the MHD equations, J. Comput. Phys. 175 (2) (2002) 645–673, https://doi.org/10.1006/jcph.2001.6961.
[27] T.S. Tricco, D.J. Price, Constrained hyperbolic divergence cleaning for smoothed particle magnetohydrodynamics, J. Comput. Phys. 231 (21) (2012) 7214–7236, https://doi.org/10.1016/j.jcp.2012.06.039.
[28] M. Brio, C.C. Wu, An upwind differencing scheme for the equations of ideal magnetohydrodynamics, J. Comput. Phys. 75 (2) (1988) 400–422, https://doi.org/10.1016/0021-9991(88)90120-9.
[29] P. Cargo, G. Gallice, Roe matrices for ideal MHD and systematic construction of Roe matrices for systems of conservation laws, J. Comput. Phys. 136 (2) (1997) 446–466, https://doi.org/10.1006/jcph.1997.5773.
[30] X. Feng, M. Zhang, A comparative study of divergence cleaning methods of magnetic field in the solar coronal numerical simulation, Front. Astron. Space Sci. 3 (2016) 6, https://doi.org/10.3389/fspas.2016.00006.
[31] S. Walch, P. Girichidis, T. Naab, A. Gatto, S.C.O. Glover, R. Wünsch, R.S. Klessen, P.C. Clark, T. Peters, D. Derigs, C. Baczynski, The SILCC (SImulating the LifeCycle of molecular Clouds) project – I. Chemical evolution of the supernova-driven ISM, Mon. Not. R. Astron. Soc. 454 (1) (2015) 238–268, https://doi.org/10.1093/mnras/stv1975.
[32] M. Bohm, R.W. Winters, D. Derigs, G.J. Gassner, S. Walch, J. Saur, An entropy stable nodal discontinuous Galerkin method for the resistive MHD equations: continuous analysis and GLM divergence cleaning, submitted to Comput. Fluids, arXiv:1711.05576.
[33] E. Tadmor, Numerical viscosity and the entropy condition for conservative difference schemes, Math. Comput. 43 (168) (1984) 369–381, https://doi.org/10.2307/2008282.
[34] T. Barth, On the role of involutions in the discontinuous Galerkin discretization of Maxwell and magnetohydrodynamic systems, in: Compatible Spatial Discretizations, Springer, 2006, pp. 69–88.
[35] M.O. Domingues, A.K.F. Gomes, S.M. Gomes, O. Mendes, B. Di Pierro, K. Schneider, Extended generalized Lagrangian multipliers for magnetohydrodynamics using adaptive multiresolution methods, ESAIM Proc. 43 (2013) 95–107, https://doi.org/10.1051/proc/201343006.
[36] A. Mignone, P. Tzeferacos, G. Bodo, High-order conservative finite difference GLM-MHD schemes for cell-centered MHD, J. Comput. Phys. 229 (2010) 5896–5920, https://doi.org/10.1016/j.jcp.2010.04.013, arXiv:1001.2832.
[37] R.-L. Jiang, C. Fang, P.-F. Chen, A new MHD code with adaptive mesh refinement and parallelization for astrophysics, Comput. Phys. Commun. 183 (8) (2012) 1617–1633, https://doi.org/10.1016/j.cpc.2012.02.030, arXiv:1204.5849.
[38] J. Mackey, A.J. Lim, Effects of magnetic fields on photoionized pillars and globules, Mon. Not. R. Astron. Soc. 412 (3) (2011) 2079–2094, https://doi.org/10.1111/j.1365-2966.2010.18043.x.
[39] T.S. Tricco, D.J. Price, M.R. Bate, Constrained hyperbolic divergence cleaning in smoothed particle magnetohydrodynamics with variable cleaning speeds, J. Comput. Phys. 322 (2016) 326–344, https://doi.org/10.1016/j.jcp.2016.06.053.
[40] P. Chandrashekar, C. Klingenberg, Entropy stable finite volume scheme for ideal compressible MHD on 2-d cartesian meshes, SIAM J. Numer. Anal. 54 (2) (2016) 1313–1340, https://doi.org/10.1137/15M1013626.
[41] F. Ismail, P.L. Roe, Affordable, entropy-consistent Euler flux functions II: Entropy production at shocks, J. Comput. Phys. 228 (15) (2009) 5410–5436, https://doi.org/10.1016/j.jcp.2009.04.021.
[42] P. Chandrashekar, Kinetic energy preserving and entropy stable finite volume schemes for compressible Euler and Navier–Stokes equations, Commun. Comput. Phys. 14 (2013) 1252–1286, https://doi.org/10.4208/cicp.170712.010313a.
[43] D. Derigs, A.R. Winters, G.J. Gassner, S. Walch, A novel averaging technique for discrete entropy stable dissipation operators for ideal MHD, J. Comput. Phys. 330 (2016) 624–632, https://doi.org/10.1016/j.jcp.2016.10.055.
[44] A.R. Winters, D. Derigs, G.J. Gassner, S. Walch, A uniquely defined entropy stable matrix dissipation operator for high Mach number ideal MHD and compressible Euler simulations, J. Comput. Phys. 332 (2017) 274–289, https://doi.org/10.1016/j.jcp.2016.12.006.
[45] S. Mishra, Entropy stable high-order schemes for systems of conservation laws, in: Modern Techniques in the Numerical Solution of Partial Differential Equations, 2011.
[46] V.V. Rusanov, The calculation of the interaction of non-stationary shock waves with barriers, Ž. Vyčisl. Mat. Mat. Fiz. 1 (1961) 267–279, https://doi.org/10.1016/0041-5553(62)90062-9.
[47] M. Wesenberg, Efficient Finite-Volume Schemes for Magnetohydrodynamic Simulations in Solar Physics, dissertation, Universität Freiburg, 2003, https://www.freidok.uni-freiburg.de/data/792.
[48] S. Gottlieb, C.-W. Shu, E. Tadmor, Strong stability-preserving high-order time discretization methods, SIAM Rev. 43 (1) (2001) 89–112, https://doi.org/10.1137/S003614450036757X.
[49] D. Derigs, G.J. Gassner, S. Walch, R.W. Winters, Entropy Stable Finite Volume Approximations for Ideal Magnetohydrodynamics, submitted to Jahresber. Dtsch. Math.-Ver., arXiv:1708.03537.
[50] P.G. LeFloch, J.M. Mercier, C. Rohde, Fully discrete, entropy conservative schemes of arbitrary order, SIAM J. Numer. Anal. 40 (5) (2002) 1968–1992, https://doi.org/10.1137/S003614290240069X.
[51] U.S. Fjordholm, S. Mishra, E. Tadmor, Arbitrarily high-order accurate entropy stable essentially nonoscillatory schemes for systems of conservation laws, SIAM J. Numer. Anal. 50 (2) (2012) 544–573, https://doi.org/10.1137/110836961.
[52] B. Schmidtmann, B. Seibold, M. Torrilhon, Relations between WENO3 and third-order limiting in finite volume methods, J. Sci. Comput., https://doi.org/10.1007/s10915-015-0151-z.
[53] D. Lee, A.E. Deane, An unsplit staggered mesh scheme for multidimensional magnetohydrodynamics, J. Comput. Phys. 228 (4) (2009) 952–975, https://doi.org/10.1016/j.jcp.2008.08.026.
[54] S.A. Orszag, C.-M. Tang, Small-scale structure of two-dimensional magnetohydrodynamic turbulence, J. Fluid Mech. 90 (01) (1979) 129–143, https://doi.org/10.1017/s002211207900210x.
[55] J. Balbás, E. Tadmor, A central differencing simulation of the Orszag Tang vortex system, IEEE Trans. Plasma Sci. 33 (2005) 470–471, https://doi.org/10.1109/TPS.2005.845282.
[56] W. Dai, P.R. Woodward, A simple finite difference scheme for multidimensional magnetohydrodynamical equations, J. Comput. Phys. 142 (2) (1998) 331–369, https://doi.org/10.1006/jcph.1998.5944.
[57] P. Londrillo, L. Del Zanna, High-order upwind schemes for multidimensional magnetohydrodynamics, Astrophys. J. 530 (2000) 508–524, https://doi.org/10.1086/308344, arXiv:astro-ph/9910086.
[58] D. Ryu, T.W. Jones, A. Frank, Numerical magnetohydrodynamics in astrophysics: algorithm and tests for multidimensional flow, Astrophys. J. 452 (1995) 785, https://doi.org/10.1086/176347, arXiv:astro-ph/9505073.
[59] J.N. Lyness, C.B. Moler, Numerical differentiation of analytic functions, SIAM J. Numer. Anal. 4 (2) (1967) 202–210, https://doi.org/10.1137/0704019.

[60] E.F. Toro, Riemann Solvers and Numerical Methods for Fluid Dynamics: A Practical Introduction, Springer, 2009.
[61] G.A. Sod, A survey of several finite difference methods for systems of nonlinear hyperbolic conservation laws, J. Comput. Phys. 27 (1) (1978) 1–31.
[62] S. Osher, Riemann solvers, the entropy condition, and difference, SIAM J. Numer. Anal. 21 (2) (1984) 217–235.
[63] P.L. Roe, D.S. Balsara, Notes on the eigensystem of magnetohydrodynamics, SIAM J. Appl. Math. 56 (1) (1996) 57–67, https://doi.org/10.1137/S003613999427084X.

4.5 Further publications not included in this thesis

Bohm, M., Winters, A. R., Gassner, G. J., **Derigs, D.**, Hindenlang, F., Saur, J., (Feb. 2018). "An entropy stable nodal discontinuous Galerkin method for the resistive MHD equations. Part I: Theory and Numerical Verification." In: *Journal of Computational Physics (in press)*. ISSN: 0021-9991.
DOI: 10.1016/j.jcp.2018.06.027. arXiv: 1802.07341.

Derigs, D., Labadie, L., Ghosh, D. S., Abel-Tibérini, L., (July 2014). "A novel high-contrast imaging technique based on optical tunneling to search for faint companions around bright stars at the limit of diffraction." In: *Advances in Optical and Mechanical Technologies for Telescopes and Instrumentation*. Vol. 9151. Proceedings of the SPIE.
DOI: 10.1117/12.2055440. arXiv: 1606.08846.

Derigs, D., Gassner, G. J., Walch, S., Winters, A. R., (Sept. 2018a). "Entropy Stable Finite Volume Approximations for Ideal Magnetohydrodynamics." In: *Jahresbericht der Deutschen Mathematiker-Vereinigung* 120.3, pp. 153–219. ISSN: 1869-7135.
DOI: 10.1365/s13291-018-0178-9. arXiv: 1708.03537.

Gatto, A., Walch, S., Naab, T., Girichidis, P., Wünsch, R., Glover, S. C. O., Klessen, R. S., Clark, P. C., Peters, T., **Derigs, D.**, Baczynski, C., Puls, J., (June 2016). "The SILCC project: III. Regulation of star formation and outflows by stellar winds and supernovae." In: arXiv: 1606.05346.

Girichidis, P., Walch, S., Naab, T., Gatto, A., Wünsch, R., Glover, S. C. O., Klessen, R. S., Clark, P. C., Peters, T., **Derigs, D.**, Baczynski, C., (Mar. 2016). "The SILCC (SImulating the LifeCycle of molecular Clouds) project - II. Dynamical evolution of the supernova-driven ISM and the launching of outflows." In: *Monthly Notices of the Royal Astronomical Society* 456, pp. 3432–3455.
DOI: 10.1093/mnras/stv2742. arXiv: 1508.06646.

Walch, S., Girichidis, P., Naab, T., Gatto, A., Glover, S. C. O., Wünsch, R., Klessen, R. S., Clark, P. C., Peters, T., **Derigs, D.**, Baczynski, C., (Nov. 2015). "The SILCC (SImulating the LifeCycle of molecular Clouds) project – I. Chemical evolution of the supernova-driven ISM." In: *Monthly Notices of the Royal Astronomical Society* 454.1, pp. 238–268.
DOI: 10.1093/mnras/stv1975. arXiv: 1412.2749.

Winters, A. R., **Derigs, D.**, Gassner, G. J., Walch, S., (Mar. 2017). "A uniquely defined entropy stable matrix dissipation operator for high Mach number ideal MHD and compressible Euler simulations." In: *Journal of Computational Physics* 332, pp. 274–289. ISSN: 0021-9991.
DOI: 10.1016/j.jcp.2016.12.006.

5 | Implementation details

I implemented my entropy-stable scheme into the multi-physics, multi-scale adaptive mesh refinement (AMR) simulation suite FLASH. Overall, I created three altogether different implementations of my entropy-stable MHD solver. In this chapter, I shortly describe the simulation framework FLASH as well as my different implementations and comment on their applicability for simulations.

5.1 The simulation code FLASH

FLASH (Fryxell et al., 2000; Flash Center for Computational Science, 2017) is a parallelized, publicly available, high performance simulation software system. It works on Eulerian grids and is capable of handling flow problems found in many common astrophysical environments. According to Dubey et al. (2009), FLASH is used by thousands of researchers in various fields. The code is written in FORTRAN90 and C. It uses the Message-Passing Interface (MPI) library for inter-processor communication and the HDF5 library for parallel I/O to achieve portability and scalability on a variety of different parallel architectures. In astrophysics, FLASH is used for simulations in the research fields of supernova explosions (SNe) and remnant evolution, X-ray bursts, galaxy formation, the evolution of the interstellar medium (ISM), stellar structures and many more. Beyond astrophysics, FLASH is also applicable to other physical applications like laser experiments at high-energy-density physics (HEDP) facilities.

The FLASH code includes physics capabilities for (magneto)hydrodynamics, flux-limited diffusion, reaction networks for nuclear burning and the formation of chemical species in the interstellar medium (ISM), various forms of Equations of State (EOS), material properties, self-gravity, and many more organized as code modules. All modules can be included and exchanged as desired. The code's architecture is designed to be flexible and extensible. Users can configure initial and boundary conditions, change algorithms, and add new physics units. My entropy stable schemes are a module that can be exchanged freely within FLASH's framework to ensure a high level of portability and flexibility.

FLASH is used within Cologne's Theoretical Astrophysics Group (TAG) for astrophysical projects, a very prominent one being the "SILCC" project introduced in Walch et al. (2015) and Girichidis et al. (2016). In the framework of SILCC, researchers from Cologne (Universität zu Köln), Garching (Max-Planck-Institut für Astrophysik), Heidelberg (Universität Heidelberg), Prague (Astronomický Ústav, the Astronomical Institute of the Czech Academy of Sciences), Cardiff (Cardiff University), and Potsdam (Leibniz-Institut für Astrophysik Potsdam) model galactic disk regions with the necessary physical complexity to understand the full life-cycle of molecular clouds.

The ultimate goal of the SILCC project is to provide self-consistent answers to questions like:

- How does stellar feedback regulate the star formation efficiency of a galaxy?
- How are molecular clouds formed and which processes destroy them?
- How are galactic outflows driven?

First results of the SILCC project have been published in Walch et al. (2015), Girichidis et al. (2016), Gatto et al. (2016), Peters et al. (2017a), and Seifried et al. (2017).

5.1.1 The modular structure

FLASH is a modular simulation code. Hence, simulations are able to approximate a wide variety of fluid simulations depending on which modules are selected.

For instance, FLASH offers three interchangeable discretization grids: a Uniform Grid (UG), a block-structured oct-tree based adaptive grid using the PARAMESH library (MacNeice et al., 2000), and a block-structured patch based adaptive grid using Chombo (Adams et al., 2015). The advantage of both PARAMESH and Chombo is that they place resolution elements only where they are needed. UG comes at a simpler implementation but notably higher computational costs.

All simulations performed with FLASH are composed out of modules coming from five categories:

Simulation modules define runtime parameters and initialize the simulation with the initial conditions of a particular simulation.

Infrastructure modules are responsible for FLASH-related housekeeping tasks such as the management of runtime parameters, the handling of input and output to and from the code, and the administration of the grid, which describes the simulation's physical domain.

Physics modules are responsible for the actual simulation of the effect of various physics that may or may not be relevant for the current simulation. They are categorized in smaller units such as

Physics/Hydro modules solve the (magneto-)hydrodynamics equations for compressible gas dynamics in one, two, or three spatial dimensions,

Physics/Eos modules add an equation of state computing the temperature, pressure, and other thermodynamic quantities needed by simulations,

Physics/Gravity modules compute gravitational source terms for the code,

Physics/sourceTerms modules compute local source terms like forcing or chemical reaction networks, or

Physics/TreeRay is a fast algorithm for radiation transport in (M)HD simulations.

Monitor modules track the progress and performance of a given simulation, they include modules like `Monitor/Logfile`, `Monitor/Profiler`, and `Monitor/Timers`.

Driver modules implement the actual time integration methods and are responsible for the general management of the interaction between all included modules. They are responsible for determining the time step Δt that is used to advance the simulation from time $t = t^{n-1}$ to t^n.

5.1.2 Time step restrictions

I implemented my new ideal GLM-MHD solver as multiple standalone `Physics/Hydro` modules selectable at setup time. During my investigations, it turned out that the time marching scheme dictated by the `Driver` modules is very restrictive and limits the applicability of my new scheme in `FLASH`:

> “ Subsequently, the routine `Driver_computeDt` (usually invoked from `Driver_evolveFlash` **at the end** of an iteration of the main evolution loop) is used to recompute Δt **for the next** evolution step. ”
>
> – `FLASH` user guide, Sec. 7.1.5

In the following, I shortly describe the time marching schemes prescribed by the two available `Driver` modules to highlight the limitations implied by this.

The `Driver/split` module

The method of “dimensional splitting” has become popular in fluid dynamics as it allows us to apply our knowledge about one-dimensional systems directly to multi-dimensional systems. Using the dimensional splitting method, one-dimensional problems along each coordinate direction are solved in turn to determine the fluxes across the faces of a multi-dimensional finite volume cell. It has proven to be an inexpensive way of extending one-dimensional high-resolution methods to higher spatial dimensions (LeVeque et al., 1998, p. 103).

The dimensionally “split” driver module implements a Strang-split method of time advancement (Strang, 1968): Each physics module updates the solution for *two* equal time steps, advancing the simulation by $2\Delta t$ in each evolution step. Given entropy-stable GLM-MHD fluxes $\boldsymbol{F}$, $\boldsymbol{G}$, and $\boldsymbol{H}$ at the interfaces, the MHD modules directly update the solution using multiple one-dimensional sweeps:

$$\boldsymbol{q}^{n,*}_{i,j,k} = \boldsymbol{q}^{n}_{i,j,k} + \frac{\Delta t}{\Delta x}(\boldsymbol{F}^{n}_{i-1/2,j,k} - \boldsymbol{F}^{n}_{i+1/2,j,k}) \tag{5.1}$$

$$\boldsymbol{q}_{i,j,k}^{n,**} = \boldsymbol{q}_{i,j,k}^{n,*} + \frac{\Delta t}{\Delta y}(\boldsymbol{G}_{i,j-1/2,k}^{n,*} - \boldsymbol{G}_{i,j+1/2,k}^{n,*}) \tag{5.2}$$

$$\boldsymbol{q}_{i,j,k}^{n+1} = \boldsymbol{q}_{i,j,k}^{n,**} + \frac{\Delta t}{\Delta z}(\boldsymbol{H}_{i,j,k-1/2}^{n,**} - \boldsymbol{H}_{i,j,k+1/2}^{n,**}) \tag{5.3}$$

This first sweep is followed by the computation and immediate application of the other `physics` modules. Thereafter, a second MHD sweep, in reversed dimensional order, is carried out:

$$\boldsymbol{q}_{i,j,k}^{n+1,*} = \boldsymbol{q}_{i,j,k}^{n+1} + \frac{\Delta t}{\Delta z}(\boldsymbol{H}_{i-1/2,j,k}^{n+1} - \boldsymbol{H}_{i+1/2,j,k}^{n+1}) \tag{5.4}$$

$$\boldsymbol{q}_{i,j,k}^{n+1,**} = \boldsymbol{q}_{i,j,k}^{n+1,*} + \frac{\Delta t}{\Delta y}(\boldsymbol{G}_{i,j-1/2,k}^{n+1,*} - \boldsymbol{G}_{i,j+1/2,k}^{n+1,*}) \tag{5.5}$$

$$\boldsymbol{q}_{i,j,k}^{n+2} = \boldsymbol{q}_{i,j,k}^{n+1,**} + \frac{\Delta t}{\Delta x}(\boldsymbol{F}_{i,j,k-1/2}^{n+1,**} - \boldsymbol{F}_{i,j,k+1/2}^{n+1,**}) \tag{5.6}$$

After another sequence of the remaining `physics` modules, the evolution loop is completed and the simulations has been advanced by two time steps of equal size: $\boldsymbol{q}_{i,j,k}^{n} \rightarrow \boldsymbol{q}_{i,j,k}^{n+2}$. After two half temporal sweeps, the can time step size can be adjusted if necessary. Furthermore, also the condition for updating the mesh refinement pattern is tested only then and local refinement is applied if required.

As indicated by the superscripts of the numerical flux functions, the `Driver/split` uses the fluid quantities at the intermediate values to compute the individual numerical fluxes. Note that these intermediate values may only be partially dimensionally updated.

The issue with the time marching of the `split` driver is immediately apparent: Based on a *previous* MHD sweep, we fix the time step for the *next two* time steps. Now, even if the solver determines that a much smaller time step is necessary for the intermediate steps due to newly evolving discontinuities or shock interactions it can likewise not be used right here, but only in the subsequent step as the solver is forced to use the predetermined time step. This directly influences the robustness and stability of the numerical scheme. **The issue of possibly unstable time steps should not be treated lightly**.

This limitation is by design. Even if the MHD solver would change the time step by itself, this would inevitably invalidate multi-physics effects already computed by, e.g., local source terms. The problem here is that their contributions have already been applied to the solution so a rescaling of the effects (necessary due to the changed Δt) is not possible. Due to memory limitations on all currently available high-performance computing platforms, `FLASH` simulations cannot afford to store historical information and retain the ability to rewind a simulation to a previous solution state once it detects that the time step is not suitable. Hence, there is no possibility to retry the computation with a smaller time step if problems are detected and the only way to mitigate such problems is setting a somewhat conservative value for the CFL condition in complex simulations.

The `Driver/unsplit` module

The `Driver/unsplit` module implements a dimensionally unsplit update of the quantities. It is the default since version `FLASH4.4` (Flash Center for Computational Science, 2017, Sec. 7.1.2.2). In contrast to the `Driver/split` module, it does only perform one sweep within a given time step and then computes the solution at the next time step. The fluxes are all computed from the same solution quantities at time step t^n (in contrast to intermediate, only partially updated values of the split scheme):

$$\begin{aligned} \boldsymbol{q}_{i,j,k}^{n+1} = \boldsymbol{q}_{i,j,k}^{n} &+ \frac{\Delta t}{\Delta x}(\boldsymbol{F}^{n}_{i-1/2,j,k} - \boldsymbol{F}^{n}_{i+1/2,j,k}) \\ &+ \frac{\Delta t}{\Delta y}(\boldsymbol{G}^{n}_{i,j-1/2,k} - \boldsymbol{G}^{n}_{i,j+1/2,k}) \\ &+ \frac{\Delta t}{\Delta z}(\boldsymbol{H}^{n}_{i,j,k-1/2} - \boldsymbol{H}^{n}_{i,j,k+1/2}) \end{aligned} \tag{5.7}$$

In general, unsplit implementations can achieve arbitrarily high accuracy, whereas split solvers are intrinsically limited in their accuracy. However, unsplit implementations have the major drawback of having to account for flows in multiple directions whereas split schemes only solve one-dimensional problems. This not only leads to (slightly) increased code complexity, but also reduces the maximum allowable time step, as the CFL condition must be fulfilled in all spatial dimensions simultaneously in contrast to have to be fulfilled for each separate spatial direction as in split methods.

Unfortunately, the unsplit implementation suffers from a similar, albeit reduced, issue with prescribed time step sizes. Like in the split driver implementation, the unsplit module fixes the time step for a given run. The restriction implied by this may be less critical than in the split case, where up to six sweeps would have to be performed with a possibly unstable time steps.

5.2 Unsplit GLM-MHD implementation

The unsplit GLM-MHD solver is the code in my second and third publications (Derigs et al., 2017; Derigs et al., 2018b). It solves the ideal GLM-MHD equations by computing the fluxes in a directionally unsplit way by updating all quantities *at once* as described in the preceding `Driver/unsplit` module subsection.

I coded this implementation for maximum flexibility to be able to exchange the fluxes, dissipation terms, spatial reconstruction, as well as temporal integration methods easily. It is fully MPI parallelized and works with adaptive meshes.

To overcome the time step size limitations described in the preceding section, this solver intentionally deviates from how `FLASH` handles the time step synchronization by manipulating internal `Driver` module variables during the evolution step to always use a suitable time step. Although the benefits for stability and usability of the scheme are immediate, this prevents me from using this solver in combination with other `Physics` modules as those modules, implemented in separate modules

("operator split"), would not see a time step that is constant in an evolution round. Accordingly, this implementation does not support the inclusion of external physics modules such as gravity or multi-species and is not suitable for general purpose multi-physics simulations.

As a testing bench, this implementation had proven to be a valuable tool during the development of my new model when I routinely derived new discrete entropy-stable fluxes with varying physical properties, including, but not limited to, alternative discretizations and source terms. It includes a variety of additional diagnosis output useful for measuring the entropic properties of a given scheme.

5.3 Split GLM-MHD implementation

The split GLM-MHD solver is an extended version of the code described in my first publication (Derigs et al., 2016). It is fully compatible with `FLASH`'s split `Driver` module and hence supports any multi-physics applications. However, due to this, it is also subject to the time step stability restrictions outlined in the description of the split driver module.

To obtain high-order spatial accuracy, I implement an extended variant of the conservative Monotone Upstream-centered Scheme for Conservation Laws (MUSCL) scheme, introduced by van Leer (1984) (see also the recent review by Toro, 2009, Sec. 13.4). The MUSCL approach implies, firstly, high-order of accuracy obtained by data reconstruction and, secondly, the reconstruction is constrained to avoid spurious oscillations.

I implement adaptive mesh refinement (AMR) flux conservation. Flux conservation is necessary when two blocks of differing refinement levels (meaning having different grid spacings) border one another and hence a necessity for stable and accurate computations with AMR.

More specifically, I implemented the MUSCL-Hancock[5] variant. This method consists of three steps to construct a discrete second-order accurate scheme. The three steps are:

Data reconstruction step: Based on a boundary extrapolation, one obtains intermediate interface values $\boldsymbol{q}_{i,\mathrm{L,R}}$

$$\boldsymbol{q}_{i,\mathrm{L,R}} = \boldsymbol{q}_i^n \mp \frac{1}{2}\boldsymbol{\Delta}_i \tag{5.8}$$

with suitable cell slopes $\boldsymbol{\Delta}_i$.

Evolution step: The intermediate interface values are evolved by a half time step

$$\overline{\boldsymbol{q}}_{i,\mathrm{R,L}} = \boldsymbol{q}_{i,\mathrm{R,L}} + \frac{1}{2}\frac{\Delta t}{\Delta x}[f(\boldsymbol{q}_{i,\mathrm{L}}) - f(\boldsymbol{q}_{i,\mathrm{R}})]. \tag{5.9}$$

Solution step: Finally, the numerical fluxes are computed from the reconstructed states.

My MUSCL-Hancock implementation is based on the description of Waagan (2009, Sec. 2) combined with the eigendecomposition I carried out for the ideal GLM-MHD system in Derigs et al. (2018b, Appendix D, p. 124f in this thesis).

[5] van Leer (1984) attributes this method to S. Hancock and the literature adopted the name MUSCL-Hancock method

5.3.1 Determination of c_h

A critical part of the GLM-MHD scheme is the correct treatment of the hyperbolic cleaning speed, c_h. In my implementation, I collect the global maximum of the fast magnetoacoustic eigenvalue found during the flux computations for each cell during the first and second dimensional sweeps. By forcing the ψ waves to be always slower than the fast magnetoacoustic waves, I ensure that the same CFL value can be use regardless of whether or not GLM corrections are applied to the solution. To match the time step computation behavior of the split driver module of `FLASH`, I communicate the new value for c_h only at the end of two time steps using the `MPI_AllReduce` subroutine.

Although this procedure might lead to less effective cleaning (c_h could potentially be larger), it ensures consistency with the way the split driver module advances the simulation and hence seems preferable. To ensure that the maximum time step is not influenced by the choice of c_h here, I offer a runtime parameter for scaling c_h (see the following section).

In the next chapter, I use this parameter to artificially increase the cleaning speed beyond the fast magnetoacoustic wave speed. As the CFL criterion is then dominated by the ψ waves, the time step shrinks accordingly.

5.3.2 Runtime parameters

For this implementation, I offer three runtime parameters to control the behavior of my GLM-MHD solver. They can be set in the parameter file `flash.par`. If not changed explicitly, they default to values I recommend.

`entropyscheme`

Using this runtime parameter, one can select the dissipation scheme used by the solver. This setting defaults to `HYBRIDWAVE`. Possible choices are:

`HYBRIDWAVE` Use selective dissipation scheme with dissipation operator (2.45) (pressure-dependent hybrid dissipation).

`FULLWAVE` Use selective dissipation scheme with dissipation operator (2.42) (wave selective dissipation).

`NOWAVE` Use selective dissipation scheme with dissipation operator (2.34) (scalar dissipation).

`H` Use entropy Jacobian $\mathbf{H}$ described in Derigs et al. (2017) as scalar dissipation operator for computing the entropy stabilization. This corresponds to eq. (2.41) in Sec. 2.6.3.

`LLF` Use local Lax-Friedrichs-like dissipation (as used in Derigs et al., 2017). This scheme is not provably entropy-stable and should only be chosen for testing the entropy behavior.

NONE No entropy stabilization is computed and applied. Note that the scheme will only be valid for purely smooth solutions as it is nearly dissipation-free (modulo the time integrator influence). Thus, physical dissipation necessary near discontinuities is not present in the scheme.

`alphadissipation`

Using this runtime parameter, users can select if they want to use additional damping on the ψ wave as described in Derigs et al. (2018b, Sec. 4.5, p. 105 in this thesis). This setting default to `TRUE`. Dedner et al. (2002), Wesenberg (2003), Tricco & Price (2012), and Derigs et al. (2018b) found that a mixed hyperbolic/parabolic ansatz may lead to the best results with respect to reduced divergence errors. When set to true, the scheme adds a parabolic diffusion to the ψ field. Through the addition of this source term, the ψ field is no longer a conserved quantity but is actively dissipated. Clearly, including such a dissipative term makes the derivation of an entropy conserving scheme impossible. As the contribution to the entropy is guaranteed to have the correct sign and dissipate as the fluid evolves (see Derigs et al., 2018b, Sec. 4.5), it integrates well into my entropy-stable scheme.

`chscaling`

This runtime parameter dictates the scale of the hyperbolic cleaning speed, discussed in Sec. 3.1, to be a fraction of the maximum fast magnetoacoustic speed encountered in the two previous solver sweeps. Setting this value to $\lesssim 0.8$ ensures that there are no overshoots in the GLM propagation due to issues arising from the time step treatment of the split driver module (see Sec. 5.1.2).

5.4 Unsplit staggered mesh (CT) implementation

In addition to the previously described implementations, I wrote an entropy stable Riemann solver for the Unsplit Staggered Mesh (USM) solver available in `FLASH4.5`. The unsplit staggered mesh unit is based on a finite-volume, high-order Godunov method combined with a constrained transport (CT) type of scheme ensuring the solenoidal constraint of the magnetic fields on a staggered mesh geometry. In this approach, the cell-centered variables such as the plasma mass density, momentum, and total plasma energy are updated via a second-order MUSCL-Hancock scheme using high-order Godunov fluxes. The cell face-centered (staggered) magnetic fields are updated using Stokes' Theorem as applied to a set of induction equations, enforcing the divergence-free constraint of the magnetic fields as described in the following.

The overall procedure of the unsplit staggered mesh scheme can be divided into the following steps (see Lee & Deane (2009), Lee (2013), and Flash Center for Computational Science (2017, Sec. 14.3.3)):

1. Data Reconstruction-evolution The solver calculates and evolves interface values for all cells by a half time step using the previously described MUSCL-Hancock algorithm. The approach makes use of a new method of "multidimensional characteristic analysis" achieved in a single time step, incorporating all flux contributions from both normal and transverse directions without the requirement to solve a set of Riemann problems (that is usually adopted in transverse flux updates). In this step, the USM scheme includes the multidimensional MHD terms in both normal and transverse directions, satisfying a perfect balance law for the terms proportional to $\nabla \cdot \boldsymbol{B}$ in the induction equations.

2. Intermediate Riemann problem An intermediate set of high-order Godunov fluxes is calculated using the cell interface values obtained from the data reconstruction-evolution step. The resulting fluxes are then used to evolve the normal fields by a half time step in the next procedure.

3. Half time step update The normal magnetic fields are evolved by a half-time step using the flux-CT method of Balsara & Spicer (1999) at cell interfaces. This method ensures the divergence-free property on a staggered grid. This intermediate update for the normal fields with the half time step data from the data reconstruction-evolution step provide second-order accurate MHD states at the cell interfaces.

4. Flux computation Using the second-order MHD states calculated from the above procedures, my entropy-stable scheme is used to obtain high-order Godunov fluxes at the cell interfaces.

5. Unsplit update of cell-centered variables The unsplit time integrations are performed using the high-order entropy-stable fluxes to update the cell-centered variables for the next time step.

6. Construction of electric fields Using the magnetic field fluxes computed by my entropy-stable MHD solver, the cell-cornered (in 2D, cell-edged in 3D) electric fields are constructed using the so-called *duality relation* between the components of the flux vector and the electric fields. As an example on a two-dimensional grid (as shown in Fig. 5.1), the $E^{n+1/2}_{z,i+1/2,j+1/2}$ field can directly be computed from

$$E^{n+1/2}_{z,i+1/2,j+1/2} = \frac{1}{4}\Big(- \boldsymbol{F}^{n+1/2}_{B_y,i+1/2,j} - \boldsymbol{F}^{n+1/2}_{B_y,i+1/2,j+1} + \boldsymbol{G}^{n+1/2}_{B_x,i,j+1/2} + \boldsymbol{G}^{n+1/2}_{B_x,i+1,j+1/2}\Big) \quad (5.10)$$

7. Flux-CT scheme The electric fields from step 6 are used to evolve the cell face-centered magnetic fields, b, by solving a set of discrete induction equations:

$$b^{n+1}_{x,i+1/2,j} = b^{n}_{x,i+1/2,j} - \frac{\Delta t}{\Delta y}\Big(E^{n+1/2}_{z,i+1/2,j+1/2} - E^{n+1/2}_{z,i+1/2,j-1/2}\Big) \quad (5.11)$$

$$b^{n+1}_{y,i+1/2,j} = b^{n}_{y,i+1/2,j} - \frac{\Delta t}{\Delta x}\Big(E^{n+1/2}_{z,i+1/2,j+1/2} - E^{n+1/2}_{z,i-1/2,j+1/2}\Big) \quad (5.12)$$

in two spatial dimensions (Yee, 1966, Lee & Deane, 2009, eq. 51 & 52).

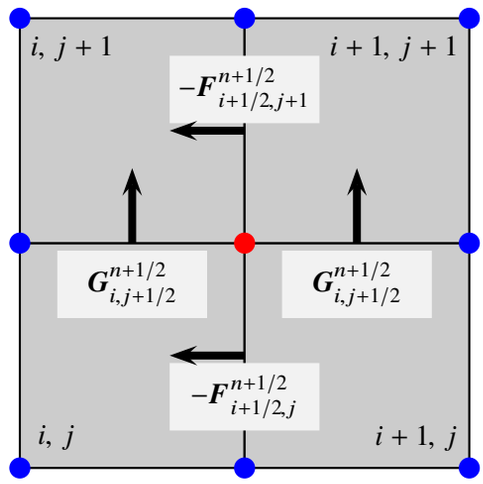

Fig. 5.1: A two-dimensional sketch of the staggered mesh in the flux-CT finite volume scheme. On the staggered mesh the numerical fluxes $\boldsymbol{F}$ and $\boldsymbol{G}$, in x- and y-direction, respectively, are collocated at the centers of cell interfaces and the electric fields E are collocated at the cell corners (blue/red dots).

The resulting magnetic fields satisfy the divergence-free constraint up to the accuracy of machine round-off errors for the chosen discretization,

$$(\nabla \cdot \boldsymbol{b})^{n+1}_{i,j} = \frac{b^{n+1}_{x,i+1/2,j} - b^{n+1}_{x,i-1/2,j}}{\Delta x} + \frac{b^{n+1}_{y,i,j+1/2} - b^{n+1}_{y,i,j-1/2}}{\Delta y}, \tag{5.13}$$

provided that the initial configuration was divergence-free, $(\nabla \cdot \boldsymbol{B})^{n}_{i,j} = 0$.

8. Reconstruct cell-centered magnetic fields Finally, the cell-centered magnetic fields are reconstructed from the divergence free cell-face magnetic fields by taking arithmetic averages of the face variables. Note that, unlike the cell-face magnetic field divergence, the cell-centered magnetic field divergence,

$$(\nabla \cdot \boldsymbol{B})^{n+1}_{i,j} = \frac{B^{n+1}_{x,i+1,j} - B^{n+1}_{x,i-1,j}}{2\Delta x} + \frac{B^{n+1}_{y,i,j+1} - B^{n+1}_{y,i,j-1}}{2\Delta y}, \tag{5.14}$$

is *not* guaranteed to vanish as I have shown in Derigs et al. (2018b, Sec. 5.3, p. 110f in this thesis).

Note that although entropy-stability is not strictly provable due to the flux-CT treatment of the magnetic fields, it may be advantageous to compute the baseline fluxes using an entropy-stable numerical scheme. An advantage of the staggered mesh formalism is that the solver's specific magnetic field divergence is always zero. Thereby, it reduces the amount of work in the solver as the non-conservative terms can safely be assumed to vanish under all circumstances.

Due to the additional computational costs, using the unsplit staggered mesh solver is not feasible for state-of-the-art multi-physics simulations. However, a future implementation of my ideal

GLM-MHD scheme into a new unsplit solver, solely operating on cell-centered quantities, may show advantageous properties with respect to accuracy and robustness at comparably high CFL numbers (see also my comment on this in the Outlook chapter).

6 | An astrophysical application

In this chapter, I will present the application of my new numerical scheme for a state-of-the-art astrophysical research topic. I discuss differences regarding solutions obtained with a standard ideal MHD solver and their possible implications on the obtained results and physical interpretations of the findings.

The formation of molecular clouds is one of the most critical steps in the star formation process. Several publications (see, e.g., Glover et al. (2010) and references therein) suggest that the structure and chemical composition of molecular clouds is largely dependent on the gas morphology's history as , under conditions predominant in molecular clouds, the dynamical and chemical timescales are of the same order.

Hence, all numerical simulations of such scenarios must account for the effects of not only magnetohydrodynamics and self-gravity, but also dust and molecular (self-)shielding, heating and cooling at different gas metallicities, molecule formation and dissociation, stellar feedback, ultraviolet (UV) radiation, X-rays, and cosmic rays from diffuse interstellar radiation.

To account for all these effects, the SILCC project[6] (Walch et al., 2015; Girichidis et al., 2016) developed an encompassing multi-physics framework with which they modeled representative regions of disk galaxies. They include the necessary physical complexity to follow the full life-cycle of molecular clouds.

A critical question in the applicability of my new scheme to astrophysical simulations is the divergence cleaning efficiency in application-ready multi-physics environments. The evidence

[6] SILCC = Simulating the Life-Cycle of molecular Clouds

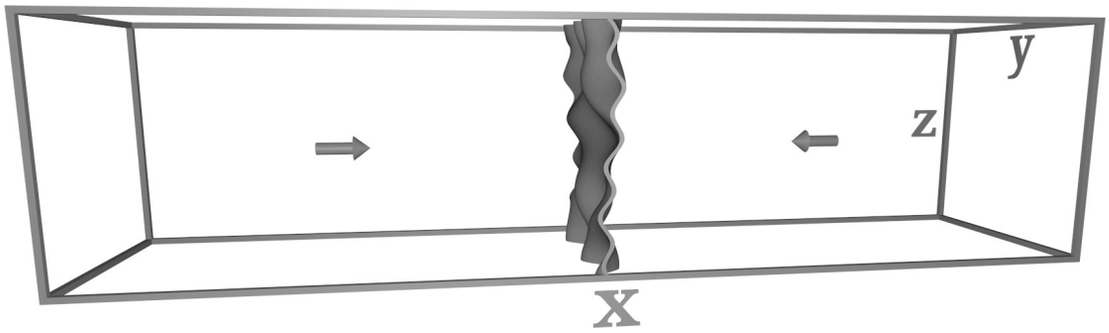

Fig. 6.1: 3D sketch of the simulation domain. Gas is inflowing towards the center of the domain where it then collides at a non-uniform interface to form turbulent structures.

presented in my papers (esp. Derigs et al., 2018b) proves high cleaning efficiency for dimensionless simulations. This chapter investigates the cleaning efficiency in full astrophysical applications.

6.1 The colliding flow model

An astrophysically interesting application is the "colliding flow" scenario where two gas flows, representative for the warm neutral medium, collide at an irregular interface. In this setup, various dynamical and thermal instabilities lead to the generation of turbulence in the collision area and eventually to the formation of a molecular cloud. Kinetic energy is naturally injected through the continually inflowing warm neutral medium onto the collision zone. The constant energy input by the inflowing gas sustains the generated turbulence self-consistently.

The usefulness of this particular scenario has been demonstrated in many publications. It has been shown that realistic clumps of molecular gas form quickly in the resulting dense molecular medium (see e.g., Ballesteros-Paredes et al., 1999; Heitsch et al., 2006; Vázquez-Semadeni et al., 2007; Hennebelle & Audit, 2007; Hennebelle et al., 2008; Banerjee et al., 2009; Clark et al., 2012; Körtgen & Banerjee, 2015; Fogerty et al., 2016; Joshi et al., 2018). Furthermore, Klessen & Hennebelle (2010) and Valdivia et al. (2016) showed that colliding flow simulations can reproduce the typical velocity dispersions and column densities observed in real molecular clouds. Due to this, simulations of colliding flows are a promising tool for studying the emergence and evolution of molecular clouds.

The particular setup I use for the simulations presented in this chapter has recently been described by Joshi et al. (2018, Sc. 3.2). I repeat their three-dimensional multi-physics simulations with my new numerical scheme to compare the properties of the generated molecular clouds. All simulations are computed with CFL = 0.5.

The sole purpose of the present discussion is the investigation of differences in the solutions and statistical properties obtained using my new Galilean-invariant entropy-stable ideal GLM-MHD scheme.

6.2 Simulation setup

In Fig. 6.1, I depict a three-dimensional sketch of the simulation setup. The computational domain has the extent $128\,\mathrm{pc} \times 32\,\mathrm{pc} \times 32\,\mathrm{pc}$ ($x \times y \times z$). It is filled with a uniform gaseous medium resembling the warm neutral medium of the ISM ($n = 1\,\mathrm{cm}^{-3}$, sound speed $c_s = 7.8\,\mathrm{km\,s}^{-1}$, corresponding to a temperature of $T = 5541\,\mathrm{K}$). The boundary conditions are set to inflow in the $x-$direction where gravity is set to isolated boundaries[7]. For the $y-$ and $z-$directions, I use fully periodic boundary conditions.

A non-uniform collision interface is established at the center of the computational domain. Inflowing warm gas colliding at the interface triggers the onset of turbulence immediately at the beginning of the simulation. The inflowing gas is modeled by directing the medium with a velocity of $v = 13.6\,\mathrm{km\,s}^{-1}$ towards the collision interface. This inflow is indicated by arrows in Fig. 6.1.

The spatial resolution of the simulations was chosen to be (a) low enough to be still affordable in terms of computational resources, and (b) high enough to resolve all interesting effects. Seifried et al., 2017, Sec. 6 recommend a resolution of $\lesssim 0.1\,\mathrm{pc}$ to obtain realistic morphological and dynamical properties in astrophysical applications. I configured the adaptive mesh refinement (AMR) to go from level 4 to 6, corresponds to a minimum grid size of 0.125 pc to approximately meet this criterion.

6.3 Non-magnetized colliding flow

Firstly, I ran the colliding flow simulation without any magnetic field to compare the hydrodynamic properties of the schemes. The temporal evolution of a few interesting simulation quantities such as the simulation time step or the global minimum temperature is plotted in Fig. 6.2. As can be seen in the uppermost plot in this figure, the amount of computational cells is of the same order compared to the `Bouchut5` scheme (Bouchut et al., 2010; Waagan et al., 2011). It is interesting to note that my solver behaves very similar and starts to deviate only at later times ($t > 20\,\mathrm{Myr}$). The slight difference in the number of computational blocks results from a different density structure that has developed during the highly non-linear simulation and should be understood as a feature of this particular simulation rather than as a general trend.

The second plot from the top in Fig. 6.2 shows the time step size used by the schemes. The arrows depict the time when the simulation first refined to the maximum allowed AMR level. We see that the overall magnitude of the time step is comparable between `Bouchut5` and my solver. In the bottom two plots of Fig. 6.2, I show the global maximum density and minimum temperature. The obtained results are in good agreement with each other.

In Fig. 6.3, I plot the cell mass distribution as two-dimensional profiles of temperature against density at $t = 28\,\mathrm{Myr}$. Three cell mass extrema can be identified in this plot:

[7] Isolated gravity boundaries mean that no gas outside of the box is considered for the gravitational potential.

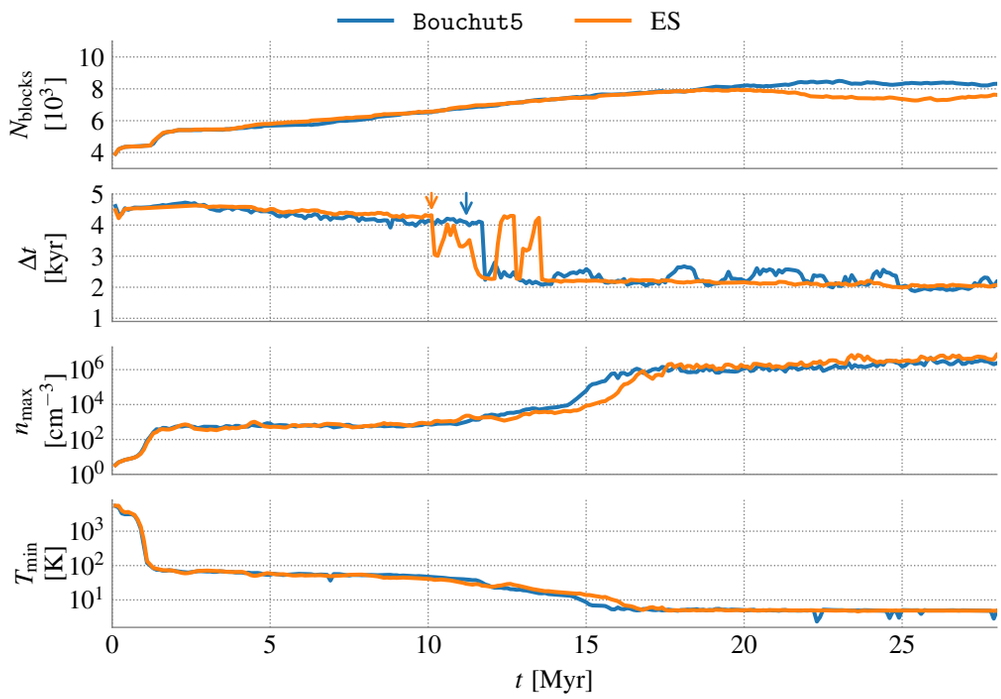

Fig. 6.2: Plot showing the temporal evolution of some simulation properties. From top to bottom: Total number of computational blocks in the grid (a computational block is composed of 8^3 cells); time step size; global maximum density (non-weighted); global minimum temperature (non-weighted).

1. A maximum in the top left corner corresponds to the inflowing warm neutral medium ($n = 1\,\text{cm}^{-3}$, $T = 5541\,\text{K}$),
2. A broad extremum around the center corresponds to gas pilled up in the collision volume ($n \approx 1 \times 10^2\,\text{cm}^{-3}$, $T \approx 100\,\text{K}$), and
3. A tail at the end of the phase plot ($n > 1 \times 10^6\,\text{cm}^{-3}$, $T < 10\,\text{K}$) corresponding to the gas that has collapsed into molecular cores.

Overall, the statistical properties of both simulations are comparable.

6.4 Magnetized colliding flow

For investigating the effect of magnetic fields on the emerging molecular cloud, an identical setup with the addition of a uniform initial magnetic field aligned with the inflow in x-direction is applied to the medium. Weis et al. (2018) investigated the evolution of the colliding flow influenced by magnetic fields varying from 0 µG to 10 µG in initial field strength. For the sake of brevity, I limit my comparison in here to one average magnetic field strength of 2.5 µG.

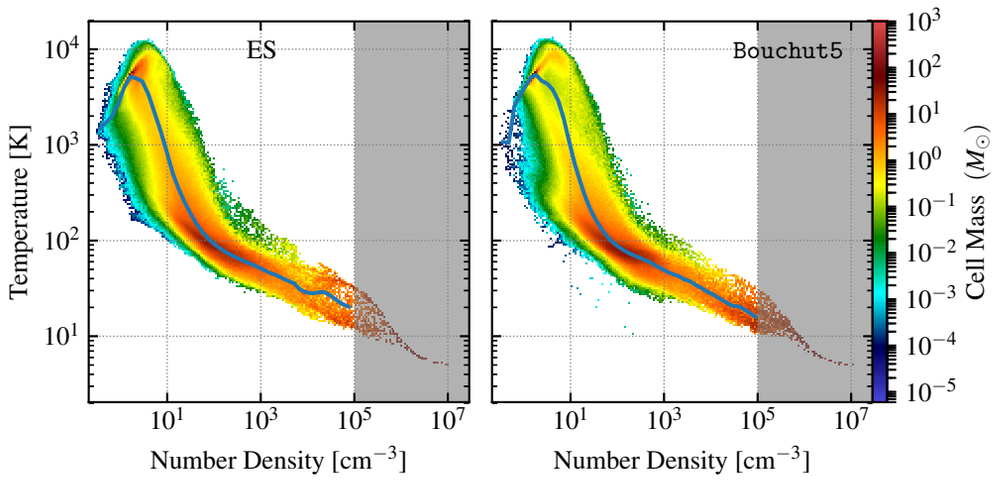

Fig. 6.3: Two-dimensional profile plots of the cell mass distribution in dependence of temperature and density at $t = 28\,\mathrm{Myr}$. The color of the pixels correspond to the mass found in a given density/temperature bin. The overplotted lines show the average temperature for a given density bin. The shaded region corresponds to gas densities that are not Jeans resolved, i.e., where the gravitational infall is no longer accurately resolvable at the given spatial resolution. Three distinct regions with high mass can be identified (see text).

In the forthcoming plots, I sometimes include two plots for the `Bouchut5` scheme, representing two different source term implementations (once with the Powell and once with the Janhunen terms). The Janhunen terms based implementation of the scheme is used in state-of-the-art simulations, e.g., by Walch et al. (2015), Girichidis et al. (2016), more recently Seifried et al. (2018a) and Weis et al. (2018). For the sake of completeness, I present a detailed discussion about the implications of this difference in implementation in the appendix of this thesis. It is of no immediate relevance for the present discussion. I primarily compare my new entropy stable scheme against the `Bouchut5` solutions with the **Powell** terms as this implementation is physically more meaningful (see appendix and also Derigs et al., 2018b, Sec. 3.8, p. 93f in this thesis).

6.4.1 The dissipation factor α

In Derigs et al. (2018b, Sec. 4.5, p. 105 in this thesis), we described a mixed hyperbolic/parabolic GLM ansatz. This approach gives very good results and has been found to be even necessary for periodic boundary conditions. The additional source term enters the ideal GLM-MHD equations in form of

$$\frac{\partial}{\partial t}\psi = -\alpha\psi, \tag{6.1}$$

with a dissipation factor $\alpha \in [0, \infty)$. In discretized form, eq. (6.1) reads

$$\psi^{n+1} = -\Delta t^n \alpha^n \psi^n. \tag{6.2}$$

In Derigs et al. (2018b), we confirmed the finding of Dedner et al. (2002) that

$$\alpha = \frac{c_h}{0.18} \tag{6.3}$$

gives satisfactory results for dimensionless simulations.

In the present astrophysical setup, however, I found that this choice is too restrictive as α is too large. This is caused by the typically very large time steps ($\Delta t \sim$ a few kyr) in conjunction with the typically very large speeds in the simulations[8] leading to a large value of c_h and hence α.

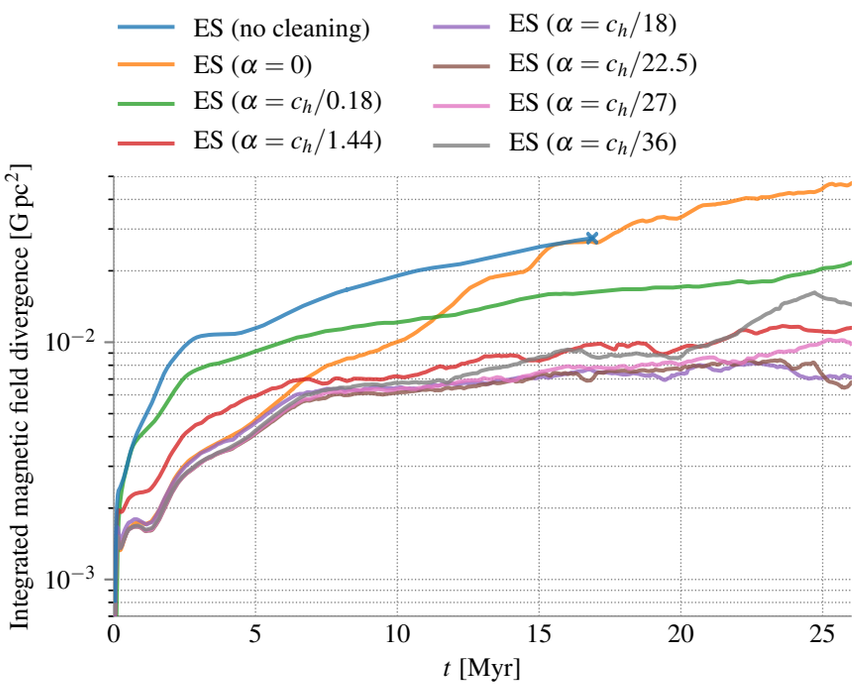

Fig. 6.4: Plot of the volume-integrated absolute magnetic field divergence. I plot difference possibilities for the dissipation parameter α. The cleaning speed is not altered ($1 \times c_h$, see also Sec. 6.4.2). The no cleaning simulation was terminated early to save computational resources. For the remainder of this work, I use $\alpha = c_h/22.5$ (brown line). This plot shows

$$|\nabla \cdot \boldsymbol{B}|_{\text{global}} = \int |\nabla \cdot \boldsymbol{B}| \, \mathrm{d}V$$

In Fig. 6.4, I plot the absolute volume-integrated magnetic field divergence for different values of the dissipation parameter α. It is obvious that magnetic cleaning is necessary in order to control the global magnetic field divergence as it otherwise grows over time as depicted by the blue line in Fig. 6.4. without divergence cleaning. We see that the mixed ansatz (hyperbolic +

[8] typically on the order of several kilometers per second

parabolic) is necessary to keep the long-term magnetic field divergence low. If one would use only hyperbolic GLM, the periodicity of the computational domain would only lead to an ever increase of complexity in the ψ field, leading to highly complex morphologies that cannot be cleaned in a timely fashion (see $\alpha = 0$, orange line). Due to various interference phenomena of ψ waves, the GLM correction can even be adverse so that the long-term magnetic field divergence can increase further when no additional damping is applied on the ψ field.

I found that a reduced parabolic dissipation factor $\alpha \sim c_h/22.5$ gives the best results over the entire evolution of the simulation. I use this value of α for the remainder of this chapter.

6.4.2 The divergence cleaning efficiency

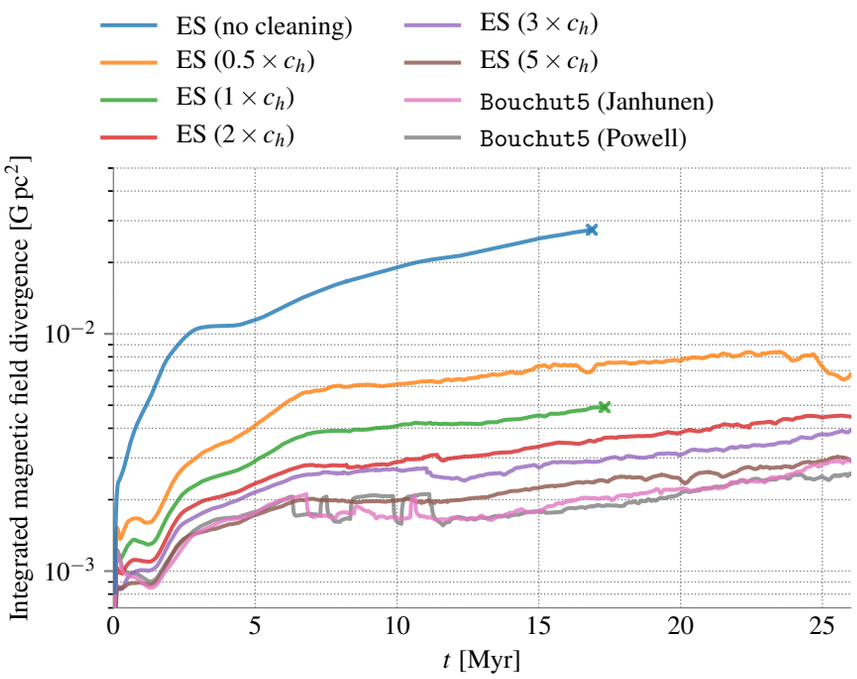

Fig. 6.5: Plot of the volume-integrated absolute magnetic field divergence for difference scalings of the cleaning speed c_h. Crosses mark simulations I terminated early to save computational resources. In the forthcoming analysis, I focus on the $5 \times c_h$ simulation as it shows the lowest global magnetic field divergence. This plot shows the same quantity as in Fig. 6.4.

In Fig. 6.5, I plot the integrated magnetic field divergence for various cleaning speeds c_h. We see that the cleaning efficiency increases with increasing cleaning speed. This is expected as the higher speeds leads to a faster transport of the ψ correction field and hence a faster correction of magnetic field divergence errors. For comparison, I add the measured integrated magnetic field divergence for the `Bouchut5` solver (once with the Janhunen and once with the Powell source term, see also the appendix of this thesis).

As described in Derigs et al. (2018b, Sec. 3.7, p. 93 in this thesis), the cleaning speed, c_h, directly influences the time step of the simulation. In my code, I compute c_h by

$$c_h = \texttt{chscaling} \times \max_{\Omega}(c_f) \tag{6.4}$$

where $\max_{\Omega}(c_f)$ is maximum fast magnetoacoustic wave speed in the entire simulation domain. The parameter `chscaling` dictates the scale of the hyperbolic cleaning speed. It is discussed in Sec. 5.3.2.

Using `chscaling` > 1, it is possible to select values for c_h that exceed $\max_{\Omega}(c_f)$. This leads to the CFL criterion being dominated by the dynamics of the GLM-waves and, hence, will shrink the (global) time step.

In my tests, I see the best cleaning behavior for the simulation with a fivefold upscaled cleaning speed, $5 \times c_h$. The increase in cleaning speed immediately reduces the time step size by a factor of five, just as expected. It is clear that such a decrease in the global time step is not feasible for large-scale astrophysical simulations. However, the purpose of this chapter is to compare the solution of my solver and the existing `Bouchut5` solver. Later in this chapter, I revisit the problem of reduced time steps and present a solution for practical astrophysical simulations.

6.4.3 Simulation properties

In Fig. 6.6, I plot the same quantities as already shown for the simulations without magnetic fields. As in the non-magnetized case, I find here that my new entropy stable scheme requires a nearly identical number of computational blocks as the `Bouchut5` run. Looking at the time step size, we see that the "ES $(1 \times c_h)$" scheme uses a comparable, but slightly smaller time step compared to the `Bouchut5` solver. This is expected, as the time step criterion for the `Bouchut5` solver is determined by a combination of the Alfvén and the hydrodynamical sound speed (Waagan et al., 2011, Sec. 2.5), whereas my scheme uses the fastest wave speed of the ideal GLM-MHD system[9] for determining the maximum time step being smaller under the same CFL condition.

As before, the global minimum temperatures obtained in the simulations are in good agreement. The ES $(5 \times c_h)$ run produces higher densities sooner in the evolution of the simulation, leading to an earlier structure formation.

[9] This is usually the magnetoacoustic wave speed, however, when c_h is scaled up, the GLM waves, $\lambda_{\pm\psi} = u \pm c_h$, provide the predominant wave speed.

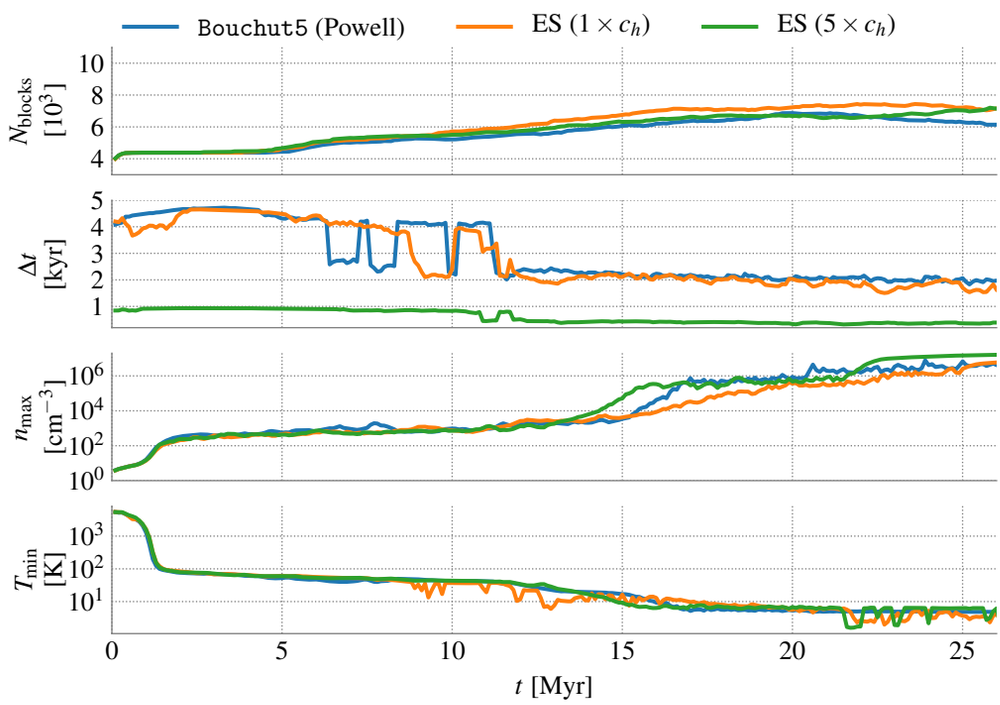

Fig. 6.6: Plot showing the temporal evolution of some simulation properties (magnetized colliding flow). From top to bottom: Total number of computational blocks in the grid; time step size; global maximum density (non-weighted); global minimum temperature (non-weighted). The arrows mark the time when the individual simulations first refined to the highest available AMR level.

6.4.4 Column densities

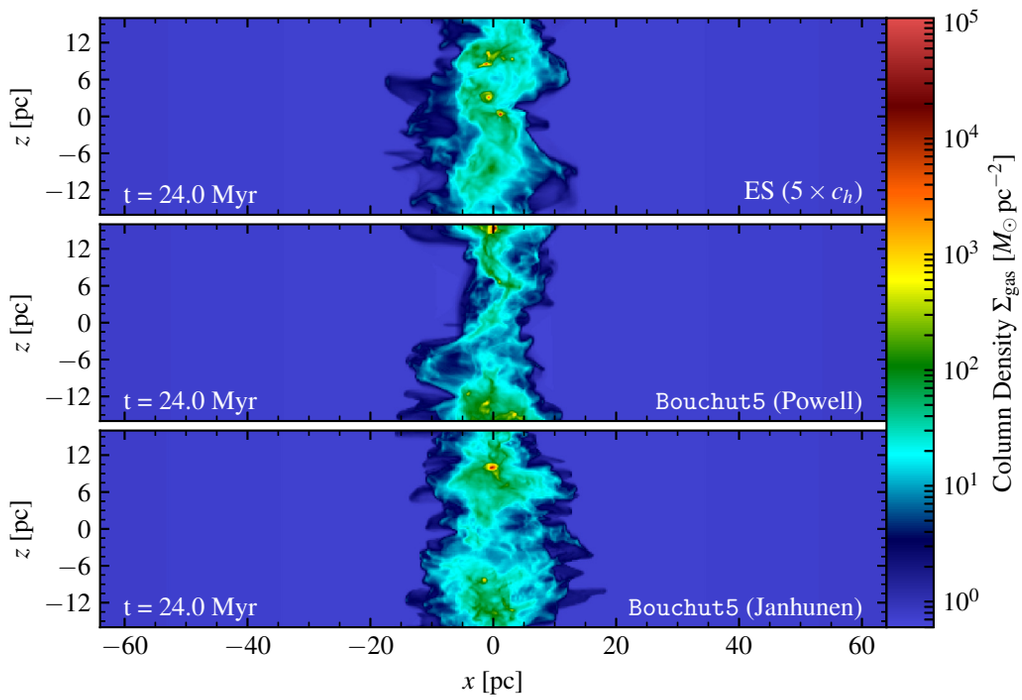

Fig. 6.7: Total gas column density at $t = 24\,\text{Myr}$. This plot shows

$$\Sigma_{\text{gas}} = \int \rho(x, y, z)\, \hat{y}\, \mathrm{d}y.$$

In Fig. 6.7, I show column density maps of the total gas by new entropy stable scheme, as well as the `Bouchut5` scheme at $t = 24\,\text{Myr}$. We see that the thickness of the collision region is similar across all three results. The most prominent difference is that a larger number of more concentrated core clumps[10] are produced by the simulation using my scheme compared to the typical clouds generated by the `Bouchut5` scheme. The `Bouchut5` (Janhunen) result is more diffuse and shows an overall less dense structure. These observations are confirmed by the evolution of the dense gas[11] mass fraction, shown in Fig. 6.8. The evolution of the ratio of dense to total gas mass in the system continuously increases due to the constant inflow of gas onto the collision interface and the gravitational collapse of gas into molecular cloud cores. At $t = 24\,\text{Myr}$, the dense gas mass fraction of the ES result lies in between the results obtained using the two `Bouchut5` results.

[10] I denote high-density regions as cores when a surface density of larger than $\Sigma_{\text{gas}} \approx 10^4\, M_\odot\,\text{pc}^{-2}$ is seen in the projection plots. Using 3D data inspection, I ensured that the identified cores are not caused by projection effects but are actual singly connected structures.

[11] $\rho \geq 2.34 \times 1.67 \times 10^{-22}\,\text{g cm}^{-3}$

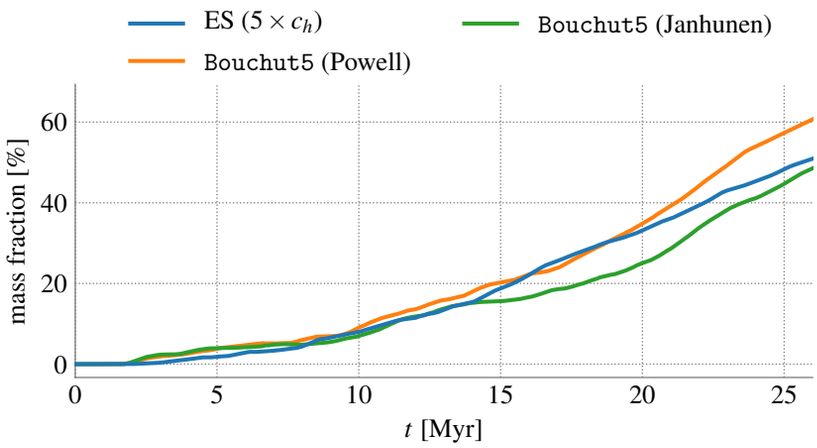

Fig. 6.8: Dense gas mass fraction ($\rho \geq 2.34 \times 1.67 \times 10^{-22}\,\mathrm{g\,cm^{-3}}$). This plot shows

$$\frac{M_\rho}{M_\text{total}} = \frac{\int \rho(x,y,z)|_{\rho \geq 2.34 \times 1.67 \times 10^{-22}\,\mathrm{g\,cm^{-3}}}\,\mathrm{d}V}{\int \rho(x,y,z)\,\mathrm{d}V}.$$

6.4.5 Plasma-β

In Fig. 6.9, I plot the mass-weighted projections of plasma-β. The beta of a plasma is the ratio of the thermal pressure p_therm to the magnetic pressure p_mag. It is used to measure their relative importance in a given fluid. In the projection plot, reddish gas is thermally dominated ($\beta > 1$), whereas blueish gas is magnetically dominated ($\beta < 1$). White regions are in an equilibrium state ($\beta \approx 1$). We see that the dynamics of the gas are slightly more magnetically dominated in the solution obtained using my entropy stable GLM-MHD solver.

For the sake of convenience, I overplot black crosses at the locations of the molecular cloud cores in Fig. 6.9. This makes it easier to see that molecular cores form both within magnetically and thermally dominated regions. This is in agreement with the results obtained using the `Bouchut5` (Powell) solver and highlights the importance of a physically consistent magnetic field treatment when studying the creation and evolution of molecular clouds in magnetized simulations.

In Fig. 6.10, I plot the temporal evolution of the magnetically dominated gas mass fraction (plasma-β criterion). We see that the temporal evolution is similar for the first $\approx 12\,\mathrm{Myr}$. Later on, my entropy stable scheme produces a slightly higher percentage of magnetically dominated gas than the `Bouchut5` solver. This is in agreement with the observations in Fig. 6.9 where we have seen extended magnetically dominated regions in the ES results but much less magnetically predominance in the `Bouchut5` (Janhunen) simulation.

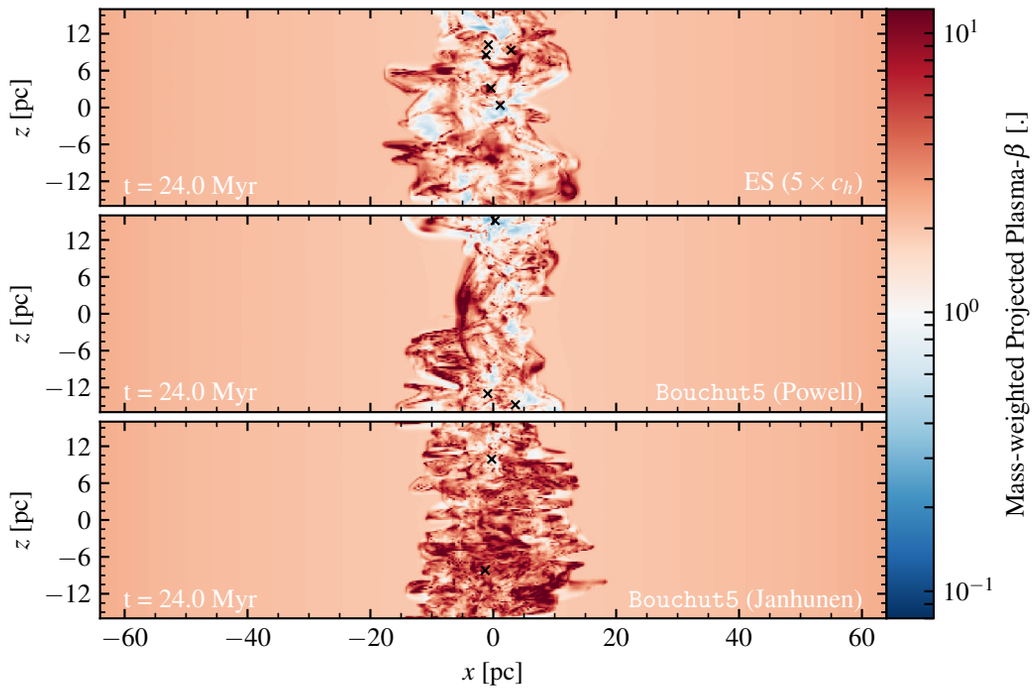

Fig. 6.9: Mass-weighted projected plasma β at $t = 24\,\mathrm{Myr}$. The black crosses correspond to the molecular cloud cores visible in the surface density plots (Fig. 6.7). This plot shows

$$\overline{\beta} = \frac{\int \beta(x,y,z)\rho(x,y,z)\,\hat{y}\,\mathrm{d}y}{\int \rho(x,y,z)\,\hat{y}\,\mathrm{d}y}, \qquad \text{with} \qquad \beta = \frac{p_\mathrm{therm}}{p_\mathrm{mag}} = \frac{nk_\mathrm{B}T}{\frac{1}{2\mu_0}\|\boldsymbol{B}\|^2}.$$

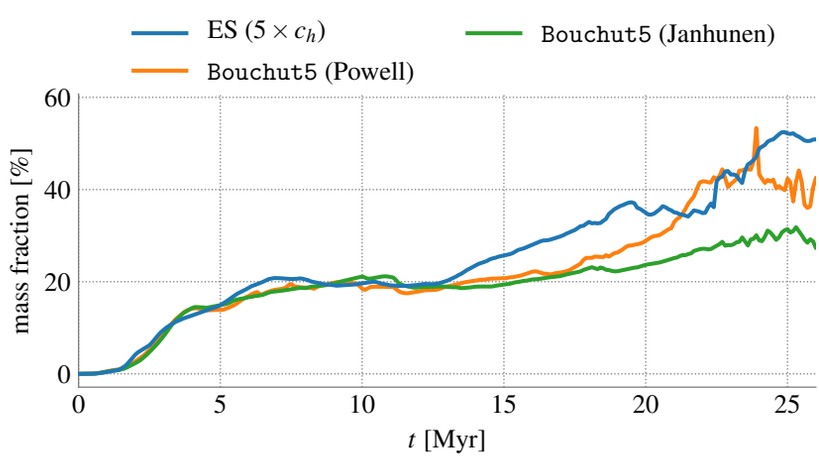

Fig. 6.10: Magnetically dominated gas mass fraction (plasma $\beta < 1$). This plot shows

$$\frac{M_{\beta<1}}{M_\mathrm{total}} = \frac{\int \rho(x,y,z)|_{\beta<1}\,\mathrm{d}V}{\int \rho(x,y,z)\,\mathrm{d}V}.$$

6.4.6 Average magnetic field

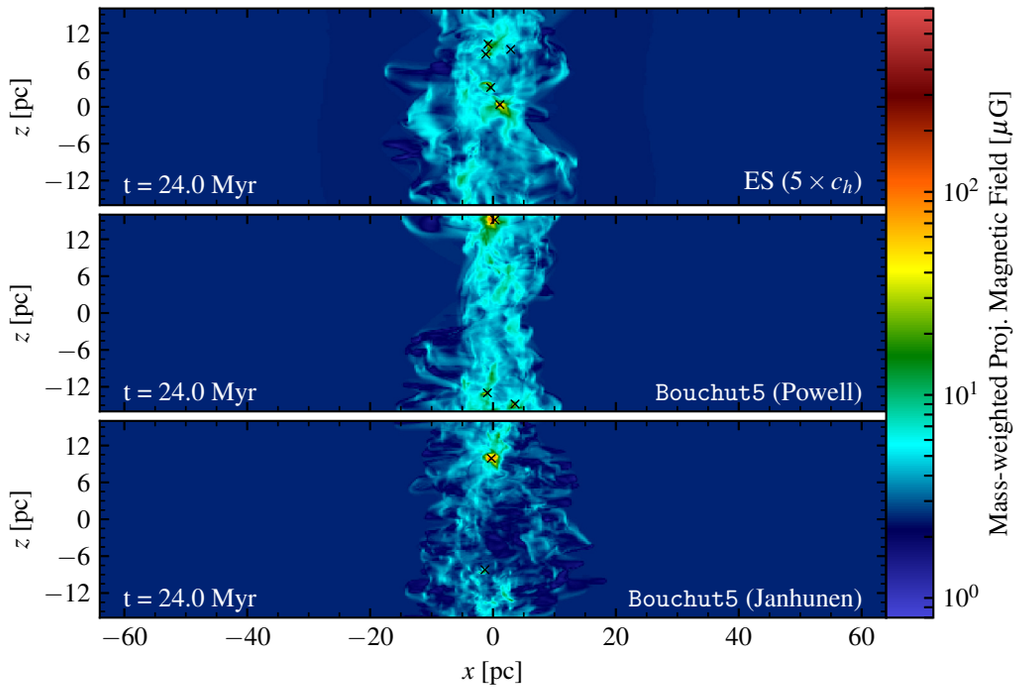

Fig. 6.11: Mass-weighted projected magnetic field strength at $t = 24\,\mathrm{Myr}$. The black crosses correspond to the molecular cloud cores visible in the surface density plots (Fig. 6.7). This plots shows

$$\overline{B} = \frac{\int \|\boldsymbol{B}(x,y,z)\| \rho(x,y,z)\, \hat{y}\, \mathrm{d}y}{\int \rho(x,y,z)\, \hat{y}\, \mathrm{d}y}.$$

In Fig. 6.11, we see that the magnetic field is dominant in some, but not all, cloud cores. The lower and more scattered magnetization found in the `Bouchut5` (Janhunen) runs is in disagreement with the other two results. However, as mentioned earlier, the Janhunen term based result is physically questionable.

The result supports the prevalence of magnetic effect in the dynamics of the forming molecular clouds.

6.4.7 Gas energies

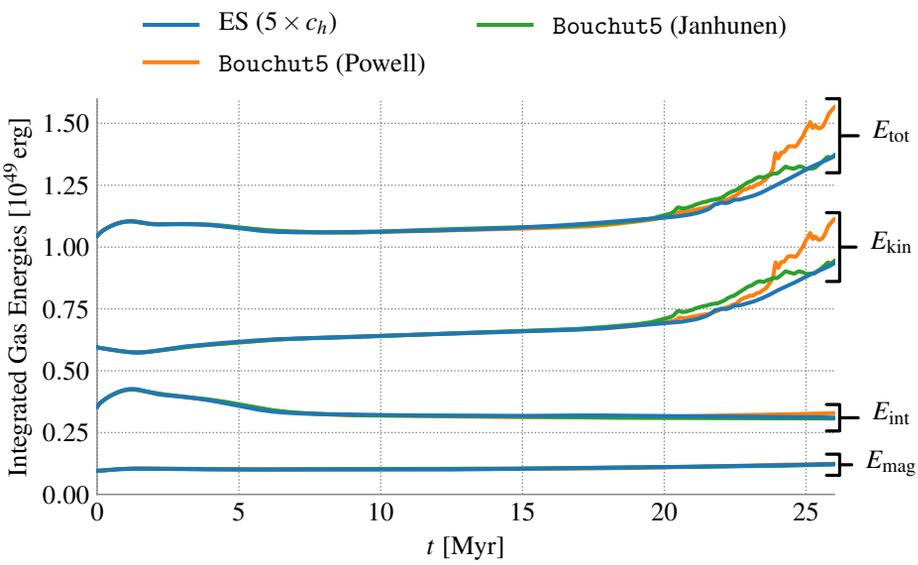

Fig. 6.12: Volume-integrated gas energies in the simulation.

In Fig. 6.12, I plot the volume-integrated fluid energies,

$$E_{\text{tot}} = \int E(x, y, z)\, \mathrm{d}V, \tag{6.5}$$

$$E_{\text{mag}} = \frac{1}{2\mu_0} \int \|\boldsymbol{B}(x, y, z)\|^2\, \mathrm{d}V, \tag{6.6}$$

$$E_{\text{kin}} = \frac{1}{2} \int \rho(x, y, z) \|\boldsymbol{u}(x, y, z)\|^2\, \mathrm{d}V, \text{ and} \tag{6.7}$$

$$E_{\text{int}} = E_{\text{tot}} - \left(E_{\text{kin}} + E_{\text{mag}}\right). \tag{6.8}$$

The GLM energy,

$$E_{\psi} = \frac{1}{2\mu_0} \int \psi(x, y, z)^2\, \mathrm{d}V, \tag{6.9}$$

is not shown as it is, at all times, several orders of magnitude smaller than the other forms of energy. Note that the gravitational energy is not contained in these plots as the MHD scheme itself is unaware of the effects of gravity (implementationwise, they are added in a separate step as source terms on momentum and kinetic energy).

We see a large agreement between the integrated energies across all three solvers. They only start to differ very late in their evolution when, e.g., the gravitational collapse into very few, very massive molecular cores becomes the dominant contribution for the generated kinetic energy in the `Bouchut5` (Powell) simulation.

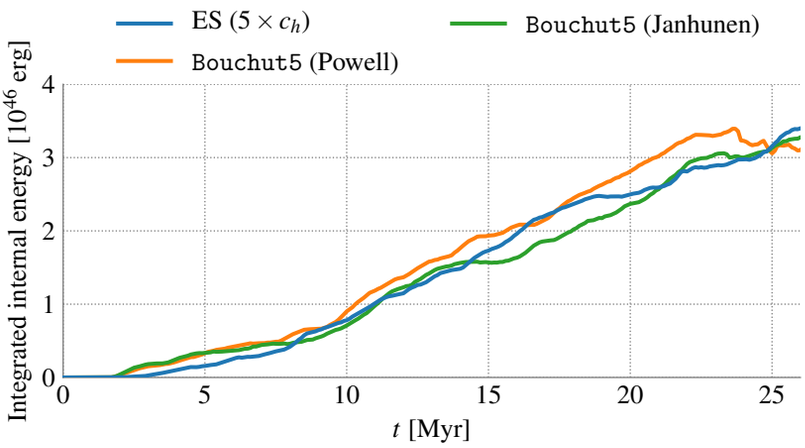

Fig. 6.13: Integrated internal energy in the dense gas ($\rho \geq 2.34 \times 1.67 \times 10^{-22}\,\mathrm{g\,cm^{-3}}$).

As the internal energy is dominated by the inflowing warm neutral medium[12], I plot the volume-integrated internal energy of only the dense gas in Fig. 6.13. We see that the integrated internal energy behaves similar across all simulations. It should, however, be noted that general statements about the behavior of the internal energy in multi-physics simulations are difficult as the gas is not only subject to adiabatic processes but also affected by heating and cooling. Especially the cooling processes are of great importance in the present simulations as the forming molecular cloud cores are, to a large degree, optically thin and can efficiently radiate away thermal energy. This cooling mechanism is likely the predominant effect in the high-density cores and continuously alters the temperatures seen by the MHD solver.

6.4.8 Temperatures

In Fig. 6.14, I show two-dimensional cell mass profiles similar to those I have shown for the simulations without magnetic fields (Fig. 6.3). They confirm that the statistical properties of the simulations are comparable with one notable difference found in the region $\rho \in [1 \times 10^3\,\mathrm{cm^{-3}}, 1 \times 10^5\,\mathrm{cm^{-3}}]$, $T \approx 100\,\mathrm{K}$. The gas found in this interval corresponds to intermediate density gas surrounding the central collision zone. This gas is visible in mass-weighted temperature projection plots (see Fig. 6.15) (located around $x = 0$, the position of the initial collision interface).

[12] Temperature of the inflowing gas: $T_{\mathrm{in}} = 5541\,\mathrm{K}$

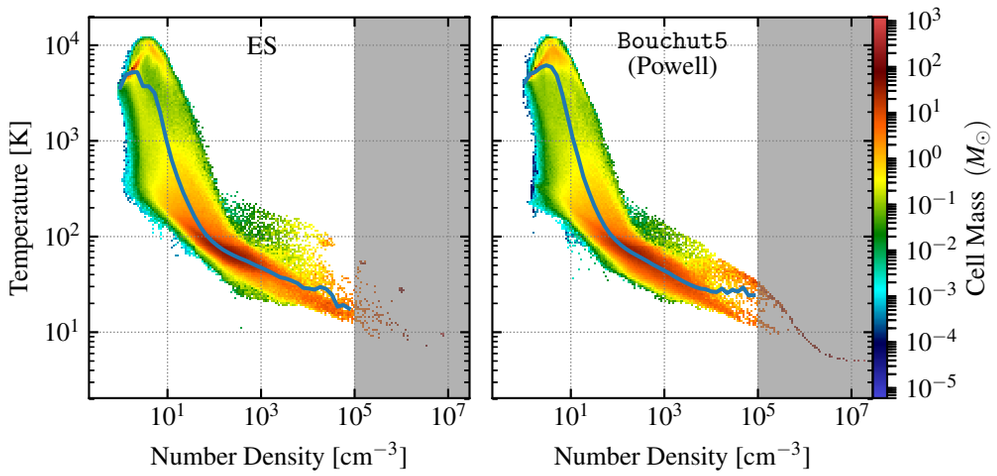

Fig. 6.14: Two-dimensional cell mass profile plots showing temperature against number density at $t = 24\,\mathrm{Myr}$. The color of the pixels correspond to the mass found in a given density/temperature bin. The overplotted lines show the average temperature for a given density bin. The shaded region corresponds to gas densities that are not Jeans resolved at the given spatial resolution.

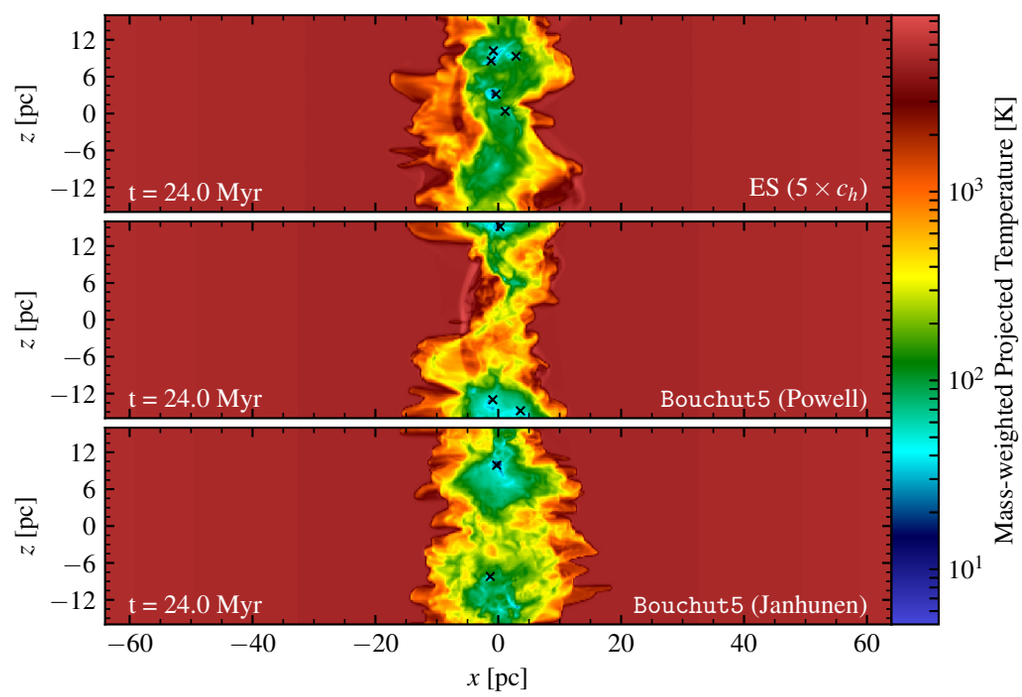

Fig. 6.15: Mass-weighted projected temperature at $t = 24\,\mathrm{Myr}$. The black crosses correspond to the molecular cloud cores visible in the surface density plots (Fig. 6.7). This plot shows

$$\overline{T} = \frac{\int T(x,y,z)\rho(x,y,z)\,\hat{y}\,\mathrm{d}y}{\int \rho(x,y,z)\,\hat{y}\,\mathrm{d}y}.$$

6.5 Applicability in state-of-the-art simulations

As I pointed out in Sec. 6.4.2, I see the best cleaning behavior for the simulation with a fivefold upscaled cleaning speed, $5 \times c_h$. As increases in cleaning speed immediately shrink the size of the global time step, it is clear that such a scheme is not feasible for large-scale astrophysical simulations. There are two solutions for this issue:

1. Implement subcycling for the MHD solver, and
2. Augment the system with a further divergence-control mechanism.

Subcycling for the MHD solver

Subcycling allows different time step sizes to be used for different parts of a simulation code. It can efficiently reduce the overall run time for a simulation when a comparably small module in the code controls the global time step. In the colliding flow simulations, the MHD solver only uses about 6 % of the overall computing time whereas other modules, such as gravity (using approximately 60 % of the total runtime), dominate the computational costs of the simulation.

The idea of subcycling is to run smaller modules several times in a row (with correspondingly reduced time steps) without enforcing the small time steps also for the other, more expensive, parts of the code. This increases the overall efficiency of the numerical implementation. In `FLASH`, subcycling is already successfully used for the chemistry module which computes the chemical evolution of the gas using a chemical network. This module regularly requires smaller time steps for its integration. Therefore, to not affect the global time step, subcycling is employed.

A similar subcycling could be implemented for the MHD solver to allow for an upscaling of the cleaning speed, c_h, at manageable additional computational costs. It would allow using a larger c_h at the same global time step without violating the CFL condition.

An additional divergence-control mechanism

A further possibility is to augment the entropy stable MHD solver with a similar post-processing divergence-control step as used, e.g., in the `Bouchut5` and other `split` MHD solvers available for `FLASH`. The entropy stable solver equipped with this divergence treatment as an *additional post-processing* step is denoted as "ES (divbdiffuse)". The post-processing step is implemented in an entropy aware manner by ensuring that neither the density not the thermal pressure change during the procedure. This requires an adjustment of the gas total energy to account for the changed magnetic field morphology caused by this post-processing step.

As can be seen in Fig. 6.16, the magnetic field divergence cleaning properties of the "ES (divbdiffuse)" are similar as in the `Bouchut5` runs and slightly improved compared to the "ES ($5 \times c_h$)" simulation.

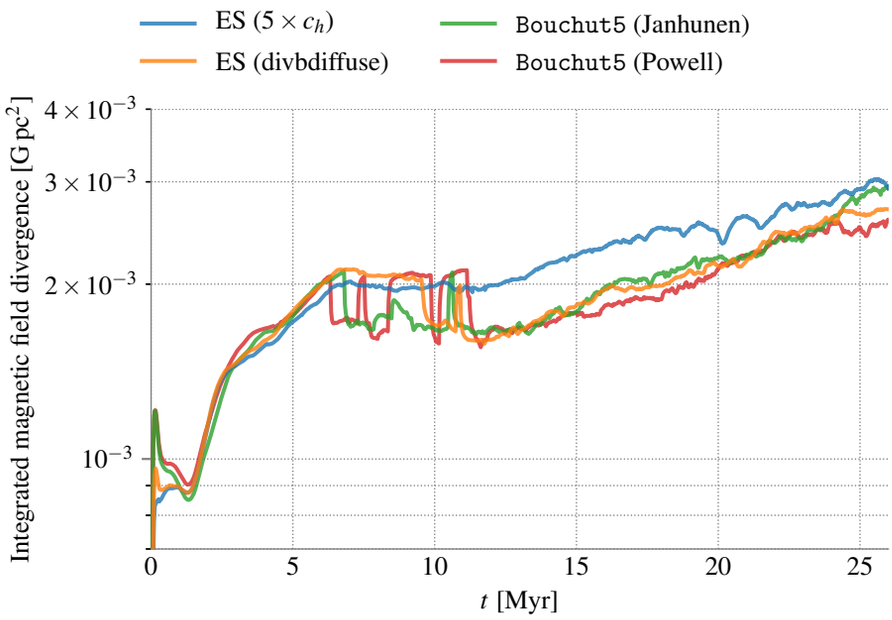

Fig. 6.16: Plot of the volume-integrated absolute magnetic field divergence. This plot shows the same quantity as in Fig. 6.5 (different scale).

In Fig. 6.17, I show the mass-weighted and maximum absolute magnetic field divergence over time. We see that all schemes agree within roughly one order of magnitude. This is in agreement with the integrated absolute magnetic field divergence plot (Fig. 6.16) and furthermore confirms that the magnetic cleaning works correctly also in the most active regions undergoing gravitational collapse.

In Fig. 6.18 – 6.21, I show similar projection plots to what I discussed in details already before. We see that the properties of the "ES (divbdiffuse)" scheme are very similar to the reference scheme. Hence, the "ES (divbdiffuse)" is a promising alternative to a GLM-only entropy stable MHD solver for the high demands of astrophysical simulations.

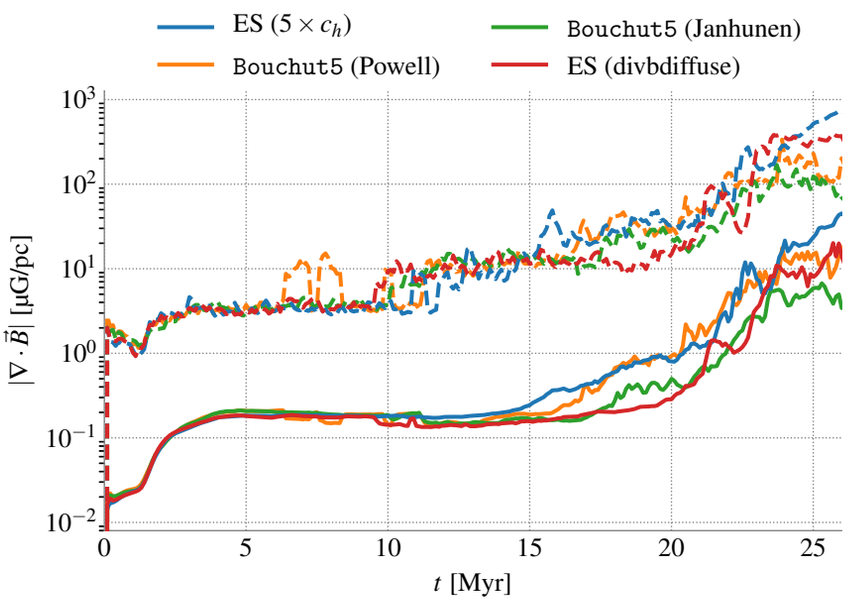

Fig. 6.17: Plot of the absolute magnetic field divergence. Solid lines: Mass-weighted average. Dashed lines: Absolute maximum in the entire domain.

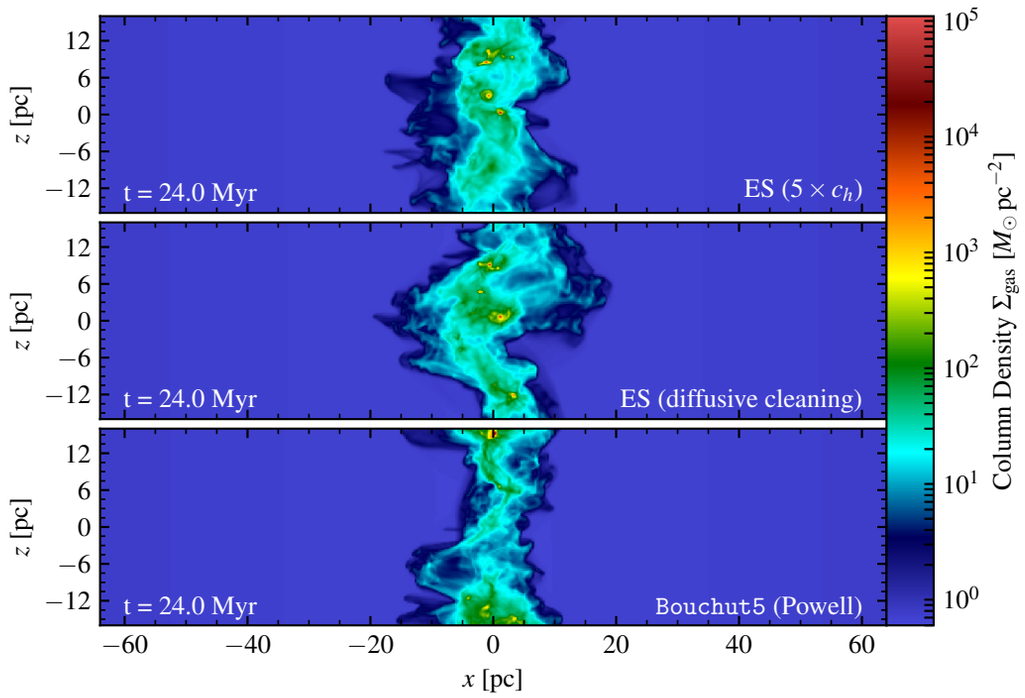

Fig. 6.18: Total gas column density at $t = 24$ Myr. Compare to Fig. 6.7.

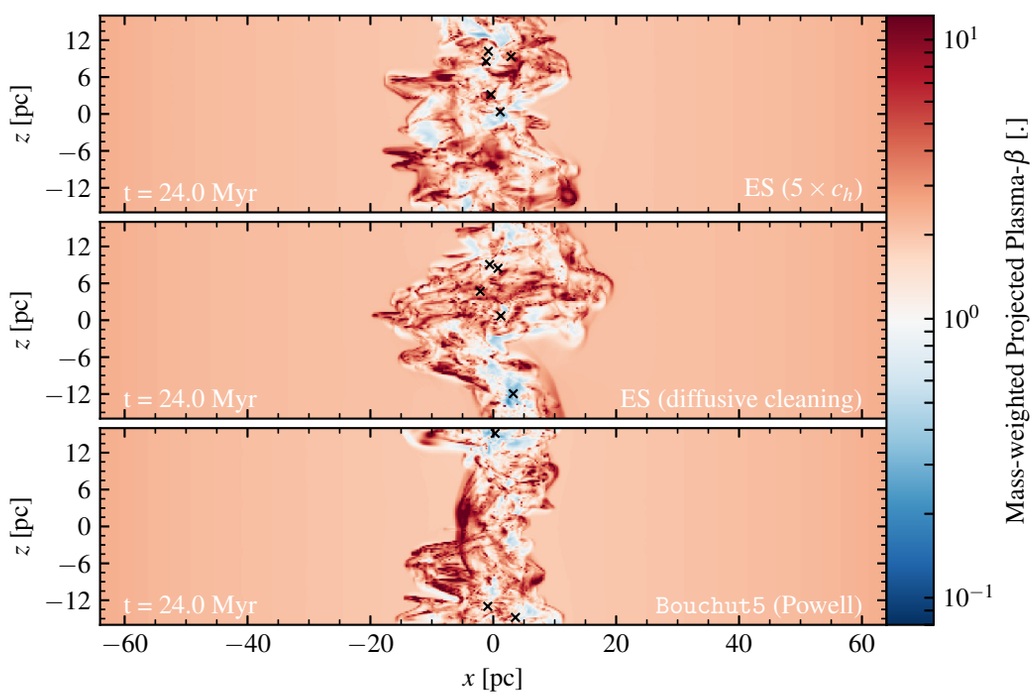

Fig. 6.19: Mass-weighted projected plasma β at $t = 24$ Myr. Compare to Fig. 6.9.

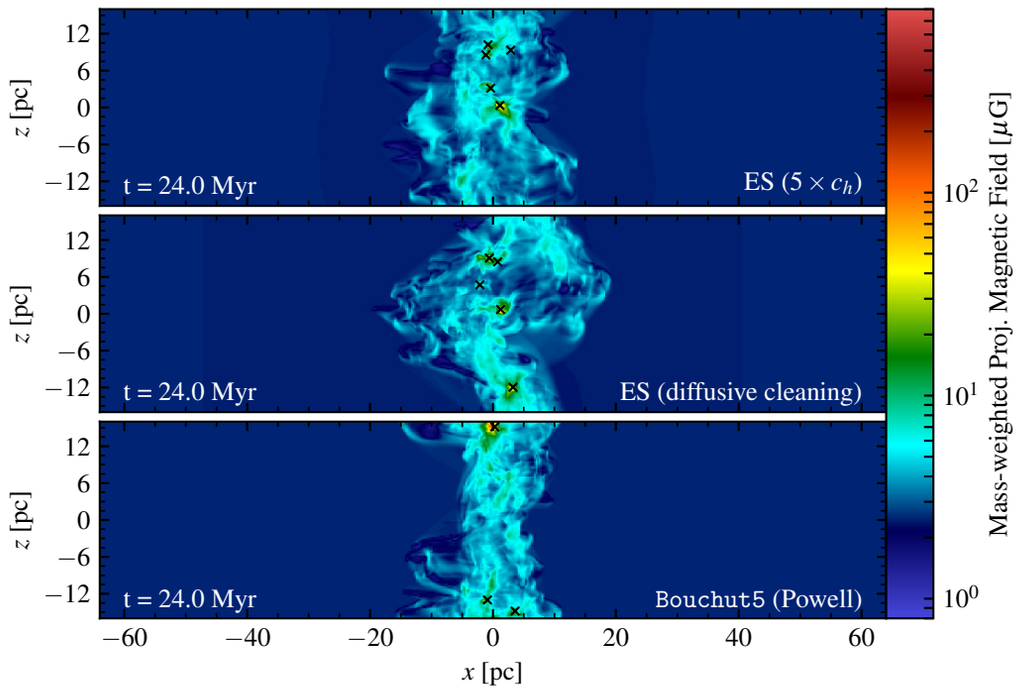

Fig. 6.20: Mass-weighted projected magnetic field strength at $t = 24\,\mathrm{Myr}$. Compare to Fig. 6.11.

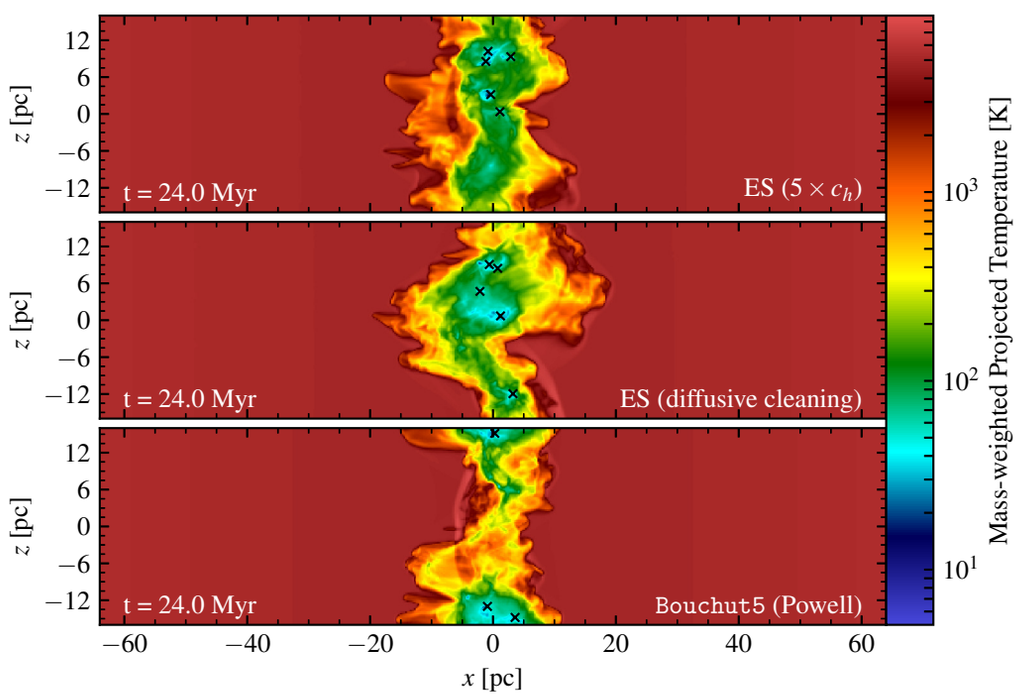

Fig. 6.21: Mass-weighted projected temperature at $t = 24\,\mathrm{Myr}$. Compare to Fig. 6.15.

6.6 Computational costs

Solver	B_0	$\overline{\Delta t}$	N_{steps}	real time	CPU hours
ES	none	3.121 kyr	5557	20.6 h	13 305 CPUh
`Bouchut5`	none	3.123 kyr	5512	19.2 h	11 728 CPUh
ES ($1 \times c_h$)	2.5 µG	2.75 kyr	6438	23.9 h	15 415 CPUh
ES ($5 \times c_h$)	2.5 µG	0.5 kyr	25 486	101.9 h	76 895 CPUh
ES (divbdiffuse)	2.5 µG	2.83 kyr	6124	24.9 h	16 064 CPUh
`Bouchut5` (Powell)	2.5 µG	2.98 kyr	5816	23.6 h	15 226 CPUh

Table 6.1: Comparison of computational resources used for the described simulations. From left to right: Numerical scheme ("solver"); initial magnetic field along inflow direction (B_0); average time step size ($\overline{\Delta t}$); number of evolution steps used by the simulation (N_{steps}); wall clock time used by the simulation (real time); computational costs accounted in total core hours (CPU hours).

In Table 6.1, I summarize the computational costs of the presented simulations. All simulations have been computed on the SuperMUC Petascale System (phase 1). Each simulation ran on 644 "thin" compute node cores (Intel© Xeon© E5-2680 CPU (Sandy Bridge) at 2.7 GHz, 2 GB memory per core, nodes connected via a non-blocking 10 GBit/s Infiniband™ FDR10 network).

The top panel in the table shows data for the simulations without magnetic fields. We see that the average time step is almost identical. The computational costs of the simulations are comparable whereas my new scheme leads to a slightly increased computational cost of 13 % compared to the `Bouchut5` scheme. These additional costs are caused by the higher complexity of the hybrid entropy stabilization as already analyzed in Derigs et al. (2017, Sec. 5, p. 76f). Using a simpler entropy stabilization (e.g., `entropyscheme=H`), the computational costs could be lowered at the cost of increased dissipation.

In the magnetized simulations, the mean time step size of my entropy stable solver is slightly smaller than the `Bouchut5` time steps. This is expected as my scheme can resolve fast magnetoacoustic waves while the `Bouchut5` solver cannot resolve these waves. Accordingly, the total number of evolution steps is about 10 % higher compared to the `Bouchut5` results. However, the total additional costs are only $\approx$ 1 % higher as my scheme is computationally more efficient per evolution step as my new scheme does not require an additional post-processing divergence cleaning step. As expected, the computational costs of the simulation with fivefold upscaled cleaning speed are about five times as expensive.

The simulation with added post-processing divergence correction ("ES (divbdiffuse)") is about 5 % more expensive compared to the `Bouchut5` (Powell) reference solution.

6.7 Summary

In this chapter, I have demonstrated the utility of my new entropy stable solver for a large-scale astrophysical application. My scheme proved to be applicable to a state-of-the-art multi-physics simulations with and without magnetic fields and can resolve fluid features accurately (see also Fig. 6.22 for a direct comparison). Its divergence cleaning properties are similar to the post-processing diffusive divergence cleaning used by the `Bouchut5` solver. The omnipresence of dynamically important magnetic fields in the entire molecular cloud indicates the importance of a physically consistent treatment of magnetic fields in this particular setup and beyond.

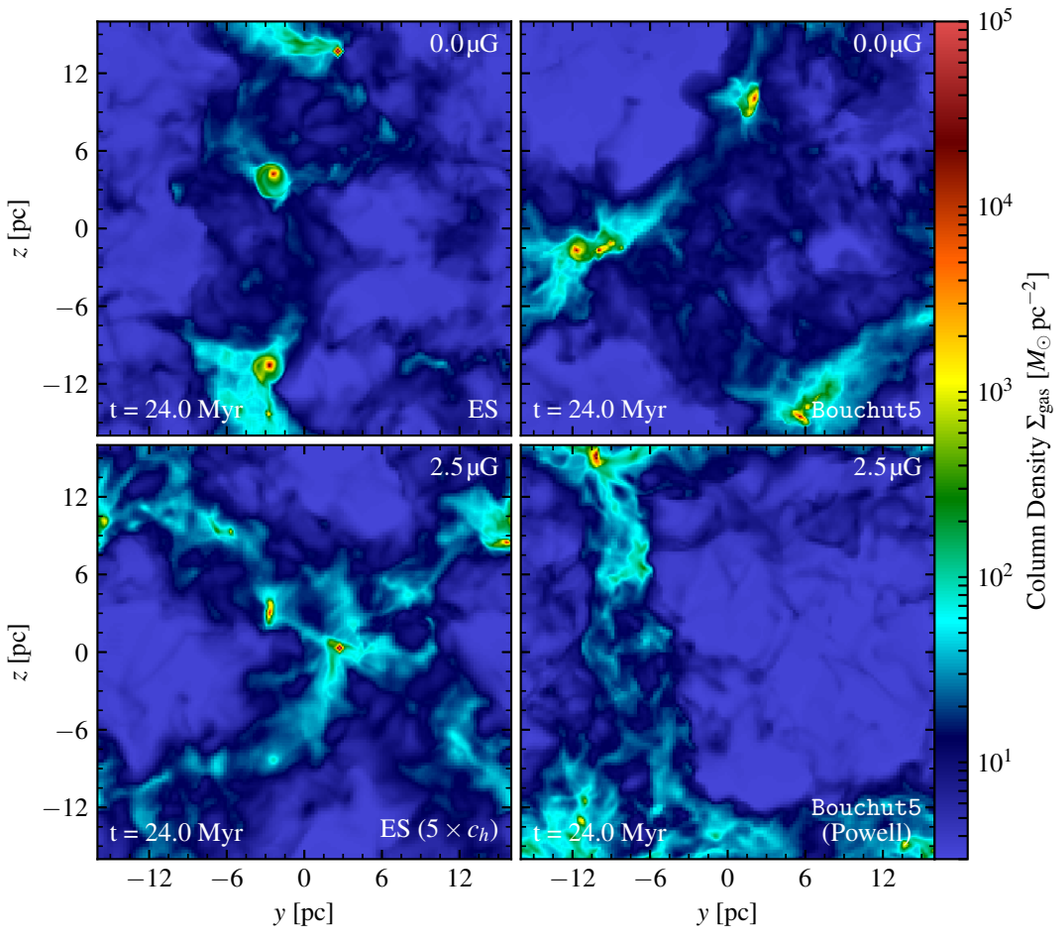

Fig. 6.22: Total gas column density at $t = 24\,\mathrm{Myr}$, projected along the x-axis. Top panel: Simulations without magnetic field. Bottom panel: Simulations with magnetic fields. Left side: ES $5 \times c_h$ result. Right side: `Bouchut5` result.
Although the simulations start from the same initial conditions, the highly non-linear character of the colliding flow model results in an entirely different evolution. The disk-like features visible in the simulations without magnetic fields are phenomena caused by the limited spatial resolution (see Seifried et al., 2017, Sec. 6).

7 | Conclusion

The aim of this work was to develop and test a new mathematical model for astrophysical simulations. This development was necessary because the traditionally used discrete form of the ideal MHD equations becomes invalid in the presence of numerically caused magnetic field divergence errors. As the ideal MHD equations have no inbuilt mechanism to control the growth of such errors, numerical schemes have to resort to so-called "divergence cleaning methods", most of which conflict with the laws of thermodynamics. To ensure a physically meaningful treatment of the simulated gas, consistency with the laws of thermodynamics was the driving design principle from the beginning of my derivations.

In my first paper in this thesis (Derigs et al., 2016), I described the implementation of a new entropy-aware high-order numerical method for MHD problems. I carefully described the implementation strategy, e.g., details about building the new solver into the adaptive mesh refinement system `PARAMESH` (MacNeice et al., 2000). I further developed a hybrid dissipation term for MHD flows that continuously blends the highly accurate selective dissipation scheme with the more dissipative scalar dissipation scheme to increase the robustness of my numerical scheme, while retaining more accurate features in smooth regions. I used a variety of tests to verify the utility, flexibility, and robustness of my numerical model for hydrodynamical and magnetohydrodynamical flows in single and multiple spatial dimensions. A detailed comparison against the other available numerical schemes for MHD in `FLASH` showed that my new entropy stable solver was the most accurate in smooth regions of a flow, and was also able to resolve strong shocks.

My second work (Derigs et al., 2017) is a follow-up paper. It highlights that special care needs to be taken when designing discrete dissipation operators for numerical schemes. I have shown that schemes designed for both hydrodynamical and magnetohydrodynamical flows may easily break down for strong shocks in moving background media. I analytically verified that the commonly used entropy conservative numerical flux function for the Euler equations of Ismail & Roe (2009) suffers from such breakdown for pressure jumps larger than a few orders of magnitude. As we expect such pressure discontinuities in strong shocks like those generated by supernova explosions, my findings are of immediate importance for the simulations concerned with plasmas under extreme conditions like in astrophysical applications. I demonstrated that the kinetic energy preserving entropy conserving (KEPEC) flux, first derived by Chandrashekar (2013) and more recently extended to ideal MHD by Winters & Gassner (2016), shows no pathological behavior even for very large pressure jumps. The KEPEC flux is the baseline flux of the solver implemented in my works.

My new contributions through this second work are two-fold: First, I showed that a straightforward discretization of the entropy Jacobian, needed to design entropy stable numerical methods, leads to an asymmetric, i.e., not provably entropy stable scheme. I presented a new technique that is convenient for the derivation of discrete entropy Jacobian operators. Secondly, I showed that it is essential to choose very specific averaging for the entries of the discrete entropy Jacobian. Further, I demonstrate that naive averaging strategies (such as commonly used arithmetic mean averaging) can quickly lead to unphysical states in cases where strong pressure jumps are present.

As a result, I establish a, for the first time, unique averaging technique for entropy stable approximate Riemann solvers. Whereas previously there have been a number of free choices in the design of numerical schemes, this work closes almost all of these uncertainties. It leaves open the unique discretization of the eigenvalues which I have presented in my third work (Derigs et al., 2018b). Together, these unique averages makes the entropy stable numerical scheme uniquely defined, giving detailed justification for the averaging on each term.

The third research paper contained in this thesis (Derigs et al., 2018b) is independent but meanwhile supplementary to the first two. In this work, I carefully described the derivation of a new physically motivated mathematical model suitable for building entropy stable numerical schemes for ideal MHD flows. In agreement with earlier publications, I choose to call my model the "ideal GLM-MHD equations". This new mathematical model can be used to build numerical methods for a number of schemes, including but not limited to, finite volume (applied in this work), finite difference, and high-order discontinuous Galerkin (see, e.g., Bohm et al., 2018) frameworks.

Whereas all entropy stable schemes for ideal MHD available in the literature to date either have insufficient magnetic field divergence treatment (e.g. through non-conservative terms), lose their favorable entropy stable properties when augmented with post-processing divergence cleaning, or are applicable in only one spatial dimension, my new scheme is free of such limitations.

My new mathematical model has the advantage of offering an effective magnetic field divergence cleaning while retaining in full agreement with thermodynamic laws. In contrast to other divergence cleaning methods, the purely hyperbolic nature of my new model makes it very attractive for parallelization on the largest scales. With this, one can acknowledge the increasingly stringent performance and scalability requirements driven by present-day trends in computing architectures.

Similar to previous GLM investigations as done by Munz et al. (2000) and Dedner et al. (2002), the idea of my model is to not enforce the divergence-free condition exactly, but to design a scheme that *evolves towards* a divergence-free state. By this, the model deliberately tolerates a certain numerically caused non-zero magnetic field divergence in the evolution of the simulations.

One notable drawback of my new mathematical model is that, as the magnetic field topology is corrected in a hyperbolic fashion, the cleaning cannot be instantaneous. Furthermore, I recommended to restrict the cleaning speed to be, at most, as fast as the fastest propagating waves in the solution. This choice was intentionally made to not alter the timestep size of multi-physics simulations. This drawback could be mitigated with, e.g., MHD solver subcycling, allowing for a substantially larger cleaning speed.

While the magnetic field morphology is corrected by the GLM waves, a certain amount of energy is temporarily removed from the magnetic field and carried by the ψ field. Hence, I found that one must account for this new type of energy to design entropy-aware methods. As the ψ energy can only come from the magnetic energy, it is natural to think of it as an additional component to the conserved fluid's total energy. Hence, the total energy equation should to be re-derived as well.

In my approach, the non-conservative terms on the right-hand side of the ideal MHD equations, initially discussed by Godunov (1972) and later rediscovered by Powell et al. (1999), naturally arise when coupling the Lorentz force with the Euler equations. Whereas the justification for using these terms previously was most often of mathematical nature as they are needed to symmetrize the equation system, I was now able to add new, solely physical motivations for these terms. Although these extra terms proportional to $\nabla \cdot \boldsymbol{B}$ have been known for decades, a physically motivated derivation was missing. It is most likely due to this lack of a physically founded interpretation that most researchers refrain from using these terms as they bring the ideal MHD equations into a strictly non-conserved form. However, as described in Derigs et al. (2018b), this commonly found lack of the proper non-conservative terms can quickly lead to unphysical behavior of the simulated fluid. For instance, the fluid could be affected by an artificial force parallel to the magnetic field lines. I thoroughly discussed this and further implications of my findings in a general framework in Derigs et al. (2018b, Sec. 2, pp. 84-88 in this thesis).

Galilean-invariance ensures that the same physical laws are valid in all inertial reference frames, and is a necessary property of any well-posed theory in non-relativistic physics. The ideal MHD equations (without non-conservative terms) are not Galilean-invariant when written in Eulerian form. Another discovery I made is that Galilean-invariance can easily and self-consistently be attained when deriving the mathematical model using the *generalized* form of Maxwell's equations.

Very recently, Bohm et al. (2018) applied my new scheme in the framework of high-order nodal discontinuous Galerkin (DG) schemes on curvilinear unstructured hexahedral meshes. They extended my ideal GLM-MHD scheme with resistive terms and demonstrated the versatility of the scheme in DG spectral element methods (DGSEM). They demonstrated that the entropy-stable GLM-MHD based DGSEM method gives increased robustness compared to standard DGSEM methods. Furthermore, they demonstrated high-order convergence rates for DGSEM with my new ideal GLM-MHD model.

I successfully applied my new ideal GLM-MHD model to a state-of-the-art application in astrophysics and compared the difference to a commonly used ideal MHD scheme utilizing a post-processing divergence cleaning method (see Chapter 6). My new scheme is currently under testing in today's largest-scale simulations which try to obtain a complete understanding of the formation of molecular clouds and star-forming regions therein carried out by Haid et al. (2018) and Seifried et al. (2018b).

To summarize, the significance of this thesis is that my work leads to the first entropy consistent hyperbolic formulation of the ideal MHD equations with effective inbuilt divergence cleaning. The ideal GLM-MHD scheme has many favorable properties, such as entropy stability ensuring consistency with the universally valid laws of thermodynamics, kinetic energy preservation

preventing the emergence of spurious kinetic energy generation, and Galilean invariance ensuring that the model describes the same physics in all reference frames. As high-performance computing facilities are pushing further towards sustainable highly power-efficient systems, they evolve more and more towards architectures featuring a larger number of machines. The purely local nature of my scheme warrants its high appeal for applications running current large-scale and the even larger-scale simulations we expect over the next decades.

8 | Outlook

Based on the developments presented in this thesis, I suggest potential follow-up works and research topics. I will shortly discuss these possible extensions herein to facilitate future projects building upon my entropy-stable GLM-MHD scheme.

One potential future project is the implementation of my scheme in arbitrary accuracy. This high-order extension is computationally feasible due to relying on simple linear combinations of fluxes.

One further project could investigate the effect of an adjustable scaling parameter in the pressure-based shock indicator used to enhance the accuracy of the hybrid dissipation scheme, in particularly for smooth flow regimes.

Furthermore, the ideal GLM-MHD system can easily be extended to include non-ideal effects such as resistivity, viscosity, and (an)isotropic thermal conduction, so work in this direction may prove be useful for future, more complex numerical simulations of plasma phenomena.

Another possible future project would be the implementation of my new entropy-stable GLM-MHD scheme into FLASH's new GLM variant of the `unsplit` solver that is currently under development. This would reduce some of the time step restrictions I discussed in Sec. 5.1.2. Unfortunately, this variant of the `unsplit` solver was not available in June 2018, so I couldn't investigate further on this topic for this thesis.

Other projects could be the implementation of subcycling as mentioned in Chapter 6 and the comparison to actual astrophysical systems using the technique of synthetic observations.

8.1 Implementation of a numerical scheme with arbitrary high-resolution

In Derigs et al. (2018b, Sec. 4.8, pp. 105-107 in this thesis), I described how one can build entropy stable schemes of arbitrarily high-order in space and time.

High temporal accuracy may be achieved by replacing the time integrator by a suitable higher-order scheme, e.g. strong stability preserving (SSP) Runge-Kutta (RK) schemes (see e.g. Gottlieb et al., 2001). However, as high-order accurate time integrators come at additional computational costs, one has to find a compromise between (temporal) accuracy and computational resources.

Fortunately, high-order accuracy in space can be achieved in a computationally very attractive way using the fact that the entropy conserving flux describes the rate of change for the quantities over an interface and, as such, is a first order derivative with respect to time over a fixed volume. Given a suitable extrapolation, one can construct arbitrarily accurate interface fluxes through simple and inexpensive linear combinations of the first-order accurate entropy conservative fluxes computed at cell interfaces in the usual way.

I carefully described the general high-order extension technique and gave the precise forms of the fluxes and non-conservative terms for up to sixth-order accuracy in my third paper. While this method is very promising for the application on purely smooth solutions (entropy *conserving* scheme), it is unclear how the high-order extension may affect the robustness of the overall entropy *stable* scheme.

As it is not possible to apply the same technique for the entropy stable part of the numerical fluxes (detailed by Fjordholm et al., 2012, Sec. 3.2) a specific reconstruction procedure has to be used to ensure high-order entropy stability. To control shock-induced oscillations, the entropy-stable fluxes should be computed from a limited reconstruction. As Fjordholm et al. pointed out, this reconstruction should preferably be done in entropy rather than in conservative variables. It may be done using high-accuracy limiting schemes such as the popular weighted essential non-oscillating scheme (WENO) by Liu et al. (1994).

It is essential to keep in mind that the amount of entropy added to the solution is based on a linearization of the ideal GLM-MHD equations. Hence, while we can ensure the *sign* in the entropy inequality, we cannot guarantee that the *amount* of added dissipation is sufficient. This can already be seen by the notable increase in robustness with the hybrid scheme that applies an extra amount of dissipation.

Whether entropy stability, as a concept, is sufficient to ensure numerical robustness at high-order accuracy remains an open question which is worthwhile for further exploration and a current field of active research (see, e.g. Svärd, 2015; Svärd, 2016).

8.2 Tunable hybridization factor

The parameter-free pressure-based smoothness indicator (2.46) I described in Sec. 2.6.3 is rather restrictive as it adds a lot of dissipation at moderate pressure jumps, e.g.,

$$\Xi(p_\mathrm{L}/p_\mathrm{R} = 10) \approx 0.86 \tag{8.1}$$

meaning that a single order of magnitude pressure jump computes 86 % of its dissipation from the more dissipative scalar part and only 14 % from the more selective dissipation term of the entropy stable scheme.

One tunable smoothness indicator would be

$$\Xi = \sqrt{\frac{|p_\mathrm{L}^\kappa - p_\mathrm{R}^\kappa|}{p_\mathrm{L}^\kappa + p_\mathrm{R}^\kappa}} \in [0, 1], \tag{8.2}$$

with a new tuning parameter $\kappa \in \mathbb{R}$. As can be seen in Fig. 8.1, a tuning parameter less than 1.0 leads to a less dissipative scheme as a lower fraction of the more diffusive scalar dissipation term is used. Obviously, the tunable smoothness indicator is identical to its parameter-free equivalent (2.46) for $\kappa = 1$.

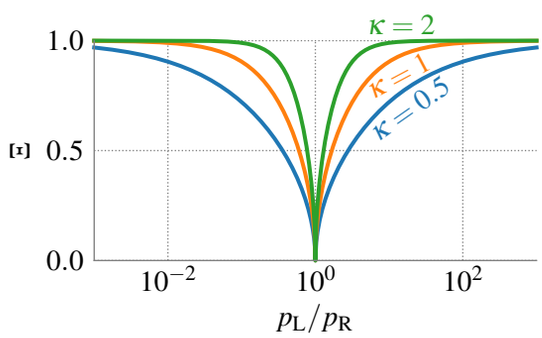

Fig. 8.1: Tunable pressure-based smoothness indicator (8.2) with parameter κ.

It should be investigated how this affects the robustness and shock resolution of the numerical method as there is substantial potential for improving the accuracy in regions that are fairly but not perfectly smooth.

8.3 Resistive MHD

Resistivity measures how collisions transport electromagnetic energy through the system. Ideal MHD is only strictly applicable when the resistivity due to these collisions is small. The diffusivity due to the resistive MHD terms leads to a break in the magnetic topology in contrast to the "frozen-in" field in the ideal MHD model.

In most astrophysical plasmas resistivity is unimportant because the plasma flows considered are, in general, perfect conductors. However, one can easily construct cases where neglecting resistivity may be physically wrong:

- coronal events (loops/flares/prominences)
- magnetized plasma above/below magnetorotationally-instable (MRI) accretion disks around stars
- planetary magnetospheres

In simpler words: if we want to study what happens when oppositely-directed regions of $\boldsymbol{B}$ are pushed together, we're forced to take resistivity seriously.

Beyond astrophysics, resistivity plays a crucial role when designing next-generation nuclear fusion devices as it requires understanding the non-linear macroscopic stability, reconnection processes and refueling approaches for burning plasmas. Due to the high cost of conducting physical experiments of nuclear fusion experiments in real devices, researchers ultimately depend on accurate numerical simulations as a tool for performing their research.

We arrive at the resistive MHD equations if we apply Ohm's law without the assumption of vanishing resistivity $\eta = 0$:

$$\boldsymbol{E} + \boldsymbol{u} \times \boldsymbol{B} = \eta \boldsymbol{J} \quad \Rightarrow \quad \boldsymbol{E} = \eta \boldsymbol{J} - \boldsymbol{u} \times \boldsymbol{B} \tag{8.3}$$

With Ampère's law (negligible displacement currents due to non-relativistic approximation),

$$\nabla \times \boldsymbol{E} = -\frac{\partial \boldsymbol{B}}{\partial t} \quad \Rightarrow \quad \frac{\partial \boldsymbol{B}}{\partial t} = -\nabla \times \boldsymbol{E}, \tag{8.4}$$

we have

$$\frac{\partial \boldsymbol{B}}{\partial t} = -\nabla \times (\eta \boldsymbol{J} - \boldsymbol{u} \times \boldsymbol{B}) \tag{8.5}$$

or, rewritten into a similar form as (2.9d),

$$\frac{\partial \boldsymbol{B}}{\partial t} + \nabla \cdot (\boldsymbol{u} \otimes \boldsymbol{B} - \boldsymbol{B} \otimes \boldsymbol{u}) + \nabla \times (\eta \boldsymbol{J}) = 0. \tag{8.6}$$

The current density, $\boldsymbol{J}$, is defined through Faraday's law,

$$\boldsymbol{J} := \nabla \times \boldsymbol{B} = \begin{bmatrix} \frac{\partial B_3}{\partial y} - \frac{\partial B_2}{\partial z} \\ \frac{\partial B_1}{\partial z} - \frac{\partial B_3}{\partial x} \\ \frac{\partial B_2}{\partial x} - \frac{\partial B_1}{\partial y} \end{bmatrix}. \tag{8.7}$$

Assuming spatially constant resistivity, I get

$$\nabla \times (\eta \boldsymbol{J}) = \eta \nabla \times \boldsymbol{J} = \eta \nabla \times \begin{bmatrix} \frac{\partial B_3}{\partial y} - \frac{\partial B_2}{\partial z} \\ \frac{\partial B_1}{\partial z} - \frac{\partial B_3}{\partial x} \\ \frac{\partial B_2}{\partial x} - \frac{\partial B_1}{\partial y} \end{bmatrix}$$

$$
\begin{aligned}
&= \eta \begin{bmatrix} (\frac{\partial B_2}{\partial x} - \frac{\partial B_1}{\partial y})_y - (\frac{\partial B_1}{\partial z} - \frac{\partial B_3}{\partial x})_z \\ (\frac{\partial B_3}{\partial y} - \frac{\partial B_2}{\partial z})_z - (\frac{\partial B_2}{\partial x} - \frac{\partial B_1}{\partial y})_x \\ (\frac{\partial B_1}{\partial z} - \frac{\partial B_3}{\partial x})_x - (\frac{\partial B_3}{\partial y} - \frac{\partial B_2}{\partial z})_y \end{bmatrix} \\
&= \eta \left\{ \begin{bmatrix} 0 \\ \frac{\partial B_1}{\partial y} - \frac{\partial B_2}{\partial x} \\ \frac{\partial B_1}{\partial z} - \frac{\partial B_3}{\partial x} \end{bmatrix}_x + \begin{bmatrix} \frac{\partial B_2}{\partial x} - \frac{\partial B_1}{\partial y} \\ 0 \\ \frac{\partial B_2}{\partial z} - \frac{\partial B_3}{\partial y} \end{bmatrix}_y + \begin{bmatrix} \frac{\partial B_3}{\partial x} - \frac{\partial B_1}{\partial z} \\ \frac{\partial B_3}{\partial y} - \frac{\partial B_2}{\partial z} \\ 0 \end{bmatrix}_z \right\}. \qquad (8.8)
\end{aligned}
$$

With this the magnetic field components of the resistive MHD fluxes are

$$
\frac{\partial \boldsymbol{B}}{\partial t} = \frac{\partial}{\partial x} \begin{bmatrix} 0 \\ u\,B_2 - v\,B_1 + \eta\left(\frac{\partial B_1}{\partial y} - \frac{\partial B_2}{\partial x}\right) \\ u\,B_3 - w\,B_1 + \eta\left(\frac{\partial B_1}{\partial z} - \frac{\partial B_3}{\partial x}\right) \end{bmatrix}. \qquad (8.9)
$$

In the next step, one has to account for the changes in the induction equation to the total energy equation:

$$
\frac{\partial E}{\partial t} = \frac{\partial}{\partial t}\left(\frac{1}{2}\rho\|\boldsymbol{u}\|^2 + \epsilon + \frac{1}{2}\|\boldsymbol{B}\|^2\right). \qquad (8.10)
$$

For the sake of convenience, I split the obtained fluxes into two components,

$$
\left(\frac{\partial \boldsymbol{B}}{\partial t}\right)_{\text{ideal}} = \frac{\partial}{\partial x} \begin{bmatrix} 0 \\ u\,B_2 - v\,B_1 \\ u\,B_3 - w\,B_1 \end{bmatrix}, \qquad \left(\frac{\partial \boldsymbol{B}}{\partial t}\right)_{\text{res.}} = \eta \frac{\partial}{\partial x} \begin{bmatrix} 0 \\ \frac{\partial B_1}{\partial y} - \frac{\partial B_2}{\partial x} \\ \frac{\partial B_1}{\partial z} - \frac{\partial B_3}{\partial x} \end{bmatrix}. \qquad (8.11)
$$

The *extra* contribution only by the resistive parts is given by:

$$
\begin{aligned}
\frac{\partial}{\partial t}\left(\frac{1}{2}\|\boldsymbol{B}\|^2\right)_{\text{res.}} &= \boldsymbol{B} \cdot \left(\frac{\partial \boldsymbol{B}}{\partial t}\right)_{\text{res.}} = \begin{bmatrix} B_1 \\ B_2 \\ B_3 \end{bmatrix} \cdot \left(\frac{\partial}{\partial x} \begin{bmatrix} 0 \\ \eta\left(\frac{\partial B_1}{\partial y} - \frac{\partial B_2}{\partial x}\right) \\ \eta\left(\frac{\partial B_1}{\partial z} - \frac{\partial B_3}{\partial x}\right) \end{bmatrix} \right) \\
&= \eta \left(B_2 (B_1)_{xy} - B_2 (B_2)_{xx} + B_3 (B_1)_{xz} - B_3 (B_3)_{xx} \right). \qquad (8.12)
\end{aligned}
$$

Due to the cross-multiplications of various non-differentiated magnetic field components with derivatives of second order, it does not seem possible to bring this contribution into a divergence form for adding it to the total energy flux. Thus, eq. (8.12) has to be added as a non-conservative term to the total energy equation. However, this is not unexpected, since – at least from the physical point of view – it seems wrong to include magnetic resistivity effects without new non-conservative terms: If reconnections happen, the magnetic energy is modified. However, the *magnetic* energy may not be solely released into *thermal*, but also into *kinetic* energy. However, there seems to be no consistent way to modify the momentum conservation law to account for such energy exchanges.

Interestingly, I have only been able to recover the equations reported in the literature (e.g., Samtaney et al., 2005, Reynolds et al., 2006, or more recently Hindenlang et al., 2016, and Bohm et al., 2018) using a mathematically invalid ansatz for the magnetic energy contribution:

$$\begin{aligned}\frac{\partial}{\partial t}\left(\frac{1}{2}\|\boldsymbol{B}\|^2\right)_{\text{res.}} &= \frac{\partial \boldsymbol{B}}{\partial x}\cdot\left(\frac{\partial \boldsymbol{B}}{\partial t}\right)_{\text{res.}} = \begin{bmatrix}(B_1)_x\\(B_2)_x\\(B_3)_x\end{bmatrix}\cdot\left(\begin{bmatrix}0\\ \eta\left(\frac{\partial B_1}{\partial y}-\frac{\partial B_2}{\partial x}\right)_x\\ \eta\left(\frac{\partial B_1}{\partial z}-\frac{\partial B_3}{\partial x}\right)_x\end{bmatrix}\right)\\ &= \eta\left((B_2)_x(B_1)_{xy}-(B_2)_x(B_2)_{xx}+(B_3)_x(B_1)_{xz}-(B_3)_x(B_3)_{xx}\right)\\ &= \eta\left\{B_2\left(\frac{\partial B_1}{\partial y}-\frac{\partial B_2}{\partial x}\right)+B_3\left(\frac{\partial B_1}{\partial z}-\frac{\partial B_3}{\partial x}\right)\right\}_x.\end{aligned} \tag{8.13}$$

This ansatz would mean that the total energy contribution of the magnetic fluxes are computed as

$$\frac{\partial}{\partial t}\left(\frac{1}{2}\|\boldsymbol{B}\|^2\right) = \boldsymbol{B}\cdot\left(\frac{\partial \boldsymbol{B}}{\partial t}\right)_{\text{ideal}} + \frac{\partial \boldsymbol{B}}{\partial x}\cdot\left(\frac{\partial \boldsymbol{B}}{\partial t}\right)_{\text{res.}} \tag{8.14}$$

in order to get the total energy contributions from the magnetic fields. This is most likely incorrect and should certainly be investigated in future works. The details provided herein should provide the necessary tools for doing so.

Entropy-stability of a potentially created resistive GLM-MHD extension is straightforward as the continuous entropy analysis technique I carefully described in Derigs et al. (2018b, Sec. 4.1, p. 95f in this thesis) can immediately be used.

8.4 Hall MHD

It is well known that Hall physics play a critical role in the accurate modeling of magnetic reconnection (Shay et al., 1999; Birn et al., 2001; Birn & Hesse, 2001; Hesse et al., 2001; Otto, 2001; Huba & Rudakov, 2002; Huba, 2005). As has been shown, Hall MHD is important to model magnetic reconnection at very small spatial and temporal scales correctly. In contrast to resistivity, the Hall effect does not break the "frozen-in" condition of the magnetic field but restructures the reconnection region.

One arrives at the Hall MHD from Ohm's law in the form:

$$\boldsymbol{E}+\boldsymbol{u}\times\boldsymbol{B} = \frac{1}{a}\boldsymbol{J}\times\boldsymbol{B} \;\Rightarrow\; \boldsymbol{E} = \frac{1}{a}\boldsymbol{J}\times\boldsymbol{B}-\boldsymbol{u}\times\boldsymbol{B} \tag{8.15}$$

with

$$a := qc, \tag{8.16}$$

where $q = n_e e$ is the electron charge, and c is the speed of light.

With Ampère's law (8.4), I can write the induction equation as

$$\frac{\partial \boldsymbol{B}}{\partial t} = -\nabla\cdot(\boldsymbol{u}\otimes\boldsymbol{B}-\boldsymbol{B}\otimes\boldsymbol{u}) - \nabla\times(a^{-1}\boldsymbol{J}\times\boldsymbol{B}), \tag{8.17}$$

or, rewritten into a similar form as (2.9d),

$$\frac{\partial \boldsymbol{B}}{\partial t} + \nabla \cdot (\boldsymbol{u} \otimes \boldsymbol{B} - \boldsymbol{B} \otimes \boldsymbol{u}) + \nabla \times (a^{-1} \boldsymbol{J} \times \boldsymbol{B}) = 0. \tag{8.18}$$

Examining the $\nabla \times (\boldsymbol{J} \times \boldsymbol{B}) = \nabla \times ((\nabla \times \boldsymbol{B}) \times \boldsymbol{B})$ term, I obtain

$$\nabla \times (\boldsymbol{J} \times \boldsymbol{B}) = \nabla \cdot (\boldsymbol{B} \otimes \boldsymbol{J} - \boldsymbol{J} \otimes \boldsymbol{B}) = \begin{bmatrix} \boldsymbol{JB}_1 & \boldsymbol{JB}_2 & \boldsymbol{JB}_3 \end{bmatrix}, \tag{8.19}$$

with

$$\boldsymbol{JB}_1 := \begin{bmatrix} 0 \\ B_2 \left(\frac{\partial B_3}{\partial y} - \frac{\partial B_2}{\partial z} \right) - B_1 \left(\frac{\partial B_1}{\partial z} - \frac{\partial B_3}{\partial x} \right) \\ B_3 \left(\frac{\partial B_3}{\partial y} - \frac{\partial B_2}{\partial z} \right) - B_1 \left(\frac{\partial B_2}{\partial x} - \frac{\partial B_1}{\partial y} \right) \end{bmatrix}, \tag{8.20}$$

$$\boldsymbol{JB}_2 := \begin{bmatrix} B_1 \left(\frac{\partial B_1}{\partial z} - \frac{\partial B_3}{\partial x} \right) - B_2 \left(\frac{\partial B_3}{\partial y} - \frac{\partial B_2}{\partial z} \right) \\ 0 \\ B_3 \left(\frac{\partial B_1}{\partial z} - \frac{\partial B_3}{\partial x} \right) - B_2 \left(\frac{\partial B_2}{\partial x} - \frac{\partial B_1}{\partial y} \right) \end{bmatrix}, \tag{8.21}$$

and

$$\boldsymbol{JB}_3 := \begin{bmatrix} B_1 \left(\frac{\partial B_2}{\partial x} - \frac{\partial B_1}{\partial y} \right) - B_3 \left(\frac{\partial B_3}{\partial y} - \frac{\partial B_2}{\partial z} \right) \\ B_2 \left(\frac{\partial B_2}{\partial x} - \frac{\partial B_1}{\partial y} \right) - B_3 \left(\frac{\partial B_1}{\partial z} - \frac{\partial B_3}{\partial x} \right) \\ 0 \end{bmatrix}. \tag{8.22}$$

With this, the magnetic field components of the Hall MHD fluxes are

$$\frac{\partial \boldsymbol{B}}{\partial t} = \frac{\partial}{\partial x} \frac{1}{a} \begin{bmatrix} 0 \\ u\, B_2 - v\, B_1 \\ +B_1 \left(\frac{\partial B_1}{\partial z} - \frac{\partial B_3}{\partial x} \right) \\ -B_2 \left(\frac{\partial B_3}{\partial y} - \frac{\partial B_2}{\partial z} \right) \\ u\, B_3 - w\, B_1 \\ +B_1 \left(\frac{\partial B_2}{\partial x} - \frac{\partial B_1}{\partial y} \right) \\ -B_3 \left(\frac{\partial B_3}{\partial y} - \frac{\partial B_2}{\partial z} \right) \end{bmatrix}. \tag{8.23}$$

Similar to the case of the resistive MHD equations, it is not clear if these additional terms can be added to the total energy equations without introducing new non-conservative terms. As magnetic reconnection is a process that changes magnetic field topology in highly conducting fluids, it is suggested to by important in several astrophysical environments and research into this direction may turn out to be very useful for future, high resolution simulations (see, e.g., Lazarian et al., 2015 for an overview of the importance of magnetic reconnection in astrophysics).

8.5 Unsplit GLM-MHD implementation of the FLASH center

The Flash Center for Computational Science is currently working on an implementation of a new unsplit MHD solver. This solver will, in contrast to the already existing staggered mesh solver, rely on a GLM implementation for appropriate divergence cleaning. Unfortunately, this solver is still in its early stages and not yet publicly available (Lee, 2018, private communication). However, as soon as this new solver is made available, it may be advantageous to implement my entropy-stable GLM-MHD scheme because it will be able to take advantage of the much less severe time step restrictions for `unsplit` solvers in `FLASH` (see Sec. 5.1.2).

8.6 Synthetic observations

Synthetic observations play an increasingly important role in astrophysics, both for interpreting real observations and for making meaningful predictions from models. In recent years, the number of synthetic observations has increased significantly (see, e.g., the review by Haworth et al., 2017).

Within the ERC Starting Grant "The radiative interstellar medium (`RADFEEDBACK`)"[13], a "synthetic observations toolbox" is currently under development. This project shall facilitate the comparison between simulations and observations by providing pipelines for atomic and molecular line as well as synthetic continuum observations.

It could be an interesting task to use synthetic observations to compare the statistics of simulations produced using my new entropy stable solver to actual observations. It would be interesting to assess if my new scheme, thanks to being Galilean invariant, entropy stable, and kinetic energy preserving, gives more realistic results.

8.7 Applicability beyond astrophysics

Nuclear fusion is a reaction in which atomic nuclei come close enough to form a different atom. The difference in mass (Δm) between the reactants and the product, caused by the difference in atomic binding energy, is manifested as the release of huge amounts of energy,

$$E_{\text{released}} = \Delta m \cdot c^2, \tag{8.24}$$

where c is the speed of light. The initial suggestion by Arthur Eddington that hydrogen fusion could be the primary source of stellar energy (Eddington, 1920), lead to the idea of controlled thermonuclear fusion for civil proposes where the released energy is harnessed for power generation.

It is speculated that global electricity needs will sextuple by the year 2100 (Clarke et al., 2014) requiring a dramatic transformation in the way in which we generate and distribute electric power.

[13] PI S. Walch, grant no. 679852

Nuclear fusion could provide the answer for the ever-growing need of energy, as the deuterium in a bathtub full of water and the lithium in a used laptop battery is sufficient to generate power for a typical family for over 50 years (Jenko, 2013). Hence, with the potential to provide clean, safe, and abundant energy, nuclear fusion has been called the "holy grail" of energy production. However, harnessing energy from fusion, the process that powers the stars in our Universe, has proven to be a tough challenge.

Energy confinement in fusion plasmas is limited by thermal losses due to turbulence (Zhumabekov, 2017). Here again, analytic models show their limitations as the necessary simplifications make them unable to predict the growth of essential plasma instabilities. As temperatures and magnetic fields vary wildly over time and space, researchers must use detailed whole-device simulations to understand the plasma's dynamics inside the reactor and to determine how sustainable fusion may be achieved.

Understanding and possibly controlling the underlying physical processes is key to achieving the right balance between fusion energy production and the heat losses associated with plasma turbulence. This will allow us to ultimately determine the size, cost, and practicability of an actual fusion reactor.

Further applications can be found, e.g., in the field of geophysics, interested, for instance, in the Earth's magnetic field. This field is not only useful for navigation but also vital for life on Earth, as it deflects cosmic ray particles as well as most of the solar wind, whose charged particles would otherwise strip away the ozone layer (Schiermeier, 2005). Without the ozone layer there would be no protection against the harmful ultraviolet radiation of the Sun.

A P P E N D I X

Non-conservative terms in the Bouchut5 solver

This appendix gives a short overview over the non-conservative term implementation in the Bouchut3/5 solvers used in the SILCC collaboration. I put this discussion in the appendix of my thesis as it is unrelated to the ideal GLM-MHD scheme. It focuses on an inconsistency I have found in the ideal MHD solver used by many international researchers. I use the Bouchut5 solver as reference solver in Chapter 6.

To highlight the differences between the non-conservative term implementations I discuss in this appendix, I shortly revise the ideal MHD equations equipped with the different non-conservative terms below (see also Derigs et al., 2018b, Sec. 3.8, p. 93f in this thesis).

From the derivations of the generalized ideal MHD equations for non-vanishing magnetic field divergence, I found that particular non-conservative terms are necessary to ensure the validity of the numerical scheme. As, on a continuous level, the magnetic field divergence, $\nabla \cdot \boldsymbol{B}$ vanishes exactly, adding these non-conservative terms is nothing else than adding zero in a clever way. However, for discrete systems, where the magnetic field divergence typically does not vanish, they turn out to be important to ensure the physical correctness of the mathematical model under $\nabla \cdot \boldsymbol{B} \neq 0$.

Conservative formulation

The ideal MHD equations without non-conservative terms read:

$$\frac{\partial}{\partial t}\begin{bmatrix}\rho\\ \rho\boldsymbol{u}\\ E\\ \boldsymbol{B}\end{bmatrix} + \nabla\cdot\begin{bmatrix}\rho\boldsymbol{u}\\ \rho(\boldsymbol{u}\otimes\boldsymbol{u}) + \left(p+\frac{1}{2}\|\boldsymbol{B}\|^2\right)\mathbf{I} - \boldsymbol{B}\otimes\boldsymbol{B}\\ \boldsymbol{u}\left(\frac{1}{2}\rho\|\boldsymbol{u}\|^2 + \frac{\gamma p}{\gamma-1} + \|\boldsymbol{B}\|^2\right) - \boldsymbol{B}(\boldsymbol{u}\cdot\boldsymbol{B})\\ \boldsymbol{u}\otimes\boldsymbol{B} - \boldsymbol{B}\otimes\boldsymbol{u}\end{bmatrix} = \mathbf{0} \tag{1a-d}$$

As I have shown in Derigs et al. (2018b, Sec. 2), the fluid feels an artificial force parallel to the magnetic field lines, in case any notable non-zero magnetic field divergence is present in the solution. This leads to physically incorrect behavior.

"Powell" non-conservative term

The non-conservative terms commonly known as the "Powell source terms" have first been described by Godunov (1972) and have later been rediscovered and described by Powell et al. (1999). I gave a solely physically motivated derivation of these non-conservative terms in Derigs et al. (2018b, Sec. 2).

The ideal MHD equations with the Powell term read:

$$\frac{\partial}{\partial t}\begin{bmatrix}\rho\\ \rho\boldsymbol{u}\\ E\\ \boldsymbol{B}\end{bmatrix} + \nabla\cdot\begin{bmatrix}\rho\boldsymbol{u}\\ \rho(\boldsymbol{u}\otimes\boldsymbol{u}) + \left(p+\frac{1}{2}\|\boldsymbol{B}\|^2\right)\mathbf{I} - \boldsymbol{B}\otimes\boldsymbol{B}\\ \boldsymbol{u}\left(\frac{1}{2}\rho\|\boldsymbol{u}\|^2 + \frac{\gamma p}{\gamma-1} + \|\boldsymbol{B}\|^2\right) - \boldsymbol{B}(\boldsymbol{u}\cdot\boldsymbol{B})\\ \boldsymbol{u}\otimes\boldsymbol{B} - \boldsymbol{B}\otimes\boldsymbol{u}\end{bmatrix} = -(\nabla\cdot\boldsymbol{B})\begin{bmatrix}0\\ \boldsymbol{B}\\ \boldsymbol{u}\cdot\boldsymbol{B}\\ \boldsymbol{u}\end{bmatrix} \tag{2a-d}$$

This scheme is also known as the "eight-wave" formulation of the ideal MHD equations as the additional terms cause any magnetic field divergence to be passively advected with the fluid:

$$\frac{\partial}{\partial t}(\nabla\cdot\boldsymbol{B}) + \nabla\cdot(\boldsymbol{u}(\nabla\cdot\boldsymbol{B})) = 0. \tag{3}$$

It may move numerically caused magnetic monopoles away from the places where they occurred but doesn't help at stagnation points of the fluid (where the fluid is at rest, i.e., $\|\boldsymbol{u}\| = 0$). At such points, magnetic field divergence accumulates.

The total energy can be affected by spurious magnetic energy generated by the moving "magnetic monopoles" in the simulation. If total energy conservation would be artificially enforced by neglecting the non-conservative term on the total energy, the internal energy, which is computed as the remainder of the subtraction of kinetic and magnetic energy from the total energy, would become incorrect.

The momentum equation correction is furthermore necessary to obtain the correct Lorenz force in case of $\nabla\cdot\boldsymbol{B} \neq 0$. If this term is not included, the fluid feels an unphysical, possibly substantial, force parallel to the magnetic field lines. This force is both, proportional to the local magnetic field $\boldsymbol{B}$, as well as to the local magnetic field divergence, $\nabla\cdot\boldsymbol{B}$:

$$\boldsymbol{F}_L\cdot\frac{\boldsymbol{B}}{\|\boldsymbol{B}\|} = -(\nabla\cdot\boldsymbol{B})\|\boldsymbol{B}\| \tag{4}$$

I carefully investigated the effect of the individual components of the Powell terms side in Derigs et al. (2018b, Sec. 2).

"Janhunen" non-conservative term

Janhunen (2000) presented a non-conservative term that adds the advection of the magnetic field divergence just like the Powell terms, but preserves the conservation in all thermodynamics quantities. Due to this reason, it has often been argued to be advantageous. However, as I have

clearly shown in Derigs et al. (2018b), this assumption is wrong as the loss of conservation in total energy and momentum equation actually is an advantageous property as these terms correct for effects caused by (unphysical) numerically caused magnetic monopoles. They are mandatory for physical correctness of the simulation.

The ideal MHD equations with the Janhunen source term read:

$$\frac{\partial}{\partial t}\begin{bmatrix}\rho\\ \rho\boldsymbol{u}\\ E\\ \boldsymbol{B}\end{bmatrix} + \nabla\cdot\begin{bmatrix}\rho\boldsymbol{u}\\ \rho(\boldsymbol{u}\otimes\boldsymbol{u}) + \left(p+\frac{1}{2}\|\boldsymbol{B}\|^2\right)\mathbf{I} - \boldsymbol{B}\otimes\boldsymbol{B}\\ \boldsymbol{u}\left(\frac{1}{2}\rho\|\boldsymbol{u}\|^2 + \frac{\gamma p}{\gamma-1} + \|\boldsymbol{B}\|^2\right) - \boldsymbol{B}(\boldsymbol{u}\cdot\boldsymbol{B})\\ \boldsymbol{u}\otimes\boldsymbol{B} - \boldsymbol{B}\otimes\boldsymbol{u}\end{bmatrix} = -(\nabla\cdot\boldsymbol{B})\begin{bmatrix}0\\ \mathbf{0}\\ 0\\ \boldsymbol{u}\end{bmatrix} \tag{5a-d}$$

The issue with the term suggested by Janhunen is that, although it does also add an eighth wave (the "divergence wave") to the solution, it does neither correct the Lorenz force nor for spurious total energy contributions in the presence of $\nabla\cdot\boldsymbol{B} \neq 0$. This is only done when adding the full Powell term.

It should also be noted that this term does not symmetrize the ideal MHD equations. As Godunov (1972) has shown, only the Powell terms can achieve this.

The Janhunen terms are used in the currently available numerical implementation of the `Bouchut3` and `Bouchut5` solvers for ideal MHD flows. This is in agreement with the description given by Waagan et al. (2011) albeit the fact that the Janhunen (rather than the Powell) term is used, is rather hidden in the statement:

> In the original FLASH code, the momentum and energy equations were also modified, which is what was actually recommended in [Powell, 1994]. We found it sufficient for stability in [Bouchut et al., 2010] and [Waagan, 2009] to **only include the Powell term for the induction equation**.

(Waagan, 2009, Section 2.3)[14]

Misleadingly, the paper continues to denote the Janhunen source term as the Powell source term in multiple places. The statement that the latter is only included in the induction equation is not repeated in the numerical results section, giving rise to the impression that with "a slightly more elaborate Powell term" (Waagan et al., 2011, Sec. 4.1) the full Powell terms are meant although this is not the case.

Even if the Janhunen term may be "sufficient for stability", using it is adverse from a physics point of view as the computed magnetic forces are incorrect.

[14] Citations changed from `numeric` to `authoryear` style.

1 Implementation details

As has been mentioned by Bouchut et al. (2010) and Waagan et al. (2011), it is essential for stability to discretize the terms in a proper upwind manner. In this section, I give the precise code I used to implement the terms into the file `hy_bou5_sources.F90` for the numerical tests shown in the subsequent sections.

1.1 Conservative formulation

```
! Only Gravity
S(ivn,i) = Uc(DENS_VAR,i)*grav(i)
S(ENER_VAR,i) = Uc(ivn,i)*Uc(DENS_VAR,i)*grav(i)
```

1.2 Powell term

```
real :: dBdx

! Powell term
dBdx = (Up(ibn,i)-Um(ibn,i))/dx(i)
S(VELX_VAR:VELZ_VAR,i) = -dBdx*Uc(MAGX_VAR:MAGZ_VAR,i)
S(ENER_VAR,i) = -dBdx*dot_product(Uc(VELX_VAR:VELZ_VAR,i),Uc(MAGX_VAR:
    MAGZ_VAR,i))
S(MAGX_VAR:MAGZ_VAR,i) = -dBdx*Uc(VELX_VAR:VELZ_VAR,i)

! Gravity
! We have to add the gravity source terms on top of the Powell terms
S(ivn,i) = S(ivn,i) + Uc(DENS_VAR,i)*grav(i)
S(ENER_VAR,i) = S(ENER_VAR,i) + Uc(ivn,i)*Uc(DENS_VAR,i)*grav(i)
```

1.3 Janhunen term

```
real :: dBdx

! Janhunen term
dBdx = (Up(ibn,i)-Um(ibn,i))/dx(i)
S(MAGX_VAR:MAGZ_VAR,i) = -dBdx*Uc(VELX_VAR:VELZ_VAR,i)

! Gravity
! The Janhunen term does neither modify the total energy nor the momentum
S(ivn,i) = Uc(DENS_VAR,i)*grav(i)
S(ENER_VAR,i) = Uc(ivn,i)*Uc(DENS_VAR,i)*grav(i)
```

2 Comparison using an astrophysical application

To compare the differences caused by the three different possibilities,

1. conservative formulation (“no Powell”),
2. Powell terms, and
3. Janhunen term,

I performed simulations of the colliding flow setup, extensively described in Chapter 6.

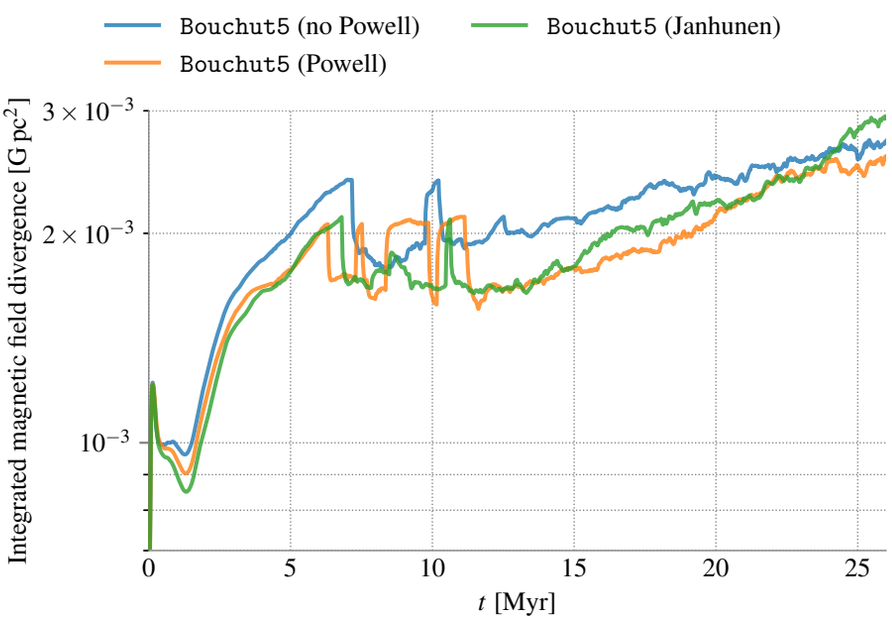

Fig. A.1: Evolution of the volume-integrated absolute magnetic field divergence

In Fig. A.1, we clearly see that the volume-integrated magnetic field divergence is similar in all simulations. This is expected as the magnetic field divergence is predominantly determined by the post-processing divergence cleaning step rather than the interior of the used numerical MHD scheme itself. Despite this, the scheme based on the Powell term proves to be advantageous for this particular setup.

In Fig. A.2, we see that the structure evolves notably different in the three simulations. This is not unexpected as minor changes can lead to very different results at later times due the highly non-linear nature of the colliding flow setup. There seems to be more dense gas in the “Powell” solution than in the “no Powell” solution or in the “Janhunen” solution. Fig. A.3 confirms this observation.

The mass-weighted magnetic field strength projection plots (Fig. A.4) again highlight the difference between the obtained solutions. The differences are even more apparent in the mass-weighted

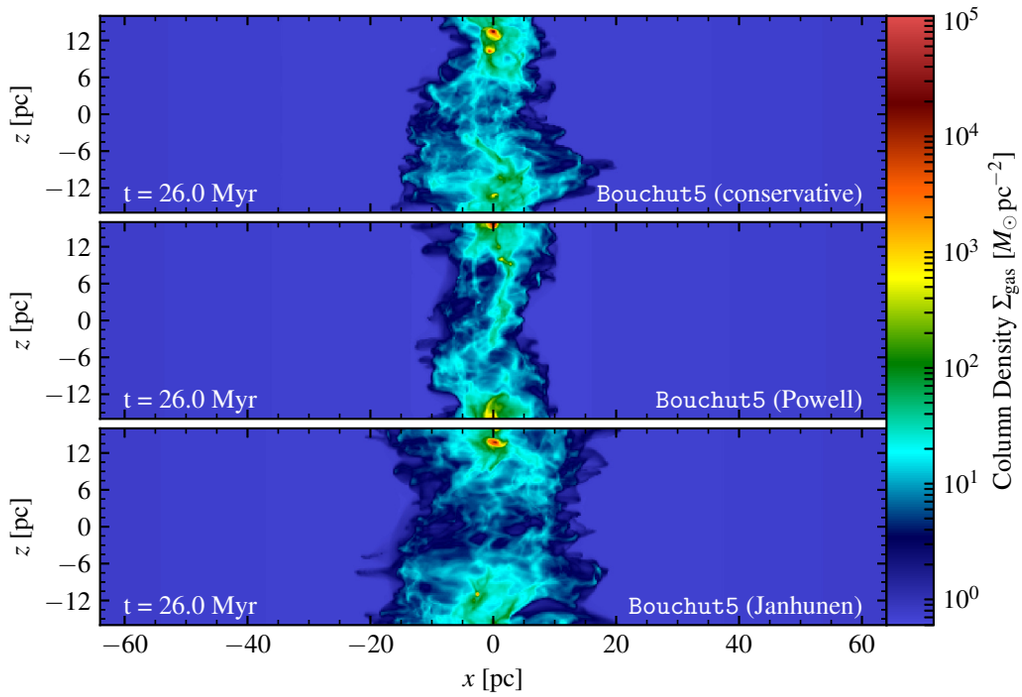

Fig. A.2: Total gas column density plot. The structure is different in all three results.

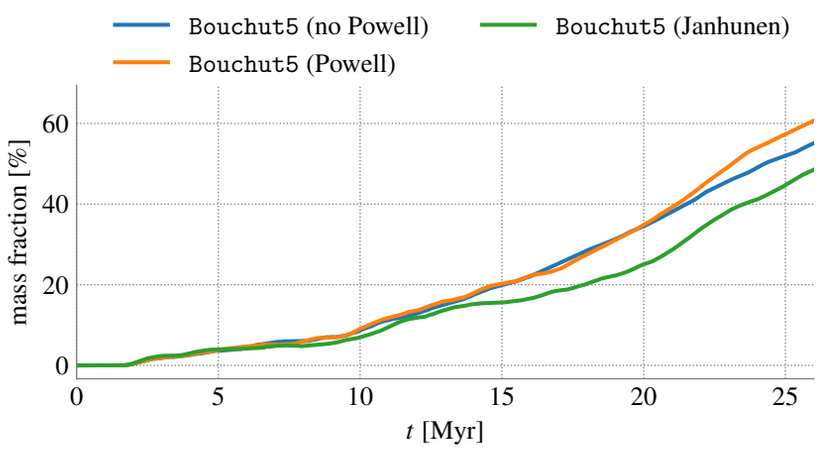

Fig. A.3: Dense gas mass ($\rho \geq 2.34 \times 1.67 \times 10^{-22}\,\mathrm{g\,cm^{-3}}$) fraction over time. There is more dense gas in the "Powell" solution that in the "no Powell" solution or the "Janhunen" solution.

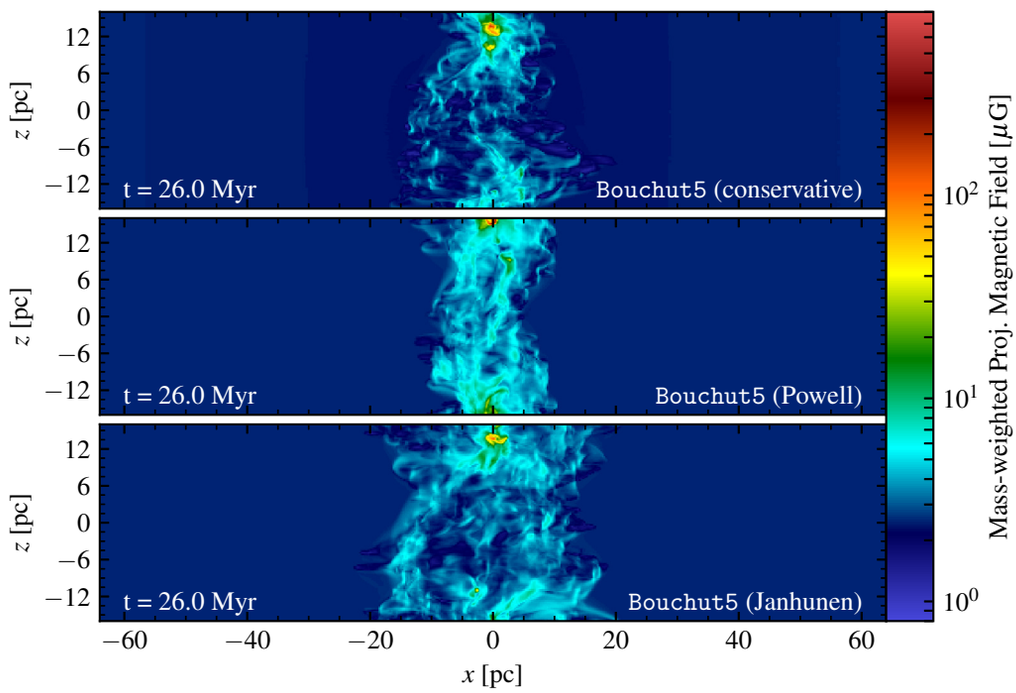

Fig. A.4: Mass-weighted projected magnetic field. The structural differences already seen in Fig. A.2 are even more predominant.

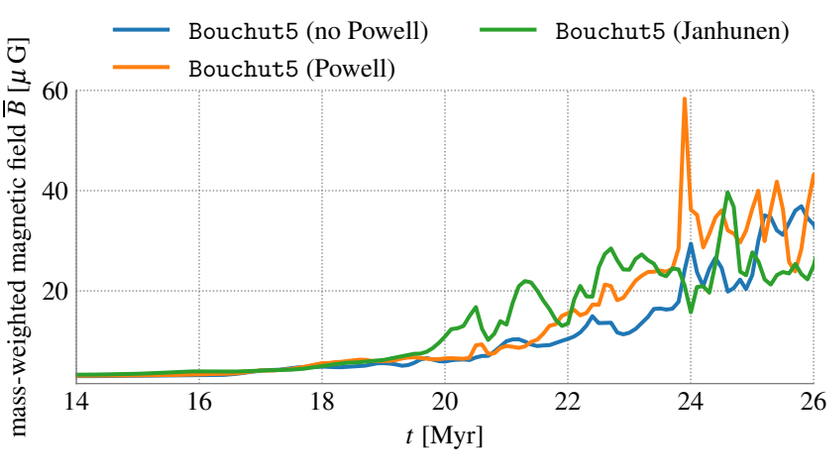

Fig. A.5: Mass-weighted average magnetic field over time. The average magnetic field is similar in all three simulations.

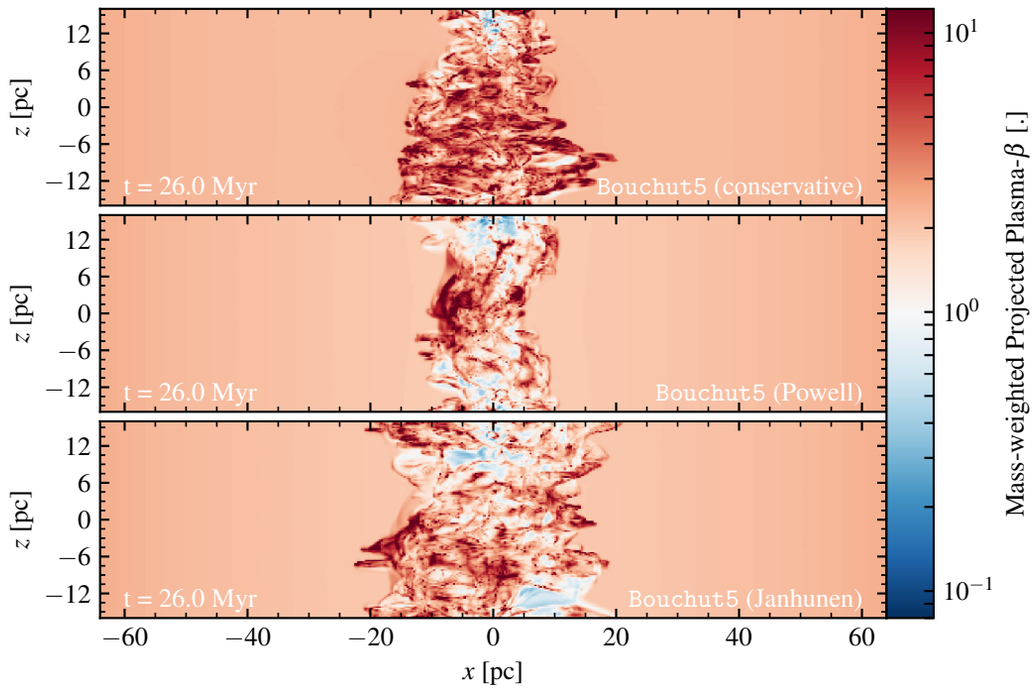

Fig. A.6: Mass-weighted projected plasma β. Blueish gas ($\beta < 1$) is magnetically dominated.

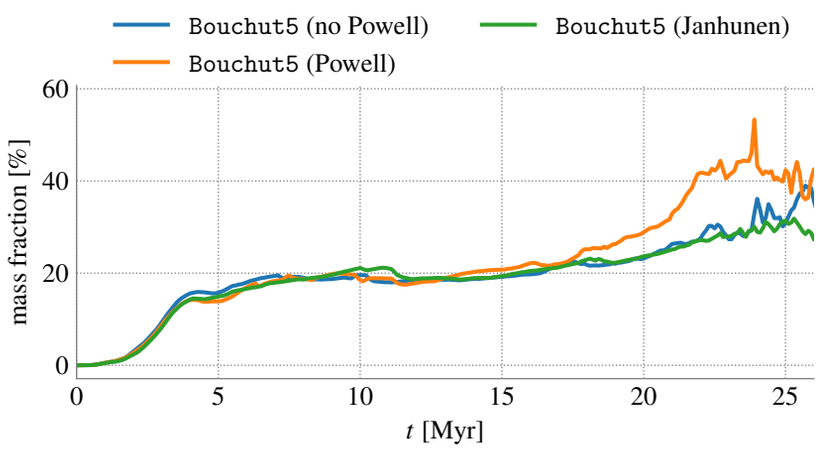

Fig. A.7: Mass fraction of the magnetically dominated gas (plasma-β criterion). The mass fraction constantly varies across the different solutions.

projected magnetic fields. However, Fig. A.5 suggests that the mass-weighted mean magnetic field is similar for all three runs.

The magnetically dominated gas mass fraction constantly varies across the different solutions as can be seen in Fig. A.7. At $t = 26\,\mathrm{Myr}$, the magnetically dominated gas mass fraction is similar for all simulations, however, as can be seen in Fig. A.6, the distribution of this gas is very different. At other simulation times, e.g., $t = 17\,\mathrm{Myr}$, the plasma $\beta < 1$ gas mass fraction is substantially smaller in the Janhunen term case (see Fig. A.7).

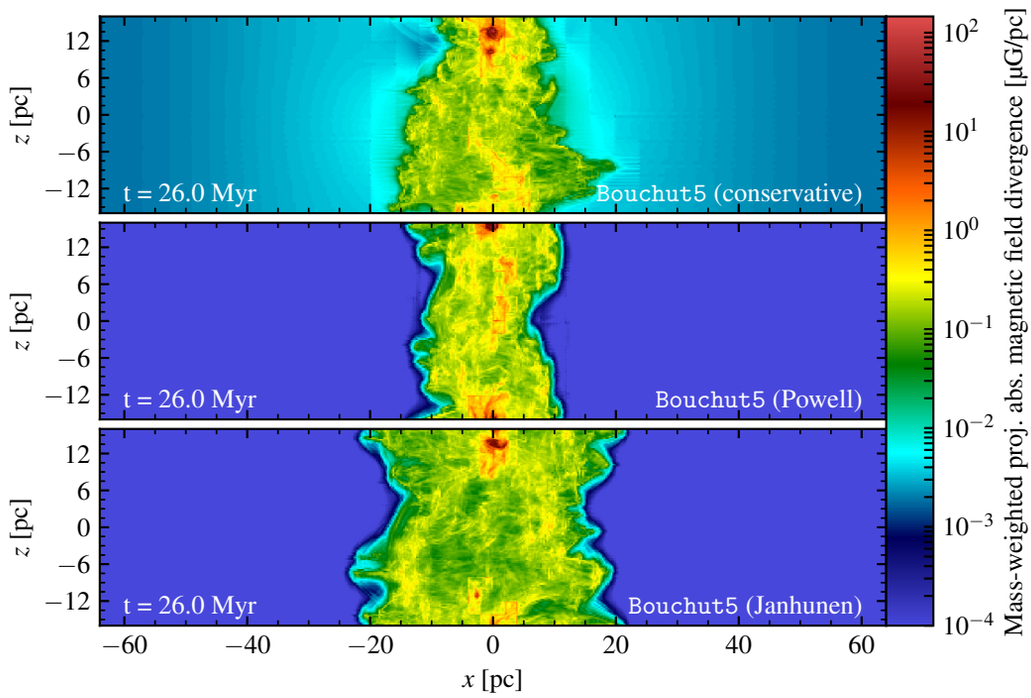

Fig. A.8: Mass-weighted projected magnetic field divergence.

Note that in all schemes the same post-processing divergence cleaning is used. In the "conservative" solution, the mass-weighted projected absolute magnetic field divergence (Fig. A.8) in the surrounding of the collision area is notably increased. However, it is still on the order of less than $\approx 0.01\,\mu\mathrm{G/pc}$ and does not contribute notably to the integrated divergence error shown in Fig. A.1.

A further difference becomes obvious when looking at the very early stages of the colliding flow simulations. As can be seen in Fig. A.9, the Janhunen variant generates notable defects in the magnetic field topology soon after the beginning of the simulation. Due to the non-linear nature of the colliding flow simulations, these small differences at early times may significantly affect the long-term evolution of the simulation.

In Fig. A.10, I plot the Lorentz force as applied by the individual numerical schemes. We see that only the Powell term based scheme applies a physically meaningful Lorentz force that is always

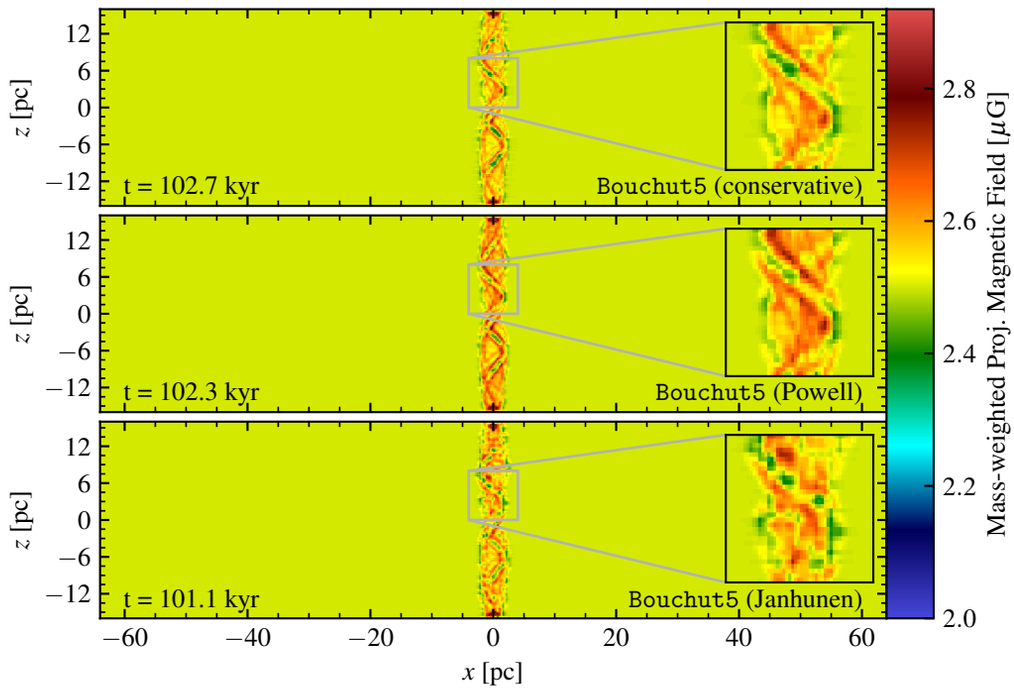

Fig. A.9: Mass-weighted projected magnetic field at $t \approx 0.1$ Myr. We see defects in the very early structure of the magnetic field where the magnetic field is more grainy than in the other two solutions.

perpendicular to the magnetic field. In the conservative case, the Lorentz force is parallel to the magnetic field almost everywhere in the inflowing medium, slightly enhancing the collapse as the force is pointing towards the central collision area. In the Janhunen term result, the behavior is exactly opposite: the Lorentz force close to the central region is pointing away from the center, i.e., the inflowing gas is slowed down shortly before the collision onto the molecular cloud occurs, giving rise to a more inflated central region as seen in Fig. A.2. This numerical experiment confirms that only the Powell term based simulation applies Lorentz forces that are physically meaningful in the sense of being always perpendicular to the magnetic field.

When looking at the volume-integrated gas energies (Fig. A.11), the difference between the solutions is most obvious. A major difference is the notably reduced growth in magnetic energy in the simulation in which the conservative formulation is used ("no Powell", blue line). As the magnetic energy is the predominant contribution to the total energy, this also explains the clearly visible difference between the run without source term (blue line) and the runs with either the Janhunen (green line) or the Powell terms (orange line). In the evolution of the kinetic energy, we see that the simulation using the Powell terms generates notably more kinetic energy in the fluid. This is most likely caused by the correct computation of the Lorentz force avoiding unphysical forces parallel to the magnetic field lines. As the initial magnetic field is aligned with inflow direction of the gas, an incorrect Lorentz force along the field lines could likely retard the

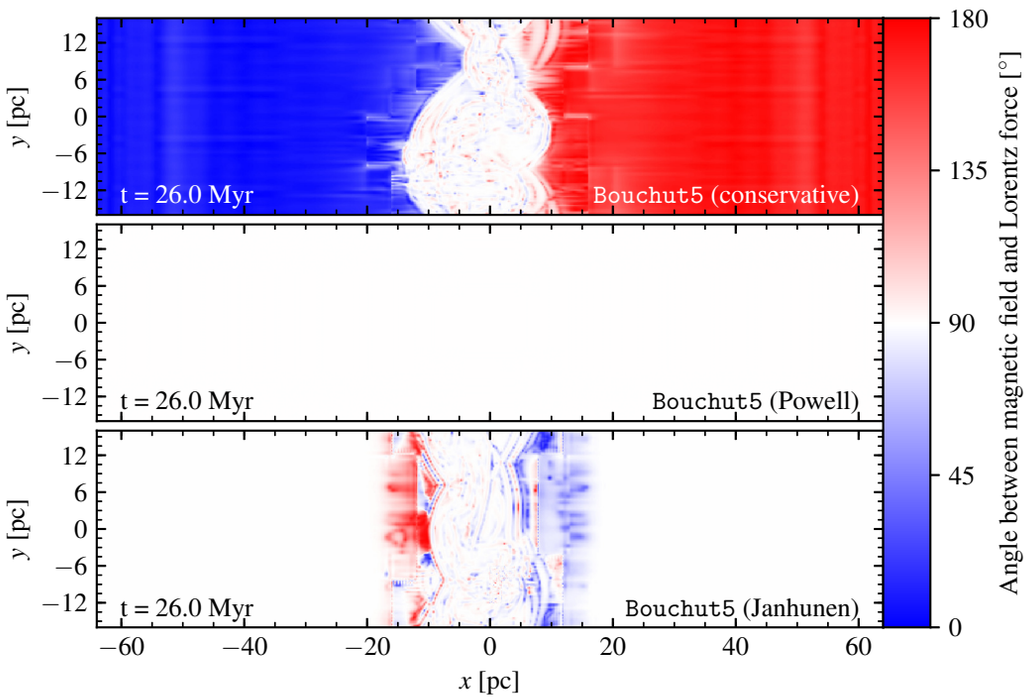

Fig. A.10: Lorentz force as applied by the numerical scheme at $t = 26\,\mathrm{Myr}$. Slice in the xy-plane at $z = 1\,\mathrm{pc}$. For both, the conservative and the Janhunen solution, the computed angle between the applied Lorentz force and the magnetic field is substantially different than 90°. With the Powell terms, the computed Lorentz force is always perpendicular with minor numerical roundoff errors ($90° \pm 6 \times 10^{-14°}$).

gravitational collapse and cause the observed slower growth of momentum.

These findings are rather concerning and should be confirmed using a different astrophysical simulation. The reckless omission of the non-conservative terms in the momentum and total energy equations often justified with wanting to recover conservation in these properties has been proven to be physically incorrect and needs to be avoided. Whereas the colliding flow model is a realistic application, its highly non-linear nature makes it rather hard to compare aspects such as the choice of the non-conservative terms. Comparative runs of simulations with less complicated physical interactions, e.g., steady state turbulence, may turn out to be useful in trying to quantify the differences for astrophysical applications.

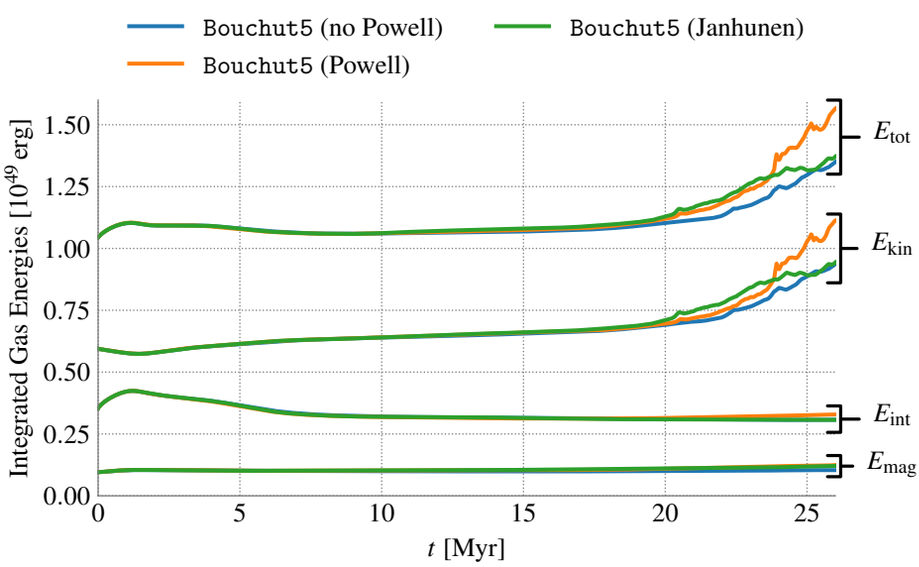

Fig. A.11: Volume-integrated gas energies. We see that the energies are in rough agreement for the Janhunen and the Powell source term whereas they start to deviate towards the end of the simulation time (collapse is much stronger in the Powell source term simulations).

Magnetic monopoles as seen by physics

Physicists often reason that magnetic monopoles are unlikely to exist as the established theory of quantum mechanics seems only possible when there are no isolated magnetic monopoles. However, Dirac (1931) showed that quantum mechanics does not preclude the existence of isolated magnetic monopoles. On the contrary, they are helpful when trying to explain the quantization of the electric charge.

Nevertheless, we phenomenologically respect the divergence-free condition (2.11) as, to this day, little experimental evidence for the existence of magnetic monopoles has been found. The scientific community is not aware of any theoretical reason why magnetic monopoles, magnets with a single north or south pole, could not exist (Rajantie, 2016).

In fact, one of the most important theoretical motivations of introducing magnetic monopoles is to obtain Maxwell's equations in symmetric form with regard to charges. The laws governing electrodynamics and magnetism are identical. This can be seen in (2.8a-d), which have a duality symmetry - the electrodynamic terms can be replaced with magnetic terms, and vice versa, in such a way that the equations are left unchanged.

One of the most notable experimental findings occurred on the night of February 14, 1982, when a group in Stanford detected a single current jump in a four-turn coil of 5 cm diameter. Within 151 days they detected a single event consistent with one Dirac unit of magnetic charge. They concluded that this event equaled that expected from a magnetic monopole (Cabrera, 1982).

However, as Cabrera's measurement has never been reproduced, it sets a low limit for both the number density as well as the magnetic charge of possibly existing magnetic monopoles. As such observations directly apply to the magnetic field divergence itself, they strongly support Gauß's law (2.11) in an asymptotic fashion. Still, the discovery of magnetic monopoles would have a massive effect on physics, and each exploration of a yet higher energy range in high energy physics triggers renewed attempts to find magnetic monopoles (see, e.g., Aad, 2012).

Although no magnetic monopoles have been found yet...

> “ ...one would be surprised if Nature had made no use of it. ”
> – Dirac (1931)

Bibliography

References are listed alphabetically by the surname of the author and grouped when authors are identical. References listed herein encompass only the scope of the thesis *excluding* the contained publications. For references used in these publications, see the Reference sections therein (pp. 67–69, pp. 79–80, and pp. 128–130).

A

Aad, G. (Dec. 2012). "Search for Magnetic Monopoles in $\sqrt{s} = 7\,\text{TeV}$ pp Collisions with the ATLAS Detector." In: *Physical Review Letters* 109.26, p. 261803. ISSN: 1079-7114. DOI: 10.1103/PhysRevLett.109.261803.

Adams, M., Schwartz, P. O., Johansen, H., Colella, P., Ligocki, T. J., Martin, D., Keen, N. D., Graves, D., Modiano, D., Van Straalen, B., McCorquodale, P., Sternberg, T. D., (Dec. 2015). *Chombo software package for AMR applications - design document*. [Online; accessed 9. May 2018]. URL: http://inspirehep.net/record/1514066.

Avillez, M. A., Breitschwerdt, D., (June 2005). "Global dynamical evolution of the ISM in star forming galaxies. I. High resolution 3D simulations: Effect of the magnetic field." In: *Astronomy and Astrophysics* 436, pp. 585–600. ISSN: 0004-6361. DOI: 10.1051/0004-6361:20042146. eprint: astro-ph/0502327.

B

Balbás, J., Tadmor, E., (Apr. 2005). "A Central Differencing Simulation of the Orszag Tang Vortex System." In: *IEEE Transactions on Plasma Science* 33, pp. 470–471. DOI: 10.1109/TPS.2005.845282.

Ballesteros-Paredes, J., Hartmann, L., Vázquez-Semadeni, E., (Dec. 1999). "Turbulent Flow--driven Molecular Cloud Formation: A Solution to the Post-T Tauri Problem?" In: *The Astrophysical Journal* 527, pp. 285–297. ISSN: 0004-637X. DOI: 10.1086/308076. eprint: astro-ph/9907053.

Balsara, D. S., Kim, J., (Feb. 2004). "A Comparison between Divergence-Cleaning and Staggered-Mesh Formulations for Numerical Magnetohydrodynamics." In: *The Astrophysical Journal* 602, pp. 1079–1090.
DOI: 10.1086/381051.

Balsara, D. S. (1998). "Total Variation Diminishing Scheme for Adiabatic and Isothermal Magnetohydrodynamics." In: *The Astrophysical Journal Supplement Series* 116.1, pp. 133–153.
DOI: 10.1086/313093.

Balsara, D. S., Spicer, D., (1999). "A staggered mesh algorithm using high order Godunov fluxes to ensure solenoidal magnetic fields in magnetohydrodynamic simulations." In: *Journal of Computational Physics* 149.2, pp. 270–292.
DOI: 10.1006/jcph.1998.6153.

Banerjee, R., Körtgen, B., (Sept. 2015). "Formation of star-forming clouds from the magnetised, diffuse interstellar medium." In: *ArXiv e-prints*. arXiv: 1509.03436.

Banerjee, R., Vázquez-Semadeni, E., Hennebelle, P., Klessen, R. S., (Sept. 2009). "Clump morphology and evolution in MHD simulations of molecular cloud formation." In: *Monthly Notices of the Royal Astronomical Society* 398, pp. 1082–1092. ISSN: 0035-8711.
DOI: 10.1111/j.1365-2966.2009.15115.x. eprint: 0808.0986.

Barth, T. (2006). "On the Role of Involutions in the Discontinuous Galerkin Discretization of Maxwell and Magnetohydrodynamic Systems." In: *Compatible Spatial Discretizations*. Ed. by D. N. Arnold, P. B. Bochev, R. B. Lehoucq, R. A. Nicolaides, & M. Shashkov. New York, NY: Springer New York, pp. 69–88.

Barth, T. J. (1999). "Numerical Methods for Gasdynamic Systems on Unstructured Meshes." In: *An Introduction to Recent Developments in Theory and Numerics for Conservation Laws*. Ed. by D. Kröner, M. Ohlberger, & C. Rohde. Vol. 5. Lecture Notes in Computational Science and Engineering. Springer Berlin Heidelberg, pp. 195–285.
DOI: 10.1007/978-3-642-58535-7_5.

Beck, R. (Oct. 2009). "Galactic and extragalactic magnetic fields – a concise review." In: *Astrophysics and Space Sciences Transactions* 5.1, pp. 43–47. ISSN: 1810-6528.
DOI: 10.5194/astra-5-43-2009.

Beck, R., Hoernes, P., (Jan. 1996). "Magnetic spiral arms in the galaxy NGC6946." In: *Nature* 379, pp. 47–49. ISSN: 0028-0836.
DOI: 10.1038/379047a0.

Beck, R. (Oct. 2001). "Galactic and Extragalactic Magnetic Fields." In: *Space Science Reviews* 99, pp. 243–260. ISSN: 0038-6308. eprint: astro-ph/0012402. URL: http://adsabs.harvard.edu/abs/2001SSRv...99..243B.

Beck, R. (Feb. 2004). "The Role of Magnetic Fields in Spiral Galaxies." In: *Astrophysics and Space Science* 289, pp. 293–302. ISSN: 0004-640X. DOI: 10.1023/B:ASTR.0000014957.31590.50. eprint: astro-ph/0212.288.

Beck, R. (Dec. 2015). "Magnetic fields in spiral galaxies." In: *Astronomy and Astrophysics Review* 24.1, p. 4. ISSN: 1432-0754. DOI: 10.1007/s00159-015-0084-4.

Bernet, M. L., Miniati, F., Lilly, S. J., Kronberg, P. P., Dessauges-Zavadsky, M., (July 2008). "Strong magnetic fields in normal galaxies at high redshift." In: *Nature* 454.7202, p. 302. DOI: 10.1038/nature07105.

Birn, J., Drake, J., Shay, M. A., Rogers, B. N., Denton, R. E., Hesse, M., Kuznetsova, M., Ma, Z. W., Bhattacharjee, A., Otto, A., Pritchett, P. L., (Mar. 2001). *Geospace Environmental Modeling (GEM) Magnetic Reconnection Challenge*. [Online; accessed 16. May 2018]. DOI: 10.1029/1999JA900449.

Birn, J., Hesse, M., (Mar. 2001). "Geospace Environment Modeling (GEM) magnetic reconnection challenge: Resistive tearing, anisotropic pressure and Hall effects." In: *J Geophys Res Space Phys* 106.A3. [Online; accessed 16. May 2018], pp. 3737–3750. ISSN: 0148-0227. DOI: 10.1029/1999JA001001.

Bohm, M., Winters, A. R., Gassner, G. J., **Derigs, D.**, Hindenlang, F., Saur, J., (Feb. 2018). "An entropy stable nodal discontinuous Galerkin method for the resistive MHD equations. Part I: Theory and Numerical Verification." In: *Journal of Computational Physics (in press)*. ISSN: 0021-9991. DOI: 10.1016/j.jcp.2018.06.027. arXiv: 1802.07341.

Bouchut, F., Klingenberg, C., Waagan, K., (June 2010). "A multiwave approximate Riemann solver for ideal MHD based on relaxation II: numerical implementation with 3 and 5 waves." In: *Numerische Mathematik* 115.4, pp. 647–679. ISSN: 0945-3245. DOI: 10.1007/s00211-010-0289-4.

Boulares, A., Cox, D. P., (Dec. 1990). "Galactic hydrostatic equilibrium with magnetic tension and cosmic-ray diffusion." In: *Astrophysical Journal* 365, pp. 544–558. ISSN: 0004-637X. DOI: 10.1086/169509.

Brackbill, J. U., Barnes, D. C., (1980). "The Effect of Nonzero $\nabla \cdot B$ on the numerical solution of the magnetohydrodynamic equations." In: *Journal of Computational Physics* 35.3,

pp. 426–430. ISSN: 0021-9991.
DOI: 10.1016/0021-9991(80)90079-0.

Brio, M., Wu, C. C., (1988). "An upwind differencing scheme for the equations of ideal magnetohydrodynamics." In: *Journal of Computational Physics* 75.2, pp. 400–422.
DOI: 10.1016/0021-9991(88)90120-9.

Burkhart, B. (Nov. 2014). *How Well Does Turbulence Theory Describe the Interstellar Medium?* Harvard-Smithsonian Center for Astrophysics, [Online; accessed 26. Apr. 2018]. URL: http://www2011.mpe.mpg.de/gamma/science/workshops/Superbubbles/talks/Burkhart.pdf.

C

Cabral, B., Leedom, L. C., (1993). "Imaging Vector Fields Using Line Integral Convolution." In: *Proceedings of the 20th Annual Conference on Computer Graphics and Interactive Techniques*. SIGGRAPH '93. Anaheim, CA: ACM, pp. 263–270. ISBN: 0-89791-601-8.
DOI: 10.1145/166117.166151.

Cabrera, B. (May 1982). "First results from a superconductive detector for moving magnetic monopoles." In: *Physical Review Letters* 48, pp. 1378–1381.
DOI: 10.1103/PhysRevLett.48.1378.

Cargo, P., Gallice, G., (1997). "Roe Matrices for Ideal MHD and Systematic Construction of Roe Matrices for Systems of Conservation Laws." In: *Journal of Computational Physics* 136.2, pp. 446–466. ISSN: 0021-9991.
DOI: 10.1006/jcph.1997.5773.

Chandrashekar, P. (Nov. 2013). "Kinetic Energy Preserving and Entropy Stable Finite Volume Schemes for Compressible Euler and Navier-Stokes Equations." In: *Communications in Computational Physics* 14 (05), pp. 1252–1286. ISSN: 1991-7120.
DOI: 10.4208/cicp.170712.010313a.

Chandrashekar, P., Klingenberg, C., (2016). "Entropy Stable Finite Volume Scheme for Ideal Compressible MHD on 2-D Cartesian Meshes." In: *SIAM Journal on Numerical Analysis* 54.2, pp. 1313–1340.
DOI: 10.1137/15M1013626.

Chiuderi, C., Velli, M., (2015). *Basics of Plasma Astrophysics*. Springer, Milano. ISBN: 978-88-470-5279-6.
DOI: 10.1007/978-88-470-5280-2.

Clapeyron, B. P. É. (1834). "Mémoire sur la puissance motrice de la chaleur." (French). In: *Journal de l'École Polytechnique*. URL: http://gallica.bnf.fr/ark:/12148/bpt6k4336791/f157.table.

Clark, P. C., Glover, S. C. O., Klessen, R. S., Bonnell, I. A., (Aug. 2012). "How long does it take to form a molecular cloud?" In: *Monthly Notices of the Royal Astronomical Society* 424, pp. 2599–2613. ISSN: 0035-8711.
DOI: 10.1111/j.1365-2966.2012.21259.x. eprint: 1204.5570.

Clarke, L. E., Fawcett, A. A., Weyant, J. P., McFarland, J., Chaturvedi, V., Zhou, Y., (May 2014). "Technology and U.S. Emissions Reductions Goals: Results of the EMF 24 Modeling Exercise." In: *Energy Journal* 35.Special. ISSN: 1944-9089.
DOI: 10.5547/01956574.35.SI1.2.

Cox, D. P. (Sept. 2005). "The Three-Phase Interstellar Medium Revisited." In: *Annual Review of Astronomy and Astrophysics* 43, pp. 337–385. ISSN: 0066-4146.
DOI: 10.1146/annurev.astro.43.072103.150615.

Crockett, R. K., Colella, P., Fisher, R. T., Klein, R. I., McKee, C. F., (Mar. 2005). "An unsplit, cell-centered Godunov method for ideal MHD." In: *Journal of Computational Physics* 203, pp. 422–448.
DOI: 10.1016/j.jcp.2004.08.021.

Crutcher, R. M. (Feb. 2004). "Observations of Magnetic Fields in Molecular Clouds." In: *The Magnetized Interstellar Medium*. Ed. by B. Uyaniker, W. Reich, & R. Wielebinski, pp. 123–132.

Crutcher, R. M. (Sept. 2012). "Magnetic Fields in Molecular Clouds." In: *Annual Review of Astronomy and Astrophysics* 50.1, pp. 29–63. ISSN: 0066-4146.
DOI: 10.1146/annurev-astro-081811-125514.

Crutcher, R. M., Wandelt, B., Heiles, C., Falgarone, E., Troland, T. H., (Dec. 2010). "Magnetic Fields in Interstellar Clouds from Zeeman Observations: Inference of Total Field Strengths by Bayesian Analysis." In: *Astrophysical Journal* 725, pp. 466–479. ISSN: 0004-637X.
DOI: 10.1088/0004-637X/725/1/466.

D

Dafermos, C. M. (2016). *Hyperbolic Conservation Laws in Continuum Physics*. 4th. Springer. ISBN: 9783662494493.
DOI: 10.1007/978-3-662-49451-6.

Dai, W., Woodward, P. R., (1998). "A Simple Finite Difference Scheme for Multidimensional Magnetohydrodynamical Equations." In: *Journal of Computational Physics* 142.2, pp. 331–369. ISSN: 0021-9991.
DOI: 10.1006/jcph.1998.5944.

Dedner, A., Kemm, F., Kröner, D., Munz, C.-D., Schnitzer, T., Wesenberg, M., (2002). "Hyperbolic divergence cleaning for the MHD equations." In: *Journal of Computational Physics* 175.2, pp. 645–673.
DOI: 10.1006/jcph.2001.6961.

Dellar, P. J. (Sept. 2001). "A Note on Magnetic Monopoles and the One-Dimensional MHD Riemann Problem." In: *Journal of Computational Physics* 172, pp. 392–398. ISSN: 0021-9991.
DOI: 10.1006/jcph.2001.6815.

Derigs, D., Labadie, L., Ghosh, D. S., Abel-Tibérini, L., (July 2014). "A novel high-contrast imaging technique based on optical tunneling to search for faint companions around bright stars at the limit of diffraction." In: *Advances in Optical and Mechanical Technologies for Telescopes and Instrumentation*. Vol. 9151. Proceedings of the SPIE.
DOI: 10.1117/12.2055440. arXiv: 1606.08846.

Derigs, D., Gassner, G. J., Walch, S., Winters, A. R., (Sept. 2018a). "Entropy Stable Finite Volume Approximations for Ideal Magnetohydrodynamics." In: *Jahresbericht der Deutschen Mathematiker-Vereinigung* 120.3, pp. 153–219. ISSN: 1869-7135.
DOI: 10.1365/s13291-018-0178-9. arXiv: 1708.03537.

Derigs, D., Winters, A. R., Gassner, G. J., Walch, S., (Apr. 2016). "A novel high-order, entropy stable, 3D AMR MHD solver with guaranteed positive pressure." In: *Journal of Computational Physics* 317, pp. 223–256. ISSN: 0021-9991.
DOI: 10.1016/j.jcp.2016.04.048. arXiv: 1605.03572.

Derigs, D., Winters, A. R., Gassner, G. J., Walch, S., (Feb. 2017). "A novel averaging technique for discrete entropy-stable dissipation operators for ideal MHD." In: *Journal of Computational Physics* 330, pp. 624–632. ISSN: 0021-9991.
DOI: 10.1016/j.jcp.2016.10.055. arXiv: 1610.06584.

Derigs, D., Winters, A. R., Gassner, G. J., Walch, S., Bohm, M., (July 2018b). "Ideal GLM-MHD: About the entropy consistent nine-wave magnetic field divergence diminishing ideal magnetohydrodynamics equations." In: *Journal of Computational Physics* 364, pp. 420–467. ISSN: 0021-9991.
DOI: 10.1016/j.jcp.2018.03.002. arXiv: 1711.06269.

Dirac, P. A. M. (1931). "Quantised Singularities in the Electromagnetic Field." In: *Proceedings of the Royal Society of London A: Mathematical, Physical and Engineering Sciences*

133.821, pp. 60–72. ISSN: 0950-1207.
DOI: 10.1098/rspa.1931.0130.

Domingues, M. O. Gomes, A. K. F. Gomes, S. M. Mendes, O. Di Pierro, B. Schneider, K. (2013). "Extended generalized Lagrangian multipliers for magnetohydrodynamics using adaptive multiresolution methods." In: *ESAIM: Proc.* 43, pp. 95–107.
DOI: 10.1051/proc/201343006.

Draine, B. (2011). *Physics of the Interstellar and Intergalactic Medium*. Princeton University Press. ISBN: 978-069112214-4.

Dubey, A., Daley, C., ZuHone, J., Ricker, P. M., Weide, K., Graziani, C., (Aug. 2012). "Imposing a Lagrangian Particle Framework on an Eulerian Hydrodynamics Infrastructure in FLASH." In: *ApJS* 201, 27, p. 27.
DOI: 10.1088/0067-0049/201/2/27.

Dubey, A., Antypas, K., Ganapathy, M. K., Reid, L. B., Riley, K., Sheeler, D., Siegel, A., Weide, K., (2009). "Extensible component-based architecture for FLASH, a massively parallel, multiphysics simulation code." In: *Parallel Computing* 35.10–11, pp. 512–522. ISSN: 0167-8191.
DOI: 10.1016/j.parco.2009.08.001.

E

Eddington, A. S. (1920). "The Internal Constitution of the Stars." In: *The Scientific Monthly* 11.4, pp. 297–303. ISSN: 00963771.

Es, B. (Apr. 2018). *Simulations for nuclear fusion*. [Online; accessed 25. Apr. 2018]. URL: https://www.cwi.nl/news/2015/simulations-nuclear-fusion.

Evans, C. R., Hawley, J. F., (Sept. 1988). "Simulation of magnetohydrodynamic flows - A constrained transport method." In: *Astrophysical Journal* 332, pp. 659–677.
DOI: 10.1086/166684.

F

Federrath, C. (July 2015). "Inefficient star formation through turbulence, magnetic fields and feedback." In: *Monthly Notices of the Royal Astronomical Society* 450, pp. 4035–4042. ISSN: 0035-8711.
DOI: 10.1093/mnras/stv941. eprint: 1504.03690.

Federrath, C. (Dec. 2016). "Magnetic field amplification in turbulent astrophysical plasmas." In: *Journal of Plasma Physics* 82.6. ISSN: 0022-3778.
DOI: 10.1017/S0022377816001069. eprint: 1610.08132.

Feng, X., Zhang, M., (Mar. 2016). "A comparative study of divergence cleaning methods of magnetic field in the solar coronal numerical simulation." In: *Frontiers in Astronomy and Space Sciences* 3, 6, p. 6.
DOI: 10.3389/fspas.2016.00006.

Ferrière, K. M. (Dec. 2001). "The interstellar environment of our galaxy." In: *Reviews of Modern Physics* 73.4, pp. 1031–1066. ISSN: 1539-0756.
DOI: 10.1103/RevModPhys.73.1031.

Fisher, T. C., Carpenter, M. H., (Nov. 2013). "High-order entropy stable finite difference schemes for nonlinear conservation laws: Finite domains." In: *Journal of Computational Physics* 252, pp. 518–557.
DOI: 10.1016/j.jcp.2013.06.014.

Fjordholm, U. S., Mishra, S., Tadmor, E., (2011). "Well-Balanced and Energy Stable Schemes for the Shallow Water Equations with Discontinuous Topography." In: *Journal of Computational Physics* 230.14, pp. 5587–5609.
DOI: 10.1016/j.jcp.2011.03.042.

Fjordholm, U. S., Mishra, S., Tadmor, E., (2012). "Arbitrarily High-order Accurate Entropy Stable Essentially Nonoscillatory Schemes for Systems of Conservation Laws." In: *SIAM Journal on Numerical Analysis* 50.2, pp. 544–573.
DOI: 10.1137/110836961.

Fjordholm, U. S., Mishra, S., Tadmor, E., (Apr. 2013). "ENO Reconstruction and ENO Interpolation Are Stable." In: *Foundations of Computational Mathematics* 13.2, pp. 139–159. ISSN: 1615-3383.
DOI: 10.1007/s10208-012-9117-9.

Flash Center for Computational Science, (Dec. 2017). *FLASH User's Guide*. Version 4.5. University of Chicago. 589 pp. URL: http://flash.uchicago.edu/site/flashcode/user_support/flash4_ug_4p5.pdf.

Fogerty, E., Frank, A., Heitsch, F., Carroll-Nellenback, J., Haig, C., Adams, M., (Aug. 2016). "Molecular cloud formation in high-shear, magnetized colliding flows." In: *Monthly Notices of the Royal Astronomical Society* 460, pp. 2110–2128. ISSN: 0035-8711.
DOI: 10.1093/mnras/stw1141. eprint: 1602.01417.

Fryxell, B., Olson, K., Ricker, P., Timmes, F. X., Zingale, M., Lamb, D. Q., MacNeice, P., Rosner, R., Truran, J. W., Tufo, H., (Nov. 2000). "FLASH: An Adaptive Mesh Hydrodynamics

Code for Modeling Astrophysical Thermonuclear Flashes." In: *ApJS* 131, pp. 273–334. DOI: 10.1086/317361.

G

Gatto, A., Walch, S., Naab, T., Girichidis, P., Wünsch, R., Glover, S. C. O., Klessen, R. S., Clark, P. C., Peters, T., **Derigs, D.**, Baczynski, C., Puls, J., (June 2016). "The SILCC project: III. Regulation of star formation and outflows by stellar winds and supernovae." In: arXiv: 1606.05346.

Girichidis, P., Walch, S., Naab, T., Gatto, A., Wünsch, R., Glover, S. C. O., Klessen, R. S., Clark, P. C., Peters, T., **Derigs, D.**, Baczynski, C., (Mar. 2016). "The SILCC (SImulating the LifeCycle of molecular Clouds) project - II. Dynamical evolution of the supernova-driven ISM and the launching of outflows." In: *Monthly Notices of the Royal Astronomical Society* 456, pp. 3432–3455.
DOI: 10.1093/mnras/stv2742. arXiv: 1508.06646.

Glatzmaiers, G. A., Roberts, P., (Sept. 1995). "A three-dimensional self-consistent computer simulation of a geomagnetic field reversal." In: *Nature* 377.6546, pp. 203–209. ISSN: 1476-4687.
DOI: 10.1038/377203a0.

Glover, S. C. O., Federrath, C., Mac Low, M.-M., Klessen, R. S., (May 2010). "Modelling CO formation in the turbulent interstellar medium." In: *Monthly Notices of the Royal Astronomical Society* 404, pp. 2–29. ISSN: 0035-8711.
DOI: 10.1111/j.1365-2966.2009.15718.x. eprint: 0907.4081.

Godunov, S. K. (1961). "An Interesting Class of Quaslinear Systems." In: *Doklady Akademii Nauk SSSR* 139, pp. 521–523.

Godunov, S. (1972). "Symmetric form of the equations of magnetohydrodynamics." In: *Numerical Methods for Mechanics of Continuum Medium* 1, pp. 26–34.

Gottlieb, S., Shu, C.-W., Tadmor, E., (2001). "Strong Stability-Preserving High-Order Time Discretization Methods." In: *SIAM Review* 43.1, pp. 89–112.
DOI: 10.1137/S003614450036757X.

Grasso, D., Rubinstein, H. R., (July 2001). "Magnetic fields in the early Universe." In: *Physics Reports* 348, pp. 163–266. ISSN: 0370-1573.
DOI: 10.1016/S0370-1573(00)00110-1. eprint: astro-ph/0009061.

Griffiths, D. J. (July 2011). *Elektrodynamik: Eine Einführung (Pearson Studium - Physik)*. (German). 3rd ed. Pearson Studium. ISBN: 978-386894057-2.

H

Haid, S., Walch, S., Naab, T., Seifried, D., Mackey, J., Gatto, A., (Aug. 2016). "Supernova blast waves in wind-blown bubbles, turbulent, and power-law ambient media." In: *Monthly Notices of the Royal Astronomical Society* 460, pp. 2962–2978. ISSN: 0035-8711. DOI: 10.1093/mnras/stw1082. eprint: 1604.04395.

Haid, S., Walch, S., Seifried, D., Wünsch, R., Dinnbier, F., Naab, T., (May 2018). "The relative impact of photoionizing radiation and stellar winds on different environments." In: *Monthly Notices of the Royal Astronomical Society*, sty1315. ISSN: 0035-8711. DOI: 10.1093/mnras/sty1315.

Hall, J. S. (Apr. 1951). "Some polarization measurements in the Pleiades and Orion regions." In: *Astronomical Journal* 56, p. 40. ISSN: 0004-6256. DOI: 10.1086/106491.

Hanasz, M., Wóltański, D., Kowalik, K., (Nov. 2009). "Global Galactic Dynamo Driven by Cosmic Rays and Exploding Magnetized Stars." In: *Astrophysical Journal* 706, pp. L155–L159. ISSN: 0004-637X. DOI: 10.1088/0004-637X/706/1/L155. eprint: 0907.4891.

Harten, A., Engquist, B., Osher, S., Chakravarthy, S. R., (1987). "Uniformly high order accurate essentially non-oscillatory schemes, III." In: *Journal of Computational Physics* 71.2, pp. 231–303. ISSN: 0021-9991. DOI: 10.1016/0021-9991(87)90031-3.

Harten, A. (1983). "On the Symmetric Form of Systems of Conservation Laws with Entropy." In: *Journal of Computational Physics* 49, pp. 151–164.

Harten, A., Lax, P. D., Leer, B., (1983). "On Upstream Differencing and Godunov-Type Schemes for Hyperbolic Conservation Laws." In: *SIAM Review* 25.1, pp. 35–61. DOI: 10.1137/1025002.

Haverkorn, M. (2015). "Magnetic Fields in the Milky Way." In: *SpringerLink*, pp. 483–506. DOI: 10.1007/978-3-662-44625-6_17.

Haworth, T. J., Glover, S. C. O., Koepferl, C. M., Bisbas, T. G., Dale, J. E., (Nov. 2017). "Synthetic observations of star formation and the interstellar medium." In: *ArXiv e-prints*. eprint: 1711.05275.

Heitsch, F., Burkert, A., (2002). "Alfvén-wave Driven Turbulence in Molecular Clouds." In: *Modes of Star Formation and the Origin of Field Populations* 285, p. 13. ISSN: 1050-3390. URL: http://adsabs.harvard.edu/abs/2002ASPC..285...13H.

Heitsch, F., Hartmann, L., (Sept. 2014). "Accretion and diffusion time-scales in sheets and filaments." In: *Monthly Notices of the Royal Astronomical Society* 443, pp. 230–240. ISSN: 0035-8711.
DOI: 10.1093/mnras/stu1147. eprint: 1406.2191.

Heitsch, F., Slyz, A. D., Devriendt, J. E. G., Hartmann, L. W., Burkert, A., (Sept. 2006). "The Birth of Molecular Clouds: Formation of Atomic Precursors in Colliding Flows." In: *The Astrophysical Journal* 648, pp. 1052–1065. ISSN: 0004-637X.
DOI: 10.1086/505931. eprint: astro-ph/0605435.

Hennebelle, P., Audit, E., (Apr. 2007). "On the structure of the turbulent interstellar atomic hydrogen. I. Physical characteristics. Influence and nature of turbulence in a thermally bistable flow." In: *Astronomy and Astrophysics* 465, pp. 431–443. ISSN: 0004-6361.
DOI: 10.1051/0004-6361:20066139. eprint: astro-ph/0612778.

Hennebelle, P., Banerjee, R., Vázquez-Semadeni, E., Klessen, R. S., Audit, E., (Aug. 2008). "From the warm magnetized atomic medium to molecular clouds." In: *Astronomy and Astrophysics* 486, pp. L43–L46. ISSN: 0004-6361.
DOI: 10.1051/0004-6361:200810165. eprint: 0805.1366.

Hennebelle, P., Ciardi, A., (Nov. 2009). "Disk formation during collapse of magnetized protostellar cores." In: *Astronomy and Astrophysics* 506, pp. L29–L32. ISSN: 0004-6361.
DOI: 10.1051/0004-6361/200913008. eprint: 0909.3190.

Hennebelle, P., Fromang, S., (Jan. 2008). "Magnetic processes in a collapsing dense core. I. Accretion and ejection." In: *Astronomy and Astrophysics* 477, pp. 9–24. ISSN: 0004-6361.
DOI: 10.1051/0004-6361:20078309. eprint: 0709.2886.

Hennebelle, P., Teyssier, R., (Jan. 2008). "Magnetic processes in a collapsing dense core. II. Fragmentation. Is there a fragmentation crisis?" In: *Astronomy and Astrophysics* 477, pp. 25–34. ISSN: 0004-6361.
DOI: 10.1051/0004-6361:20078310. eprint: 0709.2887.

Hennebelle, P., Iffrig, O., (Oct. 2014). "Simulations of magnetized multiphase galactic disc regulated by supernovae explosions." In: *Astronomy and Astrophysics* 570. ISSN: 0004-6361.
DOI: 10.1051/0004-6361/201423392. eprint: 1405.7819.

Hesse, M., Birn, J., Kuznetsova, M., (Mar. 2001). "Collisionless magnetic reconnection: Electron processes and transport modeling." In: *J Geophys Res Space Phys* 106.A3, pp. 3721–3735.

ISSN: 0148-0227.
DOI: 10.1029/1999JA001002.

Hill, A. S., Joung, M. R., Mac Low, M.-M., Benjamin, R. A., Haffner, L. M., Klingenberg, C., Waagan, K., (May 2012). "Vertical Structure of a Supernova-driven Turbulent, Magnetized Interstellar Medium." In: *Astrophysical Journal* 750. ISSN: 0004-637X. DOI: 10.1088/0004-637X/750/2/104. eprint: 1202.0552.

Hiltner, W. A. (Sept. 1951). "Polarization of Stellar Radiation. III. The Polarization of 841 Stars." In: *Astrophysical Journal* 114, p. 241. ISSN: 0004-637X. DOI: 10.1086/145465.

Hindenlang, F., Sonnendrücker, E., Hölzl, M., (July 3, 2016). "A Parallel 3D Discontinuous Galerkin Framework for Nonlinear Resistive MHD Simulations in Tokamak and Stellarator Geometries." In: *to be published.* URL: https://nrg.iag.uni-stuttgart.de/wp-content/uploads/2016/08/EPS2016_paper_hindenlang.pdf%20https://nrg.iag.uni-stuttgart.de/wp-content/uploads/2016/08/2016-07-02-EPS-Hindenlang-MHD-DGSEMposter.pdf. published.

Houde, M., Dowell, C. D., Hildebrand, R. H., Dotson, J. L., Vaillancourt, J. E., Phillips, T. G., Peng, R., Bastien, P., (Apr. 2004). "Tracing the Magnetic Field in Orion A." In: *Astrophysical Journal* 604, pp. 717–740. ISSN: 0004-637X. DOI: 10.1086/382067. eprint: astro-ph/0312365.

Huba, J. D. (Jan. 2005). "Hall magnetic reconnection: Guide field dependence." In: *Physics of Plasmas* 12.1, p. 012322. ISSN: 1070-664X. DOI: 10.1063/1.1834592.

Huba, J. D., Rudakov, L. I., (Nov. 2002). "Three-dimensional Hall magnetic reconnection." In: *Physics of Plasmas* 9.11, pp. 4435–4438. ISSN: 1070-664X. DOI: 10.1063/1.1514970.

I

Ismail, F., Roe, P. L., (2009). "Affordable, entropy-consistent Euler flux functions II: Entropy production at shocks." In: *Journal of Computational Physics* 228.15, pp. 5410–5436. DOI: 10.1016/j.jcp.2009.04.021.

J

Jackson, J. D., Witte, C., Muller, K., (July 2006). *Klassische Elektrodynamik (Überarbeitete Auflage) (German Edition)*. 4th. Walter de Gruyter. ISBN: 9783110189704.

Jameson, A. (Feb. 2008). "Formulation of Kinetic Energy Preserving Conservative Schemes for Gas Dynamics and Direct Numerical Simulation of One-Dimensional Viscous Compressible Flow in a Shock Tube Using Entropy and Kinetic Energy Preserving Schemes." In: *Journal of Scientific Computing* 34.2, pp. 188–208. ISSN: 1573-7691. DOI: 10.1007/s10915-007-9172-6.

Janhunen, P. (2000). "A positive conservative method for magnetohydrodynamics based on HLL and Roe methods." In: *Journal of Computational Physics* 160.2, pp. 649–661. DOI: 10.1006/jcph.2000.6479.

Jenko, F. (July 2013). *An introduction to turbulence in fusion plasmas I*. Max-Planck-Institut für Plasmaphysik, Garching [Online; accessed 25. Apr. 2018]. URL: http://www.physics.ucla.edu/~jenko/TURB/Jenko-1.pdf.

Jiang, R.-L., Fang, C., Chen, P.-F., (2012). "A new MHD code with adaptive mesh refinement and parallelization for astrophysics." In: *Computer Physics Communications* 183.8, pp. 1617–1633. ISSN: 0010-4655. DOI: https://doi.org/10.1016/j.cpc.2012.02.030. eprint: 1204.5849.

Joshi, P. R., Walch, S., Seifried, D., Glover, S. C. O., Weis, M., Clarke, S. D., (2018). "On the resolution requirements for modelling molecular gas formation in solar neighbourhood conditions." In: *submitted to Monthly Notices of the Royal Astronomical Society*.

K

Keeler, J. E. (Oct. 1897). "The Importance of Astrophysical Research and the Relation of Astrophysics to Other Physical Sciences." In: *Astrophysical Journal* 6, p. 271. DOI: 10.1086/140401.

Kim, C.-G., Ostriker, E. C., (Dec. 2015). "Vertical Equilibrium, Energetics, and Star Formation Rates in Magnetized Galactic Disks Regulated by Momentum Feedback from Supernovae." In: *Astrophysical Journal* 815. ISSN: 0004-637X. DOI: 10.1088/0004-637X/815/1/67. eprint: 1511.00010.

Klassen, M., Pudritz, R. E., Kirk, H., (Feb. 2017). "Filamentary flow and magnetic geometry in evolving cluster-forming molecular cloud clumps." In: *Monthly Notices of the Royal Astronomical Society* 465, pp. 2254–2276. ISSN: 0035-8711.
DOI: 10.1093/mnras/stw2889. eprint: 1605.08835.

Klessen, R. S., Hennebelle, P., (Sept. 2010). "Accretion-driven turbulence as universal process: galaxies, molecular clouds, and protostellar disks." In: *Astronomy and Astrophysics* 520. ISSN: 0004-6361.
DOI: 10.1051/0004-6361/200913780. eprint: 0912.0288.

Kong, C. (May 2011). "Comparison of Approximate Riemann Solvers." MA thesis. Berkshire, United Kingdom: University of Reading.

Körtgen, B., Banerjee, R., (Aug. 2015). "Impact of magnetic fields on molecular cloud formation and evolution." In: *Monthly Notices of the Royal Astronomical Society* 451, pp. 3340–3353. ISSN: 0035-8711.
DOI: 10.1093/mnras/stv1200. eprint: 1502.03306.

Kotarba, H., Lesch, H., Dolag, K., Naab, T., Johansson, P. H., Stasyszyn, F. A., (Aug. 2009). "Magnetic field structure due to the global velocity field in spiral galaxies." In: *Monthly Notices of the Royal Astronomical Society* 397, pp. 733–747. ISSN: 0035-8711.
DOI: 10.1111/j.1365-2966.2009.15030.x. eprint: 0905.0351.

Koyama, H., Ostriker, E. C., (Mar. 2009a). "Gas Properties and Implications for Galactic Star Formation in Numerical Models of the Turbulent, Multiphase Interstellar Medium." In: *Astrophysical Journal* 693, pp. 1316–1345. ISSN: 0004-637X.
DOI: 10.1088/0004-637X/693/2/1316. eprint: 0812.1846.

Koyama, H., Ostriker, E. C., (Mar. 2009b). "Pressure Relations and Vertical Equilibrium in the Turbulent, Multiphase Interstellar Medium." In: *Astrophysical Journal* 693, pp. 1346–1359. ISSN: 0004-637X.
DOI: 10.1088/0004-637X/693/2/1346. eprint: 0812.1848.

Kružkov, S. N. (1970). "First Order Quasilinear Equations in Several Independent Variables." In: *Mathematics of the USSR-Sbornik* 10.2, pp. 127–243.

Kuznetsov, N. N. (1976). "Accuracy of Some Approximate Methods for Computing the Weak Solutions of a First-Order Quasi-Linear Equation." In: *USSR Computational Mathematics and Mathematical Physics* 16.6, pp. 105–119.

L

Landau, L. D. (Jan. 1959). *Fluid Mechanics*. Vol. 6. Pergamon. ISBN: 9780080291420.

Lax, P. D. (Feb. 1954). "Weak solutions of nonlinear hyperbolic equations and their numerical computation." In: *Commun Pure Appl Math* 7.1, pp. 159–193. ISSN: 0010-3640. DOI: 10.1002/cpa.3160070112.

Lax, P. D. (1967). "Hyperbolic difference equations: A review of the Courant-Friedrichs-Lewy paper in the light of recent developments." In: *IBM Journal of Reseach and Development* 11.2, pp. 235–238.

Lazarian, A., Eyink, G. L., Vishniac, E. T., Kowal, G., (2015). "Magnetic Reconnection in Astrophysical Environments." In: *Magnetic Fields in Diffuse Media* 407, p. 311. DOI: 10.1007/978-3-662-44625-6_12. eprint: 1407.6356.

Lee, D. (June 2013). "A solution accurate, efficient and stable unsplit staggered mesh scheme for three dimensional magnetohydrodynamics." In: *J Comput Phys* 243, pp. 269–292. ISSN: 0021-9991. DOI: 10.1016/j.jcp.2013.02.049.

Lee, D. (Mar. 29, 2018). personal communication.

Lee, D., Deane, A. E., (Mar. 2009). "An Unsplit Staggered Mesh Scheme for Multidimensional Magnetohydrodynamics." In: *J. Comput. Phys.* 228.4, pp. 952–975. ISSN: 0021-9991. DOI: 10.1016/j.jcp.2008.08.026.

Lee, H., Hopkins, P. F., Squire, J., (Aug. 2017). "The dynamics of charged dust in magnetized molecular clouds." In: *Monthly Notices of the Royal Astronomical Society* 469, pp. 3532–3540. ISSN: 0035-8711. DOI: 10.1093/mnras/stx1097. eprint: 1612.05264.

LeFloch, P. G., Mercier, J. M., Rohde, C., (2002). "Fully Discrete, Entropy Conservative Schemes of Arbitrary Order." In: *SIAM Journal on Numerical Analysis* 40.5, pp. 1968–1992. DOI: 10.1137/S003614290240069X.

LeVeque, R. J. (1992). *Numerical Methods for Conservation Laws*. 2nd. Birkhäuser. ISBN: 9783764327231.

LeVeque, R. J. (Aug. 2008). *Numerical Methods for Conservation Laws (Lectures in Mathematics. ETH Zürich)*. Birkhäuser Verlag. ISBN: 978-376432723-1.

LeVeque, R. J., Mihalas, D., Dorfi, E. A., Müller, E., (Aug. 1998). *Computational Methods for Astrophysical Fluid Flow: Saas-Fee Advanced Course 27. Lecture Notes 1997 Swiss Society for Astrophysics and Astronomy*. Springer Science & Business Media. ISBN: 978-354064448-4.

Li, H.-B., Goodman, A., Sridharan, T. K., Houde, M., Li, Z.-Y., Novak, G., Tang, K. S., (2014). "The Link Between Magnetic Fields and Cloud/Star Formation." In: *Protostars and Planets VI*, pp. 101–123.
DOI: 10.2458/azu_uapress_9780816531240-ch005. eprint: 1404.2024.

Li, H.-B., Jiang, H., Fan, X., Gu, Q., Zhang, Y., (Aug. 2017). "The link between magnetic field orientations and star formation rates." In: *Nature Astronomy* 1. ISSN: 2397-3366.
DOI: 10.1038/s41550-017-0158. eprint: 1706.08452.

Lin, Q., Lin, J., (2007). *Finite Element Methods: Accuracy and Improvement*. 1st ed. Elsevier Science. ISBN: 9787030166562.

Liu, X.-D., Osher, S., Chan, T., (Nov. 1994). "Weighted Essentially Non-oscillatory Schemes." In: *Journal of Computational Physics* 115.1, pp. 200–212. ISSN: 0021-9991.
DOI: 10.1006/jcph.1994.1187.

Londrillo, P., Del Zanna, L., (Feb. 2000). "High-Order Upwind Schemes for Multidimensional Magnetohydrodynamics." In: *The Astrophysical Journal* 530, pp. 508–524.
DOI: 10.1086/308344. eprint: astro-ph/9910086.

Lyness, J. N., Moler, C. B., (1967). "Numerical Differentiation of Analytic Functions." In: *SIAM Journal on Numerical Analysis* 4.2, pp. 202–210.
DOI: 10.1137/0704019.

M

Mac Low, M.-M., Klessen, R. S., (Jan. 2004). "Control of star formation by supersonic turbulence." In: *Reviews of Modern Physics* 76, pp. 125–194. ISSN: 0034-6861.
DOI: 10.1103/RevModPhys.76.125. eprint: astro-ph/0301093.

Mackey, J., Lim, A. J., (2011). "Effects of magnetic fields on photoionized pillars and globules." In: *Monthly Notices of the Royal Astronomical Society* 412.3, pp. 2079–2094.
DOI: 10.1111/j.1365-2966.2010.18043.x.

MacNeice, P., Olson, K. M., Mobarry, C., de Fainchtein, R., Packer, C., (Apr. 2000). "PARAMESH: A parallel adaptive mesh refinement community toolkit." In: *Computer Physics Communications* 126, pp. 330–354.
DOI: 10.1016/S0010-4655(99)00501-9.

Marder, B. (1987). "A method for incorporating Gauss' law into electromagnetic PIC codes." In: *Journal of Computational Physics* 68.1, pp. 48–55. ISSN: 0021-9991.
DOI: 10.1016/0021-9991(87)90043-X.

Maxima, (2016). *Maxima, a Computer Algebra System. Version 5.38.1*. URL: http://maxima.sourceforge.net/.

McKee, C. F. (1999). "The Dynamical Structure and Evolution of Giant Molecular Clouds." In: *NATO Advanced Science Institutes (ASI) Series C*. Ed. by C. J. Lada & N. D. Kylafis. Vol. 540. NATO Advanced Science Institutes (ASI) Series C, p. 29. eprint: astro-ph/9901370.

Merriam, M. L. (1989). *Entropy Based Approach to Nonlinear Stability*. National Aeronautics and Space Administration.

Mignone, A., Tzeferacos, P., Bodo, G., (Aug. 2010). "High-order conservative finite difference GLM-MHD schemes for cell-centered MHD." In: *Journal of Computational Physics* 229, pp. 5896–5920.
DOI: 10.1016/j.jcp.2010.04.013. arXiv: 1001.2832 [astro-ph.HE].

Mishra, S. (Sept. 2011). "Entropy stable high-order schemes for systems of conservation laws." In: *Modern Techniques in the Numerical Solution of Partial Differential Equations*.

Mock, M. S. (1980). "Systems of conservation laws of mixed type." In: *Journal of Differential Equations* 37.1, pp. 70–88.

Moulin, F. (Aug. 2001). "Magnetic monopoles and Lorentz force." In: *Nuovo Cimento B Serie* 116, p. 869. eprint: math-ph/0203043.

Munz, C.-D., Omnes, P., Schneider, R., Sonnendrücker, E., Voß, U., (2000). "Divergence Correction Techniques for Maxwell Solvers Based on a Hyperbolic Model." In: *Journal of Computational Physics* 161.2, pp. 484–511. ISSN: 0021-9991.
DOI: 10.1006/jcph.2000.6507.

Murawski, K. (Sept. 2003). *Analytical and Numerical Methods for Wave Propagation in Fluid Media (Stability, Vibration and Control of Systems, Series A)*. World Scientific Pub Co Inc. ISBN: 9789812381552.

N

Naab, T., Ostriker, J. P., (Aug. 2017). "Theoretical Challenges in Galaxy Formation." In: *Annual Review of Astronomy and Astrophysics* 55, pp. 59–109.
DOI: 10.1146/annurev-astro-081913-040019.

Novak, G., Dotson, J. L., Li, H., (Apr. 2009). "Dispersion of Observed Position Angles of Submillimeter Polarization in Molecular Clouds." In: *Astrophysical Journal* 695, pp. 1362–1369. ISSN: 0004-637X.
DOI: 10.1088/0004-637X/695/2/1362. eprint: 0707.2818.

O

Obergaulinger, M., Cerdá-Durán, P., Müller, E., Aloy, M. A., (Apr. 2009). "Semi-global simulations of the magneto-rotational instability in core collapse supernovae." In: *Astronomy and Astrophysics* 498, pp. 241–271.
DOI: 10.1051/0004-6361/200811323. arXiv: 0811.1652.

Ogilvie, G. I. (Apr. 2016). "Lecture notes: Astrophysical fluid dynamics." In: *ArXiv e-prints*. arXiv: 1604.03835 [astro-ph.SR].

Orszag, S. A., Tang, C.-M., (1979). "Small-scale structure of two-dimensional magnetohydrodynamic turbulence." In: *Journal of Fluid Mechanics* 90.01, pp. 129–143.
DOI: 10.1017/s002211207900210x.

Osher, S. (1984). "Riemann solvers, the entropy condition, and difference." In: *SIAM Journal on Numerical Analysis* 21.2, pp. 217–235.

Otto, A. (Mar. 2001). "Geospace Environment Modeling (GEM) magnetic reconnection challenge: MHD and Hall MHD—constant and current dependent resistivity models." In: *J Geophys Res Space Phys* 106.A3, pp. 3751–3757. ISSN: 0148-0227.
DOI: 10.1029/1999JA001005.

P

Padoan, P., Nordlund, Å., (Nov. 1999). "A Super-Alfvénic Model of Dark Clouds." In: *Astrophysical Journal* 526, pp. 279–294. ISSN: 0004-637X.
DOI: 10.1086/307956. eprint: astro-ph/9901288.

Pakmor, R., Springel, V., (June 2013). "Simulations of magnetic fields in isolated disc galaxies." In: *Monthly Notices of the Royal Astronomical Society* 432, pp. 176–193. ISSN: 0035-8711.
DOI: 10.1093/mnras/stt428. eprint: 1212.1452.

Pardi, A., Girichidis, P., Naab, T., Walch, S., Peters, T., Heitsch, F., Glover, S. C. O., Klessen, R. S., Wünsch, R., Gatto, A., (Mar. 2017). "The impact of magnetic fields on the chemical evolution of the supernova-driven ISM." In: *Monthly Notices of the Royal Astronomical Society* 465, pp. 4611–4633. ISSN: 0035-8711.
DOI: 10.1093/mnras/stw3071. eprint: 1611.00585.

Peters, T., Banerjee, R., Klessen, R. S., Mac Low, M.-M., (Mar. 2011). "The Interplay of Magnetic Fields, Fragmentation, and Ionization Feedback in High-mass Star Formation." In: *Astrophysical Journal* 729. ISSN: 0004-637X.
DOI: 10.1088/0004-637X/729/1/72. eprint: 1010.5905.

Peters, T., Naab, T., Walch, S., Glover, S. C. O., Girichidis, P., Pellegrini, E., Klessen, R. S., W ünsch, R., Gatto, A., Baczynski, C., (Apr. 2017a). "The SILCC project - IV. Impact of dissociating and ionizing radiation on the interstellar medium and Hα emission as a tracer of the star formation rate." In: *MNRAS* 466, pp. 3293–3308. ISSN: 0035-8711.
DOI: 10.1093/mnras/stw3216. arXiv: 1610.06569.

Peters, T., Zhukovska, S., Naab, T., Girichidis, P., Walch, S., Glover, S. C. O., Klessen, R. S., Clark, P. C., Seifried, D., (June 2017b). "The turbulent life of dust grains in the supernova-driven, multiphase interstellar medium." In: *Monthly Notices of the Royal Astronomical Society* 467, pp. 4322–4342. ISSN: 0035-8711.
DOI: 10.1093/mnras/stx341. eprint: 1610.06579.

Planck Collaboration, Ade, P. A. R., Aghanim, N., Alves, M. I. R., Arnaud, M., Arzoumanian, D., Ashdown, M., Aumont, J., Baccigalupi, C., Banday, A. J., Barreiro, R. B., Bartolo, N., Battaner, E., Benabed, K., Benoît, A., Benoit-Lévy, A., Bernard, J.-P., Bersanelli, M., Bielewicz, P., Bock, J. J., Bonavera, L., Bond, J. R., Borrill, J., Bouchet, F. R., Boulanger, F., Bracco, A., Burigana, C., Calabrese, E., Cardoso, J.-F., Catalano, A., Chiang, H. C., Christensen, P. R., Colombo, L. P. L., Combet, C., Couchot, F., Crill, B. P., Curto, A., Cuttaia, F., Danese, L., Davies, R. D., Davis, R. J., Bernardis, P., Rosa, A., Zotti, G., Delabrouille, J., Dickinson, C., Diego, J. M., Dole, H., Donzelli, S., Doré, O., Douspis, M., Ducout, A., Dupac, X., Efstathiou, G., Elsner, F., Enßlin, T. A., Eriksen, H. K., Falceta-Gonçalves, D., Falgarone, E., Ferrière, K., Finelli, F., Forni, O., Frailis, M., Fraisse, A. A., Franceschi, E., Frejsel, A., Galeotta, S., Galli, S., Ganga, K., Ghosh, T., Giard, M., Gjerløw, E., González-Nuevo, J., Górski, K. M., Gregorio, A., Gruppuso, A., Gudmundsson, J. E., Guillet, V., Harrison, D. L., Helou, G., Hennebelle, P., Henrot-Versillé, S., Hernández-Monteagudo, C., Herranz, D., Hildebrandt, S. R., Hivon, E., Holmes, W. A., Hornstrup, A., Huffenberger, K. M., Hurier, G., Jaffe, A. H., Jaffe, T. R., Jones, W. C., Juvela, M., Keihänen, E., Keskitalo, R., Kisner, T. S., Knoche, J.,

Kunz, M., Kurki-Suonio, H., Lagache, G., Lamarre, J.-M., Lasenby, A., Lattanzi, M., Lawrence, C. R., Leonardi, R., Levrier, F., Liguori, M., Lilje, P. B., Linden-Vørnle, M., López-Caniego, M., Lubin, P. M., Macías-Pérez, J. F., Maino, D., Mandolesi, N., Mangilli, A., Maris, M., Martin, P. G., Martínez-González, E., Masi, S., Matarrese, S., Melchiorri, A., Mendes, L., Mennella, A., Migliaccio, M., Miville-Deschênes, M.-A., Moneti, A., Montier, L., Morgante, G., Mortlock, D., Munshi, D., Murphy, J. A., Naselsky, P., Nati, F., Netterfield, C. B., Noviello, F., Novikov, D., Novikov, I., Oppermann, N., Oxborrow, C. A., Pagano, L., Pajot, F., Paladini, R., Paoletti, D., Pasian, F., Perotto, L., Pettorino, V., Piacentini, F., Piat, M., Pierpaoli, E., Pietrobon, D., Plaszczynski, S., Pointecouteau, E., Polenta, G., Ponthieu, N., Pratt, G. W., Prunet, S., Puget, J.-L., Rachen, J. P., Reinecke, M., Remazeilles, M., Renault, C., Renzi, A., Ristorcelli, I., Rocha, G., Rossetti, M., Roudier, G., Rubiño-Martín, J. A., Rusholme, B., Sandri, M., Santos, D., Savelainen, M., Savini, G., Scott, D., Soler, J. D., Stolyarov, V., Sudiwala, R., Sutton, D., Suur-Uski, A.-S., Sygnet, J.-F., Tauber, J. A., Terenzi, L., Toffolatti, L., Tomasi, M., Tristram, M., Tucci, M., Umana, G., Valenziano, L., Valiviita, J., Van Tent, B., Vielva, P., Villa, F., Wade, L. A., Wandelt, B. D., Wehus, I. K., Ysard, N., Yvon, D., Zonca, A., (Feb. 2016a). "Planck intermediate results. XXXV. Probing the role of the magnetic field in the formation of structure in molecular clouds." In: *Astronomy and Astrophysics* 586. ISSN: 0004-6361. DOI: 10.1051/0004-6361/201525896. eprint: 1502.04123.

Planck Collaboration, Ade, P. A. R., Aghanim, N., Arnaud, M., Arroja, F., Ashdown, M., Aumont, J., Baccigalupi, C., Ballardini, M., Banday, A. J., Barreiro, R. B., Bartolo, N., Battaner, E., Benabed, K., Benoît, A., Benoit-Lévy, A., Bernard, J.-P., Bersanelli, M., Bielewicz, P., Bock, J. J., Bonaldi, A., Bonavera, L., Bond, J. R., Borrill, J., Bouchet, F. R., Bucher, M., Burigana, C., Butler, R. C., Calabrese, E., Cardoso, J.-F., Catalano, A., Chamballu, A., Chiang, H. C., Chluba, J., Christensen, P. R., Church, S., Clements, D. L., Colombi, S., Colombo, L. P. L., Combet, C., Couchot, F., Coulais, A., Crill, B. P., Curto, A., Cuttaia, F., Danese, L., Davies, R. D., Davis, R. J., Bernardis, P., Rosa, A., Zotti, G., Delabrouille, J., Désert, F.-X., Diego, J. M., Dolag, K., Dole, H., Donzelli, S., Doré, O., Douspis, M., Ducout, A., Dupac, X., Efstathiou, G., Elsner, F., Enßlin, T. A., Eriksen, H. K., Fergusson, J., Finelli, F., Florido, E., Forni, O., Frailis, M., Fraisse, A. A., Franceschi, E., Frejsel, A., Galeotta, S., Galli, S., Ganga, K., Giard, M., Giraud-Héraud, Y., Gjerløw, E., González-Nuevo, J., Górski, K. M., Gratton, S., Gregorio, A., Gruppuso, A., Gudmundsson, J. E., Hansen, F. K., Hanson, D., Harrison, D. L., Helou, G., Henrot-Versillé, S., Hernández-Monteagudo, C., Herranz, D., Hildebrandt, S. R., Hivon, E., Hobson, M., Holmes, W. A., Hornstrup, A., Hovest, W., Huffenberger, K. M., Hurier, G., Jaffe, A. H., Jaffe, T. R., Jones, W. C., Juvela, M., Keihänen, E., Keskitalo, R., Kim, J., Kisner, T. S., Knoche, J., Kunz, M., Kurki-Suonio, H., Lagache, G., Lähteenmäki, A., Lamarre, J.-M., Lasenby, A., Lattanzi, M., Lawrence, C. R., Leahy, J. P., Leonardi, R., Lesgourgues, J., Levrier, F., Liguori, M., Lilje, P. B., Linden-Vørnle, M., López-Caniego, M., Lubin, P. M., Macías-Pérez, J. F., Maggio, G., Maino, D., Mandolesi, N., Mangilli, A., Maris, M., Martin, P. G., Martínez-González, E., Masi, S., Matarrese, S., McGehee, P., Meinhold, P. R., Melchiorri, A., Mendes, L., Mennella, A., Migliaccio, M., Mitra, S., Miville-Deschênes, M.-A., Molinari, D., Moneti, A., Montier, L., Morgante, G., Mortlock, D., Moss, A., Munshi, D., Murphy, J. A., Naselsky, P., Nati, F., Natoli,

P., Netterfield, C. B., Nørgaard-Nielsen, H. U., Noviello, F., Novikov, D., Novikov, I., Oppermann, N., Oxborrow, C. A., Paci, F., Pagano, L., Pajot, F., Paoletti, D., Pasian, F., Patanchon, G., Perdereau, O., Perotto, L., Perrotta, F., Pettorino, V., Piacentini, F., Piat, M., Pierpaoli, E., Pietrobon, D., Plaszczynski, S., Pointecouteau, E., Polenta, G., Popa, L., Pratt, G. W., Prézeau, G., Prunet, S., Puget, J.-L., Rachen, J. P., Rebolo, R., Reinecke, M., Remazeilles, M., Renault, C., Renzi, A., Ristorcelli, I., Rocha, G., Rosset, C., Rossetti, M., Roudier, G., Rubiño-Martín, J. A., Ruiz-Granados, B., Rusholme, B., Sandri, M., Santos, D., Savelainen, M., Savini, G., Scott, D., Seiffert, M. D., Shellard, E. P. S., Shiraishi, M., Spencer, L. D., Stolyarov, V., Stompor, R., Sudiwala, R., Sunyaev, R., Sutton, D., Suur-Uski, A.-S., Sygnet, J.-F., Tauber, J. A., Terenzi, L., Toffolatti, L., Tomasi, M., Tristram, M., Tucci, M., Tuovinen, J., Umana, G., Valenziano, L., Valiviita, J., Van Tent, B., Vielva, P., Villa, F., Wade, L. A., Wandelt, B. D., Wehus, I. K., Yvon, D., Zacchei, A., Zonca, A., (Sept. 2016b). "Planck 2015 results. XIX. Constraints on primordial magnetic fields." In: *Astronomy and Astrophysics* 594. ISSN: 0004-6361. DOI: 10.1051/0004-6361/201525821. eprint: 1502.01594.

Powell, K. G. (Apr. 1994). "An approximate Riemann solver for magnetohydrodynamics (that works in more than one dimension)." In: *Technical Reports of the Institute for Computer Applications in Science and Engineering (ICASE)*. URL: https://ntrs.nasa.gov/search.jsp?R=19940028527.

Powell, K. G., Roe, P. L., Linde, T. J., Gombosi, T. I., De Zeeuw, D. L., (1999). "A solution-adaptive upwind scheme for ideal magnetohydrodynamics." In: *Journal of Computational Physics* 154.2, pp. 284–309. DOI: 10.1006/jcph.1999.6299.

Price, D. J. (2008). "Magnetic fields in Astrophysics." PhD thesis. University of Cambridge.

R

Rajantie, A. (Sept. 2016). "The search for magnetic monopoles." In: *Physics Today* 69.10, p. 40. ISSN: 0031-9228. DOI: 10.1063/PT.3.3328.

Rembiasz, T., Obergaulinger, M., Cerdá-Durán, P., Aloy, M.-Á., Müller, E., (June 2017). "On the Measurements of Numerical Viscosity and Resistivity in Eulerian MHD Codes." In: *The Astrophysical Journal Supplement Series* 230, 18, p. 18. DOI: 10.3847/1538-4365/aa6254. arXiv: 1611.05858 [astro-ph.IM].

Reynolds, D. R., Samtaney, R., Woodward, C. S., (Nov. 2006). "A fully implicit numerical method for single-fluid resistive magnetohydrodynamics." In: *Journal of Computational Physics* 219.1, pp. 144–162. ISSN: 0021-9991. DOI: 10.1016/j.jcp.2006.03.022.

Rieder, M., Teyssier, R., (Nov. 2017). "A small-scale dynamo in feedback-dominated galaxies – II. The saturation phase and the final magnetic configuration." In: *Monthly Notices of the Royal Astronomical Society* 471.3, pp. 2674–2686. ISSN: 0035-8711.
DOI: 10.1093/mnras/stx1670.

Roe, P. L., Balsara, D. S., (1996). "Notes on the eigensystem of magnetohydrodynamics." In: *SIAM Journal on Applied Mathematics* 56.1, pp. 57–67.
DOI: 10.1137/S003613999427084X.

Roe, P. L., Balsara, D. S., (July 2006). "Notes on the Eigensystem of Magnetohydrodynamics." In: *SIAM J Appl Math*.
DOI: 10.1137/S003613999427084X.

Roe, P. L. (2006). "Affordable, entropy consistent flux functions." In: *Eleventh International Conference on Hyperbolic Problems: Theory, Numerics and Applications*. Lyon.

Rusanov, V. V. (1961). "The calculation of the interaction of non-stationary shock waves with barriers." In: *Ž. Vyčisl. Mat. i Mat. Fiz.* 1, pp. 267–279. ISSN: 0044-4669.
DOI: 10.1016/0041-5553(62)90062-9.

Rusanov, V. V. (Jan. 1962). "The calculation of the interaction of non-stationary shock waves and obstacles." In: *USSR Computational Mathematics and Mathematical Physics* 1.2, pp. 304–320. ISSN: 0041-5553.
DOI: 10.1016/0041-5553(62)90062-9.

Ryu, D., Jones, T. W., Frank, A., (Oct. 1995). "Numerical Magnetohydrodynamics in Astrophysics: Algorithm and Tests for Multidimensional Flow." In: *Astrophysical Journal* 452, p. 785.
DOI: 10.1086/176347. eprint: astro-ph/9505073.

S

Samtaney, R., Colella, P., Ligocki, T. J., Martin, D. F., Jardin, S. C., (Aug. 2005). "An adaptive mesh semi-implicit conservative unsplit method for resistive MHD." In: *J Phys Conf Ser* 16.1, p. 40. ISSN: 1742-6596.
DOI: 10.1088/1742-6596/16/1/005.

Schiermeier, Q. (Mar. 2005). "Solar wind hammers the ozone layer." In: *Nature News*. ISSN: 1744-7933.
DOI: 10.1038/news050228-12.

Schmidtmann, B., Torrilhon, M., (July 2016). "A Hybrid Riemann Solver for Large Hyperbolic Systems of Conservation Laws." In: *ArXiv e-prints*.
DOI: 10.7712/100016.2395.11923. arXiv: 1607.05721 [math.NA].

Schmidtmann, B., Winters, A. R., (July 2016). "Hybrid Entropy Stable HLL-Type Riemann Solvers for Hyperbolic Conservation Laws." In: *ArXiv e-prints*.
DOI: 10.1016/j.jcp.2016.10.034. arXiv: 1607.06240 [math.NA].

Schmidtmann, B., Seibold, B., Torrilhon, M., (2015). "Relations between WENO3 and Third-Order Limiting in Finite Volume Methods." In: *Journal of Scientific Computing,*
DOI: 10.1007/s10915-015-0151-z.

Seifried, D., Banerjee, R., Klessen, R. S., Duffin, D., Pudritz, R. E., (Oct. 2011a). "Magnetic fields during the early stages of massive star formation - I. Accretion and disc evolution." In: *Monthly Notices of the Royal Astronomical Society* 417, pp. 1054–1073. ISSN: 0035-8711.
DOI: 10.1111/j.1365-2966.2011.19320.x. eprint: 1106.4485.

Seifried, D., Schmidt, W., Niemeyer, J. C., (Feb. 2011b). "Forced turbulence in thermally bistable gas: a parameter study." In: *Astronomy and Astrophysics* 526, A14. ISSN: 0004-6361.
DOI: 10.1051/0004-6361/201014373.

Seifried, D., Walch, S., Girichidis, P., Naab, T., W ünsch, R., Klessen, R. S., Glover, S. C. O., Peters, T., Clark, P., (Dec. 2017). "SILCC-Zoom: the dynamic and chemical evolution of molecular clouds." In: *MNRAS* 472, pp. 4797–4818. ISSN: 0035-8711.
DOI: 10.1093/mnras/stx2343. arXiv: 1704.06487.

Seifried, D., Walch, S., Reissl, S., Ibáñez-Mejía, J. C., (Apr. 2018a). "SILCC-Zoom: Polarisation and depolarisation in molecular clouds." In: *submitted to Monthly Notices of the Royal Astronomical Society*. eprint: 1804.10157.

Seifried, D., Walch, S., Haid, S., Girichidis, P., Naab, T., (Mar. 2018b). "Is Molecular Cloud Turbulence Driven by External Supernova Explosions?" In: *Astrophysical Journal* 855.2, p. 81. ISSN: 0004-637X.
DOI: 10.3847/1538-4357/aaacff.

Shay, M. A., Drake, J. F., Rogers, B. N., Denton, R. E., (July 1999). "The scaling of collisionless, magnetic reconnection for large systems." In: *Geophys Res Lett* 26.14, pp. 2163–2166. ISSN: 0094-8276.
DOI: 10.1029/1999GL900481.

Shay, M. A., Drake, J. F., Rogers, B. N., Denton, R. E., (Mar. 2001). "Alfvénic collisionless magnetic reconnection and the Hall term." In: *J Geophys Res Space Phys* 106.A3. [Online; accessed 16. May 2018], pp. 3759–3772. ISSN: 0148-0227.
DOI: 10.1029/1999JA001007.

Shu, F. H., Adams, F. C., Lizano, S., (1987). "Star formation in molecular clouds - Observation and theory." In: *Annual Review of Astronomy and Astrophysics* 25, pp. 23–81. ISSN: 0066-4146.
DOI: 10.1146/annurev.aa.25.090187.000323.

Sjögreen, B., Yee, H. C., Kotov, D., (May 2017). "Skew-Symmetric Splitting and Stability of High Order Central Schemes." In: *Journal of Physics Conference Series*. Vol. 837, p. 012019.
DOI: 10.1088/1742-6596/837/1/012019.

Smith, D., Ghosh, S., Dmitruk, P., Matthaeus, W. H., (Jan. 2004). "Hall and Turbulence Effects on Magnetic Reconnection." In: *Geophysical Research Letters* 31.2. ISSN: 0094-8276.
DOI: 10.1029/2003GL018689.

Sod, G. A. (1978). "A survey of several finite difference methods for systems of nonlinear hyperbolic conservation laws." In: *Journal of Computational Physics* 27.1, pp. 1–31.

Strang, G. (Sept. 1968). "On the Construction and Comparison of Difference Schemes." In: *SIAM Journal on Numerical Analysis* 5, pp. 506–517.
DOI: 10.1137/0705041.

Sur, S., Federrath, C., Schleicher, D. R. G., Banerjee, R., Klessen, R. S., (July 2012). "Magnetic field amplification during gravitational collapse - influence of turbulence, rotation and gravitational compression." In: *Monthly Notices of the Royal Astronomical Society* 423, pp. 3148–3162. ISSN: 0035-8711.
DOI: 10.1111/j.1365-2966.2012.21100.x. eprint: 1202.3206.

Susanto, A., Ivan, L., Sterck, H. D., Groth, C., (2013). "High-order central ENO finite-volume scheme for ideal MHD." In: *Journal of Computational Physics* 250, pp. 141–164. ISSN: 0021-9991.
DOI: 10.1016/j.jcp.2013.04.040.

Svärd, M. (May 2015). "Weak solutions and convergent numerical schemes of modified compressible Navier–Stokes equations." In: *Journal of Computational Physics* 288, pp. 19–51. ISSN: 0021-9991.
DOI: 10.1016/j.jcp.2015.02.013.

Svärd, M. (Dec. 2016). "Entropy solutions of the compressible Euler equations." In: *BIT Numerical Mathematics* 56.4, pp. 1479–1496. ISSN: 1572-9125.
DOI: 10.1007/s10543-016-0611-3.

T

Tadmor, E. (1984). "Numerical viscosity and the entropy condition for conservative difference schemes." In: *Mathematics of Computation* 43.168, pp. 369–381.
DOI: 10.2307/2008282.

Tadmor, E. (1987). "The numerical viscosity of entropy stable schemes for systems of conservation laws." In: *Mathematics of Computation* 49.179, pp. 91–103.
DOI: 10.2307/2008251.

Tadmor, E. (May 2003). "Entropy stability theory for difference approximations of nonlinear conservation laws and related time-dependent problems." In: *Acta Numerica* 12, pp. 451–512.

Tadmor, E. (2016). "Perfect derivatives, conservative differences and entropy stable computation of hyperbolic conservation laws." In: *Discrete and Continuous Dynamical Systems-A* 36.8, pp. 4579–4598.
DOI: 10.3934/dcds.2016.36.4579.

Thornber, B., Drikakis, D., Williams, R. J. R., Youngs, D., (May 2008). "On entropy generation and dissipation of kinetic energy in high-resolution shock-capturing schemes." In: *Journal of Computational Physics* 227.10, pp. 4853–4872. ISSN: 0021-9991.
DOI: 10.1016/j.jcp.2008.01.035.

Toro, E. F. (2009). *Riemann Solvers and Numerical Methods for Fluid Dynamics: A Practical Introduction*. Springer. ISBN: 9783662034903.

Torrilhon, M. (2012). "Krylov–Riemann Solver for Large Hyperbolic Systems of Conservation Laws." In: *SIAM Journal on Scientific Computing* 34.4, A2072–A2091.
DOI: 10.1137/110840832.

Tóth, G. (2000). "The $\nabla \cdot B = 0$ Constraint in Shock-Capturing Magnetohydrodynamics Codes." In: *Journal of Computational Physics* 161.2, pp. 605–652. ISSN: 0021-9991.
DOI: 10.1006/jcph.2000.6519.

Tricco, T. S., Price, D. J., (2012). "Constrained hyperbolic divergence cleaning for smoothed particle magnetohydrodynamics." In: *Journal of Computational Physics* 231.21, pp. 7214–7236. ISSN: 0021-9991.
DOI: j.jcp.2012.06.039.

Tricco, T. S., Price, D. J., Bate, M. R., (2016). "Constrained hyperbolic divergence cleaning in smoothed particle magnetohydrodynamics with variable cleaning speeds." In: *Journal of*

Computational Physics 322, pp. 326–344. ISSN: 0021-9991.
DOI: 10.1016/j.jcp.2016.06.053.

v

van Leer, B. (1984). "On the Relation Between the Upwind-Differencing Schemes of Godunov, Engquist–Osher and Roe." In: *SIAM Journal on Scientific and Statistical Computing* 5.1, pp. 1–20.
DOI: 10.1137/0905001.

V

Valdivia, V., Hennebelle, P., Gérin, M., Lesaffre, P., (Mar. 2016). "H2 distribution during the formation of multiphase molecular clouds." In: *Astronomy and Astrophysics* 587. ISSN: 0004-6361.
DOI: 10.1051/0004-6361/201527325. eprint: 1512.05523.

Vázquez-Semadeni, E., Banerjee, R., Gómez, G. C., Hennebelle, P., Duffin, D., Klessen, R. S., (July 2011). "Molecular cloud evolution - IV. Magnetic fields, ambipolar diffusion and the star formation efficiency." In: *Monthly Notices of the Royal Astronomical Society* 414, pp. 2511–2527. ISSN: 0035-8711.
DOI: 10.1111/j.1365-2966.2011.18569.x. eprint: 1101.3384.

Vázquez-Semadeni, E., G ómez, G. C., Jappsen, A. K., Ballesteros-Paredes, J., Gonz ález, R. F., Klessen, R. S., (Mar. 2007). "Molecular Cloud Evolution. II. From Cloud Formation to the Early Stages of Star Formation in Decaying Conditions." In: *The Astrophysical Journal* 657, pp. 870–883. ISSN: 0004-637X.
DOI: 10.1086/510771. eprint: astro-ph/0608375.

W

Waagan, K., Federrath, C., Klingenberg, C., (May 2011). "A robust numerical scheme for highly compressible magnetohydrodynamics: Nonlinear stability, implementation and tests." In: *Journal of Computational Physics* 230.9, pp. 3331–3351. ISSN: 0021-9991.
DOI: 10.1016/j.jcp.2011.01.026.

Waagan, K. (2009). "A positive MUSCL-Hancock scheme for ideal magnetohydrodynamics." In: *Journal of Computational Physics* 228.23, pp. 8609–8626.
DOI: 10.1016/j.jcp.2009.08.020.

Walch, S., Girichidis, P., Naab, T., Gatto, A., Glover, S. C. O., Wünsch, R., Klessen, R. S., Clark, P. C., Peters, T., **Derigs, D.**, Baczynski, C., (Nov. 2015). "The SILCC (SImulating the LifeCycle of molecular Clouds) project – I. Chemical evolution of the supernova-driven ISM." In: *Monthly Notices of the Royal Astronomical Society* 454.1, pp. 238–268. DOI: 10.1093/mnras/stv1975. arXiv: 1412.2749.

Weis, M., Walch, S., Seifried, D., (2018). "The virial balance of CO-clumps and -cores in magnetized colliding flows." In: *submitted to Monthly Notices of the Royal Astronomical Society*.

Wesenberg, M. (2003). "Efficient finite-volume schemes for magnetohydrodynamic simulations in solar physics." dissertation. Universität Freiburg. URL: https://www.freidok.uni-freiburg.de/data/792.

Winters, A. R., **Derigs, D.**, Gassner, G. J., Walch, S., (Mar. 2017). "A uniquely defined entropy stable matrix dissipation operator for high Mach number ideal MHD and compressible Euler simulations." In: *Journal of Computational Physics* 332, pp. 274–289. ISSN: 0021-9991.
DOI: 10.1016/j.jcp.2016.12.006.

Winters, A. R., Gassner, G. J., (Jan. 2016). "Affordable, Entropy Conserving and Entropy Stable Flux Functions for the Ideal MHD Equations." In: *Journal of Computational Physics* 304, pp. 72–108.
DOI: 10.1016/j.jcp.2015.09.055.

Wolfe, A. M., Jorgenson, R. A., Robishaw, T., Heiles, C., Prochaska, J. X., (Oct. 2008). "An 84-μG magnetic field in a galaxy at redshift z = 0.692." In: *Nature* 455.7213, p. 638.
DOI: 10.1038/nature07264.

Y

Yee, K. S. (May 1966). "Numerical solution of initial boundary value problems involving Maxwell's equations in isotropic media." In: *IEEE Trans. Antennas and Propagation* 14.3, pp. 302–307.
DOI: 10.1109/TAP.1966.1138693.

Z

Zachary, A. L., Malagoli, A., Colella, P., (1994). "A higher-order Godunov method for multidimensional ideal magnetohydrodynamics." In: *SIAM Journal on Scientific Computing*

15.2, pp. 263–284.
DOI: 10.1137/0915019.

Zamora-Avilés, M., Vázquez-Semadeni, E., Körtgen, B., Banerjee, R., Hartmann, L., (Mar. 2018). "Magnetic suppression of turbulence and the star formation activity of molecular clouds." In: *Monthly Notices of the Royal Astronomical Society* 474.4, pp. 4824–4836.
ISSN: 0035-8711.
DOI: 10.1093/mnras/stx3080.

Zhumabekov, A. (Feb. 2017). "Simulation of motions of the plasma in a fusion reactor for obtaining of future energy." In: *Journal of Physics Conference Series* 781.1, p. 012041.
ISSN: 1742-6596.
DOI: 10.1088/1742-6596/781/1/012041.

List of Figures

Eigenerklärung

Ich versichere, dass ich die von mir vorgelegte Dissertation selbständig angefertigt, die benutzten Quellen und Hilfsmittel vollständig angegeben und die Stellen der Arbeit – einschließlich Tabellen und Abbildungen –, die anderen Werken im Wortlaut oder dem Sinn nach entnommen sind, in jedem Einzelfall als Entlehnung kenntlich gemacht habe; dass diese Dissertation noch keiner anderen Fakultät oder Universität zur Prüfung vorgelegen hat; dass sie – abgesehen von den unten angegebenen Teilpublikationen – noch nicht veröffentlicht worden ist sowie, dass ich eine solche Veröffentlichung vor Abschluss des Promotionsverfahrens nicht vornehmen werde. Die Bestimmungen der Promotionsordnung sind mir bekannt. Die von mir vorgelegte Dissertation ist von Prof. Dr. Stefanie Walch-Gassner betreut worden.

Köln, 14.09.2018

Enthaltene Publikationen

Derigs, D., Winters, A. R., Gassner, G. J., Walch, S., (Apr. 2016). "A novel high-order, entropy stable, 3D AMR MHD solver with guaranteed positive pressure." In: *Journal of Computational Physics* 317, pp. 223–256. ISSN: 0021-9991.
DOI: 10.1016/j.jcp.2016.04.048. arXiv: 1605.03572.

Derigs, D., Winters, A. R., Gassner, G. J., Walch, S., (Feb. 2017). "A novel averaging technique for discrete entropy-stable dissipation operators for ideal MHD." In: *Journal of Computational Physics* 330, pp. 624–632. ISSN: 0021-9991.
DOI: 10.1016/j.jcp.2016.10.055. arXiv: 1610.06584.

Derigs, D., Winters, A. R., Gassner, G. J., Walch, S., Bohm, M., (July 2018b). "Ideal GLM-MHD: About the entropy consistent nine-wave magnetic field divergence diminishing ideal magnetohydrodynamics equations." In: *Journal of Computational Physics* 364, pp. 420–467. ISSN: 0021-9991.
DOI: 10.1016/j.jcp.2018.03.002. arXiv: 1711.06269.

Das Fachmagazin *Journal of Computational Physics* hat mir schriftlich das Recht eingeräumt, die genannten Fachartikel unverändert in dieser Dissertation abzudrucken sowie die vorliegende Arbeit über die Plattformen der Universität zu Köln für nicht-kommerzielle Nutzung unter „Open-Access" Bedingungen zur Verfügung zu stellen.